Studies of Creep Damage in the Heat-Affected Zone of 9Cr-1Mo-VNb Steel Weldments

A Dissertation Presented for the
Doctor of Philosophy
Degree
The University of Tennessee, Knoxville

John William Bohling
August 2021

Copyright © John William Bohling
All Rights Reserved.

Dedication

To my advisor, Dr. Carl "Doc" Lundin

(December 16, 1934 - March 30, 2021)

and

To my parents,

Mark and Sandra Bohling

Acknowledgements

I am deeply grateful for the patient investment of my late advisor Dr. Carl Lundin, professor of welding metallurgy and head of the Materials Joining Group (MJG) at the University of Tennessee, in taking me on as his student, teaching me, and sharing his knowledge and expertise in metallurgy and welding. He delayed his retirement and did not take eligible retirement bonuses in order to make it possible for me to finish my degree. He unexpectedly passed away in March 2021 before my defense. As his last PhD student, I dedicate this dissertation in memory of him.

I am very thankful to my dissertation committee for their patience with me and for their assistance during regular meetings and technical discussions. I would like to specifically thank Dr. Choo for agreeing to serve as my new committee chair and for his guidance about my job search; Dr. Babu for suggesting the particle analysis work and emphasis on the N:Al ratio results; and Dr. Lass for discussions on phase fractions and for volunteering to undertake the necessary calculations.

I gratefully acknowledge former MJG students Will Hoskins and Cameron Hale for their thorough metallography work in previous projects which formed the basis for much of the data contained in this dissertation. I would also like to thank my committee member Dr. Burgess and my friend Dr. Maneel Bharadwaj, both of whom were former MJG students with me, for their encouragement during my degree and for their helpful feedback and guidance. I would also like to thank many past and present staff in the UTK Department of Materials Science for their help and friendship, and Dr. Claudia Rawn at the Center for Materials Processing for providing funding support. I would also like to thank the Equity Engineering Group for providing the initial project funding and materials, and for granting permission to use this work in my dissertation.

My deepest thanks are given to my Lord and Savior Jesus Christ, whom I came to know midway through my time at UTK in June 2016. He strengthened and sustained me

during this work and brought me to the point of completing this degree. Apart from him, this dissertation would not exist at all.

Abstract

Creep strength enhanced ferritic (CSEF) steels are used in power plants for high temperature, pressure-containing welded components such as steam headers. One CSEF steel, 9Cr-1Mo-VNb or Grade 91, often exhibits localized creep deformation and cavitation in the weld heat-affected zone (HAZ), identified as Type IV creep damage. Three Grade 91 weldments were evaluated by creep testing and microstructural characterization using optical and scanning electron microscopy, combined with image analysis, to investigate microstructure evolution and creep damage. Two weldments fabricated from dissimilar base metals were used for direct comparison of creep damage in two materials simultaneously during cross-weld testing. Longitudinal creep specimens from a third weldment, with the specimen axis oriented parallel to the welding direction, were evaluated in a preliminary investigation of the effect of iso-strain loading on creep damage for two heat treatment conditions.

Dissimilar cross-weld testing showed a difference in damage susceptibility in the HAZs of three base metals with different sulfur contents and nitrogen:aluminum (N:Al) ratios. Type IV rupture in material with low N:Al ratio exhibited a significantly higher extent of creep cavitation than material with high N:Al ratio; in the low N:Al ratio material, a potential correlation was observed between greater extent of creep damage and a reduced density of fine precipitates in the base metal and intercritical HAZ, a larger subgrain size after creep exposure, and higher sulfur and aluminum contents. However, greater extent of Type IV creep damage was not unequivocally associated with lower N:Al ratio since another weldment showed greater creep damage in the material with high N:Al ratio. Base metal inclusion contents did not show a clear correlation with extent of creep damage. Longitudinal creep testing showed differences in creep damage between subcritical PWHT and N&T heat treatments; the N&T condition showed a longer rupture life despite increased creep damage and reduced creep ductility. Based

on these results, Type IV creep damage in the dissimilar cross-weld tests was proposed to depend both on base metal composition and on microstructural differences. Longitudinal creep testing is a promising technique to evaluate the effect of iso-strain loading on damage development in Grade 91 welds.

Table of Contents

Chapter 1 Introduction 1
1.1 Welded Piping in Power Generation 1
1.2 Historical and Current Problems with Creep Damage in Welded Steel Piping 1
1.3 Research Objectives 9

Chapter 2 Literature Review 11
2.1 Metallurgy of Creep Strength Enhanced Ferritic (CSEF) Steels 11
2.1.1 Morphology and Substructure of Martensite in Steels 11
2.1.2 Microstructure of CSEF Steels 15
2.1.3 Strengthening Mechanisms in CSEF Steels 22
2.1.4 Precipitation Behavior in CSEF Steels 31
2.1.5 Microstructural Changes in CSEF Steels during Tempering 38
2.1.6 Microstructural Changes in the Heat-Affected Zone of CSEF Steels 43
2.1.7 Creep Damage Development 62
2.1.8 Microstructural Evolution in CSEF Steels during Creep 78
2.1.9 Location of Type IV Creep Damage within the HAZ 99
2.1.10 Effect of Multiaxial Stress States and Constraint on Creep Behavior 101
2.2 Summary Statements from Literature Review 122

Chapter 3 Materials and Experimental Procedures 125
3.1 Materials 125
3.2 Grade 91 Weldments for Cross-Weld Creep Testing 125
3.3 Grade 91 Weldment for Longitudinal Creep Testing 128
3.4 Characterization 131
3.4.1 Metallographic Preparation and Microscopy 131
3.4.2 Cryo-Cracking 132
3.4.3 Image Processing and Analysis 134

Chapter 4 Creep Behavior and Creep Damage Characterization of Dissimilar Grade 91 Weldments 146
4.1 Characterization of Inclusion Content in Grade 91 Base Metals 146
4.2 Creep Behavior and Creep Damage Characterization of the FT-H47 Dissimilar Weldment 156
4.2.1 Characteristics of the FT-H47 Weldment Prior to Creep Exposure 156
4.2.2 Creep Results and Failure Location in the FT-H47 Weldment 175
4.2.3 Characterization of Creep Damage in the FT-H47 Weldment 175
4.2.4 Cryo-Cracking Characterization of Creep Damage in the FT-H47 Weldment 198
4.2.5 Evaluation of Microstructural Characteristics in the FT-H47 Weldment by Image Analysis 207

4.3 Creep Behavior and Creep Damage Characterization of the H13-H47 Dissimilar Weldment 221
4.3.1 Characteristics of the H13-H47 Weldment 224
4.3.2 Creep Test Results and Creep Damage in the H13-H47 Weldment 224
4.4 Discussion of Type IV Creep Damage in Dissimilar Grade 91 Weldments 233
4.4.1 Base Metal and Chemical Composition Characteristics 234
4.4.2 Microstructure Characteristics After PWHT and Creep Testing 251
4.4.3 Relevance of Evaluated Grade 91 Compositions to General Grade 91 Behavior 263
4.4.4 Relevance of Dissimilar Cross-Weld Creep Data Based on Short-Term Tests265
4.4.5 Primary Considerations in Creep Behavior of the FT-H47 and H13-H47 Dissimilar Grade 91 Weldments 269
Chapter 5 Creep Behavior and Creep Damage Characterization of Longitudinal Creep Specimens 272
5.1 Characteristics of the AEP Grade 91 Weldment 273
5.2 Creep Behavior of Longitudinal Specimens from the AEP Grade 91 Weldment. 277
5.3 Creep Damage Characterization of the 64 h Subcritically Postweld Heat-Treated Longitudinal Creep Specimen 288
5.4 Creep Damage Characterization of the Normalized and Tempered Longitudinal Creep Specimen 296
5.5 Discussion of Creep Behavior and Creep Damage in Longitudinal Specimens from the AEP Weldment 300
5.5.1 Comparison of the Longitudinal Creep Behavior of the Subcritical PWHT and N&T Heat Treatment Conditions 304
5.5.2 Comparison of 8 h and 64 h Subcritical PWHT Conditions 305
Chapter 6 Conclusions 308
6.1 Conclusions Related to Cross-Weld Creep Testing of Grade 91 Weldments with Dissimilar Base Metals 308
6.2 Conclusions Related to Creep Testing of Longitudinal Specimens from a Grade 91 Weldment 312
6.3 Research Contribution 314
Chapter 7 Future Work 315
List of References 317
Vita 328

List of Tables

Table 3-1. Measured chemical compositions of Grade 91 base metals utilized for microstructural characterization and creep testing. Standard specification limits and optimum recommended composition limits are also provided for comparison. 126

Table 3-2. Summary of heat treatment parameters for two dissimilar Grade 91 weldments (Hoskins et al., 2017) utilized for creep testing and subsequent characterization. 127

Table 4-1. Summary of inclusion data for the FT Grade 91 base metal obtained from image analysis of BSE-SEM image panoramas. Total analysis area for the FT base metal was ~25 mm^2. 147

Table 4-2. Summary of inclusion data for the H47 Grade 91 base metal obtained from image analysis of BSE-SEM image panoramas. Total analysis area for the H47 base metal was ~25 mm^2. 151

Table 4-3. Summary of statistics relating to inclusion content in two evaluated Grade 91 base metals. The values reported below (average ± 95%CI) are calculated from the five individual scans for each base metal provided in Table 4-1 and Table 4-2. 155

Table 4-5. Summary of data from measurements of ferritic subgrain size from SE-SEM micrographs obtained from three separate regions on the FT and H47 sides of the FT-H47 weldment in the PWHT condition (746°C/1 h) prior to creep testing. 222

Table 4-6. Summary of data from measurements of subgrain size from SE-SEM micrographs obtained from three separate regions on the FT and H47 sides of the FT-H47-1 cross-weld creep specimen after creep rupture testing at 627°C for 2080.4 h. When it was possible to evaluate more than one field, the average and sample standard deviation of each measured parameter were calculated and are provided in the table as (average ± SD); when only one micrograph was available, the singular values are provided in the table. 223

Table 4-7. Comparison of calculated volume fractions of $M_{23}C_6$, Z-phase, and AlN precipitates for the FT and H47 base metals at the PWHT temperature of 746°C. (Laves phase calculation was disabled for the results presented in this table.) 260

Table 5-1. Summary of heat treatment parameters and measured base metal hardness values after heat treatment for the evaluated conditions of the AEP Grade 91 SAW weldment. Hardness values obtained from Hobbs et al. (Hobbs et al., 2015). 274

List of Figures

Figure 1-1. Panorama of optical micrographs showing the typical appearance of weld deposit creep damage in 1.25Cr-0.5Mo longitudinally-seam welded hot reheat piping. The creep damage occurs in the weld deposit, immediately adjacent to the fusion line, due to a concentration of nonmetallic inclusions at this region of the weld deposit. Etchant: 2% Nital. Adapted from (Materials Joining Group, 2014). 2

Figure 1-2. Collection of creep data for Grade 91 steel showing the variation in creep properties as a function of test temperature and stress. Reproduced from Tabuchi and Takahashi (Tabuchi and Takahashi, 2012). 5

Figure 1-3. SEM micrograph illustrating the typical appearance of "Type IV" creep damage in the HAZ of a Grade 91 weldment. The creep cavitation is concentrated near the rupture location in the HAZ, at left in the micrograph, and decreases only a short distance away from rupture (at right). The dark region at left is epoxy mounting compound. 6

Figure 1-4. Scanning electron micrograph illustrating Type IV creep damage (cavitation, aligned cavitation, and micro-cracking) in the HAZ of a F91/P91 transition weld which failed after 20,000 h at 568°C. Reproduced from Brett et al. (Brett, 2007). 8

Figure 2-1. Schematic illustration of CSEF structure which is responsible for strengthening, (a) at the scale of individual grains, showing the different boundary types and (b) at the scale of individual laths within each PAG, showing M23C6 and MX precipitation along lath boundaries and small-scale MX precipitation within the matrix. Reproduced from Abe (Abe, 2008). 13

Figure 2-2. Relationship between 0.2% offset yield strength and martensite block width (plotted as the reciprocal width) for two martensitic iron alloys. The graph illustrates the inverse correlation between block width and yield strength. (Refer to Fig. 2-1 for the distinction between blocks and prior austenite grains within a martensitic microstructure.) Reproduced from Morito et al. (Morito et al., 2006). 14

Figure 2-3. Optical micrographs revealing the typical microstructure of a tempered CSEF steel (9Cr-1Mo-VNb, Grade 91) at 500X and 1000X. The martensitic structure is evident, with larger prior austenite grain boundaries (PAGBs, denoted by red arrows) containing finer substructure in the form of packets, blocks, and subgrains (formerly laths, prior to tempering). Etchant: Fry's Reagent. 16

Figure 2-4. Secondary electron SEM micrographs revealing the typical microstructure of a tempered CSEF steel (9Cr-1Mo-VNb, Grade 91). The martensitic structure is clearly evident, with larger prior austenite grains (PAGBs, red arrows) containing finer substructure, in the form of blocks and subgrains. In particular, the parallel arrangement of subgrains (preserved from the initial lath structure after normalizing and tempering) and the presence of fine carbides along the subgrain boundaries (yellow arrows) can both be observed. In (c), very fine precipitates (<<1 μm, most likely carbides) are discernible in the subgrain matrix and noted by red circles. Etchant: 10% Nital. 17

Figure 2-5. Transmission electron micrographs revealing the typical microstructure of an CSEF steel (X20CrMoV12-1) in the (a) quenched condition (b) quenched and tempered condition, 750°C/1 h. The presence of a high dislocation density within the laths in (a) and within the subgrains in (b) is clearly evident, and it can be seen that the

high aspect ratio of the initial laths (a) has been preserved in the subgrains which formed as a result of tempering (b). Also note in (b) that the subgrain width (in the narrow dimension) is <1 μm and that a subgrain boundary is visible (noted by the red arrows) at the interface between two subgrains. Adapted from Pešička et al. (Pešička et al., 2003). 20

Figure 2-6. Transmission electron micrographs comparing the substructure of two CSEF steels after extended tempering at 750°C for 100 h (a) X20CrMoV12-1 (b) 9Cr-1Mo-VNb (P91). Note that in both steels, an elongated, lath-like subgrain morphology is still apparent, but dislocation recovery has occurred which is evident by a reduction in dislocation density (e.g. compared to Fig. 2-5). Regions of reduced dislocation density, where the density is low enough that individual dislocations can be resolved, are indicated by black arrows in both micrographs. Particles along the boundaries (most likely carbides) are noted by red arrows. Adapted from Pešička et al. (Pešička et al., 2003). 21

Figure 2-7. Plot of minimum creep rate versus creep stress for five iron-base alloys, illustrating the effects and interactions of different strengthening mechanisms: alpha-Fe (base alloy, no additional strengthening); Fe-2.3W (solid solution); Fe-VNbC (precipitation); Fe-9Cr-VNbCN (precipitation strengthening and dislocation substructure from martensitic transformation); Fe-9Cr-2.3W-VNbCN (all of the preceding mechanisms). Reproduced from Maruyama et al. (Maruyama et al., 2001)... 24

Figure 2-8. Rupture time and minimum creep rate as a function of carbon content for 9Cr-3W-3Co-0.2V-0.05Nb-0.05N tempered martensite ferritic steel, at creep conditions of 650°C/140 MPa. Reproduced from Abe (Abe, 2008). 26

Figure 2-9. TEM bright-field micrograph (top) and associated EDS spectrum (bottom) revealing nanoscale MX precipitation (arrow) along a PAG boundary in a 9Cr-3W-3Co-0.2V-0.05Nb-0.05N-0.002C steel after tempering. Adapted from Taneike et al. (Taneike et al., 2004). 27

Figure 2-10. TEM bright-field micrographs from 9Cr-3W-3Co-0.2V-0.05Nb-0.05N-0.078C steel after tempering (a) extraction replica showing precipitates near a PAGB (b) thin foil showing lath-like subgrain structure. Reproduced from Abe (Abe, 2008). 28

Figure 2-11. TEM micrographs of thin foils comparing the subgrain structure observed for two martensitic iron alloys: (a) X20CrMoV12-1 tempered martensite ferritic steel, normalized but not tempered (b) Fe-10Cr binary alloy after equal channel angular pressing (ECAP), not tempered. Note the close resemblance of the two substructures in terms of subgrain width and dislocation density; although not clearly resolved, the primary difference is that carbides are present along the subgrain boundaries in (a), but not in (b). Reproduced from Kostka et al. (Kostka et al., 2007). 30

Figure 2-12. Results for determination of subgrain widths in the Fe-10Cr binary alloy. (a) schematic illustration of width dimension wi for an individual subgrain (b) cumulative frequency plots of subgrain width for Fe-10Cr in three conditions: after ECAP; after ECAP and tempering at 600°C/10 min; after ECAP, tempering, and creep at 600°C/100 MPa to 7% strain. Reproduced from Kostka et al. (Kostka et al., 2007)..... 30

Figure 2-13. Diagram of solid solubility of alloying elements in equilibrium with their corresponding precipitate(s), either carbides, nitrides, or Laves phase (Fe2(Mo,W)). Element/precipitate pairs with lower values of mole fraction are more resistant to dissolution. Reproduced from Abe (Abe, 2008). 33

Figure 2-14. Schematic illustration of precipitation on lath and block boundaries in tempered martensite ferritic steels, with either (a) MX carbonitrides forming significantly on the boundaries and within the subgrain matrix, or (b) M23C6 carbides forming on the boundaries and MX carbonitrides forming primarily within the matrix. Reproduced from Abe (Abe, 2008). 35

Figure 2-15. Evolution of number density of Z-phase and MX carbonitride particles in a Grade 91 steel during creep exposure at 600°C/70 MPa. Reproduced from Sawada et al. (Sawada et al., 2011). 36

Figure 2-16. TEM micrographs of thin foils illustrating the evolution of microstructure and dislocation density for X20 tempered martensite ferritic steel in three conditions, (a) as-quenched (b) tempered, 750°C/1 h (c) tempered, 750°C/100 h. Note the extremely high dislocation density in (a), such that individual dislocations cannot be resolved; the clear lath-like subgrain structure and the sub-grain boundary denoted by the red arrows in (b); lower dislocation density (denoted by black arrow) and more equiaxed shape of coarsened subgrains in (c). Adapted from Pešička et al. (Pešička et al., 2003). 41

Figure 2-17. TEM micrographs illustrating the microstructure evolution in a 9Cr-2W-VNb steel (a) as normalized, 1300°C/1 h, and (b) after tempering at 750°C/72.5 h. Reproduced from Sawada et al. (Sawada et al., 2003b). 42

Figure 2-18. Distribution of measured lath width in a 9Cr-2W-VNb steel in the as-normalized condition and after tempering at 750°C (1023 K) for 72.5 h. Reproduced from Sawada et al. (Sawada et al., 2003b). 44

Figure 2-19. Sequence of TEM micrographs illustrating the process of subgrain coarsening by boundary migration in a 9Cr-2W-VNb steel during in situ tempering at 730°C. Reproduced from Sawada et al. (Sawada et al., 2003b). 45

Figure 2-20. Comparison of calculated thermal cycles for Grade 92 steel with different peak temperatures. Reproduced from (Xu et al., 2017). 47

Figure 2-21. Panorama of optical micrographs illustrating the typical appearance of an HAZ in a Grade 91 CSEF weldment. The fusion line is emphasized by a narrow black line. Etchant: Fry's reagent. 47

Figure 2-22. Comparison of microstructures in the as-welded HAZ of a Grade 91 weldment (a) CGHAZ (b) FGHAZ (c) ICHAZ. 10% Nital etch, secondary electron SEM imaging. Adapted from Wang et al. (Wang et al., 2016). 50

Figure 2-23. Comparison of grain average misorientation maps for the as-welded (a) FGHAZ and (b) ICHAZ in a Grade 91 weldment. Note the coarser feature size of deformed and substructured grains in the ICHAZ. Adapted from Wang et al. (Wang et al., 2016). 51

Figure 2-24. Distribution of measured microhardness values for a Grade 91 weldment in the as-welded condition. Note that the hardness continuously decreases through the HAZ until reaching the base metal value; the as-welded condition does not exhibit a hardness dip within the HAZ, and the hardness values do not show the presence of a lower hardness overtempered zone outside the HAZ. Adapted from Wang et al. (Wang et al., 2016). 52

Figure 2-25. Schematic illustration of HAZ regions and their distinguishing features according to a classification scheme proposed specifically for CSEF steels. Note in particular that the completely transformed zone (CTZ) contains a mixture of coarse and

fine grains, showing that in this classification scheme, it is assumed that grain size has a minimal effect on overall behavior in CSEF steels. Reproduced from Xu et al. (Xu et al., 2017). 54

Figure 2-26. Ion-induced secondary electron SEM micrographs showing the variations in precipitate dissolution depending on peak temperature (noted in each micrograph) in Grade 92 simulated HAZ microstructures. Note that the simulated microstructure with a peak temperature of 1100C still exhibited a very small fraction of undissolved particles which are not readily apparent in the micrograph; thus, precipitate dissolution is still not complete at this temperature. Reproduced from Xu et al. (Xu et al., 2017)..... 55

Figure 2-27. SEM-EBSD grain orientation maps (a-d in color) and image quality maps showing 20-50° grain boundaries (e-h in grayscale) obtained from simulated HAZ microstructures in P92 steel. At the lowest peak temperature of 850°C which is below the Ac1 temperature, transformation and disruption of the original PAGBs are not evident. At 1000°C (>Ac1), complete transformation is evident, but the grain size is refined because incomplete carbide dissolution limits grain growth (cf. Fig. 2-26(b)). At Tp=1250°C (>Ac3) precipitate dissolution is complete and grain growth begins to occur. Reproduced from Xu et al. (Xu et al., 2017)..... 56

Figure 2-28. Comparison of high angle grain boundary (HAGB) and low angle grain boundary (LAGB) misorientation distributions in the FGHAZ of a P91 weldment in three conditions, (a) as-welded (b) after PWHT at 760°C/2 h, and (c) after creep rupture testing at 650°C/70 MPa. Note the significant increase in subgrain size after PWHT and also after creep testing. Reproduced from Wang and Li (Wang and Li, 2016). 58

Figure 2-29. Schematic illustration of microstructure and carbide evolution in base metal and FGHAZ for base metals subjected to different pre-weld tempering treatments. Note that in the LTT condition, the microstructure shows finer carbides which precipitated at newly-formed PAGB, compared to coarsened carbides along former PAGBs in the HTT condition. Reproduced from Yu et al. (Yu et al., 2013)..... 61

Figure 2-30. Comparison of cross-weld data for a P122 weldment, both before and after creep-testing at room temperature (solid points) and at the creep test temperature (open points). Reproduced from Li et al. (Li et al., 2003). 63

Figure 2-31. Schematic illustration of cavity nucleation mechanisms at grain boundaries. (a) sliding at ledges and triple points (b) vacancy condensation at stress concentrations (c) dislocation pileup at obstacles such as boundaries or hard particles (d) nucleation at GB particle due to combined mechanisms of (a)-(c). Reproduced from Kassner and Hayes (Kassner and Hayes, 2003)..... 66

Figure 2-32. Schematic comparison of the variation in critical cavity volume for four cases of nucleation: (a) homogeneous nucleation (b-d) heterogeneous nucleation. Note that the critical volume decreases from (a) to (d) and the nucleation probability correspondingly increases. Reproduced from Raj (Raj, 1978). 68

Figure 2-33. Modulus-normalized stress as a function of particle-matrix interfacial energy, showing that cavity nucleation significantly reduces the fracture stress. Reproduced from Raj (Raj, 1978). 68

Figure 2-34. Experimental data for creep cavity density as a function of creep strain which illustrates the different rates of cavity nucleation observed in different materials. Note that the cavity density increases with strain for all the observed materials,

indicating that continuous cavity nucleation was occurring. Reproduced from (Dyson, 1983). 71

Figure 2-35. Experimental correlation between creep ductility (as measured by fracture strain) and the change in cavity nucleation rate per incremental unit of strain. An inverse proportionality between creep ductility and change in cavity nucleation rate is evident. Reproduced from (Dyson, 1983)..... 72

Figure 2-36. Schematic curves illustrating the variation in cavity density as a function of fracture strain (εf) for different creep conditions: (a) higher stress and higher dN/dε, where cavity growth is rate-controlling (b) lower stress and dN/dε, where cavity nucleation is rate-controlling (c) lower stress and variable dN/dε, where cavity density depends on both cavity nucleation rate and growth rate. Reproduced from (Dyson, 1983). 72

Figure 2-37. Schematic illustration of vacancy diffusion adjacent to a cavity while subjected to an applied tensile stress. In the figure, the terms are defined as follows: cavity diameter (2a), tensile stress magnitude (σ), cavity separation distance (λs), and grain boundary thickness (δ). Reproduced from Kassner and Hayes (Kassner and Hayes, 2003). 74

Figure 2-38. Schematic illustration of (a) homogeneous cavity nucleation, in which cavities are present on essentially all transverse boundaries, and (b) inhomogeneous cavity nucleation, in which cavities are only present on a limited number of transverse boundaries. The transverse boundaries are perpendicular to the applied stress which is oriented in the vertical direction. 74

Figure 2-39. Measured cavity growth rate curves for two Cr-Mo steels. Several contours of cavity growth rate for unconstrained cavity growth are shown by the dashed lines; it is apparent that the measured growth rates are significantly lower than predicted by unconstrained growth. Additionally, the measured data shows a nonlinear stress dependence. Reproduced from Kassner and Hayes (Kassner and Hayes, 2003), originally from Riedel (Riedel, 1987). 76

Figure 2-40. Measured failure times as a function of applied stress for a 2.25Cr-1Mo steel (round data points). The curves correspond to predicted behavior for different combinations of instantaneous/continuous nucleation and unconstrained/constrained cavity growth. It is apparent that the experimental points correlate most nearly to the curve which represents continuous nucleation coupled with constrained growth. Reproduced from Kassner and Hayes (Kassner and Hayes, 2003), originally from Riedel (Riedel, 1987)..... 77

Figure 2-41. Evolution of M23C6 carbide size (in terms of equivalent circle diameter, ECD) as a function of exposure time at (a) 600°C and (b) 650°C. Square symbols correspond to static thermal exposure and circle symbols indicate creep exposure. Note that there is no significant change in mean diameter of M23C6 for either static or creep exposure at 600°C, while at 650°C, coarsening occurs after 4000 h during creep and 10000 h during static exposure. Reproduced from Hättestrand and Andrén (Hättestrand and Andrén, 2001)..... 80

Figure 2-42. Comparison of MX precipitate size distribution for three material states of a Grade 91 steel: as-received material, after static thermal exposure at 600°C ("head"), and after creep exposure with strain at 600°C/80 MPa ("gauge"). The durations of the static thermal exposure and creep exposure were both 113,431 h. Note that the peak value of

the size distribution (~30 nm) is essentially the same for the three states, indicating the stability of MX precipitates under these conditions. Reproduced from Panait et al. (Panait et al., 2009). 81

Figure 2-43. Cumulative probability plot of subgrain width showing the evolution of subgrain size in in X20CrMoV12-1 steel from the initial material state (normalizing, 1050°C/1 h) with different extents of tempering and/or creep exposure. Note that the largest subgrain width is for the 8% creep strain condition which occurred after 126 h of creep exposure; in comparison, extended tempering for 100 h at 750°C (static thermal exposure) resulted in less subgrain coarsening. Reproduced from Dronhofer et al. (Dronhofer et al., 2003). 83

Figure 2-44. Comparison of subgrain size distribution for three material states of a Grade 91 steel: as-received material, after static thermal exposure at 600°C ("head"), and after creep exposure with strain at 600°C/80 MPa ("gauge"). The durations of the static thermal exposure and creep exposure were both 113,431 h. Note that the peak value and narrow width of the distribution is similar in the as-received and static thermal exposure conditions, but the distribution after creep exposure broadens very significantly and the peak shifts to larger subgrain size. Based on these distributions, significant subgrain coarsening occurred in some (but not all) subgrains during creep, while essentially no coarsening took place during static thermal exposure. Reproduced from Panait et al. (Panait et al., 2009). 84

Figure 2-45. Creep curves for X20 steel after tempering (750°C/4 h) and binary Fe-10Cr alloy after tempering (600°C/0.25 h). Comparing the curves at 600°C (873 K), note the much lower creep rate for X20 versus Fe-10Cr (approx. four orders of magnitude). Reproduced from Kostka et al. (Kostka et al., 2007). 86

Figure 2-46. TEM micrographs illustrating the changes in microstructure occurring in Grade 91 steel after tempering at 765°C/0.5 h and creep at 600°C/70 MPa for different time periods. (a) As-tempered, no creep exposure (b) 9992 h creep (c) 30,030 h creep (d) 50,064 h creep (e) 70,000 h creep (f) rupture after 80,736.8 h. Note the gradual subgrain coarsening and formation of equiaxed subgrains that occurs during creep up to 70,000 h, followed by a drastic increase in size and equiaxed nature of subgrains during the final 10,736.8 h of life between (e) and (f). Reproduced from Sawada et al. (Sawada et al., 2011). 87

Figure 2-47. Schematic curves showing the relationship between creep strain and creep rate as functions of time and strain. Note that the creep rate versus time plot shows only primary (transient) and tertiary (acceleration) creep regions, without a steady state region where the creep rate is constant. Reproduced from Abe (Abe, 2015). 89

Figure 2-48. Creep curves for Grade 91 base metal in the tempered condition () for creep testing at 600°C/80 MPa. Although not emphasized by the log scale of the plot in (b), note that the majority of creep life is expended in the tertiary regime where the creep rate is increasing. Adapted from Panait et al. (Panait et al., 2009). 90

Figure 2-49. Evolution of dislocation density for different material conditions (1) through (6), as described below the graph, for an X20 (12Cr) steel. The data points show the differences in evolution of free dislocations (×, +) compared to the separate contributions to the total boundary dislocation density (ρb) from subgrains (ρb1, solid circles) and low angle boundaries (ρb2-5, empty circles). Adapted from Peŝiĉka et al. (Peŝiĉka et al., 2004). 91

Figure 2-50. Plots of measured micro hardness and subgrain (micro-grain) width as a function of time during static thermal aging (no stress) and creep exposure. Note that in (b) the subgrain width does not change definitively during static exposure, but subgrain growth does increase during creep exposure. Reproduced from Aghajani et al. (Aghajani et al., 2009). 93

Figure 2-51. Frequency plots showing the evolution of misorientation angle for an X20 steel during static thermal aging at 550°C and creep at 550°C/120 MPa. (a) Evolution of 1° (low angle) boundaries (b) Evolution of 60° (high angle) boundaries. Reproduced from Aghajani et al. (Aghajani et al., 2009). 94

Figure 2-52. Comparison of measured creep data for three different heat treatment conditions of a 9Cr-1W steel. Reproduced from Abe (Abe, 2003). 96

Figure 2-53. Comparison of TEM micrographs showing the microstructure prior to creep testing and after creep testing for three different heat treatment conditions of a 9Cr-1W steel. The initial microstructures of the three conditions are clearly different, with the extended temper material in (C) showing the greatest extent of subgrain growth prior to creep; however, the terminal microstructures after creep are qualitatively similar for the three conditions, despite the differences in rupture time. Adapted from Figures 9-11 and Table I in Abe (Abe, 2003). 98

Figure 2-54. Plot illustrating the change in creep rate during creep strain accumulation ($d \log \varepsilon / d\varepsilon$) as a function of applied stress for two 12Cr CSEF steels with different heat treatments. Reproduced from Agamennone et al. (Agamennone et al., 2006). 100

Figure 2-55. Comparison plots showing the predicted evolution of equivalent stress distribution across the notch throat diameter (0.0 mm corresponds to the center of the specimen and 3.0 mm corresponds to the notch root) for a notched creep specimen of FB2 steel (9Cr-0.5Mo-0.11V-0.21N). Note that for both less severe and more severe notches, a relaxation in the equivalent stress value is predicted to take place; the extent of relaxation at the end of the creep duration ($t/tf=1$) is slightly greater for the lower acuity notch (acuity ratio of 10). Reproduced from Niu et al. (Niu et al., 2021). 104

Figure 2-56. Comparison plots showing the predicted evolution of stress triaxiality across the notch throat diameter (0.0 mm corresponds to the center and 3.0 mm corresponds to the notch root) for a notched creep specimen of FB2 steel (9Cr-0.5Mo-0.11V-0.21N). For the less severe notch, an increase in stress triaxiality is predicted as the rupture life is expended; for the more severe notch (ratio of 24), the FEM results predict the stress triaxiality to be nearly the same throughout the creep duration. Reproduced from Niu et al. (Niu et al., 2021). 105

Figure 2-57. Comparison plots showing the predicted distribution of equivalent stress and triaxiality for a notched creep specimen of FB2 steel (9Cr-0.5Mo-0.11V-0.21N) with a notch ratio of 24. Note that in (a) the peak equivalent stress is predicted to occur at the notch root (r=3mm), while for triaxiality factor, the maximum is predicted to occur at a position slightly away from the notch root (r=~2.6mm). Reproduced from Niu et al. (Niu et al., 2021). 107

Figure 2-58. Reduction of area as a function of rupture time for plain bar creep specimens (open symbols) and for notched bar creep specimens (filled and partially filled symbols) from the same Grade 92 steel. Reproduced from Parker (Parker, 2017). 109

Figure 2-59. Comparison of uniaxial tension and multiaxial (internally pressurized tubes) creep rupture data for modified 9Cr-1Mo weldments . Reproduced from Yaguchi et al. (Yaguchi et al., 2010). 111

Figure 2-60. Predicted correlations for time to tertiary creep onset as functions of triaxiality F and maximum principal stress. Note that (a) shows a transition from notch strengthening (time to tertiary increasing with triaxiality) to notch weakening (time to tertiary decreasing with triaxiality) as stress decreases (cf. 180 MPa vs. 80 MPa). For (b), note that increased triaxiality (F>1) only leads to a reduction in time to tertiary creep when the maximum principal stress is below approx. 110 MPa. Adapted from Messner et al. (Messner et al., 2019). 114

Figure 2-61. Predicted correlations for strain at onset of tertiary creep as functions of triaxiality F and maximum principal stress. These results suggest a possible connection between increasing triaxiality and reduced rupture ductility. Adapted from Messner et al. (Messner et al., 2019). 114

Figure 2-62. Predicted contributions to the overall creep rate for different creep mechanisms as a function of triaxiality F at a fixed maximum principal stress of 120 MPa and a temperature of 600°C. Reproduced from Messner et al. (Messner et al., 2019). 115

Figure 2-63. Comparison of subgrain structure in the FGHAZ of a Grade 92 weldment (a) prior to creep testing and (b) after creep testing. (c) Plot illustrating the greater relative increase in subgrain size in the central FGHAZ (at the specimen center) as compared to the FGHAZ at the specimen surface. Adapted from Sawada et al. (Sawada et al., 2013). 117

Figure 2-64. Evaluation of mean diameter of M23C6 and MX precipitates in the base metal and FGHAZ of a Grade 92 weldment before (data point at 0 h) and after creep testing. The FGHAZ region in the center of the creep specimen and the surface FGHAZ region were evaluated separately. It is apparent that the center FGHAZ showed somewhat greater coarsening of $M_{23}C_6$ than the surface FGHAZ region; this change was attributed to the higher stress state in the center of the specimen. Reproduced from Sawada et al. (Sawada et al., 2013). 119

Figure 2-65. Schematic illustrating possible loading directions for a “weak zone” between two adjacent, stronger materials (“parent steel”). This arrangement mimics the placement of the “weak” HAZ in a Grade 91 weldment between the adjacent, higher strength weld deposit and base metal on opposing sides of the HAZ. Note that when the constituent zones are loaded in parallel, all zones are required to deform identically (iso-strain) in order to maintain interfacial continuity, and the stresses in the zones will be dissimilar. When the constituent zones are loaded in series, all zones experience identical stress while deformation proceeds uniformly (i.e. uniform shape change, in the absence of necking), but independent strains in the distinct zones are possible. Reproduced from Kimmins et al. (Kimmins et al., 1993). 120

Figure 3-1. Photograph of the AEP Grade 91 weldment prior to sectioning, showing the orientation of longitudinal creep specimens (illustrated by paper templates) parallel to the welding direction. Reproduced from (Hobbs et al., 2015). 129

Figure 3-2. Photograph of one end of the AEP Grade 91 weldment to show the sectioning plan for extraction of round longitudinal creep specimens. After polishing and macro-etching to show the weld deposit and HAZ location, six specimen locations

were marked for extraction, with each specimen centerpoint located along a line drawn through the outer portion of the HAZ. This method was used to ensure that the longitudinal creep specimens were centered on the HAZ so that the specimen gauge diameter would contain all three weldment regions (base metal, HAZ, and weld deposit). Reproduced from (Hobbs et al., 2015). 130

Figure 3-3. (A) Typical example of an microstructure of Grade 91 base metal as revealed by backscatter SEM imaging and (B) typical example of a processed image after thresholding and median filtering for inclusion analysis in ImageJ. In each image, inclusions are marked by red arrows. 135

Figure 3-4. Image sequence showing the image processing steps for particle analysis of a representative SEM micrograph from the H47 FGHAZ region at 10kx: (a) SEM micrograph after levels-adjustment so that black corresponds to the value at the far left of the original image histogram and white corresponds to the value at the far right of the histogram (b) thresholded image (c) image after applying median filter (zero pixel radius) to remove isolated stray pixels (d) image mask after particle analysis using 5-1024 pixel range and 0.15-1.00 circularity range. 139

Figure 3-5. Image sequence showing the image processing steps for particle analysis of a representative SEM micrograph from the FT FGHAZ region at 10kx: (a) SEM micrograph after levels-adjustment so that black corresponds to the value at the far left of the original image histogram and white corresponds to the value at the far right of the histogram (b) thresholded image (c) image after applying median filter (zero pixel radius) to remove isolated stray pixels (d) image mask after particle analysis using 5-1024 pixel range and 0.15-1.00 circularity range. 140

Figure 3-6. Histogram of particle area for two different SEM micrographs obtained from the H47 FGHAZ region in the FT-H47-1 cross-weld creep specimen. Both FGHAZ regions exhibit similar particle area distributions. The smallest bin size of 0.025 μm^2 shows a difference of approximately 15% between the two distributions. 142

Figure 3-7. Representative SE-SEM micrograph illustrating the procedure for measuring subgrain size according to the Abrams Three-Circle procedure described in ASTM E112. The micrograph has been overlaid with the test pattern and the boundary intersection locations have been marked for subsequent counting; yellow points are counted as single intersections and green points are counted as 1.5 intersections. 145

Figure 4-1. Histograms of particle size (in terms of area) for evaluating inclusion content in the FT base metal, showing the particle area distribution in the range of 0-60 μm. The histograms were determined based on software image analysis of BSE-SEM image panoramas obtained at 2500X from an as-polished FT base metal sample. An area of ~5 mm^2 was evaluated for each scan. 148

Figure 4-2. Box plots of particle area for evaluating inclusion content in the FT base metal. The box plot data was obtained from software image analysis of SEM-BSE image panoramas obtained at 2500X from an as-polished FT base metal sample. An area of ~5 mm^2 was evaluated for each scan for a total evaluated area of ~25 mm^2. 149

Figure 4-3. Representative optical micrograph from the FT (forging) base metal in the PWHT condition showing the presence of large inclusion “stringers” (noted by arrows). Etchant: Fry’s reagent. 150

Figure 4-4. Histograms of particle size (in terms of area) for evaluating inclusion content in the H47 base metal, showing the particle area distribution in the range of 0-60 μm.

The histograms were determined based on software image analysis of BSE-SEM image panoramas obtained at 2500X from an as-polished H47 base metal sample. An area of ~5 mm^2 was evaluated for each scan. 153

Figure 4-5. Box plots of particle area for evaluating inclusion content in the H47 base metal. Note that the main difference between the five scans is in the distribution of outliers; the characteristic quantities (mean, standard deviation, quartile range) are similar for the evaluated areas. The box plot data was obtained from software image analysis of BSE-SEM image panoramas obtained at 2500X from an as-polished H47 base metal sample. An area of ~5 mm^2 was evaluated for each scan for a total evaluated area of ~25 mm^2. 154

Figure 4-6. Optical macrograph of the FT to H47 SMAW weldment in the PWHT condition, 746°C/1 h. The red dotted lines indicate the locations of microhardness traverses which are shown in Fig. 4-17. Etchant: Fry's reagent. 157

Figure 4-7. Microstructure of the FT base metal subsequent to re-normalizing, tempering, and PWHT (746°C/1 h), as revealed with (A,B) OLM and (C,D) SEM. In (B), PAGBs are denoted by red arrows, while parallel features corresponding to tempered martensite blocks within a PAGB are denoted by blue arrows. In (C), note the clear lath-like subgrain structure with numerous fine carbides <1 μm in size along the subgrain boundaries, with additional particles <<1 μm in size within the ferritic subgrain interiors (partially visible in D). Etchant: Fry's reagent in (A, B) and 10% Nital in (C,D). 159

Figure 4-8. Microstructure of the FT CGHAZ from the FT-H47 weldment subsequent to PWHT (746°C/1 h) as revealed with (A,B) OLM and (C,D) SEM. A lath-like substructure is evident in (C,D) since this region was completely transformed to austenite during the welding thermal cycle and subsequently formed new martensite upon cooling. Compared to Fig. 4-7, a greater extent of fine particles <<1 μm in size is evident in the ferritic subgrain interior in (D) after PWHT, due to carbide dissolution and re-precipitation that occurred as a result of the CGHAZ thermal cycle and PWHT. Etchant: Fry's reagent (A, B) and 10% Nital (C,D). 160

Figure 4-9. Microstructure of the FT FGHAZ from the FT-H47 weldment in the PWHT condition, 746°C/1 h, as revealed with (A,B) OLM and (C,D) SEM. Black particle in upper left corner of (B) is an inclusion. In (C,D), note the presence of an essentially 100% equiaxed ferritic subgrain structure which formed as a result of the welding thermal cycle followed by PWHT, as compared to the lath-like structure apparent in Fig. 4-7. The micrographs in (C) and (D) clearly show ferritic subgrains (yellow) and subgrain boundaries (green); the ferritic subgrain boundaries have noticeably fewer precipitates compared to the boundaries in Fig. 4-7. Etchant: Fry's reagent (A, B) and 10% Nital (C,D). 162

Figure 4-10. Microstructure of the FT ICHAZ from the FT-H47 weldment in the PWHT condition, 746°C/1 h, as revealed with (A,B) OLM and (C,D) SEM. In (C,D), note the presence of equiaxed ferritic subgrains (yellow arrows) formed after the welding thermal cycle followed by PWHT. The ferritic subgrain boundaries (green arrows) are less populated with precipitates compared to the FT BM. Also in (C,D), the presence of undissolved, aligned carbides along former PAGBs, as shown by the dashed red lines to emphasize a PAGB outline, indicates a further decrease in the extent of carbide dissolution as compared to the original FT base metal in Fig. 4-7. Etchant: Fry's reagent (A, B) and 10% Nital (C,D)..... 164

Figure 4-11. Microstructure of the H47 base metal in the PWHT condition, 746°C/1 h, as revealed with (A,B) OLM and (C,D) SEM. Similar to Fig. 4-7, a lath-like substructure is clearly evident in (C,D) with carbides along the PAGBs. The PAGBs are noted by red arrows, block/subgrain boundaries by green arrows, and the parallel orientation of the block structure with each PAG is shown by blue arrows in (C). In (D), smaller carbides are visible within the individual subgrains; the red arrows show a junction of multiple PAGBs. Etchant: Fry's reagent (A, B) and 10% Nital (C,D). 165

Figure 4-12. Microstructure of the H47 CGHAZ from the FT-H47 weldment in the PWHT condition, 746°C/1 h, as revealed with (A,B) OLM and (C,D) SEM. A lath-like substructure is evident in (C,D) since this region was completely transformed to austenite during the welding thermal cycle and subsequently transformed to new martensite upon cooling. Compared to Fig. 4-11, a greater extent of fine particles <<1 μm in size is evident in the ferritic subgrain interior in D, due to carbide dissolution and re-precipitation that occurred as a result of the CGHAZ thermal cycle and PWHT. Etchant: Fry's reagent (A, B) and 10% Nital (C,D). 167

Figure 4-13. Microstructure of the H47 FGHAZ from the FT-H47 weldment in the PWHT condition (746°C/1 h) as revealed with (A,B) OLM and (C,D) SEM. Compared to Fig. 4-11 or Fig. 4-12, the H47 FGHAZ shows formation of equiaxed ferritic subgrains as a result of the FGHAZ thermal cycle, in which the temperature was high enough for complete re-austenitization to occur. Although significant carbide dissolution occurred, as indicated by the near-absence of carbides along former PAGBs, the peak temperature and time-at-temperature were not sufficient to produce complete carbide dissolution and re-precipitation (i.e. as occurred in the CGHAZ). Compared to Fig. 4-12, there is also a greatly reduced extent of very fine particles in the ferritic subgrain interior regions. Etchant: Fry's reagent (A, B) and 10% Nital (C,D). 168

Figure 4-14. Microstructure of the H47 ICHAZ from the FT-H47 weldment in the PWHT condition (746°C/1 h) as revealed with (A,B) OLM and (C,D) SEM. In (C,D), the presence of undissolved, aligned carbides along former PAGBs, as shown by the red arrows in (C), indicates a further decrease in the extent of carbide dissolution as compared to the original H47 base metal in Fig. 4-11. In (D), many of the ferritic subgrain boundaries (green arrows) are not populated with carbides, indicating a greater susceptibility to coarsening. Etchant: Fry's reagent (A, B) and 10% Nital (C,D). 170

Figure 4-15. Comparison of SE-SEM micrographs for the (a) FT FGHAZ region and (b) H47 FGHAZ region. The micrographs show a similar microstructural appearance in both regions, namely an equiaxed ferritic subgrain structure with some larger carbides remaining on the boundaries since the carbides were not dissolved during the thermal cycle. The majority of the fine carbides within the ferritic subgrain matrix regions (yellow arrows) were dissolved, and some of the larger carbides (white arrows) are no longer located on the ferritic subgrain boundaries, resulting in a reduced extent of boundary pinning. Etchant: 10% Nital. 171

Figure 4-16. Comparison of SE-SEM micrographs for the (a) FT ICHAZ region and (b) H47 ICHAZ region. The micrographs reveal a similar microstructural appearance in both ICHAZ regions, namely an equiaxed ferritic subgrain structure with some larger, aligned carbides remaining along the outlines of former PAGBs. Similarly to the FGHAZ, the majority of the fine carbides within the ferritic subgrain matrix regions (yellow arrows) were dissolved. Etchant: 10% Nital. 172

Figure 4-17. Microhardness traverses for the FT-H47 weldment in the PWHT condition: (A) FT side of the weld (B) H47 side of the weld. The hardness traverses are similar; the minimum hardness in the HAZ is slightly lower on the H47 side than on the FT side. Reproduced from (Hoskins et al., 2017). 174

Figure 4-18. Measured creep curve and corresponding calculated strain rate curve obtained for the "FT-H47-1" cross-weld creep specimen which was extracted from the FT-H47 weldment and tested in the PWHT condition (746°C/1 h). The creep test parameters were 627°C (1160°F) and 82.7 MPa (12 ksi). 176

Figure 4-19. Photograph of the "FT-H47-1" cross-weld creep specimen extracted from the FT-H47 weldment after PWHT at 746°C/1 h and tested at 627°C/82.7 MPa. The specimen was tested to rupture, with the rupture occurring on the FT side of the weld; although the overall elongation was low at ~0.5%, some slight local deformation at the rupture surfaces can be seen (rounding of the edges at the rupture location). 177

Figure 4-20. Macrograph of a metallographic section from the FT-H47-1 cross-weld creep specimen, PWHTed at 746°C/1 h and creep tested at 627°C/82.7 MPa and ruptured after 2080.4 h. Rupture occurred in the outer portion of the HAZ (Type IV failure) on the FT side of the weld. No macro-cracks were evident in the H47 HAZ. The loading axis during creep testing corresponds to the horizontal direction in the macrograph. Etchant: Fry's reagent. 178

Figure 4-21. Cross-section macrograph of the FT-H47-1 creep specimen showing two locations in the FT ICHAZ which were examined at higher magnification to evaluate creep damage. The creep loading axis corresponds to the horizontal direction in the micrographs. Note the evidence of localized plastic deformation at the FT HAZ, as indicated on one side by the small white arrows. Etchant: Fry's reagent. 180

Figure 4-22. SE-SEM micrograph of location ICHAZ-1A in the FT ICHAZ of the FT-H47-1 creep specimen, slightly away from the rupture location. Note the distinct delineation between the adjacent, creep undamaged region in the base metal (left) compared to the ICHAZ (right). The creep loading axis corresponds to the horizontal direction in the micrograph. The boxed region is shown at higher magnification in Fig. 4-23. Etchant: 10% Nital. 181

Figure 4-23. SE-SEM micrographs illustrating typical creep cavity morphology at the FT ICHAZ-1A location of the FT-H47-1 creep specimen, slightly away from the rupture location in the FT HAZ. The red circle highlights a particle which is clearly present at one end of the cavity; the yellow circle indicates a typical example of the slightly higher extent of fine precipitates after creep testing as compared to Fig. 4-10, suggesting that some precipitation occurred during creep. Etchant: 10% Nital. 182

Figure 4-24. SE-SEM micrograph of location ICHAZ-1B in the Forged Tee ICHAZ of the FT-H47-1 creep specimen, slightly nearer to the rupture location. Compared to Fig. 4-22, the cavity density is increased. The boxed region in the micrograph is shown at higher magnification in the micrographs in Fig. 4-25. Etchant: 10% Nital. 184

Figure 4-25. SE-SEM micrographs illustrating typical creep cavity morphology at the ICHAZ-2 location of the FT-H47-1 creep specimen. The selected creep cavity does not appear to be associated with a particle such as a nonmetallic inclusion. Etchant: 10% Nital..... 185

Figure 4-26. Cross-section macrograph of the FT-H47-1 creep specimen showing two locations in the FT FGHAZ which were examined at higher magnification to evaluate

creep damage. The creep loading axis corresponds to the horizontal direction in the micrographs. Etchant: Fry's reagent. 186

Figure 4-27. SE-SEM micrograph of location FGHAZ-1 in the FT FGHAZ of the FT-H47-1 creep specimen, slightly away from the rupture location. Similarly to the ICHAZ, the cavity density is decreased away from the rupture location. The creep loading axis corresponds to the horizontal direction in the micrograph. Etchant: 10% Nital. 187

Figure 4-28. SE-SEM micrographs illustrating creep cavity morphology at the FGHAZ-1 location of the FT-H47-1 creep specimen. Etchant: 10% Nital. 188

Figure 4-29. SE-SEM micrograph of location FGHAZ-2 in the FT FGHAZ of the FT-H47-1 creep specimen, adjacent to the rupture location (at left in image). The creep loading axis corresponds to the horizontal direction in the micrograph. Etchant: 10% Nital. ... 189

Figure 4-30. SE-SEM micrographs illustrating typical creep cavity morphology at the FT FGHAZ-2 location of the FT-H47-1 creep specimen. Note the complex, irregular shape of the cavities which appear to be located at the junction of multiple equiaxed ferritic subgrains; the cavities appear to result from separation along the subgrain boundaries. In D, small particles (most likely carbides) are visible within the cavity interior. 191

Figure 4-31. Cross-section macrograph of the FT-H47-1 creep specimen showing a selected location in the H47 HAZ which were examined at higher magnification with SEM to evaluate creep damage. The creep loading axis corresponds to the horizontal direction in the micrographs. Etchant: Fry's reagent. 192

Figure 4-32. SE-SEM micrograph of location ICHAZ-1 in the H47 ICHAZ of the FT-H47-1 creep specimen. In addition to the absence of macro-cracking on this side of the weld, note the significantly lower occurrence of cavitation compared to the FT ICHAZ (cf. Fig. 4-22). Etchant: 10% Nital. 193

Figure 4-33. SE-SEM micrographs of an isolated creep cavity at location ICHAZ-1 in the H47 ICHAZ of the FT-H47-1 creep specimen. The cavity is highly irregular and appears to be located at a boundary junction with boundary separation occurring in multiple directions. The bright area at the center of the cavity is most likely a carbide; this cavity was not associated with a nonmetallic inclusion and the cavity is not filled in the interior (i.e. if the cavity were opening around an inclusion). Etchant: 10% Nital. 194

Figure 4-34. SE-SEM micrograph of creep cavitation near location ICHAZ-2 in the H47 ICHAZ of the FT-H47-1 creep specimen. Note that while there are scattered larger cavities (n=31, average area ~5 μm), the subsequent micrographs in Fig. 4-35 also show a small cavity in the early stages of growth. Etchant: 10% Nital. 195

Figure 4-35. SE-SEM micrographs showing a small, isolated creep cavity near location ICHAZ-1 in the H47 ICHAZ of the FT-H47-1 creep specimen. The cavity is located on a short subgrain boundary segment which is oriented at an angle to the tensile loading direction during creep (horizontal in this image) and is associated with a small particle denoted by an arrow (from the SE image contrast, most likely a carbide). Etchant: 10% Nital. 196

Figure 4-36. SE-SEM micrograph of location FGHAZ-1 in the H47 FGHAZ of the FT-H47-1 creep specimen. Similarly to the H47 ICHAZ, the H47 FGHAZ shows no macro-cracking and a significantly lower occurrence of cavitation compared to the FT FGHAZ (cf. Fig. 4-27). 197

Figure 4-37. SE-SEM micrographs illustrating typical creep cavity morphology at location FGHAZ-1 in the H47 FGHAZ of the FT-H47-1 creep specimen. The cavity morphology is highly irregular and the cavity appears to be opening along a boundary junction. There are also small bright particles (most likely carbides) along the cavity perimeter and the cavity is also located adjacent to another, larger particle within the matrix. Etchant: 10% Nital. 199

Figure 4-38. Cross-section macrograph of the FT-H47-1 creep specimen showing the locations for extraction (solid red outlines) of two separate samples to reveal the creep-damaged FT HAZ and H47 HAZ regions for SEM examination, using the cryo-cracking technique. The dashed red lines in the respective samples denote the placement of circumferential notches which were used to direct crack propagation along the desired path when the samples were fractured at liquid nitrogen temperature. 200

Figure 4-39. Photograph showing the extracted, notched, and cryo-cracked samples from the FT-H47-1 creep specimen. 202

Figure 4-40. Optical fractograph showing the fracture surfaces corresponding to the lower half of each sample shown in Fig. 4-39 from the FT-H47-1 creep specimen. 203

Figure 4-41. SEM fractograph showing the fracture surface morphology revealed by cryo-cracking at Location 1 in the FT HAZ of the FT-H47-1 creep specimen, adjacent to the rupture surface (which is oxidized). 204

Figure 4-42. SEM fractographs showing the fracture surface morphology revealed by cryo-cracking at Location 1 in the FT HAZ adjacent to rupture. At this location, the fracture morphology is primary transgranular cleavage (flat features) with isolated cavities observed. The boxed regions highlight a creep cavity on the surface; small particles (most likely carbides) are present on the cavity interior surface, but a specific initiation site for the cavity is not apparent. 205

Figure 4-43. SEM fractograph showing the fracture surface morphology revealed by cryo-cracking at Location 1 in the H47 HAZ of the FT-H47-1 creep specimen. Recall that this side of the weld did not show any evidence of macro-cracking, which correlates with the predominantly transgranular fracture morphology observed in the above image. 206

Figure 4-44. SEM fractographs showing the fracture surface morphology revealed by cryo-cracking at Location 1 in the H47 HAZ. At this location, the fracture morphology is primarily transgranular cleavage (flat features) with isolated cavities observed. 208

Figure 4-45. Higher magnification SEM fractograph of the cavity interior surface in the H47 HAZ shown in Fig. 4-44. Note the regularly spaced ledges or steps that are visible on the cavity interior surface. 209

Figure 4-46. SEM fractograph showing the fracture surface morphology revealed by cryo-cracking at Location 3 in the H47 HAZ of the FT-H47-1 creep specimen. 210

Figure 4-47. SEM fractographs showing the fracture surface morphology revealed by cryo-cracking at Location 3 in the H47 HAZ. At this location, the fracture morphology is primary transgranular cleavage (flat features) with isolated cavitation; the selected cavity exhibits an irregular shape and an interior surface that is marked by the presence of small particles which most likely originated from grain/subgrain boundaries which separated during cavity growth. 211

Figure 4-48. Histograms of particle area obtained from software image analysis of representative SE-SEM micrographs of the FT and H47 base metals in the PWHT condition (746°C/1 h) prior to creep testing. (A) Histograms of particle area for the size range 0-0.6 μm^2 (B) histograms of particle area for a subset of sizes at the low end of the range, 0-0.1 μm^2. The data bar at the top of the histograms shows statistics for the full particle analysis in the respective image. Note that the particle area distributions in (A) are similar except for the smallest bin size, where the H47 base metal exhibits a significantly higher particle count which is illustrated more clearly in (B). 213

Figure 4-49. Comparison of the particle masks produced by the software image analysis procedure for the (a) FT and (b) H47 base metals in the PWHT condition. Qualitatively, the appearance matches with the histogram results in Fig. 4-48, with the H47 base metal showing a greater extent of fine particles. 214

Figure 4-50. Histograms of particle area obtained from software image analysis of individual SE-SEM micrographs obtained from the FT FGHAZ and H47 FGHAZ regions in the FT-H47 weldment in the PWHT condition (746°C/1 h). Both FGHAZ regions exhibit similar particle area distributions. 216

Figure 4-51. Histograms of particle area obtained from software image analysis of individual 10kx SE-SEM micrographs obtained from the FT ICHAZ and H47 ICHAZ regions in the FT-H47 weldment in the PWHT condition (746°C/1 h). (A) Histograms for particles in the range of 0-0.6 μm^2 in size (B) histograms for a subset of particles in the range of 0-0.1 μm^2 in size. In both cases, the H47 base metal shows a greater extent of finer size particles. In (A) and (B), the information at the top of each figure shows basic statistics for particle area from the full dataset. 217

Figure 4-52. Comparison of box plots of particle area results for the FT ICHAZ and H47 ICHAZ regions in the PWHT condition (746°C/1 h), obtained by image analysis of individual 10kx SE-SEM micrographs. The FT ICHAZ shows a greater spread around the average particle size, a larger average particle size, and a greater number of outlier particles. 218

Figure 4-53. Histograms of particle area obtained from software image analysis of individual 25kx SE-SEM micrographs obtained from the FT ICHAZ and H47 ICHAZ regions in the FT-H47 weldment in the PWHT condition (746°C/1 h). These results verify what was apparent from Fig. 4-51 in that the H47 ICHAZ region has a greater extent of finer size particles. 220

Figure 4-54. Optical macrograph of the H13 to H47 SMAW weldment in the PWHT condition, 746°C/1 h. The red dotted lines indicate the locations of microhardness traverses which are shown in Fig. 4-55. Etchant: Fry's reagent. Reproduced from (Hoskins et al., 2017). 225

Figure 4-55. Microhardness traverses for the H13-H47 weldment in the PWHT condition: (A) H13 side of the weld (B) H47 side of the weld. Reproduced from (Hoskins et al., 2017). 226

Figure 4-56. Measured creep curve obtained for the "H13-H47-2" cross-weld creep specimen which was extracted from the H13-H47 weldment and tested in the PWHT condition (746°C/1 h). Creep test parameters were altered at several points during the test in order to obtain creep rate data under different conditions; refer to the annotations above the graph for the parameters during each segment of testing. Reproduced from (Hoskins et al., 2017). 227

Figure 4-57. Photograph of the "H13-H47-2" cross-weld creep specimen extracted from the H13-H47 weldment and tested in the PWHT condition (746°C/1 h). The specimen was interrupted in the late stage of life (anticipated just prior to rupture) as shown by the formation of a significant crack on the H47 side of the weld. Refer to Fig. 4-56 for the creep curve and creep test parameters. Reproduced from (Hoskins et al., 2017). 229

Figure 4-58. Macrograph of a metallographic section from the FT-H13-2 cross-weld creep specimen, PWHTed at 746°C/1 h. Creep tested at the parameters shown in Fig. 4-56 and terminated when failure appeared imminent, after a total test time of 3022.6 h. A large macro-crack formed in the outer portion of the H47 HAZ and a small macro-crack also formed in the outer portion of the H13 HAZ (in both cases, the cracking showed Type IV characteristics). The loading axis during creep testing corresponds to the horizontal direction (left-right) in the macrograph. Etchant: Fry's reagent. Adapted from (Hoskins et al., 2017). 230

Figure 4-59. Micrographs illustrating creep damage in the ICHAZ at the HAZ-1 location on the H13 side of the H13-H47-2 cross-weld creep specimen. Etchant: 10% Nital. 231

Figure 4-60. Micrographs illustrating creep damage in the ICHAZ at the HAZ-4 location on the H47 side of the H13-H47-2 cross-weld creep specimen. Etchant: 10% Nital. 232

Figure 4-61. Literature correlation between sulfide inclusion density and sulfur content for Grade 91 and Grade 92 CSEF steels. There is a general trend between increased sulfur content and increased inclusion density, although the correlation is not linearly proportional and some materials such as Heat XA3602 deviate from this behavior. Reproduced from (*Life Management of 9%Cr Steels: Evaluation of Metallurgical Risk Factors in Grade 91 Steel Parent Material*, 2018). 239

Figure 4-62. Comparison of the size distributions of MnS inclusions observed for two Grade 91 base metals which exhibited widely different creep damage resistance. The Barrel 2 material was reported as having low creep ductility and low damage resistance (high extent of creep cavitation) while the Tee Piece 1 material exhibited a high ductility and high damage resistance (low extent of cavitation). The Barrel 2 material is seamless piping while the Tee Piece 1 material is a forging. Reproduced from (*Life Management of 9%Cr Steels: Evaluation of Metallurgical Risk Factors in Grade 91 Steel Parent Material*, 2018). 242

Figure 4-63. Comparison of the tempering resistance for multiple heats of Grade 91 steel with different N:Al ratios. The Grade 91 material with the highest N:Al ratio of 24.8 showed the highest average hardness and the smallest spread in hardness values after the most severe tempering treatment (790°C/50 h). Reproduced from (*The Benefits of Improved Control of Composition of Creep-Strength-Enhanced Ferritic Steel Grade 91*, 2014). 244

Figure 4-64. Correlation between N:Al ratio and creep ductility for Grade 91 materials with reported high inclusion density. The colored bars indicate heats with high inclusion density, while gray bars correspond to other heats which were not specifically included in this comparison. Red bars indicate low creep ductility and green bars indicate low ductility. Reproduced from (*Life Management of 9%Cr Steels: Evaluation of Metallurgical Risk Factors in Grade 91 Steel Parent Material*, 2018). 246

Figure 4-65. Effect of N:Al ratio (atomic percent basis) on creep rupture strength (a-e) and creep deformation resistance (f) of Grade 91 steel. The plots in (a-e) show the creep strength corresponding to the indicated lifetime (10kh, 200kh, or 100kh) at the indicated

test temperatures (500°C, 550°C, or 600°C). The plot in (f) shows the stress required to produce a minimum creep rate of 1E-7 per hour at 600°C. In all plots, no trend between creep strength and N:Al ratio is apparent across the evaluated range of N:Al ratio. Reproduced from (Maruyama et al., 2017). 247

Figure 4-66. Comparisons of rupture time as a function of available nitrogen content (N - Al - Ti) for 12Cr-1Mo-1W-0.3V martensitic steel when tested at temperatures of 550°C and 600°C. Note that at 600°C, for example, there is no correlation between rupture time and available nitrogen at high stress, but a clear trend becomes evident as stress decreases. Reproduced from (Abe et al., 2007). 249

Figure 4-67. Numerical simulations of chromium and carbon concentration profiles in austenite at different time steps (1 s, 60 s, 10 min, 60 min) during dissolution of cementite at 860°C. The chromium concentration profiles (thick lines) show that the initial sharp gradient of chromium content at 1 s shifts to a much broader concentration gradient after 60 min; however, complete chromium redistribution still has not occurred after 60 min. Reproduced from Zhao et al. (Zhao et al., 2006). 255

Figure 4-68. Plot of phase fraction versus temperature for the FT base metal with the composition Fe-0.125C-8.506Cr-0.110Ni-0.933Mo-0.211V-0.070Nb-0.017Al-0.041N. Laves phase calculation was disabled. Note that a small region of AlN formation (black outline region in the vicinity of 800°C) is predicted due to the higher Al content of the FT base metal (Al = 0.017 wt.%) compared with the H47 material (Al=0.002 wt.%). 258

Figure 4-69. Plot of phase fraction versus temperature for the H47 base metal with the composition Fe-0.109C-8.653Cr-0.350Ni-0.938Mo-0.208V-0.067Nb-0.002Al-0.045N. Laves phase calculation was disabled. Compared to Fig. 4-68 for the FT base metal, note that no AlN is predicted to form in the vicinity of 800°C. 259

Figure 4-70. Plot of experimental data and calculated results for cementite fraction as a function of time in a Fe-Cr-C (SAE52100) steel during isothermal exposure at 860°C. The dilatometry data and numerical results show that the rate of cementite dissolution (proportional to the slope of the cementite fraction curve) decreases significantly within the first few minutes of exposure, and complete dissolution (fraction equal to zero) is not achieved even after 30 minutes. Reproduced from Zhao et al. (Zhao et al., 2006).. 262

Figure 4-71. Graphs of creep data for a heat of Grade 91 steel with multi-region data fitting based on (a) stress and (b) temperature. Reproduced from Maruyama et al. (Maruyama et al., 2016). 268

Figure 5-1. Cross-section macrograph of the AEP Grade 91 SAW weldment in the 8 h subcritical PWHT condition (774°C/8 h). Etchant: Fry's reagent. Reproduced from (Hobbs et al., 2015). 274

Figure 5-2. Cross-section macrograph showing the representative appearance of the AEP Grade 91 SAW weldment in the 64 h subcritical PWHT condition (774°C/64 h). Etchant: Fry's reagent. Reproduced from (Hobbs et al., 2015). 275

Figure 5-3. Cross-section macrograph showing the representative appearance of the AEP Grade 91 SAW weldment in the re-normalized and tempered condition (1066°C/2 h plus 774°C/3 h). The two dashed lines indicate the locations of two hardness traverses which were performed across the former overlapped and un-overlapped regions of the HAZ; the results are presented in Fig. 5-4. Etchant: Vilella's reagent. Reproduced from (Hobbs et al., 2015). 276

Figure 5-4. Measured microhardness traverses for the AEP Grade 91 SAW weldment in two conditions: subcritical PWHT, 774°C/64 h and re-normalized and tempered (N&T), 1066°C/2 h plus 774°C/3 h. The 64 h subcritical PWHT hardness traverse shows a hardness decrease in the un-overlapped HAZ with a minimum hardness value of 176 HV500gf. In comparison, the N&T hardness traverse shows a uniform hardness across the former HAZ and base metal regions. Data obtained from (Hobbs et al., 2015). 278

Figure 5-5. Plot of measured creep strain versus elapsed test time from three longitudinal creep specimens extracted from the AEP Grade 91 submerged arc weldment. "Longitudinal" refers to the orientation of the creep sample tensile axis with respect to the welding direction in the parent weldment; the creep sample tensile axis is parallel to the welding direction. Creep testing was performed at 621°C/124 MPa. Data from (Hobbs et al., 2015). 280

Figure 5-6. Plot of creep strain rate versus elapsed test time from measured creep data obtained from three longitudinal creep specimens extracted from the AEP Grade 91 submerged arc weldment. Creep testing was performed at 621°C/124 MPa. 281

Figure 5-7. Plot of creep strain rate versus normalized test time from measured creep data obtained from three longitudinal creep specimens extracted from the AEP Grade 91 submerged arc weldment. Creep testing was performed at 621°C/124 MPa. Note that the 8 h PWHT and N&T specimens both reach their minimum creep rate at approximately the same time fraction (~0.3) while the 64 h PWHT specimen reaches the minimum creep rate at a slightly earlier fraction. Note also that the N&T specimen shows a significantly more rapid acceleration of creep rate at the very end of rupture life; this behavior is illustrated as a function of strain in Fig. 5-8. 282

Figure 5-8. Plot of creep strain rate versus average strain from measured creep data obtained from three longitudinal creep specimens extracted from the AEP Grade 91 submerged arc weldment. Creep testing was performed at 621°C/124 MPa. Note that the N&T specimen shows a faster increase of creep strain rate as strain accumulation increases into the tertiary creep regime. 284

Figure 5-9. Optical macrograph of one half of the longitudinal creep specimen in the 8 h subcritical PWHT condition from the AEP Grade 91 weldment. Creep testing was performed at 621°C/124 MPa; total elongation was 17.6%, reduction of area was 85%. The arrow shows the distortion of microstructural banding that reveals the evidence of plastic deformation. Etchant: Vilella's reagent. 285

Figure 5-10. Optical macrograph of one half of the longitudinal creep specimen in the 64 h subcritical PWHT condition from the AEP Grade 91 weldment. Creep testing was performed at 621°C/124 MPa; total elongation was 21.9%, reduction of area was 91%. The arrow shows the distortion of microstructural banding that reveals the evidence of plastic deformation. Etchant: Vilella's reagent. 285

Figure 5-11. Optical macrograph of one half of the longitudinal creep specimen in the normalized and tempered (N&T) condition from the AEP Grade 91 weldment. Creep testing was performed at 621°C/124 MPa; total elongation was 16.7%, the overall reduction of area was 59%. Note that the WM region shows significantly less reduction in area than the former HAZ and BM regions (deformation noted by arrow). Etchant: Vilella's reagent. 286

Figure 5-12. Measured profiles for reduction of area (%RA) along the gauge length of longitudinal creep samples from the AEP Grade 91 weldment. The profiles show the

change in %RA along one half of the ruptured sample; the "0 mm" location in the graph corresponds to the rupture location, and the terminal location (25 or 27 mm) corresponds to the shoulder of each creep sample. Data from (Hobbs et al., 2015). 287

Figure 5-13. Optical light macrograph showing the appearance of the 64h subcritical PWHT longitudinal creep specimen, at the rupture location. The marked regions at the 1 mm, 2 mm, 4 mm, and 8 mm locations were selected for higher magnification examination. Etchant: Vilella's reagent. 289

Figure 5-14. SE-SEM micrographs showing the microstructural appearance and extent of cavities/voids in the 64 h subcritical PWHT (774°C/64 h) longitudinal creep specimen at a distance of 1 mm from the rupture location. Note that all four individual regions in the weld show evidence of voiding/cavitation (orange arrows); additionally, the voids/cavities are distorted (elongated) due to severe plastic deformation at the 1 mm location (corresponding to 86%RA from Fig. 5-12). Etchant: Vilella's reagent.... 290

Figure 5-15. SE-SEM micrographs showing the microstructural appearance and extent of cavities/voids in the 64 h subcritical PWHT (774°C/64 h) longitudinal creep specimen at a distance of 2 mm from the rupture location. Note that all four individual regions in the weld show evidence of voiding/cavitation (orange arrows), but the extent is reduced from the 1 mm location in Fig. 5-14. The voids/cavities are still distorted (elongated) due to plastic deformation at the 2 mm location (corresponding to 77%RA from Fig. 5-12). Etchant: Vilella's reagent. 291

Figure 5-16. SE-SEM micrographs showing the microstructural appearance and extent of cavities/voids in the 64 h subcritical PWHT (774°C/64 h) longitudinal creep specimen at a distance of 4 mm from the rupture location. Note that all four individual regions in the weld show evidence of voiding/cavitation (orange arrows), but the cavity size is smaller and the extent is significantly reduced from the 1 mm location in Fig. 5-14. The voids/cavities are still slightly distorted (elongated) due to plastic deformation at the 4 mm location (corresponding to 66%RA from Fig. 5-12). Etchant: Vilella's reagent. 293

Figure 5-17. SE-SEM micrographs showing the microstructural appearance and extent of cavities/voids in the 64 h subcritical PWHT (774°C/64 h) longitudinal creep specimen at a distance of 8 mm from the rupture location. The extent of cavitation at the 8 mm location is minimal and very isolated, with only one or two cavities (orange arrows) in each micrograph; the voids/cavities are not distorted due to plastic deformation at this location (corresponding to 42%RA from Fig. 5-12). Additionally, the FGHAZ microstructure shows clear evidence of equiaxed ferritic subgrains. Etchant: Vilella's reagent. 294

Figure 5-18. SE-SEM micrographs showing the microstructural appearance and extent of cavities/voids in the 64 h subcritical PWHT (774°C/64 h) longitudinal creep specimen, in the shoulder region located 4 mm from rupture (0 %RA at this location). In all four individual regions, no evidence of voiding/cavitation is observed. The FGHAZ microstructure shows clear evidence of equiaxed ferritic subgrains, while the CGHAZ, BM, and WM show a lath-like structure. Etchant: Vilella's reagent..... 295

Figure 5-19. Optical light macrograph showing the appearance of the normalized and tempered (N&T) longitudinal creep specimen, at the rupture location. Creep testing was performed at 621°C/124 MPa; total elongation was 16.7%, the overall reduction of area was 59%, and rupture life was 481.5 h. The marked regions at the 1 mm, 2 mm, 4 mm,

and 8 mm locations were selected for higher magnification examination. The two dashed red lines indicate the location of the fusion line and the approximate location of the "former HAZ" (the HAZ which was re-transformed to austenite during the N&T heat treatment, thus essentially eliminating the HAZ microstructure gradient which had previously been present). Note the significant difference in the reduction of area for the base metal (BM) region of the specimen as compared to the weld deposit (WM). Also, even at this low magnification, more extensive cavitation (orange arrows) is evident in the WM adjacent to the rupture location. Etchant: Vilella's reagent. 297

Figure 5-20. SE-SEM micrographs showing the microstructural appearance and extent of cavities/voids in the N&T longitudinal creep specimen at a distance of 1 mm from the rupture location. All four individual regions in the weld show evidence of voiding/cavitation (orange arrows); additionally, the voids/cavities are distorted (elongated) due to plastic deformation at the 1 mm location (corresponding to 46%RA from Fig. 5-12). Etchant: Vilella's reagent. 298

Figure 5-21. SE-SEM micrographs showing the microstructural appearance and extent of cavities/voids in the N&T longitudinal creep specimen at a distance of 2 mm from the rupture location. All four individual regions in the weld show evidence of voiding/cavitation (orange arrows); the cavitation in the WM region is particularly extensive and has the appearance of micro-cracking. The voids/cavities still show some distortion due to plastic deformation at the 2 mm location (corresponding to 39%RA from Fig. 5-12). Etchant: Vilella's reagent. 299

Figure 5-22. SE-SEM micrographs showing the microstructural appearance and extent of cavities/voids in the N&T longitudinal creep specimen at a distance of 4 mm from the rupture location. The BM, former FGHAZ, and former CGHAZ regions in the weld show minor evidence of voiding/cavitation (orange arrows), but the cavitation in the WM region remains the most extensive. The voids/cavities still show slight distortion due to plastic deformation at the 4 mm location (corresponding to 34%RA from Fig. 5-12). Etchant: Vilella's reagent. 301

Figure 5-23. SE-SEM micrographs showing the microstructural appearance and extent of cavities/voids in the N&T longitudinal creep specimen at a distance of 8 mm from the rupture location. The cavitation in the BM, former FGHAZ, and former CGHAZ regions is minimal to essentially none (orange arrows), but the cavitation in the WM region remains extensive. The voids/cavities do not show evidence of elongation/distortion at the 8 mm location (corresponding to 19%RA from Fig. 5-12). Etchant: Vilella's reagent. 302

Figure 5-24. SE-SEM micrographs showing the microstructural appearance in the N&T longitudinal creep specimen in the shoulder region, at a distance of 36 mm from the rupture location. No cavitation is observed within this region due to the much lower stress (~64 MPa) during creep testing; the microstructural appearance is similar in all four individual regions due to the N&T heat treatment. Etchant: Vilella's reagent. 303

List of Abbreviations

BM	Base metal
BSE-SEM	Back-scattered electron - scanning electron microscopy
CGHAZ	Coarse-grained heat-affected zone
CSEF	Creep-strength enhanced ferritic [CSEF steel]
EBSD	Electron back-scattered diffraction
EDXS	Energy dispersive X-ray spectroscopy
FGHAZ	Fine-grained heat-affected zone
HAZ	Heat-affected zone
ICHAZ	Inter-critical heat-affected zone
OLM	Optical light microscopy
PAG	Prior austenite grain
PAGB	Prior austenite grain boundary
PWHT	Post-weld heat treatment
SE-SEM	Secondary electron - scanning electron microscopy
SEM	Scanning electron microscopy
TMFS	Tempered martensite ferritic steel
TMLS	Tempered martensite lath structure
WM	Weld metal

Chapter 1 Introduction

1.1 Welded Piping in Power Generation

Steam piping in power generation facilities, also referred to as high energy piping (HEP), operates continuously at high temperatures and pressures. Representative conditions in a standard power plant are on the order of 1000°F and 3600 psi (Jaffee, 1979), with an expected design lifetime of 30-40 years. Under these conditions, piping is susceptible to damage by a variety of different mechanisms, each having different metallurgical origins, including creep, fatigue, creep-fatigue, and thermal fatigue (Viswanathan and Stringer, 2000). As a result of the elevated temperature in conjunction with internal steam pressure, the fundamental cause of failure in HEP is usually either creep or creep in combination with fatigue (creep-fatigue). To obtain the required mechanical properties with adequate creep lifetime, Cr-Mo alloy steels are a primary material used in power generation piping systems due to their combination of high temperature strength and corrosion resistance in steam. Due to the fact these piping systems involve welded joints (whether circumferential girth welds or longitudinal seam welds), the modes and locations of creep damage occurrence and potential failure are often related to welding and its effects on metallurgical properties.

1.2 Historical and Current Problems with Creep Damage in Welded Steel Piping

Of the problems which have occurred historically in welded power piping, two of the main types have originated from either within the weld deposit immediately adjacent to the fusion line, or within the weld heat-affected zone (HAZ) in either the base metal (BM-HAZ) or within the weld deposit (WM-HAZ). The modes of creep damage have different microstructural origins and will be discussed briefly. The general appearance of weld deposit creep damage adjacent to the fusion line is illustrated in Fig. 1-1.
Fig. 1-1 depicts creep damage in a longitudinal seam weld from a 1.25Cr-0.5Mo normalized and tempered hot reheat pipeline. Creep damage is present in the form of

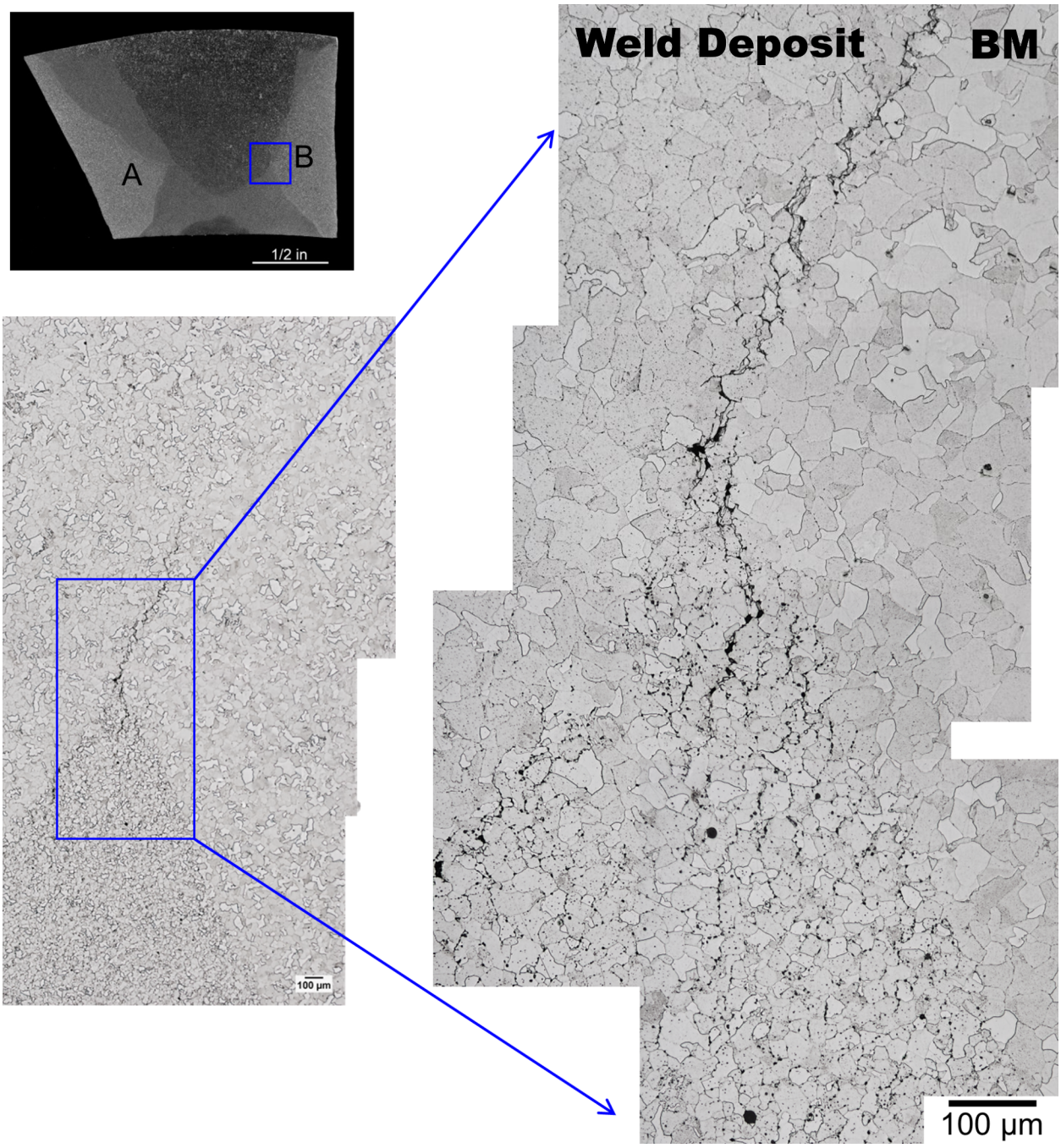


Figure 1-1. Panorama of optical micrographs showing the typical appearance of weld deposit creep damage in 1.25Cr-0.5Mo longitudinally-seam welded hot reheat piping. The creep damage occurs in the weld deposit, immediately adjacent to the fusion line, due to a concentration of nonmetallic inclusions at this region of the weld deposit. Etchant: 2% Nital. Adapted from (Materials Joining Group, 2014).

creep cavities which appear small dark spots and of micro-cracks which consist of interconnected ("coalesced") creep cavities. Notably, it is evident that a succession of micro-cracks has developed along the fusion line, which will eventually link together to form a macro-crack; this form of creep damage development is readily detectable by ultrasonic inspection and can thus be monitored during plant operation to determine a time for safe replacement. This form of creep damage was exhaustively investigated in the 1990s through a research program sponsored by the Materials Properties Council and the results published in a comprehensive report (Lundin et al., 1999) and a dissertation (Zhou, 1997). The primary conclusion from this work was that creep cavitation was linked to the presence of spherical nonmetallic inclusions in the weld deposit, which were produced during initial weld fabrication and functioned as preexisting nucleation sites for cavities due to the weak, incoherent interface between the inclusions and surrounding material.

Another type of creep damage in welded Cr-Mo piping occurs in the base metal or weld deposit HAZ. This form of damage, when occurring in the base metal HAZ, has also been identified as "Type IV" creep damage according to a classification system by Schüller et al. (Schüller et al., 1974). This type of creep damage is commonly associated with creep life significantly below expected design lifetimes and has been observed to occur in a number of different Cr-Mo steels including 1.25-0.5Mo steel and CSEF steels such as modified 9Cr-1Mo (Grade 91) or 12Cr-1Mo (X20CrMoV12-1). The history of premature failures associated with HAZs (Type IV failures) in welded components of CSEF steels has been reviewed by Francis et al. (Francis et al., 2006) and Abson and Rothwell (Abson and Rothwell, 2013), and also in EPRI Report 1018151 (*Service Experience with Grade 91 Components*, 2009). It has been shown in the literature (Kimura and Yaguchi, 2020; Tabuchi and Takahashi, 2012) that weldments of Grade 91 steels exhibit degraded creep properties compared to the creep properties of the properly heat-treated base metal, especially under certain conditions such as low stress and high

temperature or after certain thermal histories. When the creep properties of large datasets of Grade 91 base metal and weldments are compared across a range of temperatures and stresses, it is evident that the weldment creep strengths and rupture times are less than the values for base metal at equivalent temperatures, as shown for example in Fig. 1-2 with data compiled by Tabuchi and Takahashi (Tabuchi and Takahashi, 2012). The disparity in properties is generally observed to increase as test temperature increases.

One way in which the degraded creep properties of Grade 91 weldments in comparison to base metal have been addressed in industry is by the stipulation, e.g. in design codes, of a weld strength reduction factor (WSRF), also alternatively identified as a stress rupture factor or creep strength reduction factor. The WSRF at a particular temperature is defined as the ratio of the average rupture strength of a welded joint at a specified lifetime (e.g. at 100,000 h) to the average rupture strength of the base metal at the same lifetime; thus, the value of the WSRF is always between zero and one. WSRFs were introduced for Grade 91 in the ASME BPVC Section I in 2008. WSRFs as a function of temperature for different materials are given in Section I Table PG-26, which stipulates that for CSEF steels, a distinction is made between weld which receive sub-critical PWHT (below the lower critical transformation temperature) and those which are re-normalized and tempered prior to service. Although WSRFs provide a means to account for the reduced creep properties of Grade 91 weldments, they are not an ideal solution since they mostly negate one of the primary advantages of using Grade 91 to begin with over lower strength Cr-Mo steels which, it should be noted, are not as seriously affected by WSRF penalties in the ASME BPVC.

The typical appearance of Type IV creep damage is shown in Fig. 1-3 for a Grade 91 shielded metal arc weld; note that a high density of creep cavitation is present adjacent to the rupture location, on the left side of the micrograph. Only a short distance away, the cavity density decreases significantly, which shows the localized nature of Type IV

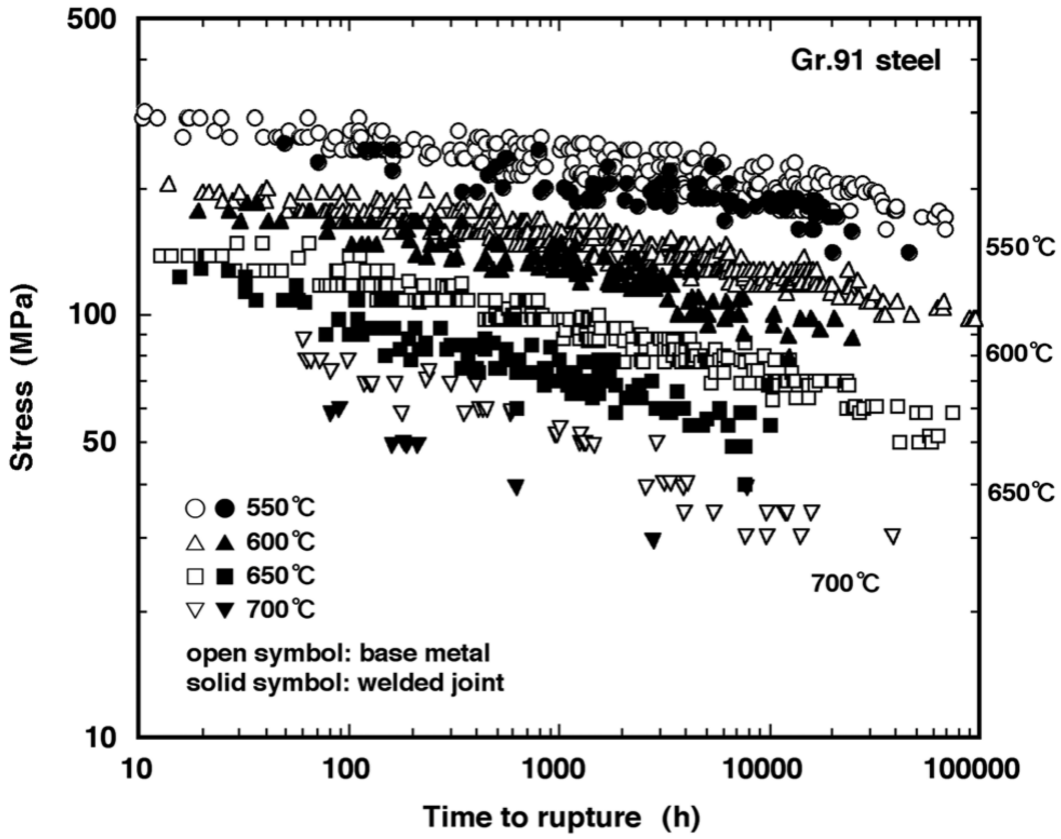


Figure 1-2. Collection of creep data for Grade 91 steel showing the variation in creep properties as a function of test temperature and stress. Reproduced from Tabuchi and Takahashi (Tabuchi and Takahashi, 2012).

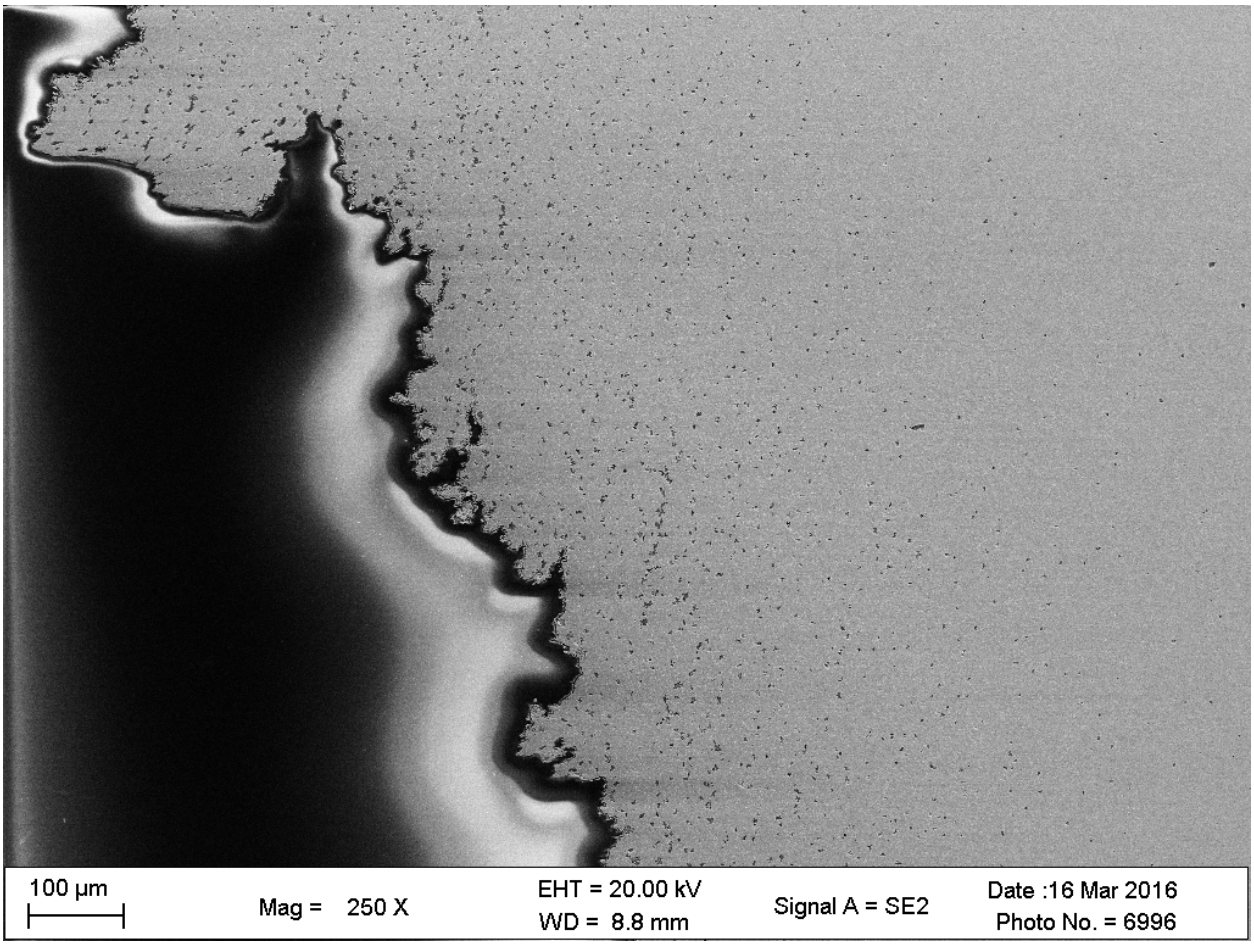


Figure 1-3. SEM micrograph illustrating the typical appearance of "Type IV" creep damage in the HAZ of a Grade 91 weldment. The creep cavitation is concentrated near the rupture location in the HAZ, at left in the micrograph, and decreases only a short distance away from rupture (at right). The dark region at left is epoxy mounting compound.

creep damage in the HAZ region. An additional example of Type IV creep damage, in which some micro-cracks have formed, is shown in Fig. 1-4, which depicts intergranularly-distributed HAZ creep cavitation in a F91/T91 transition weld (Brett, 2007). Type IV damage is considered to be less detectable by nondestructive inspection than other weld-related creep damage (e.g. of the type shown in Fig. 1-1) since Type IV creep cavitation can remain relatively isolated until near the end of component life, rather than always coalescing to form micro-/macro-cracks, e.g. as reported by Siefert et al. (Siefert et al., 2018) who did not observe macro-cracking even very near the end-of-life (~98%) for an interrupted creep specimen exhibiting a high density of HAZ cavitation. Thus, Type IV damage is considered to pose a greater danger to safe operation of power piping, since a component may proceed until nearly complete life expenditure before damage can be reliably identified.

Unlike the weld deposit inclusion-related creep damage shown in Fig. 1-1, which is considered a resolved issue with known steps for mitigation, the issue of Type IV creep damage in CSEF weldments is not fully resolved and is still an active topic of research. Some of the particular topics that have been of recent interest to the wider research community include:

1. correlation of Type IV creep damage with specific HAZ regions such as the intercritical HAZ (Siefert et al., 2019; Y. Wang et al., 2020, 2018)
2. the overall effect of chemical composition, including impurity elements, on creep properties especially creep ductility (*The Benefits of Improved Control of Composition of Creep-Strength-Enhanced Ferritic Steel Grade 91*, 2014)
3. the specific effect of boron additions to control or eliminate the formation of the susceptible Type IV HAZ region (Abe et al., 2007; Das et al., 2009; Mayr and Cerjak, 2008)

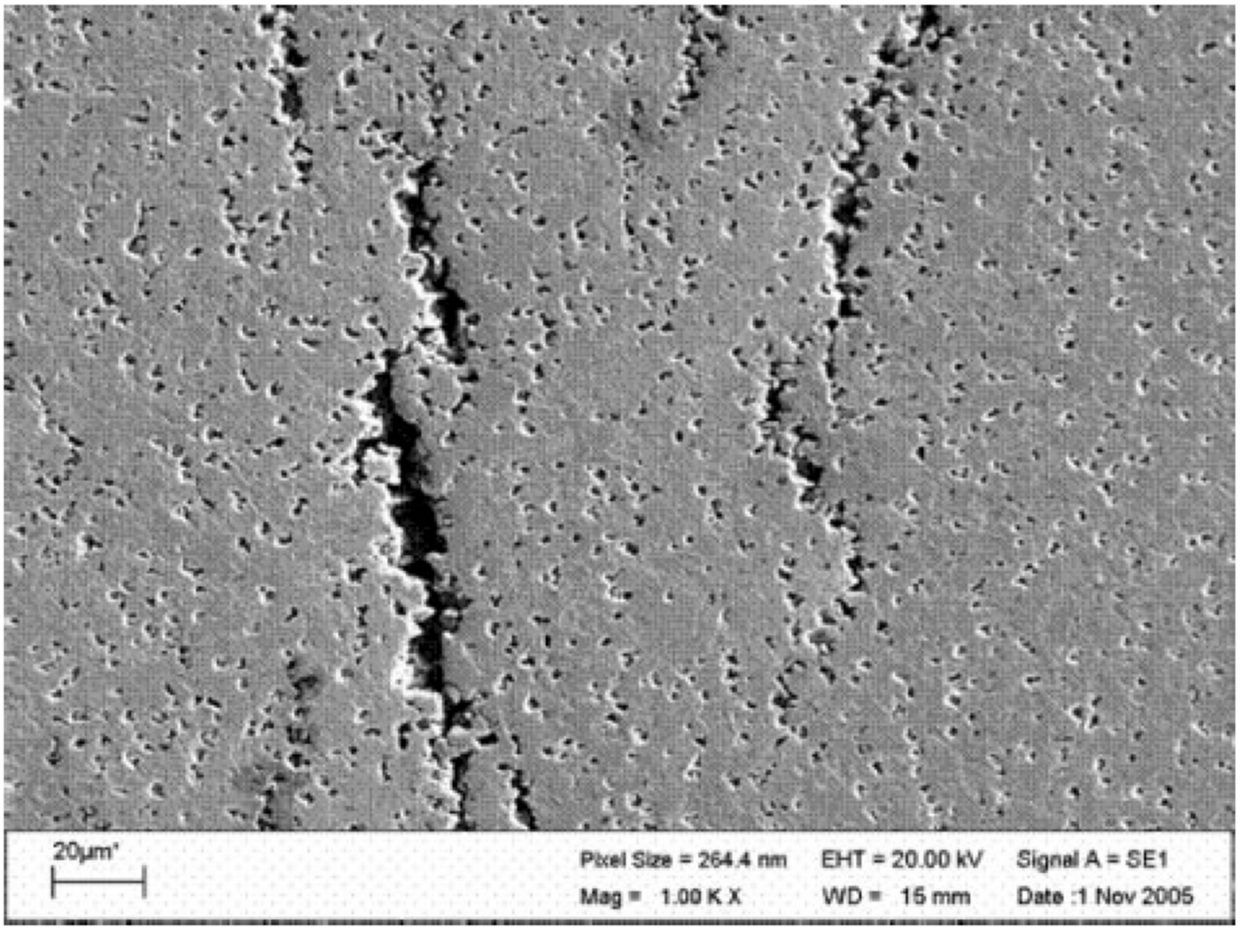


Figure 1-4. Scanning electron micrograph illustrating Type IV creep damage (cavitation, aligned cavitation, and micro-cracking) in the HAZ of a F91/P91 transition weld which failed after 20,000 h at 568°C. Reproduced from Brett et al. (Brett, 2007).

4. the effect of alternative heat treatments, such as a reduced pre-weld tempering temperature for the base metal, for improving the microstructure in the Type IV HAZ region after PWHT (Yamamoto et al., 2014; Yu et al., 2013)
5. the morphology of creep cavitation in the Grade 91 Type IV region (Parker, 2014)
6. the effect of constraint and stress state on creep damage, such as cavity nucleation and growth (Goyal et al., 2014; Goyal and Laha, 2014; Niu et al., 2021; X. Wang et al., 2020)
7. modeling and prediction of creep behavior of Grade 91, particularly microstructure-based models (Zhang et al., 2020a, 2020b)

To provide further background for understanding current research on Type IV damage in CSEF steels and the research presented in this dissertation, the literature review in Chapter 2 discusses several pertinent topics regarding creep behavior of welded CSEF steels.

1.3 Research Objectives

Based on the preceding introduction and background, this dissertation investigated specific aspects of the nature of Type IV creep damage occurring in the fine-grained and inter-critical HAZ in weldments of Grade 91 CSEF steel. The research presented herein was conducted with the following primary objectives with regard to achieving an improving understanding of the underlying mechanism(s) and factors involved in Type IV creep behavior.

The primary research objectives of the current dissertation are as follows:

1. *To investigate whether creep cavitation in the HAZ of dissimilar Grade 91 weldments is primarily associated with differences in base metal chemical composition and inclusion content, or is primarily associated with changes in microstructure in the susceptible regions of the HAZ.*

The significance of the first objective relates to identifying which material factors are more important to control in order to improve the creep properties of Grade 91 weldments.

2. *To investigate whether longitudinal loading during creep produces differences in creep behavior and damage between weld regions in a Grade 91 weldment with different heat treatment conditions.*

   The significance of the second objective relates to evaluating the effect of constrained creep deformation on Type IV creep damage in Grade 91 weldments.

Chapter 2 Literature Review

2.1 Metallurgy of Creep Strength Enhanced Ferritic (CSEF) Steels

Before properly considering the Type IV creep behavior of welded, 9-12 wt.% Cr creep strength-enhanced ferritic (CSEF) steels, it is necessary to start with an understanding of the underlying metallurgy of these alloys and of the baseline creep behavior (apart from effects of welding) at elevated temperatures. To this end, some basic metallurgy of CSEF steels—also commonly identified in the literature as tempered martensite ferritic steels (TMFS)—will be reviewed in terms of basic microstructure, descriptive terminology for that microstructure, strengthening mechanisms, precipitation behavior, and effects of tempering.

2.1.1 Morphology and Substructure of Martensite in Steels

Since CSEF steels are martensitic steels and are placed in service with a more complex microstructure than typical low carbon steels with simple ferrite/pearlite structures, consistent terminology is needed to accurately describe the distinct features of a CSEF microstructure. Although different terms have persisted in the literature, the chosen terminology used in the present work to identify the various features of a martensitic microstructure will be briefly described, beginning with the morphology and substructure of martensite. The primary type of martensite occurring in steels is alpha prime martensite with a body-centered cubic (BCC) or body-centered tetragonal (BCT) crystal structure (Maki, 2012). Within the alpha prime martensite type, five morphologies have been observed, but the two principal morphologies are lath martensite and plate (or lenticular) martensite (Krauss and Marder, 1971; Maki, 2012). The occurrence of different martensite morphologies in alpha prime martensite is influenced by several factors including Ms temperature, carbon content, austenite stacking fault energy, and critical resolved shear stress for slip or twinning. Lath martensite occurs at higher Ms temperatures and lower carbon contents, and is the morphology which occurs in a majority of commercial heat-treatable steels (Maki, 2012),

including 9Cr-1Mo-V-Nb steel (Grade 91). The distinct units comprising the microstructure of alpha prime lath martensite are packets, blocks, and laths, which are all formed within individual prior austenite grains (PAGs) during the austenite to martensite transformation upon cooling. The relationship between a single PAG and the packet, block, and lath substructure is illustrated in Fig. 2-1. The lath may be considered as the smallest unit of martensite, with typical lath width on the order of 0.2 to 0.5 μm (Maki, 2012). A block is considered as a collection of laths which are parallel to one another and have the same orientation variant, and a packet is a collection of blocks which have the same martensite habit plane (interface plane between martensite and austenite). Lath martensite exhibits further substructure within a lath, specifically the occurrence of dislocations which are formed to accommodate the transformation strain.

As a brief illustration of the effect of martensite microstructure on mechanical properties, Morito et al. (Morito et al., 2006) compared the interrelation between PAG size, block size, and yield strength in a simple Fe-0.2C alloy and a Fe-0.2C-2Mn alloy. They found that packet size increased linearly with increasing PAG size in both alloys with no apparent difference due to the Mn addition. The trend of block size (characterized as block width, measured by EBSD) was slightly different; the Fe-0.2C alloy showed a larger block size overall than Fe-0.2C-2Mn, regardless of PAG size. The block size in the Fe-0.2C alloy increased linearly with PAG size, up to a PAG size of 200 μm, after which there was a plateau in block size. In the Fe-0.2C-2Mn alloy, the block size increased linearly and continuously as the PAG size increased; as stated, the block size was decreased overall by the Mn addition. The authors attributed this change to higher hardness of the parent austenite phase due to solid solution hardening by Mn . They also reported that the 0.2% offset yield strength increased linearly with decreasing block size and that the Fe-0.2C-2Mn alloy showed overall higher yield strength than Fe-0.2C, as shown in Fig. 2-2. The main point is that the martensite

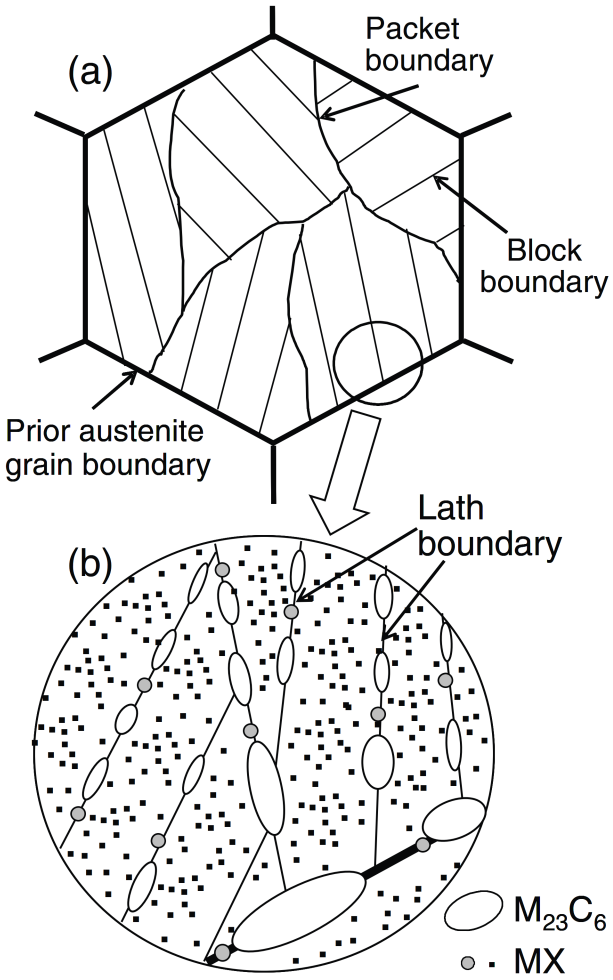


Figure 2-1. Schematic illustration of CSEF structure which is responsible for strengthening, (a) at the scale of individual grains, showing the different boundary types and (b) at the scale of individual laths within each PAG, showing M23C6 and MX precipitation along lath boundaries and small-scale MX precipitation within the matrix. Reproduced from Abe (Abe, 2008).

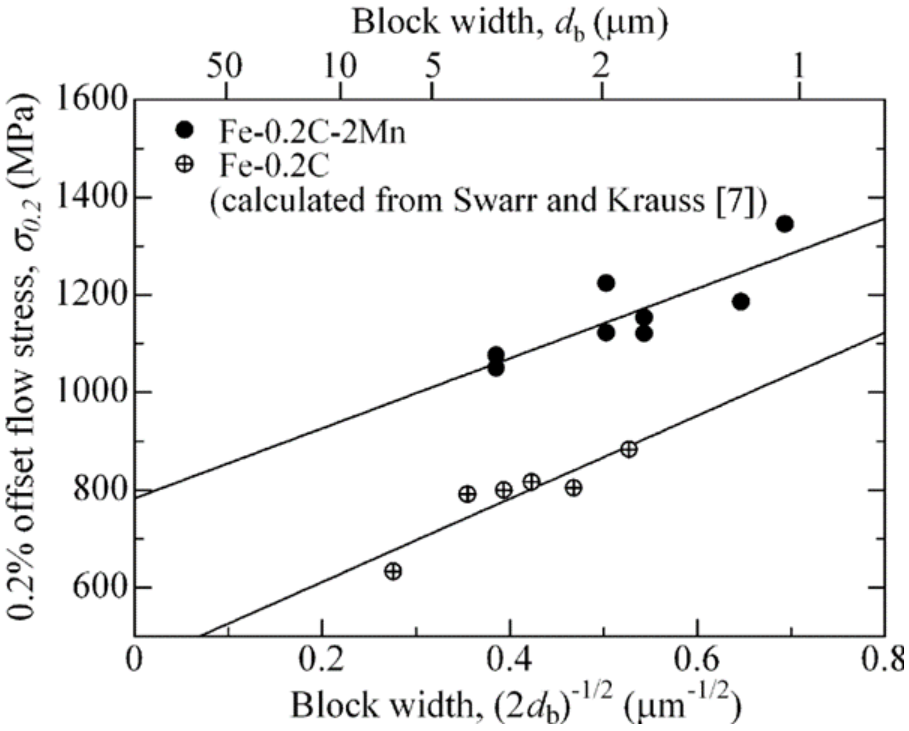


Figure 2-2. Relationship between 0.2% offset yield strength and martensite block width (plotted as the reciprocal width) for two martensitic iron alloys. The graph illustrates the inverse correlation between block width and yield strength. (Refer to Fig. 2-1 for the distinction between blocks and prior austenite grains within a martensitic microstructure.) Reproduced from Morito et al. (Morito et al., 2006).

contributes to strengthening, whether at room temperature or at elevated temperatures during creep (as will be discussed in a later section). In fact, the PAG size does not exert a significant influence on the mechanical properties (e.g. yield strength) of CSEF steels, as shown by Bonadé et al. (Bonadé et al., 2004) for two tempered Fe-Cr-C martensitic steels (Fe-9Cr-0.1C and Fe-12Cr-0.1C) which exhibited <5% difference in yield strength with a nearly 2x difference in PAG size. This indicates that a Hall-Petch relation between grain size and yield strength is not observed for tempered martensitic steels. Thus, it is expected that changes in substructure such as recovery of dislocations or an increase in lath size (i.e. lath coarsening), rather than changes in PAG size, will have a detrimental effect on yield and tensile strengths as well as creep strength; as will be discussed further, substructure can potentially be altered by heat treatment or the heat input from a welding thermal cycle. Conversely, factors which inhibit dislocation recovery or coarsening (stabilizing the substructure) will improve overall microstructural stability during creep and thus enable a greater degree of strength to be retained during long-term creep exposure.

2.1.2 Microstructure of CSEF Steels

The typical microstructure of Grade 91 CSEF steel will now be illustrated using the basic terminology discussed in the preceding section. Fig. 2-3 through Fig. 2-4 depict the typical microstructure of a tempered Grade 91 base metal as revealed by OLM and SEM examination. In the optical micrographs in Fig. 2-3, the martensitic microstructure appears as larger prior austenite grains (PAGs) containing finer substructure in the interior (packet/block/subgrains, which were formerly laths prior to tempering). Extensive carbide precipitation is also observed in the form of fine, dark particles, although the precipitation is not clearly resolved at this magnification. The scanning electron micrographs at higher magnification in Fig. 2-4 more clearly reveal the microstructure of a tempered CSEF steel. Fig. 2-4(A) reveals that the morphology of the

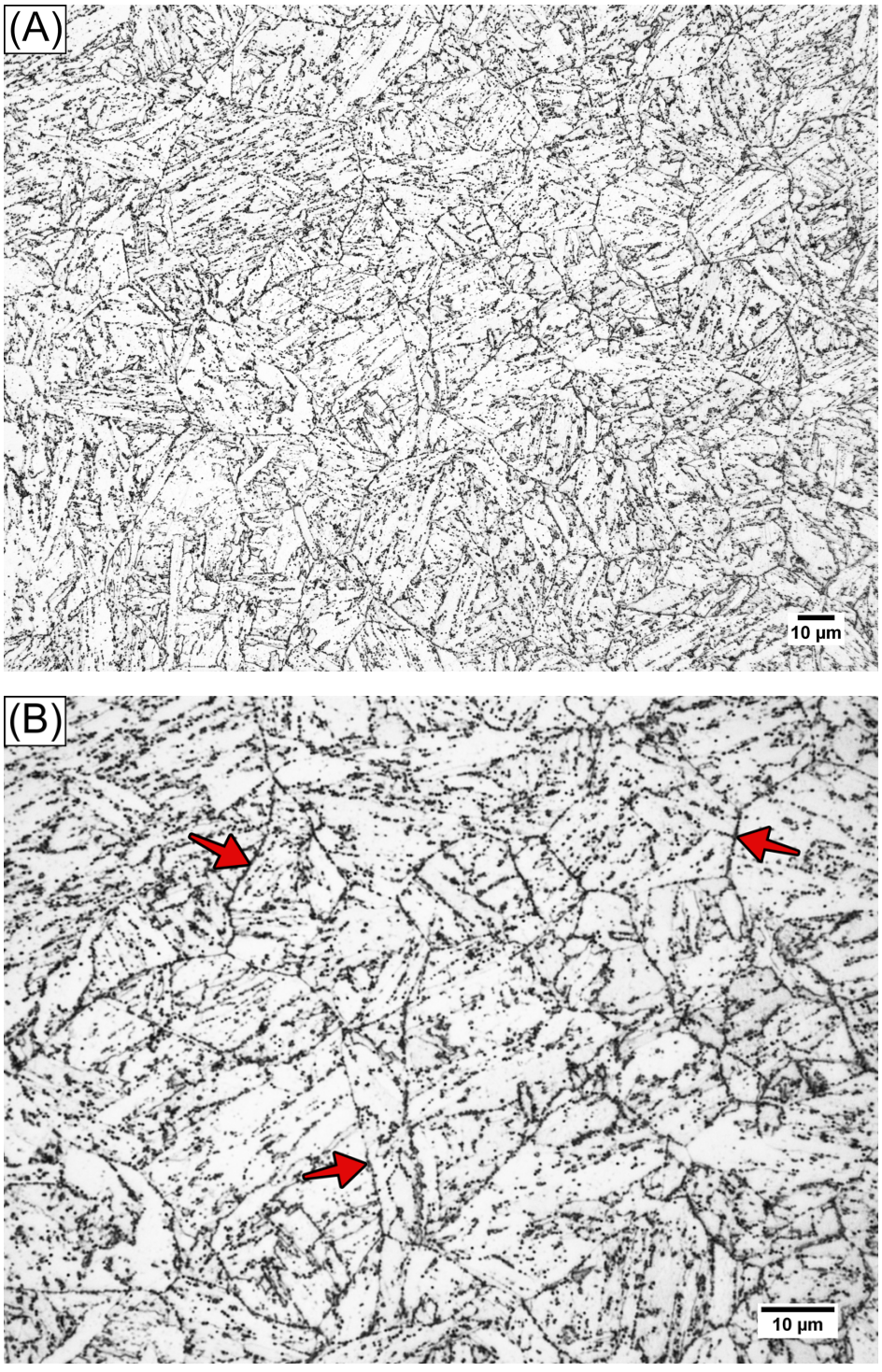
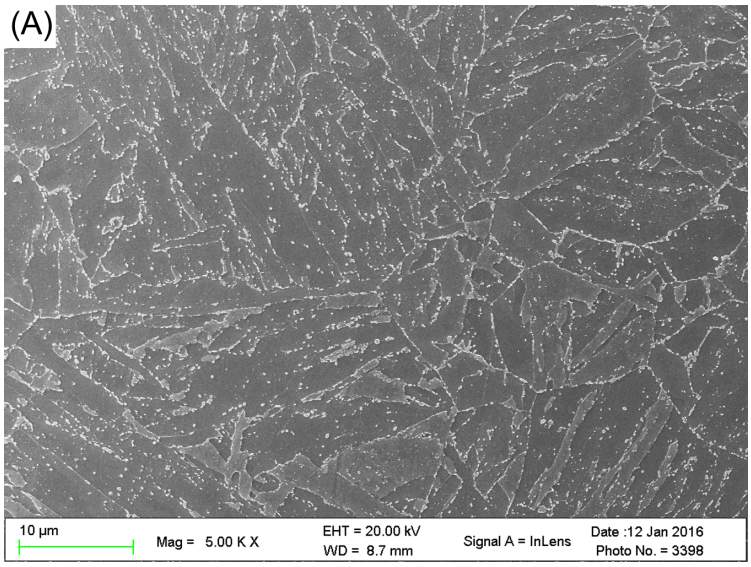
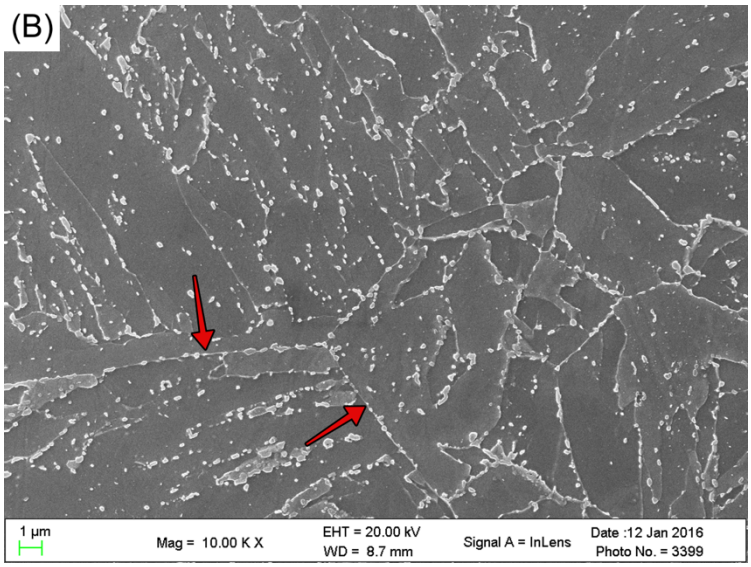


Figure 2-3. Optical micrographs revealing the typical microstructure of a tempered CSEF steel (9Cr-1Mo-VNb, Grade 91) at 500X and 1000X. The martensitic structure is evident, with larger prior austenite grain boundaries (PAGBs, denoted by red arrows) containing finer substructure in the form of packets, blocks, and subgrains (formerly laths, prior to tempering). Etchant: Fry's Reagent.

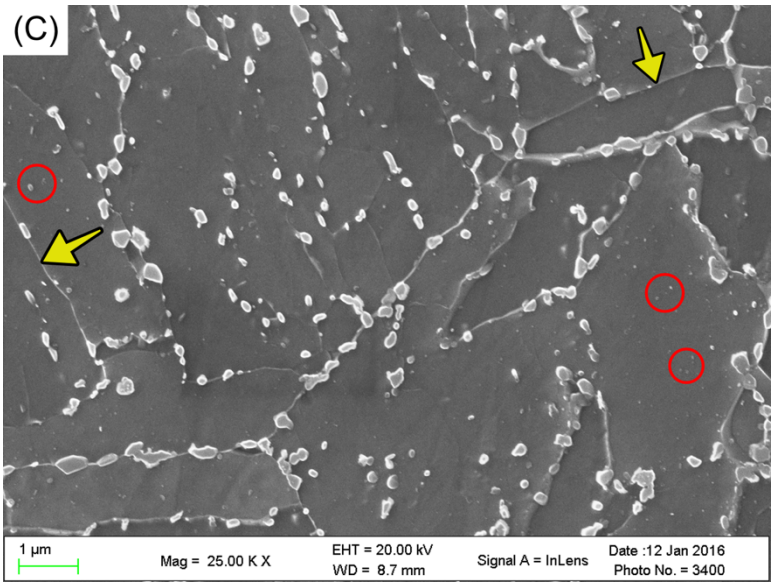


(a) 5kX SEM micrograph of Grade 91 base metal



(b) 10kX SEM micrograph of Grade 91 base metal

Figure 2-4. Secondary electron SEM micrographs revealing the typical microstructure of a tempered CSEF steel (9Cr-1Mo-VNb, Grade 91). The martensitic structure is clearly evident, with larger prior austenite grains (PAGBs, red arrows) containing finer substructure, in the form of blocks and subgrains. In particular, the parallel arrangement of subgrains (preserved from the initial lath structure after normalizing and tempering) and the presence of fine carbides along the subgrain boundaries (yellow arrows) can both be observed. In (c), very fine precipitates (<<1 μm, most likely carbides) are discernible in the subgrain matrix and noted by red circles. Etchant: 10% Nital.



(c) 25kX SEM micrograph of Grade 91 base metal

Figure 2-4 (continued)

original lath structure is preserved in the subgrains which form during tempering. In this normalized and tempered base metal, the boundaries are generally clearly defined and distinct; several different boundary types are denoted in Fig. 2-4(A), namely PAGBs and block boundaries. The clear delineation of the boundaries is due to extensive carbide precipitation along the boundaries, as shown in Fig. 2-4(B) (boundary carbides denoted by red circles). Fig. 2-4(B) also shows the parallel alignment of adjacent subgrains with a narrow aspect ratio and the presence of carbides on the subgrain boundaries; the size of the subgrain boundary carbides is under 1 μm. Fig. 2-4(C) shows the presence of fine carbides, <<1 μm in size, within the subgrain matrix as shown by the red circles; subgrain boundaries within the microstructure are indicated by yellow arrows.

Fig. 2-5 shows the typical microstructure of a tempered CSEF steel (in this case, a 12Cr CSEF steel, X20CrMoV12-1) as revealed by transmission electron microscopy in the as-quenched and tempered conditions. In both conditions, it is apparent that the microstructure is comprised of fine, parallel units with a high aspect ratio; these units identified as *laths* in the as-quenched condition, and *subgrains* after tempering. The distinction arises from the fact that lath boundaries originate from the austenite to martensite transformation, while subgrain boundaries only occur after tempering as a result of dislocation recovery (polygonization) (Dronhofer et al., 2003). In both conditions, it is evident that the microstructure contains a high density of dislocations within the laths/subgrains, such that the individual dislocations are not distinguishable (particularly in the as-quenched condition). From Fig. 2-5(B), it is apparent that the subgrain width (narrow dimension) after tempering is less than 1 μm. Although Fig. 2-5 depicts the microstructure of X20 steel, the characteristics of other CSEF steels such as Grade 91 are similar; Fig. 2-6 shows the similar microstructural appearance of X20 and Grade 91 after quenching and extended tempering (100 h at 750°C). In Fig. 2-6(B),

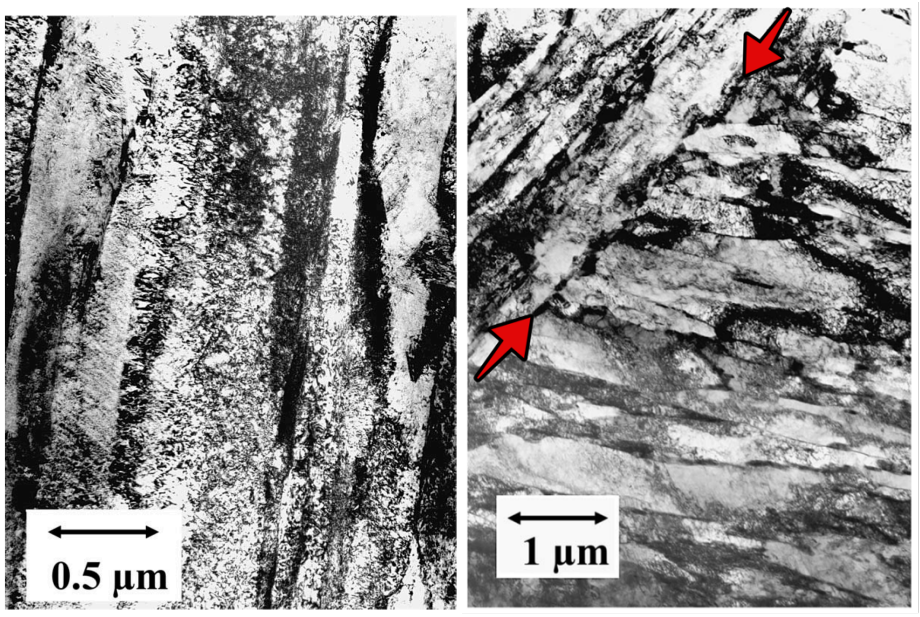


Figure 2-5. Transmission electron micrographs revealing the typical microstructure of an CSEF steel (X20CrMoV12-1) in the (a) quenched condition (b) quenched and tempered condition, 750°C/1 h. The presence of a high dislocation density within the laths in (a) and within the subgrains in (b) is clearly evident, and it can be seen that the high aspect ratio of the initial laths (a) has been preserved in the subgrains which formed as a result of tempering (b). Also note in (b) that the subgrain width (in the narrow dimension) is <1 μm and that a subgrain boundary is visible (noted by the red arrows) at the interface between two subgrains. Adapted from Pešička et al. (Pešička et al., 2003).

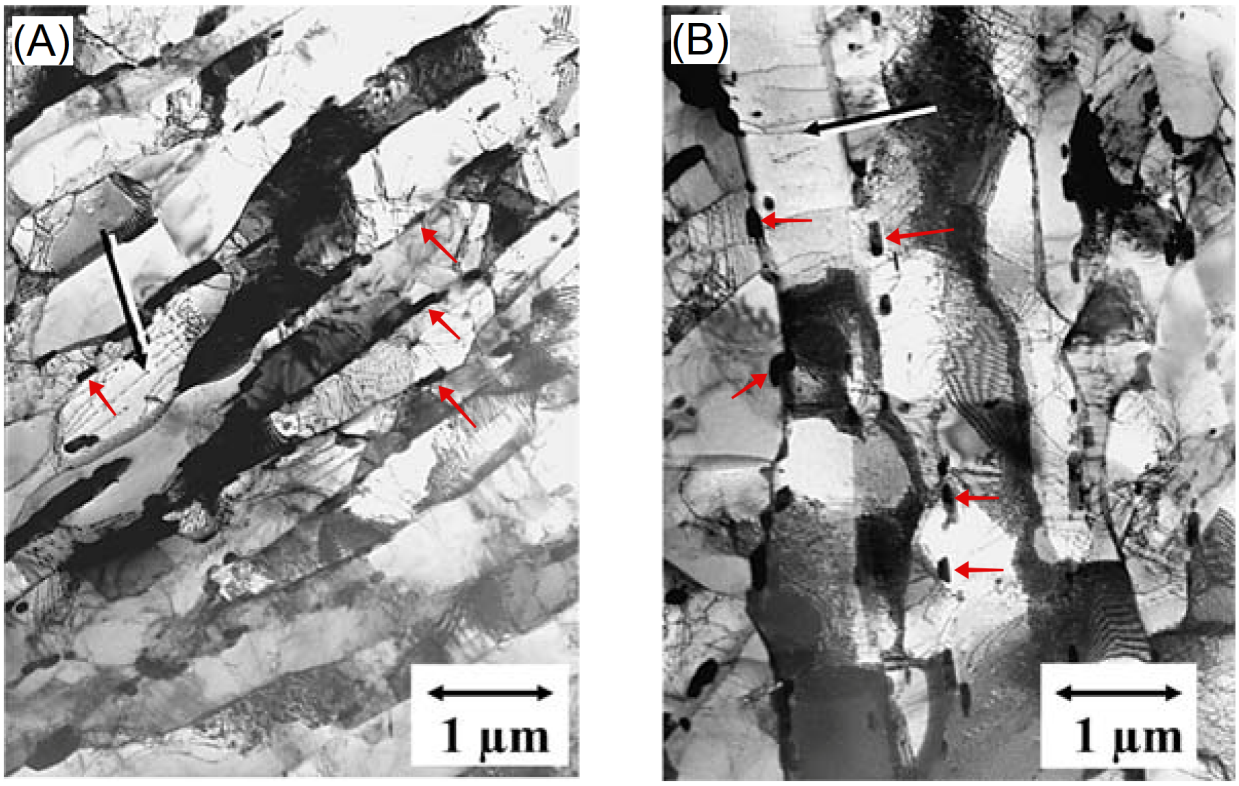


Figure 2-6. Transmission electron micrographs comparing the substructure of two CSEF steels after extended tempering at 750°C for 100 h (a) X20CrMoV12-1 (b) 9Cr-1Mo-VNb (P91). Note that in both steels, an elongated, lath-like subgrain morphology is still apparent, but dislocation recovery has occurred which is evident by a reduction in dislocation density (e.g. compared to Fig. 2-5). Regions of reduced dislocation density, where the density is low enough that individual dislocations can be resolved, are indicated by black arrows in both micrographs. Particles along the boundaries (most likely carbides) are noted by red arrows. Adapted from Pešička et al. (Pešička et al., 2003).

carbides are present along the subgrain boundaries (noted by red arrows); carbides along the boundaries comprise a fundamental aspect of the strengthening mechanism of CSEF steels as described in the following section.

2.1.3 Strengthening Mechanisms in CSEF Steels

The strengthening mechanisms in CSEF steels have been reviewed by Maruyama et al. (Maruyama et al., 2001) and by Abe (Abe, 2008). Both Maruyama et al. (Maruyama et al., 2001) and Abe (Abe, 2008) describe three primary mechanisms that contribute to the high temperature properties of CSEF steels: solid solution strengthening, precipitation strengthening, and dislocation strengthening by subgrain boundaries[1] and free dislocations (i.e., dislocations not confined within boundaries (Pešička et al., 2003)). Fundamentally, strengthening mechanisms impede plastic deformation at high temperatures by inhibiting dislocation motion. Although each mechanism presents a separate barrier to dislocation motion, there can be significant interaction between mechanisms to increase the combined strengthening effect. All three mechanisms occur to some extent in CSEF steels, but both Maruyama et al. and Abe state that the primary strengthening mechanism in CSEF steels is *dislocation strengthening* by means of lath or subgrain boundaries (i.e. "sub-boundary" or "substructure" strengthening). However, cooperative interaction between primary and secondary strengthening mechanisms is necessary to produce a material with usable long-term creep strength, since the high dislocation density required to produce satisfactory dislocation strengthening is also unavoidably accompanied by a large driving force for dislocation recovery (Maruyama et al., 2001). For this reason, dislocation strengthening on its own is not a satisfactory method for achieving stable, high creep strength over long-term exposure at low stresses as experienced in power generation. Thus, solid solution strengthening and

[1] It should be noted here that subgrain boundaries are arrangements of dislocations which reduce the local strain energy; subgrain boundaries are classified as boundaries which have a low misorientation angle (e.g. 1°) (Eggeler et al., 1987; Peŝiĉka et al., 2004).

precipitation strengthening are necessary to stabilize the primary strengthening mechanism (i.e. dislocations) at high temperature (Maruyama et al., 2001) by providing obstacles to dislocation motion and recovery. From the outset, the point should be carefully noted that the primary strengthening mechanism in CSEF steels is inherently unstable, particularly under creep conditions where plastic deformation is occurring at high temperature, and thus CSEF steels are inherently susceptible to *creep damage due to microstructural degradation* (Dyson, 1988).

The interaction of different strengthening mechanisms and the necessity of a combined approach to strengthening, such as utilized in CSEF steels, is illustrated in Fig. 2-7 from Maruyama et al. (Maruyama et al., 2001), which shows minimum creep rate versus stress for five iron-base alloys utilizing one or more of the aforementioned strengthening mechanisms. It is apparent that a noticeable strengthening effect is produced either by solid solution strengthening (Fe-2.3W) or by precipitation strengthening (Fe-VNbC with V and Nb carbides). However, greater strengthening is achieved when dislocation substructure strengthening from martensitic transformation (addition of Cr) is combined with precipitation (Fe-9Cr-VNbCN), or with the further addition of tungsten for solid solution strengthening (Fe-9Cr-2.3W-VNbCN). This last alloy is representative of the overall strengthening behavior of 9-12 wt.%. Cr CSEF steels, which contain Cr for martensitic transformation, strong carbide/nitride-forming elements such as V and Nb, and contain Mo or W for solid solution strengthening. As can be seen from the relative positions of the curves in Fig. 2-7, strengthening is not a simple, additive effect from all the mechanisms which are operative in a given alloy (Maruyama et al., 2001).

Encompassing several of the aforementioned mechanisms, Abe (Abe, 2008) stated that primary creep strengthening in a 9Cr-3Co steel originated from "sub-boundary hardening enhanced by fine distributions of precipitates along the lath and block

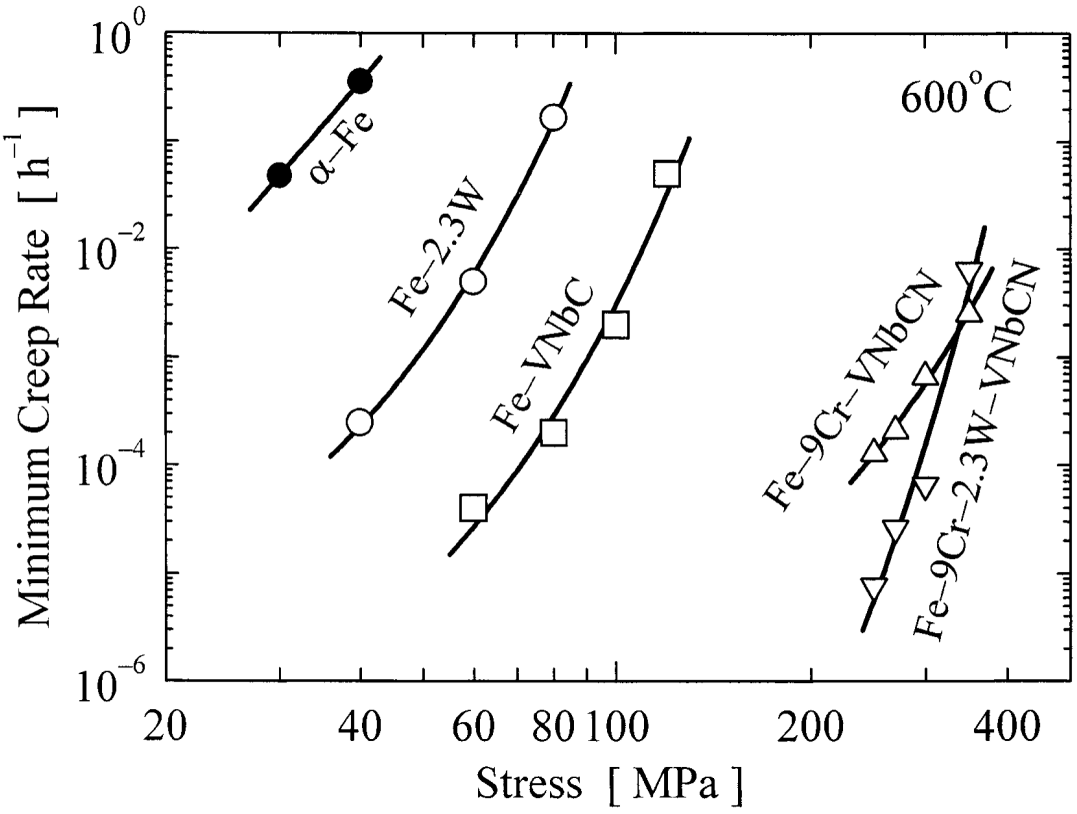


Figure 2-7. Plot of minimum creep rate versus creep stress for five iron-base alloys, illustrating the effects and interactions of different strengthening mechanisms: alpha-Fe (base alloy, no additional strengthening); Fe-2.3W (solid solution); Fe-VNbC (precipitation); Fe-9Cr-VNbCN (precipitation strengthening and dislocation substructure from martensitic transformation); Fe-9Cr-2.3W-VNbCN (all of the preceding mechanisms). Reproduced from Maruyama et al. (Maruyama et al., 2001).

boundaries." A similar definition of the strengthening mechanism for TMFS steels has been stated as "carbide stabilized substructure hardening" by Kostka et al. (Kostka et al., 2007). Abe (Abe, 2008) supported his definition with creep test results from a series of 9Cr-3W-3Co-0.2V-0.05Nb-0.05N steels which varied in carbon content from 0.002 to 0.16 wt.%. After comparing the creep properties of these steels, Abe reported that the lowest carbon content of 0.002 wt.% showed the longest time to rupture and the lowest minimum creep rate, as shown in Fig. 2-8. The microstructure of the 0.002 wt.% C alloy showed the occurrence of nanoscale (<10 nm) MX precipitates on the various boundaries (lath, block, packet) as shown in Fig. 2-9, in contrast to one of the higher carbon materials (0.078 wt.%) which exhibited coarser $M_{23}C_6$ and MX precipitates along the boundaries, as shown in Fig. 2-10. Abe attributed the more favorable creep properties of the 0.002 wt.% C material to the occurrence of the nanoscale MX precipitates, specifically to the fact that these MX precipitates were present in a higher density and were located primarily on the boundaries, as compared to the 0.078 wt.% C alloy where the MX precipitates were mainly within the grain interiors. Therefore, Abe (Abe, 2008) stated that the higher density of precipitates along the boundaries reduced the efficiency of dislocation absorption at the boundaries, thereby limiting the migration of lath and block boundaries, i.e. reducing the extent of lath coarsening, with the result of increasing the creep strength since the creep strength of CSEF steels is linked to the width of laths or blocks, rather than the PAG size.

As stated previously, it is the combined structure of a high dislocation density together with precipitates to stabilize the subgrain structure which gives TMFS/CSEF steels their strength; high dislocation density alone does not provide satisfactory strength. Kostka et al. (Kostka et al., 2007) convincingly demonstrated this fact by comparing the creep behavior of an X20 CSEF steel with that of a Fe-10Cr binary alloy with similar Cr content in order to investigate the interaction of carbides and subgrain boundaries and

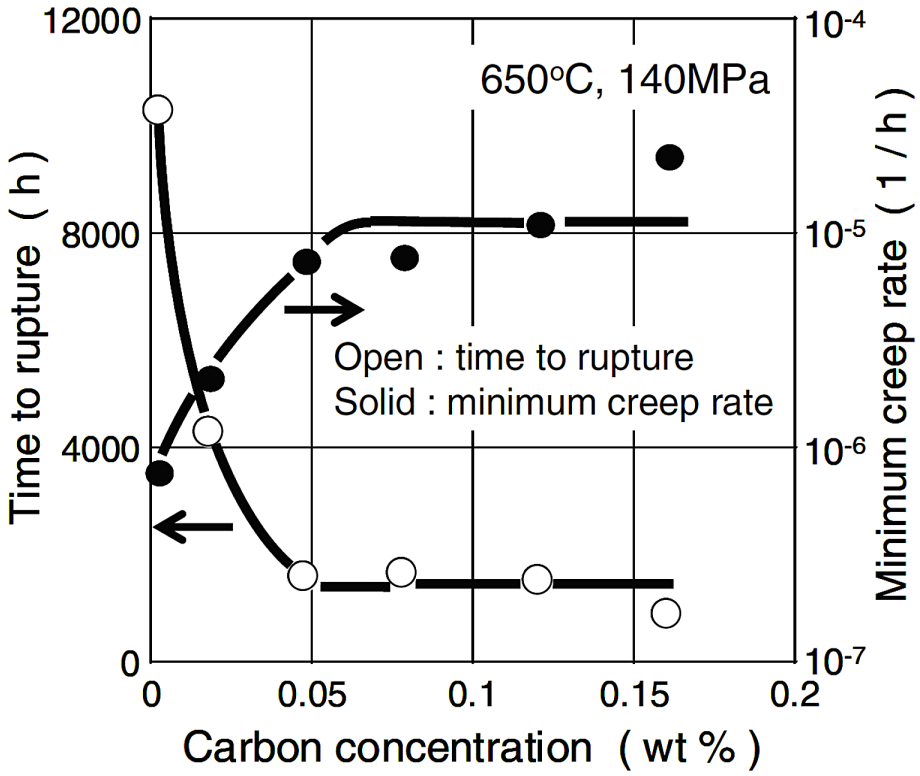


Figure 2-8. Rupture time and minimum creep rate as a function of carbon content for 9Cr-3W-3Co-0.2V-0.05Nb-0.05N tempered martensite ferritic steel, at creep conditions of 650°C/140 MPa. Reproduced from Abe (Abe, 2008).

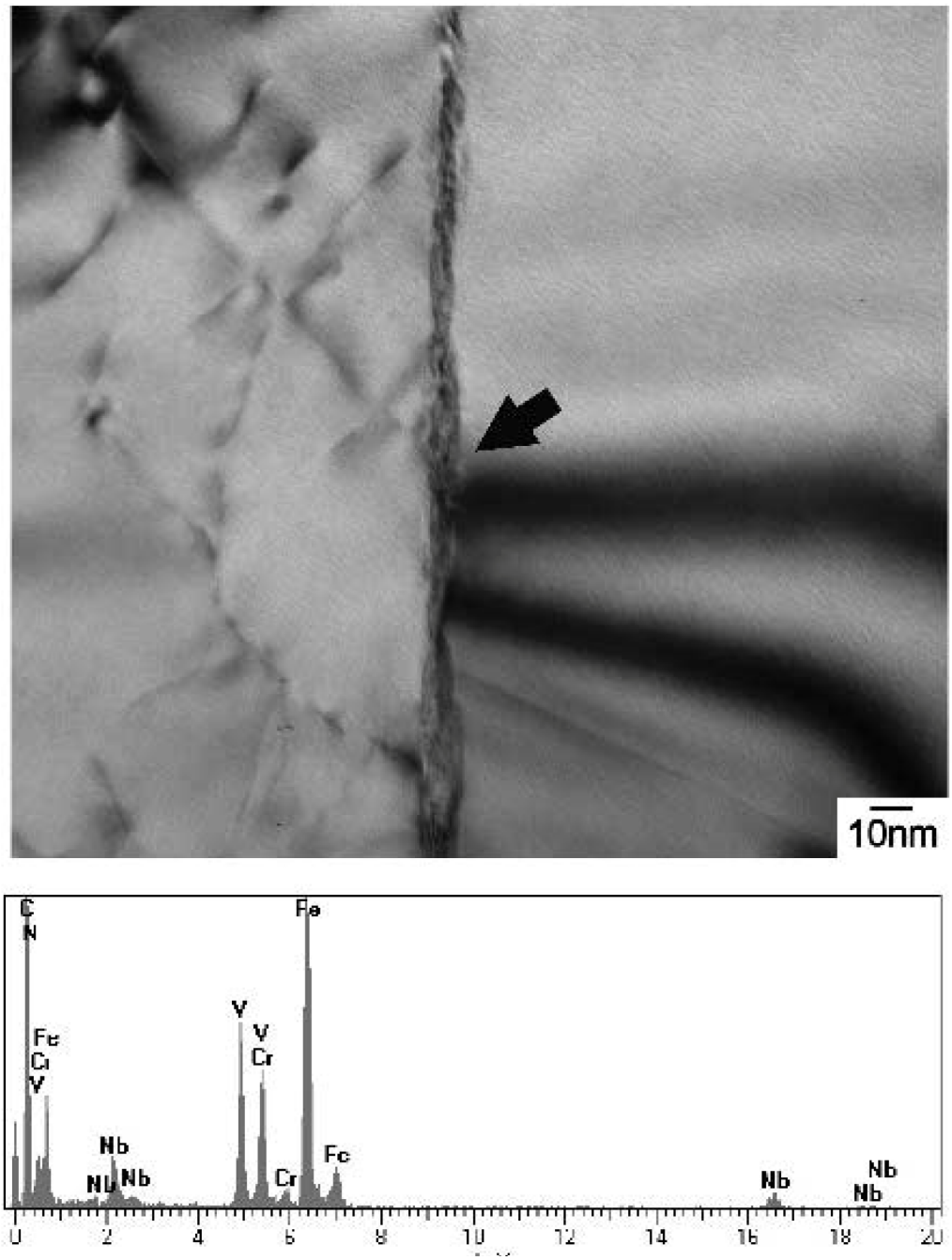


Figure 2-9. TEM bright-field micrograph (top) and associated EDS spectrum (bottom) revealing nanoscale MX precipitation (arrow) along a PAG boundary in a 9Cr-3W-3Co-0.2V-0.05Nb-0.05N-0.002C steel after tempering. Adapted from Taneike et al. (Taneike et al., 2004).

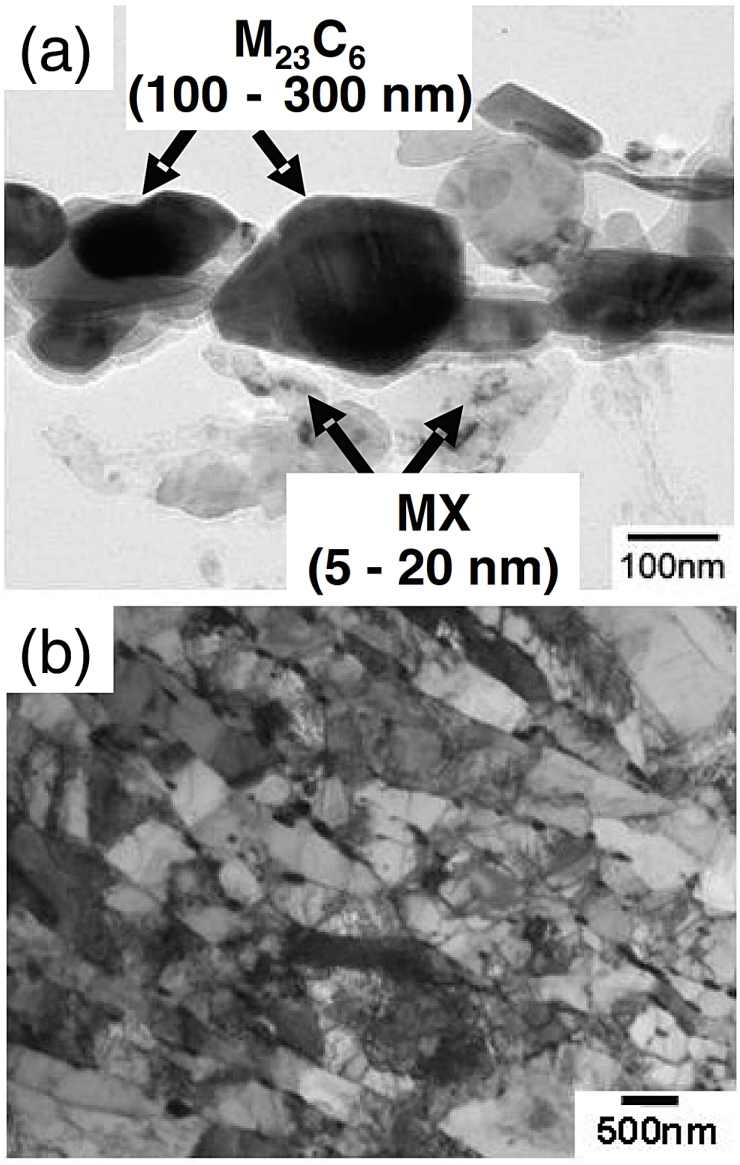


Figure 2-10. TEM bright-field micrographs from 9Cr-3W-3Co-0.2V-0.05Nb-0.05N-0.078C steel after tempering (a) extraction replica showing precipitates near a PAGB (b) thin foil showing lath-like subgrain structure. Reproduced from Abe (Abe, 2008).

the resulting effect on creep properties. In order to produce materials with similar room temperature properties (evaluated with hardness), they subjected the X20 material to typical austenitizing and tempering heat treatments while the Fe-10Cr alloy was subjected to equal channel angular pressing (ECAP) to produce an extremely-fine grained microstructure with a high dislocation density, similar to that present in the X20 material as a result of martensitic transformation. As a result of these processing steps, they produced two microstructures with qualitatively similar subgrain sizes and dislocation densities as shown in Fig. 2-11, but with the key difference being that in the X20 material, carbides were present on the subgrain boundaries, while no carbides were present (either on subgrain boundaries or elsewhere) in the Fe-10Cr alloy. They observed that the X20 material showed a minimum creep rate which was four orders of magnitude lower than Fe-10Cr (~2E-5 s-1 for Fe-10Cr and ~2E-9 s-1 for X20). Notably, TEM examination revealed the presence of a bimodal distribution of subgrain sizes in the Fe-10Cr material after creep testing, with some near the original subgrain size on the order of 0.5 μm and also some enlarged subgrains between 2 to 5 μm in size. On the basis of the increases in subgrain size and a resulting probability plot of subgrain size (see Fig. 2-12), Kostka et al. (Kostka et al., 2007) concluded that recrystallization occurred in the Fe-10Cr alloy during creep. In the pre-creep condition (ECAP + tempering at 600°C/10 min), they indicated that a high dislocation density was still observed and that some subgrain growth had already occurred; they did not comment on how the dislocation density changed after creep testing. In comparison, the X20 material after creep testing did not show a bimodal distribution of subgrain sizes, and although some subgrain growth was observed, the increase in subgrain size was smaller than in Fe-10Cr. From this observation, the authors stated that recrystallization had occurred in the Fe-10Cr binary alloy, but not in the X20 alloy. They attributed this difference in microstructure to the presence of carbide particles on the subgrain boundaries in the X20 material. More specifically, they reported that carbides on subgrain boundaries acted to stabilize the boundaries, thereby limiting recrystallization

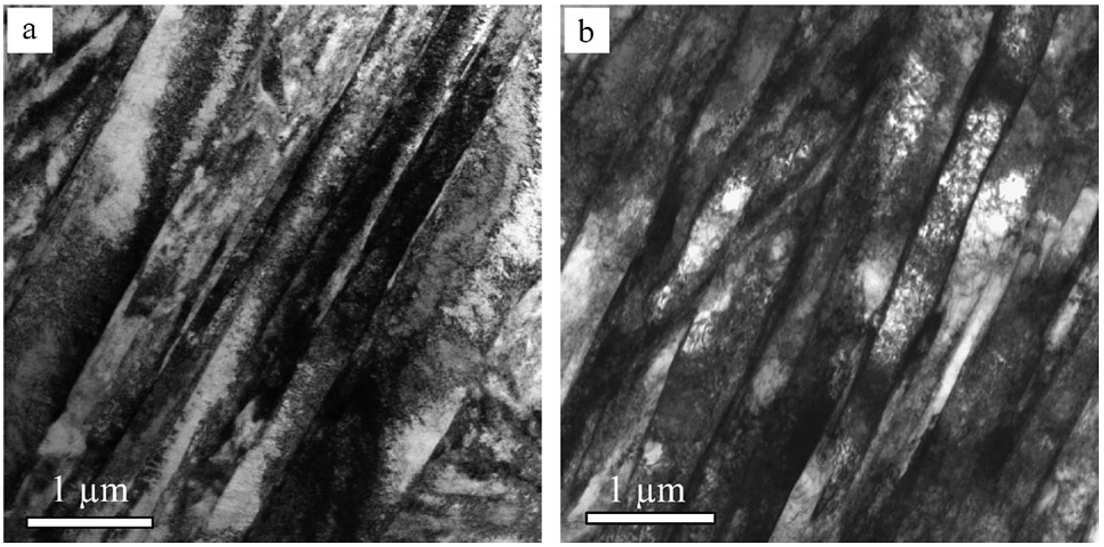


Figure 2-11. TEM micrographs of thin foils comparing the subgrain structure observed for two martensitic iron alloys: (a) X20CrMoV12-1 tempered martensite ferritic steel, normalized but not tempered (b) Fe-10Cr binary alloy after equal channel angular pressing (ECAP), not tempered. Note the close resemblance of the two substructures in terms of subgrain width and dislocation density; although not clearly resolved, the primary difference is that carbides are present along the subgrain boundaries in (a), but not in (b). Reproduced from Kostka et al. (Kostka et al., 2007).

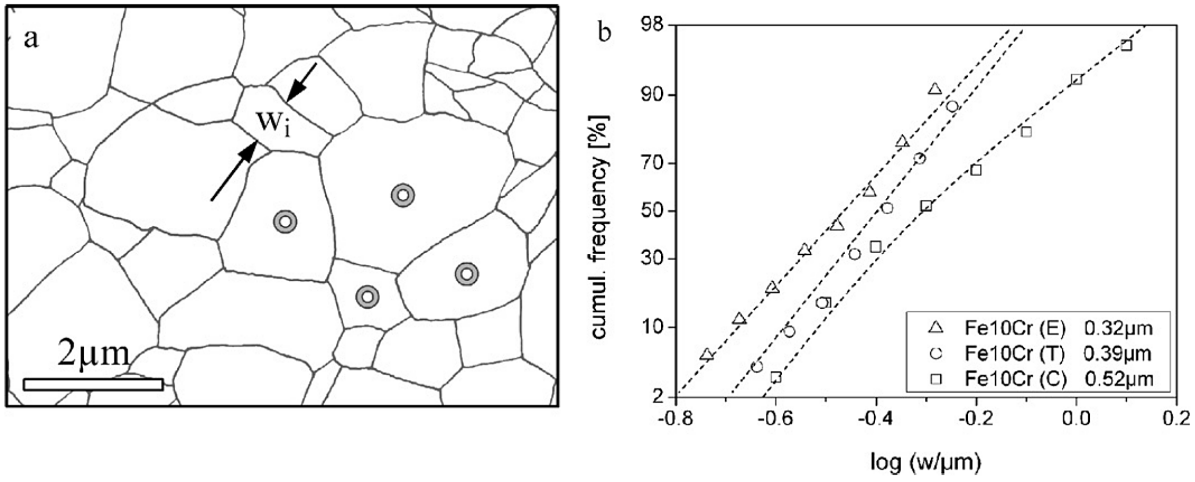


Figure 2-12. Results for determination of subgrain widths in the Fe-10Cr binary alloy. (a) schematic illustration of width dimension wi for an individual subgrain (b) cumulative frequency plots of subgrain width for Fe-10Cr in three conditions: after ECAP; after ECAP and tempering at 600°C/10 min; after ECAP, tempering, and creep at 600°C/100 MPa to 7% strain. Reproduced from Kostka et al. (Kostka et al., 2007).

and growth of the subgrains (and concurrent recombination/recovery of boundaries and dislocations). Based on these observations, they proposed the term "carbide stabilized substructure hardening" as a description of the creep strengthening mechanism in TMFS/CSEF steels. This terminology was proposed because the presence of carbides was considered to directly inhibit dislocation motion and also inhibit the recrystallization and growth of deformed subgrains (substructure).

The preceding discussion of the overall strengthening mechanism in CSEF steels such as Grade 91 emphasized the cooperative contributions of fundamental strengthening mechanisms and showed the necessity of subgrain boundary stabilization by precipitates (e.g. carbides and carbo-nitrides). The characteristics of secondary precipitation in CSEF steels are discussed in the following section with the goal of understanding how strengthening in CSEF steels may be affected by detrimental changes to precipitate size, spacing, or distribution, such as would occur within the heat-affected zone (HAZ) of a weld.

2.1.4 Precipitation Behavior in CSEF Steels

From the preceding description of strengthening mechanisms, the creep strength of CSEF steels such as Grade 91 originates from a fine-scale dislocation substructure which is stabilized from degradation (boundary migration and subgrain coarsening) during creep exposure by precipitates located on subgrain boundaries and within subgrain interiors. In an early publication, Vitek and Klueh (Vitek and Klueh, 1983) studied the carbide precipitation reactions which occurred in 9Cr-1Mo-VNb (modified 9Cr-1Mo) and 12Cr-1Mo-V-W CSEF steels as a function of heat treatment. The primary variables were austenitizing time and temperature, cooling rate from the austenitizing temperature, and tempering time and temperature. In both materials, they observed that the principal carbides were M23C6 carbides, along with some MC-type carbides containing Nb and V in the modified 9Cr material. Their studies showed that carbide precipitation was essentially complete after one hour of tempering at temperatures

between 700-780°C; however, after one hour of tempering at 650°C, the 9Cr-1Mo-VNb alloy showed incomplete precipitation[2]. Vitek and Klueh also measured hardness for various tempering conditions and found that while hardness decreased with more intensive tempering, the extent of precipitation did not vary (precipitate fraction, as measured by electrolytic extraction), leading them to hypothesize that the change in hardness resulted from coarsening of precipitates and subgrain structure.

Abe (Abe, 2008) reviewed the considerations for effective precipitation behavior in 9Cr tempered martensite ferritic steels (TMFS) to achieve good long-term creep performance. To achieve a stable microstructure and satisfactory long-term creep strength, it is necessary to prevent subgrain coarsening when a creep stress is being applied; the movement of subgrain boundaries during creep is effectively impeded by distributions of small, closely-spaced precipitates along the boundaries and within the subgrain matrix, in which the precipitates pin the boundaries as shown schematically in a previous figure (Fig. 2-1). Thus, coarsening of precipitates along the subgrain boundaries must be prevented because coarsening results in an increase in particle size as well as a increase in interparticle spacing. Several factors affecting the coarsening rate of precipitates (and consequently, of subgrains) include growth caused by diffusion, particularly along enhanced diffusion paths such as PAGBs, and the nucleation and growth of other phases which may consume the desirable strengthening phases during long-term creep exposure. The diffusion-controlled growth of precipitates is related to the solid solubility of the precipitates (either carbides or nitrides) in the matrix, with the coarsening rate becoming larger as the solid solubility increases. Thus, Abe showed in Fig. 2-13 that V- and Nb-containing precipitates such as NbN, VN, NbC, and VC are desirable because they have lower solid solubility. TiN and TiC, while more stable than

[2] This phenomenon has been intentionally utilized recently (e.g. by Yu et al. (Yu et al., 2013)), regarding the utilization of lower pre-weld tempering temperatures as a potential means for manipulating the carbide characteristics and evolution in CSEF steels to achieve more optimal properties after welding.

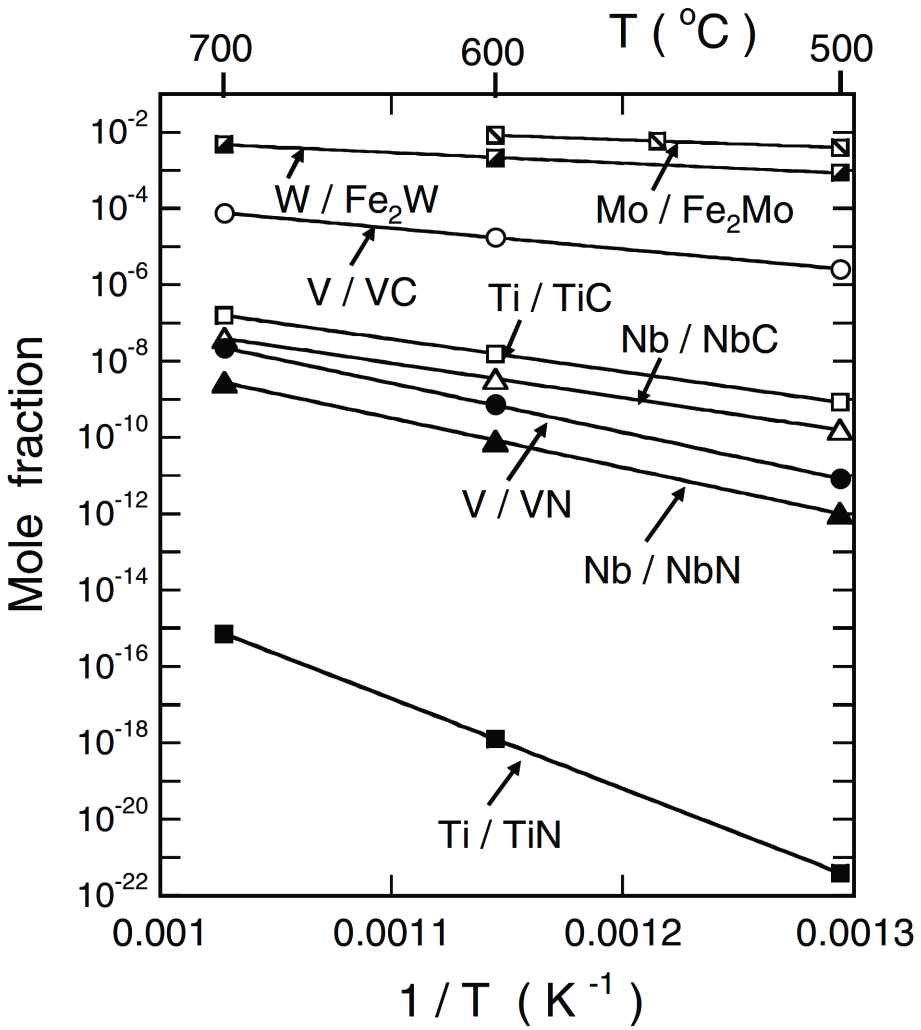


Figure 2-13. Diagram of solid solubility of alloying elements in equilibrium with their corresponding precipitate(s), either carbides, nitrides, or Laves phase (Fe2(Mo,W)). Element/precipitate pairs with lower values of mole fraction are more resistant to dissolution. Reproduced from Abe (Abe, 2008).

(Nb,V)N or (Nb,V)C, are so stable that these phases cannot be dissolved and re-precipitated by heat treatment. Notably, the common M23C6 carbides such as those formed in the 9Cr-1Mo-0.1C alloy (P9 alloy, predecessor to Grade 91) are less resistant to coarsening as reported by Wey et al. (Wey et al., 1981). Thus, Abe (Abe, 2008) considers that optimum precipitation characteristics in 9Cr TMFS can be obtained by increasing the proportion of MX carbonitrides and reducing the proportion of M23C6 carbides, and also by stabilizing M23C6 against coarsening by altering the solid solubility or interfacial energy of the carbide. The relative proportion of M23C6 can be decreased by lowering the carbon content, which increases the number of MX carbonitrides; furthermore, with lower carbon content, the MX carbonitrides more preferentially form on subgrain boundaries. This preferred microstructure is illustrated schematically in Fig. 2-14.

Precipitation behavior in CSEF base metals can also encompass other constituents besides carbides or carbonitrides, such as Laves phases, delta ferrite, and Z-phase. Of these, Z-phase and Laves phase are more commonly reported for 9Cr CSEF steels, while delta ferrite formation is a known issue in 12Cr steels due to ferrite stabilization from the higher Cr content. It is not completely clear whether these phases are entirely detrimental to creep performance, or whether they may partially contribute to strengthening under certain conditions. Sawada and coworkers (Sawada et al., 2011) observed the presence of Z-phase in P91 steel after creep exposure for 30,000 h at 600°C/70 MPa; the Z-phase particles were observed to gradually increase in size up to rupture. After 50,000 h, V- and Nb-containing MX precipitates significantly decreased in extent as shown in Fig. 2-15, leading to the hypothesis that Z-phase precipitation occurred at the expense of MX particles. However, this hypothesis is not uniformly supported by others in the literature. Panait et al. (Panait et al., 2010) studied the microstructure evolution in a Grade 91 steel after long-term creep exposure (>100,000 h) at 600°C/80 MPa. The characterization results indicated that after creep, four precipitate

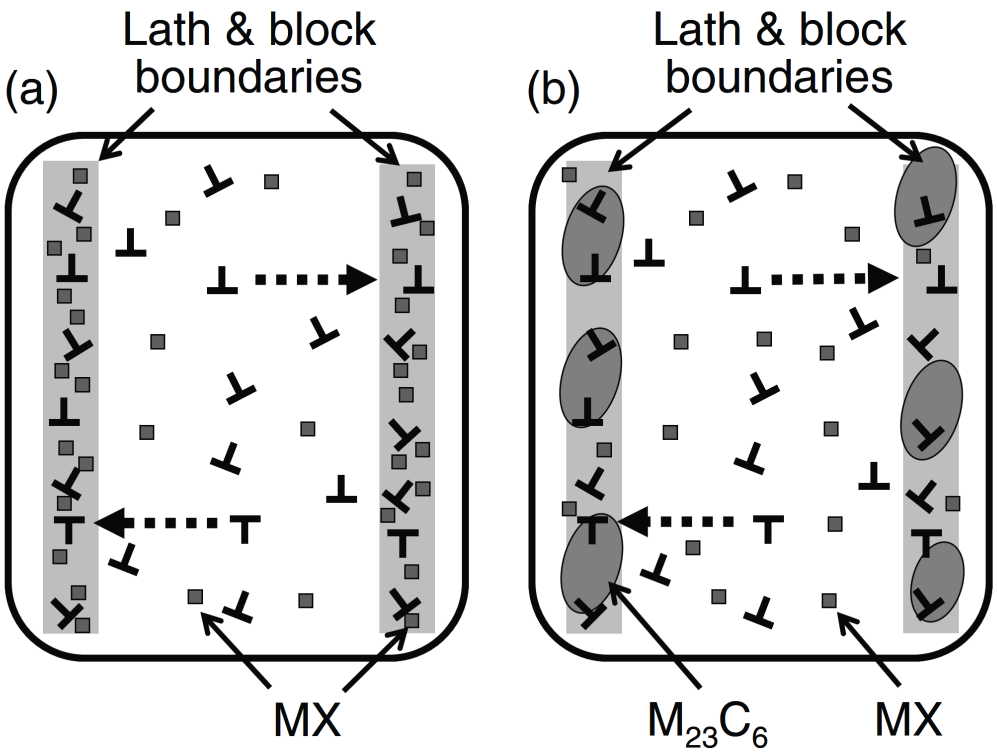


Figure 2-14. Schematic illustration of precipitation on lath and block boundaries in tempered martensite ferritic steels, with either (a) MX carbonitrides forming significantly on the boundaries and within the subgrain matrix, or (b) M23C6 carbides forming on the boundaries and MX carbonitrides forming primarily within the matrix. Reproduced from Abe (Abe, 2008).

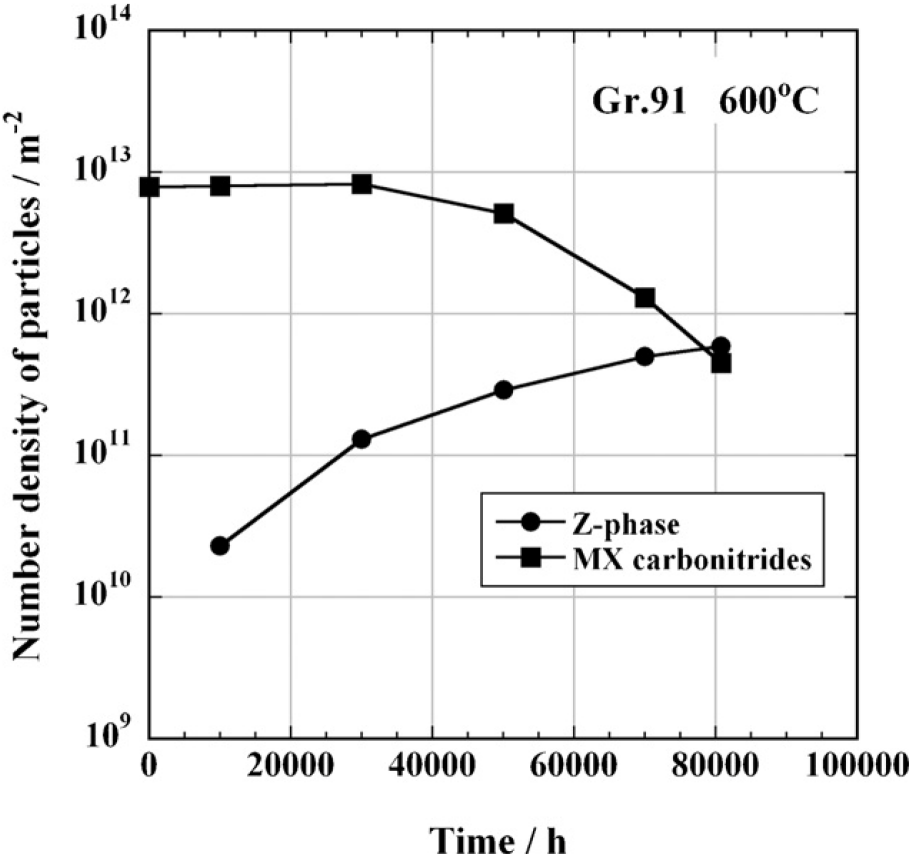


Figure 2-15. Evolution of number density of Z-phase and MX carbonitride particles in a Grade 91 steel during creep exposure at 600°C/70 MPa. Reproduced from Sawada et al. (Sawada et al., 2011).

types were present: M23C6 carbides, MX carbonitrides, Laves phase, and "modified" Z-phase. Panait et al. pointed out from the literature that Z-phase is considered to precipitate by consuming MX particles after long exposure times, which is detrimental to creep strength. After creep exposure, the microstructure examined by Panait et al. showed evidence of significant changes including precipitation and growth of large Laves phase particles which the authors indicated were associated with cavitation. Additionally regarding Z-phase, Panait et al. noted that while a small percentage of Z-phase was observed as large particles, TEM investigation showed the continued presence of MX carbonitrides after creep, raising the question of whether Z-phase truly has an effect on reducing the MX precipitate fraction and thereby reducing creep strength. Furthermore, the dependence of Z-phase formation on temperature is not clear since there are apparently conflicting reports in the literature. Sawada et al. (Sawada et al., 2008) reported that Z-phase formed after creep testing at 600°C in a Grade 91 steel with reduced Ni content and tempered at 760°C, but not in the same steel tempered at 680°C. In contrast, Agamennone et al. (Agamennone et al., 2006) noted a potential connection between extended time, lower-temperature double-step tempering (at 570°C+700°C) and the formation of Z-phase along PAGBs in a 12Cr CSEF steel after creep exposure at 650°C.

Precipitation of Laves phase enriched in Mo (and also W if added as an alloying element) during creep has been observed by a number of investigators, such as Watanabe et al. (Watanabe et al., 2006) for a Grade 91 steel tested at 600°C/80 MPa. Sawada et al. (Sawada et al., 2013) observed Laves phase in the base metal and the FGHAZ of welded Grade 92 steel after creep exposure at 650°C/60 MPa/10559.2 h. It is considered that Laves phase formation occurs at temperatures below 650°C, such that a higher temperature range of 650 to 750°C was intentionally chosen by Sawada et al. in another study (Sawada et al., 2003a) as a temperature range to avoid Laves phase. Panait et al. (Panait et al., 2010) stated that the effect from Laves phase precipitation

could reduce the solid solution strengthening contribution in the matrix and thereby reduce creep strength.

In summary, the preceding sections together have discussed the microstructure and strengthening mechanisms of tempered martensite ferritic steels and modified 9Cr steel (Grade 91) in particular, in order to establish the following: due to the inherent instability of dislocation-strengthened microstructures during creep deformation, the creep behavior of tempered martensite ferritic steel weldments will depend on the microstructural degradation caused by the welding thermal cycle and the subsequent evolution of this degraded microstructure when subjected to creep exposure during service.

2.1.5 Microstructural Changes in CSEF Steels during Tempering

Tempering of CSEF steels involves heat treatment at temperatures which are typically less than the lower critical transformation temperature (i.e. below A_1). The most important changes occurring in CSEF steels during tempering are related to the strengthening mechanism (carbide-stabilized substructure hardening) discussed in a preceding section of the literature review. This strengthening mechanism is thermodynamically unstable and thus the microstructure of CSEF steels evolves during heat treatment. The changes in structure include precipitation and coarsening of secondary phases, reduction in dislocation density, and formation and coarsening of subgrains from the initial martensite lath structure. These structural changes produce corresponding changes in mechanical properties, including decrease in hardness and room temperature strength, and changes in creep strength which vary with tempering time and temperature.

Because the primary strengthening mechanism in CSEF steels depends on stabilization of the dislocation substructure by precipitates, the thermal stability and evolution of precipitates will greatly affect the subsequent microstructural changes and properties.

During a high temperature exposure such as tempering, the diffusional processes will occur which either favor precipitate growth and coarsening or precipitate dissolution. Under static conditions (no strain), the behavior is dependent upon the specific precipitate and its free energy and solid solubility, the exposure temperature, and the relative kinetics of growth versus dissolution. As shown earlier in Fig. 2-13, solid solubility varies depending on the specific carbide chemistry and is related to the free energies of the carbide, the alloying element when dissolved in austenite, and the interfacial energies of the carbide and austenite, as a function of temperature. At the typical tempering temperatures e.g. 775°C for Grade 91 CSEF steel, particle coarsening is the predominant process.

Another primary changes which occurs during tempering of CSEF steels is the formation of subgrains. Subgrain structure refers to ordered structural arrangements which are present at length scales smaller than the size of individual grains (PAGBs) or blocks. Most specifically, subgrains refer to a structure in which regions of lower dislocation density (subgrain interiors) are surrounded by regions of higher dislocation density (subgrain boundaries); the subgrain boundaries are lower-energy arrangements (networks) of dislocations, thereby creating low-misorientation angle boundaries between adjacent subgrains; the term "micro-grain" is preferred by some authors (e.g. Refs. (Dronhofer et al., 2003; Peŝička et al., 2004)). Once subgrains (micro-grains) have formed, microstructure evolution continues during tempering and coarsening occurs. Coarsening is characterized by increasing subgrain size as measured by the width in the narrow dimension and also by decreasing aspect ratio of subgrains in which the subgrain shape becomes less acicular and more equiaxed. Ghassemi-Armaki et al. (Ghassemi-Armaki et al., 2013) concluded that subgrain coarsening under static conditions (such as tempering) was caused by the prior coarsening of M23C6 carbides leading to increased inter-particle spacing; since the M23C6 carbides form preferentially on subgrain boundaries and impede boundary motion due to pinning force, an increase

in inter-particle spacing corresponds to increased boundary mobility and thus results in subgrain coarsening.

With regard to dislocation density, in CSEF steels the martensitic transformation upon cooling from austenite results in a high dislocation density within the martensite laths, as described previously. Because the high dislocation density is associated with a high elastic strain energy, there is a driving force for strain energy reduction that leads to microstructural changes during tempering, even for short periods. Pešička et al. (Pešička et al., 2003) showed that tempering for times as short as 15 minutes at a typical tempering temperature of 750°C resulted in an order-of-magnitude decrease in dislocation density (from ~10E14/m^2 to ~1E14/m^2), which was unaltered by further tempering up to 1 h, and only decreased further (~0.1E14/m^2) after extended tempering for 100 h. The microstructures of the initial martensite and the tempered conditions after 1 h and 100 h are compared in Fig. 2-16. It is apparent that the extremely high dislocation density in the as-quenched structure (high enough that individual dislocations are completely indistinguishable) is reduced after one hour of tempering, but the fine lath-like substructure is preserved. After extended tempering for 100 h at 750°C, further reduction in dislocation density is apparent such that individual dislocations are apparent as denoted by the black arrow in Fig. 2-16(C). Sawada et al. (Sawada et al., 2003b) showed further evidence via TEM in situ tempering of normalized P91 steel that martensitic lath recovery and a decrease in dislocation density occurred during tempering. The overall microstructure in the TEM in situ tempered condition and a comparative sample tempered in a conventional furnace (750°C for 72.5 h) are shown in Fig. 2-17 where it is apparent that a subgrain structure formed after tempering and the dislocation density decreased within the subgrains. In situ TEM characterization at lower tempering temperatures revealed that the lath recovery proceeded by movement of lath boundaries, elimination of small laths, and an increase in average lath width. The distribution of lath widths before and after tempering is

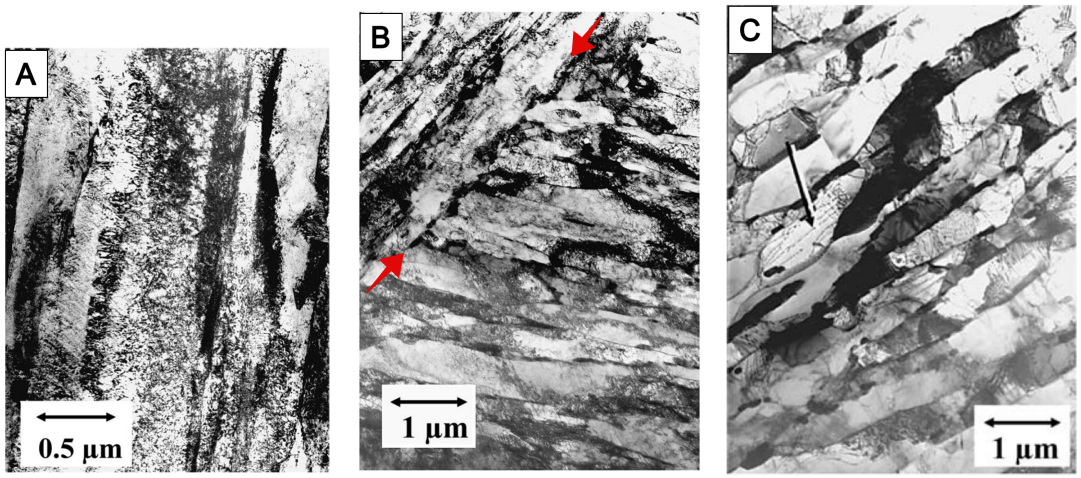


Figure 2-16. TEM micrographs of thin foils illustrating the evolution of microstructure and dislocation density for X20 tempered martensite ferritic steel in three conditions, (a) as-quenched (b) tempered, 750°C/1 h (c) tempered, 750°C/100 h. Note the extremely high dislocation density in (a), such that individual dislocations cannot be resolved; the clear lath-like subgrain structure and the sub-grain boundary denoted by the red arrows in (b); lower dislocation density (denoted by black arrow) and more equiaxed shape of coarsened subgrains in (c). Adapted from Pešička et al. (Pešička et al., 2003).

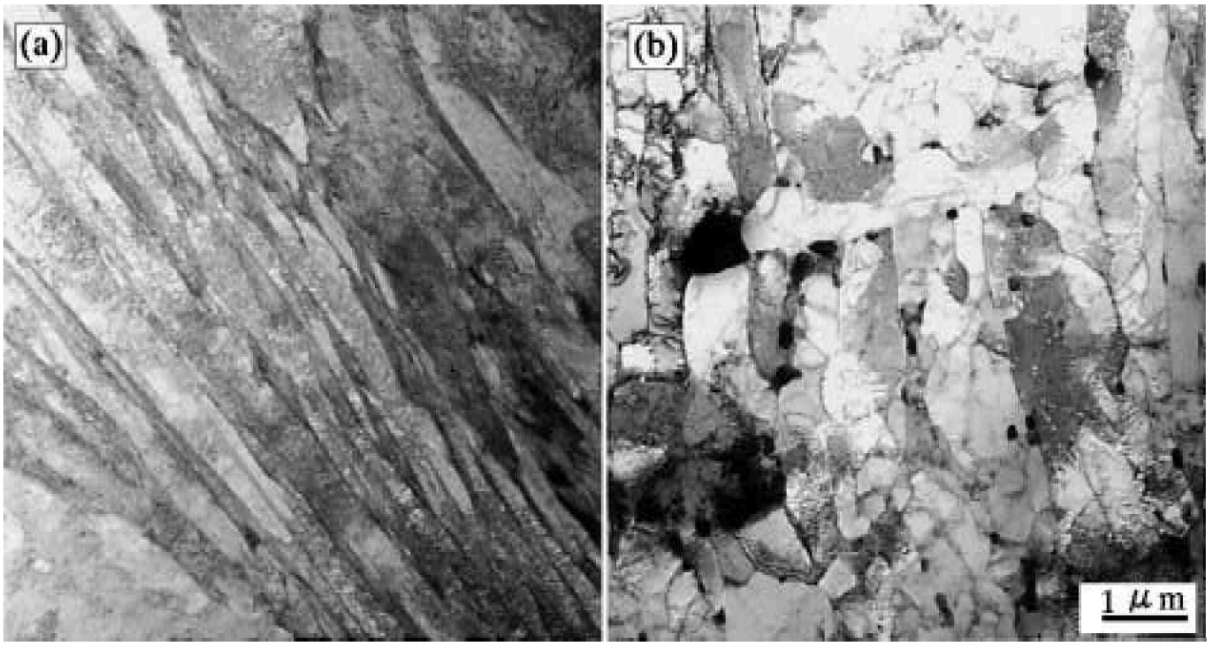


Figure 2-17. TEM micrographs illustrating the microstructure evolution in a 9Cr-2W-VNb steel (a) as normalized, 1300°C/1 h, and (b) after tempering at 750°C/72.5 h. Reproduced from Sawada et al. (Sawada et al., 2003b).

shown in Fig. 2-18. TEM micrographs showed that boundary migration occurred by a repeated process of localized bulges forming and advancing in adjacent portions of a boundary as depicted in Fig. 2-19. However, this process did not necessarily occur simultaneously on different lath boundaries, which indicates a dependence on the specific boundary characteristics such as local strain and misorientation angle. Thus, an important observation from this work is that recovery of the lath structure is not necessarily homogeneous, with recovery proceeding more slowly in some regions compared to others. This behavior can be explained from the perspective that while strain from the martensitic transformation is the driving force for recovery, the transformation strain is not uniform in different laths. The phenomenon of non-uniform recovery with formation and growth of sub-grains was also observed by Kostka et al. (Kostka et al., 2007) after creep of a martensitic Fe-10Cr alloy subjected to ECAP processing.

2.1.6 Microstructural Changes in the Heat-Affected Zone of CSEF Steels

Previous sections of this literature review have considered the microstructure and resulting creep behavior of 9-12 wt.% Cr CSEF steels in terms of the base metal. From this discussion, it is clear that the desirable creep behavior of steels such as Grade 91 is dependent on producing and maintaining an optimal microstructural condition (tempered martensite lath structure, or TMLS), and alteration of this microstructure will result in degradation of creep properties. Because CSEF steels must typically be welded during the fabrication of actual, in-service equipment for industry, the effect of the welding thermal cycle on the TMLS microstructure is a fundamental consideration for the creep behavior of CSEF weldments.

During welding, the base metal regions adjacent to the weld deposit experience a temperature excursion by rapid heating to a certain peak temperature, followed by cooling to the initial plate temperature. This temperature excursion is called the welding thermal cycle. As distance from the fusion line increases, at each point relative

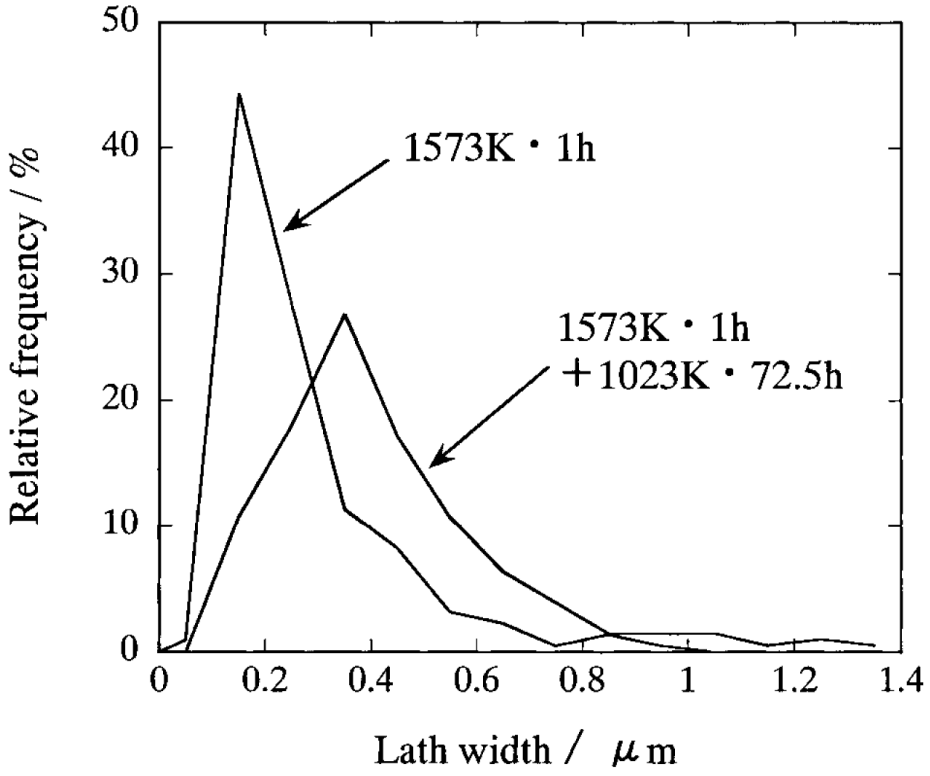


Figure 2-18. Distribution of measured lath width in a 9Cr-2W-VNb steel in the as-normalized condition and after tempering at 750°C (1023 K) for 72.5 h. Reproduced from Sawada et al. (Sawada et al., 2003b).

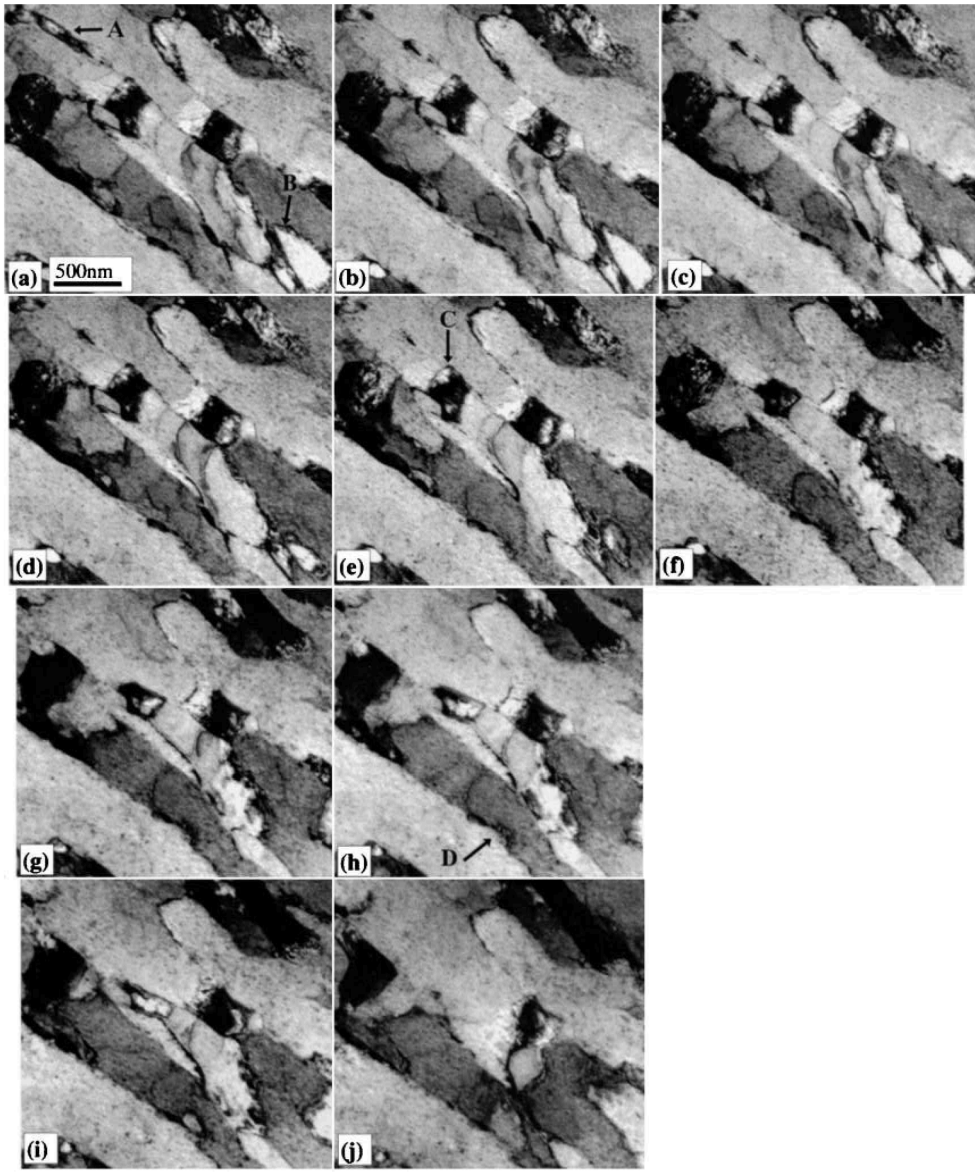


Figure 2-19. Sequence of TEM micrographs illustrating the process of subgrain coarsening by boundary migration in a 9Cr-2W-VNb steel during in situ tempering at 730°C. Reproduced from Sawada et al. (Sawada et al., 2003b).

to the fusion line, the associated peak temperature will decrease and the heating and cooling rates will become more gradual; see Fig. 2-20 for a comparison of calculated thermal cycles at various distances from the fusion line. Furthermore, at each point the associated thermal cycle will exhibit both a certain peak temperature and certain duration where the temperature exceeds metallurgically important temperatures, namely the lower and upper critical transformation temperatures (Ac1 and Ac3, respectively) for steels[3]; additionally, each thermal cycle has an associated cooling rate, e.g. which can be characterized by the t8->5 time which is the time required to cool from 800°C to 500°C. Thus, welding produces a continuous gradient of altered microstructure adjacent to the fusion line, with the nature and extent of alteration depending on peak temperature, time-at-temperature, and the temperature-dependent transformations which occur in the material upon heating and cooling. This region of altered microstructure is categorized as the heat-affected zone (HAZ).

The HAZ is commonly divided into sub-regions based on microstructure characteristics, such as those occurring in Cr-Mo steels, including the coarse-grained HAZ (CGHAZ), fine-grained HAZ (FGHAZ), intercritical HAZ (ICHAZ), and in some classification schemes, the over-tempered zone (OTZ). An example of the typical appearance of a HAZ in Grade 91 steel, labeled accordingly, is shown by the optical micrographs in Fig. 2-21. Although this HAZ classification is widely used, there is some disagreement in the literature regarding the proper terminology for describing the HAZ in 9-12 wt.%. Cr CSEF steels (or steels with a tempered martensitic lath structure). Many investigations on Grade 91 weldments utilize the commonly-accepted terminology (although it is not always consistently applied), but Siefert et al. (Siefert et al., 2019) emphasized that the CG/FG/ICHAZ descriptors are hold-overs from research which

[3] Note that Ac1 and Ac3 must be specified when discussing the transformations which occur in the HAZ of steels, rather than Ae1 and Ae3, since welding is a highly non-equilibrium process where Ac1/Ac3 may differ significantly from the Ae1/Ae3 values, which are the values that are commonly predicted by thermodynamic calculation approaches.

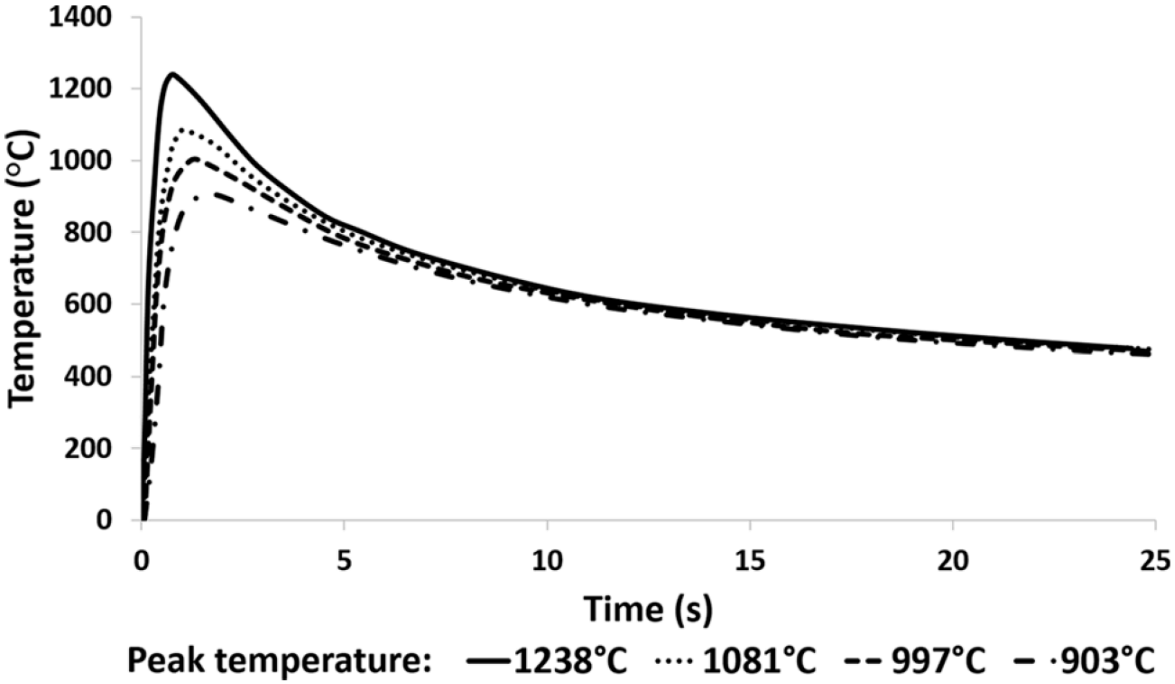


Figure 2-20. Comparison of calculated thermal cycles for Grade 92 steel with different peak temperatures. Reproduced from (Xu et al., 2017).

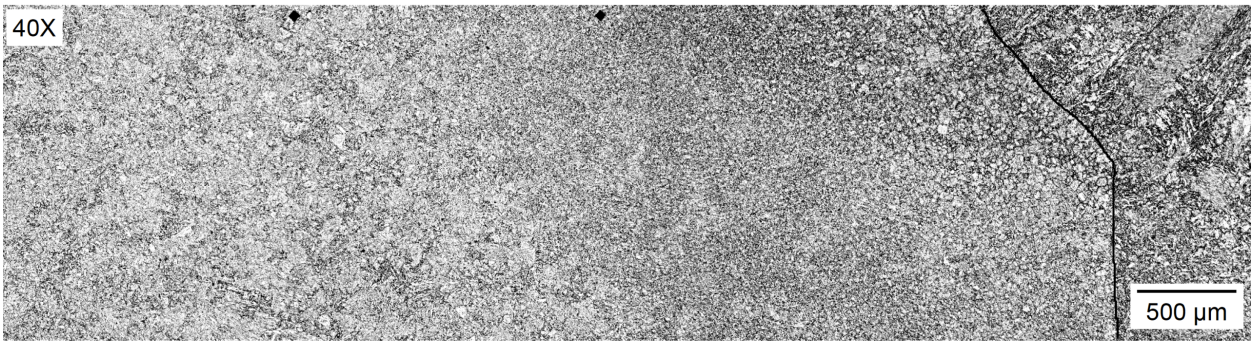


Figure 2-21. Panorama of optical micrographs illustrating the typical appearance of an HAZ in a Grade 91 CSEF weldment. The fusion line is emphasized by a narrow black line. Etchant: Fry's reagent.

investigated the behavior of earlier, lower-alloy Cr-Mo steels such as 2-1/4Cr-1Mo, and thus may not be appropriate to CSEF steels. The lower-alloy Cr-Mo steels generally have bainitic microstructures and thus, Siefert et al. (Siefert et al., 2019) state that the HAZ transformations which occur are fundamentally different from those occurring in martensitic CSEF steels such as P91. For this reason, Siefert et al. (Siefert et al., 2019) argued that the existing HAZ terminology is invalid for CSEF steels; based on other published research (Xu et al., 2017), they proposed to describe the HAZ regions using different terminology related to the extent of transformation produced by the welding thermal cycle. According to this terminology, there are three distinct microstructural regions which result from welding: the fully-transformed zone (FTZ), the partially-transformed zone (PTZ), and the over-tempered zone (OTZ) (Siefert et al., 2019; Xu et al., 2017). This terminology eliminates the distinction between the CGHAZ and FGHAZ, which both experience complete transformation to austenite during the thermal cycle.

Aside from the issue of which terminology is used to describe the HAZ, the metallurgical transformations occurring in the HAZ of 9-12Cr CSEF/TMLS steels such as Grade 91, Grade 92, and X20CrMoV12-1 have been investigated in detail by several authors (Wang et al., 2018b, 2016; Wang et al., 2017; Xu et al., 2017) and summarized in review papers (Abson and Rothwell, 2013; Francis et al., 2006). Wang and co-workers have conducted several studies on the microstructural characteristics and evolution in the HAZ of Grade 91 steels (Wang et al., 2018a, 2017, 2016). Wang et al. (Wang et al., 2016) compared the microstructural changes in the as-welded (not postweld heat treated) HAZ of a P91 steel weldment with the base metal; they utilized the traditional classification of HAZ sub-regions as previously mentioned. In common with many recent investigations of CSEF steels, the EBSD technique in the SEM (known as orientation imaging microscopy, OIM) was used to definitively characterize the various HAZ regions by revealing distinguishing microstructural features which are not

apparent with optical microscopy or secondary electron imaging in the SEM. Specifically, Wang et al. (Wang et al., 2016) used EBSD to distinguish different boundary types in the HAZ microstructures, such as PAGBs (high misorientation angle boundaries) and sub-grain boundaries (low misorientation angle), and also to evaluate the degree of strain within individual grains as a means of identifying which grains were recrystallized, transformed, or untransformed/overtempered. Wang et al. observed that in the CGHAZ, complete dissolution of carbides occurred, which permitted significant PAG growth to occur due to the loss of grain boundary pinning. EBSD analysis showed that the CGHAZ retained a more lath-like structure after cooling, which is consistent with complete transformation to austenite and subsequently to martensite. In comparison, they reported that the FGHAZ showed the smallest PAG size of 5 μm together with the presence of some undissolved carbides (as shown in Fig. 2-22(b)) and a more equiaxed grain structure than either the base metal or the CGHAZ. EBSD analysis revealed a non-uniform distribution of localized strain within the FGHAZ microstructure; localized strain is correlated with dislocation density and recrystallization, so the non-uniform strain distribution indicated that recrystallization had occurred during the FGHAZ thermal cycle. The ICHAZ showed a mixture of recrystallized, substructured, and deformed grains, with a larger substructure feature size than the FGHAZ, cf. (a) and (b) in Fig. 2-23. Additionally, the ICHAZ showed a further reduction in kernel average misorientation which indicated a lower extent of localized strain, which correlated with reduced dislocation density due to tempering of untransformed grains. The microhardness distribution in the as-welded HAZ (see Fig. 2-24) indicated continuously decreasing hardness with distance from the fusion line, until the base metal hardness level was attained; the weldment did not exhibit either a hardness dip in the HAZ or an over-tempered region in the as-welded condition.

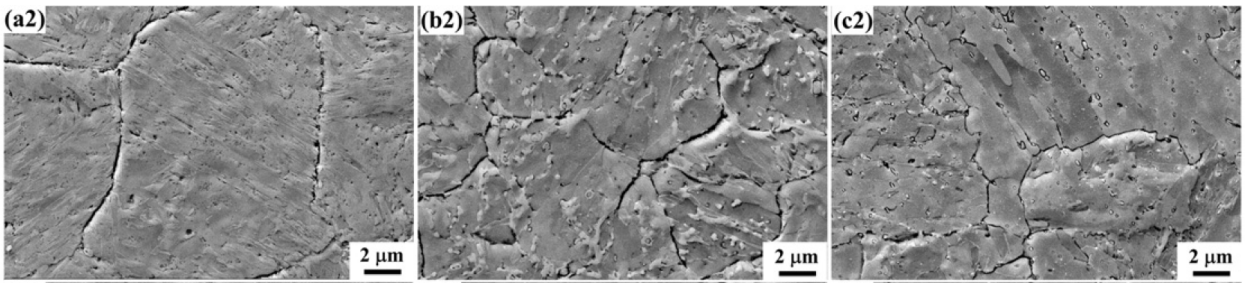


Figure 2-22. Comparison of microstructures in the as-welded HAZ of a Grade 91 weldment (a) CGHAZ (b) FGHAZ (c) ICHAZ. 10% Nital etch, secondary electron SEM imaging. Adapted from Wang et al. (Wang et al., 2016).

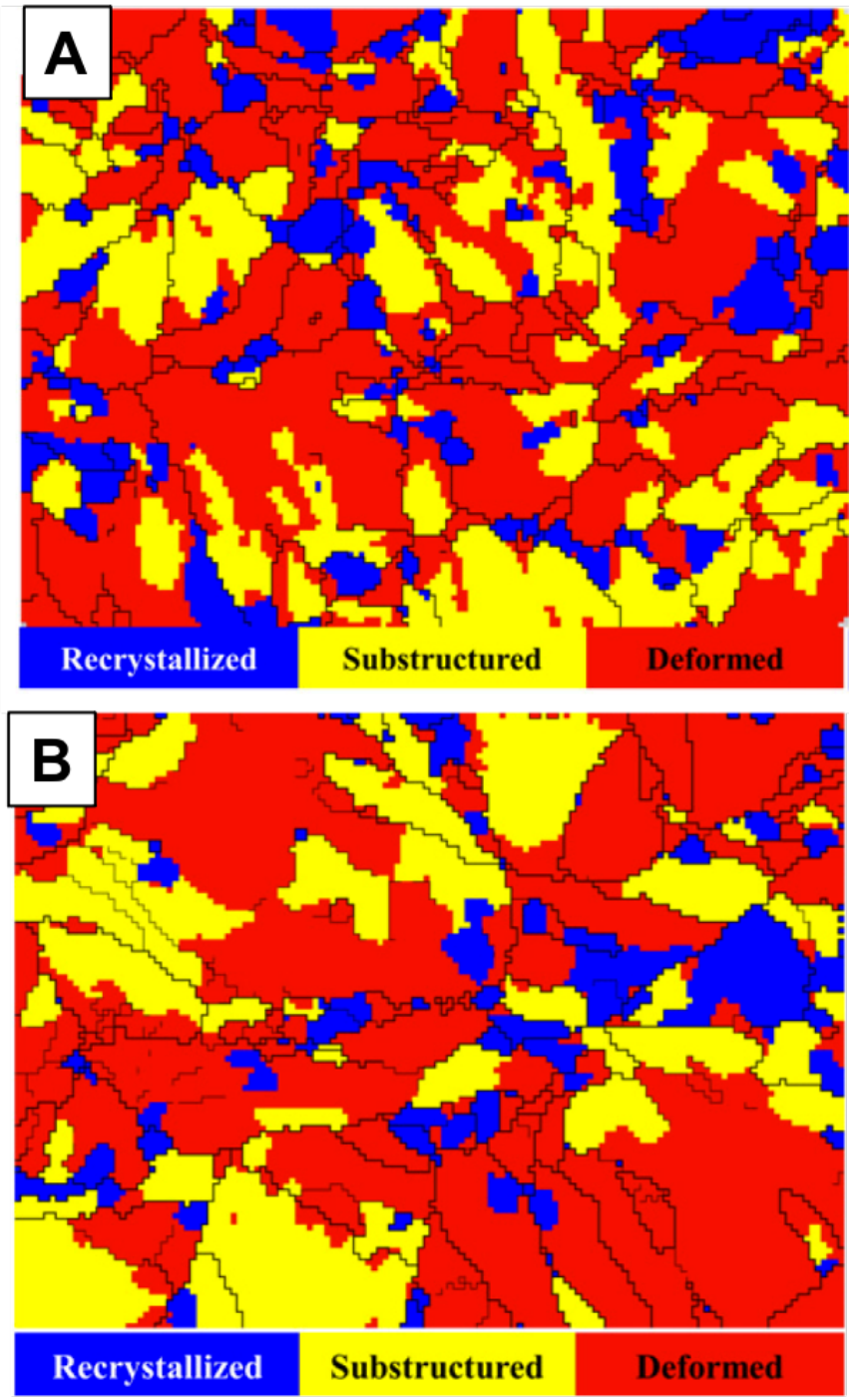


Figure 2-23. Comparison of grain average misorientation maps for the as-welded (a) FGHAZ and (b) ICHAZ in a Grade 91 weldment. Note the coarser feature size of deformed and substructured grains in the ICHAZ. Adapted from Wang et al. (Wang et al., 2016).

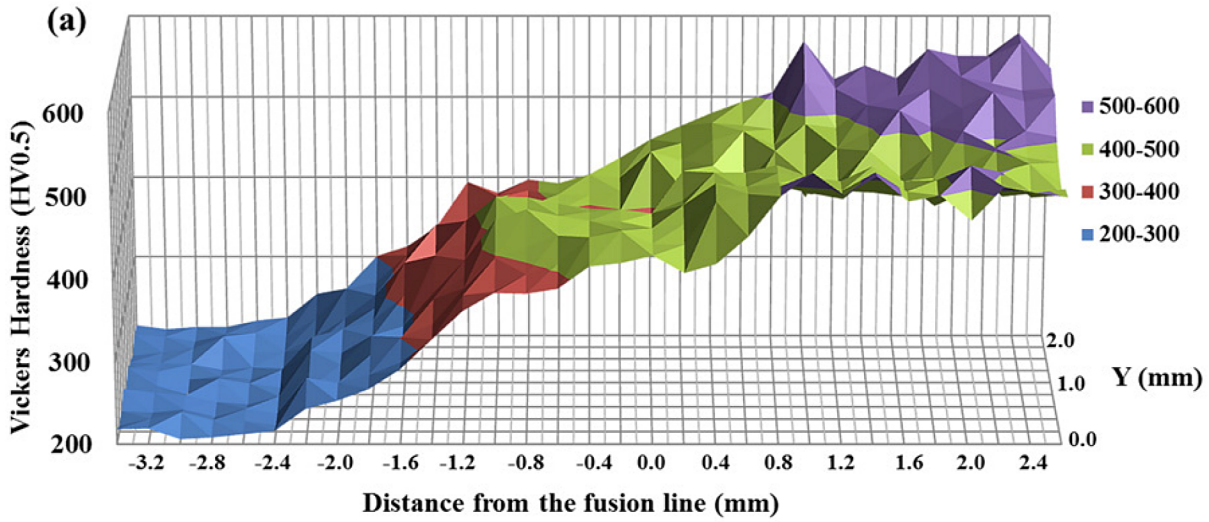


Figure 2-24. Distribution of measured microhardness values for a Grade 91 weldment in the as-welded condition. Note that the hardness continuously decreases through the HAZ until reaching the base metal value; the as-welded condition does not exhibit a hardness dip within the HAZ, and the hardness values do not show the presence of a lower hardness overtempered zone outside the HAZ. Adapted from Wang et al. (Wang et al., 2016).

Similarly for another CSEF steel (Grade 92), Xu et al. (Xu et al., 2017) conducted a detailed investigation of the microstructural changes which occurred in the as-welded heat-affected zone of a bead-on-plate weld in Grade 92 (9Cr-0.5Mo-1.8W-VNb) steel and in simulated HAZ specimens subjected to specific peak temperatures relative to the Grade 92 transformation temperatures. From the characterization, the authors categorized the HAZ in Grade 92 steel into three microstructurally distinct sub-regions: the completely transformed zone (CTZ); the partially transformed zone (PTZ); and the overtempered zone (OTZ). These sub-regions are illustrated schematically in Fig. 2-25 and are the basis of the alternate HAZ classifications scheme mentioned earlier in this section. In these sub-regions, the extent of transformation (either complete or partial) is in reference to both the extent of austenitization and the dissolution of pre-existing secondary precipitates. In the CTZ, corresponding to a peak temperature >Ac3, ion beam-induced microscopy revealed that at 1100°C (Ac3 + 43C°), nearly all of the secondary precipitates were dissolved (see Fig. 2-26). However, fully complete dissolution of all precipitates was only noted at a peak temperature of 1250°C (Ac3+193C°). EBSD showed that above Ac1, the high angle grain boundaries (corresponding to prior austenite grain boundaries) were somewhat refined compared to the original base metal PAGB size, indicating that transformation occurred. For peak temperatures in the intercritical region (Ac1<Tp<Ac3), for example 1000°C (Ac3 minus 57C°), although precipitate dissolution occurred, a definite number of precipitates remained and were not dissolved (see Fig. 2-26(b)). Consequently, significant refinement of the areas delineated by high angle boundaries (PAGB), as shown in Fig. 2-27, was observed because the incomplete precipitate dissolution inhibited grain growth that would otherwise occur. Their results also showed that the acicular subgrain structure from the original base metal was mostly absent at a peak temperature slightly below Ac3. It is worth emphasizing that in this temperature rate (PTZ, between Ac1 and Ac3), the lath-like subgrain structure which is characteristic of CSEF steels and which provides a primary source of strengthening (from subgrain boundaries) has been almost

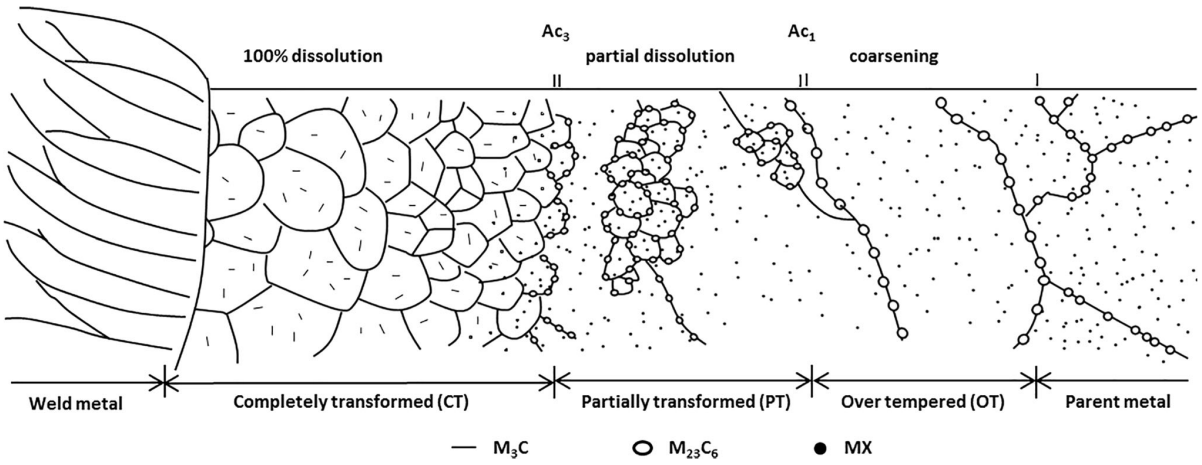


Figure 2-25. Schematic illustration of HAZ regions and their distinguishing features according to a classification scheme proposed specifically for CSEF steels. Note in particular that the completely transformed zone (CTZ) contains a mixture of coarse and fine grains, showing that in this classification scheme, it is assumed that grain size has a minimal effect on overall behavior in CSEF steels. Reproduced from Xu et al. (Xu et al., 2017).

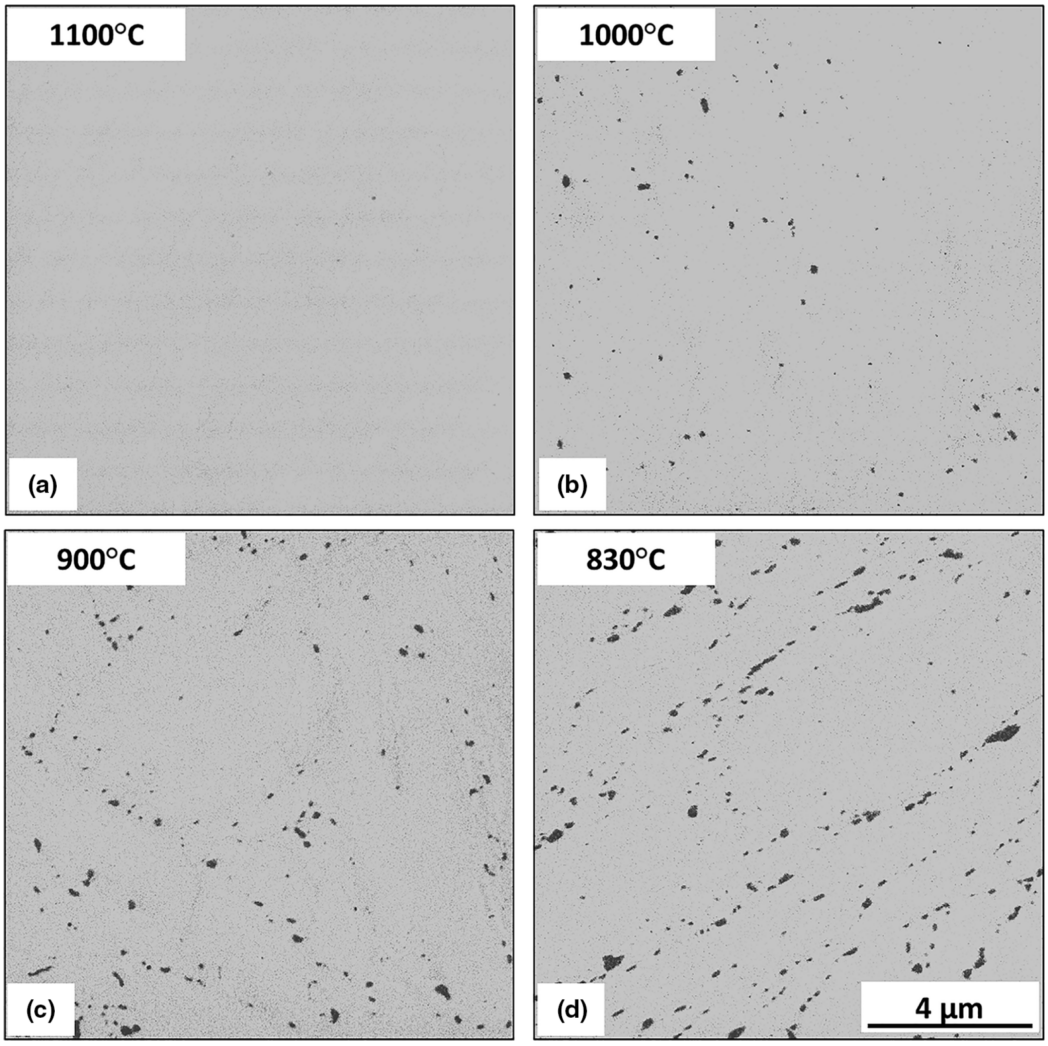


Figure 2-26. Ion-induced secondary electron SEM micrographs showing the variations in precipitate dissolution depending on peak temperature (noted in each micrograph) in Grade 92 simulated HAZ microstructures. Note that the simulated microstructure with a peak temperature of 1100C still exhibited a very small fraction of undissolved particles which are not readily apparent in the micrograph; thus, precipitate dissolution is still not complete at this temperature. Reproduced from Xu et al. (Xu et al., 2017).

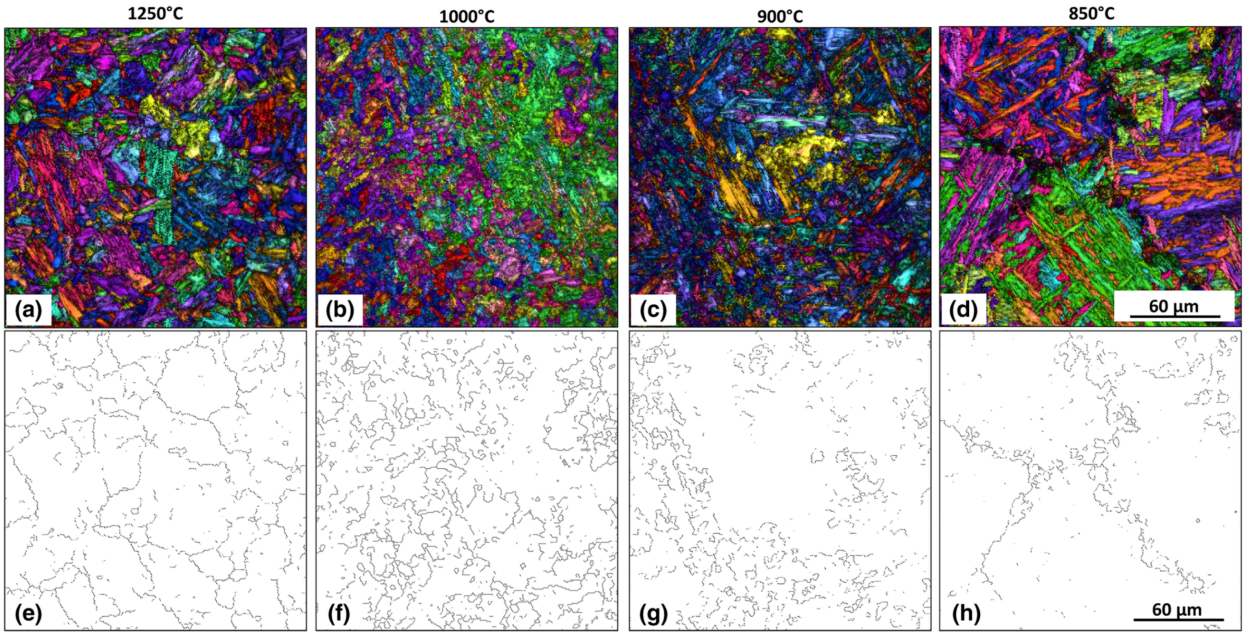


Figure 2-27. SEM-EBSD grain orientation maps (a-d in color) and image quality maps showing 20-50° grain boundaries (e-h in grayscale) obtained from simulated HAZ microstructures in P92 steel. At the lowest peak temperature of 850°C which is below the Ac1 temperature, transformation and disruption of the original PAGBs are not evident. At 1000°C (>Ac1), complete transformation is evident, but the grain size is refined because incomplete carbide dissolution limits grain growth (cf. Fig. 2-26(b)). At Tp=1250°C (>Ac3) precipitate dissolution is complete and grain growth begins to occur. Reproduced from Xu et al. (Xu et al., 2017).

fully eliminated and replaced with equiaxed subgrains, suggesting that the PTZ region will be weak in creep.

2.1.6.1 Effect of Postweld Heat Treatment on Heat-Affected Zone Characteristics

After fabrication, weldments from CSEF steels must be given a PWHT to comply with code requirements, which stipulate PWHT as a means to relieve residual stresses and improve toughness. During the PWHT, the altered microstructure in the HAZ undergoes further evolution similar to tempering of base metal. The maximum allowable PWHT temperature for CSEF steels is intentionally chosen to be below the Ac1 temperature; thus, no transformation to austenite takes place during a correctly performed PWHT. Wang et al. investigated the microstructure evolution during PWHT of the FGHAZ (Wang and Li, 2016) and ICHAZ regions (Wang et al., 2018a) in Grade 91 weldments. In the FGHAZ (Wang and Li, 2016), PWHT resulted in coarsening of carbides and partial breakdown of the as-welded TMLS structure to form a more equiaxed ferrite grain structure; coarsened subgrains (retaining some lath character) and equiaxed grains were both observed. The coarsened carbides were noted to be located on PAGBs and former martensite lath boundaries. Partial microstructure recovery during PWHT and a resulting mixed microstructure were revealed by EBSD analysis which showed that the formation of a more equiaxed structure was accompanied by an increase in the density of high angle boundaries increases while the density of low angle boundaries (associated with lath structure and/or subgrains) decreased (see the comparison in Fig. 2-28).

Regarding the microstructure in the ICHAZ, Wang et al. (Wang et al., 2018a) characterized the ICHAZ of a Grade 91 weldment after PWHT. In their work, Wang et al. 2018 characterized the ICHAZ as the creep-susceptible region within the HAZ, and showed by Auger spectroscopy mapping that in the as-welded condition, the ICHAZ exhibited variations in Cr concentration on a grain-to-grain level, but after PWHT, this

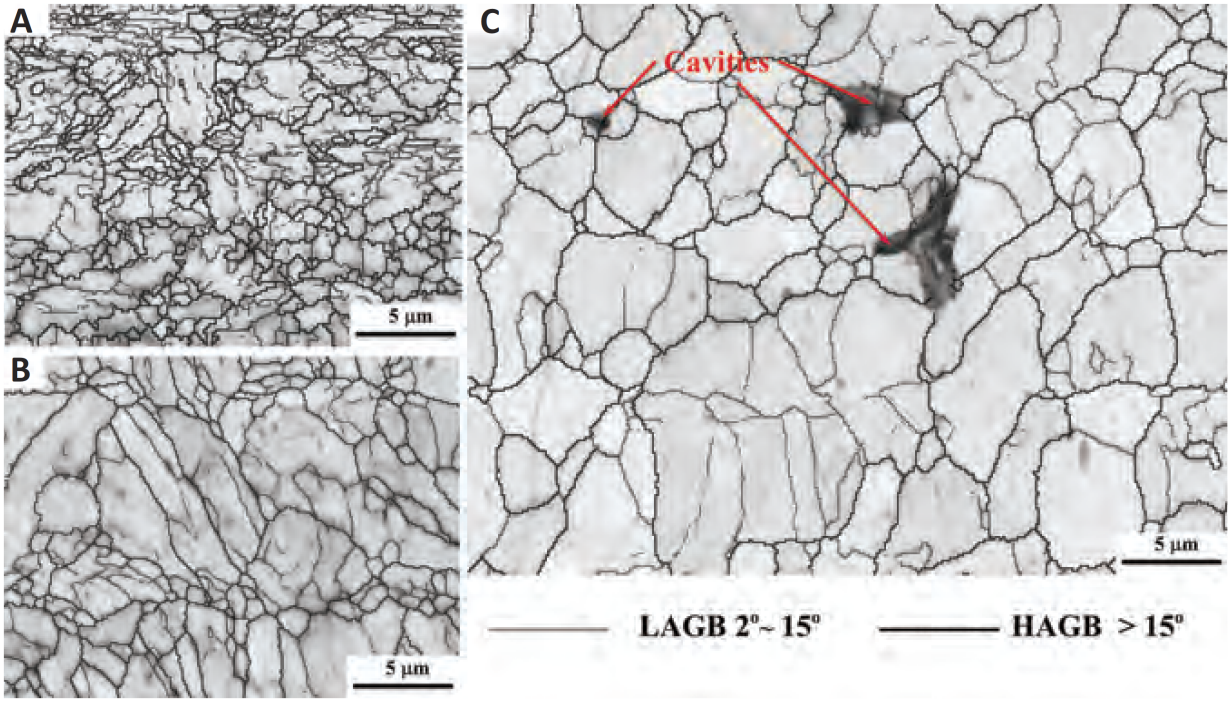


Figure 2-28. Comparison of high angle grain boundary (HAGB) and low angle grain boundary (LAGB) misorientation distributions in the FGHAZ of a P91 weldment in three conditions, (a) as-welded (b) after PWHT at 760°C/2 h, and (c) after creep rupture testing at 650°C/70 MPa. Note the significant increase in subgrain size after PWHT and also after creep testing. Reproduced from Wang and Li (Wang and Li, 2016).

localized chemical segregation appeared to decrease but then was found to increase after creep; the authors used this observation as the basis to propose that grain-to-grain local segregation (potentially due to incomplete of Cr-rich M23C6 carbides) could lead to grain-to-grain variations in transformation stability of ferrite vs. austenite and thus to non-uniformity in ferrite to austenite transformation during the ICHAZ thermal cycle and produce the mixed ICHAZ microstructure. However, the small magnitude of the effect (only 5C° difference in transformation temperature depending on Cr concentration) seems inadequate to explain the significant microstructural inhomogeneity in the ICHAZ.

Yu et al. (Yu et al., 2013) showed that the initial base metal temper has an effect on the precipitate characteristics which develop in the HAZ (such as the FGHAZ) during PWHT, with a subsequent effect on creep properties. They compared two base metals, one of which was tempered at a low temperature of 650°C (LTT) while the other was tempered at a typical PWHT temperature of 760°C (HTT). After welding and PWHT it was observed that in the LTT condition, M23C6 carbides had fully dissolved in the FGHAZ and then precipitated again along grain and subgrain boundaries after PWHT. In contrast, in the HTT condition, M23C6 carbides were not completely dissolved during the FGHAZ thermal cycle and thus carbide coarsening occurred during PWHT. The difference in carbide dissolution among the HAZ regions is partly related to the stability of the carbide (see Fig. 2-13), but it is also related to the dissolution kinetics; the closer the carbides are to equilibrium when dissolution begins, the more time (and/or higher temperature) is required to fully dissolve the carbide. Thus, for the LTT condition, the fine carbides present after the low initial temper were not close to equilibrium and were readily dissolved during the short FGHAZ thermal cycle. The complete dissolution of carbides in the LTT condition enabled re-precipitation and growth of fine carbides during PWHT since the matrix composition was at the expected level (i.e. all carbide-forming elements were in solution for subsequent precipitation).

However, in the HTT condition, incomplete carbide dissolution led to carbide coarsening and also depletion of carbide-forming elements in the matrix. The coarsened carbides were no longer located on grain or subgrain boundaries; rather, the coarsened carbides only showed the location and size of the former PAG boundaries since the carbides are typically aligned along the former boundary. Both of these processes and their effect on the precipitate characteristics which are produced by PWHT are illustrated schematically in Fig. 2-29. This figure shows that for CSEF steels, a lower initial tempering temperature is advantageous for producing the desirable carbide-stabilized substructure.

In terms of mechanical properties, PWHT causes a decrease in hardness throughout the HAZ and weld deposit, such that the hardness differential between the weld deposit, HAZ, and base metal is significantly reduced (Wang et al., 2018a). Hardness data from Wang and Li (Wang and Li, 2016) showed that after PWHT, the hardness appeared fairly uniform within the FGHAZ and ICHAZ regions, with only a minor observable minimum in hardness within the FGHAZ/ICHAZ. In contrast, Siefert et al. (Siefert et al., 2019) reported a hardness minimum in the "overtempered zone" (OTZ) just outside the HAZ. The reason for this discrepancy regarding the uniformity of hardness within the FGHAZ/ICHAZ, between Wang and Li and Siefert et al., could be due to the higher PWHT temperature employed by Wang and Li (760°C vs. 675°C, respectively). Shassere et al. (Shassere et al., 2016) showed that a Grade 91 steel subject to an aus-forming/aus-aging thermo-mechanical treatment (TMT) at 800C showed a lesser extent of softening in the FGHAZ region after PWHT at 760°C as compared to base metal with a standard N&T heat treatment, as determined by microhardness measurements.

Most reported microhardness data for weldments are obtained at room temperature, but Li et al. (Li et al., 2003) performed Vickers hardness measurements across P122 (12Cr) weldments at both room temperature and at 650°C (the creep test temperature), in both the PWHTed and creep-tested conditions. Their results showed that the

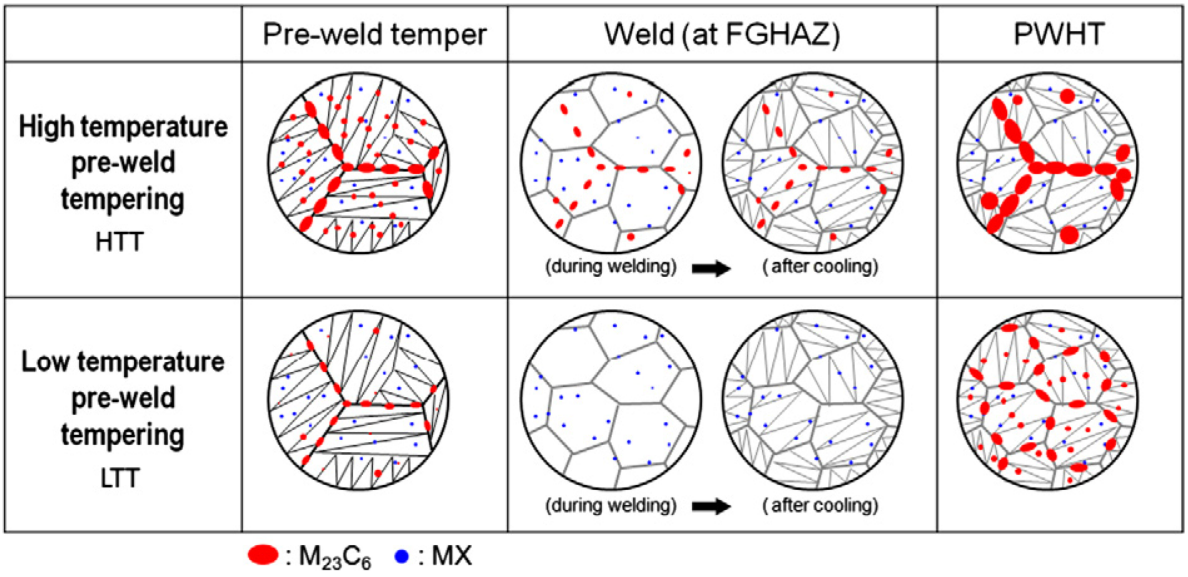


Figure 2-29. Schematic illustration of microstructure and carbide evolution in base metal and FGHAZ for base metals subjected to different pre-weld tempering treatments. Note that in the LTT condition, the microstructure shows finer carbides which precipitated at newly-formed PAGB, compared to coarsened carbides along former PAGBs in the HTT condition. Reproduced from Yu et al. (Yu et al., 2013).

minimum hardness location occurred at the same distance (3 mm) away from the fusion line, both before and after creep-testing and both at room temperature and 650°C. The location of the minimum hardness values corresponded closely to the Type IV rupture location, as shown in Fig. 2-30; the minimum hardness occurs at the same distance from the fusion line both before and after creep testing, so it seems that the low hardness values adjacent to the rupture location, after testing, cannot be dismissed merely as strain-induced softening. This suggests that while differences in room temperature and elevated temperature hardness do exist, the results for welds are similar enough that room temperature measurements will not be misleading about the weldment properties and behavior.

2.1.7 Creep Damage Development

In considering the failure of welded components due to creep loading at high temperature and stress, it is important to understand the mechanism(s) by which an initially sound weldment develops the microstructural defects associated with creep processes, principally creep cavitation and cracking. Beginning with creep cavitation, damage accumulates and eventually leads to linking of creep cavities to form micro-cracks and macro-cracks, ending in final component failure. It is necessary to understand how these steps occur: whether in sequence or simultaneously, and also whether they occur only at a specific stage of creep exposure or occur continuously (e.g. continuous nucleation of cavities). Understanding how these processes occur can provide direction about why damage development may proceed differently in different materials, for example in the 9-12 wt.% Cr CSEF steels compared to lower alloy Cr-Mo steels such as P11 and P22. It has been proposed (Siefert and Parker, 2016) that the damage development in CSEF steels proceeds in such a way that the linking of cavities into micro-cracks (which are detected by ultrasonic NDE) is delayed compared to lower-alloy Cr-Mo steels, with the result that damage cannot be reliably detected until component life is nearly consumed. Thus, it is important to understand damage

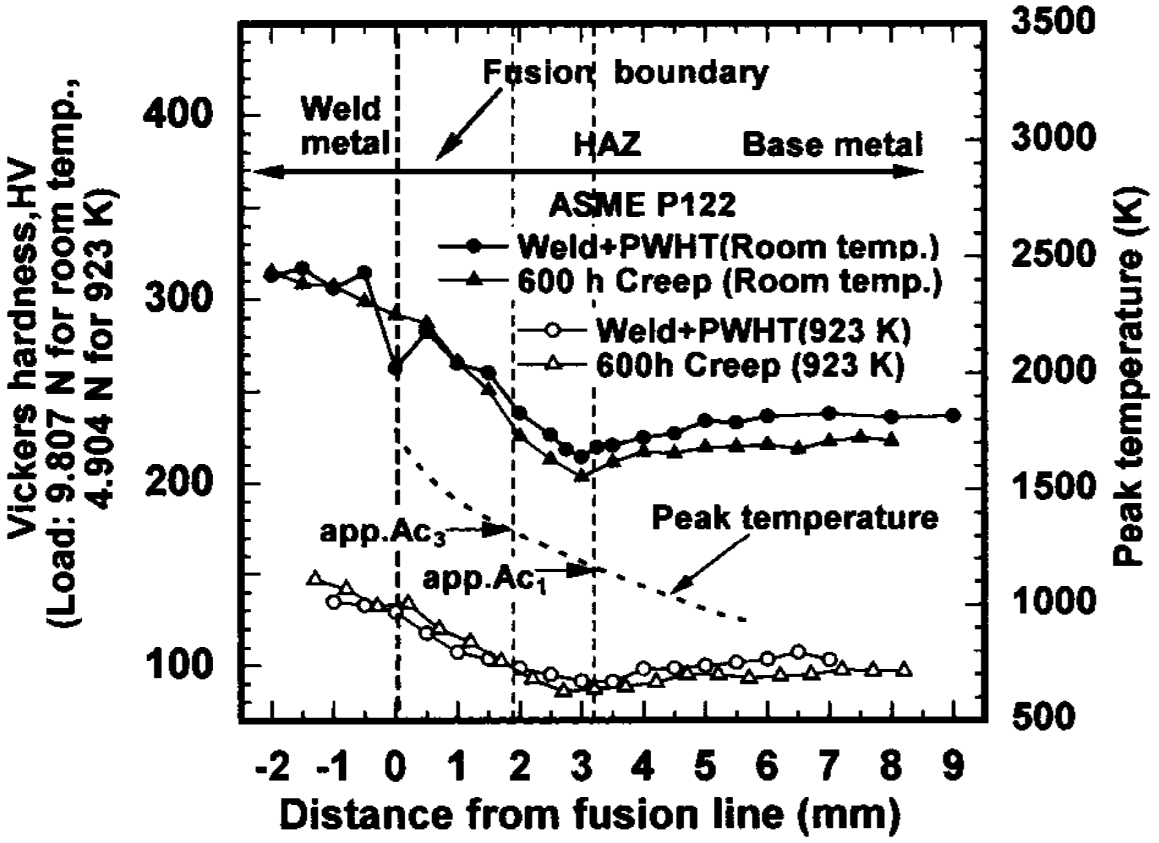


Figure 2-30. Comparison of cross-weld data for a P122 weldment, both before and after creep-testing at room temperature (solid points) and at the creep test temperature (open points). Reproduced from Li et al. (Li et al., 2003).

development processes because this development affects the considerations of component inspection and remaining life when a certain level of damage is present/detected. To this end, the evolution of creep damage in CSEF steels is discussed in base metals as a starting point, followed by considering the additional complications introduced by creep loading of weldments. Two principal aspects of creep damage development, cavity nucleation and cavity growth, are discussed in subsequent sections of this review.

In addition to the processes of cavity nucleation and growth, creep damage development must also be considered with regard to the metallurgy of CSEF steels and the resulting mechanical properties. Generally, the response of a material to constant loading at elevated temperature (its creep behavior) is considered to depend on two different material properties, creep strength and creep ductility. These properties are not necessarily linked, as has been shown experimentally (*Life Management of 9%Cr Steels: Evaluation of Metallurgical Risk Factors in Grade 91 Steel Parent Material*, 2018) where creep testing of Grade 91 steel has revealed materials which exhibit high creep strength with low ductility or high creep strength with high ductility. A material's creep strength influences creep deformation, which describes how the material responds elastically and plastically to the creep load as a function of time. In contrast, a material's creep ductility (measured at rupture either by elongation or reduction in area) affects the development of creep damage, which can be considered to include the nucleation, growth, and coalescence of creep cavities, followed by development of micro-cracking and macro-cracking leading to rupture. For CSEF steels, the overall creep behavior includes both deformation susceptibility (related to strength) and damage susceptibility (related to ductility) (*Life Management of 9%Cr Steels: Evaluation of Metallurgical Risk Factors in Grade 91 Steel Parent Material*, 2018); microstructural evolution during creep is one of the primary factors which affects both creep deformation and creep damage development. Thus, the different aspects of microstructural evolution in CSEF steels

during creep are also discussed in the following sections. Lastly, the effects of temperature and stress on all the preceding processes are also discussed since laboratory creep testing is often conducted under different conditions than actual in-service creep conditions due to the long test times that are required to replicate service conditions.

2.1.7.1 Nucleation of Creep Cavities

Cavity nucleation considers how creep cavities or creep voids, a type of microstructural discontinuity, develop within the initial microstructure. Several factors are important to consider with regard to cavity nucleation, specifically:

i. whether cavities nucleate preferentially at specific microstructural features, such as PAG boundaries, martensite lath/block boundaries (for untempered martensite), subgrain boundaries (tempered martensite, aka ferritic), or particles (such as non-metallic inclusions).
ii. whether cavities are nucleated during an initial stage and then growth proceeds with minimal additional nucleation (discrete nucleation), or are nucleated continuously during creep exposure (continuous nucleation), with the location of nucleation possibly changing as the "most favorable" sites are consumed first.

Cavity nucleation behavior can be first considered in a general sense for metals. From a fundamental mechanism perspective, Kassner and Hayes (Kassner and Hayes, 2003) have summarized potential cavity nucleation mechanisms (which are not fully understood) in metals as being related to stress concentrations at grain boundaries. These stress concentrations are potentially produced in the following ways which are illustrated in Fig. 2-31:

1. sliding of the interconnected grains at triple junctions
2. vacancy diffusion and accumulation at triple junctions
3. sliding and locking of grain boundary ledges

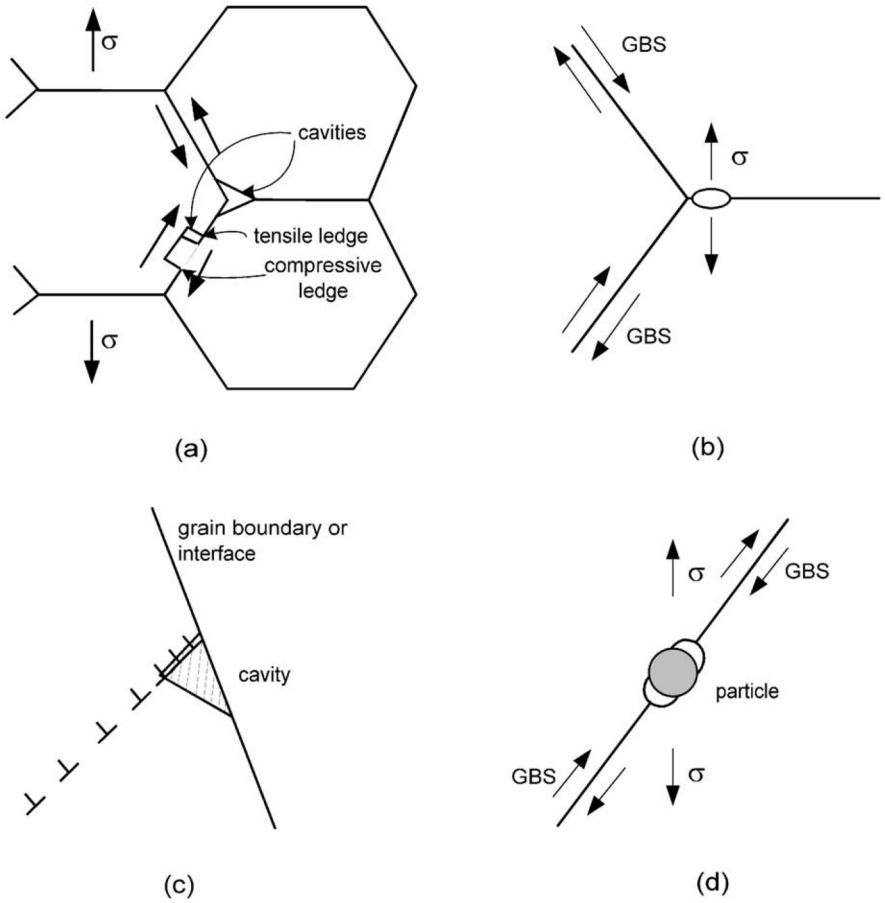


Figure 2-31. Schematic illustration of cavity nucleation mechanisms at grain boundaries. (a) sliding at ledges and triple points (b) vacancy condensation at stress concentrations (c) dislocation pileup at obstacles such as boundaries or hard particles (d) nucleation at GB particle due to combined mechanisms of (a)-(c). Reproduced from Kassner and Hayes (Kassner and Hayes, 2003).

4. particles which function as obstacles on grain boundaries: particles have an associated particle-matrix interface which may be coherent or incoherent, and thus affect the propensity for stress concentration

Regarding cavitation at particles, Raj (Raj, 1978) analyzed the nucleation of cavities at grain boundaries and secondary phase particles from the viewpoint of kinetics, in which he considered the formation of stable cavities from vacancy clusters. Raj proposed that for a stable cavity to form, a random "decohesion" event occurs, e.g. along a grain boundary interface, which can produce a stable cavity if the decohesion/discontinuity is equal to or greater in size than the critical cavity radius. The size of the critical cavity radius is related to the change in free energy resulting from the formation of the cavity; therefore, the critical radius is dependent on the applied stress across the boundary, the cavity volume, the interfacial energy of the cavity surfaces, the surface area of the nucleated cavity, the grain boundary energy, and grain boundary area that is consumed when the cavity is formed. According to Raj's analysis, the available heterogeneous nucleation sites will be more or less favorable for nucleation based on the resulting volume of the critical cavity at each site type, as illustrated in Fig. 2-32. Thus, nucleation at a triple point between a secondary phase particle and grain boundary is the most favorable site, since it requires the smallest cavity volume. The nucleation site will also affect the value of the apparent "threshold stress" for nucleation, with stress providing the driving force for cavity nucleation. The variation of threshold stress with different nucleation sites (here, different particle shapes) is shown in Fig. 2-33 and it can be seen that all of the particle shapes allow nucleation at much lower stresses than the theoretical tensile strength of the interface. Raj's analysis also incorporates grain boundary sliding and the resulting stress concentrations at grain boundary particles, which is more prevalent during transient creep.

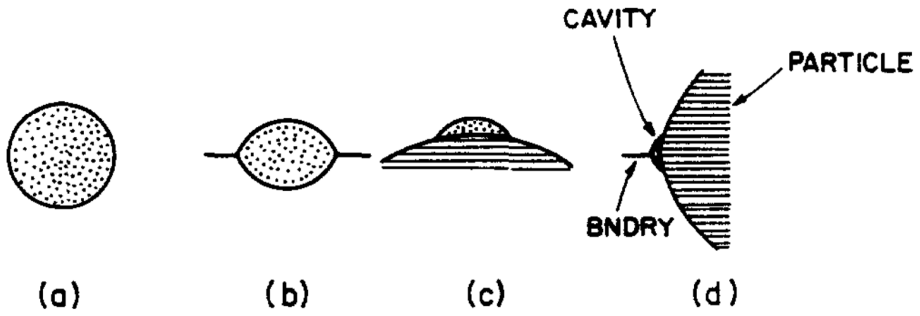


Figure 2-32. Schematic comparison of the variation in critical cavity volume for four cases of nucleation: (a) homogeneous nucleation (b-d) heterogeneous nucleation. Note that the critical volume decreases from (a) to (d) and the nucleation probability correspondingly increases. Reproduced from Raj (Raj, 1978).

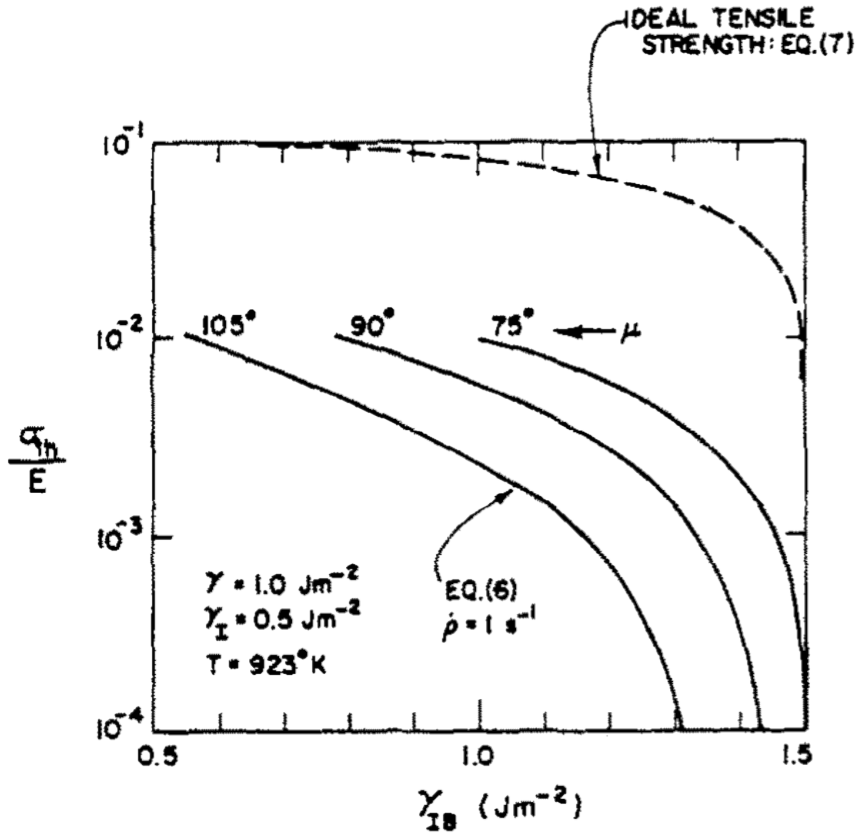


Figure 2-33. Modulus-normalized stress as a function of particle-matrix interfacial energy, showing that cavity nucleation significantly reduces the fracture stress. Reproduced from Raj (Raj, 1978).

Cavitation at particles was investigated experimentally by George and co-workers (George et al., 1987a, 1987b) using dilute alloys of iron with carefully controlled additions of specific elements such as sulfur, carbon, and phosphorus. These elements were added in order to identify which second phase particles (e.g. sulfides, carbides, etc.) could act as nucleation sites for creep cavities and whether cavities nucleated preferentially on specific particle types. The primary findings were summarized in Benci et al. (Benci et al., 1988); their experiments showed that occurrence of cavity nucleation on second phase particles did in fact vary depending on the elements added. Sulfides were identified as the preferred nucleation site for cavities, since for alloys which had sulfur in sufficient concentration to form sulfides at the creep temperature (700°C), cavities always nucleated on sulfides, particularly sulfides which were located on PAGBs. When sulfur content was reduced below the solubility limit, sulfides were not present and cavities were observed to nucleate on oxide particles. However, this behavior was also found to be dependent on carbon and phosphorus content, due to the effect of these elements on strengthening the particle-matrix interface. At the lowest sulfur levels (estimated 1ppm sulfur), they did not observe cavitation in any of the samples tested. Furthermore, when carbon was added to these low-sulfur alloys at sufficient levels to produce grain boundary and matrix carbide precipitation, the tensile tests showed high ductility and transgranular failure rather than (brittle) intergranular failure. Recently for CSEF weldments, Wang et al. (Wang et al., 2018b) has postulated that oxide inclusions in weld deposits may act as creep cavity nucleation sites and thus be responsible for the observed preferential rupture in the weld deposit after certain heat treatments (where the temperature exceeds Ac1).

A further consideration regarding cavity nucleation is whether nucleation occurs in a defined, distinct period during the initial stage of creep (discrete nucleation) to establish a stable cavity population followed mainly by growth and little additional nucleation, or whether continuous nucleation during creep leads to a cavity population that is

continually increasing either to some plateau value or to the time of rupture. The reason that this consideration is important is that it has implications for which mechanisms may control final creep rupture. In the first case, if the cavity population is nearly constant at a given value during the majority of creep life, then final rupture should be controlled by cavity growth. However, if continuous nucleation occurs, then final rupture may be controlled by either nucleation rate, growth rate, or by a combination of the two, as pointed out by Dyson (Dyson, 1983) who reviewed the phenomenon of continuous nucleation of creep cavities in regard to intergranular creep rupture. The two main viewpoints proposed as the rate controlling process for time to rupture, namely cavity growth and cavity nucleation, may both be proportional to the creep strain rate. However, the distinguishing consideration is that models which assign cavity growth as the controlling process assume that all cavities are nucleated simultaneously, which appears contrary to experimental evidence as indicated by Dyson. Rather, Dyson cites several experimental studies which directly measured the cavity density (to determine the fraction of cavitated boundary length) as functions of strain or time during creep. These experimental results suggested that the number of cavities continued to increase during the test duration, that *creep strain* was the parameter which correlated with cavity density, and that the cavity nucleation rate appeared linearly proportional to strain during the initial portion of creep (see Fig. 2-34), although the proportionality varied considerably with different materials. From these studies, Dyson also indicated that creep rupture ductility was found to be inversely related to the creep cavity nucleation rate as shown in Fig. 2-35.

Dyson also stated that there is an interaction between applied stress, strain to rupture, and cavity nucleation rate, such that three possible regimes of rupture behavior with varying contributions of cavity nucleation vs. cavity growth. The plot in Fig. 2-36 shows that at lower stress (longer rupture time), there is more cavity growth and thus cavity nucleation is the limiting factor. In contrast, at high stress and high nucleation rate,

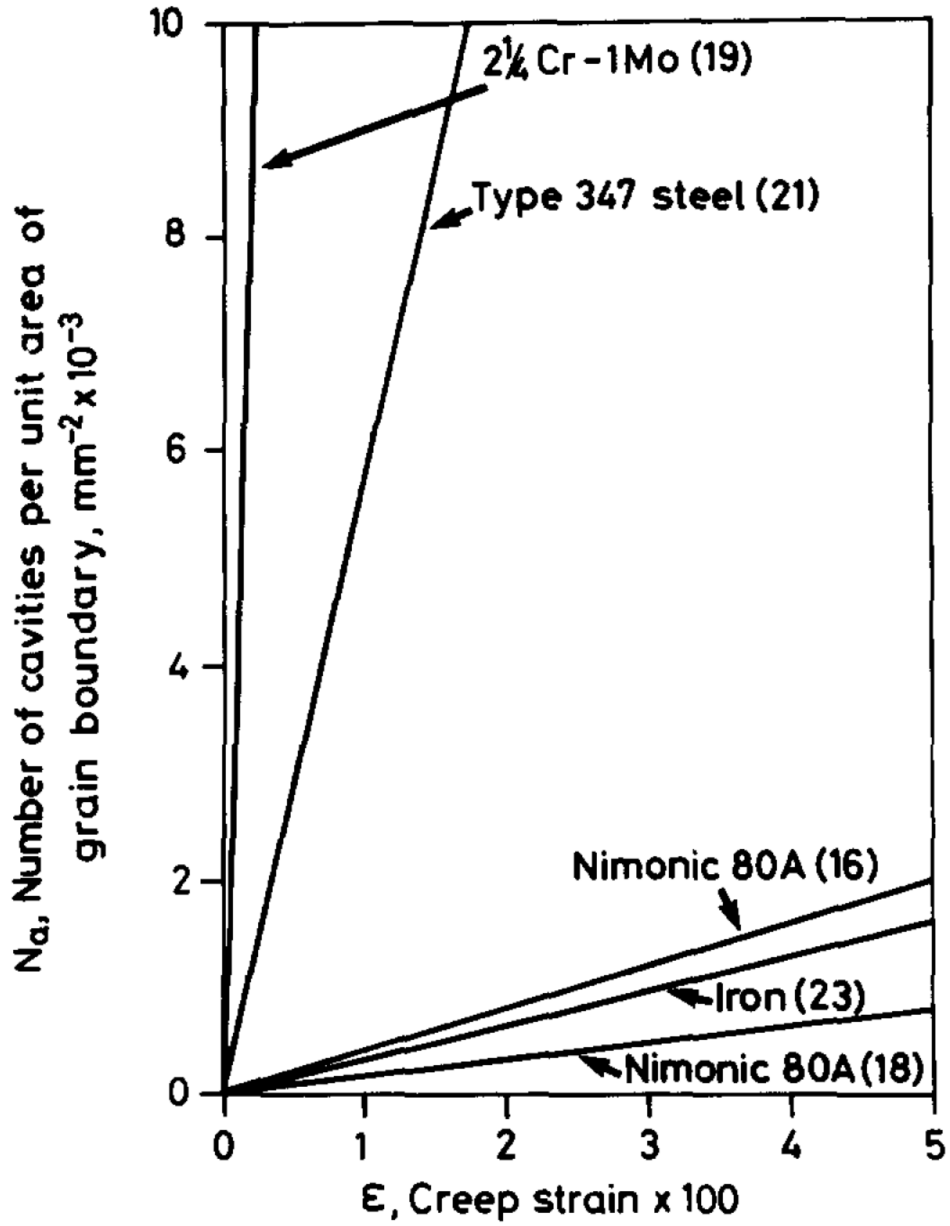


Figure 2-34. Experimental data for creep cavity density as a function of creep strain which illustrates the different rates of cavity nucleation observed in different materials. Note that the cavity density increases with strain for all the observed materials, indicating that continuous cavity nucleation was occurring. Reproduced from (Dyson, 1983).

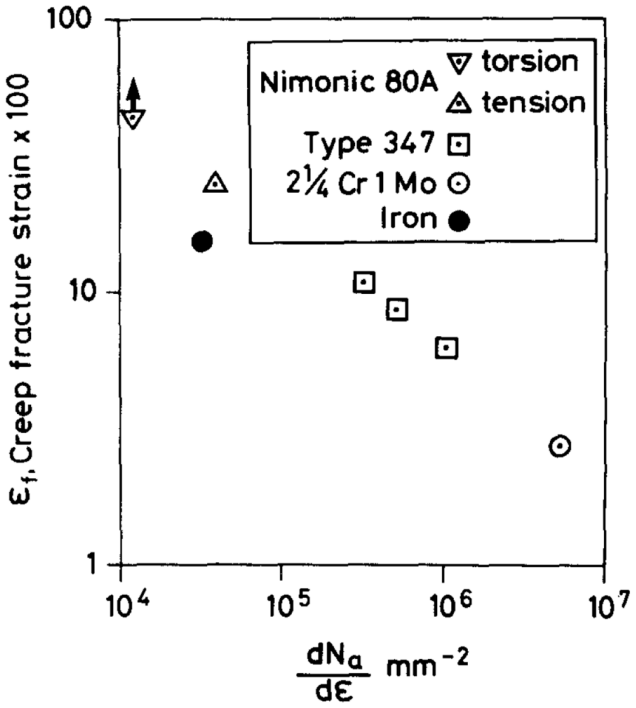


Figure 2-35. Experimental correlation between creep ductility (as measured by fracture strain) and the change in cavity nucleation rate per incremental unit of strain. An inverse proportionality between creep ductility and change in cavity nucleation rate is evident. Reproduced from (Dyson, 1983).

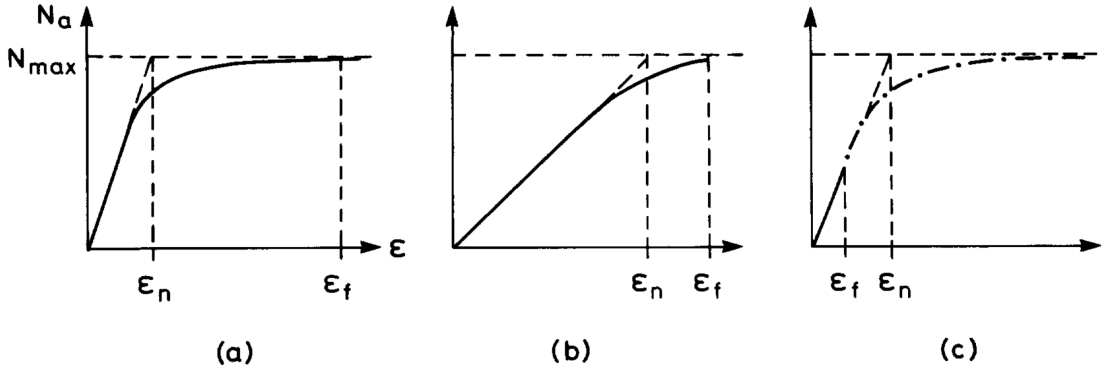


Figure 2-36. Schematic curves illustrating the variation in cavity density as a function of fracture strain (εf) for different creep conditions: (a) higher stress and higher dN/dε, where cavity growth is rate-controlling (b) lower stress and dN/dε, where cavity nucleation is rate-controlling (c) lower stress and variable dN/dε, where cavity density depends on both cavity nucleation rate and growth rate. Reproduced from (Dyson, 1983).

cavity growth will be relatively low and the rupture strain will be much greater than the strain to initiate cavity nucleation. When these two regimes are interacting, then the strain at rupture cannot be readily predicted since the cavity growth rate is inter-dependent on the nucleation rate. Additionally, Dyson stated that impurity element levels and pre-straining prior to creep exposure could affect the cavity nucleation rate; in the latter case, he showed experimentally that pre-straining led to an increased cavity density compared to solution annealed material (in this case, for Nimonic 80A).

2.1.7.2 Growth of Creep Cavities

Once creep cavities have been nucleated within a microstructure, cavity growth commences and may occur by several potential mechanisms. In the literature, understanding of growth mechanisms has not been unanimous, but Kassner and Hayes (Kassner and Hayes, 2003) summarized the potential mechanisms in their review as (i) unconstrained diffusional growth, (ii) grain boundary sliding, (iii) constrained diffusional growth, and (iv) plasticity. In the diffusional growth mechanisms, cavity growth occurs by diffusive flow of vacancies in the presence of a tensile stress either along grain boundaries, across the cavity surfaces, or within the grain matrix (bulk), as illustrated in Fig. 2-37. Diffusive cavity growth may be further sub-divided as either unconstrained or constrained, which is related to whether cavitation occurs uniformly through the microstructure (unconstrained) such that the majority of grain boundaries are cavitated, or whether cavitation occurs in a more limited manner such that only a fraction of boundaries are cavitated (heterogeneous nucleation). Heterogeneous cavity nucleation is the type of behavior in which constrained diffusive growth is more likely to occur since the overall cavity density the comparison is illustrated in Fig. 2-38. Eggeler (Eggeler, 1989) reported this type of creep damage for a 12Cr-Mo-V steel, which exhibited a heterogeneous cavity distribution (areas with both high or low cavity density) with cavities located on PAGBs and also within the PAG matrix.

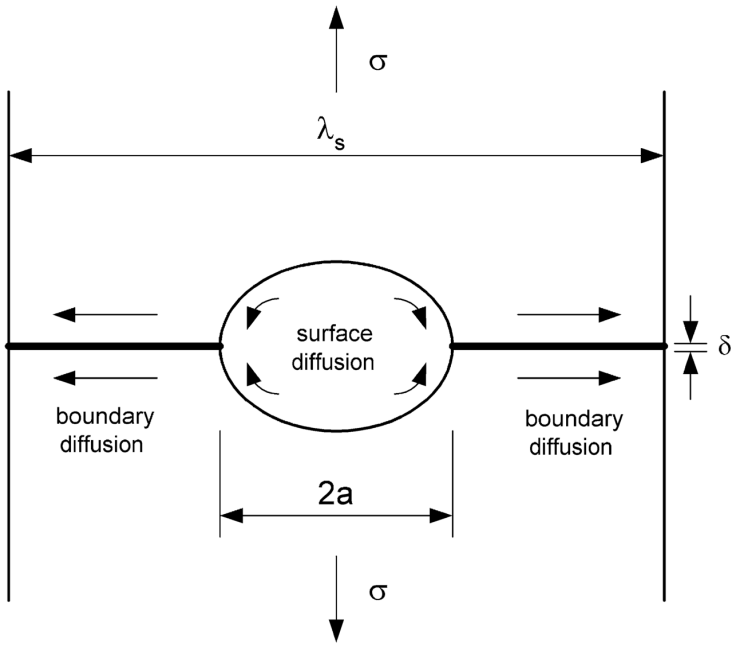


Figure 2-37. Schematic illustration of vacancy diffusion adjacent to a cavity while subjected to an applied tensile stress. In the figure, the terms are defined as follows: cavity diameter (2a), tensile stress magnitude (σ), cavity separation distance (λs), and grain boundary thickness (δ). Reproduced from Kassner and Hayes (Kassner and Hayes, 2003).

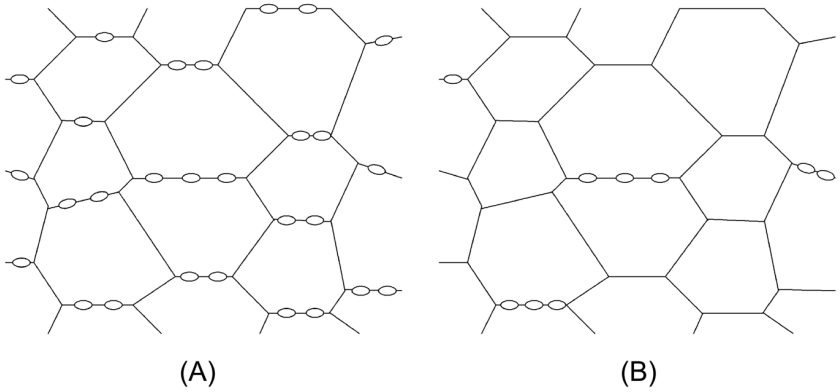


Figure 2-38. Schematic illustration of (a) homogeneous cavity nucleation, in which cavities are present on essentially all transverse boundaries, and (b) inhomogeneous cavity nucleation, in which cavities are only present on a limited number of transverse boundaries. The transverse boundaries are perpendicular to the applied stress which is oriented in the vertical direction. Reproduced from Kassner and Hayes (Kassner and Hayes, 2003).

In the case of constrained diffusive cavity growth, cavity growth which would otherwise occur freely due to diffusive processes is limited by creep plasticity (dislocation-controlled creep) of the surrounding material which is not cavitated. Thus, the diffusional growth rate of cavities is constrained by the creep rate of surrounding matrix regions. One of the early discussions on constrained diffusional growth was due to Dyson (Dyson, 1976). A primary difference between unconstrained and constrained diffusive cavity growth is that unconstrained growth predicts a linear dependence on stress together with an activation energy on the order of that for grain boundary diffusion, while constrained growth predicts a nonlinear variation of growth rate with stress. As Kassner points out, experiments with Cr-Mo steels have shown that the cavity growth rate exhibits a stress dependence which more closely accords with the predictions of constrained growth than with unconstrained growth, as illustrated in Fig. 2-39. Fig. 2-39 shows a plot of measured cavity growth rates for two different steels as a function of applied stress; the dashed contour lines in the plot indicate the linear dependence on stress which would be expected for unconstrained (homogeneous) nucleation. However, the measured growth rates exhibit a non-linear stress dependence, especially for the 2.25Cr-1Mo material. Furthermore, as previously discussed regarding cavity nucleation (see section Nucleation of creep cavities), it is generally considered that cavity nucleation occurs continuously during creep and thus there is a further potential interaction with constrained cavity growth. Riedel (Riedel, 1987) indicated that the combined effect of continuous nucleation and constrained growth could be represented by the equation:

$$t_f = \left[\frac{kT}{5\Omega\delta D_{gb}\sigma}\right]^{2/5}\left(\frac{\omega_f}{\dot{N}}\right)^{3/5}$$

Fig. 2-40 shows rupture time data as function of stress reported by Riedel (Riedel, 1987) for a 2.25Cr-1Mo steel. The figure shows several curves corresponding to predicted

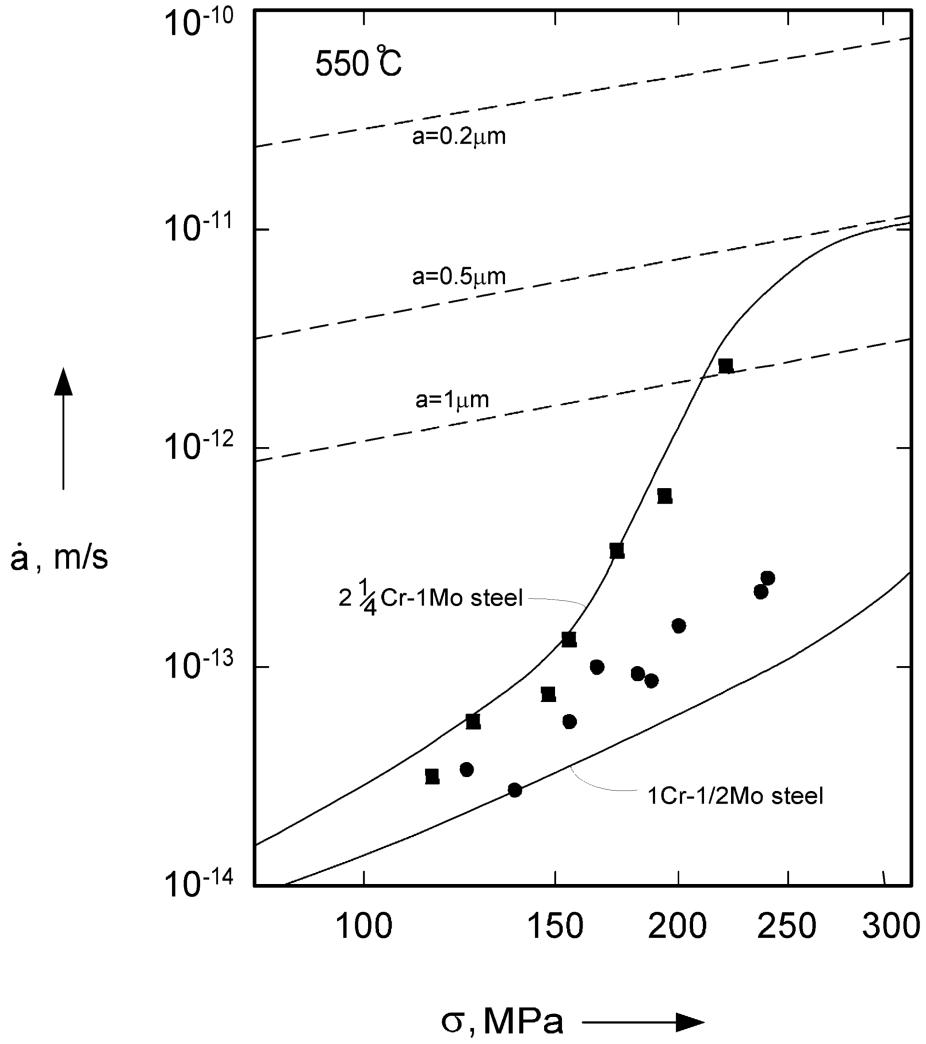


Figure 2-39. Measured cavity growth rate curves for two Cr-Mo steels. Several contours of cavity growth rate for unconstrained cavity growth are shown by the dashed lines; it is apparent that the measured growth rates are significantly lower than predicted by unconstrained growth. Additionally, the measured data shows a nonlinear stress dependence. Reproduced from Kassner and Hayes (Kassner and Hayes, 2003), originally from Riedel (Riedel, 1987).

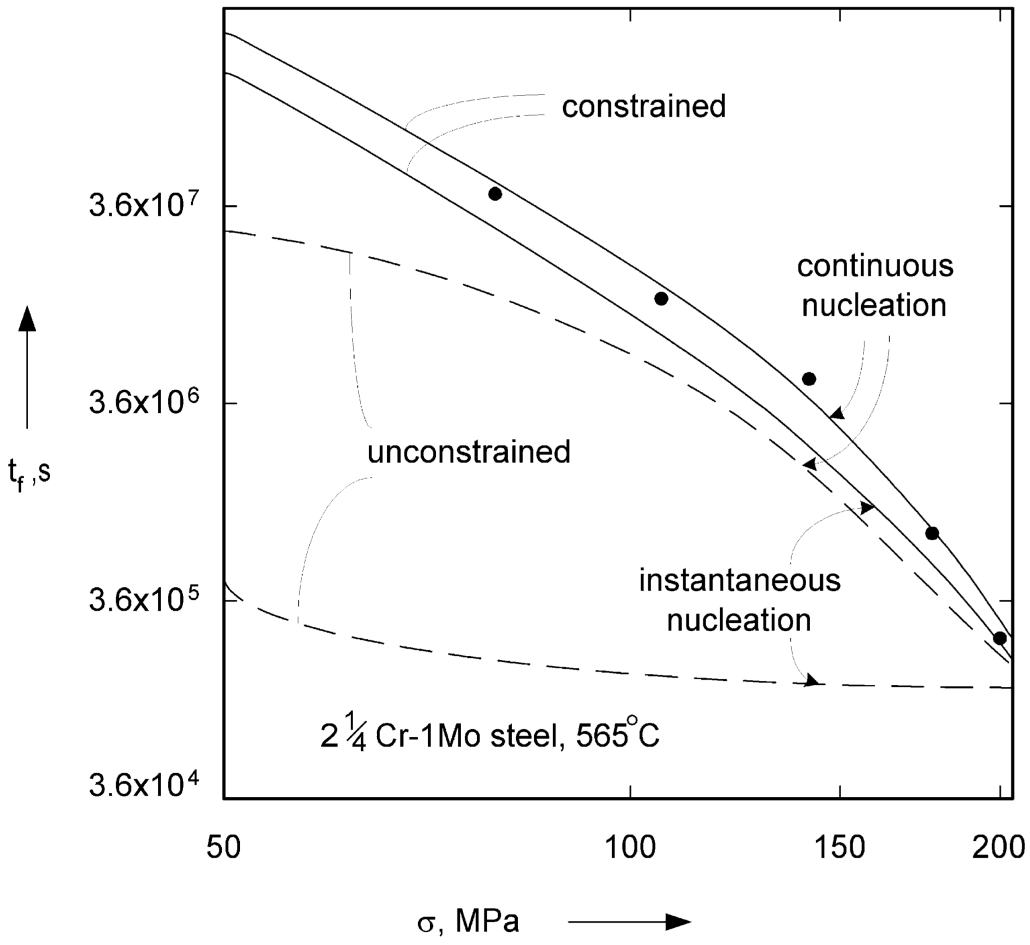


Figure 2-40. Measured failure times as a function of applied stress for a 2.25Cr-1Mo steel (round data points). The curves correspond to predicted behavior for different combinations of instantaneous/continuous nucleation and unconstrained/constrained cavity growth. It is apparent that the experimental points correlate most nearly to the curve which represents continuous nucleation coupled with constrained growth. Reproduced from Kassner and Hayes (Kassner and Hayes, 2003), originally from Riedel (Riedel, 1987).

behavior for different nucleation and growth mechanisms; the combination of continuous cavity nucleation and constrained growth correlates most closely with the experimental points.

2.1.8 Microstructural Evolution in CSEF Steels during Creep

The microstructural changes which occur in CSEF steels during creep are similar to those which occur during tempering, namely coarsening of precipitates and increasing inter-particle spacing, consequent coarsening of subgrains due to the reduction in subgrain boundary pinning, reduction in dislocation density, and changes in the boundary misorientation angle distribution comprised of low-angle and high-angle boundaries (Aghajani et al., 2009; Peŝiĉka et al., 2004). All of these microstructural changes decrease the creep strength of the material and thereby contribute to creep deformation and accumulation of creep strain. Abe (Abe, 2003) has stated that the transition from primary creep to acceleration creep is primarily caused by microstructure evolution that occurs during creep exposure, not by localized plastic deformation and stress concentration from necking or from creep damage accumulation. Compared to tempering, in which the material is subject only to static aging (thermal exposure in the absence of applied stress), some of the microstructural evolution processes in CSEF steels may occur more readily during creep, either in extent or rate of change. Thus, static aging experiments are only of limited value in predicting the long-term stability of the tempered martensitic lath structure (TMLS) in CSEF steels.

As previously discussed, the presence of fine precipitates on the subgrain boundaries is critical to the ability of CSEF steels to maintain good long-term creep strength, because high dislocation density on its own is not a stable strengthening mechanism under creep conditions (Kostka et al., 2007). Thus, precipitate coarsening is especially detrimental to the creep properties of CSEF steels and precedes the loss of strength by changes in subgrain structure and dislocation density. Hättestrand and Andrén

(Hättestrand and Andrén, 2001) showed for P92 steel that $M_{23}C_6$ carbides coarsened slightly during creep at 600°C while no coarsening was observed for static aging. At 650°C, the extent of coarsening was similar between static aging vs. creep, but coarsening occurred more rapidly during creep, as illustrated in Fig. 2-41; note the similar particle sizes at ~4,000 h creep and ~10,000 h aging for the two conditions. It should be noted that increased tendency for coarsening during creep depends upon the precipitate type, since the same authors also reported no difference in MX carbonitride evolution (either for particle size or volume fraction) between static aging vs. creep at either 600°C or 650°C. Panait et al. (Panait et al., 2009) reported similar results regarding MX precipitates in a Grade 91 steel after more than 100,000 h creep exposure at 600°C/80 MPa; as shown in Fig. 2-42, there is minimal change in the size of MX precipitates between the as-received, thermally-aged, and creep-exposed material states. Variable microstructure evolution was also observed by Ghassemi-Armaki et al. (Ghassemi-Armaki et al., 2013) for static thermal exposure and creep exposure of Grade 91 steel. They reported that coarsening of subgrains and increased inter-particle spacing of $M_{23}C_6$ precipitates were observed during static thermal exposure at 650°C and 700°C, but not at 550°C or 600°C, while spacing of MX precipitates remained unchanged at all temperatures during static aging. Compared with the static aging condition, for creep exposure it was reported that both $M_{23}C_6$ and MX showed some increase in inter-particle spacing during testing at 700°C and stresses of 40 MPa or 50 MPa, but comparing the two, the spacing of $M_{23}C_6$ was greater.

As a consequence of accelerated precipitate coarsening and increased subgrain boundary mobility as the inter-particle spacing increases, thus decreasing the pinning force, increased coarsening of subgrains is also observed during creep of tempered martensite ferritic steels, as reported in the literature for both short-term and long-term creep experiments (Abe, 2004; Aghajani et al., 2009; Dronhofer et al., 2003; Eggeler et al., 1987; Ghassemi Armaki et al., 2011; Panait et al., 2009). Dronhofer et al. (Dronhofer et

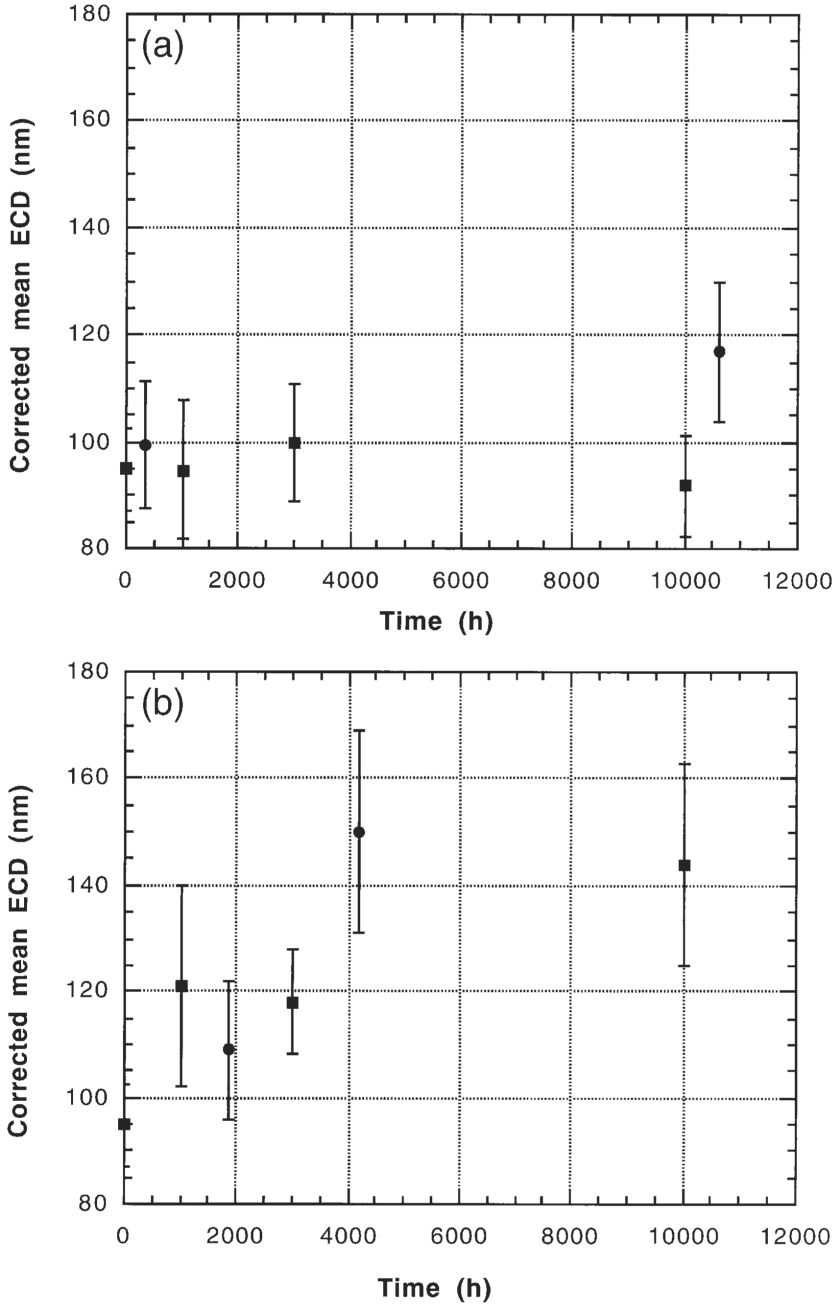


Figure 2-41. Evolution of M23C6 carbide size (in terms of equivalent circle diameter, ECD) as a function of exposure time at (a) 600°C and (b) 650°C. Square symbols correspond to static thermal exposure and circle symbols indicate creep exposure. Note that there is no significant change in mean diameter of M23C6 for either static or creep exposure at 600°C, while at 650°C, coarsening occurs after 4000 h during creep and 10000 h during static exposure. Reproduced from Hättestrand and Andrén (Hättestrand and Andrén, 2001).

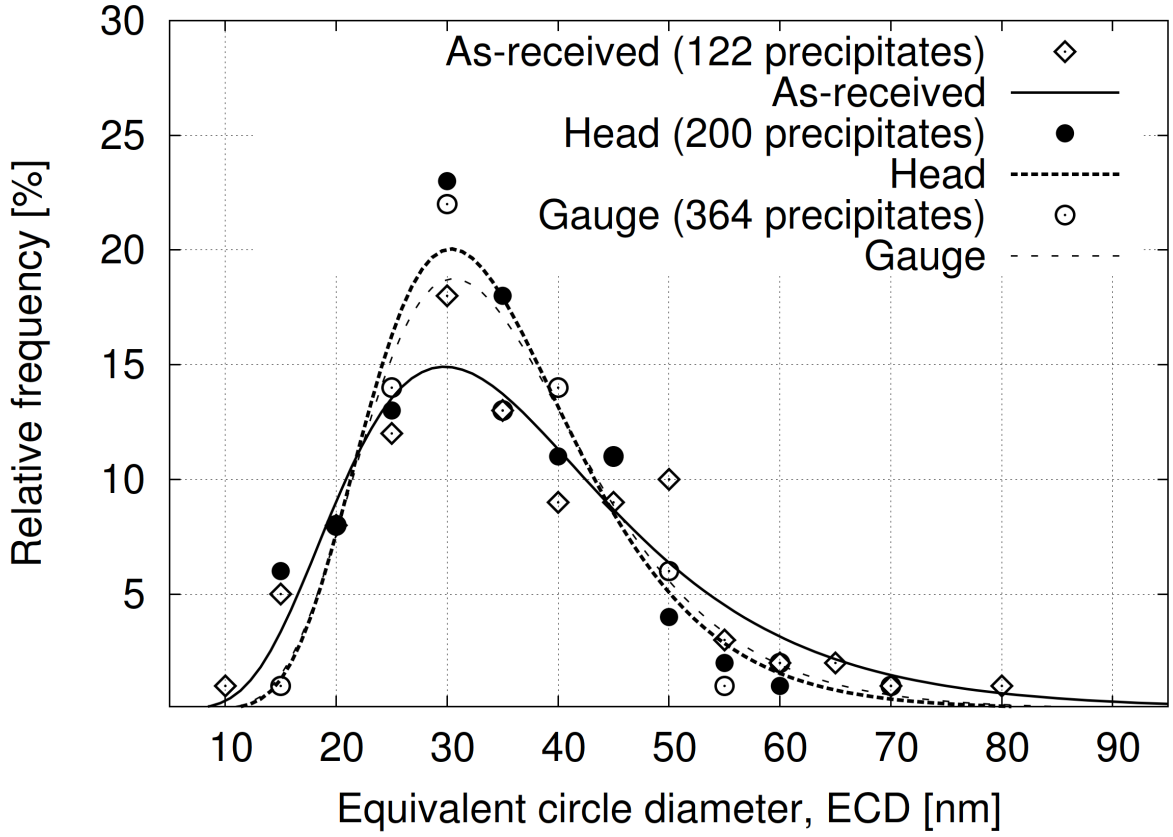


Figure 2-42. Comparison of MX precipitate size distribution for three material states of a Grade 91 steel: as-received material, after static thermal exposure at 600°C ("head"), and after creep exposure with strain at 600°C/80 MPa ("gauge"). The durations of the static thermal exposure and creep exposure were both 113,431 h. Note that the peak value of the size distribution (~30 nm) is essentially the same for the three states, indicating the stability of MX precipitates under these conditions. Reproduced from Panait et al. (Panait et al., 2009).

al., 2003) showed that subgrain growth was greater during short-term creep of X20CrMoV12-1 steel compared to static aging of a similar duration, as illustrated in Fig. 2-43 for a distribution plot of subgrain width. During very long-term creep exposure at 600°C/80 MPa lasting over 100,000 h, Panait et al. 2009 (Panait et al., 2009) showed by TEM measurements that the subgrain size distribution after creep was significantly affected by the presence of strain (see Fig. 2-44), in that the size distribution became much broader and with a larger value for average width as compared to the size distribution for a region with the same duration of thermal (no strain) exposure. Ghassemi Armaki et al. (Ghassemi Armaki et al., 2011) also reported some differences in the subgrain size evolution for Cr-2W-0.4Mo-1Cu-VNb steels during static aging as compared with creep exposure, and showed furthermore that subgrain and precipitate evolution depended on Cr content. For 9Cr-2W-0.4Mo-1Cu-VNb steel, after creep at 650°C/98 MPa the subgrain size was on the order of 600 nm, but after 10,000 h static aging at the same temperature, the subgrain size was on the order of 450 nm. It was observed that the steel with a 9%Cr content showed the most stable microstructure after long-term creep exposure.

Although significant subgrain coarsening occurs in most 9-12Cr CSEF steels during creep, experiments by Kostka et al. (Kostka et al., 2007) demonstrated the critical role of precipitates in stabilizing the subgrain structure to delay the formation of equiaxed subgrains. By comparing a martensitic X20 steel with a Fe-10Cr alloy subjected to severe plastic deformation to obtain a high dislocation density similar to that of a tempered martensite ferritic steel, the authors showed that the precipitate-free binary Fe-10Cr alloy exhibited a significantly higher primary creep rate (four orders of magnitude) and also exhibited extensive dislocation recovery and recrystallization along with subgrain growth after creep exposure at 600°C/100 MPa, as compared to the X20 steel at the same conditions. It should be noted that while subgrain growth occurred in the X20 steel, a “lath-like” subgrain structure was retained; in contrast, the precipitate-free alloy

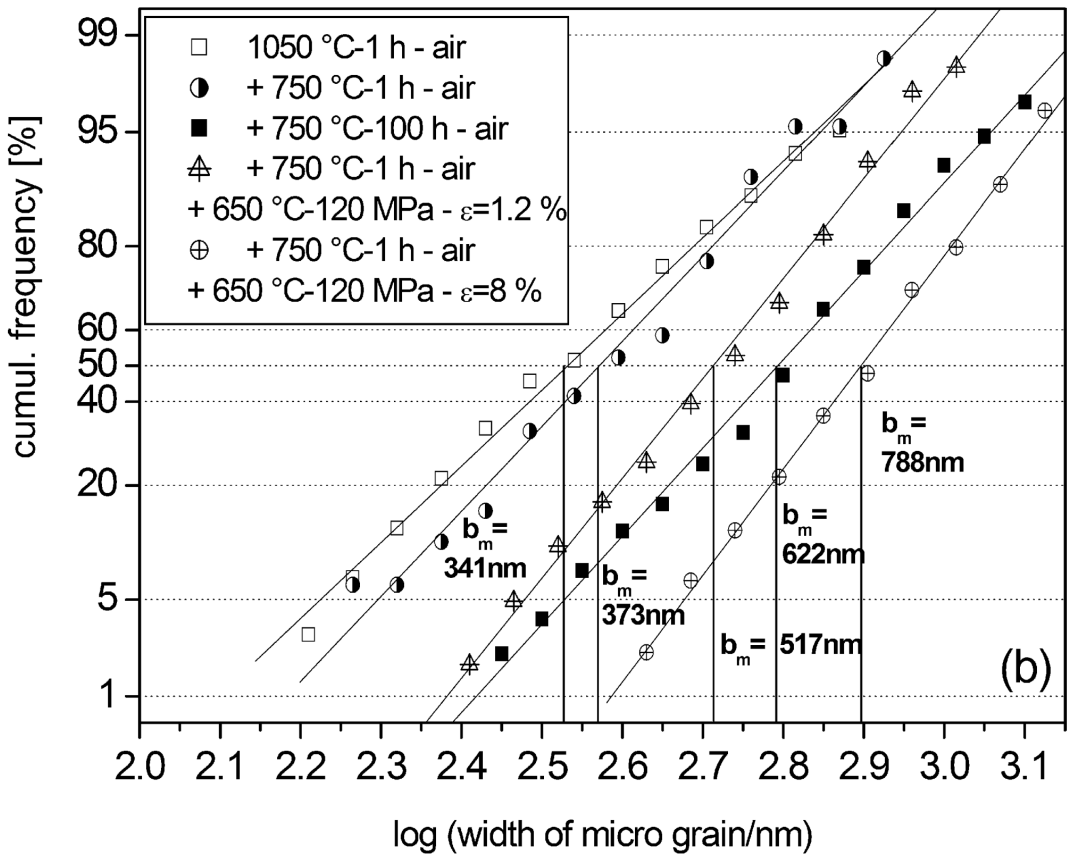


Figure 2-43. Cumulative probability plot of subgrain width showing the evolution of subgrain size in in X20CrMoV12-1 steel from the initial material state (normalizing, 1050°C/1 h) with different extents of tempering and/or creep exposure. Note that the largest subgrain width is for the 8% creep strain condition which occurred after 126 h of creep exposure; in comparison, extended tempering for 100 h at 750°C (static thermal exposure) resulted in less subgrain coarsening. Reproduced from Dronhofer et al. (Dronhofer et al., 2003).

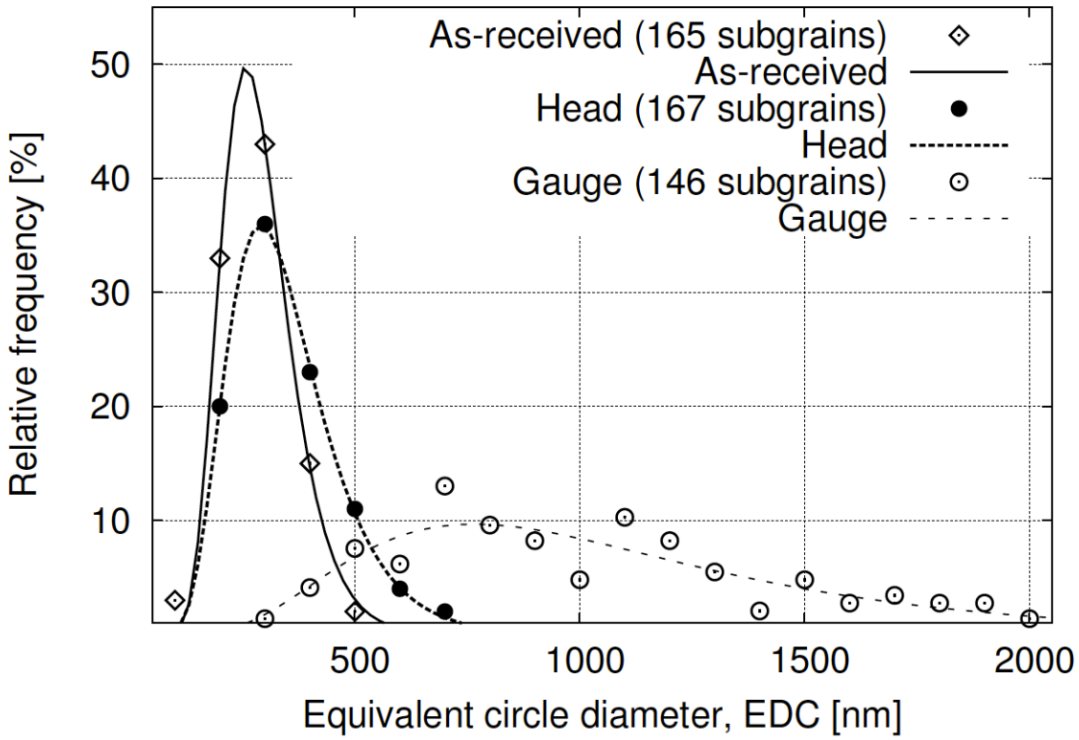


Figure 2-44. Comparison of subgrain size distribution for three material states of a Grade 91 steel: as-received material, after static thermal exposure at 600°C ("head"), and after creep exposure with strain at 600°C/80 MPa ("gauge"). The durations of the static thermal exposure and creep exposure were both 113,431 h. Note that the peak value and narrow width of the distribution is similar in the as-received and static thermal exposure conditions, but the distribution after creep exposure broadens very significantly and the peak shifts to larger subgrain size. Based on these distributions, significant subgrain coarsening occurred in some (but not all) subgrains during creep, while essentially no coarsening took place during static thermal exposure. Reproduced from Panait et al. (Panait et al., 2009).

exhibited recrystallization and formation of equiaxed subgrains, leading to greatly increased strain accumulation (see strain rate vs. strain plot in Fig. 2-45). However, even with the presence of precipitates on subgrain boundaries (as in TMFS steels), an equiaxed subgrain structure will eventually form. Sawada et al. (Sawada et al., 2011) showed that the subgrain structure of a Grade 91 steel was stable to ~30,000 h of creep exposure at 600°C/70 MPa, with subgrain growth observable after 50,000 h, a sudden increase in growth after ~70,000 h, and a fully equiaxed subgrain structure at rupture after ~80,000 h. This evolution in subgrain structure during creep is illustrated by the TEM micrographs in Fig. 2-46; the authors also noted that the sudden increase in subgrain growth at ~70,000 h corresponding to the region of the creep curve exhibiting a rapid increase in strain. Abe (Abe, 2015) also made an association between an increased rate of microstructural recovery (e.g. subgrain coarsening) and the tertiary or acceleration regime of the creep curve. Abe further noted that when testing a 9Cr-1W steel with different initial microstructures, the final hardness values and final microstructures after creep exposure were qualitatively similar, exhibiting subgrain coarsening and dislocation recovery with a more equiaxed subgrain structure. This suggests that 9Cr-type tempered martensite ferritic steels may exhibit microstructural change toward a typical "terminal" microstructure associated with tertiary creep and rupture, with varying times required to reach this microstructural condition according to the initial microstructure.

During creep, CSEF steels also exhibit further changes in dislocation density (beyond what occurs in tempering) as dislocation motion, dislocation interactions with adjacent dislocations and subgrain boundaries, and dislocation recovery all occur, which influence creep strength and creep deformation. The changes in dislocation density vary with dislocation type, since dislocations may be present either as free dislocations within the subgrain matrix or as boundary dislocations within a subgrain

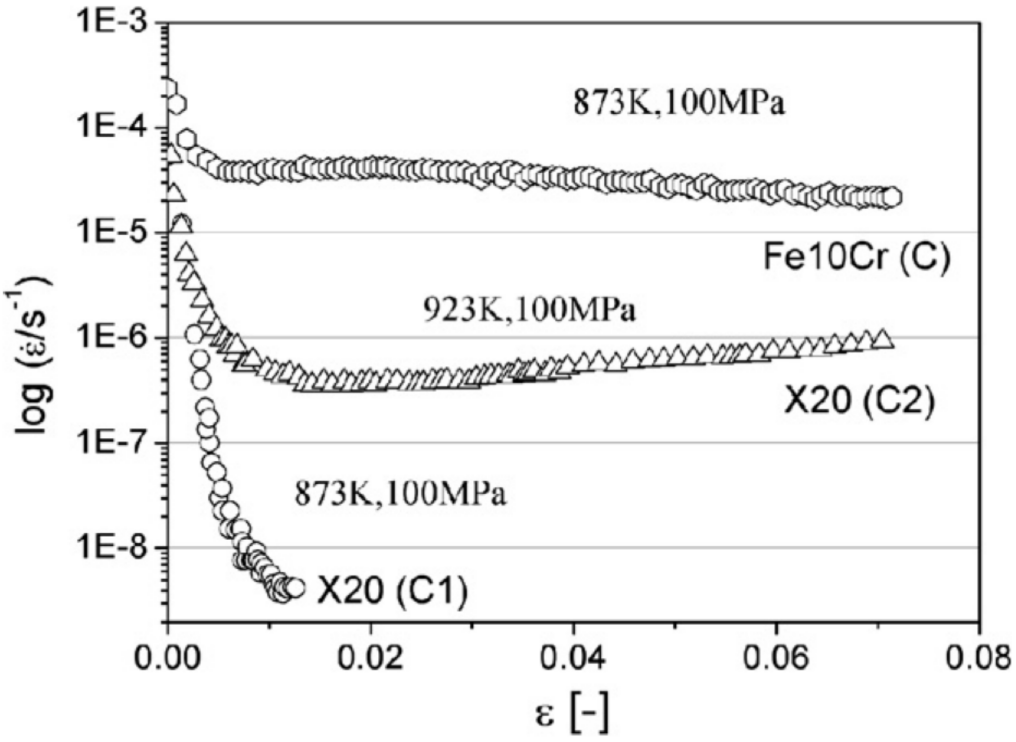


Figure 2-45. Creep curves for X20 steel after tempering (750°C/4 h) and binary Fe-10Cr alloy after tempering (600°C/0.25 h). Comparing the curves at 600°C (873 K), note the much lower creep rate for X20 versus Fe-10Cr (approx. four orders of magnitude). Reproduced from Kostka et al. (Kostka et al., 2007).

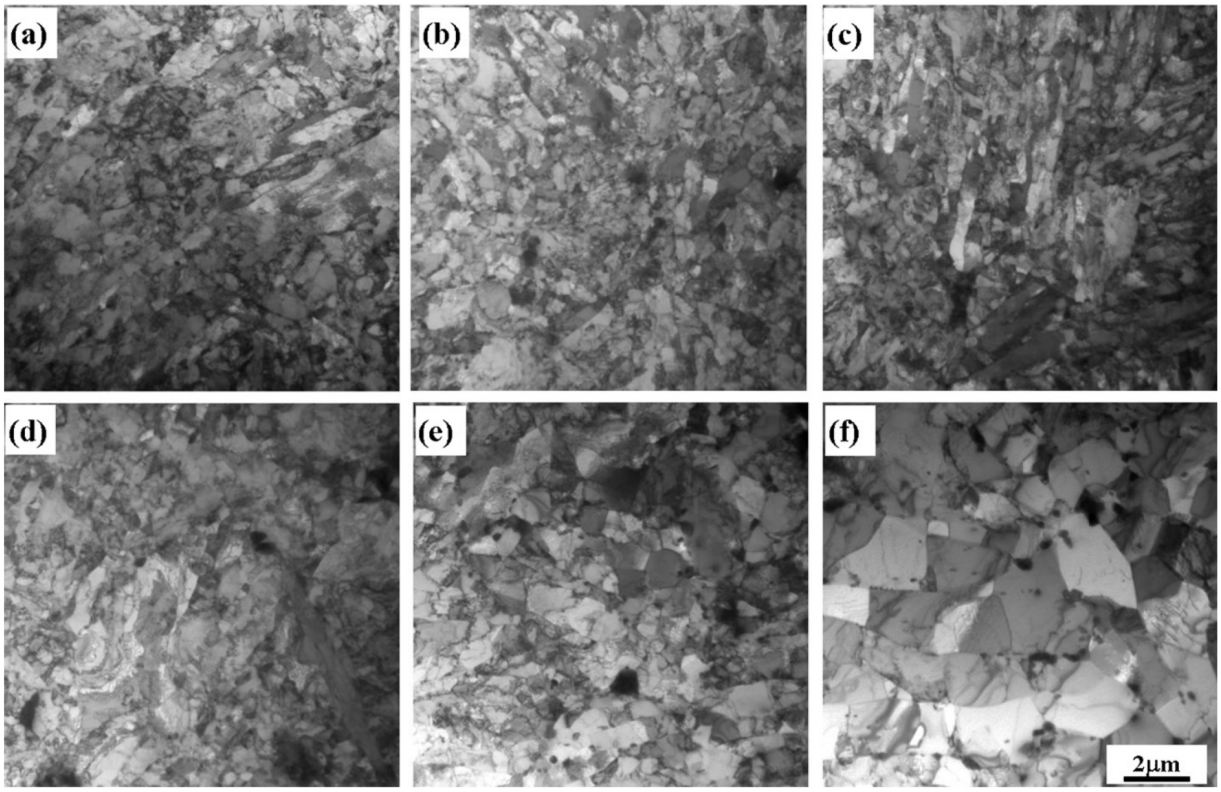


Figure 2-46. TEM micrographs illustrating the changes in microstructure occurring in Grade 91 steel after tempering at 765°C/0.5 h and creep at 600°C/70 MPa for different time periods. (a) As-tempered, no creep exposure (b) 9992 h creep (c) 30,030 h creep (d) 50,064 h creep (e) 70,000 h creep (f) rupture after 80,736.8 h. Note the gradual subgrain coarsening and formation of equiaxed subgrains that occurs during creep up to 70,000 h, followed by a drastic increase in size and equiaxed nature of subgrains during the final 10,736.8 h of life between (e) and (f). Reproduced from Sawada et al. (Sawada et al., 2011).

boundary[4] (Peŝiĉka et al., 2004). Abe (Abe, 2015) and Pešička et al. (Pešička et al., 2003) have reported for CSEF steels such as P91 and X20 that the initial region of the creep curve where the creep rate is sharply decreasing (transient or primary creep regime, as shown schematically in Fig. 2-47 or experimentally in Fig. 2-48) corresponds to decreasing dislocation density. Pešička et al. (Pešička et al., 2003) additionally stated that the role of dislocations in creep deformation of CSEF steels cannot be limited solely to that of obstacles to motion and plastic deformation (as proposed by (Maruyama et al., 2001)), but rather that dislocations are also "carriers" of plastic deformation. In a later publication (Peŝiĉka et al., 2004), the same concept was re-stated by Peŝiĉka et al. and slightly extended to point out that the function of dislocations as either obstacles to, or carriers of, plastic deformation may depend on strain rate.

The changes in dislocation density also show differences when comparing between static aging and creep, as discussed for subgrain and precipitate evolution. Peŝiĉka et al. (Peŝiĉka et al., 2004) stated that static dislocation recovery during thermal exposure occurs more slowly than dynamic recovery occurring during creep. They considered different degrees of recovery "intensity" (temperature or stress exposure leading to substructure recovery) for different material states of a X20 steel and divided the substructure boundaries into two categories, subgrain boundaries with angles $< 1°$ and micrograin boundaries with angles of 2-5°, and reported that with increasing recovery "intensity," the frequency of micrograin boundaries decreased while the subgrain boundaries increased in frequency. They also showed that the density of free dislocations decreased more rapidly than boundary dislocations (see Fig. 2-49), from which they conclude that free dislocations and their recovery are related to primary creep (as stated by Abe (Abe, 2015)).

[4] Subgrains are lower-energy arrangements of dislocations, comprised of the subgrain matrix regions (lower dislocation density) and subgrain boundaries (networks of higher dislocation density).

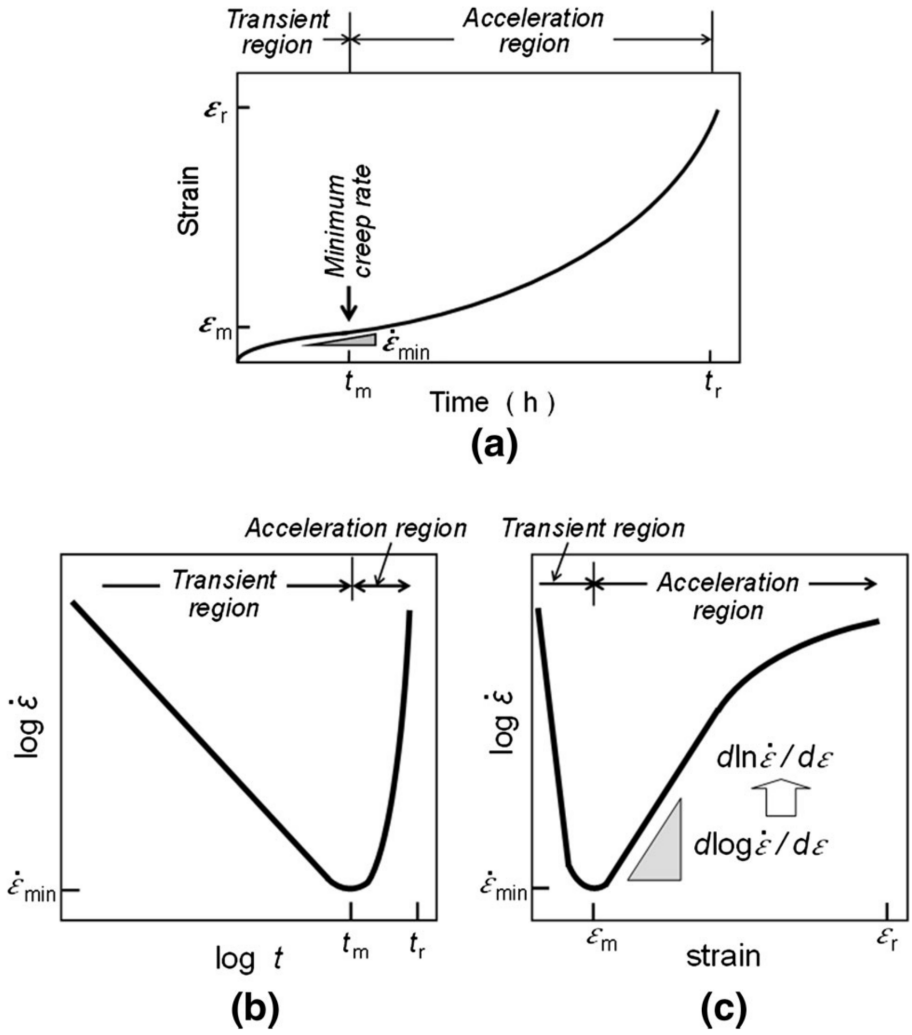


Figure 2-47. Schematic curves showing the relationship between creep strain and creep rate as functions of time and strain. Note that the creep rate versus time plot shows only primary (transient) and tertiary (acceleration) creep regions, without a steady state region where the creep rate is constant. Reproduced from Abe (Abe, 2015).

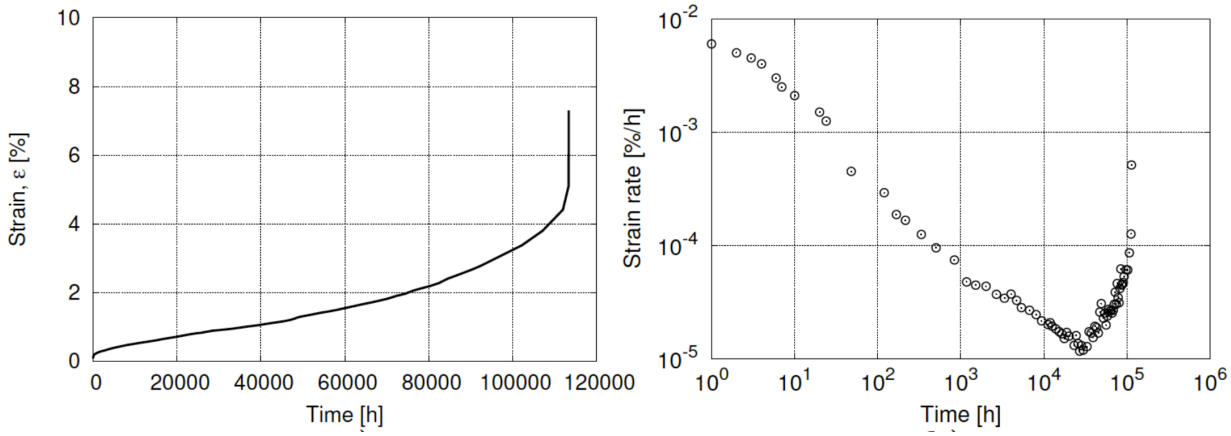
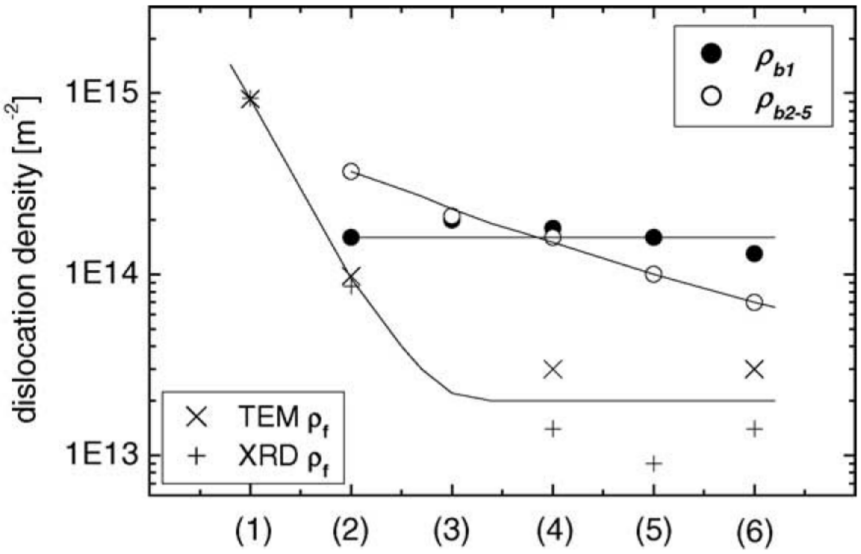


Figure 2-48. Creep curves for Grade 91 base metal in the tempered condition () for creep testing at 600°C/80 MPa. Although not emphasized by the log scale of the plot in (b), note that the majority of creep life is expended in the tertiary regime where the creep rate is increasing. Adapted from Panait et al. (Panait et al., 2009).



(1): Solution annealed 1050 °C for 1 h and water quenched
(2): (1) + tempering at 750 °C for 1 h
(3): (1) + tempering at 750 °C for 4 h
(4): (2) + creep at 650 °C, 120 MPa, 1.2% strain
(5): (1) + long term aging at 750 °C for 100 h
(6): (2) + creep at 650 °C, 120 MPa, 8% strain

Figure 2-49. Evolution of dislocation density for different material conditions (1) through (6), as described below the graph, for an X20 (12Cr) steel. The data points show the differences in evolution of free dislocations (×, +) compared to the separate contributions to the total boundary dislocation density (ρb) from subgrains (ρb1, solid circles) and low angle boundaries (ρb2-5, empty circles). Adapted from Peŝiĉka et al. (Peŝiĉka et al., 2004).

Lastly, microstructural evolution during creep also includes changes in the characteristics of low-angle and high-angle boundaries at different length scales (e.g. PAG, packet, block, lath/subgrain, in decreasing order of size). As summarized previously, low-angle boundaries are typically considered to correspond to misorientation angles of a few degrees or less, and are divided by some researchers (e.g. Peŝiĉka et al (Peŝiĉka et al., 2004)) into "subgrain" boundaries with angles ≤1° and "micrograin" boundaries with angles of 2-5°. High-angle boundaries are generally associated with prior austenite grain boundaries, although Peŝiĉka et al. (Peŝiĉka et al., 2004) has also reported that some micrograin boundaries are also high angle boundaries. It is has been shown (Aghajani et al., 2009) that the subgrain boundaries (≤1°) increase in frequency during creep, but do not increase in frequency during static aging, as shown in the misorientation angle frequency plots in Fig. 2-51; in contrast, the high angle boundaries do not change during either creep or static aging. Based on the fact that an increase in subgrain widths in this material was also reported, a correlation can be made that the lowest boundaries (≤1°) are the boundaries which are involved in recovery processes that lead to subgrain coarsening. This could either be due to an inherent instability of the ≤1° boundaries, or it could indicate the presence of other factors, e.g. evolution of precipitates which are located on the ≤1° boundaries leading to increased boundary mobility and coarsening. It is interesting that Aghajani et al. (Aghajani et al., 2009) noted that room temperature hardness values do not shown a correlation with presence/absence of precipitates on subgrain boundaries, but rather were inversely correlated with increases in subgrain width (see Fig. 2-50). This could possibly be a partial explanation for why room temperature hardness measurements have been considered mostly ineffective in identifying creep-susceptible regions in weldment HAZs: due to the fact that extensive subgrain coarsening has not yet occurred (having only experienced the PWHT which is typically on the order of 2 h), but extensive changes in precipitates *have* occurred which are not distinguishable by hardness.

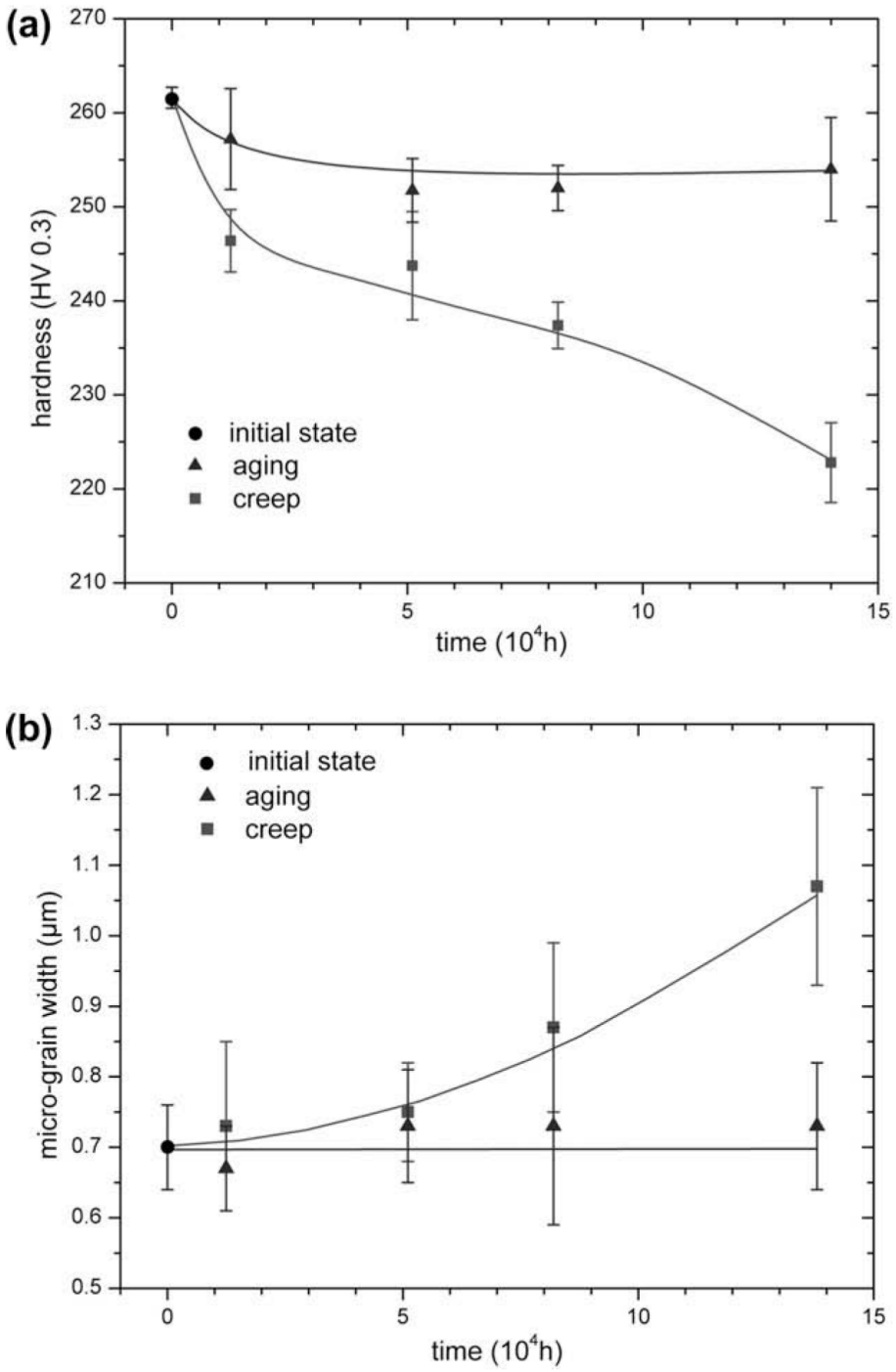


Figure 2-50. Plots of measured micro hardness and subgrain (micro-grain) width as a function of time during static thermal aging (no stress) and creep exposure. Note that in (b) the subgrain width does not change definitively during static exposure, but subgrain growth does increase during creep exposure. Reproduced from Aghajani et al. (Aghajani et al., 2009).

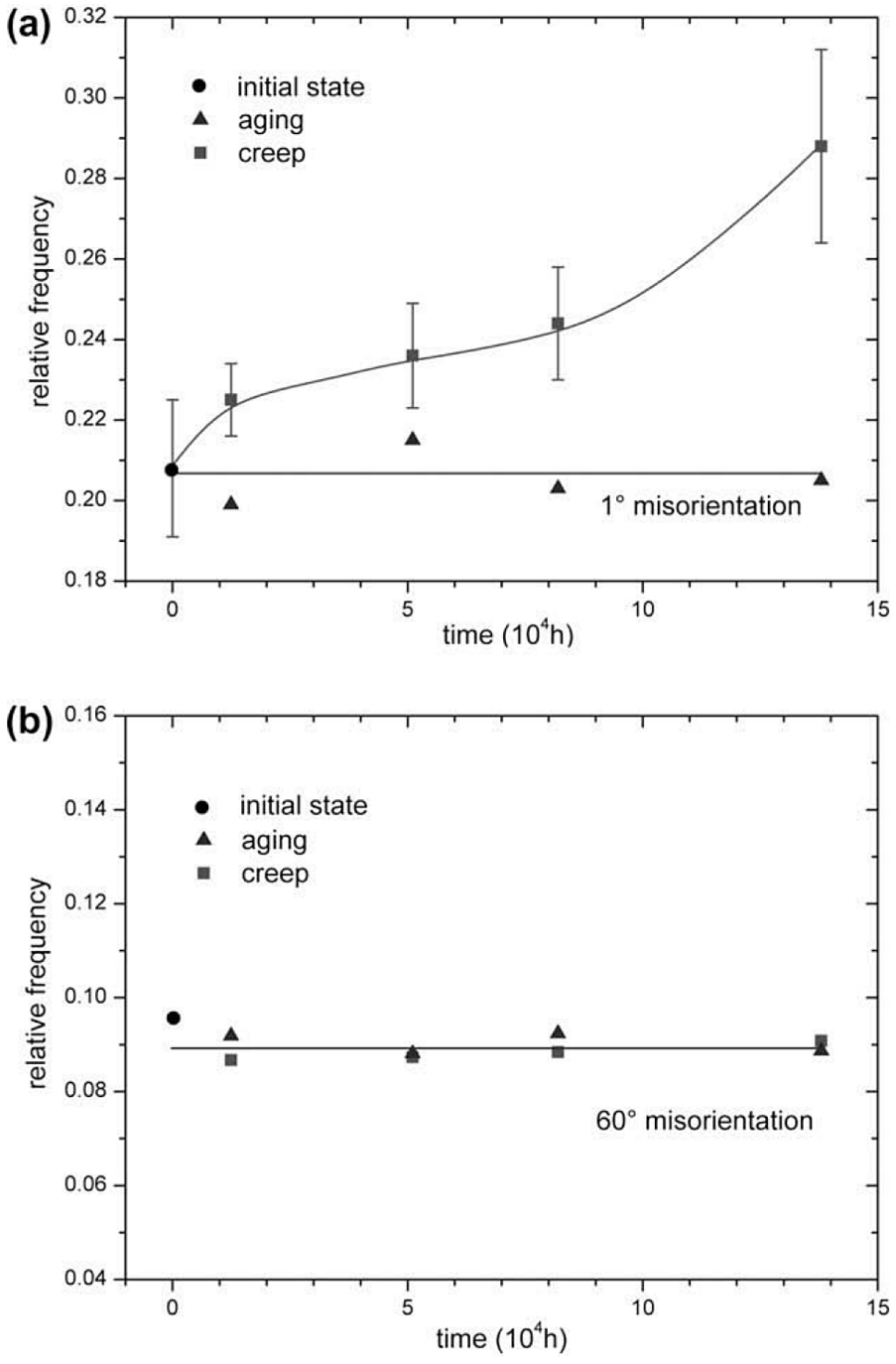


Figure 2-51. Frequency plots showing the evolution of misorientation angle for an X20 steel during static thermal aging at 550°C and creep at 550°C/120 MPa. (a) Evolution of 1° (low angle) boundaries (b) Evolution of 60° (high angle) boundaries. Reproduced from Aghajani et al. (Aghajani et al., 2009).

2.1.8.1 Effect of Tempering on Subsequent Creep Rupture Life and Creep Deformation

Tempering has a significant effect on the creep behavior of CSEF steels. Tempering heat treatments for CSEF steels are normally specified below the lower critical transformation temperature, resulting in microstructural evolution (although not transformation to austenite). Regardless of whether tempering is applied to a base metal after austenitization or to a weldment in the form of a postweld heat treatment, the microstructural changes induced by tempering have a subsequent effect on the creep deformation behavior of CSEF steels. The manner of this effect on creep properties will be described herein in a general sense with regard to base metals; the effect on weldment behavior will be addressed in a later section.

As discussed previously in Section "Microstructural changes in CSEF steels during tempering," the principal microstructural changes occurring during tempering of CSEF steels are (in descending order of extent) reduction in dislocation density, coarsening of precipitates, and coarsening of subgrains. The effect of these changes on subsequent creep behavior, namely creep deformation (properties such as strength and strain rate) and rupture time has been reported by several investigators. Abe (Abe, 2003) compared creep behavior and microstructural characteristics of 9Cr-1W steel in three conditions: quenched, quenched and tempered (750°/1h), and quenched and extended temper (750°C/20h). The results showed that a standard tempering treatment of 750°C/1 h yielded a 50% increase in rupture life compared to the as-quenched material; however, an extended temper of 750°C/20 h produced a 30% decrease in life compared to the as-quenched condition. The creep rate plots for the three conditions in Fig. 2-52 reveal that all three materials exhibit transient and acceleration creep regions without a steady state region. The slope of creep rate vs. time is similar for all three conditions, with the quenched material exhibiting a slightly more rapid decrease in rate. The extended temper condition showed the shortest time to reach the minimum creep rate, while the standard temper showed the lowest minimum creep rate and the longest time to reach

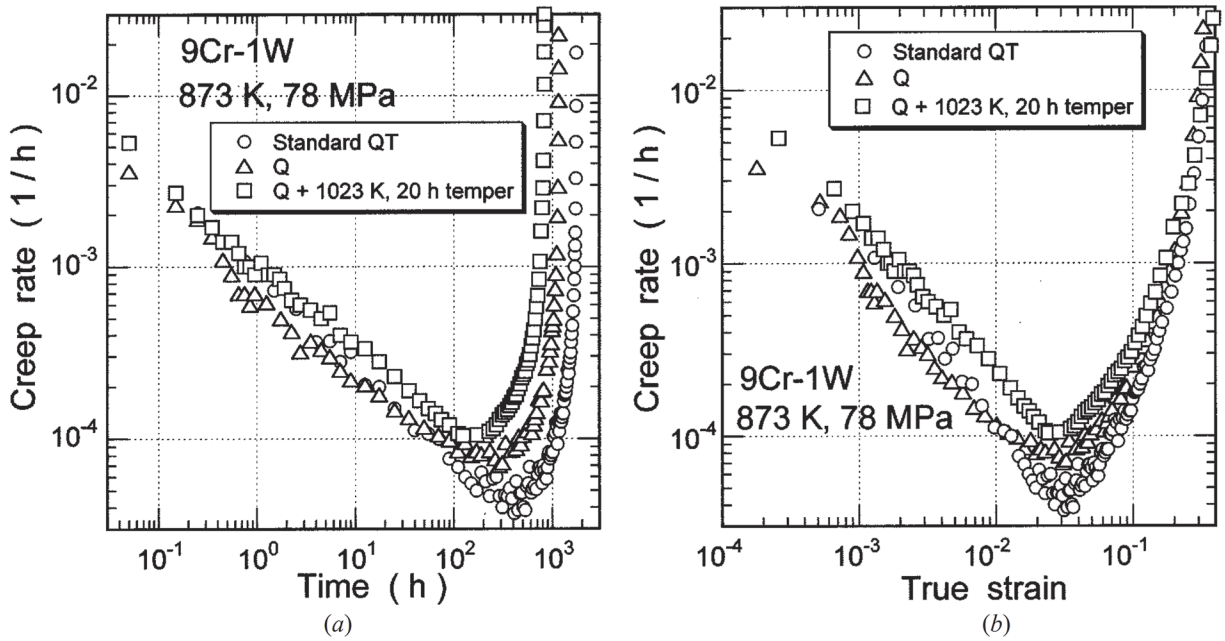


Figure 2-52. Comparison of measured creep data for three different heat treatment conditions of a 9Cr-1W steel. Reproduced from Abe (Abe, 2003).

the minimum creep rate. After reaching the minimum creep rate, all three materials showed similar slope of creep rate in the acceleration region. This suggests that the differences in rupture times originate from differences in the length of time required to attain the minimum creep rate. Additionally, the majority of creep life consumption and creep strain accumulation occurred in the acceleration creep regime where the creep rate is increasing, as shown in Fig. 2-52.

Regarding the microstructures of the three material conditions shown in Fig. 2-53, the standard Q&T (750°C/1 h) showed carbide precipitation (dark spots) and some sub-grain recovery compared to the 750°C/20 h condition. It is noteworthy that the final microstructures of the materials after creep show substantial similarity despite the range in rupture life, and the hardness values post-creep were also similar. Specifically, all three materials show a structure of equiaxed, coarsened sub-grains and coarsened carbides. Based on this observation together with the absence of creep cavitation and also that these materials showed similar acceleration of creep rate, Abe postulated that the acceleration creep behavior was due to microstructural evolution (e.g. carbide coarsening, sub-grain coarsening) rather than creep damage or stress concentration due to localized plastic deformation (necking).

Agamennone et al. (Agamennone et al., 2006) compared the creep behavior of two 12Cr CSEF steels with different tempering treatments and found that initial trends in creep behavior changed during testing. One material received a standard temper of 760°C/2 h while the other received an extended temper at lower temperatures (570°C/10 h plus 700°C/8 h). The extended temper material initially showed a greater resistance to creep deformation , since the minimum creep rate was smaller (at low strain, i.e. early in creep life). However, the low temperature tempering was also associated with a more rapid increase in creep rate as creep strain accumulation occurred (i.e. steeper slope of d log $\varepsilon/d\varepsilon$). This difference suggested that the low tempered material showed less microstructural stability during creep. Additionally, the extended low temper condition

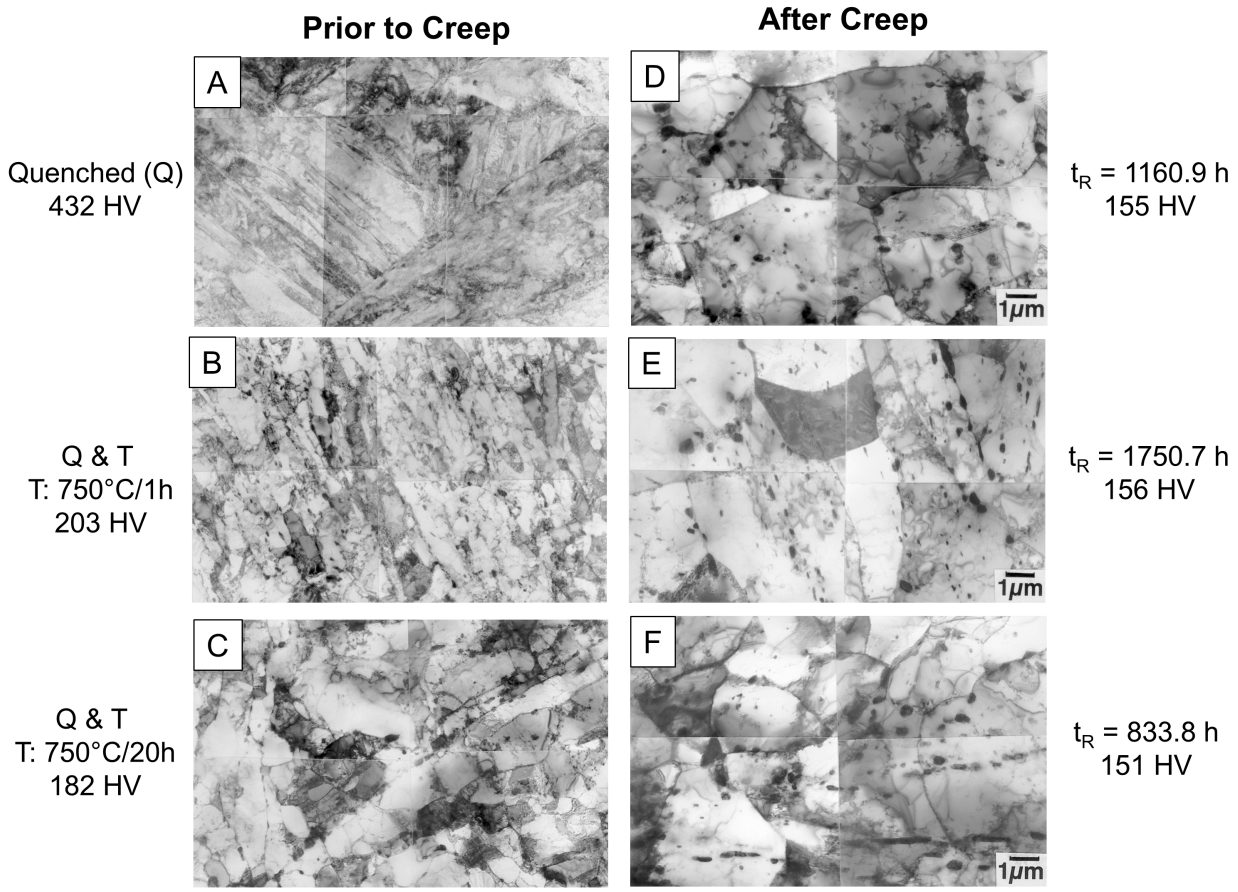


Figure 2-53. Comparison of TEM micrographs showing the microstructure prior to creep testing and after creep testing for three different heat treatment conditions of a 9Cr-1W steel. The initial microstructures of the three conditions are clearly different, with the extended temper material in (C) showing the greatest extent of subgrain growth prior to creep; however, the terminal microstructures after creep are qualitatively similar for the three conditions, despite the differences in rupture time. Adapted from Figures 9-11 and Table I in Abe (Abe, 2003).

showed a significantly higher slope in the tertiary creep regime, as shown by the plot in Fig. 2-54. Based on their TEM results, the authors reported that the low tempered material showed formation of M2X-type precipitates and Z-phase (which precipitated along subgrain boundaries within PAG), in addition to the VX precipitates.

2.1.9 Location of Type IV Creep Damage within the HAZ

The specific location of Type IV creep damage occurrence within the HAZ has historically been a point of debate within the literature, as to whether or not Type IV failure occurs in the FGHAZ or the ICHAZ. A definitive correlation between specific HAZ regions and Type IV rupture locations has been complicated by several factors, namely that for both intentional and unintentional reasons, the FGHAZ and ICHAZ have not always been separately distinguished in published results. On some occasions both regions have been intentionally treated as one, i.e. regions with fine-grained and intercritical microstructural characteristics are grouped together and identified as the FGHAZ (such as in Li et al. (Li et al., 2003) and in Zhang et al. (Zhang et al., 2020)). In other cases, it may not be clear whether the rupture location or the location of maximum extent of creep damage (for terminated specimens) is in the FGHAZ or in the ICHAZ, since the boundary between these two regions is not a distinct transition but corresponds to a continuous gradient of peak temperature and thus a continuous gradient of microstructure.

Despite these differences, the recent literature which has been able to utilize microscopy techniques such as EBSD agrees that the location for Type IV creep damage corresponds to the intercritical HAZ (Wang et al., 2020, 2018a) or the partially transformed zone (PTZ) (Siefert et al., 2019). These two terms are essentially synonymous and refer to the microstructures produced by exposure to peak temperatures which are intermediate between the lower and upper critical transformation temperatures. A distinct characteristic of this region is that some parts of the microstructure are transformed

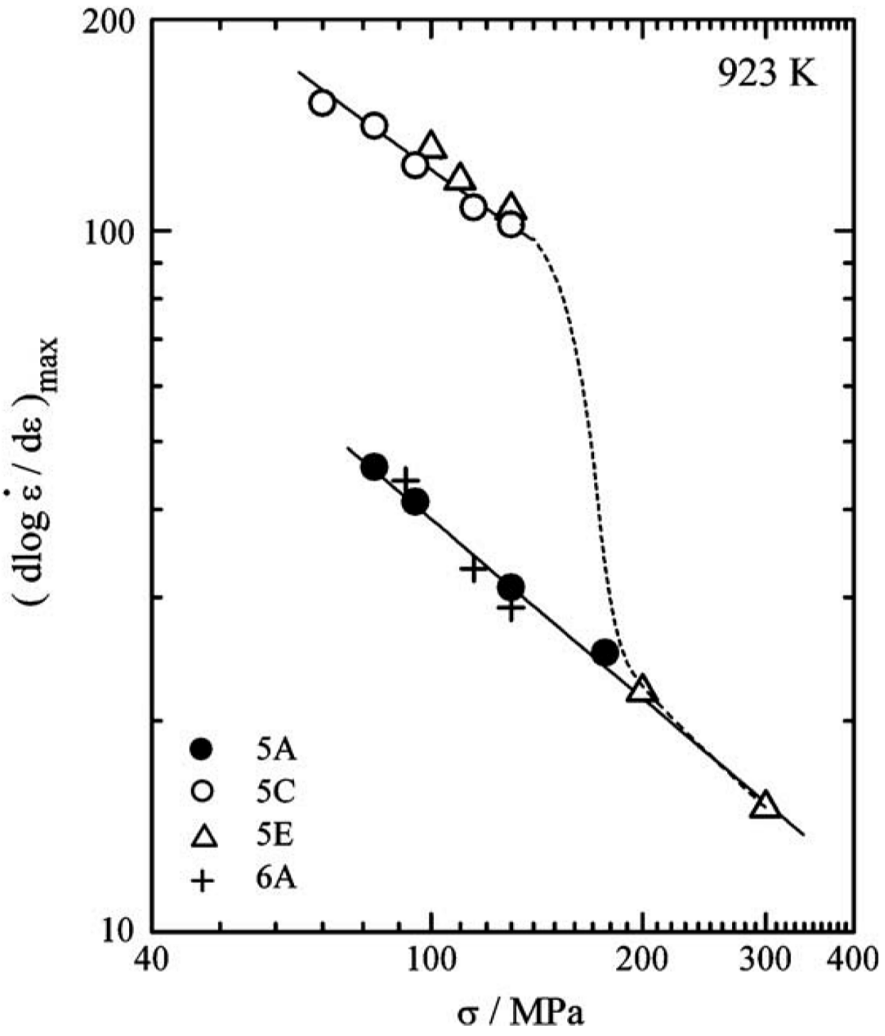


Figure 2-54. Plot illustrating the change in creep rate during creep strain accumulation (d log ε/dε) as a function of applied stress for two 12Cr CSEF steels with different heat treatments. Reproduced from Agamennone et al. (Agamennone et al., 2006).

during the heating portion of the welding thermal cycle while other regions remain untransformed and are simply tempered.

However, it is apparently still debated whether Type IV rupture consistently occurs in the HAZ region exhibiting the lowest hardness values (softening). Wang et al. (Wang et al., 2020, 2018a) conducted cross-weld creep testing of a Grade 91 FCAW weldment at 650°C and 70 MPa and observed Type IV failure. After comparing the as-welded, PWHTed, and creep-tested conditions, they determined that failure occurred in the ICHAZ and that the ICHAZ exhibited the lowest hardness in all three conditions. Siefert et al. (Siefert et al., 2019) performed creep testing on a Grade 91 SMAW weldment at 625°C/60 MPa and 625°C/80 MPa and observed Type IV failure, but they indicated that the failure location (rupture location together with maximum extent of cavitation) did not coincide with the region exhibiting the lowest hardness values. They characterized the minimum hardness values as occurring toward the "overtempered" zone just beyond and adjacent to the HAZ, where the peak temperature did not exceed the measured Ac1 temperature. They identified the Type IV failure location as occurring within the "partially transformed" zone (PTZ), similarly to the results of Wang et al., but the PTZ did not exhibit the greatest occurrence of low hardness values.

2.1.10 Effect of Multiaxial Stress States and Constraint on Creep Behavior

The creep behavior of weldments under multiaxial stress states (i.e., biaxial or triaxial) is important to consider because it corresponds to the conditions of actual components in service. Given that the majority of creep test data is gathered from uniaxial creep tests of base-metal and cross-weld specimens, and these datasets are typically used for high temperature design, it is necessary to understand the influence of multiaxial stress on creep behavior to identify departures from simple uniaxial behavior. It is generally impractical to conduct multiaxial creep testing of full-sized components in their actual loading conditions, although some investigators have gone to significant effort to perform creep testing of large components, such as the work of Masuyama et al.

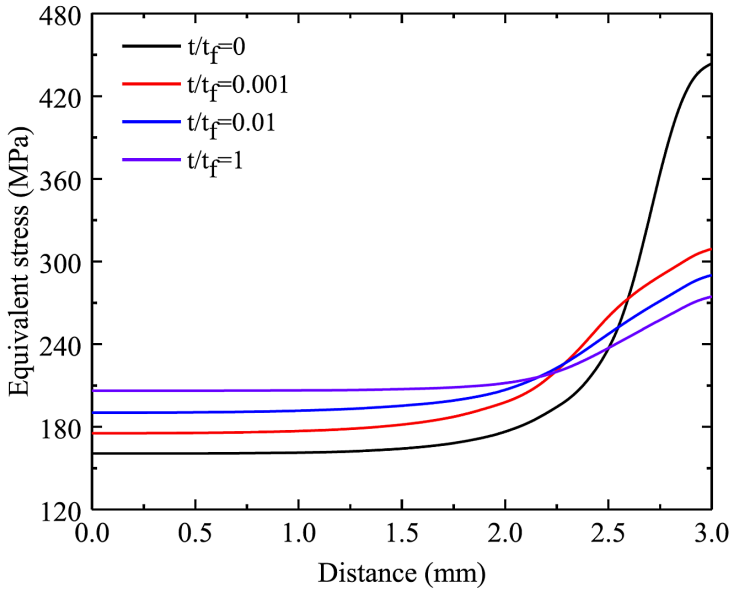
(Masuyama, 2010) and Komai et al. (Komai et al., 2016). Thus, the influence of multiaxial stress is typically investigated by typical laboratory size specimens, such as uniaxial creep testing of notched, round bar specimens in tension or creep testing of internally pressurized, welded tubes. Internally pressurized tubes directly produce multiaxial stresses in the weld, while uniaxial tensile loading of a notched specimen produces triaxial tension at the notch root (Goodall and Skelton, 2004). The importance of multiaxial stress concerning Type IV behavior of weldments arises from the potential effect of a multiaxial stress state on creep damage accumulation in regard to damage location and accumulation rate.

Multiaxial stresses which are present in actual weldments during high temperature service may arise from several potential sources. First, multiaxial stresses may simply originate from the applied stresses on the weldment, such as in a piping system: system loads from improperly adjusted hangers and supports, bending loads not adequately accounted for during design, etc. Another source of multiaxial stresses is mechanical constraint, which may be thought of as the condition in which the deformation or mechanical response of a material is physically "constrained" or limited, in comparison to the condition where the material can deform freely in response to all applied stresses. The restriction of deformation causes additional stresses to be present which would otherwise be zero if deformation occurred freely. Constraint occurs, for example, in the condition of plane strain which occurs in solids when one dimension (such as thickness) is significantly larger than the other two dimensions (Dieter, 1986a). Multiaxial stresses can also occur due to the presence of stress concentrations, which may be defined as a discontinuity which produces a nonuniform stress distribution. In weldments, stress concentrations can arise from physical and geometrical characteristics such as notches, grooves, or abrupt changes in section size; the presence of a notch introduces a local stress concentration and also a triaxial stress state at the notch root (Dieter, 1986a), although the stress is not uniform across the minimum section area plane (at the root)

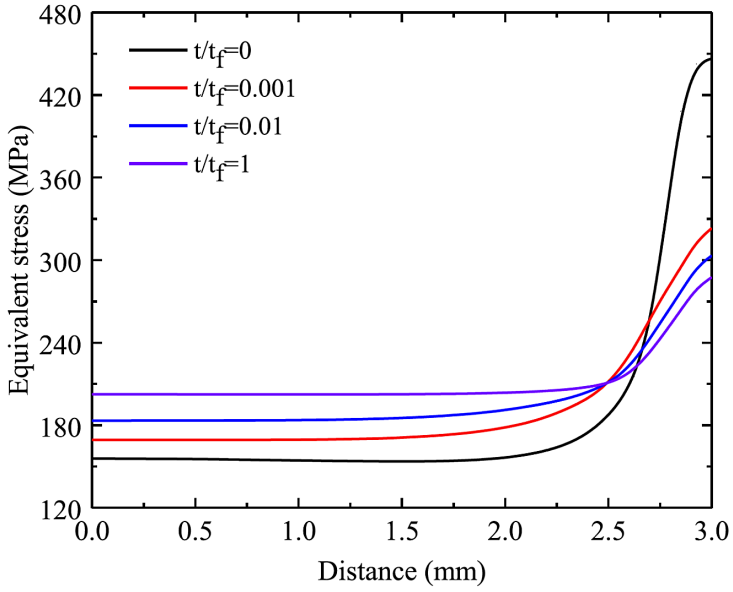
(Goodall and Skelton, 2004). Stress concentrations can arise from mechanical property differences (i.e. a "metallurgical" notch) such as differences in strength and hardness found in dissimilar metal welds or across the different regions within a heat-affected zone. Regardless of their source, the effect of multiaxial stresses on creep damage development is an important consideration for understanding the creep behavior of 9-12Cr CSEF steels and Type IV behavior of weldments, and the fact that stress state effects continue to be an active area of research to the present time (see for example, Niu et al. (Niu et al., 2021)) suggests that the interactions are not yet fully understood.

Two aspects which will be considered regarding the effect of multiaxial stress are its general effect on microstructure and creep damage evolution followed by a consideration of whether multiaxial stress has an especial, increased role in causing Type IV creep behavior (preferential creep damage in the ICHAZ). As discussed in previous sections of the literature review, microstructural evolution in CSEF steels is altered in the presence of stress such as during creep exposure, in comparison to thermal exposure alone (without stress); for example, in the presence of stress there is increased coarsening of $M_{23}C_6$ carbides which leads to decreased restriction of sub-boundary movement and greater propensity for coarsening. In their recent paper, Niu et al. (Niu et al., 2021) reported similar findings in that they observed a correlation between microstructural changes and the stress state produced in notched creep specimens of FB2 steel. In regions where the stress triaxiality and equivalent stress were increased, they reported increased carbide precipitation.

Niu et al. (Niu et al., 2021) also predicted by FEM analysis that stress relaxation in the vicinity of the notch would occur during creep for different notch severities (see Fig. 2-55 and Fig. 2-56), in that the equivalent stress decreased as a function of creep life.

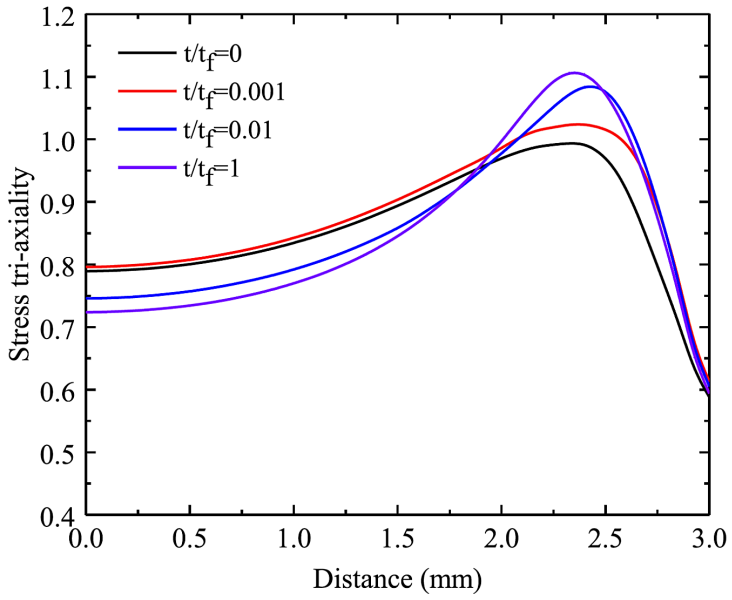


(a) Notch acuity ratio of 10

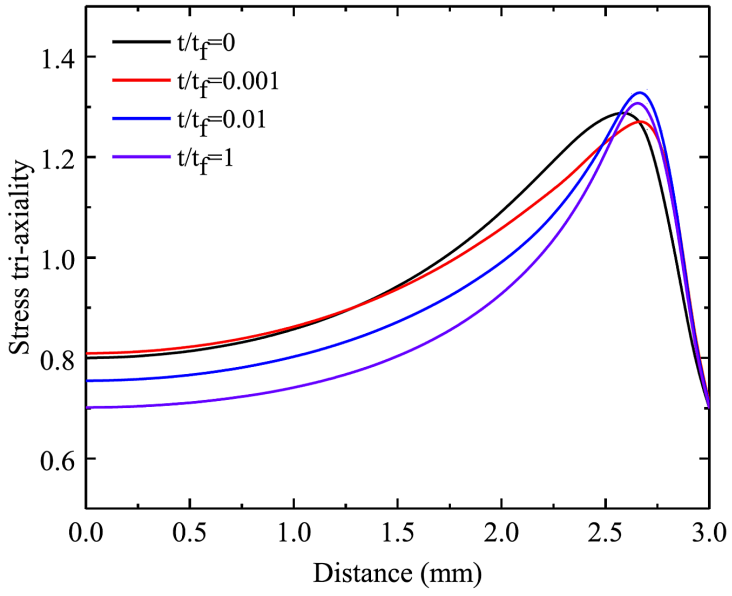


(b) Notch acuity ratio of 24

Figure 2-55. Comparison plots showing the predicted evolution of equivalent stress distribution across the notch throat diameter (0.0 mm corresponds to the center of the specimen and 3.0 mm corresponds to the notch root) for a notched creep specimen of FB2 steel (9Cr-0.5Mo-0.11V-0.21N). Note that for both less severe and more severe notches, a relaxation in the equivalent stress value is predicted to take place; the extent of relaxation at the end of the creep duration (t/tf=1) is slightly greater for the lower acuity notch (acuity ratio of 10). Reproduced from Niu et al. (Niu et al., 2021).



(a) Notch acuity ratio of 10



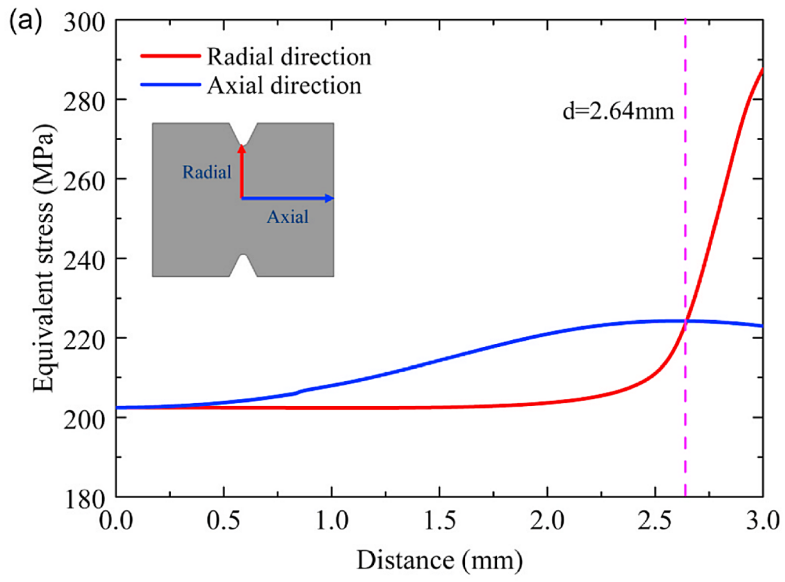
(b) Notch acuity ratio of 24

Figure 2-56. Comparison plots showing the predicted evolution of stress triaxiality across the notch throat diameter (0.0 mm corresponds to the center and 3.0 mm corresponds to the notch root) for a notched creep specimen of FB2 steel (9Cr-0.5Mo-0.11V-0.21N). For the less severe notch, an increase in stress triaxiality is predicted as the rupture life is expended; for the more severe notch (ratio of 24), the FEM results predict the stress triaxiality to be nearly the same throughout the creep duration. Reproduced from Niu et al. (Niu et al., 2021).

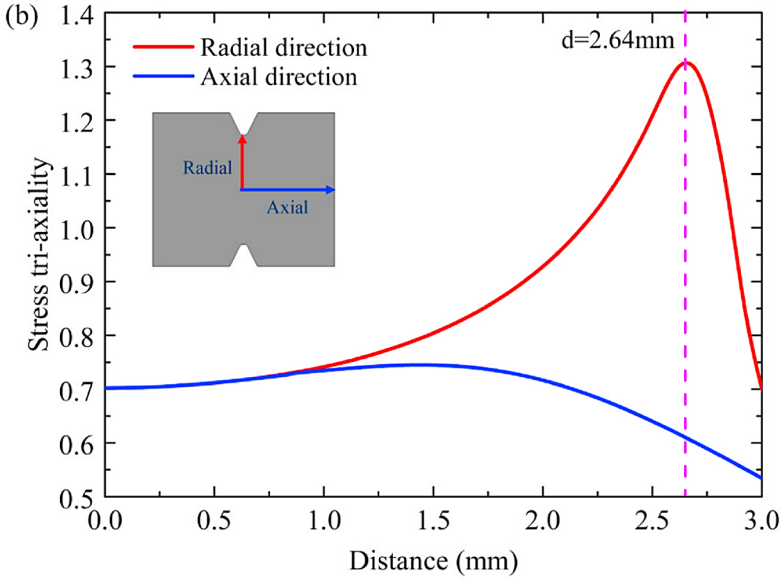
However, the stress triaxiality factor[5] was predicted to increase during creep for the lesser notch severity (acuity ratio of 10), while remaining nearly the same throughout creep for the higher notch severity (acuity ratio of 24). Furthermore, the authors (Niu et al., 2021) reported that creep cavitation was most extensive in regions near the notch root in the notched creep specimens, regions which their numerical model indicated were correlated with the maximum triaxiality (see Fig. 2-57; cavitation was less extensive at the notch center (center of the specimen).

The simplest loading condition that can be considered for a material under load is that of a homogenous material subjected to uniaxial loading (e.g. uniaxial tension). In this scenario, the material in the gauge volume is homogenous and the load is applied along one axis only. In uniaxial loading of a ductile material, only one principal stress is active and all of the shear stresses are zero, with the result that the material deforms uniformly (constant volume conditions) until necking begins. The onset of necking leads to a triaxial stress state (hydrostatic tension) (Dieter, 1986b) in the necked region which results in void formation, void growth, and eventually final failure. Obviously, conditions of homogeneous materials and simple uniaxial loading rarely if ever occur in the case of welded components subjected to complex service loading at elevated temperatures. Stresses in real components are generally multiaxial, and for the great majority of weldments, the high temperature properties of the weld deposit, heat-affected zone, and base metal are different. Even when nominally matching filler metals and/or PWHT are used to make the mechanical behavior of weld metal and base metal as similar as possible, variations will remain which are difficult to eliminate (e.g. due to slight composition differences between WM and BM, microstructure differences between WM and BM, unequal response to PWHT, etc.). Therefore, real weldments will

[5] Triaxiality factor is defined as the ratio of the hydrostatic stress or mean stress (the mean of the three principal stresses) to the equivalent stress, e.g. the von Mises equivalent stress or other equivalent stress parameter.



(a) Equivalent stress



(b) Stress tri-axiality

Figure 2-57. Comparison plots showing the predicted distribution of equivalent stress and triaxiality for a notched creep specimen of FB2 steel (9Cr-0.5Mo-0.11V-0.21N) with a notch ratio of 24. Note that in (a) the peak equivalent stress is predicted to occur at the notch root (r=3mm), while for triaxiality factor, the maximum is predicted to occur at a position slightly away from the notch root (r=~2.6mm). Reproduced from Niu et al. (Niu et al., 2021).

be inherently and unavoidably inhomogeneous. In addition to general considerations of material inhomogeneity and multiaxial stress states, additional factors further complicate the creep behavior of weldments, including the effects of stress concentration in weldments, constraint in the heavy wall welded piping used in power generation, and strain localization due to creep property mismatch. These factors will now be discussed in a general sense and also as they specifically apply to Grade 91 weldments.

Constraint may occur in a weldment in several different ways. Constraint can vary with piping wall thickness, with thicker piping experiencing a higher degree of constraint. This would be the case whether or not a weldment is present. It is important to note that this is one of the primary reasons that creep-testing of full-size or "jumbo" creep specimens which encompass the entire thickness of a weld, as it will be placed in service, are highly preferable compared to smaller cross-weld specimens (e.g. standard 12.7 mm round) which are extracted from a larger weldment, since the smaller specimen will not exhibit constraint effects that will occur in the weldment in service. Apart from thickness, further constraint may occur due to the local differences in creep properties of adjoining regions of a weldment, e.g. regions with higher creep strength may constrain (limit) the creep deformation of adjoining regions with lower creep strength which, when tested alone (unconstrained or free to deform), would otherwise exhibit higher creep deformation. In effect, the existence of regions with varying creep properties creates a "metallurgical notch," meaning a stress concentration that arises from metallurgical, than geometrical, factors. This term and its effects have been shown, for example, by Manjoine for weldments in austenitic stainless steels (Manjoine, 1982).

Constraint may also affect the creep ductility of a material, whether in the case of base metals or for weldments. In the first instance, Parker (Parker, 2017) reported findings which showed a decreasing trend of creep ductility as test times increased, for the same Grade 92 steel (see Fig. 2-58). This trend was observed for both notched and plain

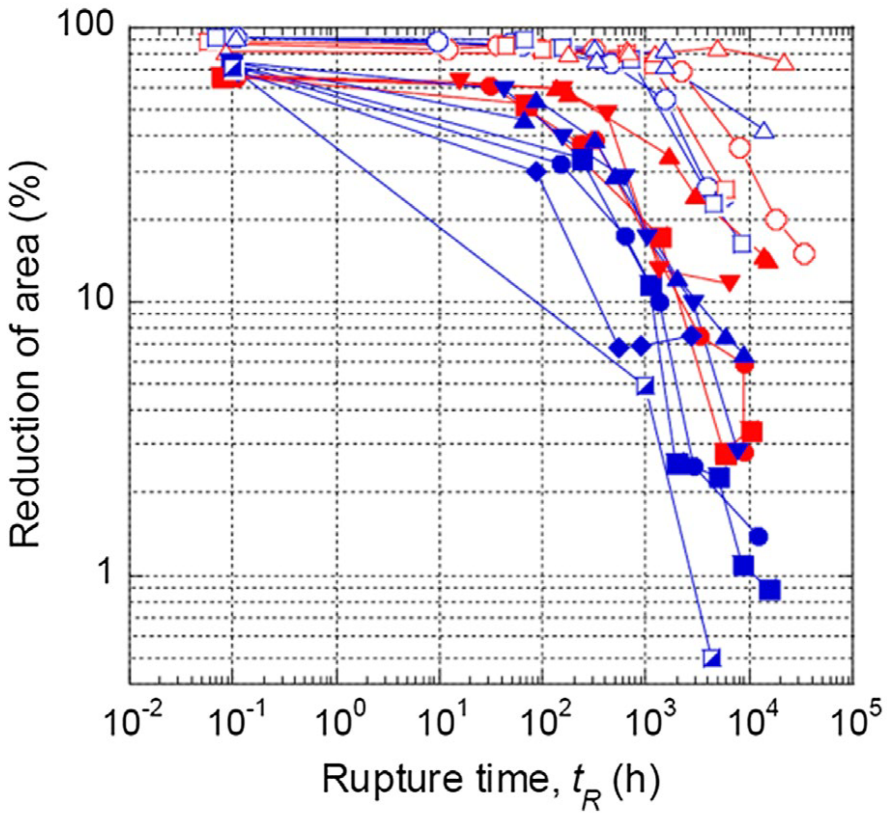


Figure 2-58. Reduction of area as a function of rupture time for plain bar creep specimens (open symbols) and for notched bar creep specimens (filled and partially filled symbols) from the same Grade 92 steel. Reproduced from Parker (Parker, 2017).

specimens, but the magnitude of the ductility decrease at long times was larger for notched specimens. Parker associated these results with an increased notch sensitivity, but based on what he stated earlier in the paper, it appears that the notch sensitivity of Grade 92 depends on stress—that Grade 92 is notch sensitive only at comparatively low stresses. In the second instance, Yaguchi et al. (Yaguchi et al., 2010) compared the uniaxial and multiaxial creep behavior of P91 and P122 CSEF weldments, and reported that both loading modes showed similar creep behavior in terms of creep strength and rupture life (see Fig. 2-59). Additionally, they reported that specimens in both loading modes failed by Type IV except at higher stresses (>150 MPa for P91). However, they found that the multiaxial specimens (which were internally pressurized) showed significantly reduced creep ductility, on the order of 0.5 to 2% circumferential strain.

The degree of stress concentration or constraint can be affected by weld-related geometrical factors, primarily the weld groove angle. Stevick (Stevick, 1994) used finite element analysis to show that for weldments which have differences in creep properties between weld deposit and base metal, the stress concentration will increase with increasing weld groove angle from 0 to 45 degrees, to a maximum stress concentration of ~1.9. In his work, Stevick considered the case of a N&T weldment in which the HAZ is eliminated, so that the weld deposit and base metal are the only regions. The change in stress concentration with groove angle is also interdependent on the magnitude of the creep property difference between regions, which Stevick characterized using a ratio of strain rate; when the strain rate constant ratio of weld to base metal (Bw/Bm) increased from 2.5 to 15 with a constant weld angle of 45 degrees which is the most severe case, the stress concentration increased from ~1.3 to ~1.9.

The general consideration is that higher degrees of constraint will be accompanied by higher stress triaxiality, such that the applied mean stress on the component will be effectively increased due to triaxiality. This higher triaxiality is associated with a greater propensity for cavity formation, since triaxial stresses are reportedly responsible for

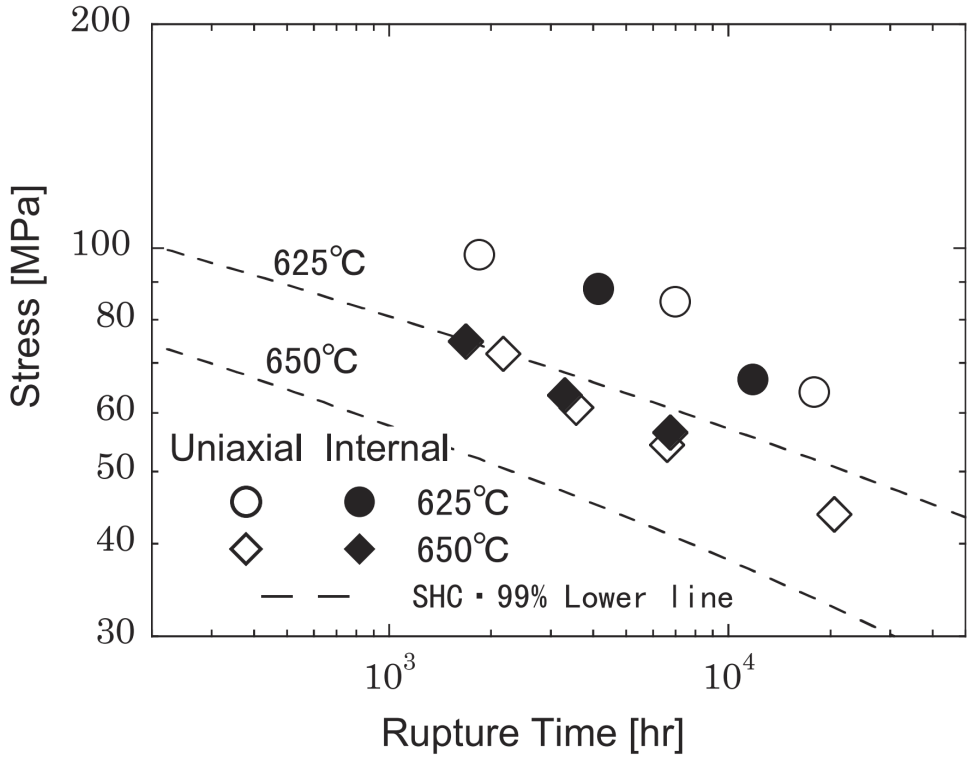


Figure 2-59. Comparison of uniaxial tension and multiaxial (internally pressurized tubes) creep rupture data for modified 9Cr-1Mo weldments . Reproduced from Yaguchi et al. (Yaguchi et al., 2010).

cavity growth. In the presence of higher stress triaxiality, such as a geometrical (or metallurgical) notch, a material may be classified as either of the following under creep conditions: notch weakening, which means that the material exhibits lower rupture life compared to a notch-free specimen, or (ii) notch strengthening, meaning that the material exhibits greater rupture life compared to a notch-free specimen. The notch-sensitivity of a specific material can vary with applied stress, so within these categories, further distinctions may be made to indicate trends in behavior, i.e. to indicate that a material is notch-strengthening but exhibits a decreasing strengthening effect with increasing triaxiality (Messner et al., 2019).

This complex intertwining of behaviors is the situation which occurs with Grade 91 under creep conditions. The most basic consideration, which is the effect of triaxial stress on the creep performance of Grade 91 base metal without the present of a weld, has been examined in several publications. Goyal et al. (Goyal et al., 2014) performed creep rupture testing of Grade 91 steel using smooth and U-notched specimens under uniaxial loading, across a range of notch severity, and used the finite element method together with continuum damage mechanics to develop a model to compare the creep rupture behavior of the smooth vs. notched specimens. The tests were conducted at the same temperature (600°C) as the investigations of (Messner et al., 2019; Nassif et al., 2019) and Kimura et al. (Kimura et al., 2009); however, the lowest stress tested was 110 MPa, compared to the minimum of 80 MPa in the work of Messner et al. Similarly to Messner et al. (Messner et al., 2019), Goyal and co-workers (Goyal et al., 2014) found that the creep rupture life increased with increasing degree of notch severity (higher constraint) and higher applied stress. Additionally, the creep rupture ductility was found to decrease in the notched specimens; the extent of the decrease was greater with higher constraint and lower stress.

The effect of notches (e.g. stress triaxiality) on the creep behavior of Grade 91 steel was also investigated by Messner, Nassif, and co-workers (Messner et al., 2019; Nassif et al.,

2019) using an FEM approach. The authors developed a physically-based crystal plasticity finite element model for creep rupture (Nassif et al., 2019) and applied the model to consider several aspects of creep rupture behavior in Grade 91 steel (Messner et al., 2019). The authors found that their model predicted variations in notch sensitivity for Grade 91 steel, depending on applied stress and triaxiality. They noted that design codes do not typically distinguish variations in notch effects for a given material, but usually classify a material as categorically notch-weakening or notch-strengthening. Specifically, their model (Nassif et al., 2019) predicted that Grade 91 exhibits relative notch-strengthening behavior when maximum principal stress is high or when triaxiality is low, while notch-weakening behavior is expected to occur at low stress and when triaxiality increases. They also noted that notch sensitivity may also be a function of notch severity (i.e. notch "sharpness" or notch acuity).

It is interesting to note that the results of Messner et al. (Messner et al., 2019) predict a transition in notch behavior from relative notch weakening to relative notch strengthening at a stress of approximately 100 MPa at 600°C, which coincides with commonly-used parameters for creep-rupture testing of Grade 91 materials and weldments. Fig. 2-60 and Fig. 2-61 show the model results which predict that at low stress, Grade 91 will exhibit a decrease in $t_{tertiary}$ (time to onset of tertiary creep) as triaxiality increases.[6] Fig. 2-60 also shows more specifically that in the stress range of 100-125 MPa, a transition from notch weakening to notch strengthening is predicted to occur as stress triaxiality increases.

In addition, Messner et al. (Messner et al., 2019) also used their model to examine the predicted contributions to the overall creep rate from different creep mechanisms as a function of stress triaxiality. The results shown in Fig. 2-62 reveal that at lower

[6] It should be noted here that the authors' model results show the time to onset of tertiary creep ($t_{tertiary}$) rather than rupture time, because the boundary conditions of the model could not predict the localized deformation (necking) that occurs at the end-of-life of a rupture specimen.

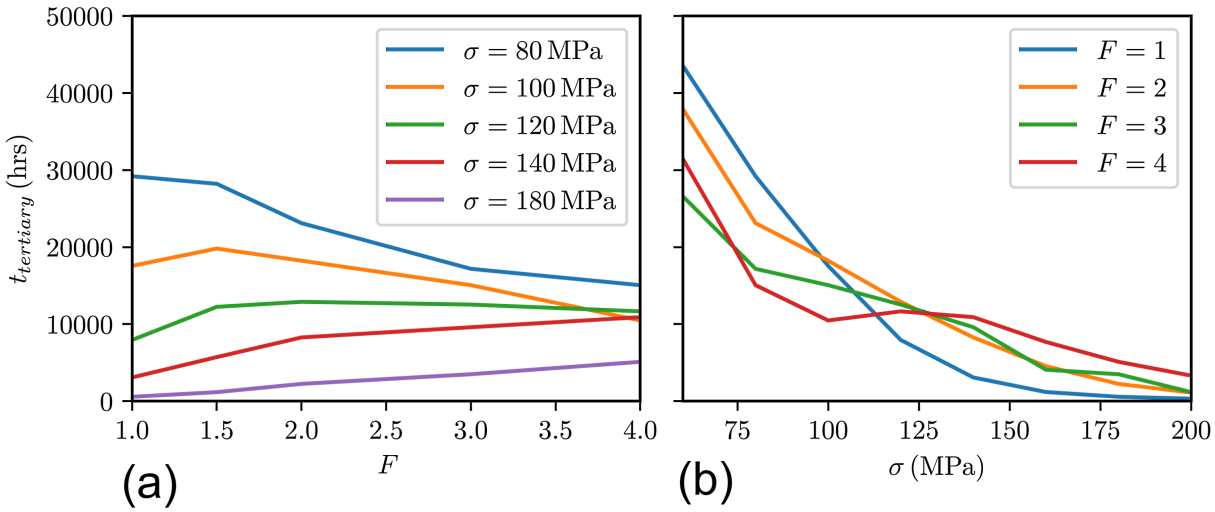


Figure 2-60. Predicted correlations for time to tertiary creep onset as functions of triaxiality F and maximum principal stress. Note that (a) shows a transition from notch strengthening (time to tertiary increasing with triaxiality) to notch weakening (time to tertiary decreasing with triaxiality) as stress decreases (cf. 180 MPa vs. 80 MPa). For (b), note that increased triaxiality (F>1) only leads to a reduction in time to tertiary creep when the maximum principal stress is below approx. 110 MPa. Adapted from Messner et al. (Messner et al., 2019).

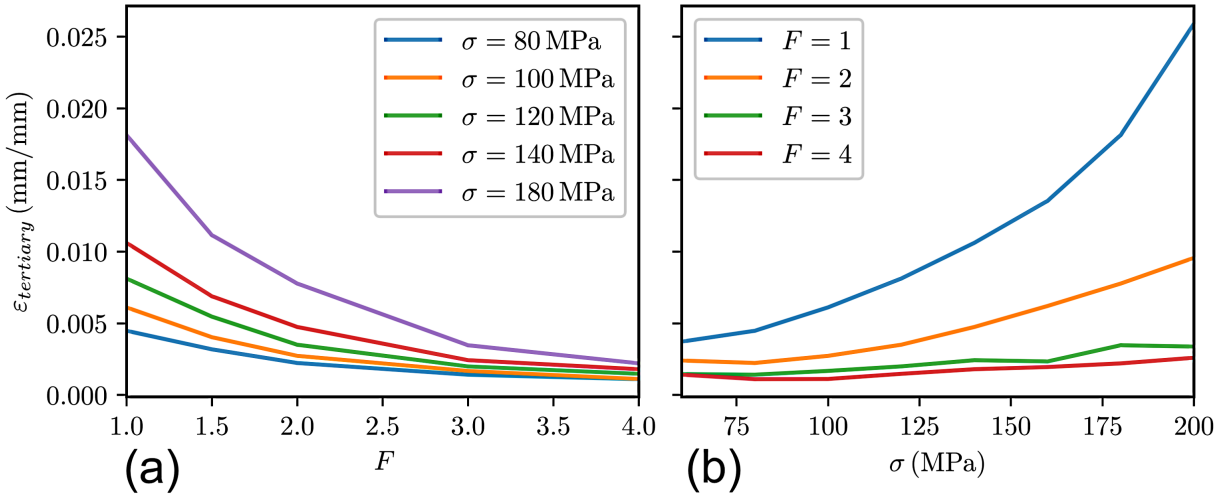


Figure 2-61. Predicted correlations for strain at onset of tertiary creep as functions of triaxiality F and maximum principal stress. These results suggest a possible connection between increasing triaxiality and reduced rupture ductility. Adapted from Messner et al. (Messner et al., 2019).

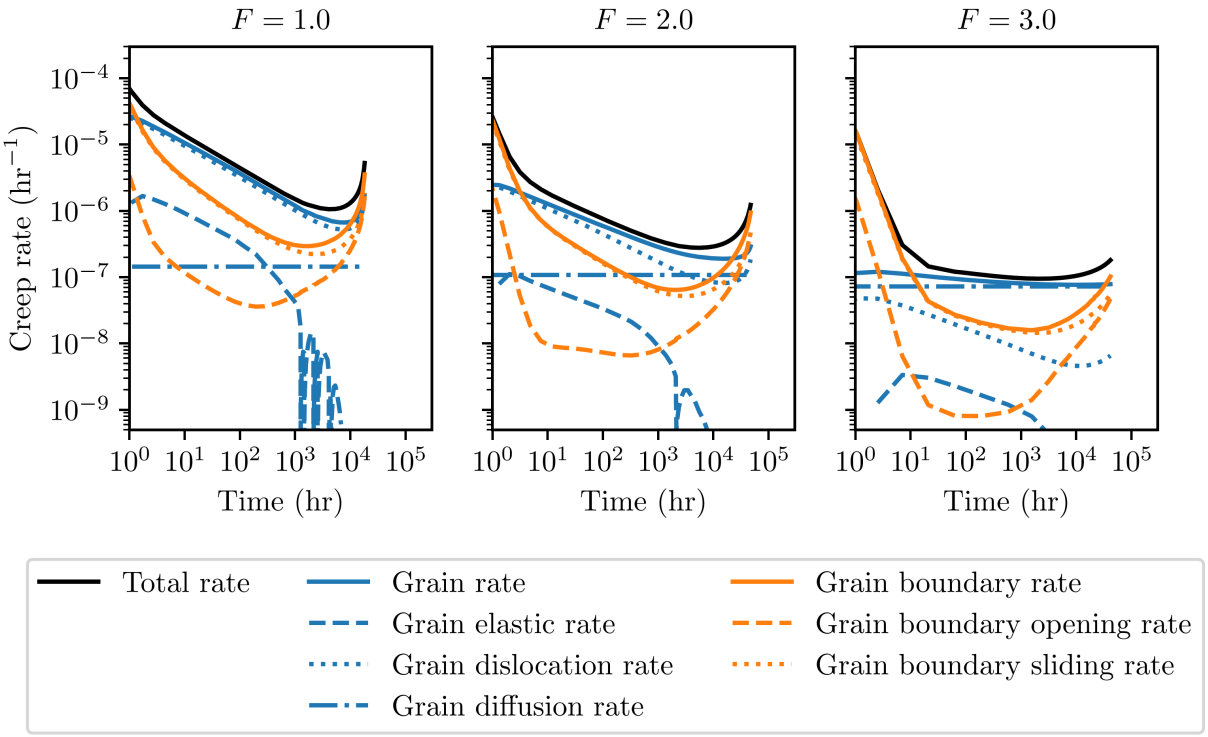


Figure 2-62. Predicted contributions to the overall creep rate for different creep mechanisms as a function of triaxiality F at a fixed maximum principal stress of 120 MPa and a temperature of 600°C. Reproduced from Messner et al. (Messner et al., 2019).

triaxiality, the creep rate appears to proceed directly from primary to tertiary creep, as has been observed experimentally by some investigators, e.g. by Abe et al. (Abe et al., 1992) for 9Cr-2W steel. However, when triaxiality increases from F=1 to F=3, a region of secondary creep is predicted to occur. Additionally, at high triaxiality, grain boundary sliding is predicted to have the greatest contribution to creep rate during the early stage of creep, after which the main contribution is expected to be from grain interior diffusion creep. This is in contrast to lower triaxiality (when F=1 or F=2) where grain interior dislocation creep is expected to predominate over the diffusion contribution.

2.1.10.1 Effect of Multiaxial Stress on Creep Behavior of Welds

Furthermore, the consideration of constraint leads to questions of the extent of constraint within weldment HAZs during creep. If evidence for constraint is not observed experimentally, then any considerations of the effects of constraint on cavity nucleation, growth, and linkage are not supportable. In this regard, Sawada et al. (Sawada et al., 2013) investigated the effect of stress state on creep behavior of Grade 92 weldments by evaluating subgrain size, dislocation density, and precipitate size in the base metal and FGHAZ regions to determine if the stress state affected creep damage and microstructural evolution in these regions. The subgrain structure of the FGHAZ and the corresponding measurements of subgrain size are shown in Fig. 2-63 from Sawada et al. (Sawada et al., 2013). Fig. 2-63 shows that the FGHAZ exhibited a partially equiaxed structure prior to creep testing; this behavior was attributed to inadequate carbide precipitation on lath boundaries (thus allowing lath boundary migration) due to incomplete dissolution of carbides during the FGHAZ thermal cycle. Although subgrain growth occurred in both the BM and FGHAZ during creep and the subgrain size was larger in the FGHAZ than in the BM, a significant difference in subgrain growth was not observed between the surface and central regions of the FGHAZ. Sawada et al. (Sawada et al., 2013) concluded that stress triaxiality (surface vs. central regions) therefore did not influence the subgrain size, but this may not agree with other

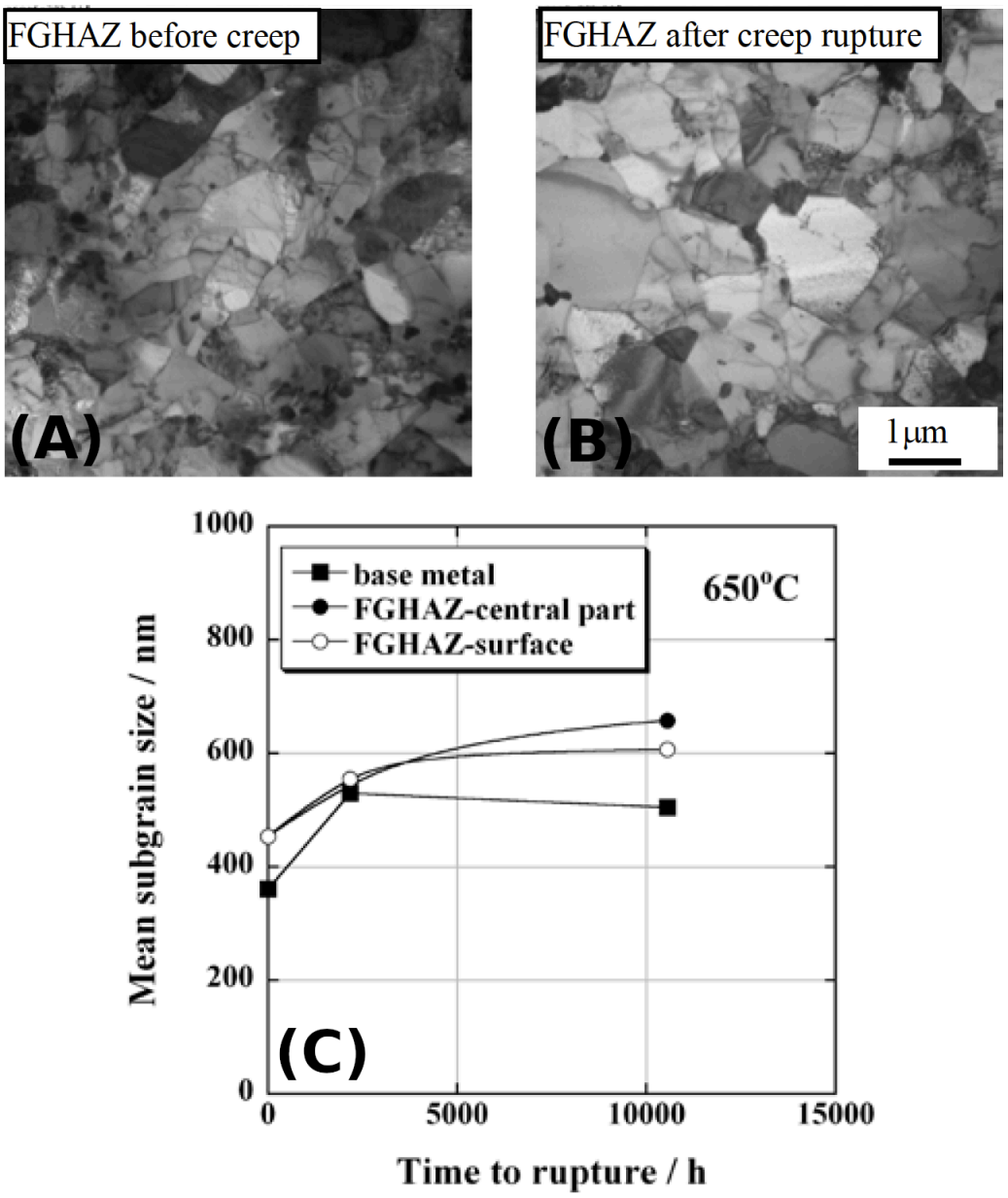


Figure 2-63. Comparison of subgrain structure in the FGHAZ of a Grade 92 weldment (a) prior to creep testing and (b) after creep testing. (c) Plot illustrating the greater relative increase in subgrain size in the central FGHAZ (at the specimen center) as compared to the FGHAZ at the specimen surface. Adapted from Sawada et al. (Sawada et al., 2013).

literature. The authors also measured dislocation density in the different regions after creep testing and again found that the reduction in dislocation density was higher in the FGHAZ in the base metal, but no significant difference in behavior was observed between the center and surface regions of the FGHAZ. With regard to precipitates, Sawada et al. (Sawada et al., 2013) observed Laves phase in both regions and an increase in size of $M_{23}C_6$ carbides in both regions, although the increase was greater in the FGHAZ than in the BM. Furthermore, they reported greater coarsening of $M_{23}C_6$ in the central FGHAZ region than in the surface region, as shown in Fig. 2-64. On this basis, they proposed that stress multiaxiality increases $M_{23}C_6$ coarsening in the FGHAZ during creep, and in support of this statement they referred to other published work that showed increased coarsening of $M_{23}C_6$ in the vicinity of a creep crack tip, where stress multiaxiality is higher.

Based on work reported in the literature, it seems that the degree of constraint and its effects may vary with the material and also with its inherent creep ductility. According to the work reported by Kimmins and Smith (Kimmins and Smith, 1998), based on their investigation of Type IV creep behavior in 0.5Cr-Mo-V steel weldments, the deformation characteristics of Type IV in this material seem to indicate that constraint is not a significant factor for rupture life.

2.1.10.2 Comparison of Iso-Stress and Iso-Strain Loading in a Weldment

With regard to constraint in welded joints, it is helpful to compare two different loading conditions. In the first condition, the weldment is loaded perpendicular to the welding direction, so that the different weld regions (weld deposit, HAZ sub-regions, and base metal) are loaded sequentially (iso-stress). It should be remembered that the different weld regions exhibit different creep properties (creep strength, creep rate) due to their differing microstructures. In the second condition, the weld regions are loaded parallel to the welding direction, i.e. in the iso-strain condition. These two loading conditions are illustrated schematically in Fig. 2-65. The sequential loading orientation corresponds

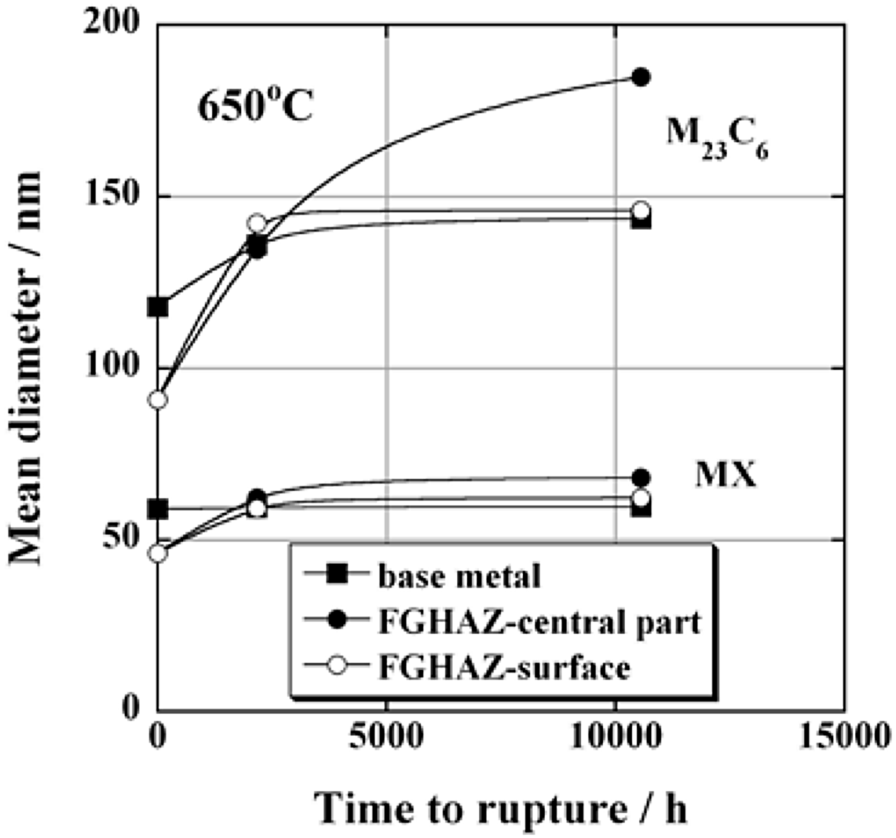


Figure 2-64. Evaluation of mean diameter of M23C6 and MX precipitates in the base metal and FGHAZ of a Grade 92 weldment before (data point at 0 h) and after creep testing. The FGHAZ region in the center of the creep specimen and the surface FGHAZ region were evaluated separately. It is apparent that the center FGHAZ showed somewhat greater coarsening of $M_{23}C_6$ than the surface FGHAZ region; this change was attributed to the higher stress state in the center of the specimen. Reproduced from Sawada et al. (Sawada et al., 2013).

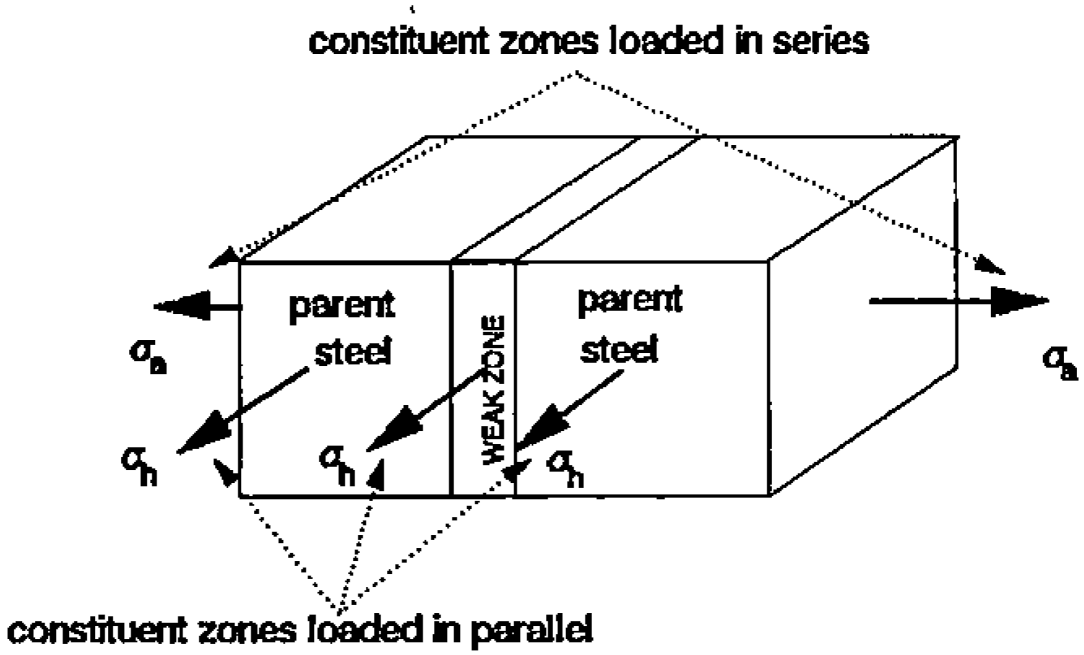


Figure 2-65. Schematic illustrating possible loading directions for a "weak zone" between two adjacent, stronger materials ("parent steel"). This arrangement mimics the placement of the "weak" HAZ in a Grade 91 weldment between the adjacent, higher strength weld deposit and base metal on opposing sides of the HAZ. Note that when the constituent zones are loaded in parallel, all zones are required to deform identically (iso-strain) in order to maintain interfacial continuity, and the stresses in the zones will be dissimilar. When the constituent zones are loaded in series, all zones experience identical stress while deformation proceeds uniformly (i.e. uniform shape change, in the absence of necking), but independent strains in the distinct zones are possible. Reproduced from Kimmins et al. (Kimmins et al., 1993).

to the loading experienced by longitudinal seam welds due to the hoop stress in piping or a cylindrical pressure vessel, while the parallel loading orientation corresponds to the loading experienced by circumferential girth welds due to the hoop stress or seam welds due to the axial stress. These two conditions are discussed by Kimmins et al. (Kimmins et al., 1993) in regard to the interactions between the different weld regions with different properties and the effect of constraint (deformation of weak regions being limited by adjacent/surrounding stronger regions) on the weldment behavior as a whole. As pointed out by Kimmins et al., the classic illustration of the effect of constraint is the fact that a soldered joint, consisting of a thin layer of soft solder or braze material sandwiched between surrounding sheets of "strong" base metal, exhibits higher strength than might be intuitively expected based on the low strength of the solder material. A similar configuration may be simplistically assumed for weldments with the HAZ, specifically the ICHAZ sub-region, comprising the weak layer surrounded by the stronger weld deposit and base metal. Considering this arrangement, if constraint is indeed limiting the deformation of the weakest region, then the creep strength of the weldment should be higher (and/or with a lower creep rate) than the respective properties of the ICHAZ when tested separately.

The disagreement does not appear to be quickly resolved based on the reported experimental evidence reported in the literature either in opposition to, or in support of, the importance of multiaxial stresses resulting from constraint. In opposition to the importance of constraint in Type IV, Kimmins and Smith (Kimmins and Smith, 1998) reported for 0.5Cr-Mo-V steel weldments that similar creep lives were observed for cross-weld tests and creep tests of singular regions of simulated HAZ material, which they concluded was an indication that significant constraint (leading to a multiaxial stress state) likely was not present in the cross-weld. They further supported their assertion regarding the minimal role of constraint in governing Type IV behavior by building a finite element model in which they showed that constraint could be relaxed

during creep by removing the requirement for strain compatibility between regions, such as might occur due to creep deformation by grain boundary sliding. In contrast to this, Kussmaul et al. (Kussmaul et al., 1993) reported for X20CrMoV12-1 (12Cr) steel weldments that at intermediate stress of 171 MPa, creep rupture occurred in the HAZ of cross-weld specimens with the rupture time being nearly the same as for base metal specimens tested at the same stress, and being much longer than for creep specimens of simulated HAZ material; this would appear to contradict the results of Kimmins and Smith who reported similar rupture times for simulated HAZ specimens and cross-weld specimens. However, some complicating factors in Kussmaul et al. include a relatively low test temperature of 550°C and the use of intermediate stresses above the range typically associated with Type IV.

2.2 Summary Statements from Literature Review

Based on the review of the literature, the following statements have been compiled in an attempt to summarize the general consensus of researchers on some of the main points regarding creep behavior of CSEF steels and their weldments. Some of this information is already summarized in the relevant review papers, but some has been conducted after the publication of the aforementioned reviews.

1. The high temperature strength of CSEF steels is achieved by precipitate stabilized substructure hardening, in which strengthening primarily originates from a fine-scale structure of dislocations and subgrains/subgrain boundaries, which are stabilized against recovery by precipitates distributed on the boundaries and within subgrain interiors. Without precipitate stabilization, recovery of free dislocations and subgrain boundaries is significantly accelerated.
2. Considering the base metal behavior, the degradation of the optimal tempered martensite lath structure (TMLS) of CSEF steels such as Gr. 91 and X20 occurs in the form of carbide coarsening, subgrain coarsening, and reduction of dislocation density to eventually form equiaxed subgrains with relatively low dislocation

density. This microstructure recovery may occur non-uniformly within the material, particularly while creep deformation is progressing (t<tR), e.g. since there are inherent random variations in initial dislocation density.

3. Type IV creep failure in CSEF weldments is associated with a microstructural region exhibiting partial transformation of the original, TMLS structure that is characteristic of the properly heat-treated base metal. In this partially transformed region, the microstructure is a mixture of grains which transformed to austenite and back to martensite during the thermal cycle, together with grains which did not transform to austenite and were merely tempered during the thermal cycle.
4. In published research which only uses optical microscopy to identify failure location or characterize microstructure in CSEF weldments, the identification or association of Type IV failure location may not be truly definitive in terms of the FGHAZ vs. ICHAZ, since these regions appear microstructurally similar at the comparatively low magnifications of OLM. Characterization should be performed with SEM, and ideally in conjunction with EBSD, to accurately distinguish the ICHAZ from the FGHAZ for correlation with the location of creep damage.
5. The individual sub-regions in the HAZ exhibit inherently different creep properties (e.g. creep rate) when compared with one another or with the base metal. Within the HAZ, the FGHAZ and ICHAZ exhibit higher creep rates than the CGHAZ or b
6. Regarding cavitation in CSEF steels, short creep rupture lives have been associated with higher inclusion content when comparing base metals with similar strength levels, and an association between cavitation and second phase particles such as inclusions has also been noted. However, it appears that a specific correlation between particle (inclusion) number density and cavity

number density has not been clearly established. Irregular cavity shapes (non-spherical) have also been reported in CSEF steels.

7. Regarding creep damage in the Type IV (HAZ) region of CSEF steels, there is a distribution of cavitation across the HAZ with the peak extent of cavitation occurring in the partially transformed region (ICHAZ or PTZ), although cavitation also occurs in the FGHAZ and in the overtempered zone where the peak temperature is <Ac1.
8. Localized strain accumulation occurs in the HAZ during creep. Although the overall strain in Type IV failure is low, strain is concentrated in the HAZ during creep deformation as reported for both lower Cr-Mo and P91 steels, and it appears that for cross-welds with identical base metals on both sides, strain accumulates similarly on both sides as expected before final rupture occurs on one side preferentially.
9. Although less attention has been given to the effect of welding parameters on Type IV behavior, the weld groove angle and the preheat temperature have been noted to have an effect on Type IV failure propensity, with rupture life increasing as preheat temperature increased and increasing as weld groove angle (included angle) decreased toward 0°. The reason for the effect of preheat temperature has not been explained and could be a possible area for microstructural study.

Chapter 3 Materials and Experimental Procedures

3.1 Materials

Four different Grade 91 base metals were utilized in the current dissertation research. The designations and chemical compositions of the Grade 91 base metals are listed in Table 3-1 along with the standard specification limits for Grade 91 according to ASME Section II Part A (ASME SA-387 Gr. 91) and the optimum composition ranges for Grade 91 as recommended by the Electric Power Research Institute (EPRI), which were implemented with slight modifications as ASME code case 2864. Of the materials listed in Table 3-1, materials H47, H13, and AEP were originally in plate product form, while the FT material was a forging product. Based on the data in Table 3-1, the base metals met the required ASME composition limits with the exception of carbon content for the FT base metal, which was slightly higher than the allowable upper limit.

3.2 Grade 91 Weldments for Cross-Weld Creep Testing

Two weldments were utilized in the current dissertation for post-creep test characterization of base metal composition and microstructure characteristics of dissimilar Grade 91 weldments. The two weldments were originally fabricated as part of a previous industry project (Hoskins et al., 2017) for cross-weld creep testing using three base metals designated as Forged Tee (FT), Header 47 (H47), and Header 13 (H13), whose chemical compositions are listed in Table 3-1. One weldment was comprised of the FT and H47 base metals ("FT to H47 Weldment") and the other was comprised of the H13 and H47 base metals ("H47 to H13 Weldment"). The plate thicknesses were nominally 25 mm (1 inch) and the plates were heat-treated with a normalizing and tempering treatment prior to welding, according to the heat treatments listed in Table 3-2. The weldments were fabricated using the SMAW process with a square-groove or butt joint geometry; E9015 electrodes were utilized with a backing plate. After welding, the two weldments were given a PWHT according to the parameters given in Table 3-2.

Table 3-1. Measured chemical compositions of Grade 91 base metals utilized for microstructural characterization and creep testing (Hoskins et al., 2017). Standard specification limits and optimum recommended composition limits are also provided for comparison.

Element (wt.%)	H47	FT	H13	AEP	ASME II Part A SA-387 Gr.91 Cl.1 (2010)	EPRI Recommended Limits (2014), Report 3002003472
C	0.109	0.125	0.099	0.105	0.08-0.12	0.08-0.12
Mn	0.480	0.475	0.489	0.43	0.30-0.60	0.30-0.50
P	0.008	0.010	0.009	0.009	<0.025	<0.01
S	0.003	0.008	0.001	0.002	<0.025	<0.005
Si	0.290	0.287	0.320	0.323	0.20-0.50	0.20-0.40
Ni	0.350	0.110	0.351	0.14	<0.40	<0.20
Cr	8.653	8.506	8.809	8.700	8.00-9.50	8.00-9.50
Mo	0.938	0.933	0.956	0.91	0.85-1.05	0.85-1.05
V	0.208	0.211	0.207	0.211	0.18-0.25	0.18-0.25
Al	0.002	0.017	0.003	0.028	<0.04	<0.02
Cu	0.126	0.142	0.110	0.115	-	<0.10
H (ppm)	1.200	-	1.100	-	-	-
N	0.045	0.041	0.034	0.0488	0.03-0.07	0.035-0.07
Sn	0.008	0.008	0.007	0.0116	-	<0.01
As	0.007	0.007	0.005	0.0066	-	<0.012
Co	0.0150	0.0140	0.0140	0.014	-	-
Pb	0.0008	<0.001	<0.001	0.00004	-	<0.001
B	0.0004	<0.001	0.0007	0.0003	-	<0.001
Sb	0.002	0.001	0.002	0.001	-	<0.003
Nb	0.067	0.070	0.069	0.069	0.06-0.10	0.06-0.1
Ca	0.0001	-	0.0229	0.0007	-	-
O	0.0054	0.0025	0.0064	0.0034	-	-
Ti	<0.001	0.002	0.001	0.002	<0.01	<0.01
Zr	<0.001	<0.001	<0.001	<0.001	<0.01	<0.01
W	0.002	0.039	0.002	0.004	-	-
N:Al	22.50	2.41	11.33	1.74	0.75-1.75	>4.0

Table 3-2. Summary of heat treatment parameters for two dissimilar Grade 91 weldments (Hoskins et al., 2017) utilized for creep testing and subsequent characterization.

Weldment Information	Base Metal Re-Normalization and Temper Prior to Weldment Fabrication	Postweld Heat Treatment
FT-H47 FT (forging) and H47 (plate)	Normalize: 1066°C/70 min Temper: 774°C/30 min	746°C/1 h
H13-H47 H13 (plate) and H47 (plate)	Normalize: 1053°C/30 min Temper: 774°C/1 h	746°C/1 h

As part of the previous industry project (Hoskins et al., 2017), cross-weld creep specimens were extracted from each weldment after fabrication and PWHT. The cross-weld specimens had gauge cross-sectional dimensions of 22.10×13.72 mm (0.87006×0.54032 inches) with a resulting gauge area of 303.3 mm^2 (0.47011 in^2), and a gauge length of 81.3 mm (3.2 inches). This specimen size was near the full plate thickness of the original weldments in order to obtain "jumbo" or "feature size" creep samples which more closely replicate the behavior of service weldments. Constant-load creep testing was performed by Materials Technology Corporation in Ann Arbor, MI. For some specimens, the stress and temperature were maintained at a constant value throughout the test. For other specimens, the stress and/or temperature were changed at one or more points during testing in order to obtain creep rates under different conditions for calculation of creep life using the Omega method (Prager, 2000).[7] Average elongation over the gauge length was recorded for each specimen throughout the test duration to record the overall strain versus time behavior.

3.3 Grade 91 Weldment for Longitudinal Creep Testing

A third weldment designated "AEP" was utilized for creep testing and subsequent characterization of longitudinal oriented creep specimens. The AEP weldment was previously fabricated and utilized for several previous studies (Hobbs et al., 2015; Lundin and Liu, 1999) and some of the metallographic samples, creep specimens, and data were made available for the current dissertation research. The extraction of longitudinal creep specimens was previously conducted as shown in Fig. 3-1 and Fig. 3-2. Fig. 3-1 shows the weldment top surface with the schematic layout and orientation of the longitudinal creep samples (shown by the white paper templates) with respect to the welding direction. The longitudinal samples were extracted in an orientation parallel to the welding direction and with the specimen centerline placed at

[7] The Omega calculations were part of the previous project and will not be addressed in the current dissertation.

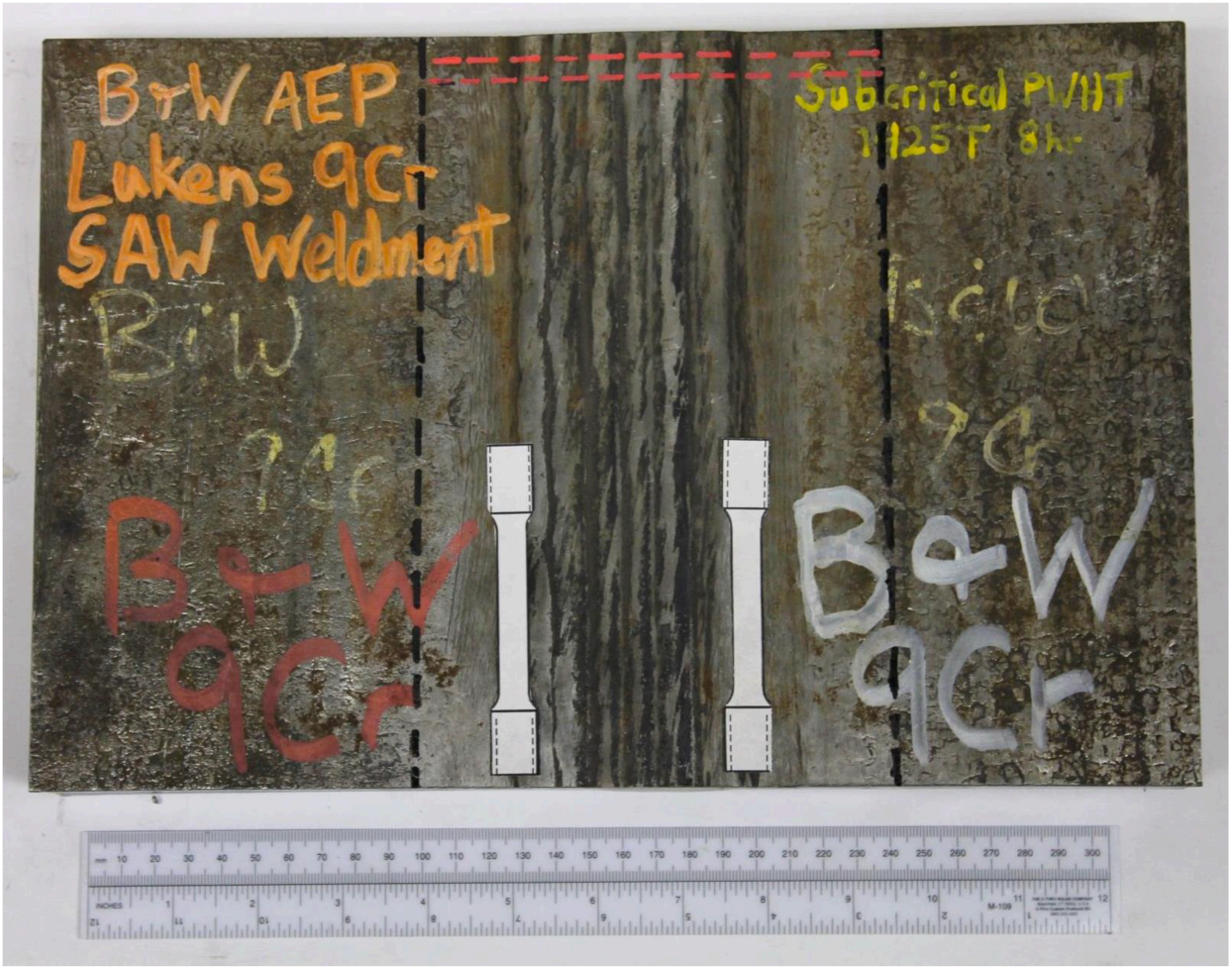


Figure 3-1. Photograph of the AEP Grade 91 weldment prior to sectioning, showing the orientation of longitudinal creep specimens (illustrated by paper templates) parallel to the welding direction. Reproduced from (Hobbs et al., 2015).

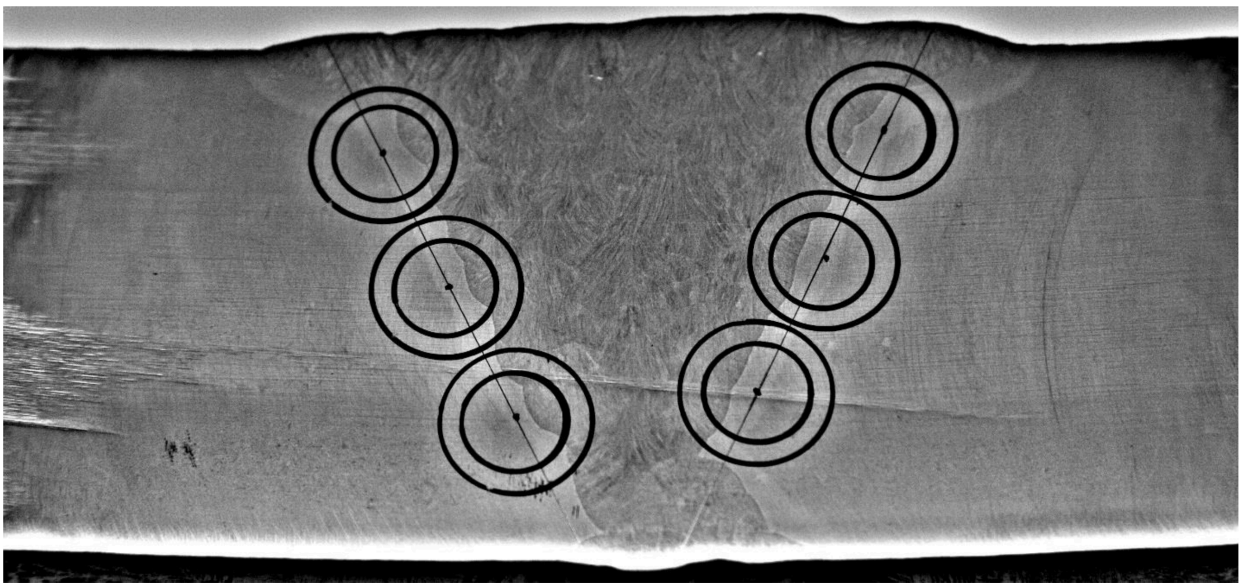


Figure 3-2. Photograph of one end of the AEP Grade 91 weldment to show the sectioning plan for extraction of round longitudinal creep specimens. After polishing and macro-etching to show the weld deposit and HAZ location, six specimen locations were marked for extraction, with each specimen centerpoint located along a line drawn through the outer portion of the HAZ. This method was used to ensure that the longitudinal creep specimens were centered on the HAZ so that the specimen gauge diameter would contain all three weldment regions (base metal, HAZ, and weld deposit). Reproduced from (Hobbs et al., 2015).

the fusion line, in order for the specimen diameter to contain all of the relevant weldment regions (BM, HAZ, and WM). This can be more clearly seen in Fig. 3-2, which shows the placement of six longitudinal creep specimens through the weldment thickness. After specimen extraction and machining, constant-load creep testing was performed by Materials Technology Corporation in Ann Arbor, MI. The longitudinal specimens were tested to rupture at a condition of 621°C/124 MPa. Subsequent to creep testing, characterization was performed on one half of each ruptured creep specimen, including the measurement of ductility (%RA) along the gauge length, sectioning and mounting, microhardness testing, and optical and scanning electron microscopy.

3.4 Characterization

3.4.1 Metallographic Preparation and Microscopy

Mounted samples were prepared for microscopy using standard metallographic techniques, consisting of wet grinding with SiC grinding paper at 240 grit and 400 grit, diamond polishing on nylon cloth using 9 μm, 6 μm, and 3 μm diamond paste for durations of 5 minutes each, and a final polishing step of 0.05 μm colloidal silica on Imperial cloth for 5 minutes. The polished samples were etched with one of several etchants depending on the desired characterization method. Samples which were characterized by optical microscopy were etched with dilute Fry's Reagent for a duration of 5 to 10 s. The full strength reagent, as reported in standard metallography texts such as Vander Voort (Vander Voort, 1999), was diluted 2:1 with anhydrous ethanol. For samples which were characterized by SEM, freshly polished samples were etched by immersion in 10% Nital (10 mL nitric acid, 90 mL high purity methanol) for 2-4 minutes. For samples which were characterized both by optical microscopy and scanning electron microscopy, the sample was first etched for optical microscopy and then re-polished with colloidal silica before re-etching with 10% Nital for SEM examination. Subsequent to etching, optical micrographs were obtained at 4076×3116 pixel resolution with bright-field illumination using a Nikon MA-200 inverted

metallograph with a DS-U2 digital camera. Scanning electron micrographs were obtained at resolutions of either 1024×768 or 3072×2304 using a Zeiss LEO 1525 field-emission scanning electron microscope and a Phenom XL desktop scanning electron microscope.

3.4.2 Cryo-Cracking

"Cryo-cracking" is a technique for creating pristine fracture surfaces of a sample or material for subsequent fractographic evaluation, such as with the SEM (Lundin et al., 1998). This technique has been used extensively to evaluate creep damage (cavitation and micro/macro-cracking) in Cr-Mo steel weldments, for example in the results reported by the MPC HEP program (Lundin et al., 1999) and by Zhou (Zhou, 1997) for longitudinally seam-welded Cr-Mo piping. The advantages of this technique for evaluating creep damage are that the possibility of contamination of features of interest, e.g. creep cavitation, during the preparation process is greatly reduced, and additionally that the damage is revealed three dimensionally rather than as a 2D planar surface as in the case of a polished metallographic sample.

In the current research, cryo-cracking was conducted on samples from selected Grade 91 weldments in order to characterize creep damage (creep cavitation and micro-/macro-cracking) within the HAZ regions. For each selected weldment, cryo-cracking was performed according to the following procedure:

1. At the desired examination location, e.g. corresponding to a creep crack or region of preferential creep damage, notch the sample around the circumference using a Dremel tool with an abrasive cutting wheel. The purpose of the notch is to ensure that fracture occurs through the desired examination location by creating a stress concentration and by directing the path of fracture propagation.

2. After notching, clean the samples in methanol, dry them in warm air, and then immerse them in liquid nitrogen for 10-15 minutes or until the samples reach a stable temperature as evidenced by minimal bubbling in the nitrogen bath.
3. After temperature stabilization, rapidly remove the sample from the liquid nitrogen using tongs or tweezers, clamp the sample firmly into a bench vise with the notch slightly above the level of the vise jaw, and then fracture the sample by striking it with a heavy hammer blow. *Note*: for this step, it is imperative that the elapsed time between removing the sample from the bath and fracturing the sample is as short as possible, to minimize the temperature increase of the sample above liquid nitrogen temperature. If the sample temperature is allowed to increase too much, the sample might deform plastically rather than fracturing in a brittle manner at the desired location. If this occurs, the location of interest will be in an altered condition and a new sample for cryo-cracking must be obtained before repeating the procedure.
4. Quickly unclamp the fractured sample piece from the vise, then take this piece and the loose fractured piece and immerse both pieces in methanol and allow to warm up to ambient temperature. The use of a methanol bath is necessary to prevent oxidation of the fracture surfaces by condensed moisture, which would occur if the fractured pieces were allowed to warm up in air.

If the sample does not fracture after two or three rapid hammer blows, the sample should be returned to the nitrogen bath and re-equilibrated until bubbling stops. The sample fracturing process may then be repeated. If the sample still does not fracture after two or three hammer blows, the sample should be immersed in methanol to warm to ambient temperature. The notch depth should then be increased by further cutting with the Dremel tool to reduce the thickness of material that must be fractured, before repeating the cryo-cracking procedure.

3.4.3 Image Processing and Analysis

Software image analysis with FIJI/ImageJ (Abràmoff et al., 2004) was utilized for several different characterization steps in the dissertation research to obtain microstructural data for comparing the creep performance of different samples. Image analysis was used to evaluate the following aspects:

- inclusion content of the initial Grade 91 base metals, in terms of average inclusion size (area, μm^2) and areal density (inclusions/mm^2)
- microstructural characteristics of different regions within the Grade 91 weldment specimens, including precipitate size (area, μm^2) and areal density (particles/mm^2) and lath/subgrain size (mean lineal intercept l, in μm)

The specific procedures for each of these evaluations are described in the following subsections.

3.4.3.1 Evaluation of Inclusion Content in Grade 91 Base Materials

Inclusion analysis was performed on two Grade 91 base metals (refer to Table 3-1) to determine the representative, average inclusion area and areal density for each material. The inclusion analysis was performed using backscatter contrast SEM imaging at a magnification of 2500X; for each base metal, a total area of 25 mm^2 was analyzed by capturing ~5 mm^2 image panoramas at five locations in each base metal sample. The panoramas were captured at an image resolution of 2048x2048 pixels per tile and the final resolution of the panoramas was on the order of 4 pixels/μm. The image panoramas were processed according to the following procedure to obtain thresholded images (see example in Fig. 3-3) for performing inclusion analysis using the particle analyzer function in ImageJ (Abràmoff et al., 2004) to determine the average inclusion size and average inclusion density (number/mm^2).

1. Set the image scale using the scale marker from the acquired SEM panorama.
2. Crop the panorama to remove the data bar and stitched edges.

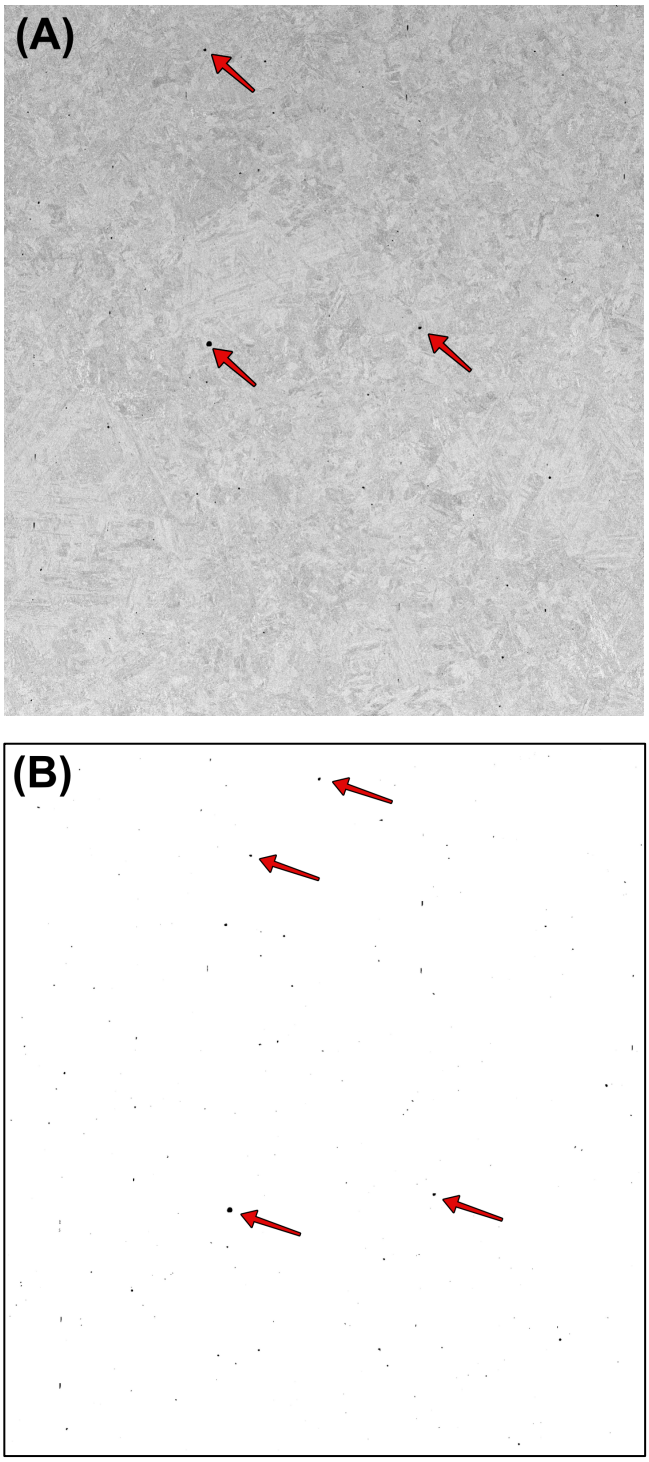


Figure 3-3. (A) Typical example of an microstructure of Grade 91 base metal as revealed by backscatter SEM imaging and (B) typical example of a processed image after thresholding and median filtering for inclusion analysis in ImageJ. In each image, inclusions are marked by red arrows.

3. Apply Gaussian blur to a copy of the cropped panorama, using a kernel size of 150, to create a blurred image for normalizing the brightness/contrast across the entire image. This step was performed to eliminate the brightness/contrast gradient from the top to bottom of the panorama.
4. Subtract the blurred image from the cropped image to normalize brightness/contrast.
5. Apply binary thresholding to the normalized image remove the background and leave only inclusions (black on white background). The threshold level was manually selected for each image while examining the image at high magnification in ImageJ to eliminate as much of the matrix area as possible while not altering the inclusion sizes.
6. Apply a median filter (radius: 0 pixels) to the thresholded image to remove stray or isolated pixels.
7. Use Particle Analyzer function in ImageJ to obtain measurements of features in the thresholded images (area, circularity, max. Feret diameter, bounding ellipse angle). A lower limit of 1 μm on particle size was applied to remove isolated pixels from the measurement results.
8. It was found that some image stitching artifacts were present in the panoramas in the form of short, vertical line segments at some of the image tile boundaries. Data filtering to mitigate these artifacts was performed by removing measurements with both an ellipse angle of $80° < x < 90°$ (i.e. nearly perpendicular to the horizontal axis of the image) and an aspect ratio (AR) > 2. Prior to removal, in each panorama a number of flagged artifacts were manually examined to verify that the flagged features were truly artifacts. After this data reduction, the data was sorted by AR and particles with AR>2 and angles near the cut-off, e.g. near 90° were manually examined to remove any additional artifacts which were slightly outside the selected range.

3.4.3.2 Evaluation of Microstructure in Grade 91 Weldments by Image Analysis

Image analysis was performed on SE-SEM micrographs obtained from different weld regions of the FT-H47 weldment and the H13-H47 weldment in the PWHT condition. The goal of the image analysis was to obtain data for semi-quantitative comparison of different regions within each dissimilar Grade 91 weldment, e.g. for a comparison of FT ICHAZ versus H47 ICHAZ characteristics, in order to relate possible differences in microstructural characteristics to differences in creep behavior. The microstructural characteristics were evaluated and compared from SEM micrographs of polished and etched metallographic samples; the etchant utilized was 10% Nital. The image measurements included the following data: average particle size and/or particle size distribution, particle number density, and grain/subgrain size. The procedures for the particle analysis and grain/subgrain analysis are described separately in the following text.

Concerning the evaluation of precipitates from the SEM micrographs, the precise identification of particles as correlating to a specific carbide type was not possible because the micrographs were secondary electron images and thus the image contrast was primarily topographical rather than compositional. Only a general determination of particle type could be inferred from background knowledge of CSEF steels, namely that the larger particles on the subgrain boundaries after PWHT are most likely $M_{23}C_6$ carbides and that small/fine particles within the subgrain matrix are most likely MX carbonitrides. Considering these limitations, image analysis was performed on the micrographs using ImageJ according to the following procedure:

1. Calibrate the image using the known scale factors for each magnification.
2. Perform binary thresholding on 8-bit grayscale images to remove the matrix regions (background) and leave only the particles with the image field. The threshold level was checked and adjusted as necessary for each region (CGHAZ,

FGHAZ, etc.) to ensure as much as possible, that the matrix grayscale values were being thresholded without excessively removing particles/carbides from the image.

3. A median filter (radius = zero pixels) was applied to the image after thresholding to remove stray/isolated pixels.
4. Particle analysis was performed in ImageJ using a particle size range of 5-2048 pixels. Multiple analyses were performed while varying the particle circularity range from 0 to 1, 0.15 to 1, and 0.3 to 1. The circularity range was adjusted in order to obtain the best possible exclusion of non-particle features from the particle analysis (e.g. segments of subgrain boundaries which exhibited similar contrast to particles). For some images, it was necessary to manually remove grain boundary segments from the thresholded images; where this manual cleaning was necessary, it was performed prior to the ImageJ/FIJI particle analysis.
5. The average particle area, Feret diameter, and areal number density of particles were determined for each region using the image analysis results and the calibrated image dimensions.

As an illustration of the above procedure, Fig. 3-4 shows an image sequence for the H47 FGHAZ region to proceed from a levels-adjusted SEM micrograph to the final image mask for measurement of particle characteristics. Fig. 3-4(A) shows the SEM micrograph after levels adjustment to align the black point/white point in the output with the extreme values at the far left and far right of the histogram. Fig. 3-4(B) shows the image after thresholding has been applied; Fig. 3-4(C) shows the image after median filtering (pixel radius of zero) to remove stray pixels, followed by Fig. 3-4(D) which shows the image mask output from the particle analysis module in ImageJ using a particle size range of 5-1024 px and a circularity range of 0.15-1.00. These ranges were chosen to eliminate "potential" particles which were below a reasonable detection limit based on the resolution of the SEM micrographs. Similarly, Fig. 3-5 shows a

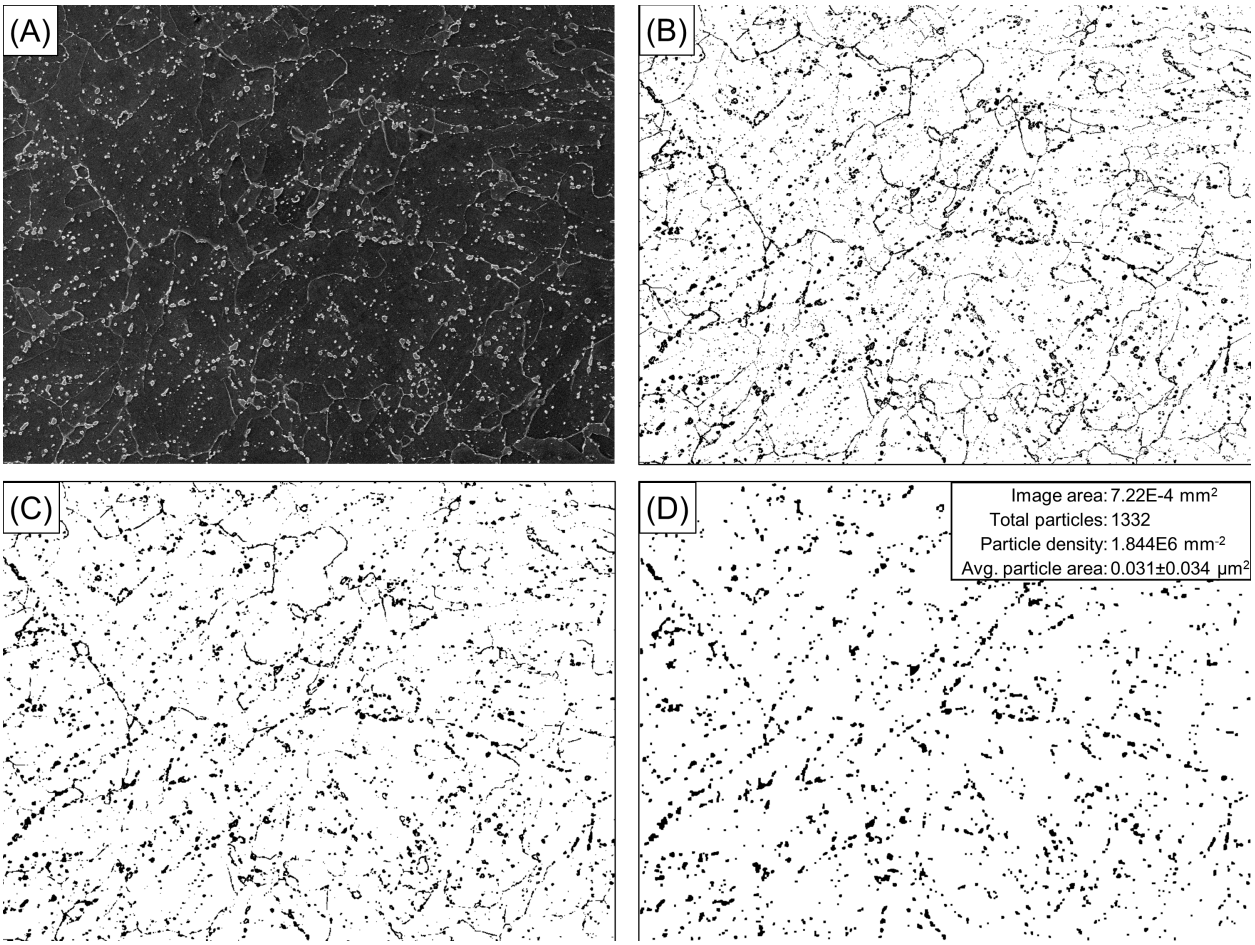


Figure 3-4. Image sequence showing the image processing steps for particle analysis of a representative SEM micrograph from the H47 FGHAZ region at 10kx: (a) SEM micrograph after levels-adjustment so that black corresponds to the value at the far left of the original image histogram and white corresponds to the value at the far right of the histogram (b) thresholded image (c) image after applying median filter (zero pixel radius) to remove isolated stray pixels (d) image mask after particle analysis using 5-1024 pixel range and 0.15-1.00 circularity range.

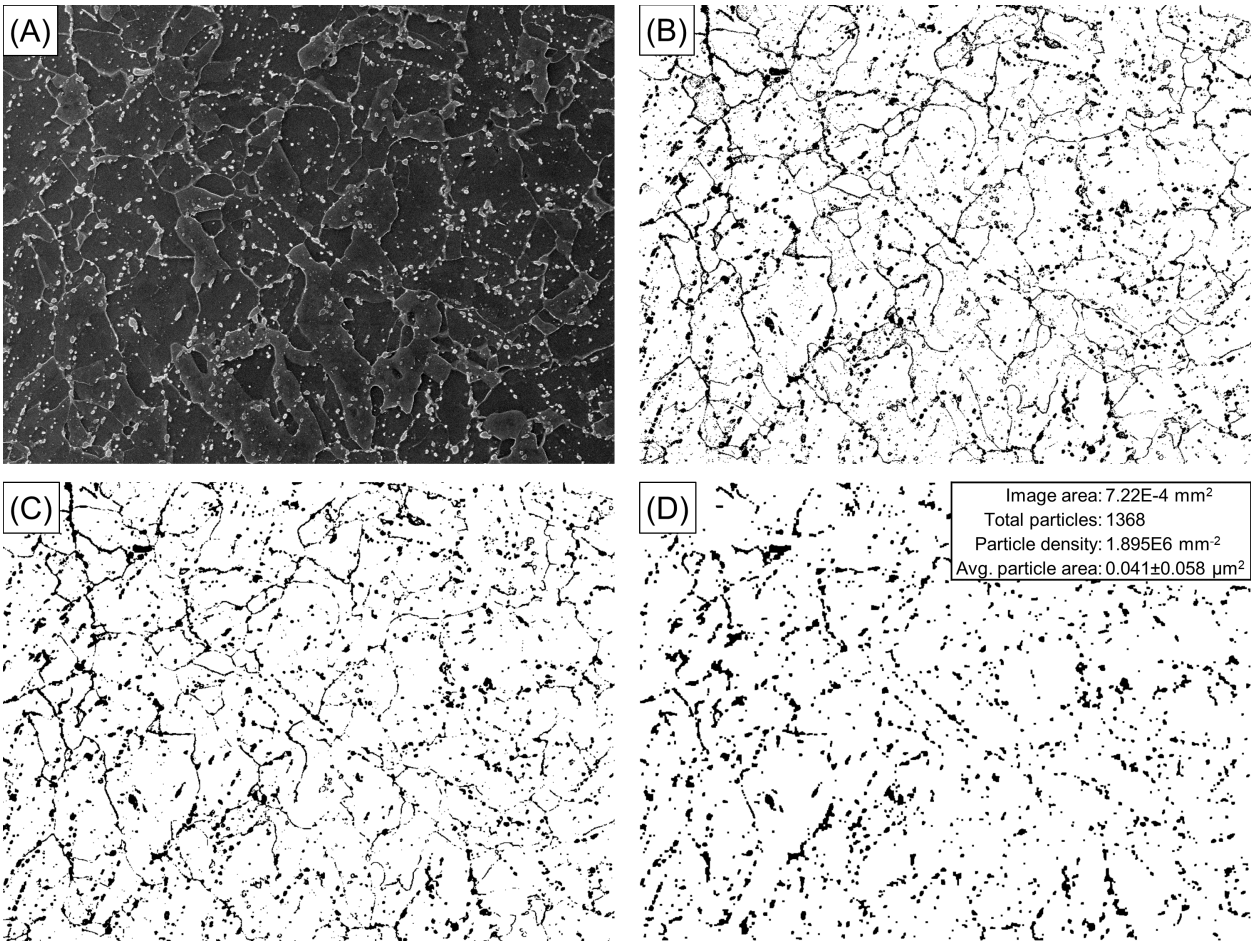


Figure 3-5. Image sequence showing the image processing steps for particle analysis of a representative SEM micrograph from the FT FGHAZ region at 10kx: (a) SEM micrograph after levels-adjustment so that black corresponds to the value at the far left of the original image histogram and white corresponds to the value at the far right of the histogram (b) thresholded image (c) image after applying median filter (zero pixel radius) to remove isolated stray pixels (d) image mask after particle analysis using 5-1024 pixel range and 0.15-1.00 circularity range.

representative image sequence for the FT FGHAZ region to proceed from a levels-adjusted SEM micrograph to the final image mask for measurement of particle characteristics. Summary statistics for each evaluated image were obtained including average particle area and standard deviation, total particle count, and areal density of particles.

Following from this procedure, it was necessary to check the consistency of the technique and provide some verification for the use of single images as a data source, which was necessary due to limited availability of samples. As mentioned in the opening section of this chapter, the dissimilar Grade 91 weldments were part of a previous industry-sponsored project (Hoskins et al., 2017) and most of the samples were returned to the sponsor at the conclusion of the project. Thus, the weldment samples in the PWHT condition were not available for obtaining additional or replicate micrographs in the various weld regions in order to increase the number of analyzed fields (which, of course, is desirable for better accuracy of the results). In the case of the H47 FGHAZ region where duplicate micrographs had been obtained previously, a comparison of the particle analysis results was conducted to show whether the particle distribution was similar between the two regions. Fig. 3-6 shows histograms of particle area values for two individual 10kx micrographs obtained from the H47 FGHAZ region of the FT-H47 weldment in the PWHT condition. The histogram and the accompanying statistics at the top of the figure show that both FGHAZ micrographs are similar in terms of particle characteristics. The difference in the smaller particle count at the left of the histogram, approximately 15% difference for the smallest bin size, is potentially due to the limitation of the image resolution (1024x768 pixels) of the micrographs. At the image resolution of 1024x768, a particle size of 0.025 μm^2 is equivalent to 27 px^2. Based on this result, it may be concluded that single images can provide usable data for performing a semi-quantitative comparison of particle characteristics such as particle area and areal number density.

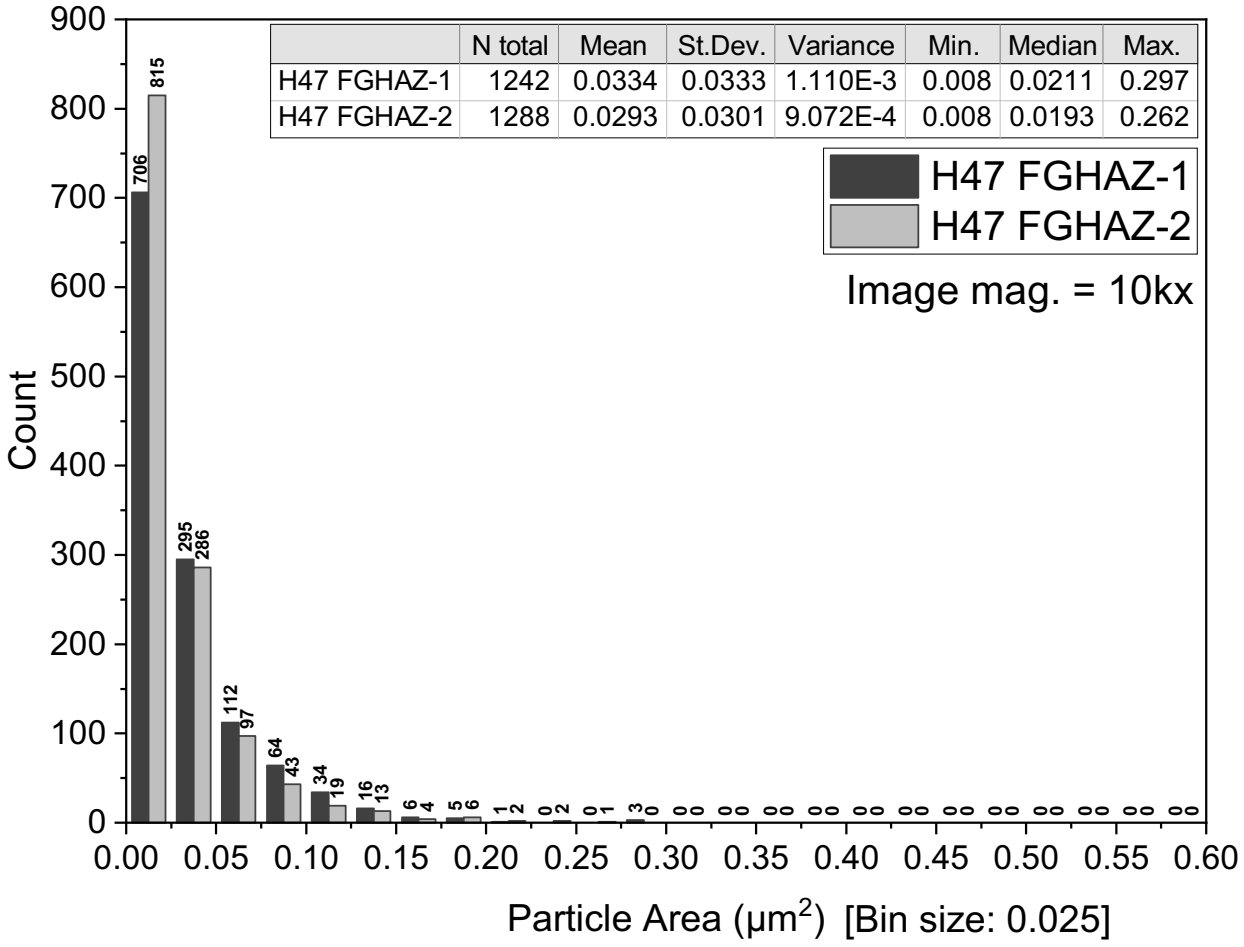


Figure 3-6. Histogram of particle area for two different SEM micrographs obtained from the H47 FGHAZ region in the FT-H47-1 cross-weld creep specimen. Both FGHAZ regions exhibit similar particle area distributions. The smallest bin size of 0.025 μm^2 shows a difference of approximately 15% between the two distributions.

An additional aspect of evaluating the microstructure of various regions in the Grade 91 weldments was related to the subgrain size. To perform this analysis, SEM micrographs in the PWHT and creep-tested conditions were processed in ImageJ in order to measure the dimensions of the subgrains. The measurement method applied to the micrographs was the circular intercept method, specifically the Abrams Three-Circle Procedure described in ASTM E112-13 "Standard test methods for determining average grain size" (*Standard Test Methods for Determining Average Grain Size*, 2013). The circular intercept method was used because it avoids the uncertainty of having test lines end within subgrain interiors and it also automatically accounts for non-equiaxed grain structures. Generally, due to limited sample availability and data, only a single micrograph was available for evaluation for the PWHT condition; for some cases in the creep-test condition, multiple micrographs were available and were analyzed as noted in the results for specific cases. The circular intercept method yielded microstructure parameters P_L (the number of grain boundary intersections per unit of test line) and l (mean lineal intercept length); a larger lineal intercept length corresponds to a larger grain size and a larger ASTM grain size number. The analysis in ImageJ was conducted according to the following procedure.

1. A test overlay consisting of three concentric circles centered in the image frame was applied to each SE-SEM micrograph using ImageJ and the ConcentricCircles plugin. The sum of the circle circumferences (true length at the selected image magnification) was calculated to find the total test line length for the calculation of P_L and l. For micrographs obtained a 10kx with an image resolution on the order of 1024x768px, three circles having a radius of 345, 272.5, and 200 pixels respectively were used.
2. For each micrograph, the number of grain boundary intersections with each circle of the test overlay were manually counted and tabulated using the point count function in ImageJ. In accordance with ASTM E112, intersections of the test

overlay with a boundary triple point were counted as 1.5 intersections, and points where the test overlay intersected or touched a boundary tangentially were counted as single intersections.

   a. when counting the boundary intersections, boundaries which obviously corresponded to PAGBs (e.g. by the clear presence of many aligned carbides) were excluded from the count.
   b. additionally, for micrographs from creep-tested samples, intersections between the test overlay and the edges of creep cavities were excluded from the count.

3. For each micrograph, the total number of boundary intersections was determined as the number of single intersections plus twice the number of triple intersections. Then the number of intersections was divided by the true test line length, which was equal to the sum of circumferences in pixels multiplied by the image scale factor, to calculate the value of PL. Lastly, this value was inverted to obtain the lineal intercept length (μm).
4. Where possible, the average value and standard deviation of the lineal intercept length were calculated.

An example micrograph illustrating the three-circle test pattern with markers to denote the boundary intersection locations in shown in Fig. 3-7.

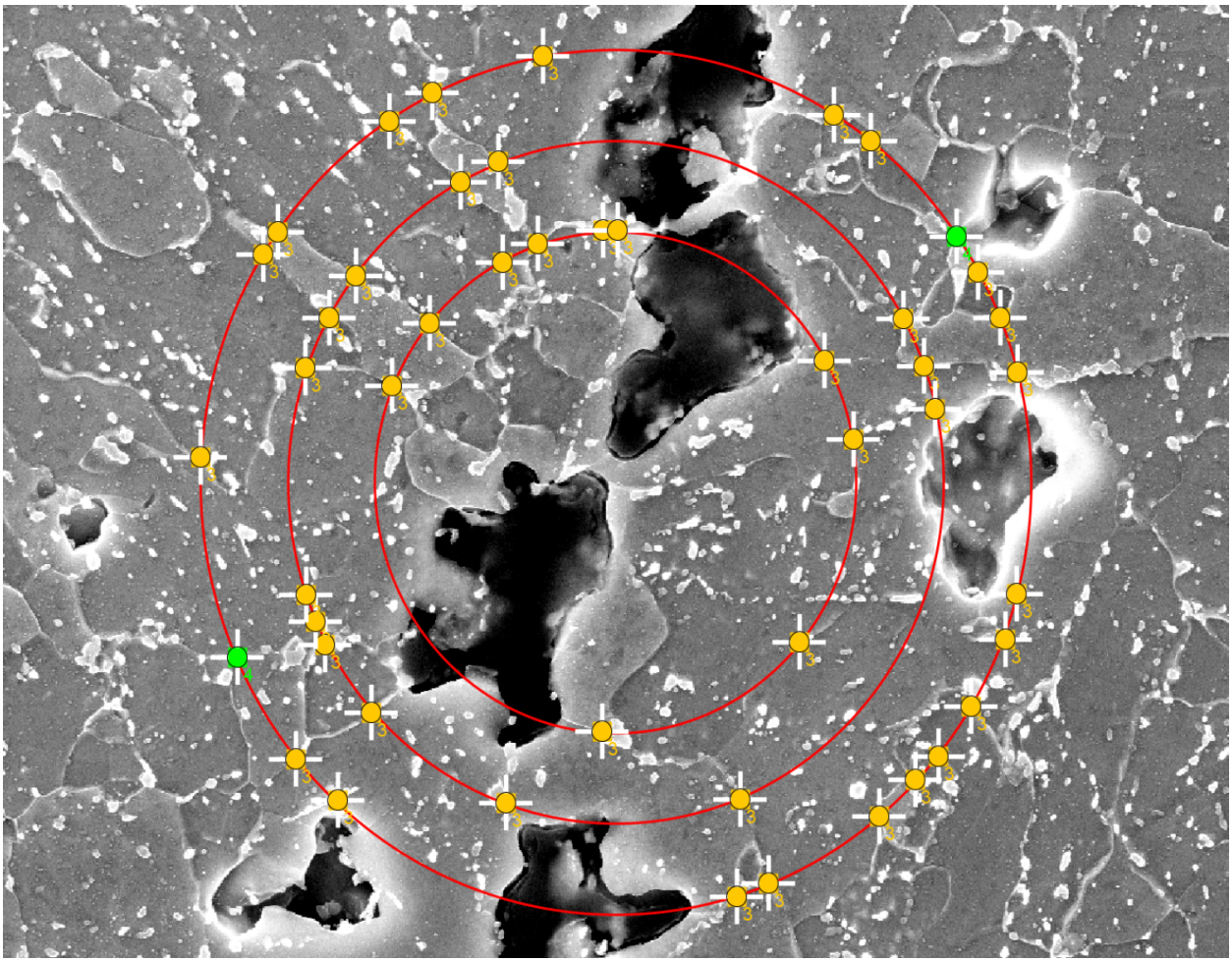


Figure 3-7. Representative SE-SEM micrograph illustrating the procedure for measuring subgrain size according to the Abrams Three-Circle procedure described in ASTM E112. The micrograph has been overlaid with the test pattern and the boundary intersection locations have been marked for subsequent counting; yellow points are counted as single intersections and green points are counted as 1.5 intersections.

Chapter 4 Creep Behavior and Creep Damage Characterization of Dissimilar Grade 91 Weldments

4.1 Characterization of Inclusion Content in Grade 91 Base Metals

As described in Section 3.4.3.1, two different Grade 91 base metals (FT and H47 as denoted in Materials) were characterized to evaluate the average inclusion density in order to determine whether differences in inclusion content could be correlated to the observed differences in Type IV creep damage occurrence. The results for the average inclusion density of the FT base metal are summarized in Table 4-1. A histogram of the measured inclusion data in the range of 0-50 μm is shown in Fig. 4-1; the full dataset with summary statistics is presented in the box plot in Fig. 4-2. Table 4-1 shows that the inclusion density in the FT material was on the order of 50 to 60 particles/mm^2 and the average inclusion size (in terms of area) is in the range of ~4 to 8 μm^2. The average inclusion density for the FT material would be classified as a low inclusion density heat according to the categories published by EPRI (*Life Management of 9%Cr Steels: Evaluation of Metallurgical Risk Factors in Grade 91 Steel Parent Material*, 2018). The box plots in Fig. 4-2 show that the FT base metal exhibits significant spread in the particle size distribution since there is a large "tail" of outlier particles that are significantly larger than the average particle size, e.g. for "FT Scan-2" which exhibit a large outlier particle (area of nearly 500 μm^2). A representative micrograph showing the typical appearance of the large outlier inclusions is shown in Fig. 4-3. The statistics in Fig. 4-2 also show that the median particle size is fairly uniform for the different scans, indicating that the average size is significantly affected by the outlier particles.

The results for the determination of average inclusion density for the H47 base metal are summarized in Table 4-2. Table 4-2 shows that the total inclusion count varies across the different image areas examined (each ~5 mm^2 in size) and thus the resulting calculated value for inclusion density varies from 61 to 92 mm^{-2}. However, the mean

Table 4-1. Summary of inclusion data for the FT Grade 91 base metal obtained from image analysis of BSE-SEM image panoramas. Total analysis area for the FT base metal was ~25 mm^2.

Name	Image area (mm^2)	Total Count of Inclusions > 1 μm^2	Inclusion Number Density (1/mm^2)	Total Inclusion Area in Image (μm^2)	Inclusion Area Fraction in Image	Mean Inclusion Size (Area, μm^2)	Median Inclusion Size (μm^2)
FT Scan-1	5.28	256	49	1243	2.35E-4	4.85	1.372
FT Scan-2	5.10	332	65	2554	5.01E-4	7.69	1.424
FT Scan-3	5.19	322	62	2397	4.62E-4	7.44	1.498
FT Scan-4	5.18	266	51	1197	2.31E-4	4.50	1.379
FT Scan-5	5.21	275	53	1032	1.98E-4	3.75	1.401

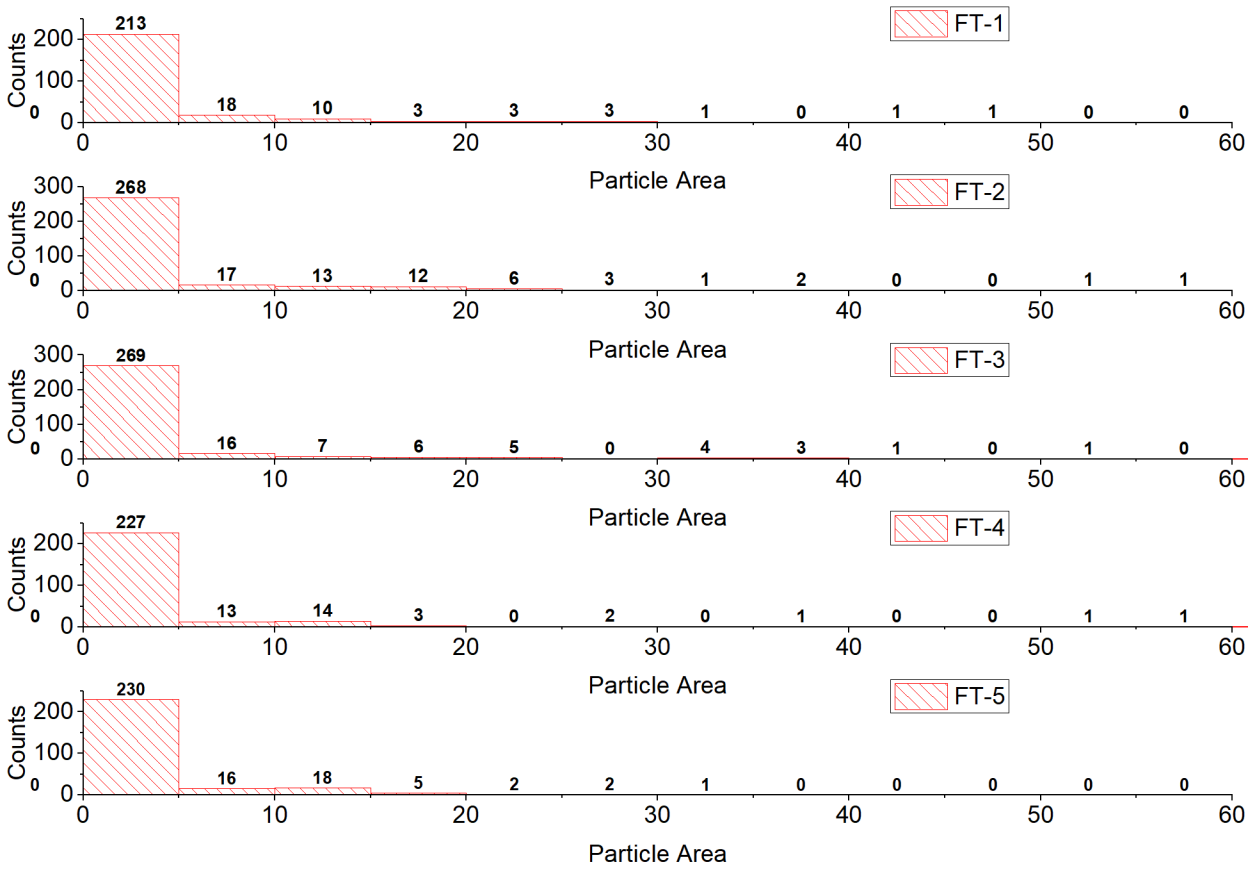
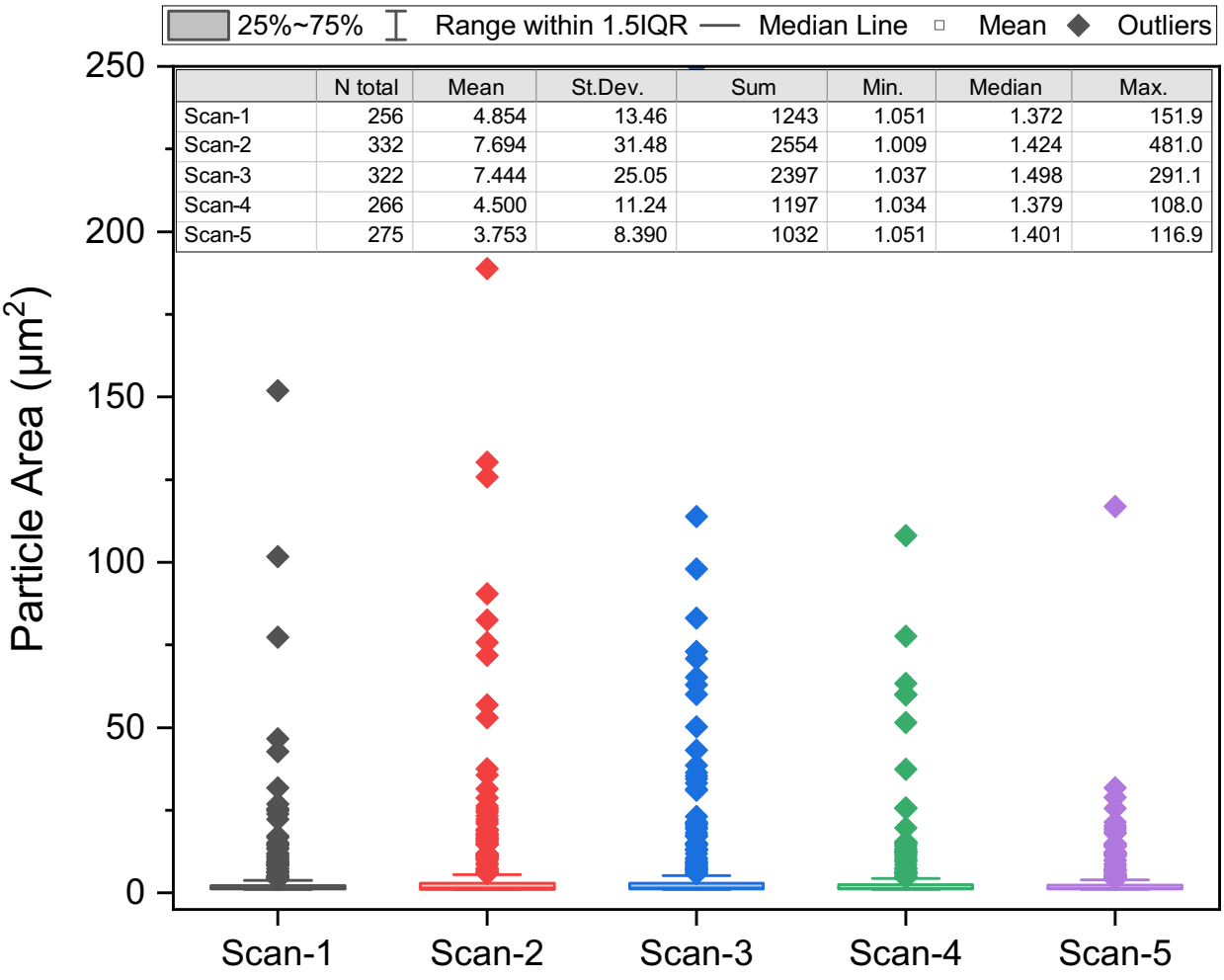


Figure 4-1. Histograms of particle size (in terms of area) for evaluating inclusion content in the FT base metal, showing the particle area distribution in the range of 0-60 μm. The histograms were determined based on software image analysis of BSE-SEM image panoramas obtained at 2500X from an as-polished FT base metal sample. An area of ~5 mm^2 was evaluated for each scan.



	N total	Mean	St.Dev.	Sum	Min.	Median	Max.
Scan-1	256	4.854	13.46	1243	1.051	1.372	151.9
Scan-2	332	7.694	31.48	2554	1.009	1.424	481.0
Scan-3	322	7.444	25.05	2397	1.037	1.498	291.1
Scan-4	266	4.500	11.24	1197	1.034	1.379	108.0
Scan-5	275	3.753	8.390	1032	1.051	1.401	116.9

Figure 4-2. Box plots of particle area for evaluating inclusion content in the FT base metal. The box plot data was obtained from software image analysis of SEM-BSE image panoramas obtained at 2500X from an as-polished FT base metal sample. An area of ~5 mm² was evaluated for each scan for a total evaluated area of ~25 mm².

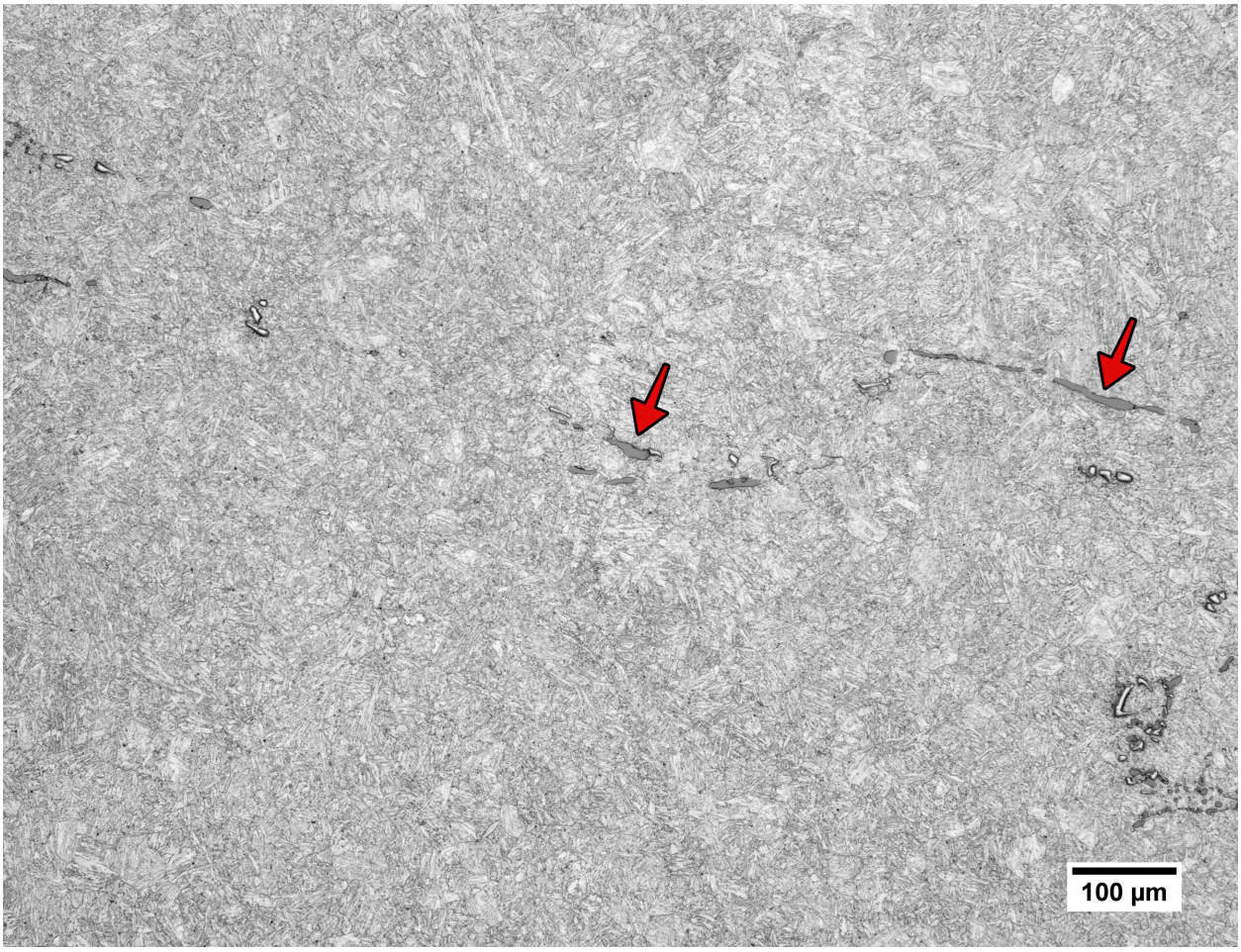


Figure 4-3. Representative optical micrograph from the FT (forging) base metal in the PWHT condition showing the presence of large inclusion "stringers" (noted by arrows). Etchant: Fry's reagent.

Table 4-2. Summary of inclusion data for the H47 Grade 91 base metal obtained from image analysis of BSE-SEM image panoramas. Total analysis area for the H47 base metal was ~25 mm^2.

Name	Image area (mm^2)	Total Count of Inclusions > 1 μm^2	Inclusion Number Density (1/mm^2)	Total Inclusion Area in Image (μm^2)	Inclusion Area Fraction in Image	Mean Inclusion Size (μm^2)	Median Inclusion Size (μm^2)
H47 Scan-1	5.07	467	92	1737	3.43E-4	3.72	2.38
H47 Scan-2	5.06	460	91	1698	3.36E-4	3.69	2.38
H47 Scan-3	5.16	364	71	1406	2.72E-4	3.86	2.22
H47 Scan-4	5.08	397	78	1631	3.21E-4	4.11	2.41
H47 Scan-5	5.06	308	61	1130	2.99E-4	3.67	2.46

inclusion size (measured in terms of particle area) for each image is similar and except for the fourth image, the total inclusion area is also fairly consistent. The particle area histograms for the examined H47 base metal regions are shown in Fig. 4-4 and it is apparent that the four different regions exhibit identical trends in particle area distribution. Compared to the H13 data shown subsequently, the outlier inclusions in the H47 base metal , i.e. the inclusion sizes which occur much less frequently than the majority, are smaller than those in H13; Fig. 4-4 shows that the majority of the inclusions were <10 μm^2 in size in each of the analyzed H47 image panoramas. Fig. 4-5 shows box plots of inclusion area for the same H47 image areas and it is apparent both qualitatively from the graphs and from the summary data within the graph that the characteristic quantities of each area are similar. The graph in Fig. 4-5 shows that the main difference is the number and scatter of outlier inclusions. Based on the measured inclusion density, H47 would be classified as a "medium inclusion density heat" according to the classification scheme reported by EPRI (*Life Management of 9%Cr Steels: Evaluation of Metallurgical Risk Factors in Grade 91 Steel Parent Material*, 2018). Table 4-3 summarizes the inclusion results for the FT and H47 base metals for comparison. The summary shows that due to the large variability in the FT inclusion characteristics between the five measurement areas, the average total inclusion count and average inclusion density are nominally lower than the H47 base metal; however, the ranges of values overlap between the FT and H47 materials in both cases, indicating that a clear distinction in inclusion density cannot be made. There is also significant overlap in the average values for total inclusion area, inclusion area fraction, and mean inclusion size due to the scatter in the FT inclusion data and the presence of the large outlier inclusions. Only for median inclusion size is there a distinct difference between the FT and H47 base metal, where the FT base metal actually shows a smaller value of median inclusion size.

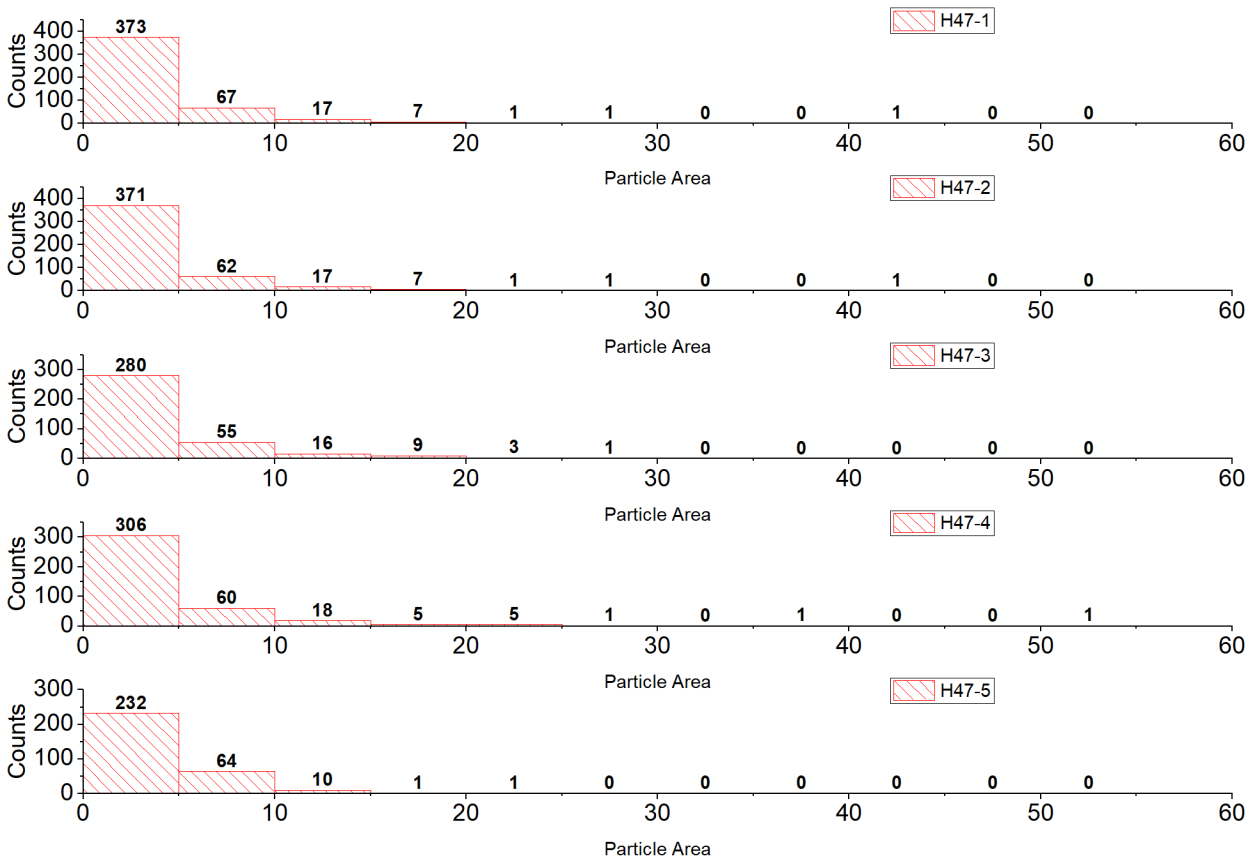
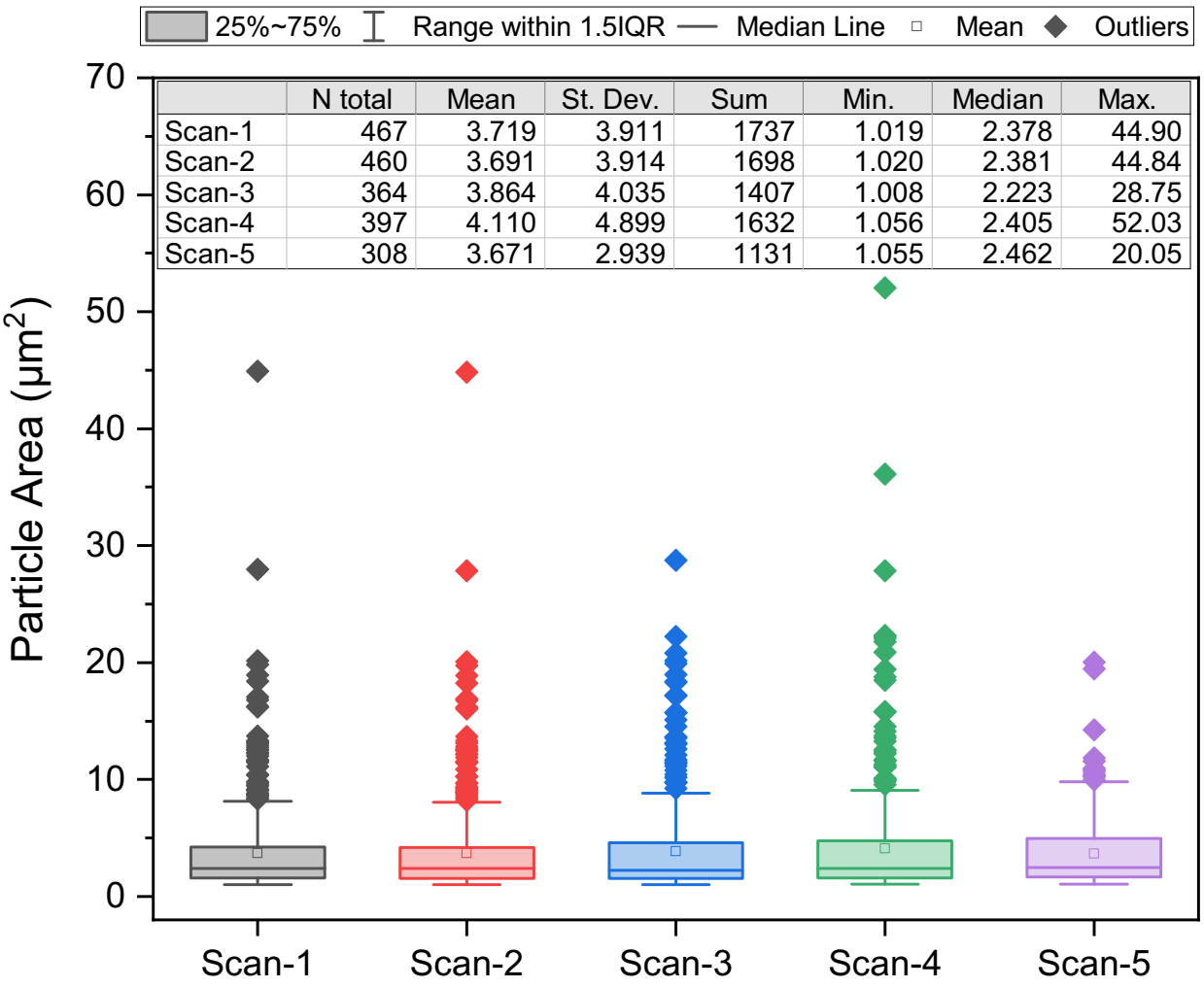


Figure 4-4. Histograms of particle size (in terms of area) for evaluating inclusion content in the H47 base metal, showing the particle area distribution in the range of 0-60 μm. The histograms were determined based on software image analysis of BSE-SEM image panoramas obtained at 2500X from an as-polished H47 base metal sample. An area of ~5 mm^2 was evaluated for each scan.



	N total	Mean	St. Dev.	Sum	Min.	Median	Max.
Scan-1	467	3.719	3.911	1737	1.019	2.378	44.90
Scan-2	460	3.691	3.914	1698	1.020	2.381	44.84
Scan-3	364	3.864	4.035	1407	1.008	2.223	28.75
Scan-4	397	4.110	4.899	1632	1.056	2.405	52.03
Scan-5	308	3.671	2.939	1131	1.055	2.462	20.05

Figure 4-5. Box plots of particle area for evaluating inclusion content in the H47 base metal. Note that the main difference between the five scans is in the distribution of outliers; the characteristic quantities (mean, standard deviation, quartile range) are similar for the evaluated areas. The box plot data was obtained from software image analysis of BSE-SEM image panoramas obtained at 2500X from an as-polished H47 base metal sample. An area of ~5 mm² was evaluated for each scan for a total evaluated area of ~25 mm².

Table 4-3. Summary of statistics relating to inclusion content in two evaluated Grade 91 base metals. The values reported below (average ± 95%CI) are calculated from the five individual scans for each base metal provided in Table 4-1 and Table 4-2.

	Total Count of Inclusions >1 μm^2	Inclusion Number Density ($1/mm^2$)	Total Inclusion Area (μm2)	Inclusion Area Fraction	Mean Inclusion Size (μm^2)	Median Inclusion Size (μm^2)
FT Base Metal	290 ± 43	56 ± 8.8	1685 ± 904	3.3E-4 ± 1.8E-4	5.6 ± 2.2	1.4 ± 0.063
H47 Base Metal	399 ± 83	79 ± 16	1520 ± 314	3.0E-4 ± 6.3E-5	3.8 ± 0.23	2.4 ± 0.11

4.2 Creep Behavior and Creep Damage Characterization of the FT-H47 Dissimilar Weldment

As described in the Materials and Experimental Procedures section, a Grade 91 test weldment from a previous industry project (Hoskins et al., 2017) was utilized for investigating potential factors on the occurrence and extent of Type IV creep damage. The weldment was previously fabricated by a third party for metallurgical characterization and creep testing using two dissimilar Grade 91 base metals, identified as "FT" and "H47." In the following sections, the results of creep testing and subsequent characterization by optical light microscopy and scanning electron microscopy; "cryo-cracking" fractography in the SEM; and image analysis of microstructure using SEM micrographs are presented. The results are subsequently discussed in a following section with regard to the development of creep damage in the heat-affected zone (Type IV creep damage) and a comparison of creep damage susceptibility in the HAZs of the FT and H47 base metals.

4.2.1 Characteristics of the FT-H47 Weldment Prior to Creep Exposure

The Grade 91 weldment designated as "FT-H47" was characterized in the PWHT condition to document the microstructure and microhardness prior to creep exposure. An optical macrograph of the FT-H47 weldment is shown in Fig. 4-6. The selected weld geometry utilized a weld groove angle of zero degrees and thus the fusion line was perpendicular to the loading axis during subsequent creep testing. It has been shown in literature (Francis et al., 2009) that a zero- or low-angle groove geometry produces optimum creep performance for Grade 91 welds compared to angles such as 30° or 45°; therefore, the resulting creep behavior of the FT-H47 weld may be attributed more specifically to the inherent base metal HAZ characteristics with a minimal effect from the weld geometry. Since the zero degree angle produces optimum performance (longest rupture time), this configuration will also tend to emphasize differences in performance between the two base metals HAZs.

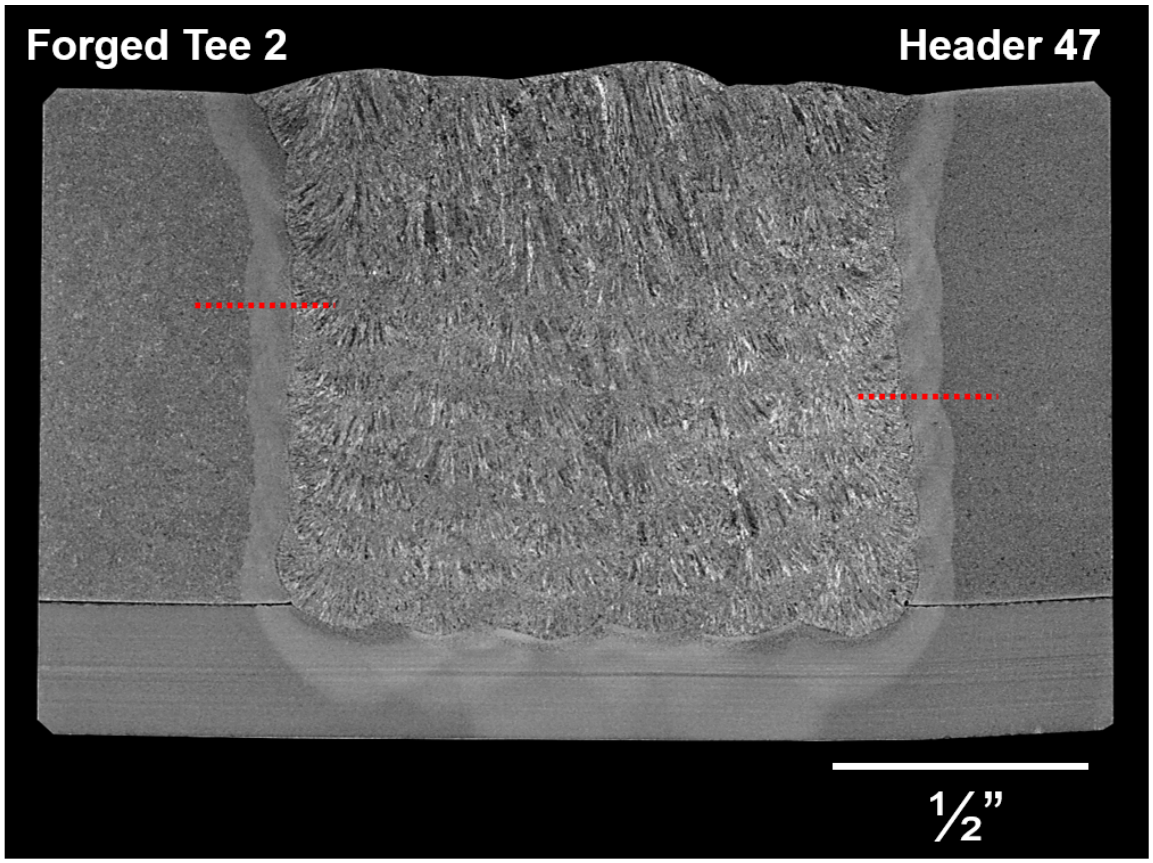


Figure 4-6. Optical macrograph of the FT to H47 SMAW weldment in the PWHT condition, 746°C/1 h. The red dotted lines indicate the locations of microhardness traverses which are shown in Fig. 4-17. Etchant: Fry's reagent.

The microstructures of the base metal, HAZ regions (CG/FG/ICHAZs), and weld deposit of the FT-H47 weldment were characterized in the etched condition using OLM and SEM. These corresponding microstructures for the FT-H47 weldment are shown beginning in Fig. 4-7. The FT and H47 base metals were evaluated in more detail regarding inclusion content in Section Characterization of Inclusion Content in Grade 91 Base Metals, but generally speaking, both base metals exhibited a tempered martensite ferritic structure (TMFS) as discussed previously (refer to Section 2.1.2 and Fig. 2-1 in the literature review).

Fig. 4-7 shows OLM and SEM micrographs of the FT base metal subsequent to normalizing, tempering, and PWHT. The OLM micrograph in Fig. 4-7(B) shows the overall grain structure; representative PAGBs are visible (red arrows) and some parallel features indicating the block substructure of the tempered martensite are also visible by blue arrows in (B). The lath-like structure is more clearly apparent in the SEM micrograph in Fig. 4-7(C); PAGBs decorated with carbides are apparent (red arrows) along with parallel blocks (blue arrows) and block boundaries (green arrows). Similarly in Fig. 4-7(D), PAGBs, blocks, and block boundaries are visible; note that the boundaries are decorated with carbides, but that some portions of the boundaries, e.g. particularly the block boundaries as shown by the green arrows in (D), do not show continuous carbide precipitation. This is most likely a result of slight carbide coarsening during tempering and PWHT, and also the fact that in this Grade 91 composition, the primary boundary carbides are $M_{23}C_6$ carbides rather than MX carbonitrides and M23C6 carbides are larger and coarsen more readily (refer to Fig. 2-14 for $M_{23}C_6$ vs. MX comparison on boundaries).

Fig. 4-8 shows the OLM and SEM micrographs of the FT CGHAZ region subsequent to PWHT. Compared to the FT base metal, the PAG size has increased due to grain growth resulting from the high peak temperature in the CGHAZ (~>1300°C); the high peak

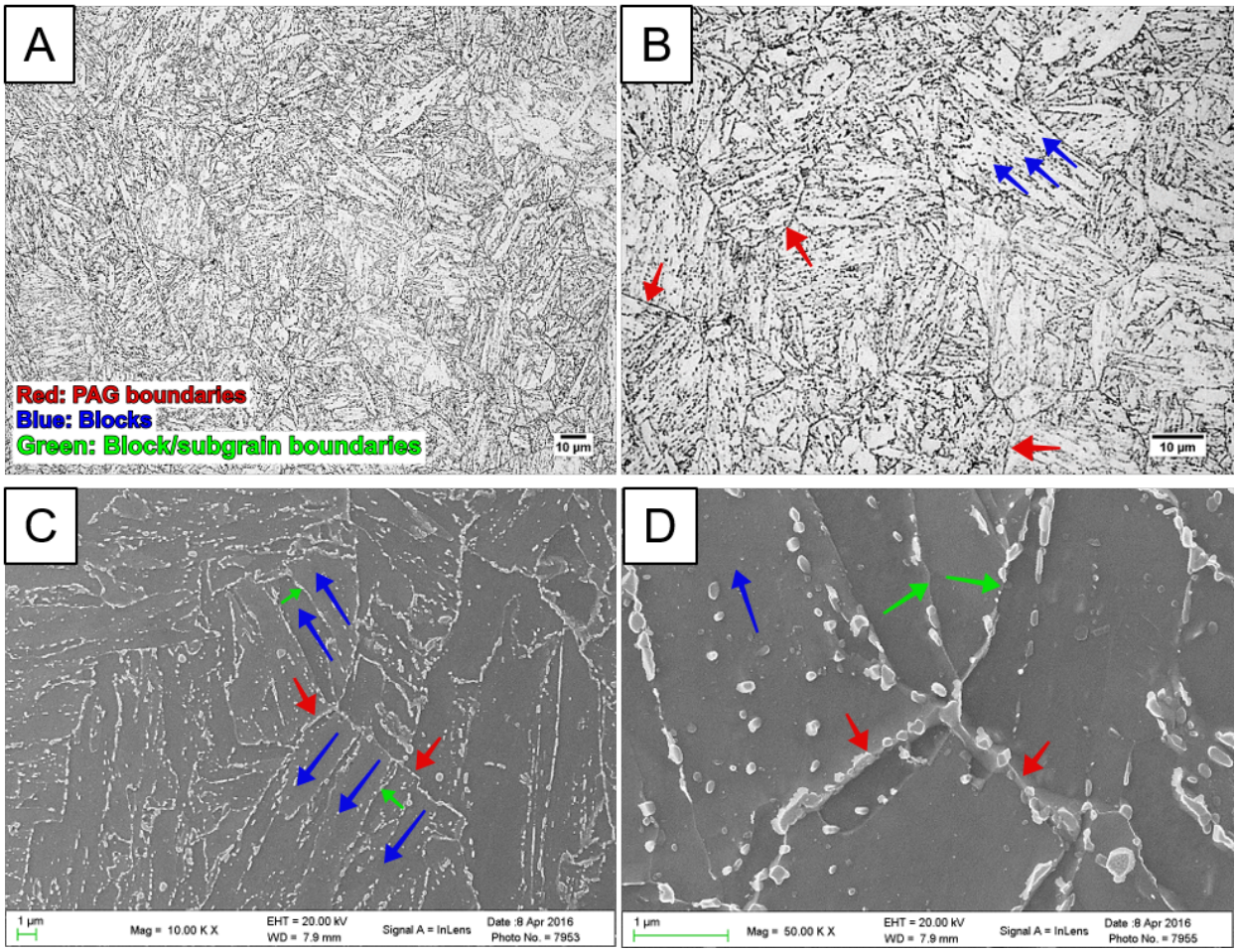


Figure 4-7. Microstructure of the FT base metal subsequent to re-normalizing, tempering, and PWHT (746°C/1 h), as revealed with (A,B) OLM and (C,D) SEM. In (B), PAGBs are denoted by red arrows, while parallel features corresponding to tempered martensite blocks within a PAGB are denoted by blue arrows. In (C), note the clear lath-like subgrain structure with numerous fine carbides <1 μm in size along the subgrain boundaries, with additional particles <<1 μm in size within the ferritic subgrain interiors (partially visible in D). Etchant: Fry's reagent in (A, B) and 10% Nital in (C,D).

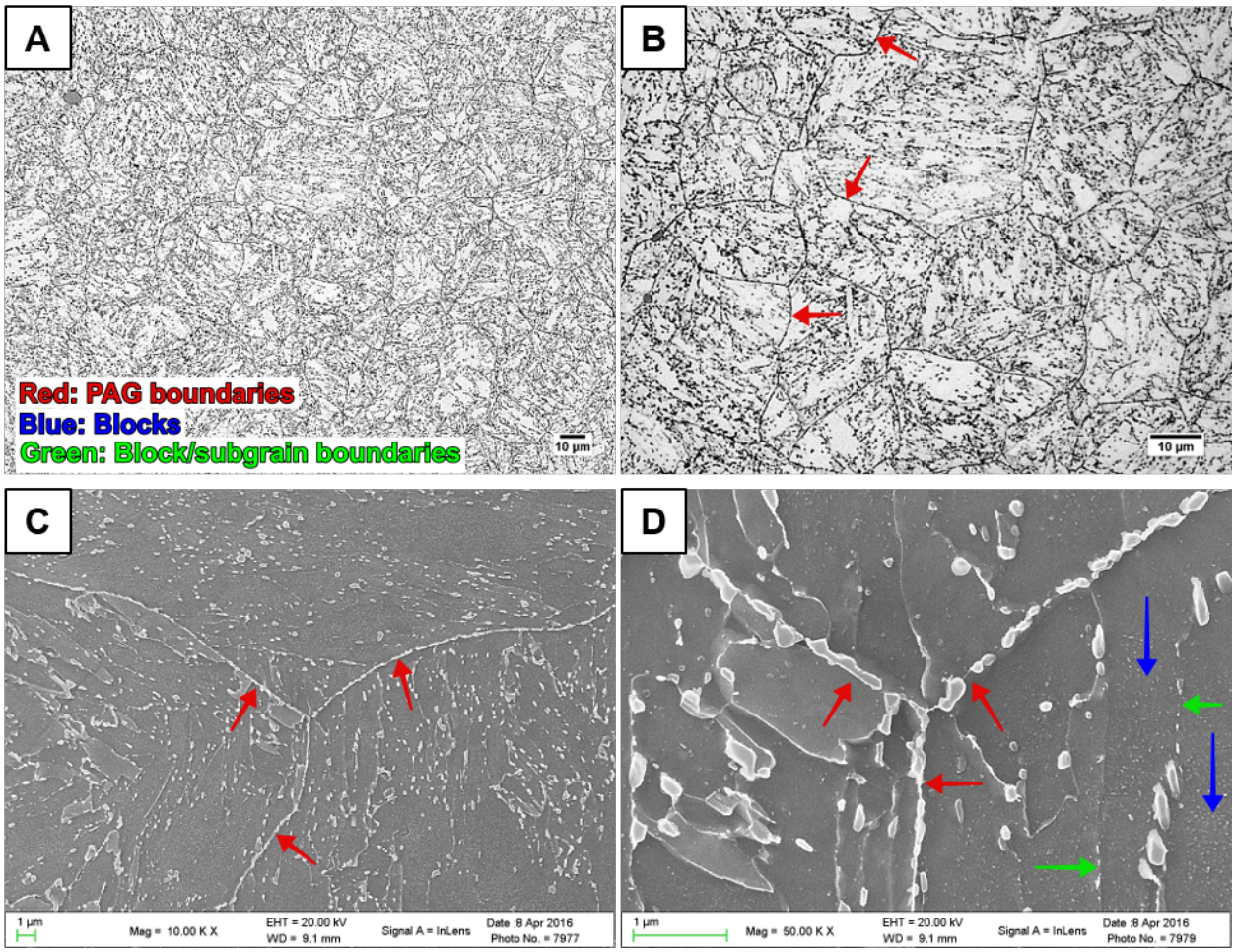


Figure 4-8. Microstructure of the FT CGHAZ from the FT-H47 weldment subsequent to PWHT (746°C/1 h) as revealed with (A,B) OLM and (C,D) SEM. A lath-like substructure is evident in (C,D) since this region was completely transformed to austenite during the welding thermal cycle and subsequently formed new martensite upon cooling. Compared to Fig. 4-7, a greater extent of fine particles <<1 μm in size is evident in the ferritic subgrain interior in (D) after PWHT, due to carbide dissolution and re-precipitation that occurred as a result of the CGHAZ thermal cycle and PWHT. Etchant: Fry's reagent (A, B) and 10% Nital (C,D).

temperature leads to complete dissolution of precipitates which would normally inhibit grain growth (grain growth occurs in the austenite phase). The OLM micrograph in Fig. 4-8(B) shows the overall grain structure with larger PAGBs visible. In the SEM micrograph in Fig. 4-8(C), the enlarged PAG size is very clearly visible with well-defined PAGBs (red arrows); the martensite substructure (blocks) is much more indistinct than in Fig. 4-7(C). Nearly continuous carbide precipitation along the PAGB is apparent in (C) and also in (D), which shows a PAGB triple junction. The carbides along the PAGBs are most likely $M_{23}C_6$ carbides; due to the complete dissolution of carbides during the CGHAZ thermal cycle and subsequent re-precipitation during tempering and PWHT, a significant extent of very fine precipitation within the substructure is also apparent (red circles), mores than in Fig. 4-7(D).

Fig. 4-9 illustrates the OLM and SEM microstructure of the FT FGHAZ region subsequent to PWHT. Compared to either the FT base metal or the FT CGHAZ, the PAGBs are much less distinct, as can be seen from the OLM micrograph in Fig. 4-9(B); faint outlines of PAGBs are noted in the figure. At higher magnification with SEM in Fig. 4-9(C), it is apparent that the parallel, aligned lath-like features which occur clearly in the FT base metal (Fig. 4-8) are mostly absent from the FGHAZ. Instead, the lath-like structure has been almost entirely replaced with equiaxed ferritic subgrains, which are denoted by yellow arrows. It is also apparent from Fig. 4-9(C) that the lower visibility of PAGBs is due to the fact that grain refinement has occurred since the carbides which typically decorate the PAGBs have been significantly (although not fully) dissolved and thus there is still a limitation on grain growth after the on-heating transformation to austenite (unlike in the CGHAZ). The SEM micrograph in Fig. 4-9(D) shows that the equiaxed ferritic subgrain interiors are mainly lacking the fine precipitates that were observed in the CGHAZ; this is due to incomplete carbide dissolution on heating, such that there is a reduced extent of carbon in solution to be available for re-precipitation upon cooling. Several individual subgrains and subgrain boundaries are shown in

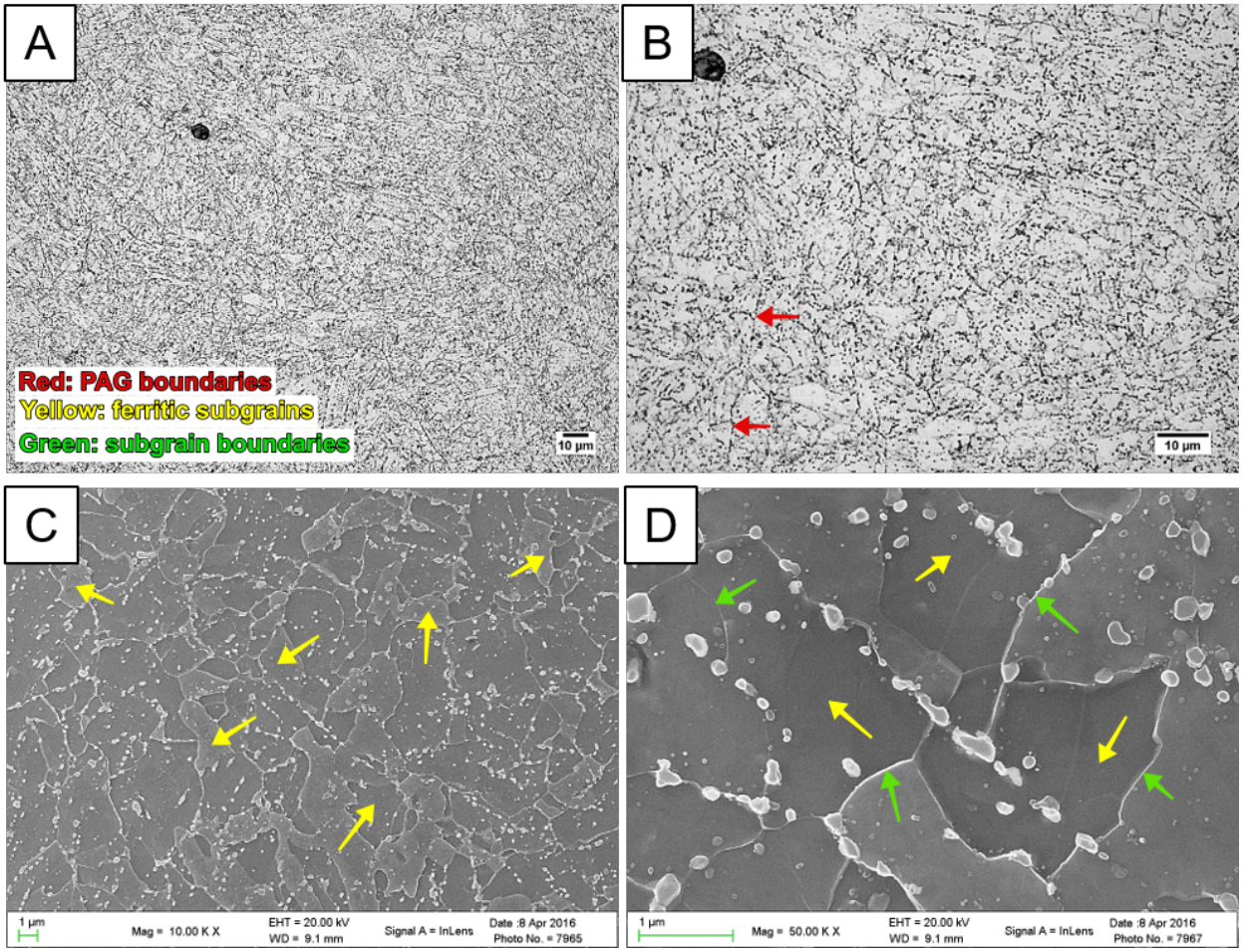


Figure 4-9. Microstructure of the FT FGHAZ from the FT-H47 weldment in the PWHT condition, 746°C/1 h, as revealed with (A,B) OLM and (C,D) SEM. Black particle in upper left corner of (B) is an inclusion. In (C,D), note the presence of an essentially 100% equiaxed ferritic subgrain structure which formed as a result of the welding thermal cycle followed by PWHT, as compared to the lath-like structure apparent in Fig. 4-7. The micrographs in (C) and (D) clearly show ferritic subgrains (yellow) and subgrain boundaries (green); the ferritic subgrain boundaries have noticeably fewer precipitates compared to the boundaries in Fig. 4-7. Etchant: Fry's reagent (A, B) and 10% Nital (C,D).

Fig. 4-9(D).

Lastly, Fig. 4-10 shows the microstructure revealed by OLM and SEM within the FT IHCAZ region of the fabricated weldment, subsequent to PWHT. Compared to the previous regions, the FT ICHAZ bears some similarity with the FGHAZ since the lath-like structure of the BM has been disrupted by the thermal cycle. However, since only partial on-heating transformation to austenite occurs in the ICHAZ, the lath-like substructure is not completely removed and the resulting ferritic subgrains are less randomly oriented although still equiaxed. Some ferritic subgrains (slightly equiaxed) are denoted (yellow arrows) in the SEM micrograph in Fig. 4-10(C). Furthermore, due to the lower peak temperature, as described earlier in the literature review, a lesser degree of carbide dissolution occurs (further reduced as compared to the CHGAZ and FGHAZ) and thus there are regions which still exhibit aligned carbides corresponding to the location of a former PAGB. The outlines of some former PAGBs are shown by red dashed lines and red arrows in Fig. 4-10(C). The SEM micrograph in Fig. 4-10(D) shows that the very fine precipitation in the ferritic subgrain interior is mostly absent, e.g. the ferritic subgrains denoted by yellow arrows. One shortcoming of the SE-SEM characterization is that the mixed nature of the microstructure in the ICHAZ is not readily discernible; in Fig. 4-10(C) and (D), it is difficult to identify subgrains which transformed to austenite during heating versus grains which did not transform but were simply tempered. The importance of this distinction lies in the fact that an untransformed and tempered grain will experience microstructure recovery and thus exhibit a reduced dislocation density.

The corresponding microstructures for the H47 side of the weld are shown beginning with Fig. 4-11. Fig. 4-11 shows the H47 base metal in the PWHT condition as revealed by OLM and SEM examination; from these micrographs, the H47 base metal has a generally similar appearance to the FT base metal (cf. Fig. 4-7(C) with Fig. 4-11(C)). In Fig. 4-11(B), some PAGBs are visible as noted by red arrows in the OLM micrograph;

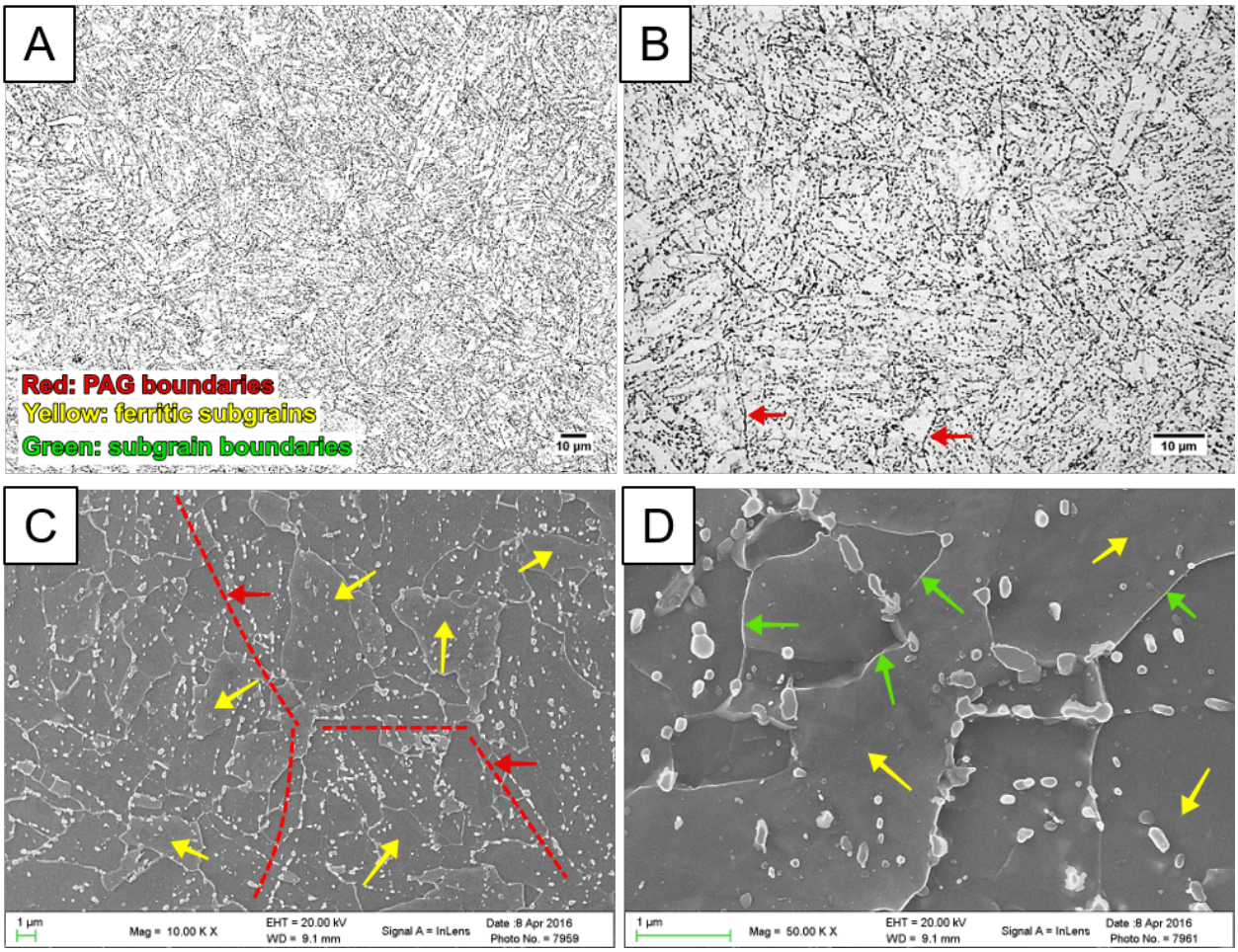


Figure 4-10. Microstructure of the FT ICHAZ from the FT-H47 weldment in the PWHT condition, 746°C/1 h, as revealed with (A,B) OLM and (C,D) SEM. In (C,D), note the presence of equiaxed ferritic subgrains (yellow arrows) formed after the welding thermal cycle followed by PWHT. The ferritic subgrain boundaries (green arrows) are less populated with precipitates compared to the FT BM. Also in (C,D), the presence of undissolved, aligned carbides along former PAGBs, as shown by the dashed red lines to emphasize a PAGB outline, indicates a further decrease in the extent of carbide dissolution as compared to the original FT base metal in Fig. 4-7. Etchant: Fry's reagent (A, B) and 10% Nital (C,D).

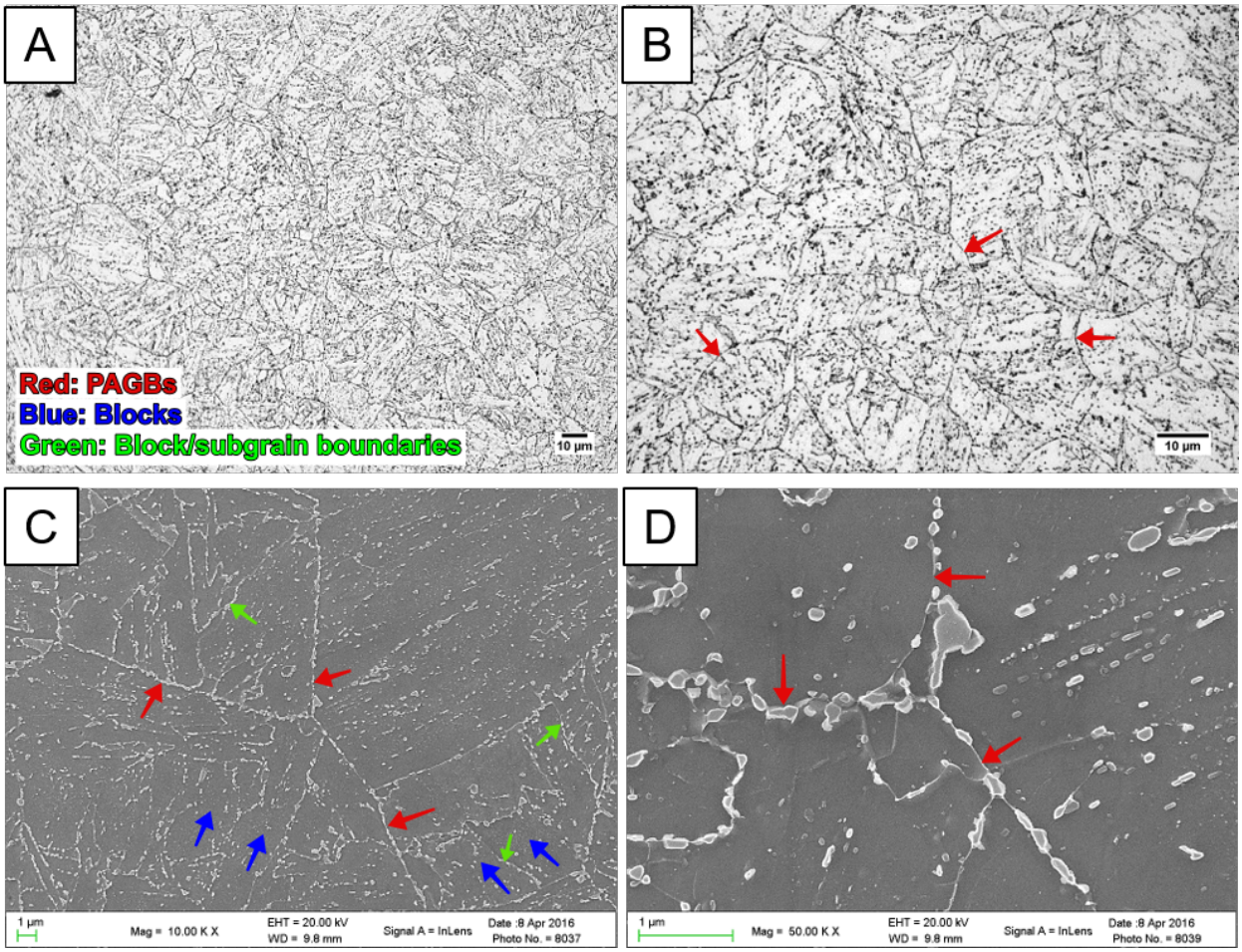


Figure 4-11. Microstructure of the H47 base metal in the PWHT condition, 746°C/1 h, as revealed with (A,B) OLM and (C,D) SEM. Similar to Fig. 4-7, a lath-like substructure is clearly evident in (C,D) with carbides along the PAGBs. The PAGBs are noted by red arrows, block/subgrain boundaries by green arrows, and the parallel orientation of the block structure with each PAG is shown by blue arrows in (C). In (D), smaller carbides are visible within the individual subgrains; the red arrows show a junction of multiple PAGBs. Etchant: Fry's reagent (A, B) and 10% Nital (C,D).

PAGBs are more clearly seen in Fig. 4-11(C), where the PAGBs (red arrows) are decorated with aligned carbides which are most likely M23C6. Block and/or subgrain boundaries are also shown in Fig. 4-11(C) and (D) along with parallel features which most likely illustrate the block structure within a PAG. Fig. 4-11(D) shows that there are some fine precipitates (<<1 μm) within the interiors of the ferritic subgrains. Note that in the BM, the ferritic subgrains (no longer martensitic laths since tempering has occurred) still retain a lath-like elongated morphology; the subgrains have not become equiaxed during PWHT.

The microstructure of the H47 CGHAZ after PWHT is depicted in Fig. 4-12. The OLM micrograph in Fig. 4-12(B) shows that the PAGBs appear prominently and are clearly visible (red arrows). The lath-like tempered martensite ferritic structure (TMFS) is also visible in this region of the HAZ due to the complete transformation to austenite on heating and subsequent re-formation of martensite upon cooling. In the SEM micrograph in Fig. 4-12(C), the PAGBs are clearly outlined with carbide particles, most probably $M_{23}C_6$; these boundaries (red arrows) mainly correspond to high angle boundaries within the microstructure. The aligned block substructure is also visible within the interior of some of the PAGs. In the higher magnification SEM micrograph of Fig. 4-12(D), it is apparent that carbides are nearly continuous along the PAGBs and that finer carbides are present along the block/subgrain boundaries and also within the ferritic subgrain interior (particles denoted by a red circle). Comparing this to the FT CGHAZ microstructure (Fig. 4-8), both CGHAZ microstructures are similar in terms of the characteristics revealed by OLM and SE-SEM.

The H47 FGHAZ microstructure in the PWHT condition is shown in Fig. 4-13 by OLM and SE-SEM micrographs. After the FGHAZ thermal cycle and PWHT, the PAGBs are mostly indistinct in the OLM micrographs especially at 500X in Fig. 4-9(A). A few remnant PAGBs are visible in Fig. 4-9, but the PAGBs are mostly discontinuous and interrupted (broken up) due to the grain refinement that has occurred in this region.

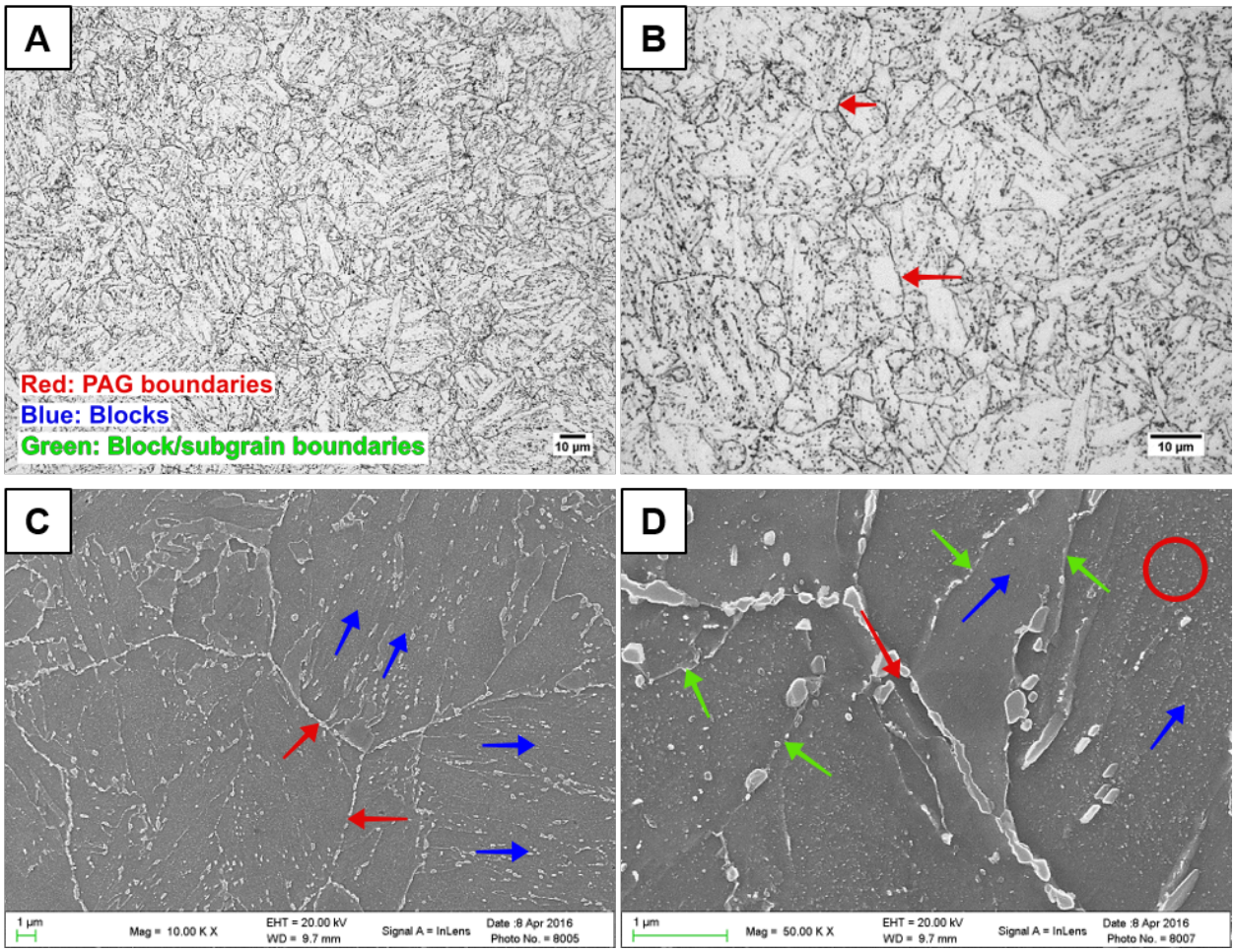


Figure 4-12. Microstructure of the H47 CGHAZ from the FT-H47 weldment in the PWHT condition, 746°C/1 h, as revealed with (A,B) OLM and (C,D) SEM. A lath-like substructure is evident in (C,D) since this region was completely transformed to austenite during the welding thermal cycle and subsequently transformed to new martensite upon cooling. Compared to Fig. 4-11, a greater extent of fine particles <<1 μm in size is evident in the ferritic subgrain interior in D, due to carbide dissolution and re-precipitation that occurred as a result of the CGHAZ thermal cycle and PWHT. Etchant: Fry's reagent (A, B) and 10% Nital (C,D).

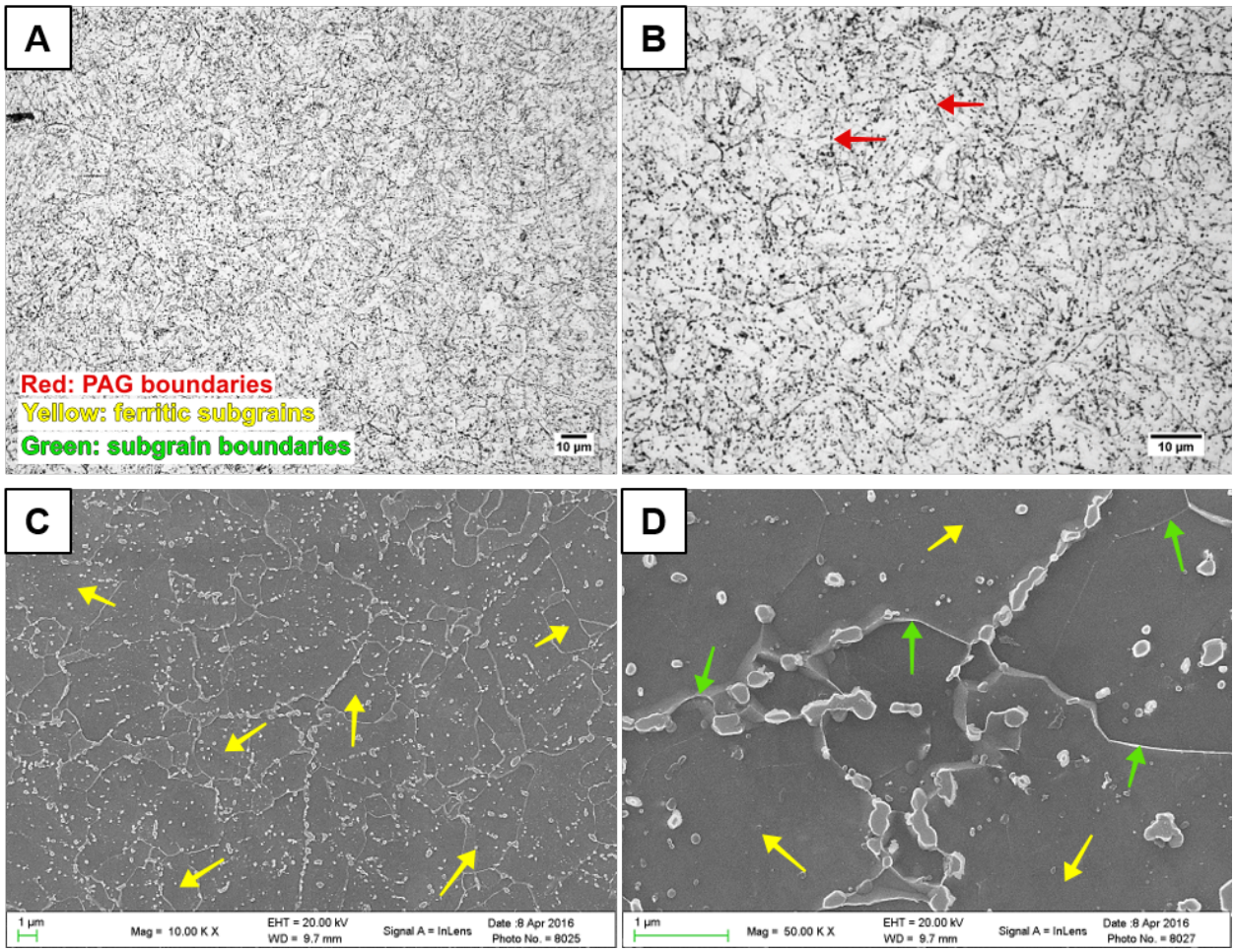


Figure 4-13. Microstructure of the H47 FGHAZ from the FT-H47 weldment in the PWHT condition (746°C/1 h) as revealed with (A,B) OLM and (C,D) SEM. Compared to Fig. 4-11 or Fig. 4-12, the H47 FGHAZ shows formation of equiaxed ferritic subgrains as a result of the FGHAZ thermal cycle, in which the temperature was high enough for complete re-austenitization to occur. Although significant carbide dissolution occurred, as indicated by the near-absence of carbides along former PAGBs, the peak temperature and time-at-temperature were not sufficient to produce complete carbide dissolution and re-precipitation (i.e. as occurred in the CGHAZ). Compared to Fig. 4-12, there is also a greatly reduced extent of very fine particles in the ferritic subgrain interior regions. Etchant: Fry's reagent (A, B) and 10% Nital (C,D).

The SEM micrograph in Fig. 4-9(C) shows that the TMFS of the original base metal has been replaced by an equiaxed ferritic subgrain structure, in which the ferritic subgrains (representative indication by yellow arrows) do not exhibit the parallel, aligned orientation of the TMFS, but are more random in shape and orientation. Some partial remnants of former PAGBs are visible in Fig. 4-9(C), as shown by segments of aligned carbides; the aligned carbides indicate where precipitation occurred along a PAGB in the original base metal microstructure. In Fig. 4-9(D), some coarsened carbides from a remnant PAGB are visible and also portions of ferritic subgrain boundaries (green arrows) which are devoid of any precipitates; additionally, the ferritic subgrain interiors show a minimal amount of fine carbides as compared to the H47 CGHAZ.

Fig. 4-14 shows OLM and secondary electron SEM micrographs for the H47 ICHAZ subsequent to PWHT. In the OLM micrographs, the PAGBs (representative PAGBs shown by red arrows) are less prominent than in the H47 base metal or CGHAZ, but are more clearly visible than in the H47 FGHAZ. In Fig. 4-14(C), the SEM micrograph shows that remnants of several PAGBs are clearly visible in the form of two PAGB junctions and a horizontal PAGB segment. These remnant PAGBs are more clearly visible in the ICHAZ because the lower peak temperature in the ICHAZ corresponds to a lesser extent of carbide dissolution during heating than in the FGHAZ, and thus carbides along the PAGBs are less fully dissolved. In Fig. 4-14(D), the formation of a more equiaxed, ferritic subgrain structure can be observed along with a reduced extent of fine precipitates within the ferritic subgrain interior. Already after PWHT, many of the ferritic subgrain boundaries (green arrows) are not stabilized with carbides, which indicates a greater potential for recovery and coarsening during subsequent creep exposure.

Since the FGHAZ and ICHAZ are the primary susceptible regions for creep damage, these regions from the FT and H47 HAZs are compared directly in Fig. 4-15 and Fig. 4-16 for the FGHAZ and ICHAZ, respectively. The microstructures of the FT and

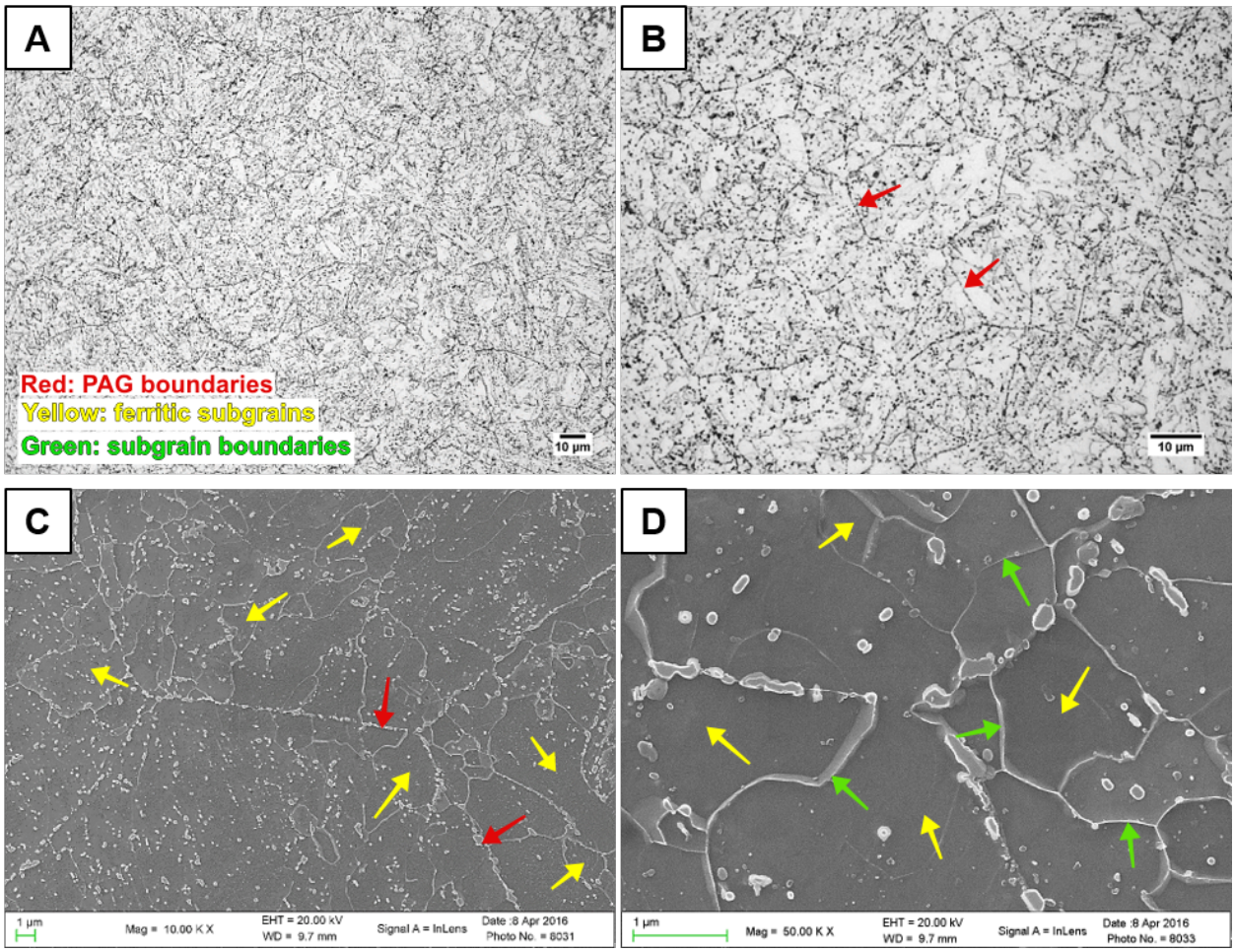


Figure 4-14. Microstructure of the H47 ICHAZ from the FT-H47 weldment in the PWHT condition (746°C/1 h) as revealed with (A,B) OLM and (C,D) SEM. In (C,D), the presence of undissolved, aligned carbides along former PAGBs, as shown by the red arrows in (C), indicates a further decrease in the extent of carbide dissolution as compared to the original H47 base metal in Fig. 4-11. In (D), many of the ferritic subgrain boundaries (green arrows) are not populated with carbides, indicating a greater susceptibility to coarsening. Etchant: Fry's reagent (A, B) and 10% Nital (C,D).

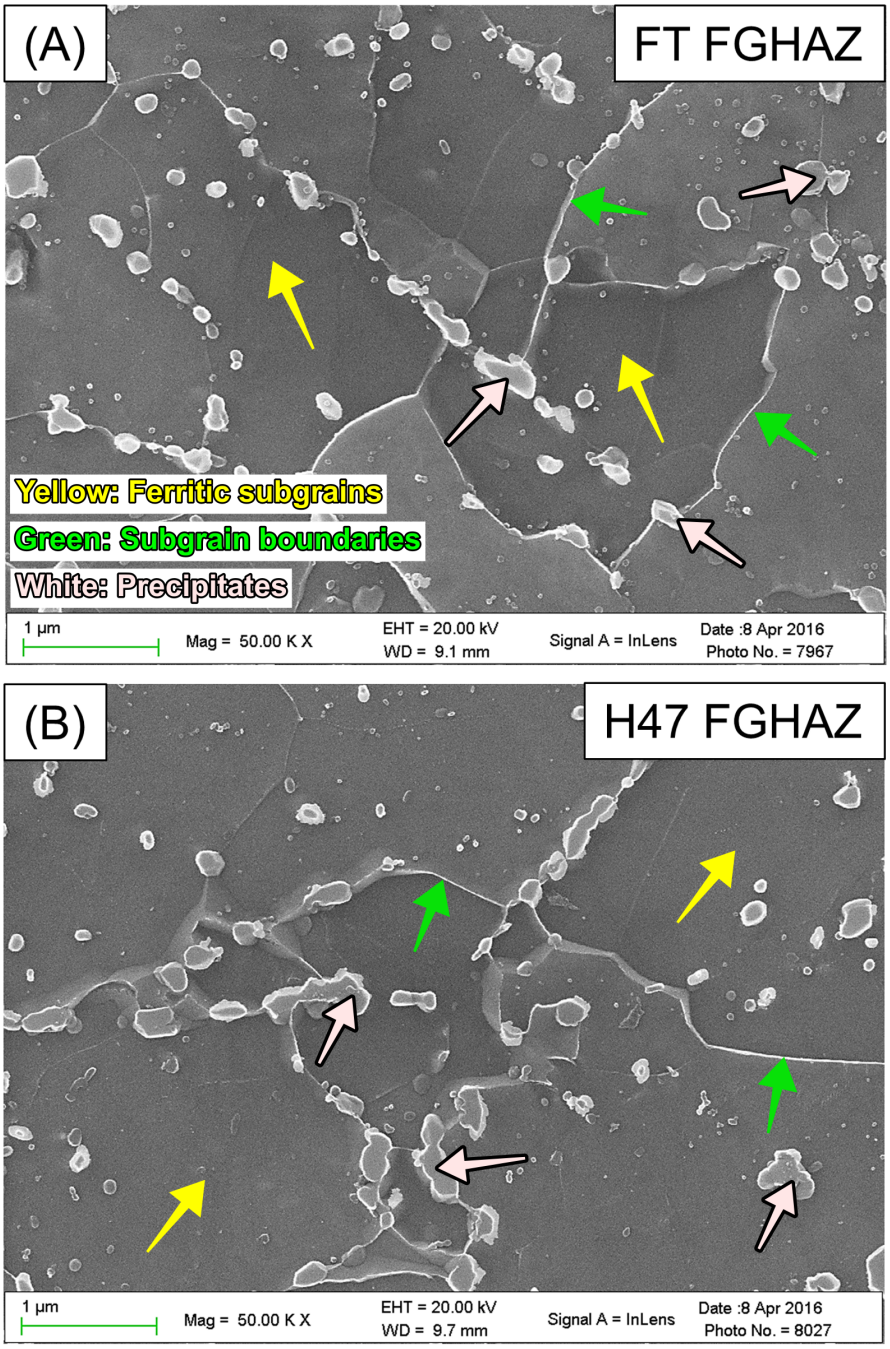


Figure 4-15. Comparison of SE-SEM micrographs for the (a) FT FGHAZ region and (b) H47 FGHAZ region. The micrographs show a similar microstructural appearance in both regions, namely an equiaxed ferritic subgrain structure with some larger carbides remaining on the boundaries since the carbides were not dissolved during the thermal cycle. The majority of the fine carbides within the ferritic subgrain matrix regions (yellow arrows) were dissolved, and some of the larger carbides (white arrows) are no longer located on the ferritic subgrain boundaries, resulting in a reduced extent of boundary pinning. Etchant: 10% Nital.

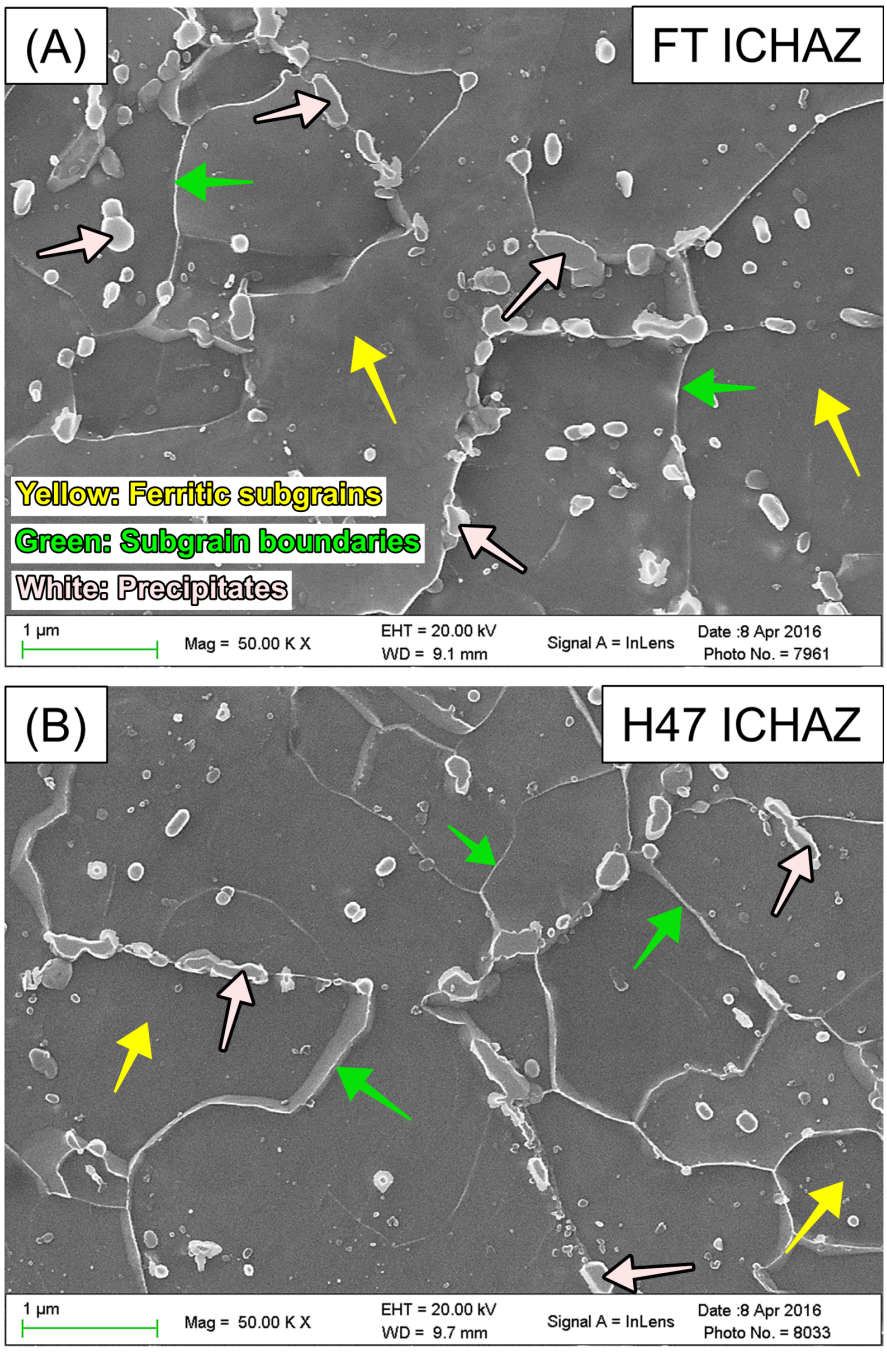


Figure 4-16. Comparison of SE-SEM micrographs for the (a) FT ICHAZ region and (b) H47 ICHAZ region. The micrographs reveal a similar microstructural appearance in both ICHAZ regions, namely an equiaxed ferritic subgrain structure with some larger, aligned carbides remaining along the outlines of former PAGBs. Similarly to the FGHAZ, the majority of the fine carbides within the ferritic subgrain matrix regions (yellow arrows) were dissolved. Etchant: 10% Nital.

H47 FGHAZ in Fig. 4-15 and of the ICHAZ in Fig. 4-16 appear qualitatively similar by SE-SEM examination. In both FGHAZ regions, the initial TMFS has been replaced by an equiaxed ferritic subgrain structure; it is clear from the enlarged 50kx micrographs that the ferritic subgrain interior regions are mostly depleted of fine precipitates (such as are present in the CGHAZ, see Fig. 4-12) and that the subgrain boundaries are less populated with precipitates than either the CGHAZ or base metal conditions. It is also apparent that many of the larger precipitates (white arrows) are no longer located on subgrain boundaries, but are within the subgrain interior regions, where the precipitates are not effective at pinning the boundaries against coarsening. Fig. 4-16 shows a similar microstructural appearance in the FT and H47 ICHAZ regions from the enlarged 50kx micrographs. Both ICHAZ microstructures consist of equiaxed ferritic subgrains with few precipitates in the subgrain interiors; there is some evidence of larger aligned carbides and also of larger isolated carbides within the subgrain interiors. Additionally, there is a significant fraction of the subgrain boundary length which is not populated with precipitates.

Comparison of the mechanical properties of the FT-H47 dissimilar Grade 91 weldment was evaluated by microhardness traverses in the PWHT condition, which are provided in Fig. 4-17 (Hoskins et al., 2017). The minimum hardness value in both traverses is located at or just beyond the optically-discernible transition from the HAZ to base metal. The minimum and maximum HAZ hardness values for the FT and H47 traverses are 209/277 HV500gf and 204/286 HV500gf, respectively. The minimum HAZ hardness has sometimes been used as an indicator of propensity for Type IV creep damage; however, the values for the FT and H47 hardness traverses indicate that the minimum hardness in both HAZs is similar, so any differences in creep behavior between the FT HAZ and H47 HAZ are not attributable to a significant difference in the minimum HAZ hardness. Based on these traverses, the location of minimum hardness in the HAZ agrees with the observations of other investigators such as Siefert et al. (Siefert et al.,

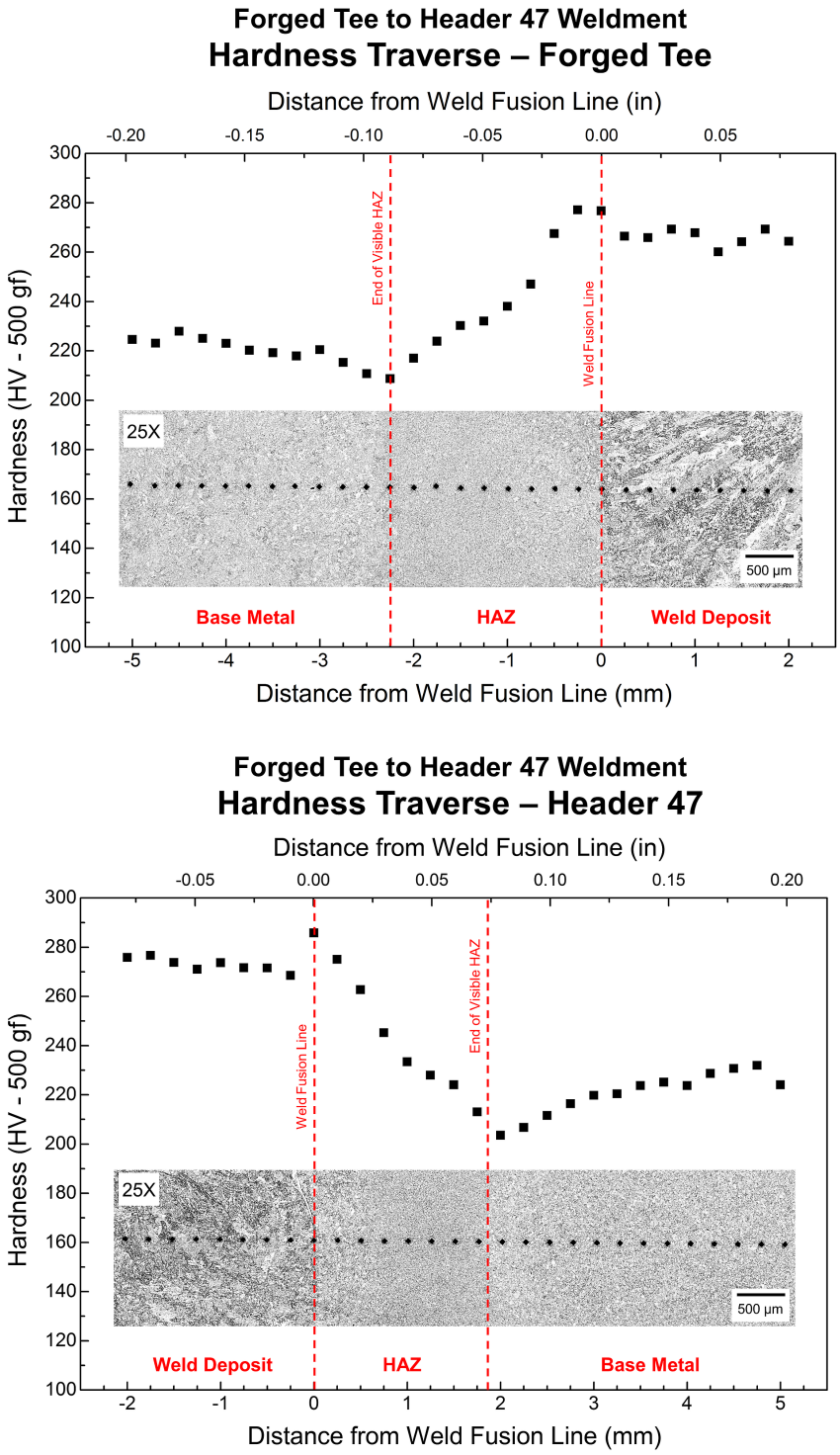


Figure 4-17. Microhardness traverses for the FT-H47 weldment in the PWHT condition: (A) FT side of the weld (B) H47 side of the weld. The hardness traverses are similar; the minimum hardness in the HAZ is slightly lower on the H47 side than on the FT side. Reproduced from (Hoskins et al., 2017).

2019) in which the minimum hardness location after PWHT is located beyond the optically-discernible HAZ, which Siefert et al. characterized as the overtempered zone (where no transformation to austenite occurred during the welding thermal cycle).

4.2.2 Creep Results and Failure Location in the FT-H47 Weldment

After fabrication and PWHT, the FT-H47 weldment was subject to cross-weld creep rupture testing at conditions of 627°C (1160°F) and 82.7 MPa (12 ksi). Plots of creep strain and creep strain rate and the corresponding macrograph of the post-test "FT-H47-1" creep specimen from the FT-H47 weldment are shown in Fig. 4-18 and Fig. 4-19, respectively. From the creep curve and the photograph in Fig. 4-19, it is apparent that the "FT-H47-1" cross-weld specimen ruptured on the FT side of the weld with a very low overall level of ductility (<1% elongation), although in the photograph some localized necking can be seen at the rupture surfaces. The creep strain rate plot in Fig. 4-18 shows that a period of "steady-state" creep was evident between ~400 h to ~2000 h, shortly prior to final tertiary acceleration and rupture; it should be noted that this data corresponds to the overall average creep strain rate across the entire gauge length. A macrograph of the FT-H47-1 cross-weld specimen after sectioning and metallographic preparation is shown in Fig. 4-20. From this figure, it is evident that the FT-H47-1 specimen failed in the Type IV mode since the macroscopically-apparent damage location is in the outer region of the HAZ toward the base metal. Comparing the two base metals, only the HAZ on the FT side exhibits macro-cracking leading to rupture; therefore, on the basis of the observed damage location, the FT base metal may be qualitatively ranked as exhibiting a higher susceptibility to Type IV creep damage than the H47 base metal.

4.2.3 Characterization of Creep Damage in the FT-H47 Weldment

The FT-H47-1 creep specimen was examined with OLM and SEM to investigate the nature of the creep damage that occurred in the weldment. Overall, creep damage in the form of creep cavitation and macro-cracking was observed in the FGHAZ and ICHAZ

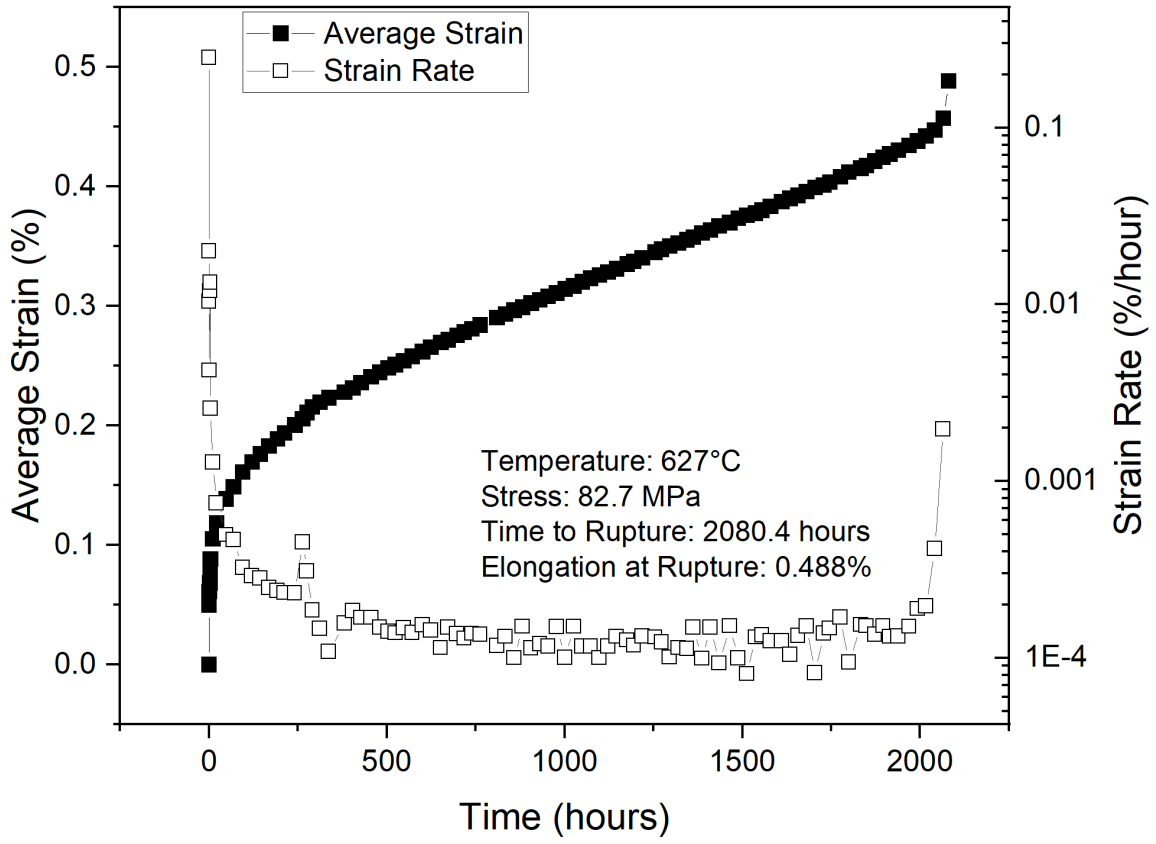


Figure 4-18. Measured creep curve and corresponding calculated strain rate curve obtained for the "FT-H47-1" cross-weld creep specimen which was extracted from the FT-H47 weldment and tested in the PWHT condition (746°C/1 h). The creep test parameters were 627°C (1160°F) and 82.7 MPa (12 ksi).



Figure 4-19. Photograph of the "FT-H47-1" cross-weld creep specimen extracted from the FT-H47 weldment after PWHT at 746°C/1 h and tested at 627°C/82.7 MPa. The specimen was tested to rupture, with the rupture occurring on the FT side of the weld; although the overall elongation was low at ~0.5%, some slight local deformation at the rupture surfaces can be seen (rounding of the edges at the rupture location).

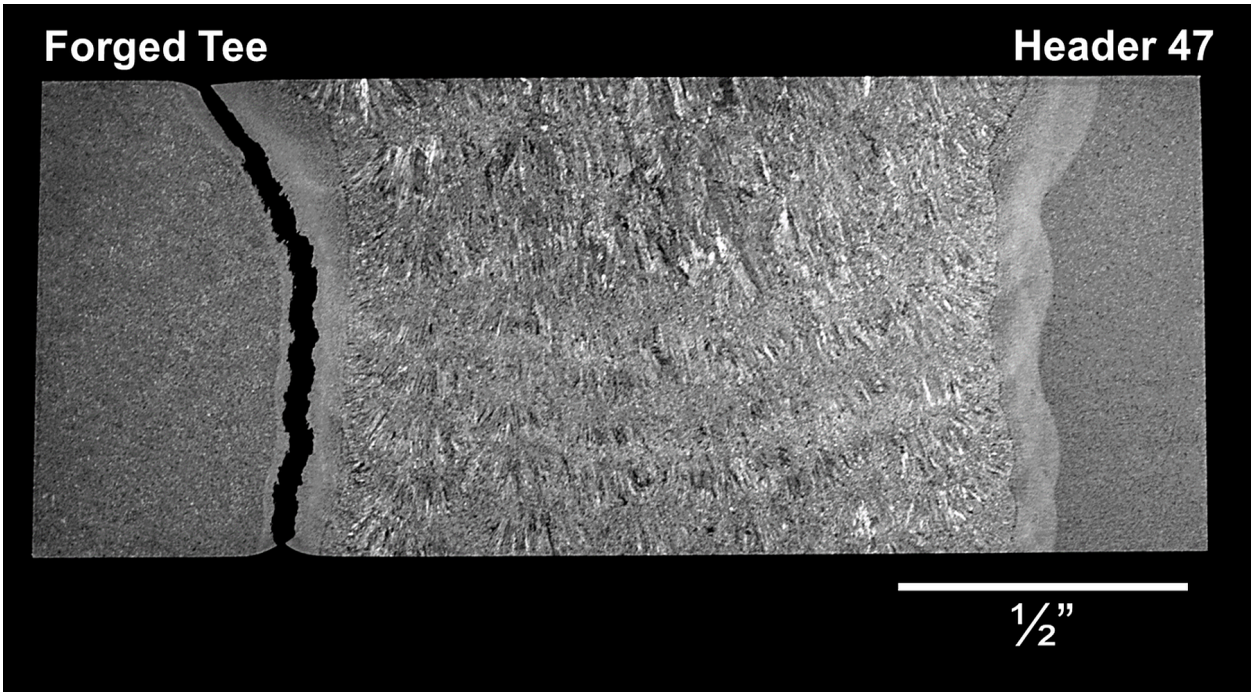


Figure 4-20. Macrograph of a metallographic section from the FT-H47-1 cross-weld creep specimen, PWHTed at 746°C/1 h and creep tested at 627°C/82.7 MPa and ruptured after 2080.4 h. Rupture occurred in the outer portion of the HAZ (Type IV failure) on the FT side of the weld. No macro-cracks were evident in the H47 HAZ. The loading axis during creep testing corresponds to the horizontal direction in the macrograph. Etchant: Fry's reagent.

regions of the weldment; creep cavitation was not observed in the base metal, CGHAZ, or weld deposit regions. Fig. 4-21 shows the FT-H47-1 creep specimen macrograph with marked locations for higher magnification examination in the FT ICHAZ. The macrograph shows that creep rupture occurred in the outer portion of the FT HAZ toward the base metal, near the transition from the HAZ into the base metal; this places the rupture location in the Type IV region. Some evidence of localized plastic deformation in the HAZ is also evident in the vicinity of rupture as shown by the reduction of area (see small white arrows in the macrograph. In contrast, the H47 side of the weld shows no discernible plastic deformation and no evidence of macro-cracking.

The micrographs obtained from locations ICHAZ-1 and ICHAZ-2 in the middle of the creep specimen (corresponding to the middle of the weld, in the through-thickness direction, i.e. approximately midway between the weld face and the weld root) are shown beginning in Fig. 4-22. Fig. 4-22 shows the extent of creep damage at the transition between the outer boundary of the FT HAZ and the base metal; the appearance reveals a distinct delineation between creep-damaged and undamaged areas immediately adjacent to each other at this location. This region, which is slightly away from the rupture location, corresponds to the lower temperature range of the ICHAZ where the expected peak temperature is slightly above Ac1. The boxed region in the micrograph is shown at higher magnification in Fig. 4-23.

A representative example of the cavity appearance at the FT ICHAZ location is shown in Fig. 4-23. Fig. 4-23(A) shows that cavitation is fairly concentrated but isolated at this location in the ICHAZ. A selected cavity is examined at higher magnification in Fig. 4-23(B) and is revealed to be slightly irregular in shape, not spherical or polyhedral. Fig. 4-23(B) shows that a particle (circled) is present at one corner of the cavity. Based on its similar contrast to surrounding particles in the SEM, the particle is most likely a coarsened carbide rather than a nonmetallic inclusion. Also in Fig. 4-22, the equiaxed

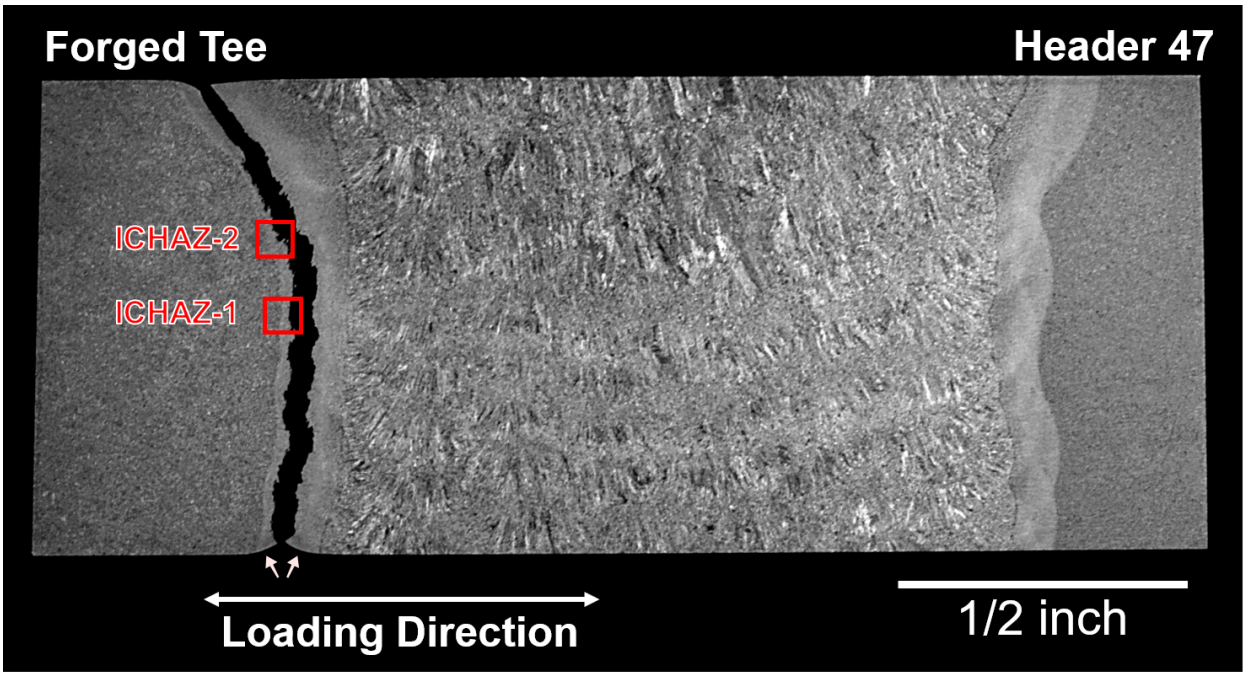


Figure 4-21. Cross-section macrograph of the FT-H47-1 creep specimen showing two locations in the FT ICHAZ which were examined at higher magnification to evaluate creep damage. The creep loading axis corresponds to the horizontal direction in the micrographs. Note the evidence of localized plastic deformation at the FT HAZ, as indicated on one side by the small white arrows. Etchant: Fry's reagent.

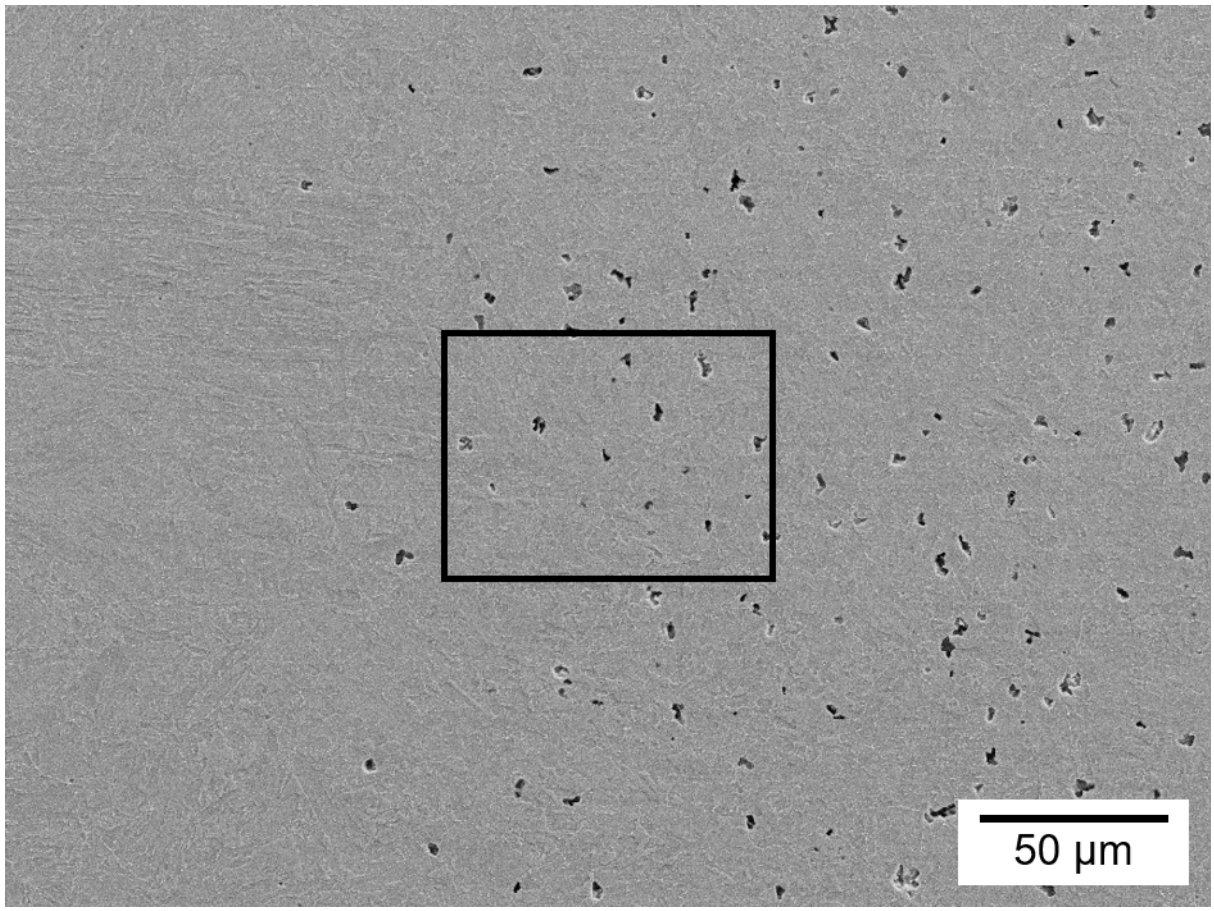


Figure 4-22. SE-SEM micrograph of location ICHAZ-1A in the FT ICHAZ of the FT-H47-1 creep specimen, slightly away from the rupture location. Note the distinct delineation between the adjacent, creep undamaged region in the base metal (left) compared to the ICHAZ (right). The creep loading axis corresponds to the horizontal direction in the micrograph. The boxed region is shown at higher magnification in Fig. 4-23. Etchant: 10% Nital.

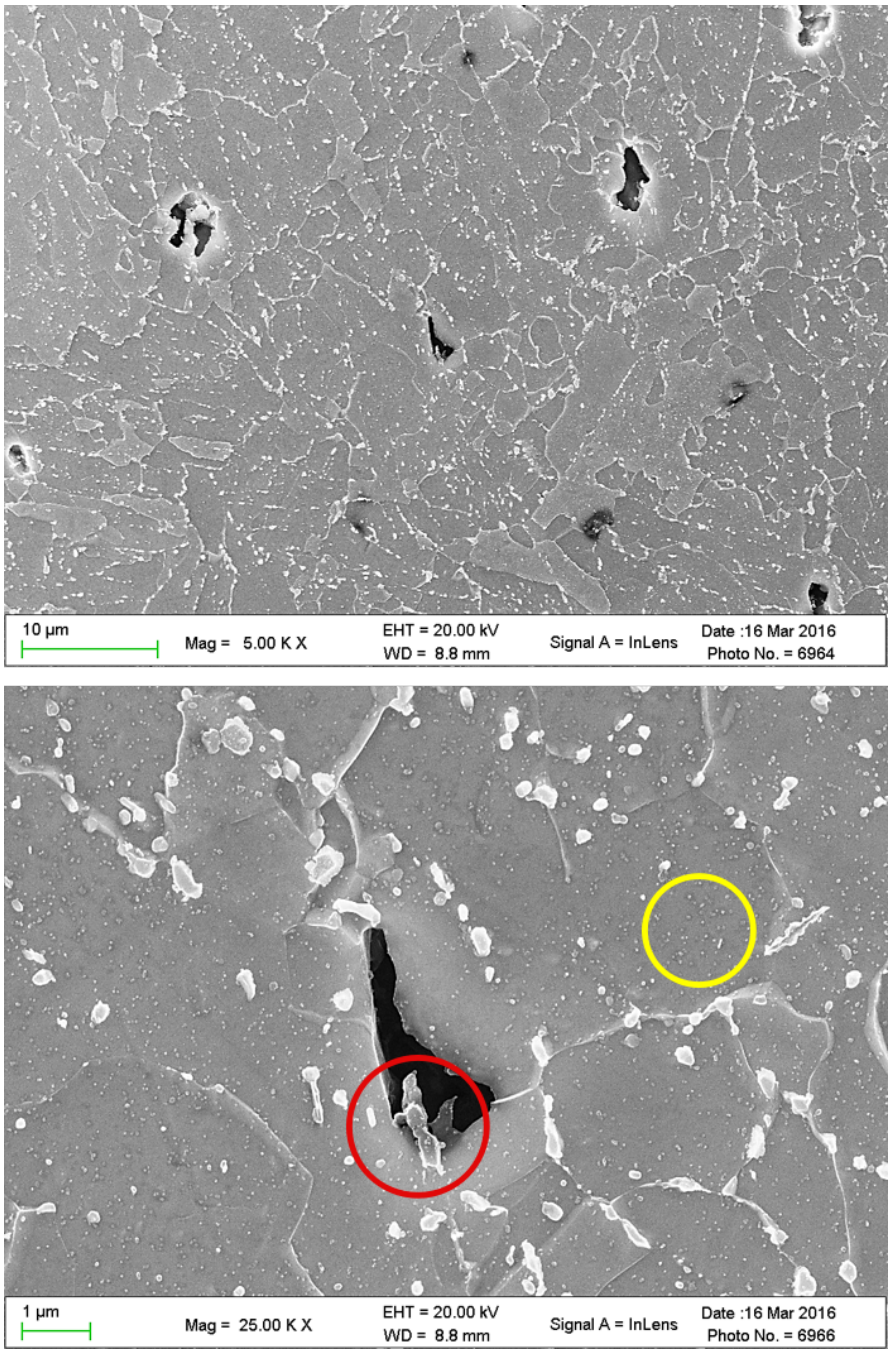


Figure 4-23. SE-SEM micrographs illustrating typical creep cavity morphology at the FT ICHAZ-1A location of the FT-H47-1 creep specimen, slightly away from the rupture location in the FT HAZ. The red circle highlights a particle which is clearly present at one end of the cavity; the yellow circle indicates a typical example of the slightly higher extent of fine precipitates after creep testing as compared to Fig. 4-10, suggesting that some precipitation occurred during creep. Etchant: 10% Nital.

ferritic subgrain structure is still evident at the conclusion of creep-testing; there are some portions of the ferritic subgrain boundaries which remain unpopulated with carbides. It is evident also that some fine precipitation occurred in the subgrain interior regions during creep (see the yellow circle).

Nearer to rupture at FT ICHAZ locations 1 and 2, the cavitation density increased and the cavity appearance remained irregular, as shown in Fig. 4-24 and Fig. 4-25. Fig. 4-24 shows that although the cavity density is increased adjacent to rupture, the cavities are still essentially completely isolated with only minimal coalescence or link-up. Additionally, cavitation is not entirely uniform over the field of view; there are some regions where cavitation is less extensive as shown by red arrows. The boxed region in the micrograph is shown at higher magnification in the micrographs in Fig. 4-25. Fig. 4-25 shows the typical cavity appearance at an ICHAZ location adjacent to rupture on the FT side of the weld; the cavities in Fig. 4-25 appear to result from separation of multiple subgrain boundaries. It is apparent that even adjacent to rupture, extensive alignment of cavities and formation of micro-cracks are not observed.

The characteristics of creep damage in the FT FGHAZ in the FT-H47-1 creep specimen were evaluated at two locations near the mid-thickness of the specimen. The two locations, FT FGHAZ-1 and FGHAZ-2, are denoted in Fig. 4-26. Cavitation in the FGHAZ appears similar to that in the ICHAZ, as shown in Fig. 4-27 through Fig. 4-29. Fig. 4-27 shows the cavity appearance at a location in the FGHAZ slightly away from the rupture location, across from the FT ICHAZ-1 location; away from rupture, the cavity density is decreased. Fig. 4-28 shows several cavities which are not associated with nonmetallic inclusions; the correlation between the cavity edges (i.e. matching edges) in Fig. 4-28(c) indicates that the cavity opened along a boundary intersection. Adjacent to the rupture location in the FGHAZ, the cavity density increased and there is some evidence of aligned cavitation, although the majority of cavities remain isolated even at rupture. The cavity characteristics in the FT FGHAZ are shown at higher

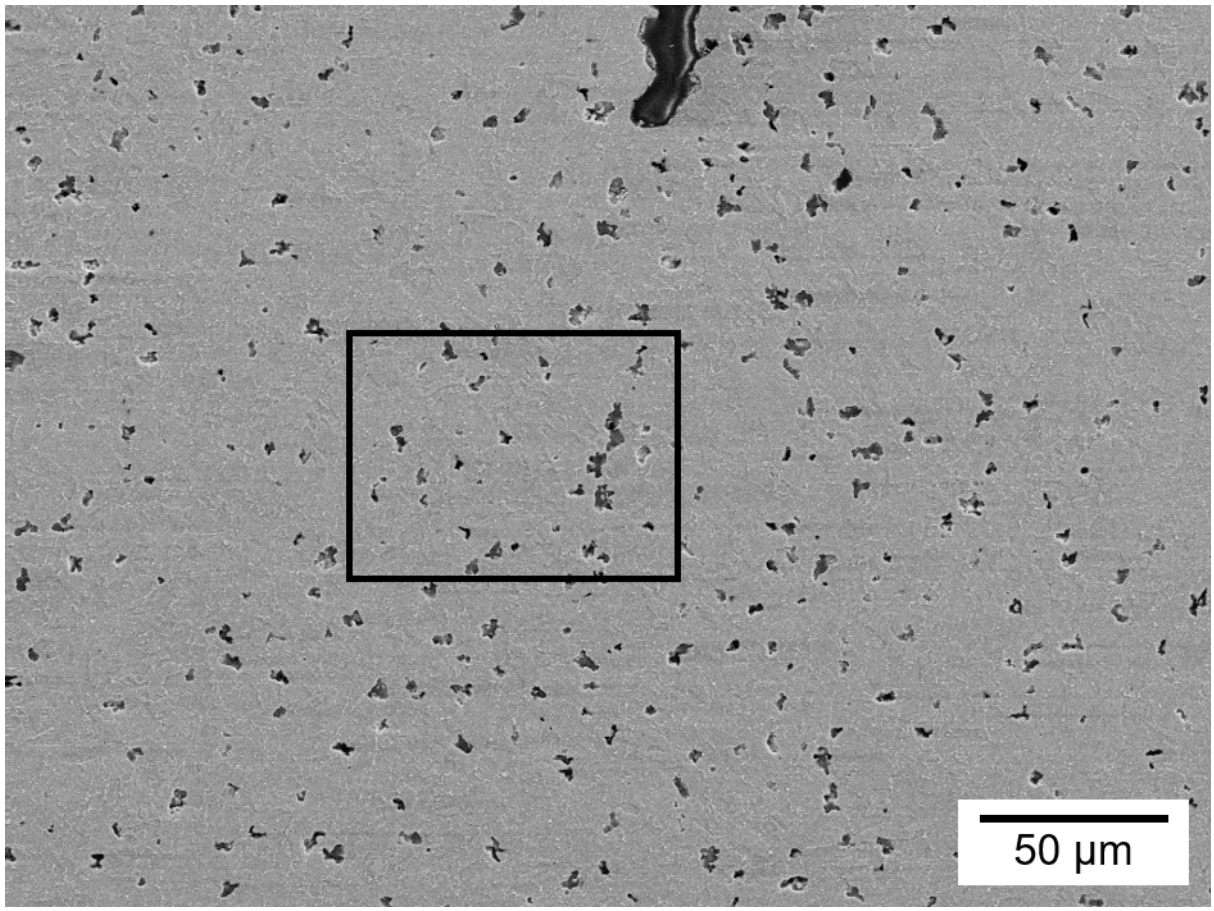


Figure 4-24. SE-SEM micrograph of location ICHAZ-1B in the Forged Tee ICHAZ of the FT-H47-1 creep specimen, slightly nearer to the rupture location. Compared to Fig. 4-22, the cavity density is increased. The boxed region in the micrograph is shown at higher magnification in the micrographs in Fig. 4-25. Etchant: 10% Nital.

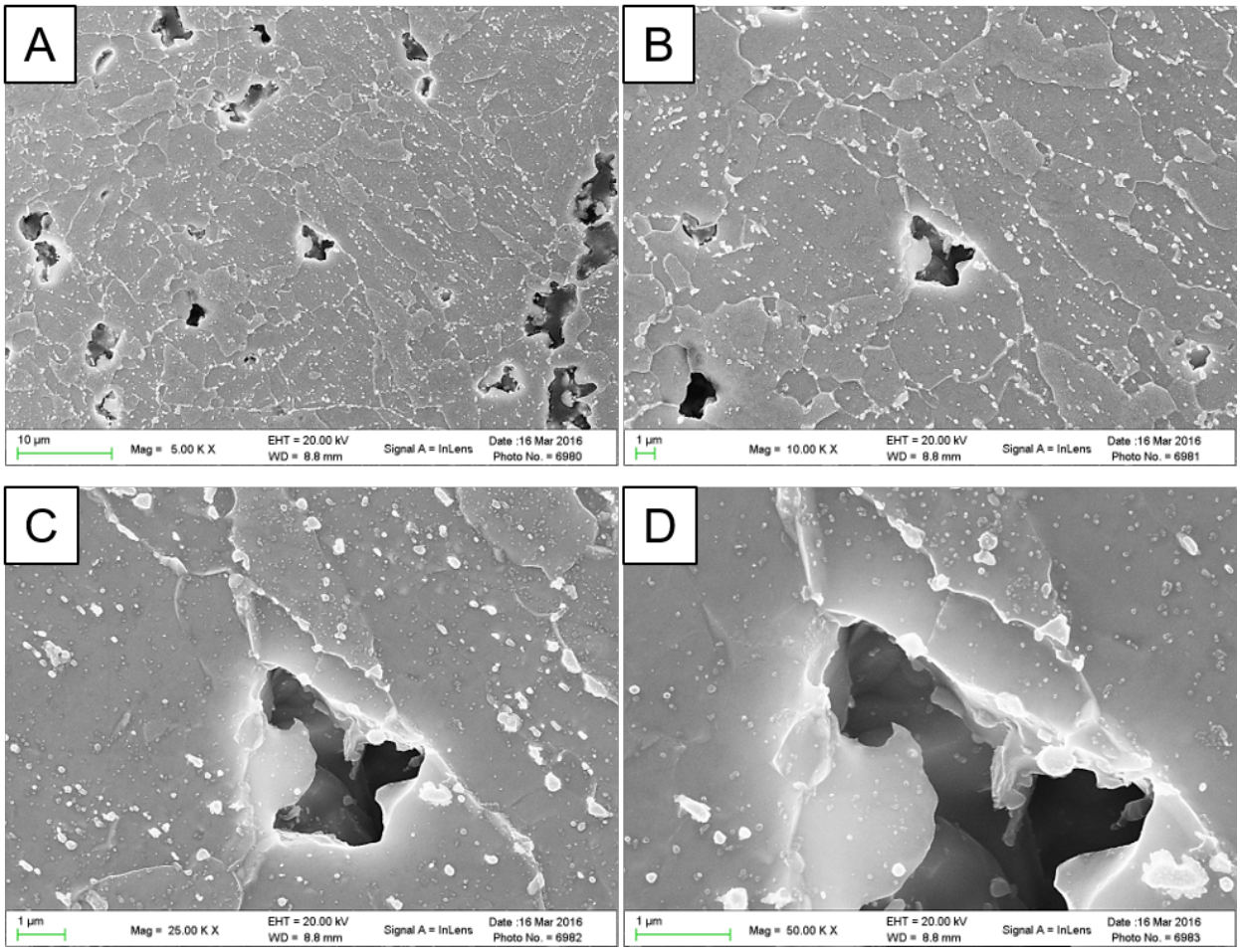


Figure 4-25. SE-SEM micrographs illustrating typical creep cavity morphology at the ICHAZ-2 location of the FT-H47-1 creep specimen. The selected creep cavity does not appear to be associated with a particle such as a nonmetallic inclusion. Etchant: 10% Nital.

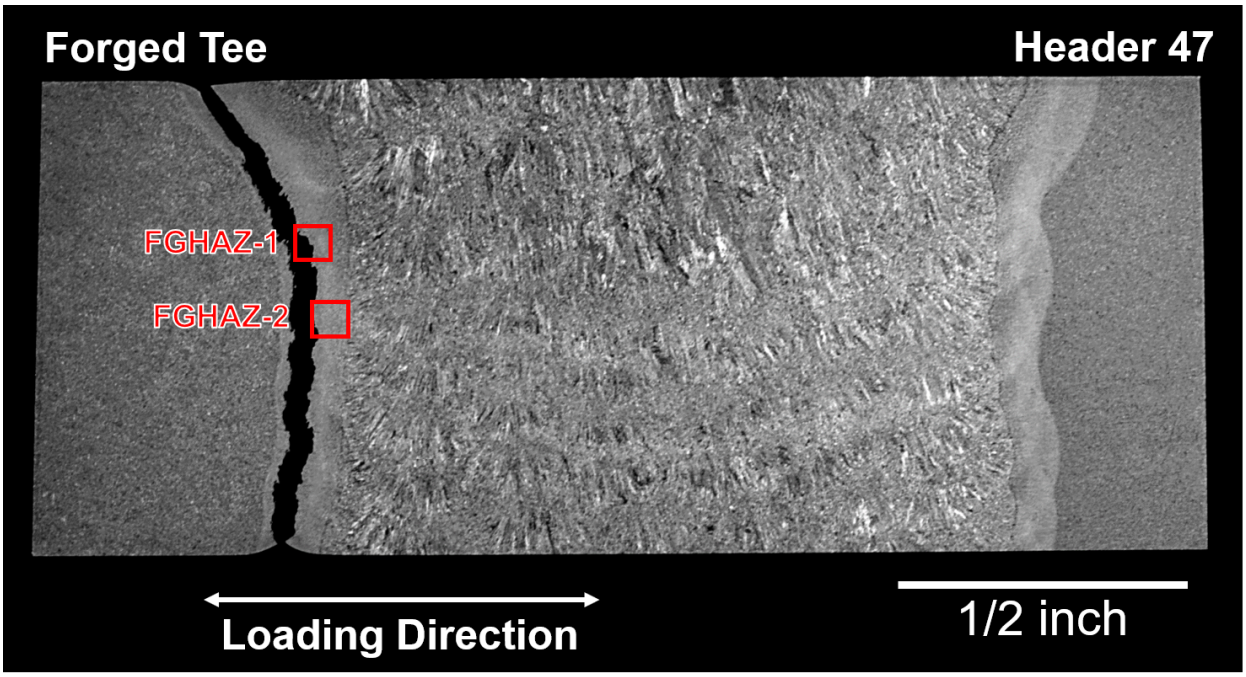


Figure 4-26. Cross-section macrograph of the FT-H47-1 creep specimen showing two locations in the FT FGHAZ which were examined at higher magnification to evaluate creep damage. The creep loading axis corresponds to the horizontal direction in the micrographs. Etchant: Fry's reagent.

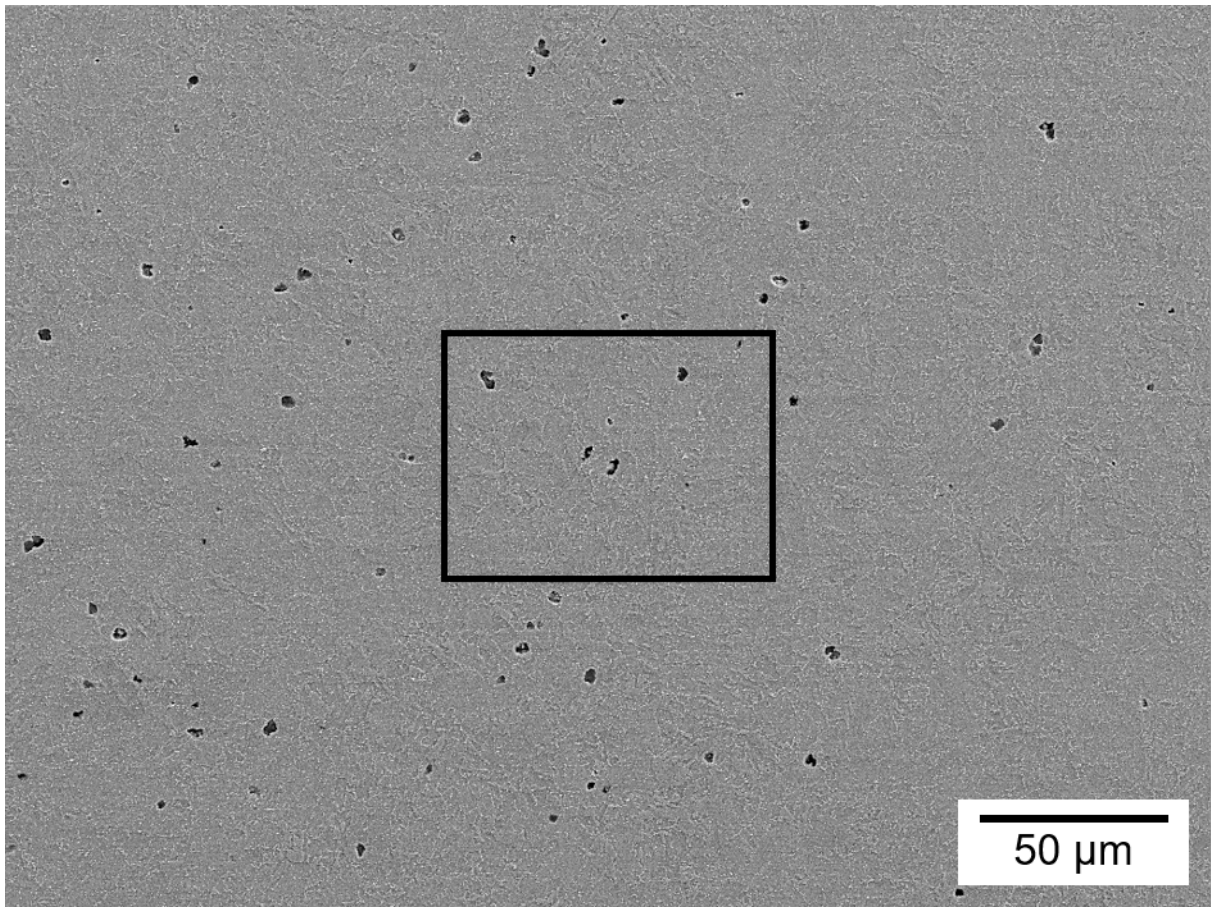


Figure 4-27. SE-SEM micrograph of location FGHAZ-1 in the FT FGHAZ of the FT-H47-1 creep specimen, slightly away from the rupture location. Similarly to the ICHAZ, the cavity density is decreased away from the rupture location. The creep loading axis corresponds to the horizontal direction in the micrograph. Etchant: 10% Nital.

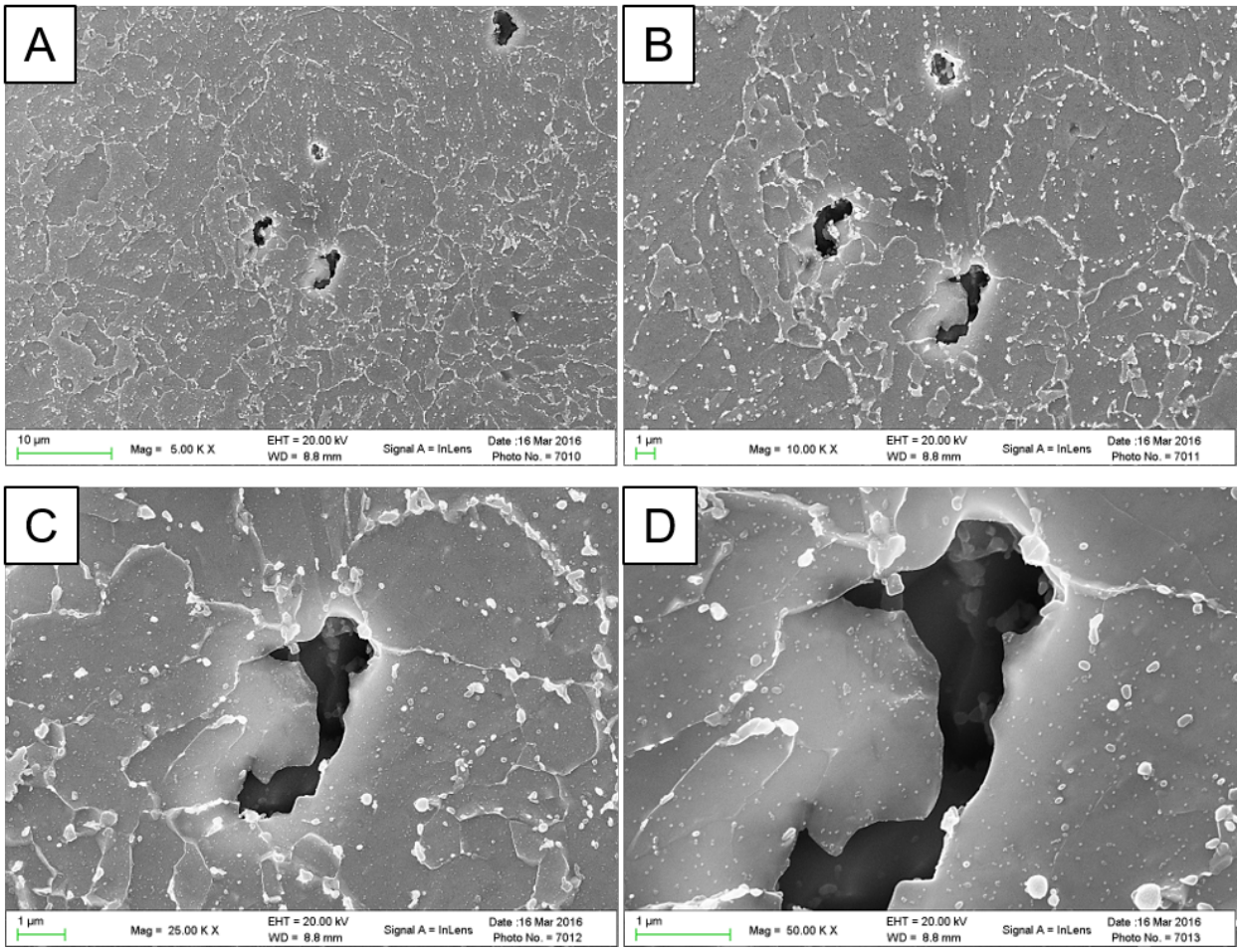


Figure 4-28. SE-SEM micrographs illustrating creep cavity morphology at the FGHAZ-1 location of the FT-H47-1 creep specimen. Etchant: 10% Nital.

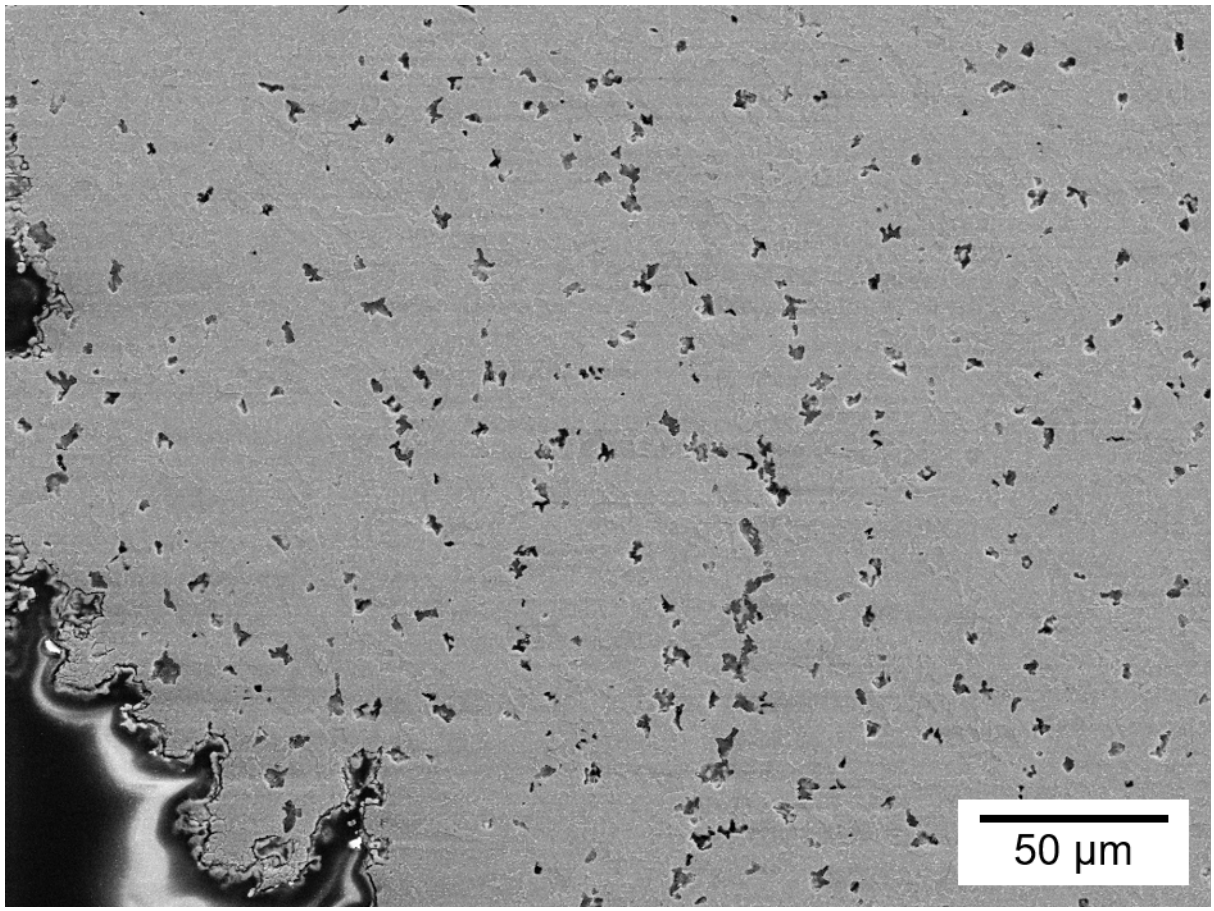


Figure 4-29. SE-SEM micrograph of location FGHAZ-2 in the FT FGHAZ of the FT-H47-1 creep specimen, adjacent to the rupture location (at left in image). The creep loading axis corresponds to the horizontal direction in the micrograph. Etchant: 10% Nital.

magnification in the micrographs in Fig. 4-30, and the cavity morphology is generally irregular and complex in shape.

The characteristics of creep cavitation were also examined in the H47 side of the weld in the FT-H47-1 creep specimen. As shown previously in the FT-H47-1 macrograph, the H47 side of the weld did not develop macroscopic creep damage in the HAZ during testing. Fig. 4-31 shows a macrograph identifying the selected location for examination within the HAZ on the H47 side of the specimen. Fig. 4-32 obtained from the upper half of the specimen thickness, in the through-weld direction, shows that the creep cavitation extent is significantly lower in the H47 ICHAZ as compared to the FT side of the weld (cf. Fig. 4-22 and Fig. 4-24 from the FT-ICHAZ). The general cavity appearance in the H47 ICHAZ is similar, however, to that in the FT ICHAZ, with the cavitation exhibiting an irregular morphology as revealed in Fig. 4-33. This figure shows a cavity located partly along a former PAGB (red outlines) as indicated by the presence of aligned carbides, and the cavity itself is located at a boundary junction; a small particle which is most likely a carbide is located within the middle of the cavity. SEM examination in the ICHAZ also revealed the presence of small cavities (<1 μm) such as shown in Fig. 4-34 and Fig. 4-35. Fig. 4-35 shows that the cavity is located on a short subgrain boundary segment within a former PAG (the aligned carbides of the former PAGB are visible in the micrograph) and the cavity is also associated with a small particle (an apparent carbide). The existence of this small cavity in the same field of view as a number of other larger cavities (~5 μm) as shown in Fig. 4-34 suggests that continuous cavity nucleation is occurring during creep and that cavities are present in different stages of growth at the time of rupture. The extent of creep damage was also evaluated in the FGHAZ region of the H47 side of the cross-weld creep specimen at the same location shown in Fig. 4-31. Fig. 4-36 shows the appearance of isolated creep cavitation in the H47 FGHAZ, where no macro-cracking is observed and the relative density of cavitation is significantly less than the corresponding FT FGHAZ region. The

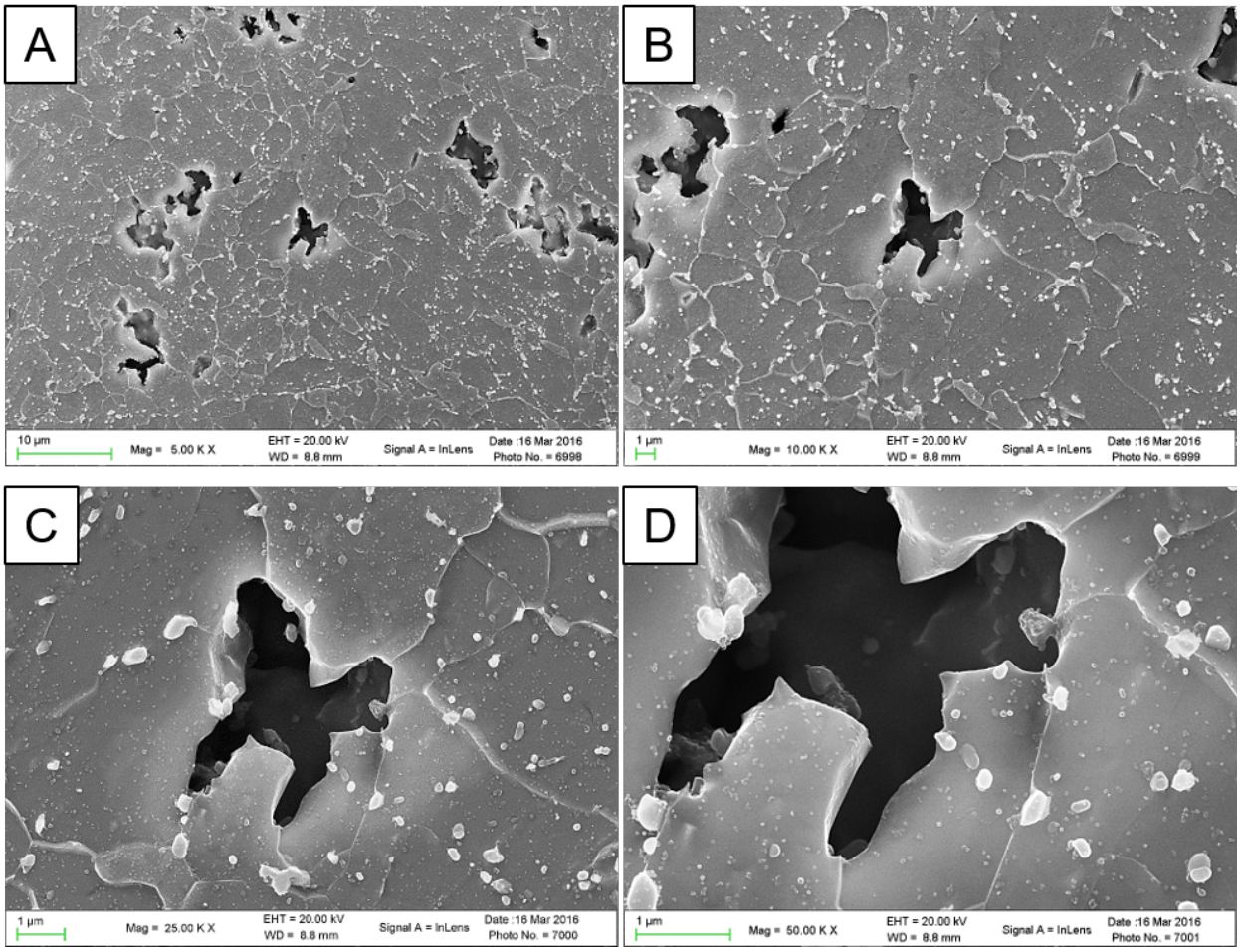


Figure 4-30. SE-SEM micrographs illustrating typical creep cavity morphology at the FT FGHAZ-2 location of the FT-H47-1 creep specimen. Note the complex, irregular shape of the cavities which appear to be located at the junction of multiple equiaxed ferritic subgrains; the cavities appear to result from separation along the subgrain boundaries. In D, small particles (most likely carbides) are visible within the cavity interior.

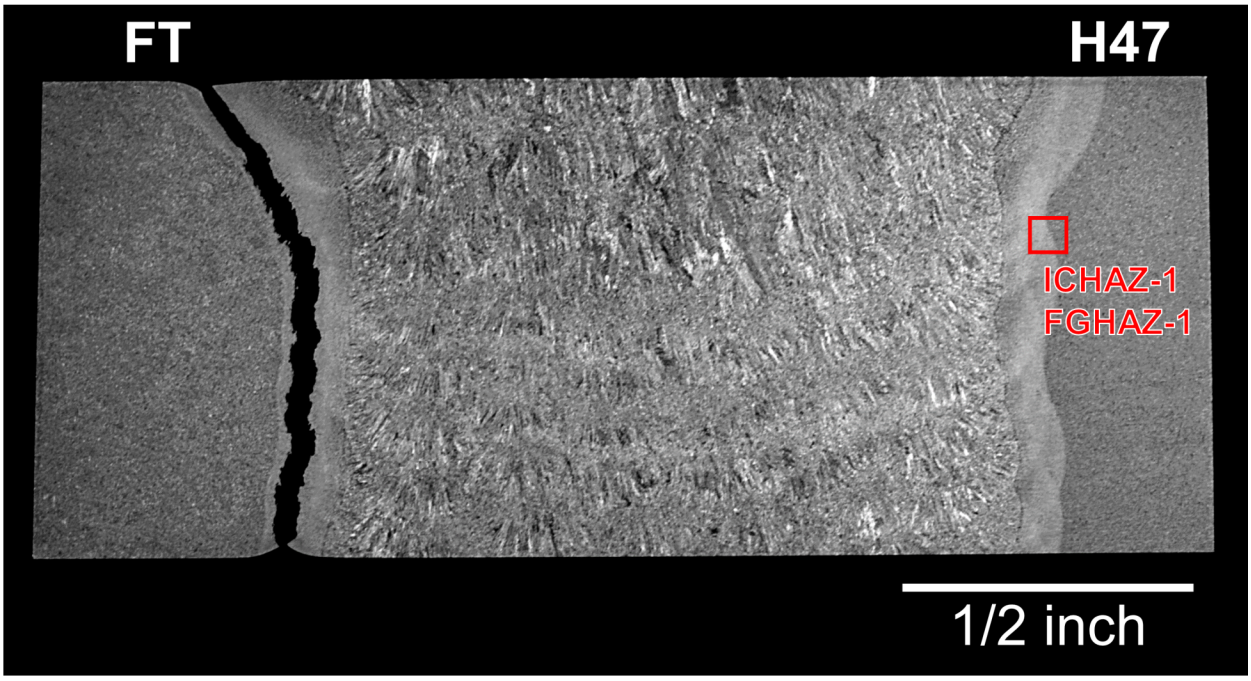


Figure 4-31. Cross-section macrograph of the FT-H47-1 creep specimen showing a selected location in the H47 HAZ which were examined at higher magnification with SEM to evaluate creep damage. The creep loading axis corresponds to the horizontal direction in the micrographs. Etchant: Fry's reagent.

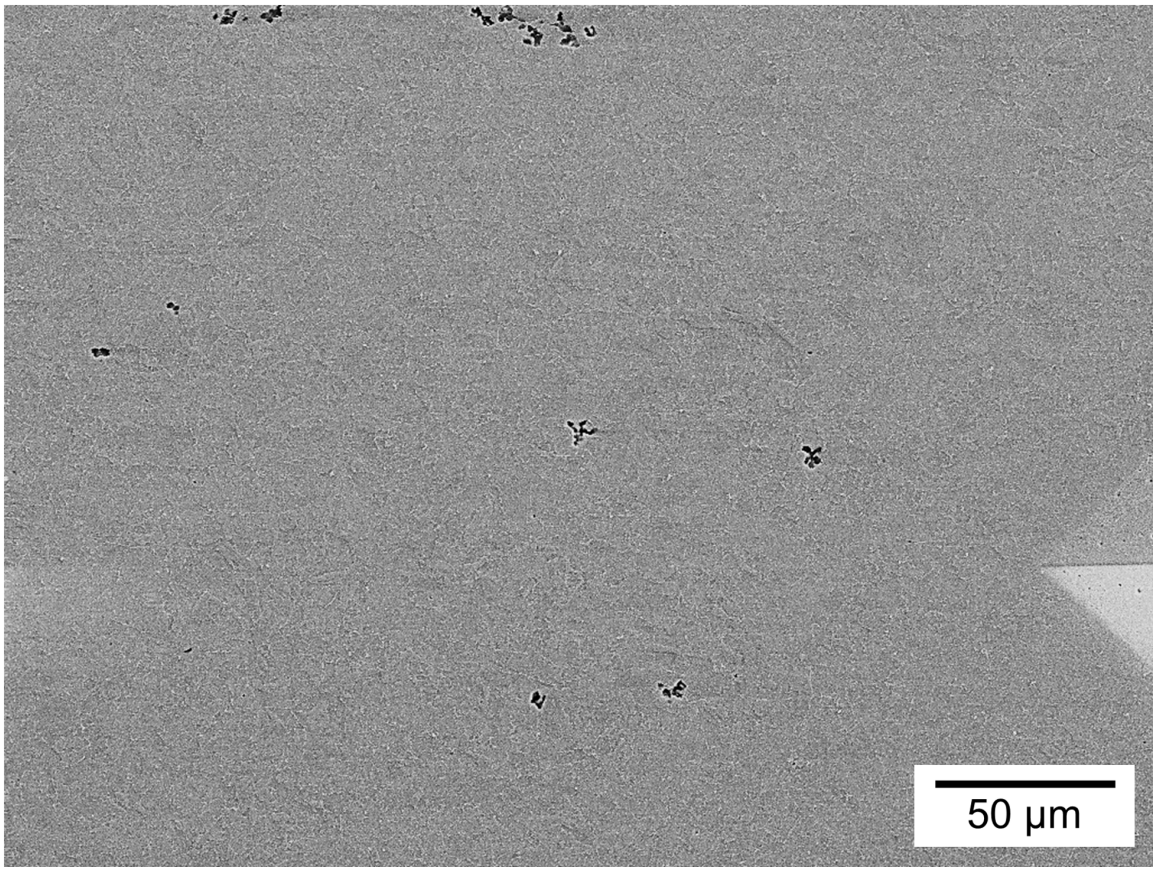


Figure 4-32. SE-SEM micrograph of location ICHAZ-1 in the H47 ICHAZ of the FT-H47-1 creep specimen. In addition to the absence of macro-cracking on this side of the weld, note the significantly lower occurrence of cavitation compared to the FT ICHAZ (cf. Fig. 4-22). Etchant: 10% Nital.

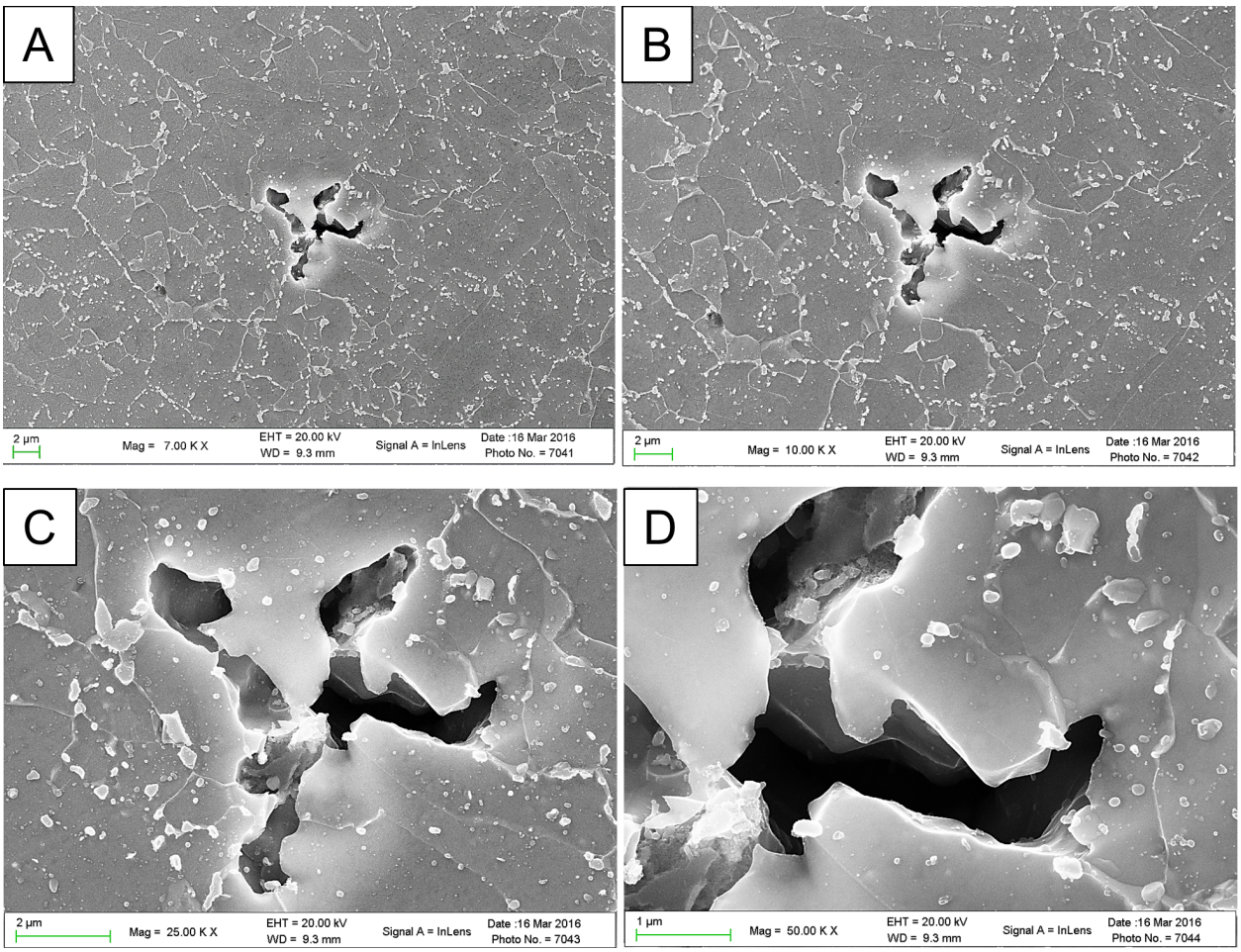


Figure 4-33. SE-SEM micrographs of an isolated creep cavity at location ICHAZ-1 in the H47 ICHAZ of the FT-H47-1 creep specimen. The cavity is highly irregular and appears to be located at a boundary junction with boundary separation occurring in multiple directions. The bright area at the center of the cavity is most likely a carbide; this cavity was not associated with a nonmetallic inclusion and the cavity is not filled in the interior (i.e. if the cavity were opening around an inclusion). Etchant: 10% Nital.

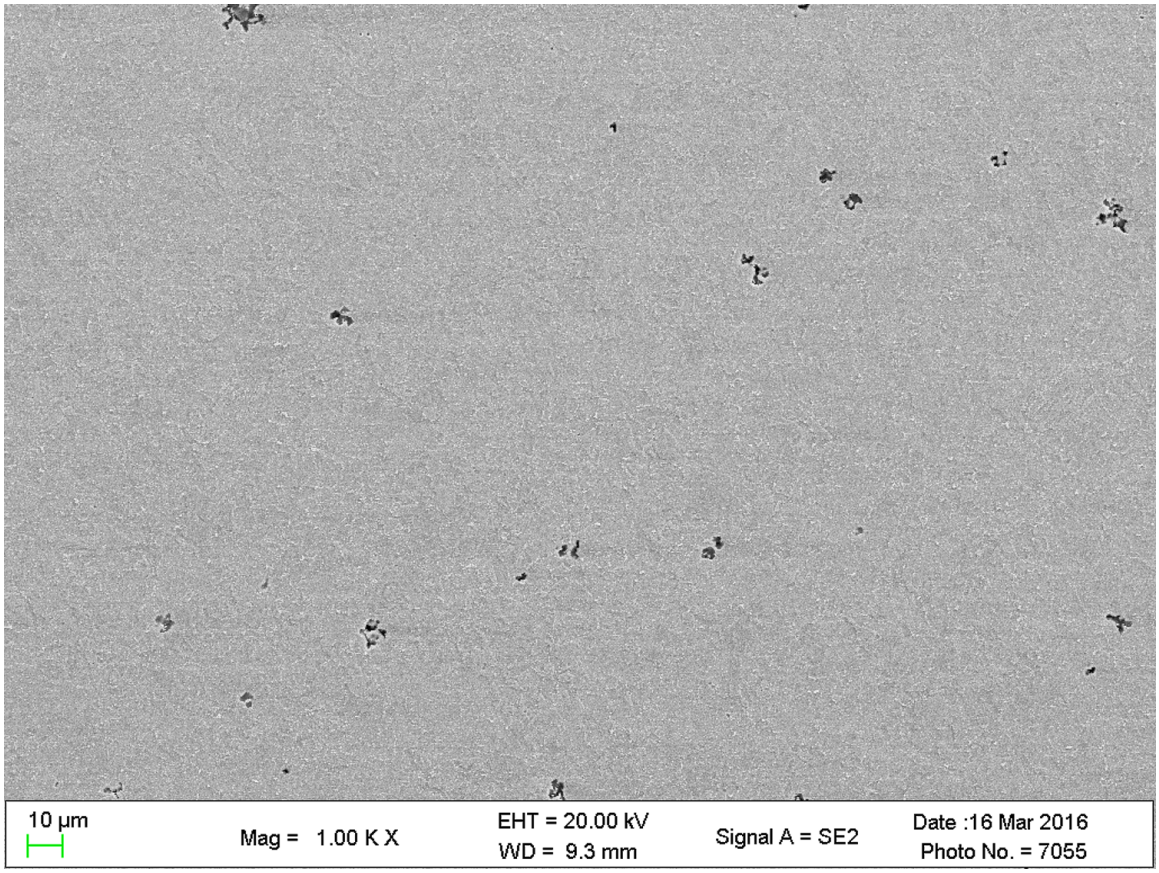


Figure 4-34. SE-SEM micrograph of creep cavitation near location ICHAZ-2 in the H47 ICHAZ of the FT-H47-1 creep specimen. Note that while there are scattered larger cavities (n=31, average area ~5 μm), the subsequent micrographs in Fig. 4-35 also show a small cavity in the early stages of growth. Etchant: 10% Nital.

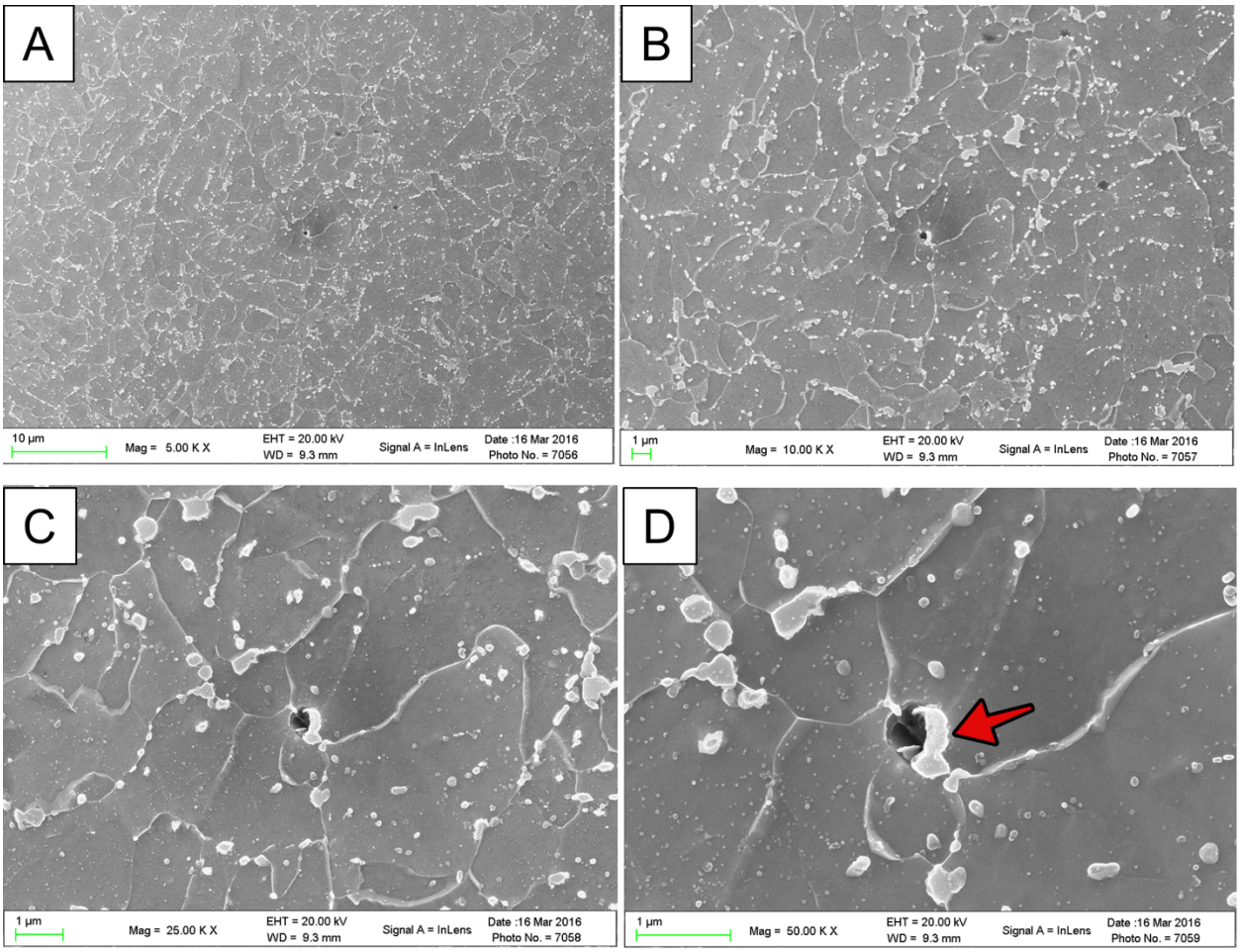


Figure 4-35. SE-SEM micrographs showing a small, isolated creep cavity near location ICHAZ-1 in the H47 ICHAZ of the FT-H47-1 creep specimen. The cavity is located on a short subgrain boundary segment which is oriented at an angle to the tensile loading direction during creep (horizontal in this image) and is associated with a small particle denoted by an arrow (from the SE image contrast, most likely a carbide). Etchant: 10% Nital.

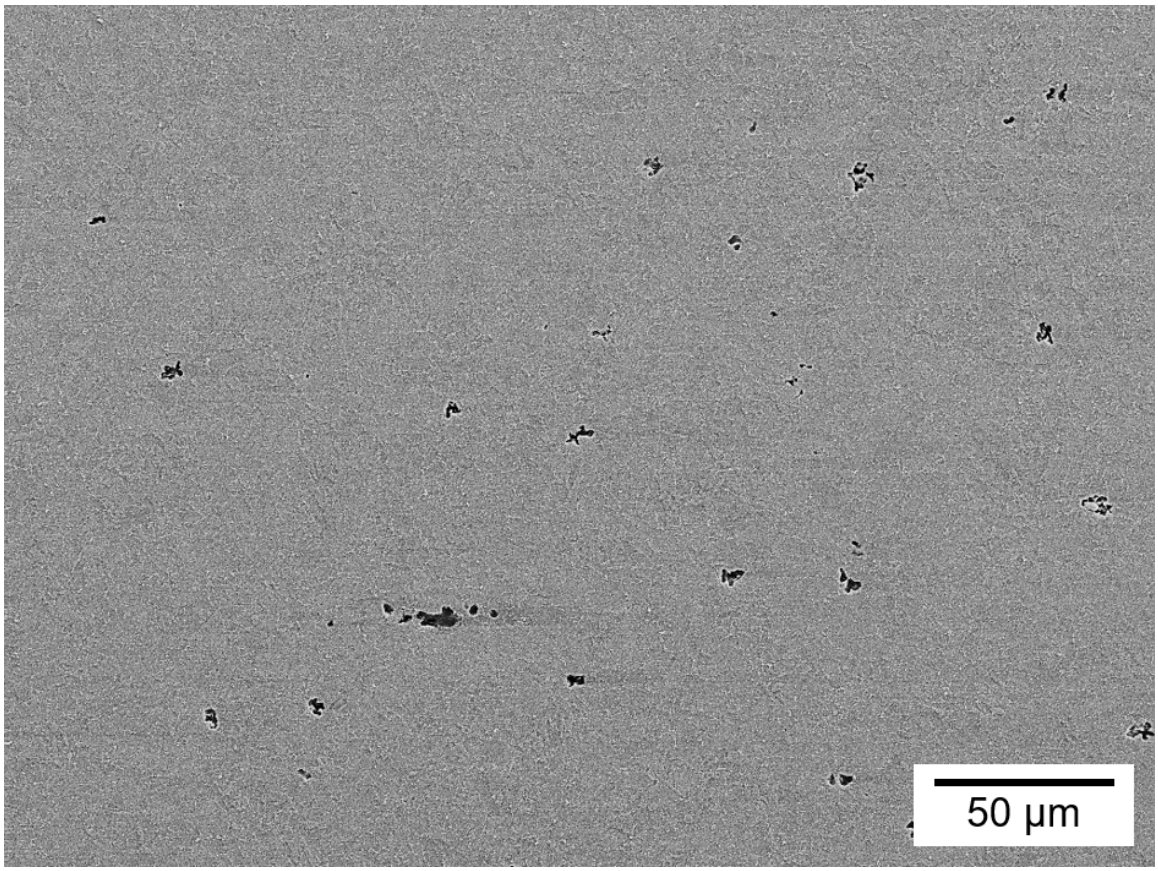


Figure 4-36. SE-SEM micrograph of location FGHAZ-1 in the H47 FGHAZ of the FT-H47-1 creep specimen. Similarly to the H47 ICHAZ, the H47 FGHAZ shows no macro-cracking and a significantly lower occurrence of cavitation compared to the FT FGHAZ (cf. Fig. 4-27).

cavitation at the H47 FGHAZ-1 location is shown at higher magnification in Fig. 4-37 and the cavity appearance is similar to other regions, with a complex cavity morphology and small particles visible within the cavity. Small bright particles (most likely carbides) are also visible at some locations around the cavity perimeter and the cavity appears to be located adjacent to another larger, particle within the matrix.

Based on comparison of the macroscopic and microscopic characteristics of creep cavitation in the FT-H47-1 creep specimen, the H47 base metal exhibited a lower susceptibility to Type IV creep damage than the FT base metal under the same testing condition (627°C, 82.7 MPa, 2080.4 h).

4.2.4 Cryo-Cracking Characterization of Creep Damage in the FT-H47 Weldment

To further evaluate the characteristics of creep damage, the Cryo-Cracking technique (Lundin et al., 1998) was employed to reveal the three-dimensional appearance of creep cavitation in the HAZ regions of the FT-H47 and H13-H47 Grade 91 SMAW weldments. The Cryo-Cracking technique involves cooling a sample below its ductile-to-brittle transition temperature (e.g. using liquid nitrogen) and then breaking the sample to produce matching fracture surfaces which expose any existing discontinuities within the sample (porosity, creep cavitation, crack surfaces, etc.) without producing any plastic deformation to distort these features, as would otherwise occur if the sample were fractured at room temperature. This technique was used to expose creep cavitation and creep damage (macro-cracks) in the tested creep specimens, as will now be discussed for the FT-H47-1 specimen.

Fig. 4-38 shows a macrograph of the FT-H47-1 cross-weld creep specimen, corresponding to a thin slice which was extracted from the middle of the specimen width. The solid red outlines on the left and right sides of the macrograph denote the removal of two specimens for cryo-cracking, containing the FT and H47 HAZs, respectively. The dashed red lines correspond to the locations of notches which were

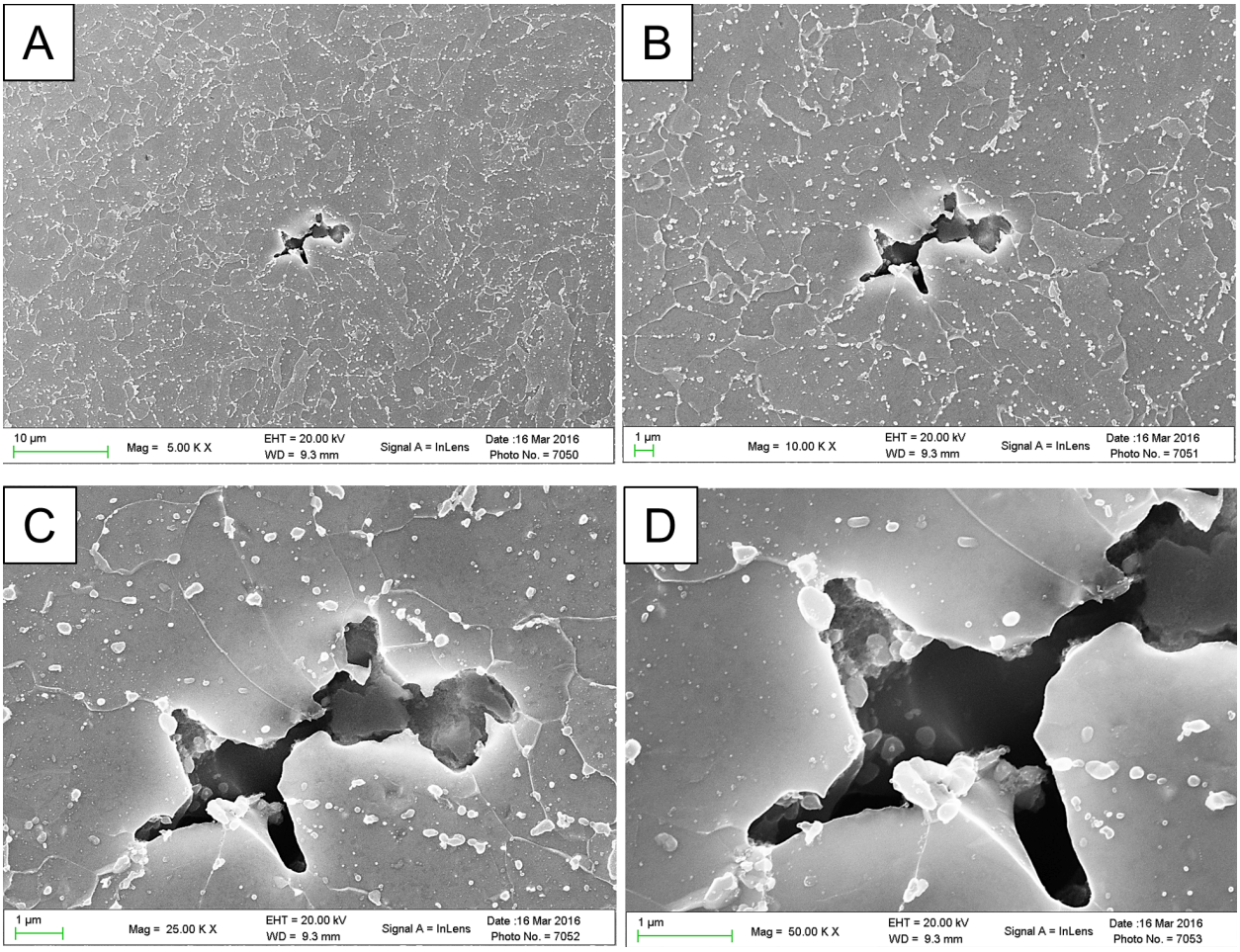


Figure 4-37. SE-SEM micrographs illustrating typical creep cavity morphology at location FGHAZ-1 in the H47 FGHAZ of the FT-H47-1 creep specimen. The cavity morphology is highly irregular and the cavity appears to be opening along a boundary junction. There are also small bright particles (most likely carbides) along the cavity perimeter and the cavity is also located adjacent to another, larger particle within the matrix. Etchant: 10% Nital.

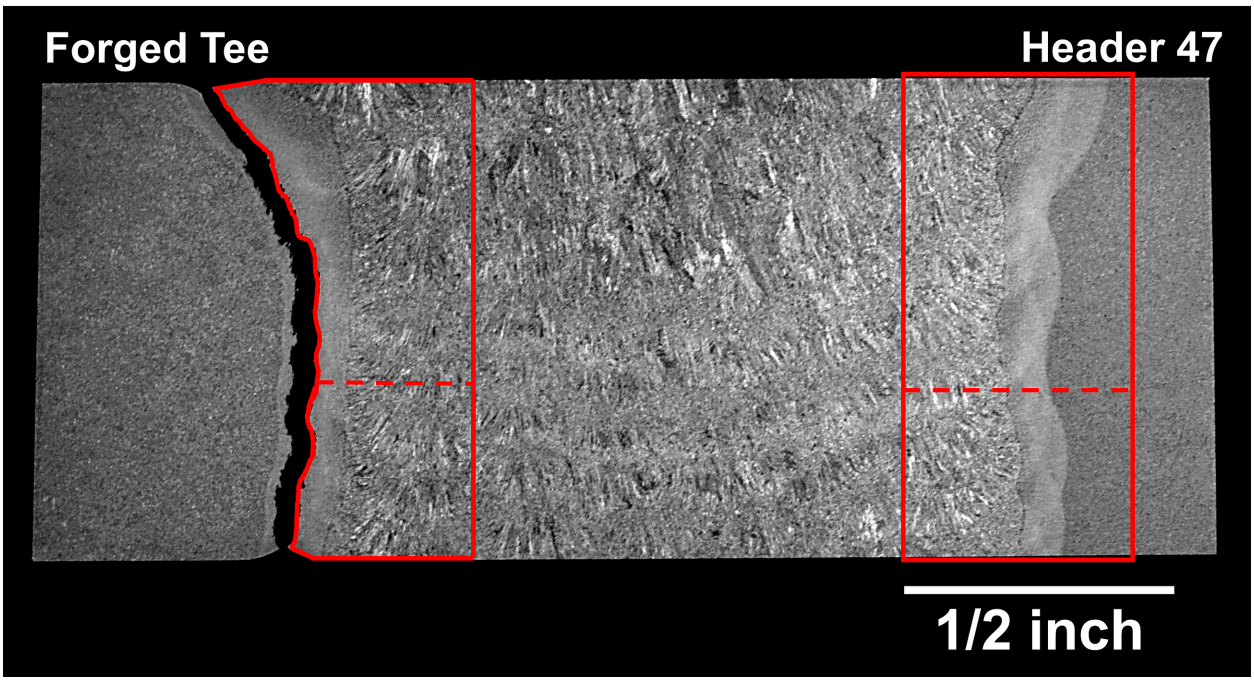


Figure 4-38. Cross-section macrograph of the FT-H47-1 creep specimen showing the locations for extraction (solid red outlines) of two separate samples to reveal the creep-damaged FT HAZ and H47 HAZ regions for SEM examination, using the cryo-cracking technique. The dashed red lines in the respective samples denote the placement of circumferential notches which were used to direct crack propagation along the desired path when the samples were fractured at liquid nitrogen temperature.

cut around the samples; the notches were created to direct the path of crack propagation through the regions of creep damage in the HAZs when fractured at liquid nitrogen temperature. Fig. 4-39 shows the fractured pieces after cryo-cracking, arranged in their original configuration, while Fig. 4-40 shows the fracture surfaces of both samples as produced by cryo-cracking, with the weld deposit, HAZ, and BM regions labeled on each surface. Fig. 4-41 shows a cryo-cracked fracture surface location in the FT HAZ, adjacent to the rupture[8] surface (noted on the left), and Fig. 4-42 shows the fracture morphology at this location. The fracture surface exhibited primarily transgranular cleavage with some isolated creep cavities, as shown in the SEM fractographs; the fractographs show that the cavity shape is irregular (identical to the two dimensional SEM evolution) and that the cavity interior surface is "decorated" with small particles, most likely carbides. However, the cavity is not clearly associated with a specific particle, in the sense that the cavity could be said to "nucleate" or "initiate" at a particle such as a non-metallic inclusion. This observation suggests that the particles are present on the interior surface simply because subgrain boundaries are the primary location for carbides and the cavity growth occurred at the intersection of subgrain boundaries, according to the description by Benci et al. (Benci et al., 1988), and not because the cavity nucleated at any of these particles.

A second cryo-cracked sample from the FT-H47-1 creep specimen was obtained from the H47 side of the weld, as shown on the right hand side in Fig. 4-38. SEM fractography was conducted for the lower fracture half of this specimen as shown in Fig. 4-40. The corresponding SEM fractography results for the H47 side of the FT-H47-1 creep specimen are shown in Fig. 4-43 through Fig. 4-45. Fig. 4-43 shows the fracture surface appearance at location 1 within the FGHAZ on the H47 side of the weld; the

[8] Note that the terms fracture surface and rupture surface are used intentionally to distinguish between the creep crack surfaces resulting from final creep rupture and the surfaces newly produced by cryo-cracking.

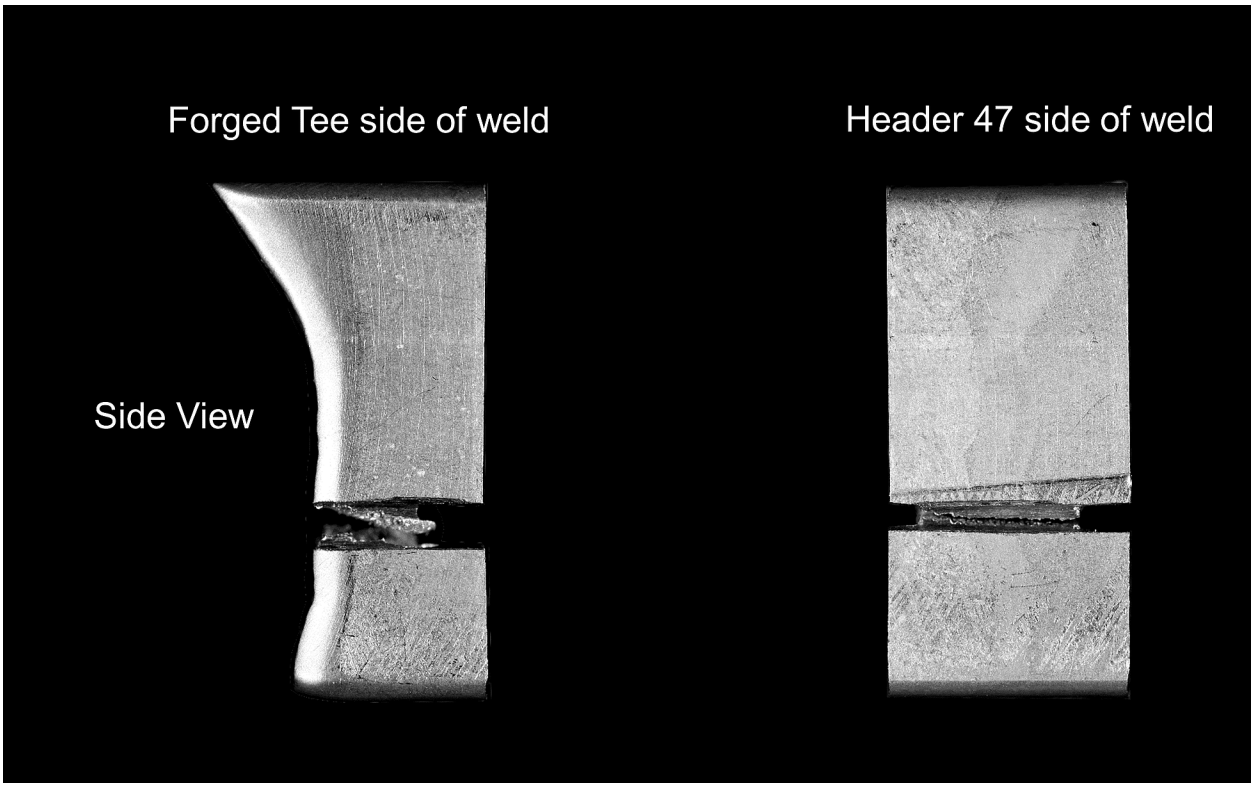


Figure 4-39. Photograph showing the extracted, notched, and cryo-cracked samples from the FT-H47-1 creep specimen.

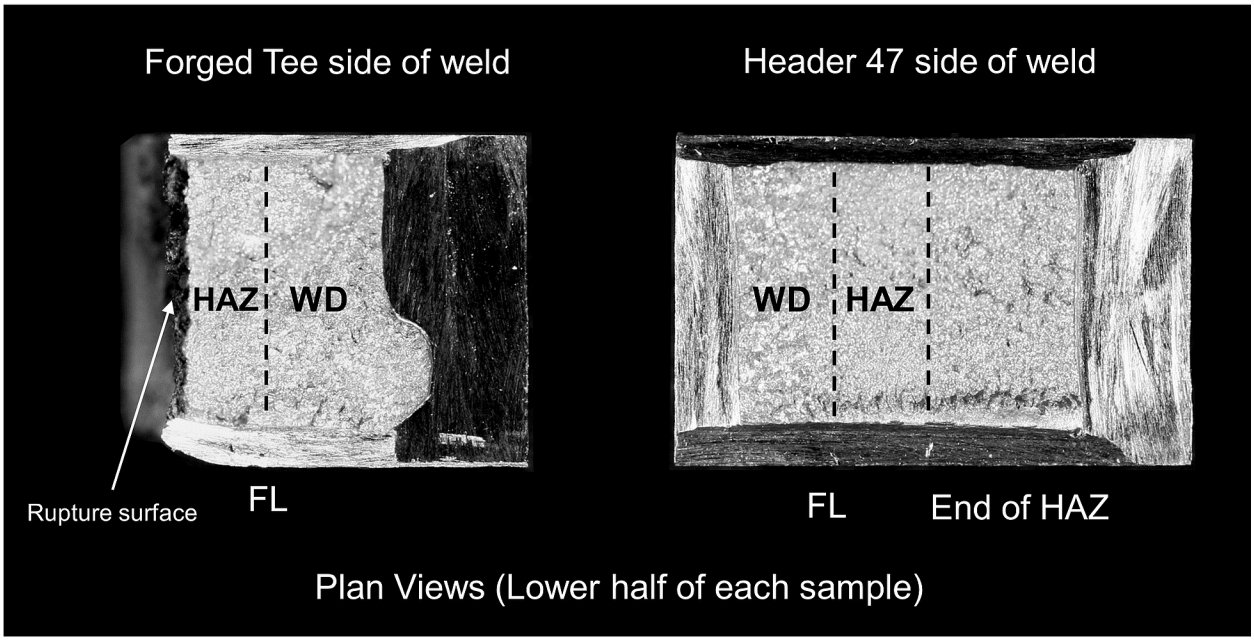


Figure 4-40. Optical fractograph showing the fracture surfaces corresponding to the lower half of each sample shown in Fig. 4-39 from the FT-H47-1 creep specimen.

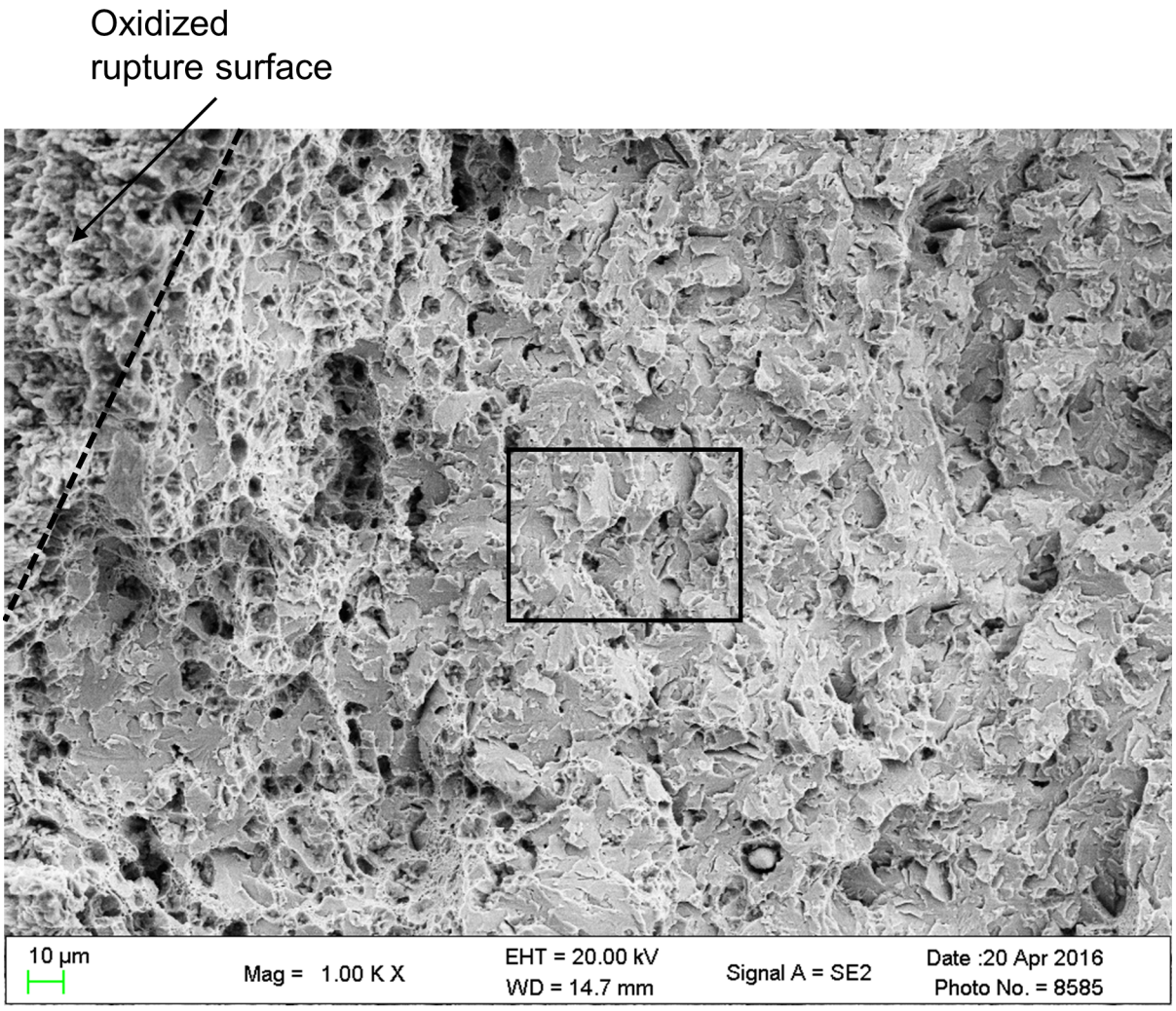


Figure 4-41. SEM fractograph showing the fracture surface morphology revealed by cryo-cracking at Location 1 in the FT HAZ of the FT-H47-1 creep specimen, adjacent to the rupture surface (which is oxidized).

Forged Tee Side – Location 1 – Adjacent to Rupture (FGHAZ)

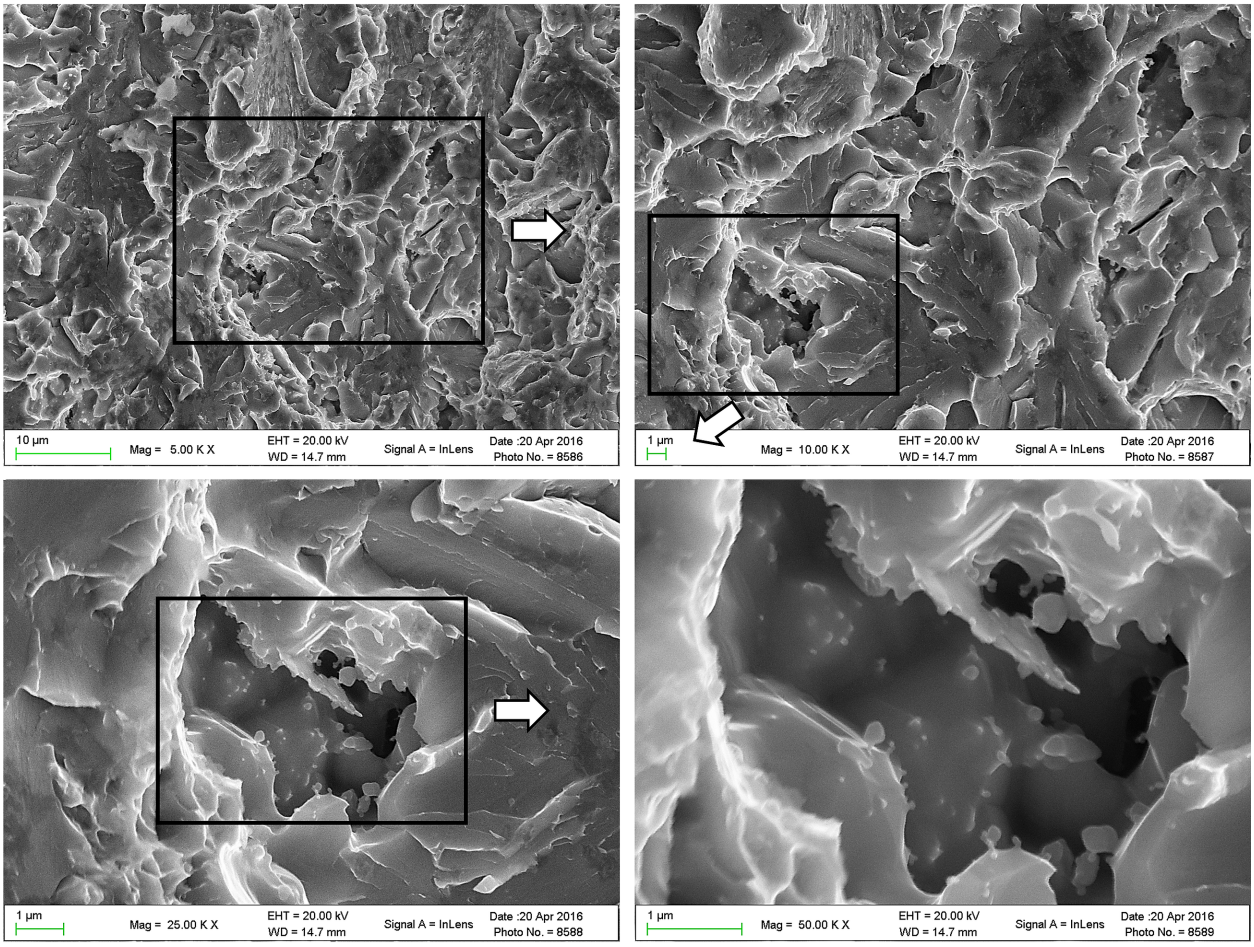


Figure 4-42. SEM fractographs showing the fracture surface morphology revealed by cryo-cracking at Location 1 in the FT HAZ adjacent to rupture. At this location, the fracture morphology is primary transgranular cleavage (flat features) with isolated cavities observed. The boxed regions highlight a creep cavity on the surface; small particles (most likely carbides) are present on the cavity interior surface, but a specific initiation site for the cavity is not apparent.

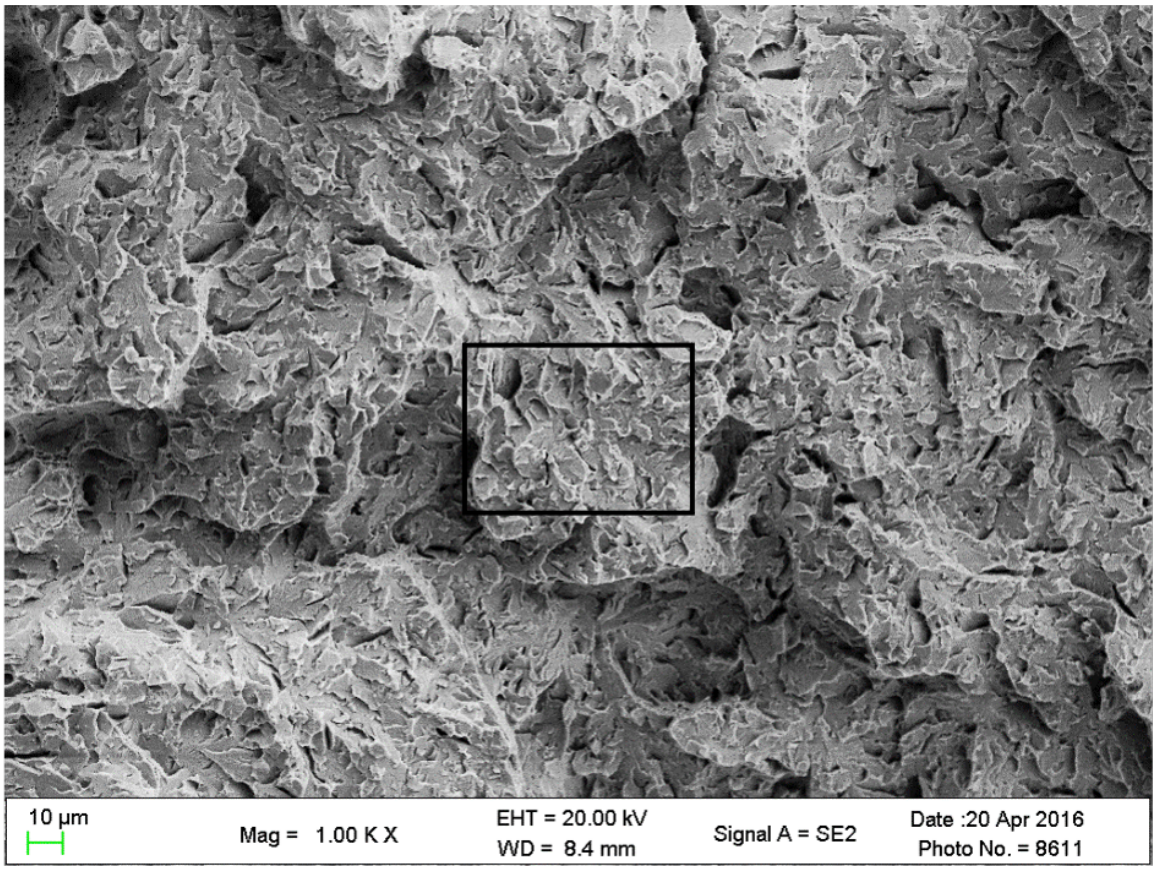


Figure 4-43. SEM fractograph showing the fracture surface morphology revealed by cryo-cracking at Location 1 in the H47 HAZ of the FT-H47-1 creep specimen. Recall that this side of the weld did not show any evidence of macro-cracking, which correlates with the predominantly transgranular fracture morphology observed in the above image.

corresponding higher magnification fractographs in Fig. 4-44 indicate that the extent of creep cavitation is qualitatively lower than in the FT HAZ, and the fracture morphology at the H47 FGHAZ appears more transgranular and smooth than in the FT FGHAZ. The cavity interior surface is depicted more clearly in the SEM image in Fig. 4-45, where regularly spaced, geometric features (similar to ledges or steps) were observed at various areas. At another location in the H47 HAZ, the cryo-crack fracture surface at low magnification in Fig. 4-46 shows the primarily transgranular morphology, while the higher magnification fractographs in Fig. 4-47 show the irregular cavity shape (in agreement with the OLM results) and the presence of small particles on the cavity interior surface without any clear nucleation or initiation site.

4.2.5 Evaluation of Microstructural Characteristics in the FT-H47 Weldment by Image Analysis

As demonstrated in the previous sections, an asymmetric extent of HAZ creep damage was observed in the FT-H47 cross-weld specimen. The FT side of the weldment exhibited a much higher occurrence of creep damage, with significant cavitation adjacent to the rupture faces where creep crack propagation proceeded through the outer portion of the HAZ. The characterization results from OLM and SEM microscopy of the FT-H47 weldment in the PWHT condition, prior to creep testing, did not reveal clear differences from simple examination of the images that could explain the differences in creep behavior between the two dissimilar sides of the weld. A method for evaluating and comparing the PWHTed, pre-creep FT and H47 HAZ microstructures in a more quantitative (i.e. semi-quantitative) manner using the previously available data was thereby undertaken using software image analysis with ImageJ, according to the procedure described in the Image Processing and Analysis section. The image analysis included determination of particle size distribution and areal density (particles/mm^2) and of subgrain size using the three-circle intercept method. Micrograph magnifications of 10kx and 25kx were selected in order to provide a general overview (10kx) of the subgrain structure and boundary precipitates along

Header 47 Side – Location 1 – FGHAZ

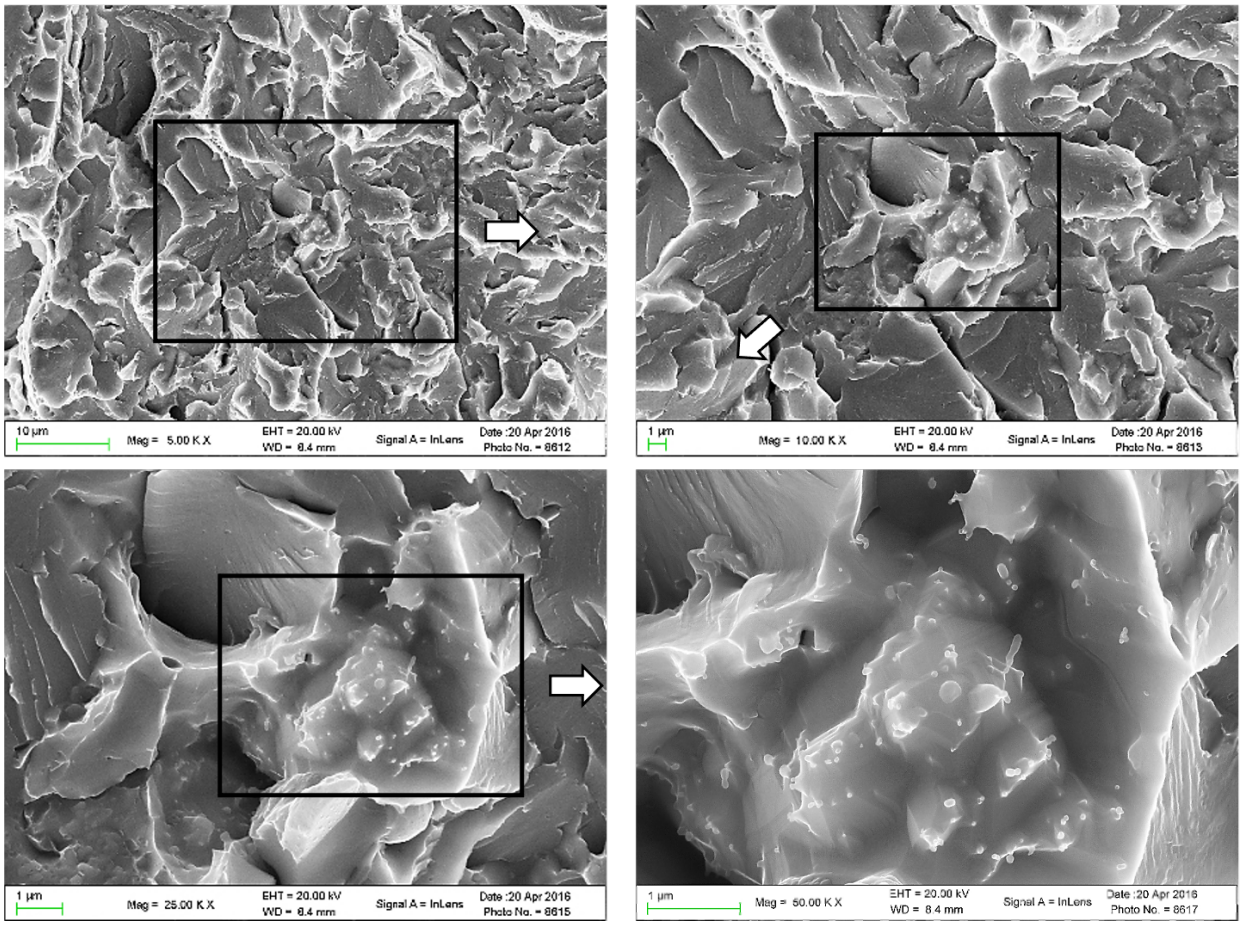


Figure 4-44. SEM fractographs showing the fracture surface morphology revealed by cryo-cracking at Location 1 in the H47 HAZ. At this location, the fracture morphology is primarily transgranular cleavage (flat features) with isolated cavities observed.

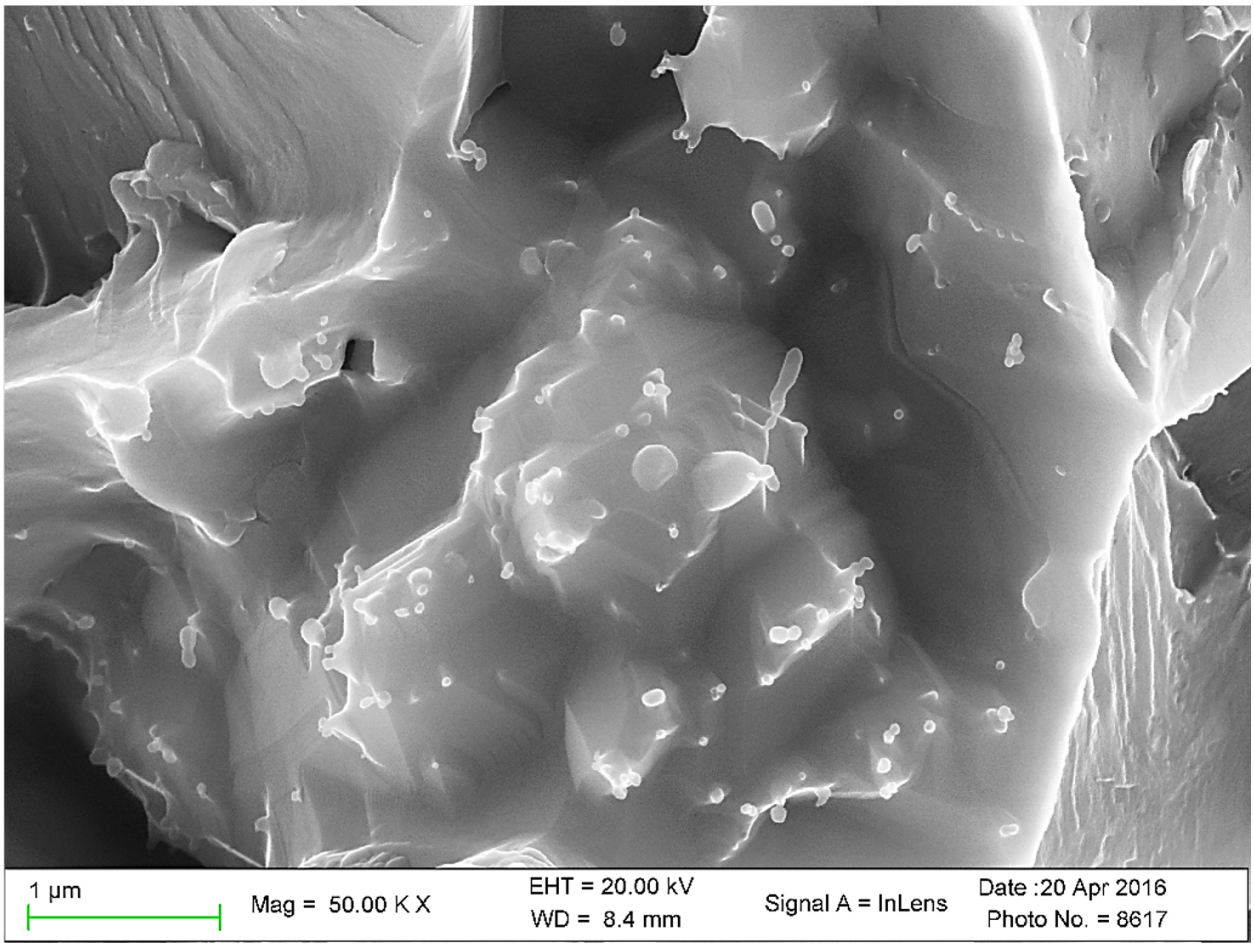


Figure 4-45. Higher magnification SEM fractograph of the cavity interior surface in the H47 HAZ shown in Fig. 4-44. Note the regularly spaced ledges or steps that are visible on the cavity interior surface.

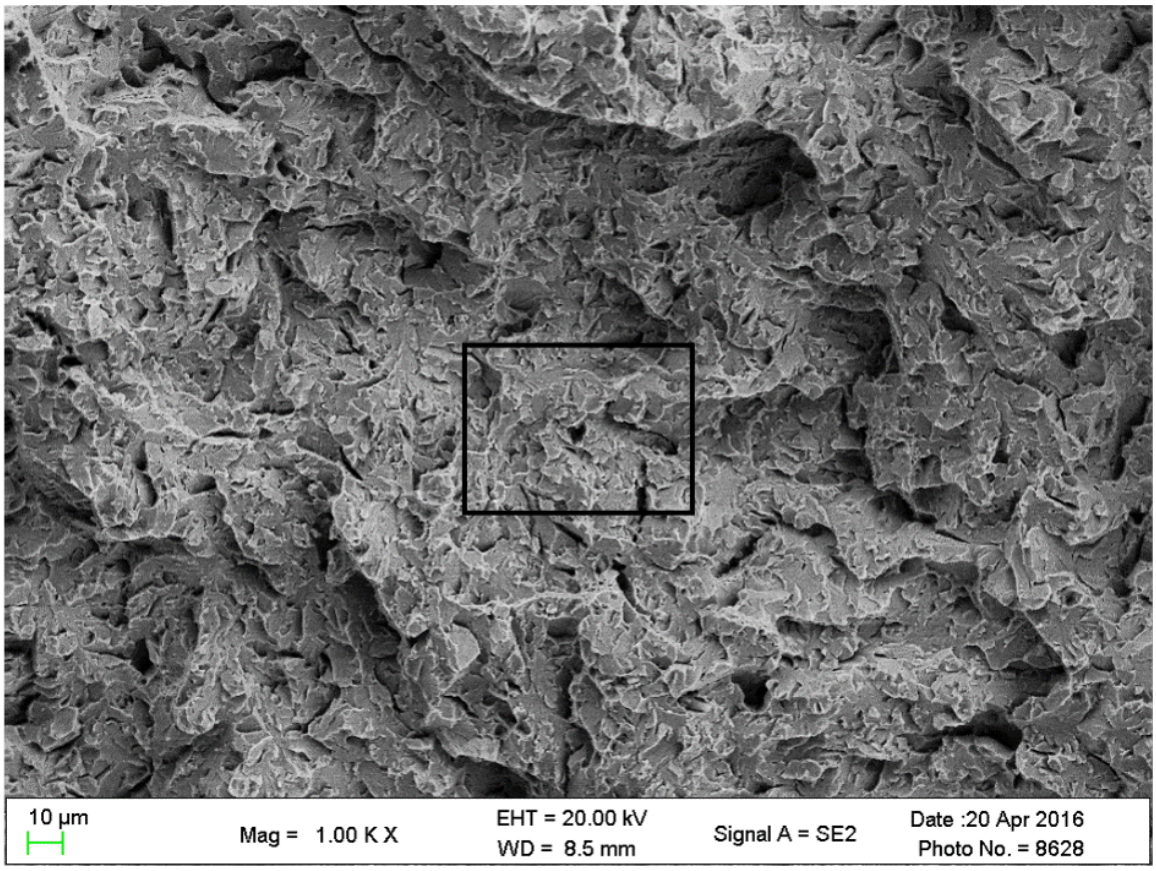


Figure 4-46. SEM fractograph showing the fracture surface morphology revealed by cryo-cracking at Location 3 in the H47 HAZ of the FT-H47-1 creep specimen.

Header 47 Side – Location 3 – FGHAZ

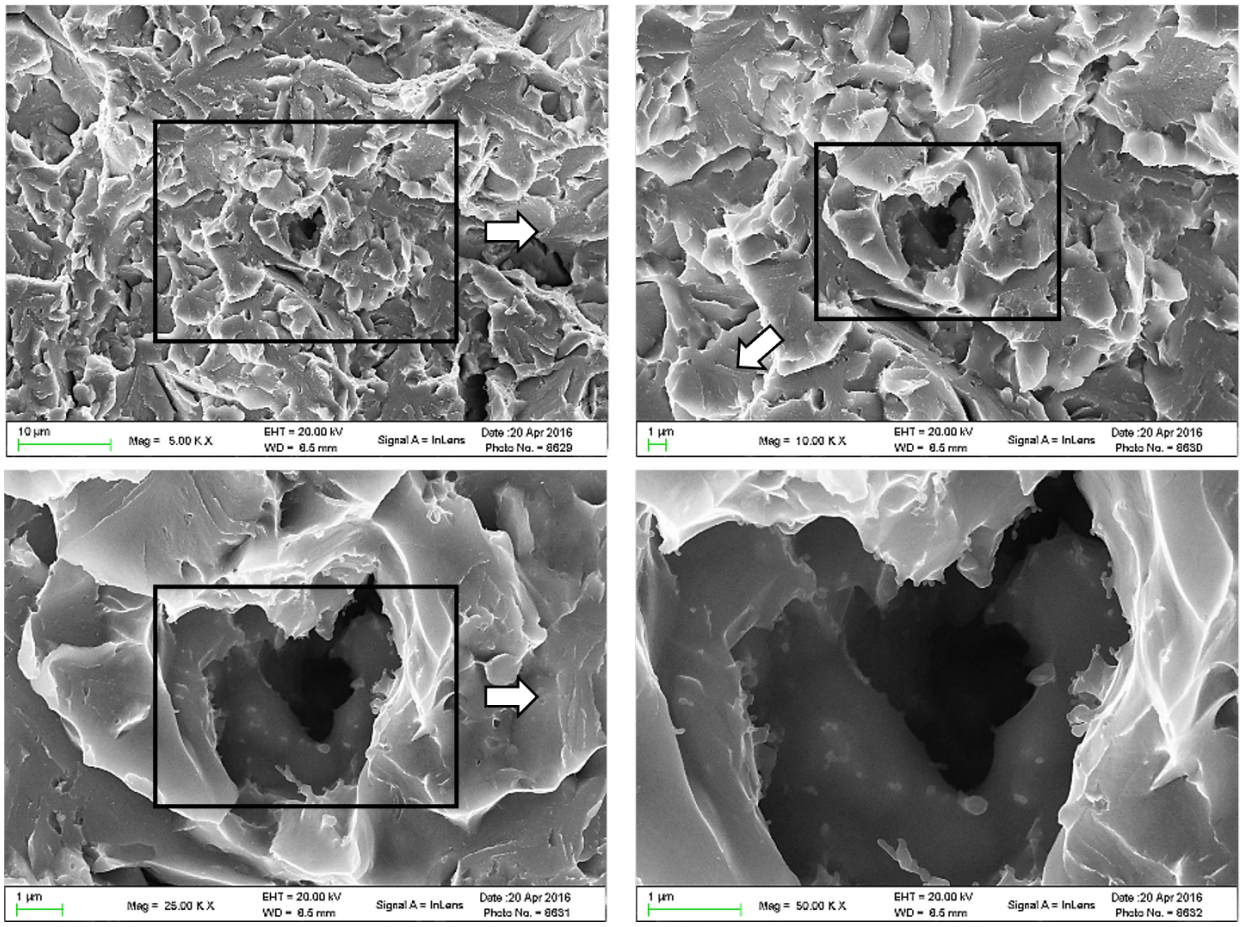


Figure 4-47. SEM fractographs showing the fracture surface morphology revealed by cryo-cracking at Location 3 in the H47 HAZ. At this location, the fracture morphology is primary transgranular cleavage (flat features) with isolated cavitation; the selected cavity exhibits an irregular shape and an interior surface that is marked by the presence of small particles which most likely originated from grain/subgrain boundaries which separated during cavity growth.

with a higher magnification view (25kx) to reveal any differences in fine precipitation within the subgrain matrix regions. The results are presented and discussed first for particle size and particle density, followed by measurements of subgrain size, for different regions within the FT and H47 sides of the weld in the PWHT condition, namely the BM, FGHAZ, and ICHAZ regions.

4.2.5.1 Particle Analysis of the FT and H47 Base Metals after Postweld Heat Treatment

Fig. 4-48 shows the particle analysis results for the FT and H47 base metals in the PWHT condition (746°C/1 h) when evaluated at a magnification of 10kx. Fig. 4-48(A) shows that the particle distributions are very similar except at the lowest size range of <0.025 μm^2, where the H47 base metal exhibits a significantly higher particle count. The difference in the particle distributions at the low end of the size range is illustrated more clearly in Fig. 4-48(B), which shows that the H47 base metal contains a greater extent of particles whose sizes are in the vicinity of 0.01 μm^2. The overall particle densities are 2.32E6 particles/mm^2 for the FT base metal and 2.86E6 articles/mm^2 for the H47 base metal, respectively. Fig. 4-49 shows a comparison of the final particle masks from the image analysis and it can be seen qualitatively that the "spread" of apparent particle size in the masks is in agreement with the histograms. Comparing the total particle area between the two base metal micrographs and also the upper ends of the histograms, the FT base metal showed a larger total particle area (73.534 μm^2) and had a higher relative occurrence of larger particles compared to the H47 base metal. Comparing the measured carbon content between the two materials (given in Table 3-1), the FT material has a higher carbon content of 0.125 wt.% compared to 0.109 wt.% for the H47 material. Both materials received identical normalizing, tempering, and PWHT treatments; the samples were heat treated together in the same batch at all three steps, so the differences in particle characteristics are not due to heat treatment differences. Thus, the higher total particle area in the FT base metal agrees with the

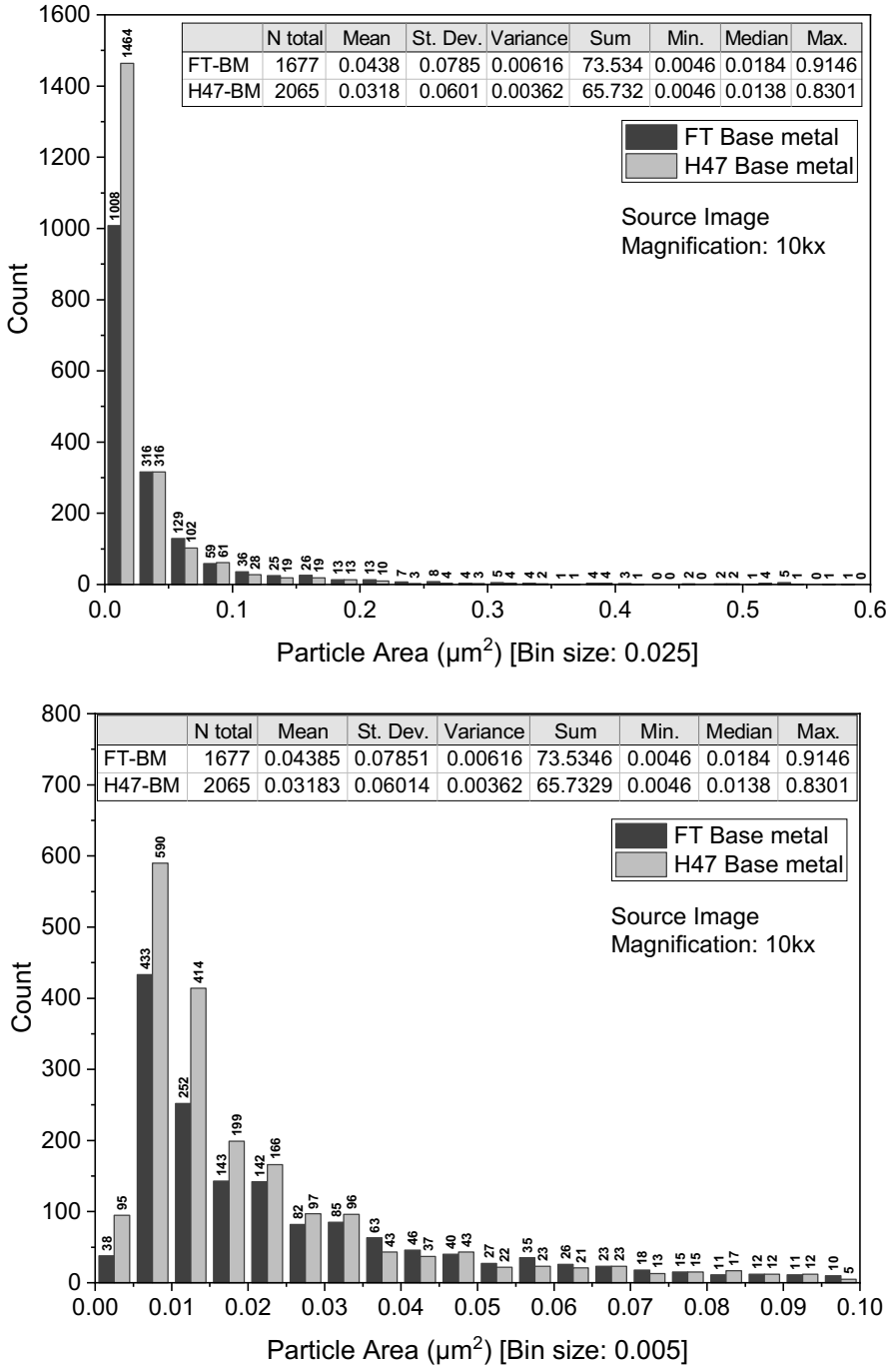


Figure 4-48. Histograms of particle area obtained from software image analysis of representative SE-SEM micrographs of the FT and H47 base metals in the PWHT condition (746°C/1 h) prior to creep testing. (A) Histograms of particle area for the size range 0-0.6 μm^2 (B) histograms of particle area for a subset of sizes at the low end of the range, 0-0.1 μm^2. The data bar at the top of the histograms shows statistics for the full particle analysis in the respective image. Note that the particle area distributions in (A) are similar except for the smallest bin size, where the H47 base metal exhibits a significantly higher particle count which is illustrated more clearly in (B).

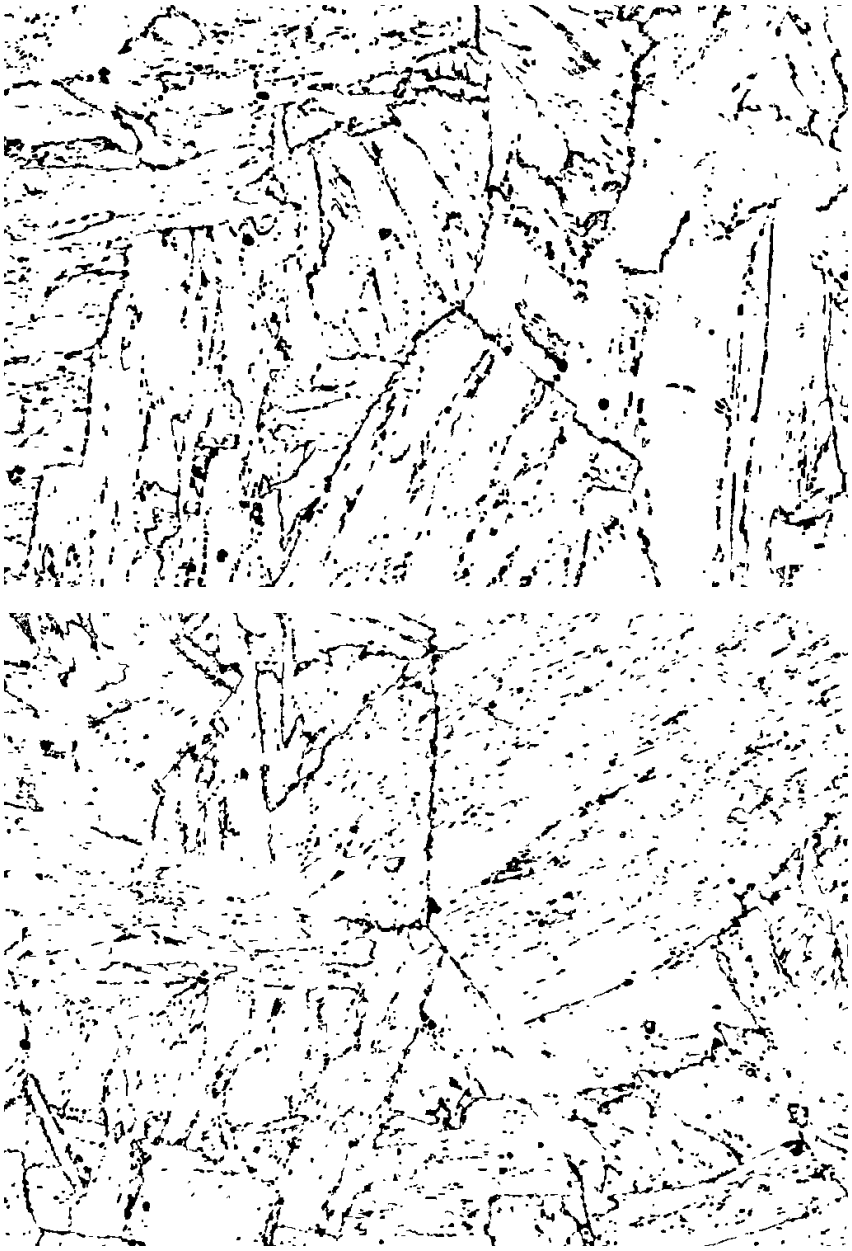


Figure 4-49. Comparison of the particle masks produced by the software image analysis procedure for the (a) FT and (b) H47 base metals in the PWHT condition. Qualitatively, the appearance matches with the histogram results in Fig. 4-48, with the H47 base metal showing a greater extent of fine particles.

higher carbon content as compared with the H47 material. The slightly higher extent of large particles suggests that more carbide coarsening occurred in the FT material during tempering and PWHT and potentially that the FT material is less microstructurally stable at high temperature. This possibility is explored further in the Discussion of Type IV Creep Damage in Dissimilar Grade 91 Weldments.

4.2.5.2 Particle Analysis of HAZ Regions after Postweld Heat Treatment and Creep Testing

The particle analysis results for the H47 FGHAZ and FT FGHAZ regions in the PWHT condition (746°C/1 h) are compared beginning in Fig. 4-50. Fig. 4-50 shows comparative histograms for the FT-FGHAZ and H47-FGHAZ region, determined from individual SE-SEM micrographs at 10kX. At this magnification, the visible particles primarily correspond to grain boundary precipitates (most likely $M_{23}C_6$ carbides) and to larger particles within the grain interiors; small precipitates in the grain interiors are not quantifiable at this magnification. Fig. 4-50 suggests that the particle area distribution is similar for the two different FGHAZ regions (FT and H47) within the FT-H47 weldment.

Fig. 4-51 similarly shows histograms for individual 10kx SE-SEM micrographs from the FT and H47 ICHAZ regions within the weldment. Based on Fig. 4-51(A), the FT-ICHAZ region shows a reduced extent of the smallest size range of precipitates ($\leq 0.025\ \mu m^2$) compared to the H47-ICHAZ. Additionally, the FT-ICHAZ shows a greater extent of larger, outlier particles than the H47 ICHAZ as shown in the box plot in Fig. 4-52. To further clarify these results, a subset of the data in Fig. 4-51 was re-plotted as a new histogram with smaller bin size to separate the $\leq 0.025\ \mu m^2$ particle data. These histograms are given in Fig. 4-51(B) and show that the difference in the fine particle count is most noticeable at 10kx for particles which are around $0.01\ \mu m^2$ in size.

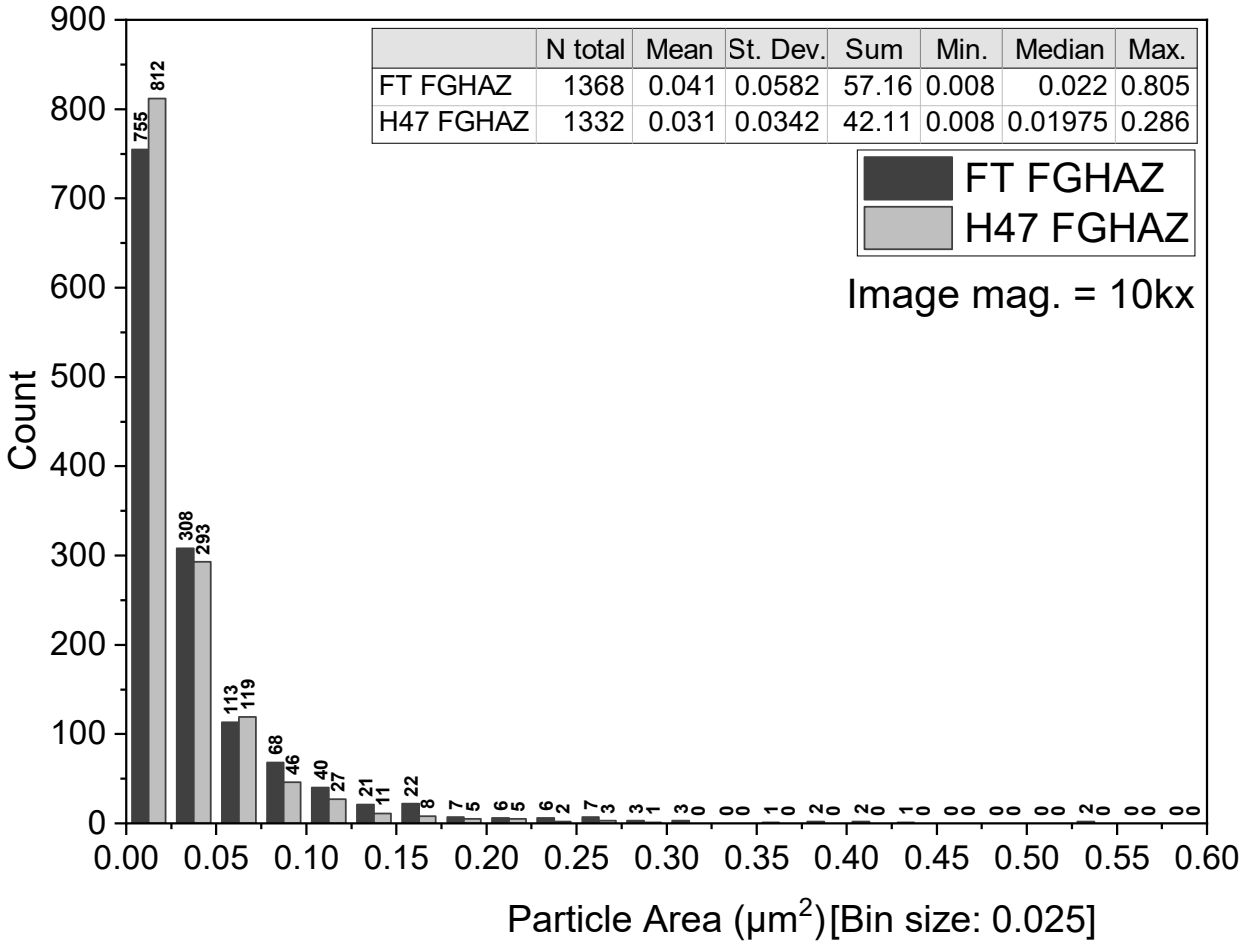


Figure 4-50. Histograms of particle area obtained from software image analysis of individual SE-SEM micrographs obtained from the FT FGHAZ and H47 FGHAZ regions in the FT-H47 weldment in the PWHT condition (746°C/1 h). Both FGHAZ regions exhibit similar particle area distributions.

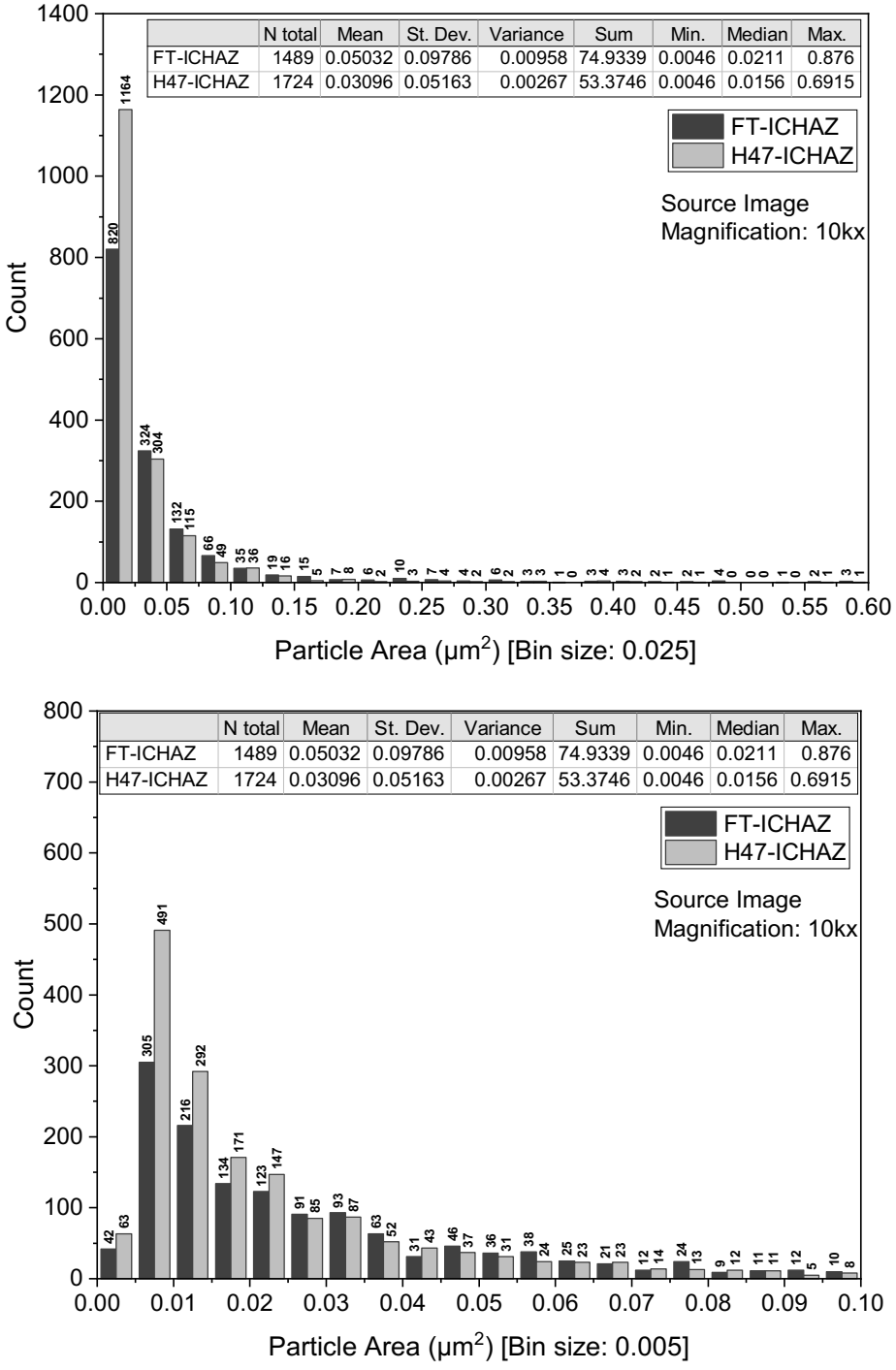


Figure 4-51. Histograms of particle area obtained from software image analysis of individual 10kx SE-SEM micrographs obtained from the FT ICHAZ and H47 ICHAZ regions in the FT-H47 weldment in the PWHT condition (746°C/1 h). (A) Histograms for particles in the range of 0-0.6 μm^2 in size (B) histograms for a subset of particles in the range of 0-0.1 μm^2 in size. In both cases, the H47 base metal shows a greater extent of finer size particles. In (A) and (B), the information at the top of each figure shows basic statistics for particle area from the full dataset.

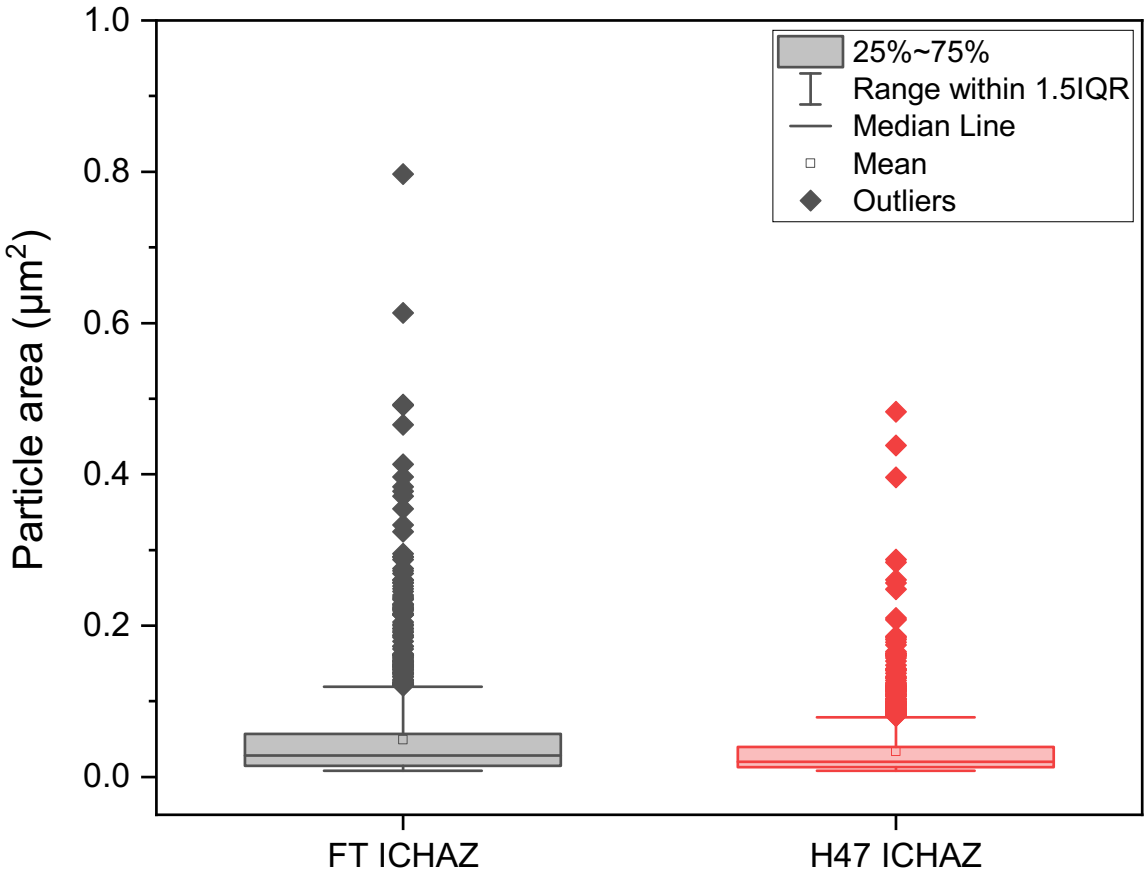


Figure 4-52. Comparison of box plots of particle area results for the FT ICHAZ and H47 ICHAZ regions in the PWHT condition (746°C/1 h), obtained by image analysis of individual 10kx SE-SEM micrographs. The FT ICHAZ shows a greater spread around the average particle size, a larger average particle size, and a greater number of outlier particles.

For further verification of the difference in fine precipitates, SE-SEM micrographs from the FT-H47 weld in the PWHT condition at a higher magnification of 25kx were evaluated with a similar image analysis procedure. Fig. 4-53 shows the histograms of particle size obtained at this magnification and the histograms confirm that the H47 ICHAZ shows a greater extent of the smallest particles, compared to the FT ICHAZ. Additionally, the 25kx histograms illustrate that the 10kx micrographs are not able to adequately resolve particles smaller than approximately 0.01 μm^2. Altogether, the particle analysis results suggest reduced strengthening on the FT side of the weld as compared to the H47 side in general and specifically for the FT ICHAZ compared to the H47 ICHAZ. A larger fraction of smaller particles is more effective at inhibiting dislocation motion and recovery (subgrain coarsening) and thus the H47 BM and H47 ICHAZ would be expected to be more microstructurally stable during creep than the corresponding FT regions.

4.2.5.3 Measurement of Ferritic Subgrain Size after PWHT and Creep Testing

In addition to the particle characteristics, the ferritic subgrain size was also measured and compared for the FT and H47 base metal, FGHAZ, and ICHAZ regions in the PWHT condition to explore a potential correlation with the asymmetric HAZ creep damage in the FT-H47-1 creep specimen. Previously obtained SE-SEM micrographs were used for measuring the ferritic subgrain size in the base metal, FGHAZ, and ICHAZ regions according to the procedure described in Evaluation of microstructure in Grade 91 weldments by image analysis. As described previously, the base metal regions retained a lath-like subgrain structure with elongated subgrains, while the FGHAZ and ICHAZ regions show evidence of microstructure recovery with a more equiaxed subgrain structure; however, in both cases the structure consists of ferritic subgrains since the weldment is in the PWHT condition. The results for ferritic subgrain size of the FT and H47 materials across the three different regions after PWHT are summarized

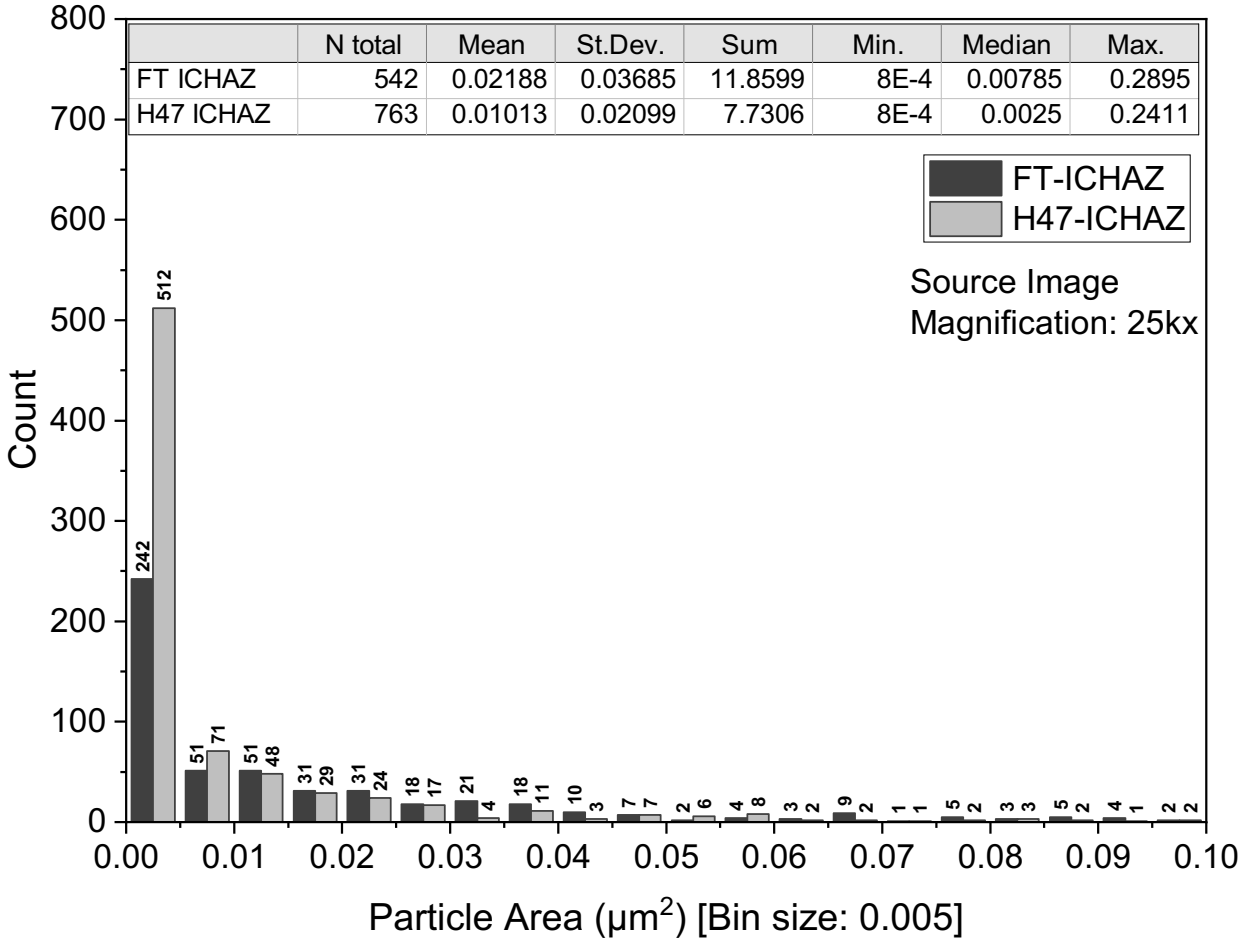


Figure 4-53. Histograms of particle area obtained from software image analysis of individual 25kx SE-SEM micrographs obtained from the FT ICHAZ and H47 ICHAZ regions in the FT-H47 weldment in the PWHT condition (746°C/1 h). These results verify what was apparent from Fig. 4-51 in that the H47 ICHAZ region has a greater extent of finer size particles.

in Table 4-5. Table 4-5 shows that the FT regions generally have smaller lineal intercept values than the corresponding H47 regions; smaller lineal intercept values correspond to smaller equivalent grain/subgrain sizes and thus the FT regions can be characterized as showing a smaller ferritic subgrain size. However, it should be noted that the differences in subgrain size are not large, e.g. for the FT versus H47 base metal and FT versus H47 ICHAZ, so it is possible that the differences are within a reasonably expected scatter in the data. Based on the measured subgrain sizes in the creep-exposed condition as reported in Table 4-6, for which more data was available and statistics could be determined, the standard deviation of the subgrain sizes were typically on the order of several tenths of a micron. If a standard deviation of $\pm 0.2\ \mu$m is assumed as a best-case value, then the results in Table 4-5 show that the base metal and ICHAZ regions are probably within the scatter.

To examine the change in ferritic subgrain size during creep exposure, a similar set of measurements was performed using SE-SEM micrographs obtained from the FT and H47 base metal, ICHAZ, and FGHAZ regions of the FT-H47-1 creep specimen after rupture at 2080.4 h. The results from the ferritic subgrain measurements in the creep-exposed condition are shown in Table 4-6. Table 4-6 shows that the FT FGHAZ has a slightly higher value for the lineal intercept (corresponding to a slightly larger equivalent subgrain size) compared to the H47 FGHAZ. Similarly, the FT ICHAZ region after creep testing shows a slightly larger lineal intercept value than the H47 ICHAZ, corresponding to a larger subgrain size. Both of these results together indicate that the HAZ on the FT side of the FT-H47 dissimilar Grade 91 weldment experienced more microstructural recovery, in the form of subgrain coarsening, than the H47 side.

4.3 Creep Behavior and Creep Damage Characterization of the H13-H47 Dissimilar Weldment

In conjunction with the previously discussed characterization of the FT-H47 weldment, another dissimilar Grade 91 weldment fabricated, creep-tested, and characterized as

Table 4-5. Summary of data from measurements of ferritic subgrain size from SE-SEM micrographs obtained from three separate regions on the FT and H47 sides of the FT-H47 weldment in the PWHT condition (746°C/1 h) prior to creep testing.

Material and Region	Measured number of boundary intercepts for 10kx images	Lineal intercept l for 10kx images (μm)
FT base metal	73.5	2.12
H47 base metal	65.5	2.38
FT FGHAZ	78.5	1.98
H47 FGHAZ	59	2.64
FT ICHAZ	83	1.88
H47 ICHAZ	70.5	2.21

Table 4-6. Summary of data from measurements of subgrain size from SE-SEM micrographs obtained from three separate regions on the FT and H47 sides of the FT-H47-1 cross-weld creep specimen after creep rupture testing at 627°C for 2080.4 h. When it was possible to evaluate more than one field, the average and sample standard deviation of each measured parameter were calculated and are provided in the table as (average ± SD); when only one micrograph was available, the singular values are provided in the table.

Material and Region	Measured number of boundary intercepts for 10kx images	Lineal intercept l for 10kx images (μm)
FT base metal	68.5	2.27
H47 base metal	46	3.38
FT FGHAZ	53 ± 13	3.07 ± 0.72
H47 FGHAZ	77 ± 0.71	2.03 ± 0.019
FT ICHAZ	51 ± 3.5	3.06 ± 0.22
H47 ICHAZ	68.5 ± 10.6	2.30 ± 0.36

part of the same industry project (Hoskins et al., 2017) was evaluated to enable a further comparison of the possible effect of N:Al ratio on Type IV creep behavior. In the H13-H47 weldment, the H13 and H47 base metals had N:Al ratios of 11.55 and 22.50, respectively. The following sections present a condensed summary of the H13-H47 creep specimen characterization in order to compare the Type IV creep damage in this weldment to the creep damage observed in the FT-H47 weldment.

4.3.1 Characteristics of the H13-H47 Weldment

An optical macrograph of the H13 to H47 weldment is shown in Fig. 4-54 and it is apparent that the macroscopic appearance is very similar to the FT-H47 weldment shown previously in Fig. 4-6. Comparative microhardness traverses for the H13-H47 weldment in the PWHT condition, corresponding to the red dashed lines in Fig. 4-54, are given in Fig. 4-55. Similar trends in hardness are observed for the H13-H47 weldment in the PWHT condition as for the FT-H47 weldment (refer to Fig. 4-17); the minimum and maximum hardness values for the H13 and H47 traverses are 209/208 HV500gf and 209/293 HV500gf, respectively. The microhardness data indicated that the FT-H47 and H13-H47 dissimilar weldments are expected to be similar in room-temperature mechanical properties and that any differences between the two weldments in terms of creep damage development would most likely not originate from hardness differences.

4.3.2 Creep Test Results and Creep Damage in the H13-H47 Weldment

Cross-weld creep testing was conducted on the "Header 13 to Header 47" (H13-H47) Grade 91 SMA weldment, previously characterized in the PWHT condition, as part of a previous industry project (Hoskins et al., 2017) according to the parameters described in Materials and Experimental Procedures. Fig. 4-56 shows the creep curve for the "H13-H47-2" cross-weld creep specimen which was tested at constant stress with temperature changes in order to measure creep rate values under different conditions (for Omega method testing which is not described in this dissertation). The creep parameters were

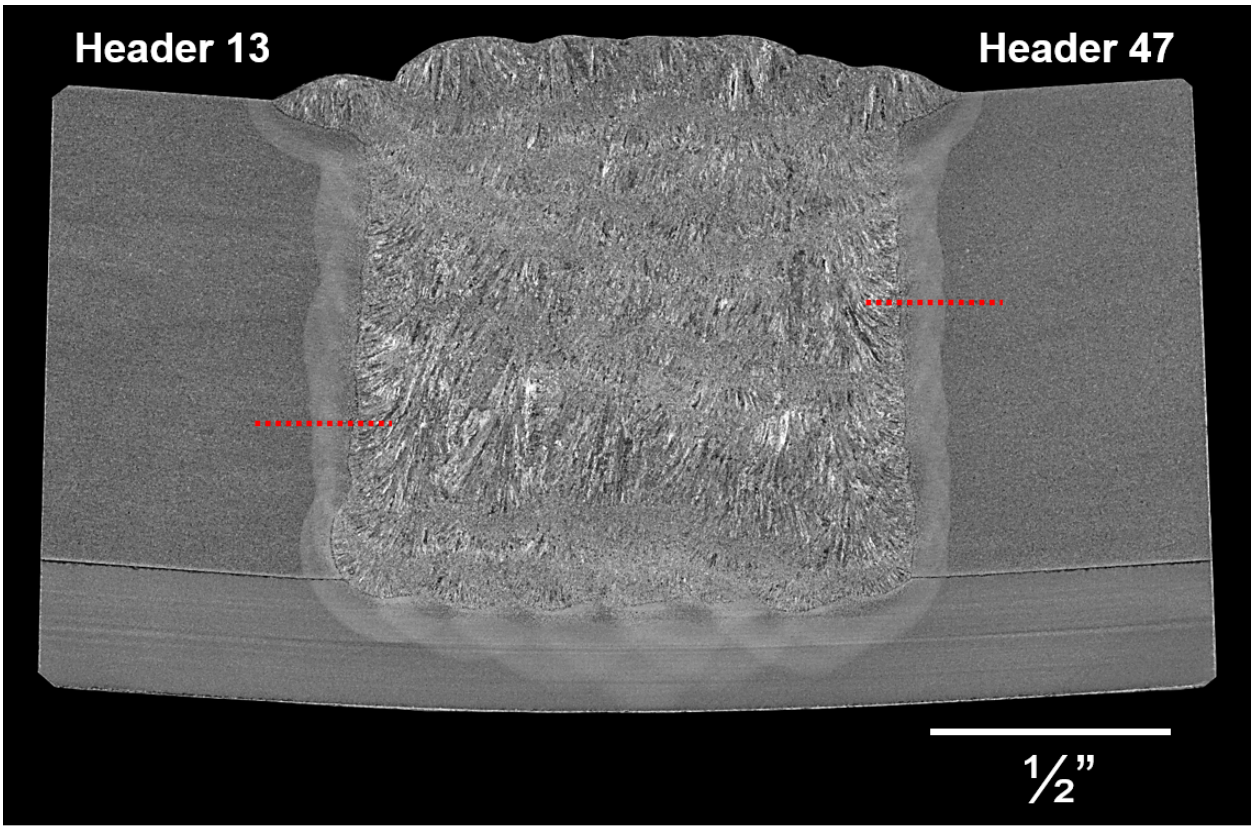


Figure 4-54. Optical macrograph of the H13 to H47 SMAW weldment in the PWHT condition, 746°C/1 h. The red dotted lines indicate the locations of microhardness traverses which are shown in Fig. 4-55. Etchant: Fry's reagent. Reproduced from (Hoskins et al., 2017).

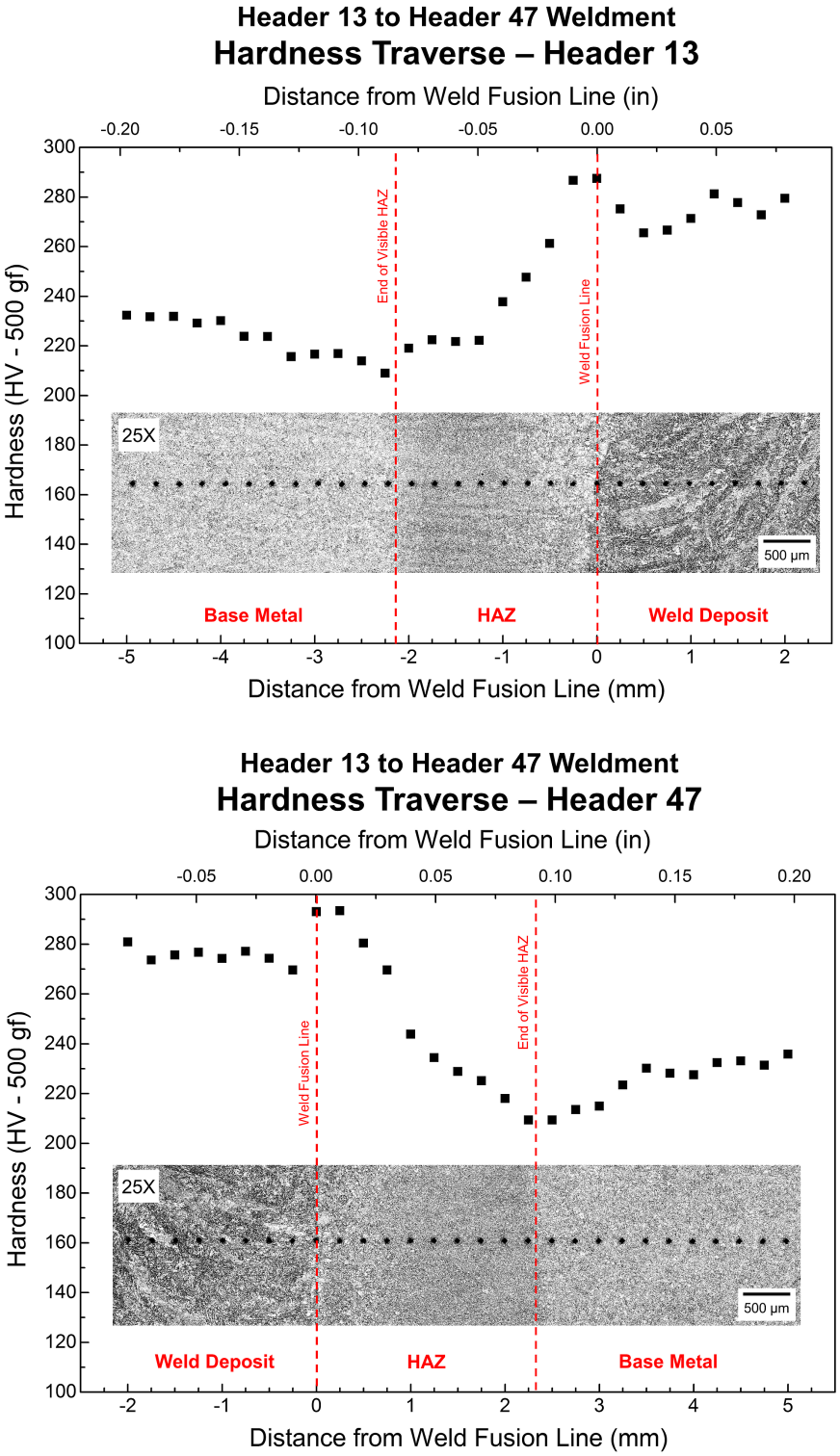


Figure 4-55. Microhardness traverses for the H13-H47 weldment in the PWHT condition: (A) H13 side of the weld (B) H47 side of the weld. Reproduced from (Hoskins et al., 2017).

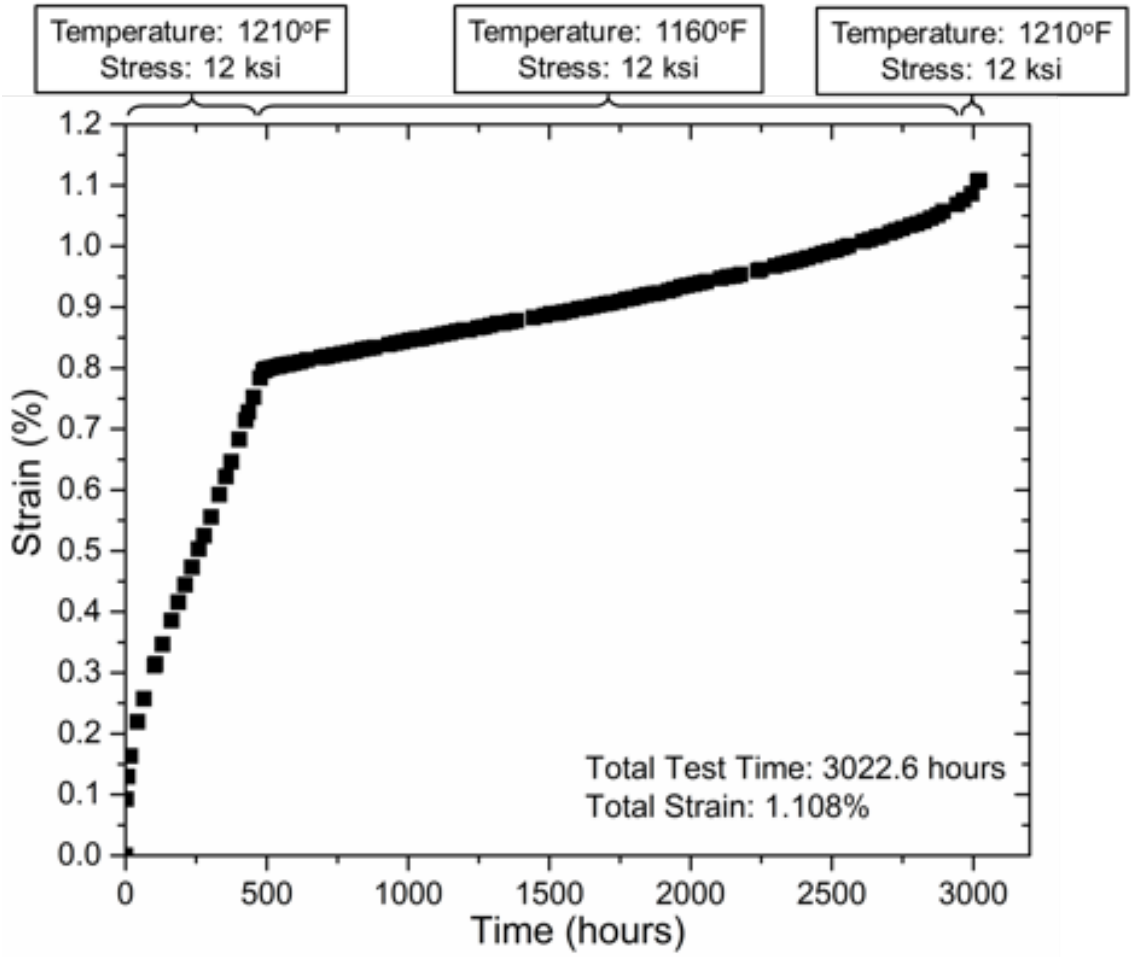


Figure 4-56. Measured creep curve obtained for the "H13-H47-2" cross-weld creep specimen which was extracted from the H13-H47 weldment and tested in the PWHT condition (746°C/1 h). Creep test parameters were altered at several points during the test in order to obtain creep rate data under different conditions; refer to the annotations above the graph for the parameters during each segment of testing. Reproduced from (Hoskins et al., 2017).

different from those for FT-H47 weldment and thus a direct cross-comparison cannot be made between the creep damage responses of the different HAZ regions (e.g. the H13 HAZ cannot be directly compared to the behavior of the FT HAZ); however, qualitative comparisons were still possible since the H47 base metal was utilized in both specimens and its creep damage behavior could be used as a "baseline."

A macrograph of the ruptured H13-H47 cross-weld specimen (see Fig. 4-57) after sectioning and metallographic preparation is shown in Fig. 4-58. From this figure, the H13-H47 specimen failed in the Type IV mode, similarly to the FT-H47 specimen in Fig. 4-20, since the macroscopically-apparent damage location is in the outer region of the H47 HAZ toward the base metal. While the FT-H47-1 specimen showed macro-cracking (rupture) only on one side (FT side), in the H13-H47-2 specimen a large macro-crack is present in the H47 HAZ and a smaller macro-crack is visible in the H13 HAZ. Simply on the basis of the observed damage locations in both specimens, it can be deduced that the base metals may be qualitatively ranked in terms of their susceptibility to Type IV creep damage, in increasing order (increasing susceptibility to Type IV creep damage) of H13, H47, and FT.

Representative micrographs showing the extent of Type IV creep damage in the H13 and H47 regions of the H13-H47 weldment are given in Fig. 4-59 and Fig. 4-60. Fig. 4-59 show a compilation of micrographs revealing the nature of Type IV creep damage near the top of the weld on the H13 side, adjacent to the micro-crack which developed in the HAZ. The optical micrograph in Fig. 4-59 shows a relatively high density of creep cavitation adjacent to the micro-crack propagation path, with the damage decreasing significantly over a short distance (several hundred microns). The SEM micrographs show the appearance of creep cavities in the H13 ICHAZ region at higher magnification and it is apparent that the cavity morphology is complex and irregular, with a similar appearance to creep cavitation in the FT-H47 weldment; additionally, the cavitation is still significantly isolated in nature, even at a location adjacent to rupture. Fig. 4-60

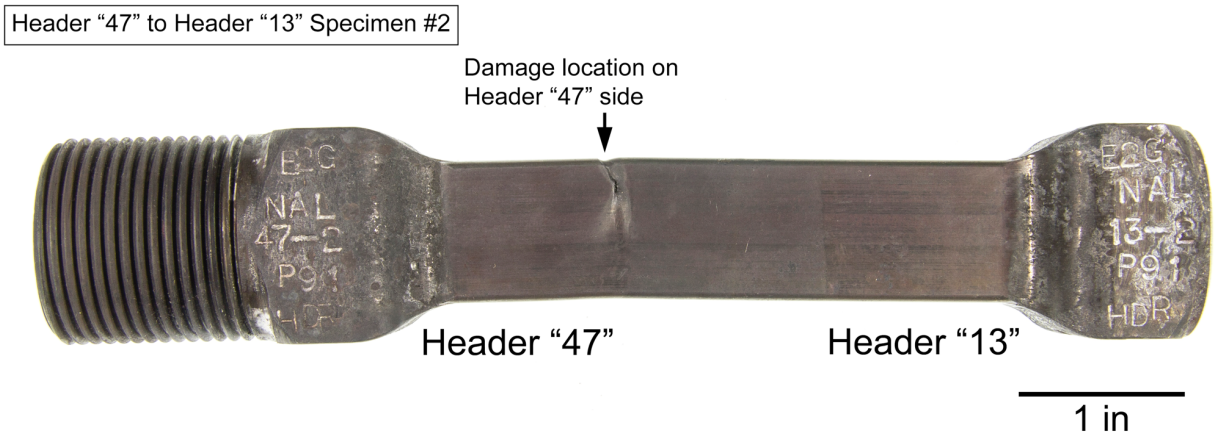


Figure 4-57. Photograph of the “H13-H47-2” cross-weld creep specimen extracted from the H13-H47 weldment and tested in the PWHT condition (746°C/1 h). The specimen was interrupted in the late stage of life (anticipated just prior to rupture) as shown by the formation of a significant crack on the H47 side of the weld. Refer to Fig. 4-56 for the creep curve and creep test parameters. Reproduced from (Hoskins et al., 2017).

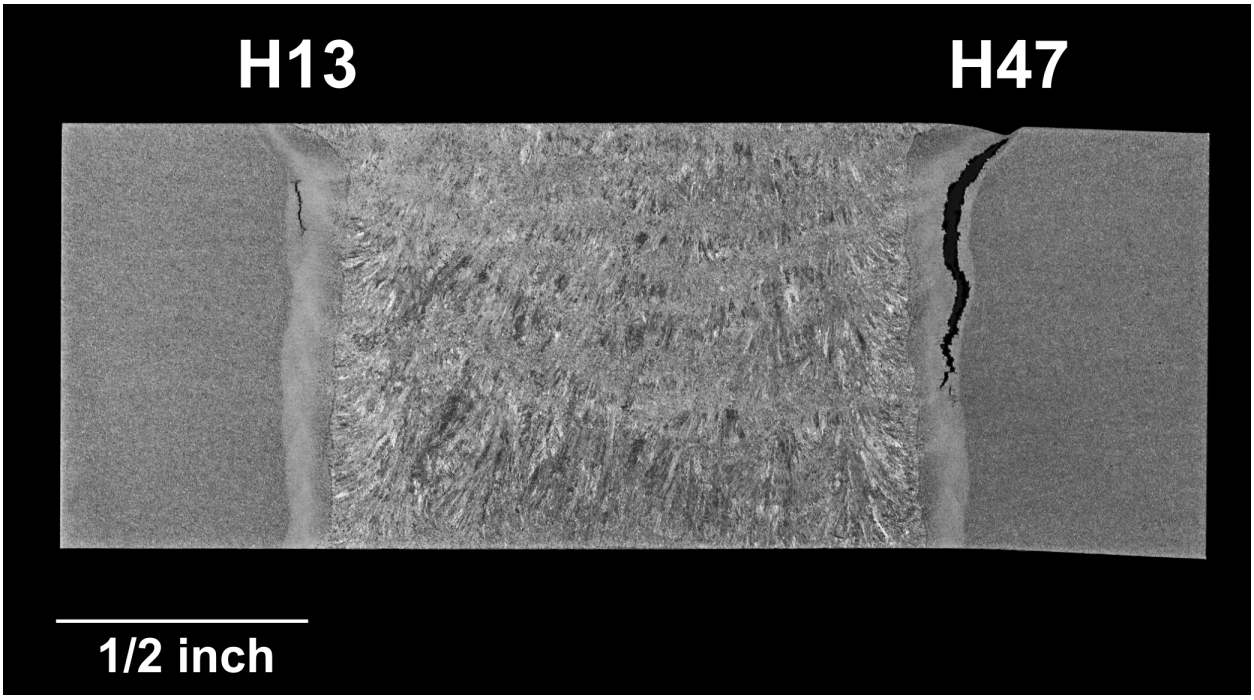


Figure 4-58. Macrograph of a metallographic section from the FT-H13-2 cross-weld creep specimen, PWHTed at 746°C/1 h. Creep tested at the parameters shown in Fig. 4-56 and terminated when failure appeared imminent, after a total test time of 3022.6 h. A large macro-crack formed in the outer portion of the H47 HAZ and a small macro-crack also formed in the outer portion of the H13 HAZ (in both cases, the cracking showed Type IV characteristics). The loading axis during creep testing corresponds to the horizontal direction (left-right) in the macrograph. Etchant: Fry's reagent. Adapted from (Hoskins et al., 2017).

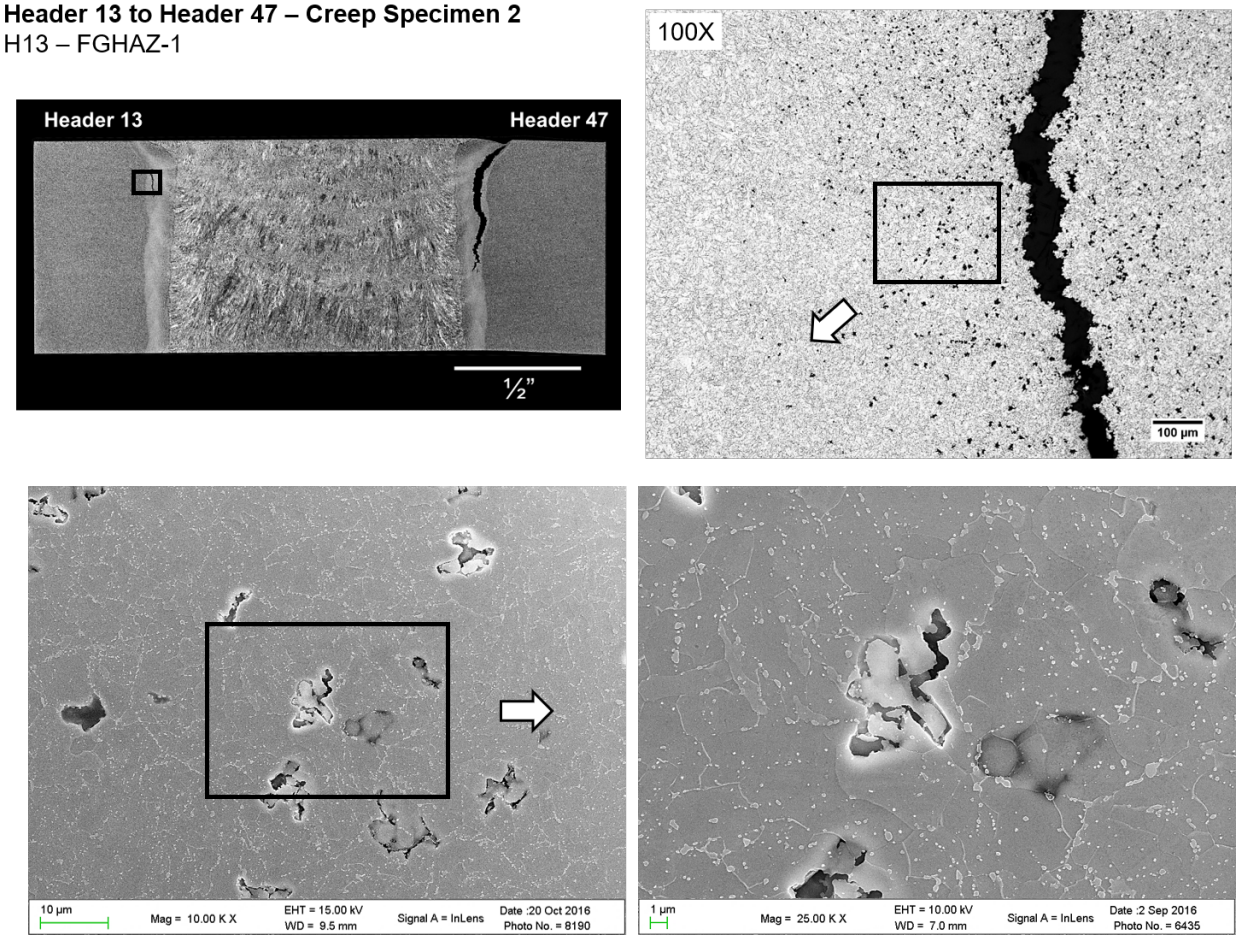


Figure 4-59. Micrographs illustrating creep damage in the ICHAZ at the HAZ-1 location on the H13 side of the H13-H47-2 cross-weld creep specimen. Etchant: 10% Nital.

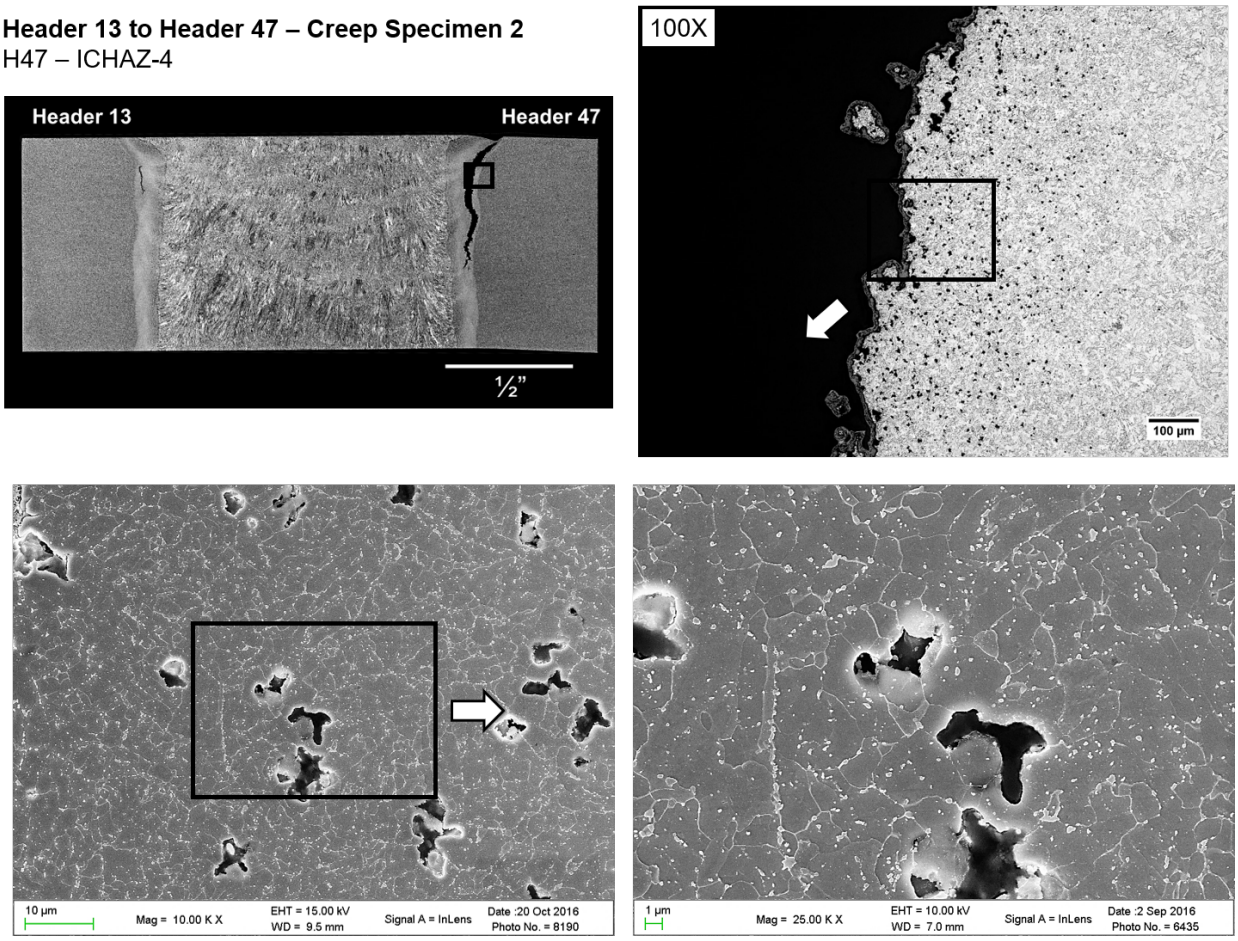


Figure 4-60. Micrographs illustrating creep damage in the ICHAZ at the HAZ-4 location on the H47 side of the H13-H47-2 cross-weld creep specimen. Etchant: 10% Nital.

shows a compilation of micrographs illustrating the extent of Type IV creep damage near the top of the weld, adjacent to the large macro-crack in the H47 HAZ. The optical micrograph shows a significant extent of isolated creep cavitation adjacent to the macro-crack propagation path; the corresponding SEM micrographs similarly show evidence of complex and irregular cavity morphology. Based on the micrographs in Fig. 4-59 and Fig. 4-60, the creep cavitation density appears to be of the same order of magnitude adjacent to the cracks on both sides of the H13-H47 creep specimen. However, the larger macro-crack on the H47 HAZ side of the weldment corresponds to a more advanced state of creep damage than the H13 side, and thus it can be concluded that the H47 material showed a greater susceptibility to Type IV creep damage accumulation than the H13 material.

4.4 Discussion of Type IV Creep Damage in Dissimilar Grade 91 Weldments

The results which were presented for the FT-H47 and H13-H47 dissimilar weldments showed that both weldments exhibited a non-uniform extent of Type IV creep damage on either side of the weld, particularly so for the FT and H47 HAZs. To recap briefly for the ruptured FT-H47 specimen, creep rupture occurred on the FT side of the weld accompanied by a slight amount of local plastic deformation and a high extent of creep cavitation in the FT HAZ, while the H47 HAZ showed essentially no plastic deformation and exhibited a much lower extent of creep cavitation at the time of rupture on the FT side. In contrast, in the terminated H13-H47 specimen, the H13 and H47 HAZs showed a more similar overall extent of damage and cracking was present in both HAZs, although the cracking was much more advanced (macro-cracking with probable imminent rupture) in the H47 HAZ. In order to understand the reason for these differences in creep deformation and Type IV creep damage based on the results presented in the previous sections of this chapter, possible explanations for the difference in creep damage development are discussed for the FT-H47 weldment and, to a lesser degree, the H13-H47 weldment in terms of the following:

- the base metal characteristics including chemical composition and inclusion content;

- microstructural characteristics of the base metals and HAZ regions in the PWHT and creep tested conditions.

After discussing the occurrence of Type IV creep damage in the FT-H47 and H13-H47 dissimilar Grade 91 weldments, several considerations regarding the relevance of the results to the general behavior of Grade 91 weldments are also discussed. Specifically, considerations of the limited number of Grade 91 materials involved in the current work (three heats used for dissimilar cross-weld testing) and of the short-term nature of the creep test data are addressed. Lastly, an overview is presented of proposed primary factors which influenced the development of Type IV creep damage in the currently evaluated dissimilar weldments.

4.4.1 Base Metal and Chemical Composition Characteristics

4.4.1.1 General Correlations Related to Chemical Composition and Type IV Creep Damage

In the recent literature, the effect of chemical composition on Grade 91 creep performance of base metals and of weldments (Type IV) has been of primary interest, and thus this aspect will be discussed in more detail first regarding a potential explanation for the difference in creep damage occurrence in the FT and H47 HAZ regions. Considering chemical composition in general, EPRI publications (*Life Management of 9%Cr Steels: Evaluation of Metallurgical Risk Factors in Grade 91 Steel Parent Material*, 2018; *The Benefits of Improved Control of Composition of Creep-Strength-Enhanced Ferritic Steel Grade 91*, 2014) as well as work by other researchers (Abe, 2010; Maruyama et al., 2017; Sawada et al., 2014) have considered some composition-related explanations for variations in creep strength of CSEF steels. EPRI's recommendations for composition limits for Grade 91 are discussed in "The Benefits of Improved Control of Composition of Creep-Strength-Enhanced Ferritic Steel Grade 91" (*The Benefits of Improved Control of*

Composition of Creep-Strength-Enhanced Ferritic Steel Grade 91, 2014) and these values were shown for comparison to the measured FT and H47 compositions in Table 3-1. The FT and H47 base metals conform to all the requirements of the applicable ASME standard and to nearly all the requirements of the stricter EPRI recommendations. The exceptions where the FT and H47 materials deviate from the EPRI recommendations are the H47 nickel content (0.350 wt.% Ni) which exceeds the recommended value of <0.20 wt.% Ni, and the FT and H47 copper contents (0.126 wt.% and 0.142 wt.%, respectively) which exceed the recommended value of <0.10 wt.% Cu. These deviations of the FT and H47 compositions from the published EPRI guidelines are discussed further along with potential effects of specific elements which satisfied the guideline values.

Regarding the Ni content, the main detrimental effects are summarized (*The Benefits of Improved Control of Composition of Creep-Strength-Enhanced Ferritic Steel Grade 91*, 2014) as a tendency to exacerbate microstructure recovery, to potentially form embrittling grain-boundary phases in conjunction with impurity elements, and to promote detrimental grain boundary segregation of elements such as Sb and Si. At a basic level, the considerations regarding Ni content do not explain the FT-H47 weld behavior since the H47 side with higher Ni content showed the lower extent of Type IV creep damage. As discussed in more detail later, the estimated A1 temperature for both materials is identical irrespective of the significantly higher Ni content of H47, so there is no expected effect of the Ni content on tempering resistance. The validity of the Ni<0.20 wt.% recommendation has been questioned by Maruyama et al. (Maruyama et al., 2017), regarding the sufficiency of the data used as the basis for showing the benefit of the reduced Ni content to improve creep performance of Grade 91. Maruyama et al. reported that their evaluation of multiple Grade 91 heats showed no correlation between rupture strength and Ni content. They noted that Cr content was the only evaluated element in their study which showed a correlation with creep strength in the low stress/intermediate temperature regime, which was attributed to the influence of

higher Cr content on reducing the rate of subgrain recovery and growth. In contrast to the Ni content, the Cr content correlation is in more agreement with the FT and H47 base metal behavior since the H47 base metal has higher Cr content than FT (8.653 wt.% vs. 8.506 wt.%, respectively).

With regard to impurity element content, the main detrimental elements to Grade 91 creep performance are identified as S, As, Cu, Sn, and Sb (*Life Management of 9%Cr Steels: Evaluation of Metallurgical Risk Factors in Grade 91 Steel Parent Material*, 2018). The recent recommendation by EPRI for Grade 91 steel is for the target sulfur content to be ≤0.003 wt.% and the H47 base metal meets this requirement, while the FT material has more than twice the sulfur content at 0.008 wt.%. Research on metallurgical risk factors in Grade 91 steel has suggested that sulfur content is the primary correlating factor with low creep ductility (*Life Management of 9%Cr Steels: Evaluation of Metallurgical Risk Factors in Grade 91 Steel Parent Material*, 2018). Thus, the sulfur content difference between the two materials agrees with the trend of creep damage occurrence and is a possible explanation for the observed difference. However, the other impurity elements are not as clearly in agreement: although the FT material does have higher Cu content (0.142 wt.%) compared to the H47 level (0.126 wt.%), both materials have identical As content (0.007 wt.%); the FT material has lower Sb content than H47; and both materials have the same Sn content. The effect of copper on Grade 91 creep performance is not very clear in the literature; reportedly a correlation was observed between poor creep ductility and Cu content as re-stated by EPRI [*The Benefits of Improved Control of Composition of Creep-Strength-Enhanced Ferritic Steel Grade 91* (2014), but the same original authors also reported in a different publication (Masuyama et al., 2004) that Cu content did not have an effect on creep behavior of Grade 91 at 600°C. Furthermore, EPRI has recommended relaxing their earlier recommendation on Cu content from <0.10 wt.% Cu to <0.15 wt.%, which both FT and H47 materials then satisfy. Thus, the

Cu content of the two materials does not appear to be significant in explaining the creep damage difference.

The effect of chemical composition on critical transformation temperature was also considered as a possible explanation for the difference in Type IV creep damage extent for the FT and H47 base metals. Although the FT and H47 base metals received identical N&T heat treatment prior to welding and also received identical PWHT heat treatments, differences in the lower and upper critical transformation temperatures (A_1 and A_3) between the two materials could possibly lead to unequal severity of tempering and unequal alteration of microstructure. The equilibrium lower transformation temperature was chosen as the basis for comparison since PWHT represents a quasi-steady state condition and PWHT is intentionally conducted below the A1 to avoid forming a partially-transformed microstructure. Below the A1, a disparity in severity of tempering and microstructural evolution could occur in the following manner: if the selected PWHT temperature (746°C) is near the A1 temperature of one material while being significantly lower than the A_1 temperature of the other material, such a difference could lead to a more susceptible microstructure (more severely tempered during PWHT) in one HAZ as compared to the other. To explore this possibility, predictive formulae for the A_1 temperature of Grade 91 steels as developed by Wang (Wang, 2010) were utilized to estimate the A_1 temperatures for the FT and H47 base metals. Wang reported that the formula for the A_1 temperature of Grade 91 steel containing 0.12-0.40 wt.% Cu is given by:

A1 (°C) = 2113 - 243*C* - *174*N + 87.5*Si* - *24.4*Mn + 16.676*Cr2* – *271.81*Cr - 365.45*Ni2* + *153.05*Ni + 164*Mo2* - *299.2*Mo + 1320*V2* - *570*V - 194.3Cu2 + 83.9*Cu (Eq. 4-1)

Using this formula and the measured chemical compositions given in Table 3-1, the A_1 temperatures of the FT and H47 base metals were estimated to be *806°C* and *808°C*, respectively. The PWHT temperature of 746°C is quite close to the calculated A_1

temperatures of both materials (~0.9 A_1) and there is essentially no difference in the A_1 temperatures of the two base metals. Thus, the relative effect of the PWHT temperature, with regard to microstructure alteration, cannot account for the difference in creep damage development between the FT and H47 sides of the weldment.

Considering the fact that the FT material is a forging and the H47 material is plate, Jabar et al. (Jabar et al., 2021) showed that different product forms of Grade 91 steel exhibit significantly different chemical segregation patterns with a consequent effect on precipitate formation. They evaluated the segregation of Mo, Cr, Nb, and V in a Grade 91 barrel piece (from a seamless pipe section formed by drawing) and a Grade 91 forging, and they reported that the barrel piece showed evidence of banding oriented parallel to the barrel axis while the forging showed a much more random segregation pattern. The most significant segregation was observed for Mo and Nb and the segregation of these elements resulted in a factor of two difference in Laves phase content when comparing solute-enriched and solute-depleted segregated regions. Although only Laves phase was quantified, the authors pointed out that elemental segregation will affect the formation of other secondary phases also, not only Laves phase. The results of Jabar et al. demonstrate that elemental segregation in different Grade 91 product forms affects the resulting precipitate formation and thus the same behavior may be expected for the FT (forging) and H47 (plate) base metals in the current work.

4.4.1.2 Correlation of Base Metal Inclusion Content with Type IV Creep Damage

Additionally with regard to chemical composition, the results for base metal inclusion content were also considered for understanding the differences in creep cavitation behavior between the FT and H47 base metals. Data from the literature (*Life Management of 9%Cr Steels: Evaluation of Metallurgical Risk Factors in Grade 91 Steel Parent Material*, 2018) has indicated that there is a general correlation between increasing sulfur content and higher inclusion density, as shown in Fig. 4-61; however this is not exclusively the

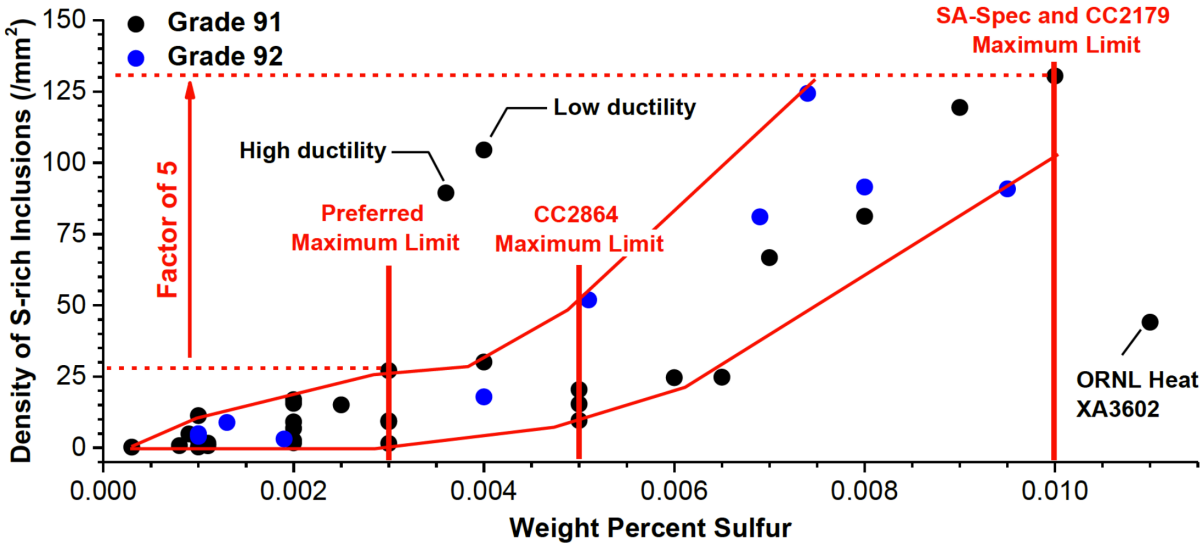


Figure 4-61. Literature correlation between sulfide inclusion density and sulfur content for Grade 91 and Grade 92 CSEF steels. There is a general trend between increased sulfur content and increased inclusion density, although the correlation is not linearly proportional and some materials such as Heat XA3602 deviate from this behavior. Reproduced from (*Life Management of 9%Cr Steels: Evaluation of Metallurgical Risk Factors in Grade 91 Steel Parent Material*, 2018).

case since some higher sulfur materials did not exhibit a high inclusion density. This is similar to the current research in which the highest sulfur material, the FT forging, did not exhibit a higher average inclusion density than the H47 material. The inclusion analysis of the H47 base metal based on backscatter SEM imaging at 2500x indicated that the inclusion density was on the order of 60-90 mm^{-2} (average: 80 mm^{-2}) which is classified as a "medium level" inclusion density, which has been associated with low/high creep ductility (*Life Management of 9%Cr Steels: Evaluation of Metallurgical Risk Factors in Grade 91 Steel Parent Material*, 2018). In comparison, the FT base metal showed an inclusion density on the order of 50-60 mm^{-2} (average: 56 mm^{-2}) which is categorized as a "low level" inclusion density heat. However, it must be noted that the average inclusion density values of the FT material are significantly affected by the variability between different measurement areas. Table 4-3 previously showed also that the inclusion characteristics for the FT and H47 base metals are fairly similar to one another. The inclusion density of the FT material is slightly lower than the H47 material, and the median inclusion size is also slightly lower in the FT material, while there is not a meaningful difference in area fraction and mean inclusion size. As noted earlier, the mean inclusion size of the FT material in particular is skewed by the presence of significantly larger outlier particles. Some data from the literature has indicated that for mechanical properties in general at room temperature and high temperature, inclusions can act as stress concentration sites in the matrix, with the stress concentration effect being dependent on the inclusion morphology and size (Arreola-Herrera et al., 2018; Wang et al., 2020). Comparing Fig. 4-2 and Fig. 4-5, the inclusion particle distribution for the FT material is much broader than for the H47 material, as would be reasonably expected for a forging compared to plate since the plate would experience more total deformation during forming with greater break-up of inclusions.

Comparing the trends in the FT and H47 inclusion results with the characterized Type IV creep damage shown in Section OLM and SEM Characterization of Creep Damage in

the FT-H47 Weldment, it is apparent that the inclusion results do not show a correspondingly significant difference with the observed Type IV cavitation. The difference in cavitation extent is much greater than the difference in inclusion density or inclusion area fraction, as shown by comparing the qualitative damage appearance in Fig. 4-22 for the FT ICHAZ and in Fig. 4-34 for the H47 ICHAZ; these two figures compare a "less damaged" FT ICHAZ region with a "more damaged" H47 ICHAZ to give a worst case comparison. The difference in inclusion density between the FT and H47 materials is significantly less than that reported (*Life Management of 9%Cr Steels: Evaluation of Metallurgical Risk Factors in Grade 91 Steel Parent Material*, 2018) for two heats of Grade 91 steels which showed significantly different creep damage tolerance. The two heats identified as B2 (barrel piece, seamless pipe product) and TP1 (forged tee product) exhibited inclusion density values of 141.6 features/mm^2 and 17.8 features/mm^2, respectively, with the corresponding inclusion distribution shown in Fig. 4-62. In this case, the B2 material had higher content of sulfur and aluminum (0.010 wt.% S and 0.040 wt.% Al) than the TP1 material with 0.002 wt.% S and 0.020 wt.% Al. These general trends line up with FT and H47 materials in terms of sulfur and aluminum content (see Table 3-1). However, the TP1 material with fewer inclusions and less creep damage exhibited a greater degree of elemental segregation and Laves phase formation than the B2 material, as shown by Jabar et al. (Jabar et al., 2021); these factors would initially seem to be detrimental to creep behavior of the TP1 material, so the reason for the improved creep damage resistance of the TP1 material is not completely clear.

4.4.1.3 Correlation of Nitrogen to Aluminum (N:Al) Ratio with Type IV Creep Damage

Lastly, another compositional factor discussed in the literature regarding its potential effect on Type IV creep behavior of Grade 91 weldments is the nitrogen to aluminum ratio (N:Al ratio). The significance of the N:Al ratio in Type IV creep behavior reportedly arises from ensuring adequate N content for forming MX precipitates after

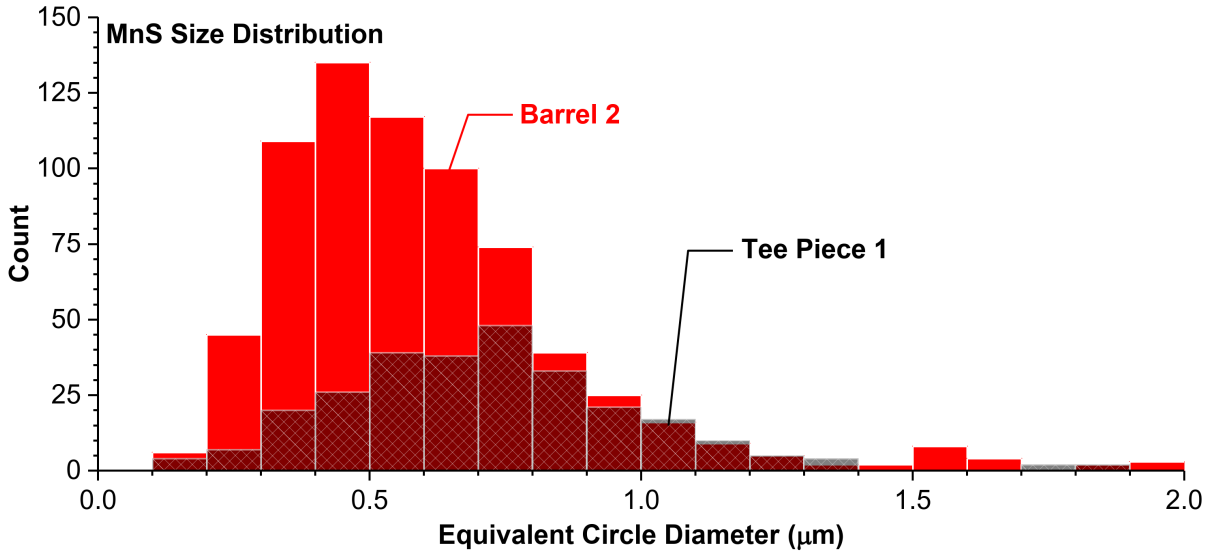


Figure 4-62. Comparison of the size distributions of MnS inclusions observed for two Grade 91 base metals which exhibited widely different creep damage resistance. The Barrel 2 material was reported as having low creep ductility and low damage resistance (high extent of creep cavitation) while the Tee Piece 1 material exhibited a high ductility and high damage resistance (low extent of cavitation). The Barrel 2 material is seamless piping while the Tee Piece 1 material is a forging. Reproduced from (*Life Management of 9%Cr Steels: Evaluation of Metallurgical Risk Factors in Grade 91 Steel Parent Material*, 2018).

accounting for the consumption of N by nitride-forming elements such as Al and Ti, and concurrently from controlling the formation of aluminum nitrides which have been associated with reduced Grade 91 creep strength (*The Benefits of Improved Control of Composition of Creep-Strength-Enhanced Ferritic Steel Grade 91*, 2014). As discussed in the literature review, maintaining optimum MX precipitation is desirable for stabilizing the tempered martensitic lath structure because MX precipitates are considered more effective than $M_{23}C_6$ carbides for impeding substructure recovery, since MX precipitates generally show a greater resistance to coarsening during creep than $M_{23}C_6$. Correspondingly, a high N:Al ratio is recommended by some researchers (*The Benefits of Improved Control of Composition of Creep-Strength-Enhanced Ferritic Steel Grade 91*, 2014), based on the preceding statements and also on data indicating a correlation between higher N:Al ratio and greater resistance to hardness degradation during tempering as shown in Fig. 4-63. A minimum N:Al ratio of four, on a weight percent basis, has been recommended (*The Benefits of Improved Control of Composition of Creep-Strength-Enhanced Ferritic Steel Grade 91*, 2014) based on this data and also based on data from Brett et al. (Brett et al., 2005) which empirically correlated low N:Al ratio values to an increased extent of creep cracking in stub welds.

Historically, the relevant standards for Grade 91 such as ASME SA-387 have not included a requirement for N:Al ratio, and have only included broad limits for Al and N content. This most likely originates from the fact that N:Al ratio was not included in the original ORNL specifications for commercial production of Grade 91 steel (DiStefano, 1986). However, the aforementioned findings have led to the proposal and introduction of a new category of Grade 91 steel, i.e. Grade 91 "Class 2" conforming to the stricter composition limits developed by EPRI (*The Benefits of Improved Control of Composition of Creep-Strength-Enhanced Ferritic Steel Grade 91*, 2014) with a minimum required N:Al ratio of four. This new specification has recently been introduced in the ASME Boiler and Pressure Vessel Code as a code case (Maruyama et al., 2017). The

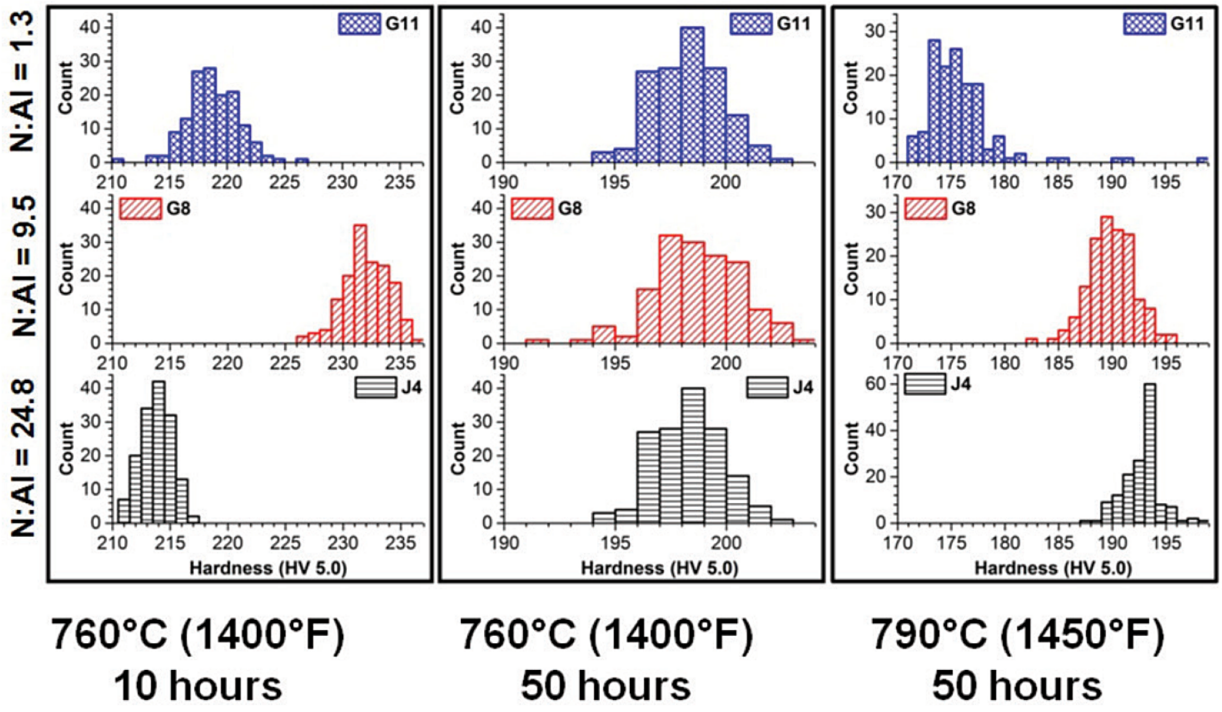


Figure 4-63. Comparison of the tempering resistance for multiple heats of Grade 91 steel with different N:Al ratios. The Grade 91 material with the highest N:Al ratio of 24.8 showed the highest average hardness and the smallest spread in hardness values after the most severe tempering treatment (790°C/50 h). Reproduced from (*The Benefits of Improved Control of Composition of Creep-Strength-Enhanced Ferritic Steel Grade 91*, 2014).

stated intention of developing and introducing the new composition limits with stricter controls on certain elements is to avoid cracking problems during alloy production/processing, to minimize embrittlement, and to minimize the occurrence of Grade 91 material with low creep ductility (*The Benefits of Improved Control of Composition of Creep-Strength-Enhanced Ferritic Steel Grade 91*, 2014). Such a correlation between low N:Al ratio and low creep ductility has also been reported in the literature as shown by the data in Fig. 4-64 (*Life Management of 9%Cr Steels: Evaluation of Metallurgical Risk Factors in Grade 91 Steel Parent Material*, 2018). Notably, the introduction of the new Grade 91 composition does not appear to be intended to eliminate the occurrence of Type IV cracking in Grade 91 weldments or to lead to a re-consideration of the currently mandated weld strength reduction factors (e.g. in the ASME Boiler and Pressure Vessel Code Section I, Table PG-26) which severely reduce the feasibility of subcritically postweld heat-treated CSEF weldments including Grade 91.

Despite the recent shift in the ASME code to include a Grade 91 specification with a requirement on N:Al ratio, there is disagreement in the literature regarding the magnitude and importance of the effect of N:Al on Type IV creep behavior of Grade 91 weldments. Some contrary data was published by Maruyama et al. (Maruyama et al., 2017) in which they examined potential reasons for variability in creep strength among fourteen different Grade 91 heats, encompassing plate and tube products. In their results, shown in Fig. 4-65, Maruyama et al. reported no correlation between N:Al ratio and creep strength considering a data set in which N:Al ratio varied from <4 to 100. Accordingly, Maruyama et al. took the position that higher values of the N:Al ratio, greater than the stoichiometric ratio of 7.7 by atomic percent (corresponding to a ratio of 4 by weight percent), are not correlated with better creep performance. Thus, in their view it is only necessary to have nitrogen content greater than the aluminum content in order to form "a sufficient number of fine MX precipitates" (Maruyama et al., 2017),

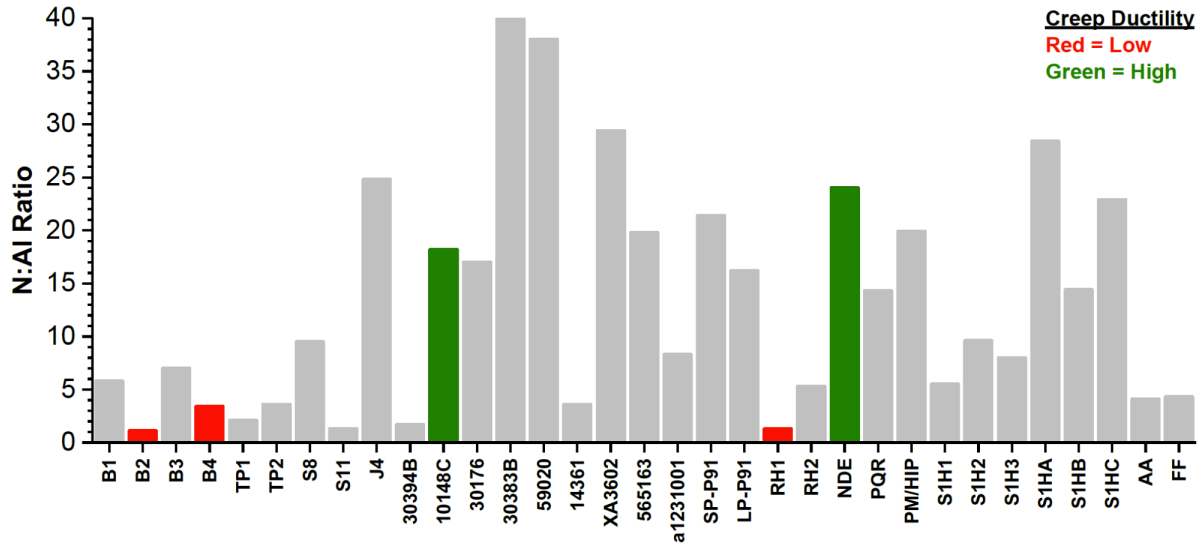


Figure 4-64. Correlation between N:Al ratio and creep ductility for Grade 91 materials with reported high inclusion density. The colored bars indicate heats with high inclusion density, while gray bars correspond to other heats which were not specifically included in this comparison. Red bars indicate low creep ductility and green bars indicate low ductility. Reproduced from (*Life Management of 9%Cr Steels: Evaluation of Metallurgical Risk Factors in Grade 91 Steel Parent Material*, 2018).

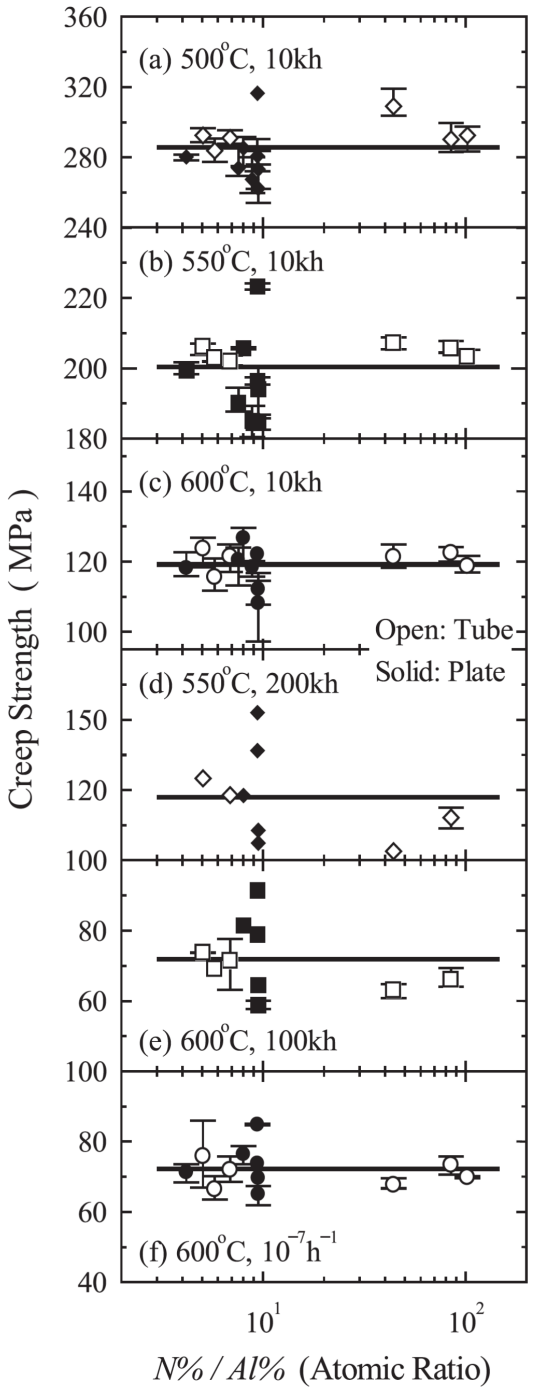


Figure 4-65. Effect of N:Al ratio (atomic percent basis) on creep rupture strength (a-e) and creep deformation resistance (f) of Grade 91 steel. The plots in (a-e) show the creep strength corresponding to the indicated lifetime (10kh, 200kh, or 100kh) at the indicated test temperatures (500°C, 550°C, or 600°C). The plot in (f) shows the stress required to produce a minimum creep rate of 1E-7 per hour at 600°C. In all plots, no trend between creep strength and N:Al ratio is apparent across the evaluated range of N:Al ratio. Reproduced from (Maruyama et al., 2017).

although this is admittedly qualitative. Abe has pointed out (Abe, 2008) that the important variable is the free nitrogen after considering nitrogen consumption by AlN and TiN. In this regard, Abe et al. (Abe et al., 2007) showed a positive correlation, given in Fig. 4-66, between increased available nitrogen content and rupture time for 12Cr-1Mo-1W-0.3V martensitic steel. Available nitrogen was defined as N content minus Al and Ti content, and a proportional correlation between increasing available nitrogen and increased rupture time was shown at lower stresses (<100 MPa) that are more typical of service conditions; notably, no correlation was apparent at higher stresses, e.g. >200 MPa. It seems that BN formation should also be considered and the available nitrogen should be adjusted for boron content; thus the free nitrogen available for MX precipitate formation may be taken as

$$\text{Available N} = \text{wt.\% N} (\text{wt.\% Ti} - \text{wt.\% Al} - \text{wt.\% B}) \qquad \text{(Eq. 4-2)}$$

The role of N:Al ratio on reducing the formation of AlN has also been used (*The Benefits of Improved Control of Composition of Creep-Strength-Enhanced Ferritic Steel Grade 91*, 2014) as an argument to support the requirement for a minimum value of N:Al ratio. However, the precise mechanism by which AlN formation increases the creep damage susceptibility of Grade 91 steel remains unclear (*Life Management of 9%Cr Steels: Evaluation of Metallurgical Risk Factors in Grade 91 Steel Parent Material*, 2018). Brett et al. (Brett et al., 2005) showed a correlation between decreasing N:Al ratio and an increased occurrence of cracking in stub welds and pointed out that the presence of AlN particles had been observed in Grade 91 material with poor creep strength. However, direct observation of the proposed mechanism, i.e. a reduction of MX precipitate fraction due to AlN formation in materials with low N:Al ratio, with a consequent reduction in substructure stabilization, appears to be lacking.

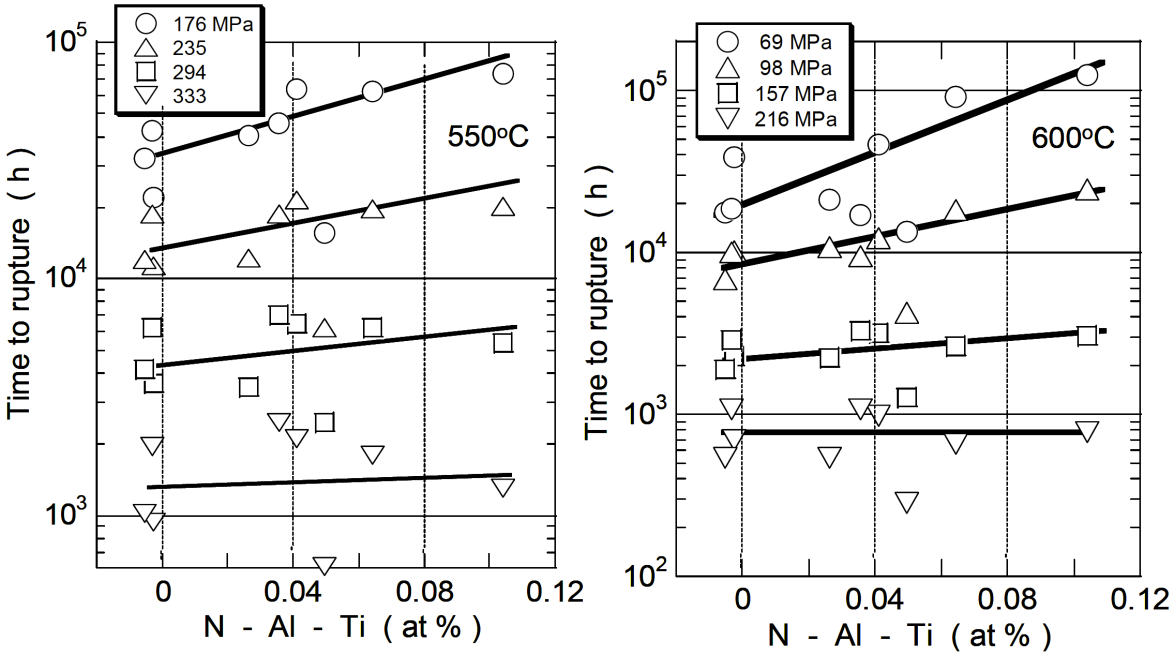


Figure 4-66. Comparisons of rupture time as a function of available nitrogen content (N - Al - Ti) for 12Cr-1Mo-1W-0.3V martensitic steel when tested at temperatures of 550°C and 600°C. Note that at 600°C, for example, there is no correlation between rupture time and available nitrogen at high stress, but a clear trend becomes evident as stress decreases. Reproduced from (Abe et al., 2007).

Considering this information from the literature, the creep behavior of the three Grade 91 base metals evaluated in the current dissertation suggests a lower importance of the N:Al ratio on controlling the Type IV creep damage susceptibility. Recalling from Table 3-1, the H47 base metal has an N:Al ratio of 22.5 compared to a N:Al ratio of 2.41 for the FT material, while the H13 material has an intermediate N:Al ratio of 11.33. As shown in the creep damage characterizations described previously in this chapter, both dissimilar weldments (FT-H47 and H13-H47) showed the formation of Type IV creep damage in HAZ. The difference in N:Al ratios for the FT-H47 dissimilar weldment agreed with the observed extent of creep damage since the FT material showed a much greater extent of Type IV creep damage than the H47 material. However, the trend did not hold for the H13-H47 weldment, since the H13 material with a lower N:Al ratio (approximately 50% lower) exhibited a reduced extent of Type IV damage than the higher N:Al ratio, H47 material as shown in Fig. 4-58. For the purpose of further comparison, based on the statements of Abe et al. (Abe et al., 2007) and the proposed adjusted equation in Eq. 4-2, the calculated available nitrogen values for the FT, H47, and H13 base metals are 0.021 wt.%, 0.0416 wt.%, and 0.0293 wt.%, respectively, based on the measured Al, Ti, and B contents of the three base metals. The same disagreement in behavior is apparent when considering available nitrogen as when considering N:Al ratio, in that the H13 material with a lower available nitrogen showed decreased Type IV creep damage compared to the H47 material with higher available nitrogen. Therefore, the observations from the current work suggested that N:Al ratio alone is not an unequivocal indicator of Type IV creep damage susceptibility regardless of other factors.

Additionally, as shown previously in Fig. 4-48 and Fig. 4-51, the H47 material shows a greater extent of fine precipitates in the base metal and ICHAZ of the weldment in the PWHT condition. Although these precipitates were not positively identified due to the limitations of SEM for analyzing fine particles, based on literature it is reasonable to

infer that the fine particles observed in H47 are MX precipitates, and thus there is a possible connection between the higher N:Al ratio of H47 and the greater proportion of fine precipitates, and consequently a potential connection with the lower extent of creep damage in the H47 HAZ. However, this connection between higher N:Al ratio in H47 and greater extent of fine precipitates cannot be stated definitively since the complete prior processing history of the FT and H47 materials is unknown; factors originating from prior processing, such as precipitate coarsening during forging or annealing with a subsequent effect on particle dissolution and re-precipitation during welding, may have influenced the precipitate size distributions in the FT and H47 ICHAZs in addition to any influence of N:Al ratio.

4.4.2 Microstructure Characteristics After PWHT and Creep Testing

The microstructural evaluation for the FT-H47 weldment in the PWHT and creep-exposed conditions as reported in Section 4.2.5 Evaluation of Microstructural Characteristics in the FT-H47 Weldment by Image Analysis revealed several differences which correlated with the observed extent of Type IV creep damage in the FT and H47 HAZs. The results of the microstructure analysis showed (i) differences in the precipitate size distribution and density in the FT and H47 ICHAZ regions which correlated with similar trends observed in the initial base metal condition after PWHT (described in Evaluation of Grade 91 Base Materials), and (ii) differences in subgrain size which aligned with the trends in precipitate characteristics. These observations suggested that the changes in subgrain size could be linked to precipitate evolution, as expected based on the discussion of carbide-stabilized substructure hardening in the literature review. These two aspects, precipitate characteristics and subgrain size, are discussed further in this section to understand how the microstructure of the FT and H47 HAZ regions contributed to the preferential occurrence of Type IV creep damage and to consider possible explanations for the FT and H47 microstructure differences.

The first aspect of the FT and H47 microstructures relating to the relative extent of Type IV creep damage is the size distribution and density of precipitates in the HAZ. The literature review established that obtaining and maintaining a fine dispersion of $M_{23}C_6$ and MX precipitates on subgrain boundaries and within the subgrain interiors is necessary for optimum creep properties in CSEF steels, since these precipitates impede subgrain coarsening by acting as obstacles to dislocation motion and recovery. The FT ICHAZ showed a reduced fraction of fine precipitates compared to the H47 ICHAZ as shown in Fig. 4-51 and Fig. 4-53. Fig. 4-51 showed an approximately 30-40% decrease in particles between 0.005 to 0.015 μm^2 in size, while Fig. 4-53 showed an approximately 50% decrease in particles <0.005 μm^2. As Maruyama has stated, the strengthening effect is inversely proportional to the precipitate size and thus a material with a greater extent of fine precipitates (H47) will exhibit greater strengthening. Thus, the lesser extent of fine precipitation in the FT ICHAZ is identified as a primary cause of the apparent difference in microstructural stability between the FT and H47 HAZs since precipitates are responsible for impeding subgrain coarsening.

The trend in the FT versus H47 ICHAZ precipitate distributions is linked to the initial base metal precipitate condition. Fig. 4-48 showed that the FT and H47 base metals contained different amounts of fine precipitates after PWHT. Although FT and H47 material in the pre-weld, N&T condition was not available for evaluation in the current research, it is reasonable to presume that the same general trend in particle distribution in the N&T condition would be preserved through the PWHT exposure. The majority of precipitation in FT and H47 would have already occurred during the pre-weld temper, based on the results of Vitek and Klueh (Vitek and Klueh, 1983) where precipitation in Grade 91 is complete after tempering at 700-780°C for 1 h; the known N&T heat treatment for the FT and H47 base metals is similar to this level of tempering. Assuming that the PWHT precipitate distribution is representative of the N&T precipitate distribution, the effect of the base metal precipitate condition on the ICHAZ precipitate

distribution after PWHT—and therefore on the precipitate distribution at the beginning of creep exposure—is due to the thermal exposure of the various HAZ thermal cycles and re-precipitation afterward during PWHT. These factors are in turn influenced by the kinetics of carbide dissolution.

The kinetics of carbide dissolution have an effect on the final precipitate condition of the FT and H47 ICHAZs at the start of creep exposure. When creep exposure begins, the ICHAZ has proceeded through a sequence of conditions—the initial BM tempering, the HAZ thermal cycle, and tempering during PWHT—each of which involves heating and cooling and thus a combination of simultaneous precipitate formation and dissolution can be expected (Robson and Bhadeshia, 1996). Precipitation during the initial tempering step and during PWHT are affected by the extent of precipitate dissolution during the prior thermal exposure (austenitization and the HAZ thermal cycle, respectively). The extent of dissolution will affect the availability of alloying elements in solid solution and also the preferential growth of remaining undissolved particles at the expense of newly precipitating fine particles. Liu et al. (Liu et al., 1991) showed for a Fe-Cr-C alloy that while complete transformation from ferrite to austenite occurred rapidly at a temperature within the austenite single phase field, slightly above the A_3 temperature, carbide dissolution proceeded much more slowly. After heat treatment of the alloy at 735°C for 300 h to produce an equilibrium microstructure of spheroidized cementite in ferrite, the authors reported that some undissolved cementite was still present after exposure for 10^4 s at 910°C. Furthermore, they reported that the carbide size decreased slowly during the dissolution heat treatment; the average particle size only decreased by ~10% during dissolution exposure times between 1 s to 1000 s. From these results, it is clear that the microstructural condition has a significant effect on the expected completion of dissolution—when the initial microstructure is near equilibrium or metastable equilibrium, complete dissolution will only occur after extended periods of time. Zhao et al. (Zhao et al., 2006) states that the carbide dissolution rate in the Fe-

Cr-C system is related to the interface velocity between the carbide and austenite, which in turn is proportional to the C and Cr diffusivities, the interfacial concentrations of C and Cr in austenite and cementite, and the slope of the concentration profile at the interface. Fig. 4-67 from Zhao et al. illustrates that the concentration slope decreases as dissolution proceeds, with the effect that the rate of dissolution decreases and thus, complete dissolution is expected to require extended times.

Considering these results in application to the HAZ of CSEF steels, the effect of initial precipitate size on subsequent dissolution and re-precipitation has been demonstrated experimentally for Grade 91 welds by Yu et al. (Yu et al., 2013) who showed that the pre-weld tempering condition (standard temperature vs. "low" temperature) alters the resulting precipitate distribution in the HAZ. Where there has been discussion in the literature regarding the proper terminology for the HAZ microstructural regions (e.g. CG/FG/IC-HAZ versus CTZ/PTZ/OTZ), it seems probable that there is a region in the HAZ where complete structural transformation occurs from a ferritic matrix into austenite, but complete carbide dissolution may not occur—i.e., a connection between complete structural transformation and complete carbide dissolution cannot be assumed as seems to be the case in the CTZ/PTZ terminology proposed by Xu et al. (Xu et al., 2017).

The effect of the precipitate distribution on creep behavior is apparent in the FT and H47 results for the ferritic subgrain size. As reported in Table 4-6, the ferritic subgrain size in the FT ICHAZ after creep exposure was larger than in the H47 ICHAZ; the same trend was observed for the FT FGHAZ compared to the H47 FGHAZ. These results suggested that the FT HAZ was less microstructurally stable during creep than the corresponding H47 HAZ, and therefore the FT HAZ experienced a greater degree of microstructure recovery compared to the H47 HAZ. This observation agrees with the higher extent of creep damage in the FT HAZ and with Type IV failure locating occurring in the FT HAZ rather than in the H47 HAZ, in the following aspects. As

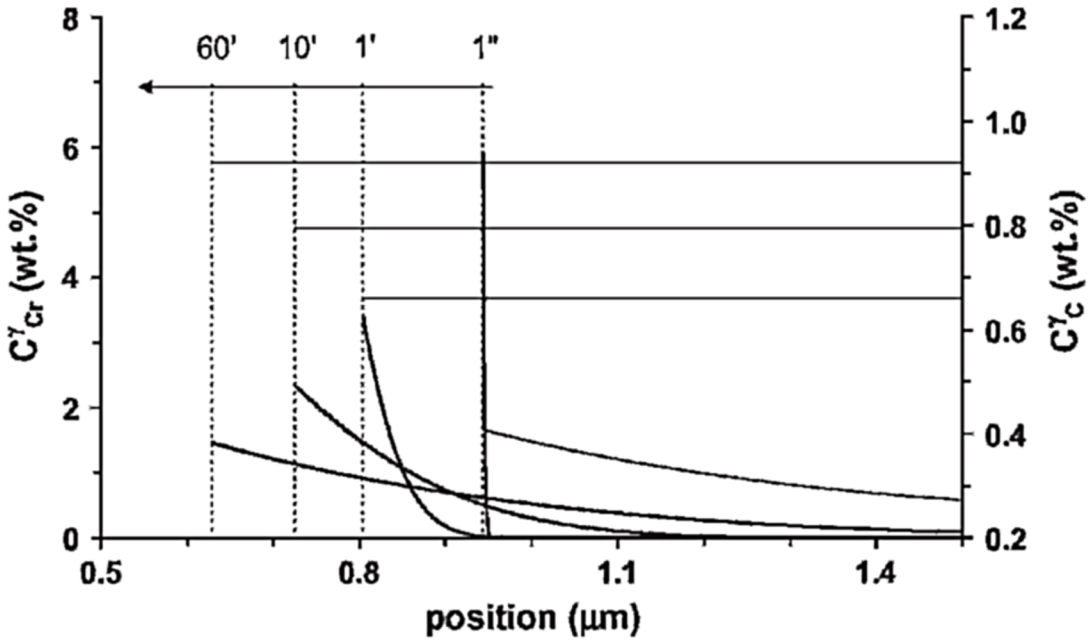


Figure 4-67. Numerical simulations of chromium and carbon concentration profiles in austenite at different time steps (1 s, 60 s, 10 min, 60 min) during dissolution of cementite at 860°C. The chromium concentration profiles (thick lines) show that the initial sharp gradient of chromium content at 1 s shifts to a much broader concentration gradient after 60 min; however, complete chromium redistribution still has not occurred after 60 min. Reproduced from Zhao et al. (Zhao et al., 2006).

described initially in the literature review, any loss of strengthening or stabilizing precipitates in CSEF microstructures will lead to an increased propensity for subgrain boundary motion and dislocation motion which will increase the degree of microstructure recovery. The work of Dyson (Dyson, 1983) proposed that cavity growth and cavity density were correlated with the accumulation of creep strain; similarly, Hales (Hales, 1994) proposed that low ductility creep failure was connected with constrained cavity growth occurring at lower stresses and creep strain rates. Furthermore, Kostka et al. (Kostka et al., 2007) showed that a dislocation-strengthened substructure without any stabilizing precipitates will exhibit a much higher creep rate than a substructure with precipitates (refer to Fig. 2-45). Abe [@abeEffectQuenching2003] also reported that 9Cr-1W steels with different initial microstructures (i.e. quenched, or quenched and tempered) showed similar final microstructures after creep rupture, even though the time required for rupture varied significantly, which seemed to indicate that microstructural evolution in 9Cr steels proceeds from the initial, lath-like TMLS toward an equiaxed ferritic subgrain structure with coarsened precipitates and reduced dislocation density (e.g. see Fig. 2-53 and Fig. 2-46).

The preceding discussion has described the observed differences in the precipitate distributions in the FT and H47 ICHAZ and base metals and considered how the precipitate distribution at each processing step affects the final precipitate distribution at the beginning of creep exposure, followed by further precipitate evolution during creep. However, these differences cannot be attributed to the *intermediate* heat treatment and welding of the FT and H47 materials, due to the fact that FT and H47 experienced the same thermal history during re-N&T, welding, and PWHT since they were processed in the same batch during all heat treatment steps. It is possible that the precipitate distribution of the *initial* microstructure, e.g. that which formed directly after forging or hot rolling, could have an influence on the later microstructure if the initial

precipitate distribution was significantly coarsened; however, this information on the initial processing and microstructure was not available for the FT or H47 base metals. Concerning elements which are involved in MX formation, including Nb and V, both materials have nearly identical V and Nb content with H47 being slightly lower in both cases, so these elements are not responsible for the greater extent of fine precipitates in the H47 ICHAZ. Therefore, potential explanations were further investigated to understand the differences in precipitate and subgrain characteristics that were observed between the two sides of the weldment.

To explore the possible effect of chemical composition differences on the precipitate distributions in the FT and H47 base metals and HAZs, phase fractions as a function of temperature for the FT and H47 base metals were calculated using Thermo-Calc and the TCFE9 database. For the calculations, the weight fractions of C, Cr, Ni, Mo, V, Nb, Al, and N were utilized from the measured FT and H47 chemical compositions given in Table 3-1; the balance of each composition was taken as Fe. It should be remembered here that both of the base metals met the required ASME composition limits for Grade 91 Class 1 with the exception of the FT carbon content which was very slightly above the upper limit. Fig. 4-68 shows the calculated phase fractions for the FT base metal considering the effects of C, Cr, Ni, Mo, V, Nb, Al, and N, while Fig. 4-69 shows the calculated phase fractions for the H47 base metal with the same elements.

Several differences in the expected phases for the FT and H47 base metals may be noted from the calculated results. Table 4-7 shows a comparison of the calculated volume fractions of $M_{23}C_6$, Z-phase, and AlN for these two Grade 91 compositions at the PWHT temperature of 746°C. It is apparent that the FT base metal is predicted to have a slightly greater fraction of $M_{23}C_6$, as expected due to its higher carbon content. The FT base metal is predicted to show a small region of AlN formation just above the PWHT temperature (very small amount at 746°C); a small temperature overshoot during PWHT could bring the material into this phase field. AlN has been identified as a

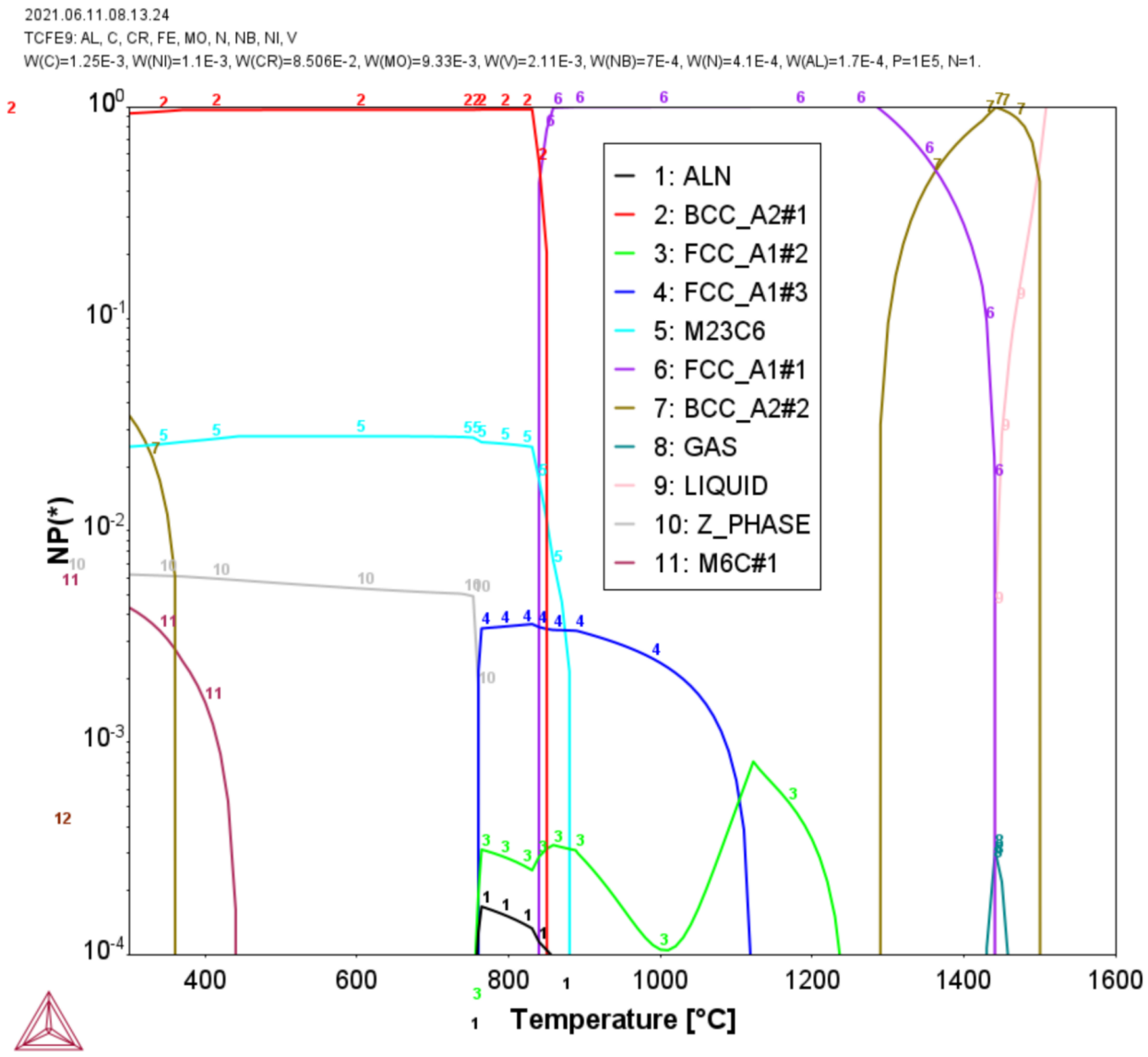


Figure 4-68. Plot of phase fraction versus temperature for the FT base metal with the composition Fe-0.125C-8.506Cr-0.110Ni-0.933Mo-0.211V-0.070Nb-0.017Al-0.041N. Laves phase calculation was disabled. Note that a small region of AlN formation (black outline region in the vicinity of 800°C) is predicted due to the higher Al content of the FT base metal (Al = 0.017 wt.%) compared with the H47 material (Al=0.002 wt.%).

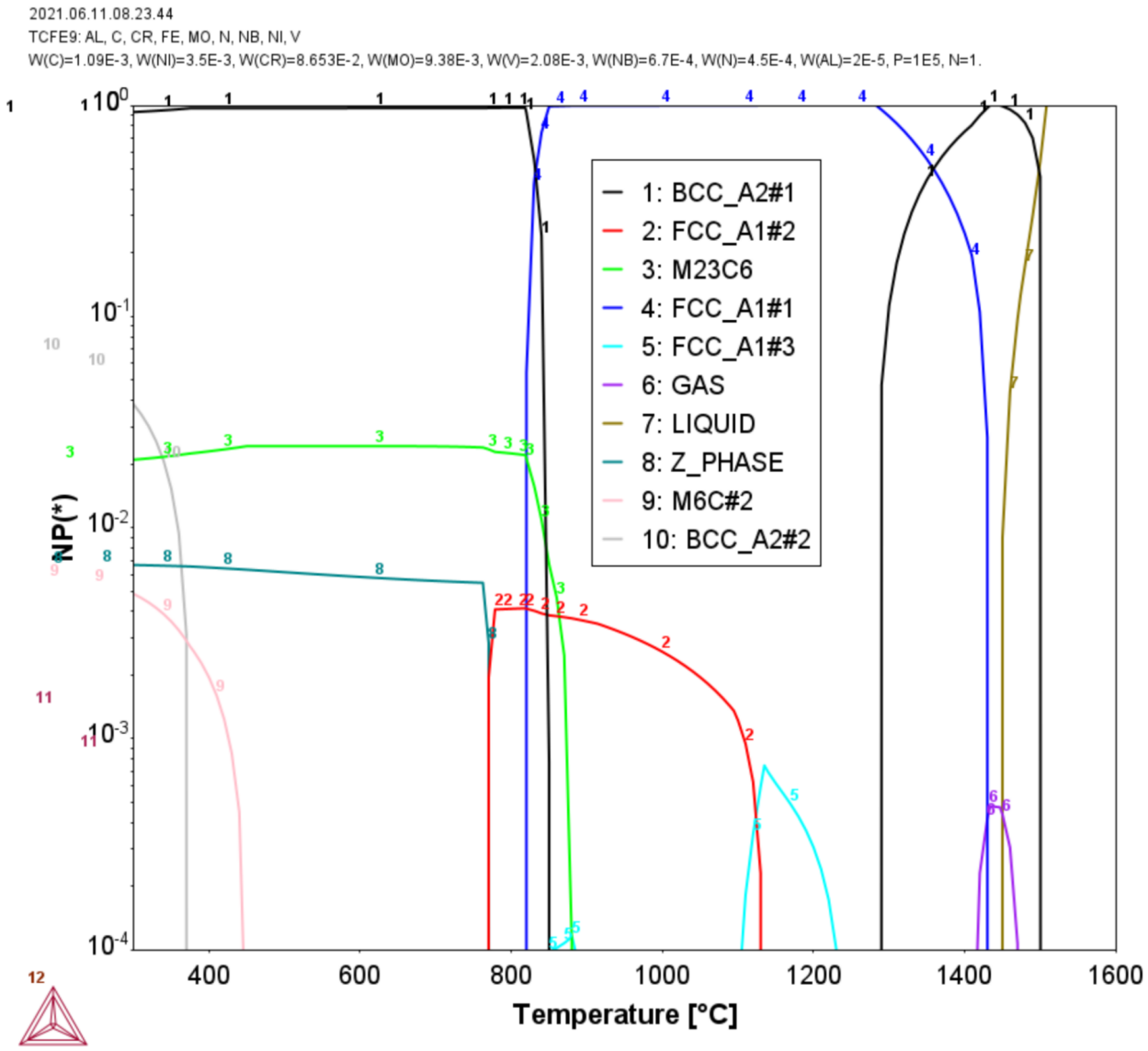


Figure 4-69. Plot of phase fraction versus temperature for the H47 base metal with the composition Fe-0.109C-8.653Cr-0.350Ni-0.938Mo-0.208V-0.067Nb-0.002Al-0.045N. Laves phase calculation was disabled. Compared to Fig. 4-68 for the FT base metal, note that no AlN is predicted to form in the vicinity of 800°C.

Table 4-7. Comparison of calculated volume fractions of $M_{23}C_6$, Z-phase, and AlN precipitates for the FT and H47 base metals at the PWHT temperature of 746°C. (Laves phase calculation was disabled for the results presented in this table.)

Precipitate Phase of Interest	Precipitate Volume Fraction in FT Base Metal, Fe-0.125C-8.506Cr-0.110Ni-0.933Mo-0.211V-0.070Nb-0.017Al-0.041N	Precipitate Volume Fraction in H47 Base Metal: Fe-0.109C-8.653Cr-0.350Ni-0.938Mo-0.208V-0.067Nb-0.002Al-0.045N
$M_{23}C_6$	2.45E-2	2.14E-2
Z-phase	4.75E-3	5.26E-3
AlN	2.43E-5	n/a

detrimental phase for creep performance of Grade 91 steel by some researchers (*Life Management of 9%Cr Steels: Evaluation of Metallurgical Risk Factors in Grade 91 Steel Parent Material*, 2018), so the predicted formation of AlN could be a possible explanation for the greater creep damage extent in the FT material. The diffusivity matrix for the FT and H47 base metals was also examined and no significant differences were found, indicating that at least with the evaluated elements, the differences in the precipitate distributions are not due to differences in diffusivity which would affect carbide dissolution or coarsening. While the presented Thermo-Calc results are based on the measured bulk compositions of the two base metals, it is very important to consider that the local compositions may differ significantly from the nominal bulk composition (as determined by macro-scale chemical analysis methods such as atomic emission spectroscopy or mass spectrometry), due to elemental segregation. As already mentioned from the work of Jabar et al. (Jabar et al., 2021), elemental segregation varies in extent in different product forms (forged material vs. pipe material) and thus the deviation of local chemistry within a given HAZ region from the nominal FT and H47 bulk compositions will vary as well.

Zhao et al. (Zhao et al., 2006) showed for cementite dissolution in Fe-Cr-C (SAE52100) steel that the dissolution rate of cementite was non-uniform during isothermal holding at 860°C, as shown in Fig. 4-70, with the initial rate of dissolution occurring rapidly (up to a time of ~3 min) followed by a significantly slower rate of dissolution which did not reach completion even after 30 min hold time. This is in line with the theoretical approach and results of Ågren and Vassilev (Ågren and Vassilev, 1984) who remarked that there are three separate stages of cementite dissolution governed by different rate-controlling processes, namely, carbon diffusion in austenite, chromium diffusion in cementite, and chromium diffusion in austenite.

These results indicate that the initial precipitate size in a Grade 91 base metal is critically important for achieving complete dissolution of precipitates during the HAZ

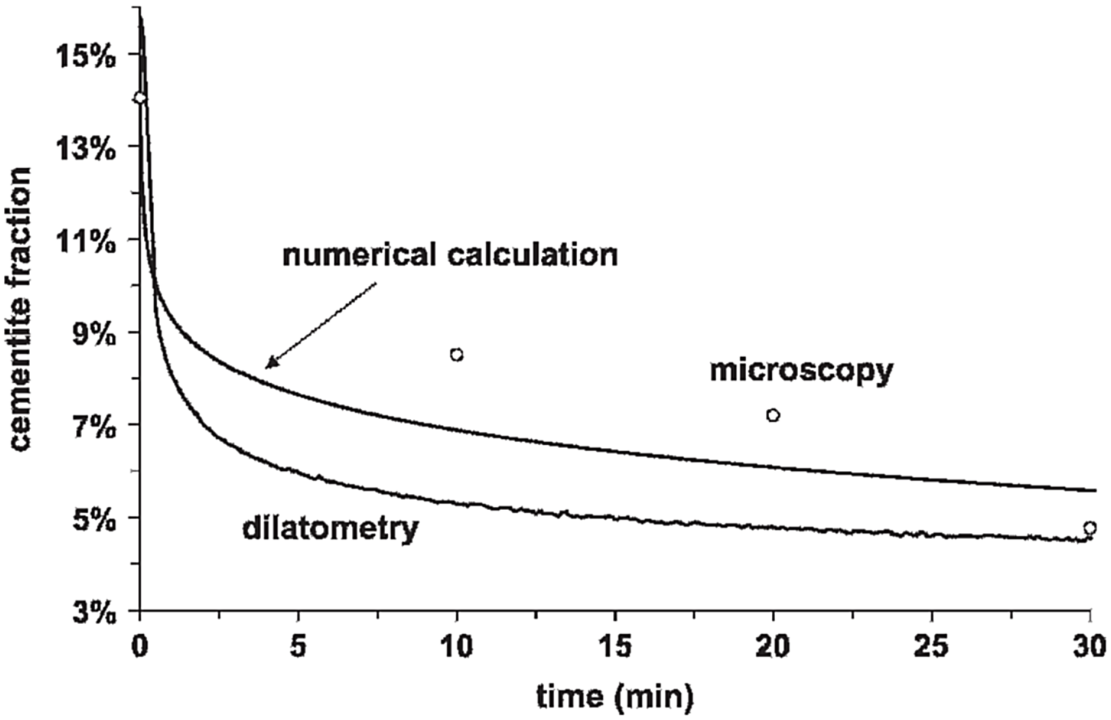


Figure 4-70. Plot of experimental data and calculated results for cementite fraction as a function of time in a Fe-Cr-C (SAE52100) steel during isothermal exposure at 860°C. The dilatometry data and numerical results show that the rate of cementite dissolution (proportional to the slope of the cementite fraction curve) decreases significantly within the first few minutes of exposure, and complete dissolution (fraction equal to zero) is not achieved even after 30 minutes. Reproduced from Zhao et al. (Zhao et al., 2006).

thermal cycle in order to obtain maximum re-precipitation of carbides along the newly-formed lath/subgrain boundaries (boundaries which form as a result of the transformation from the ferritic structure to austenite upon heating, followed by transformation to martensite upon cooling). Without adequate precipitation of carbides along the lath/subgrain boundaries, the creep behavior of the FG/ICHAZ will be more similar to the creep behavior of a dislocation-strengthened, carbide-free material, e.g. the Fe-10Cr binary alloy reported by Kostka et al. (Kostka et al., 2007) which showed markedly increased creep rate compared to a material with a carbide-stabilized dislocation structure.

4.4.3 Relevance of Evaluated Grade 91 Compositions to General Grade 91 Behavior

A potential question about the results presented for the cross-weld creep testing of dissimilar Grade 91 weldments (consisting of the FT, H47, and H13 base metals) relates to the applicability and relevance of this limited number of Grade 91 heats for predicting general behavior of Grade 91 weldments. It is true that only three Grade 91 heats cannot represent the vast spectrum of Grade 91 compositions that can be potentially encountered in service, even if the consideration is limited to Grade 91 materials which meet the ASME BPVC composition requirements. These requirements, which were previously listed in Table 3-1 for comparison with the measured compositions, have fairly broad allowable ranges or high minimum limits for some of the elements, including elements of primary importance such as Cr (Maruyama et al., 2017), Al and N (Abe, 2010), and impurity elements such as S (*The Benefits of Improved Control of Composition of Creep-Strength-Enhanced Ferritic Steel Grade 91*, 2014). It has been noted (*The Benefits of Improved Control of Composition of Creep-Strength-Enhanced Ferritic Steel Grade 91*, 2014) that these ranges may be different than the recommended ranges proposed by ORNL (DiStefano, 1986) during the initial development of Grade 91. Due to the broad ranges or high minimum limits, it is possible to produce heats which

nominally meet the ASME specification, but which differ significantly in the content of important elements and thus exhibit significant differences in creep behavior.

In spite of the inherent limitation of only three heats, the three particular Grade 91 heats used in the current research are useful and valid for examining Type IV creep behavior of dissimilar Grade 91 weldments for the following reasons. First, two of the three Grade 91 heats (H13 and H47 which are plate materials) meet all but one of the stricter requirements of the EPRI recommended composition for Grade 91 that was published in 2014 (*The Benefits of Improved Control of Composition of Creep-Strength-Enhanced Ferritic Steel Grade 91*, 2014). The third heat, FT which is a forging material, meets all but two of the recommended composition requirements, with one of the differences being a significant deviation above the maximum allowable sulfur content (0.008 wt.%. vs. the limit of 0.005 wt.%). The recommended composition was subsequently adopted as an ASME code case to create a new category of Grade 91 material, e.g. Grade 91 "Class 2" material in ASME SA-387. With the introduction of this classification into the ASME code, it is expected that more Grade 91 material with the tighter composition limits will be placed into service, and thus the Type IV creep behavior of materials which are slightly out-of-tolerance on certain elements (as can be expected during commercial production) should be of interest to industry users of Grade 91. The behavior of "nearly compliant" Grade 91 heats will permit industry to further clarify the importance of compositional factors in Grade 91 creep performance, and will also add to the available literature data on the "new" Class 2 category of Grade 91 material.

Additionally, the composition differences between the three evaluated heats are focused on some of the elements which are variously considered to be of primary importance in the literature, such as Cr, S, Ni, Al, and N:Al ratio. Importantly, the differences in many of the other elements are small and thus the compositions are otherwise similar apart from the elements of interest. This is particularly the case with the H47 and H13 materials, which are both plate materials and differ primarily in the amounts of S, Cr,

N, Cu, and Mo (only an ~0.02 wt.% difference). Both of these base metals are very similar in other elements of potential concern, such as other impurity elements including As, Sn, Sb (*Life Management of 9%Cr Steels: Evaluation of Metallurgical Risk Factors in Grade 91 Steel Parent Material*, 2018). Thus, even though only three heats were included in the current program of creep testing of dissimilar weldments, the compositions of these heats should be of interest to industry and thus the results

Finally, the inter-comparisons between the three heats, in terms of the observed characteristics of Type IV creep damage in each weldment, are useful even comparing only three heats. Although only qualitative comparisons are possible between the FT-H47 and H13-H47 weldments due to the different heat treatment and creep conditions, the inter-comparisons between the two base metals in each dissimilar weldment are still valid. Within each weldment, care was taken to heat treat both materials together (e.g. the FT and H47 pieces for the FT-H47 weld were re-normalized and tempered together in the same furnace load) to minimize the possible influence of heat treatment variations. Thus, the differences between the Type IV creep damage extent in each weldment are expected to only be due to the response of each material to the applied heat treatments (which will depend on prior processing history) and to chemical composition.

4.4.4 Relevance of Dissimilar Cross-Weld Creep Data Based on Short-Term Tests

Another potential question regarding the relevance and applicability of the preceding discussion of the creep behavior of dissimilar Grade 91 welds is related to the short durations of the creep tests. As pointed out by Maruyama et al. (Maruyama et al., 2020), typical operating lifetimes for power plant components can exceed 10^5 hours and thus the creep properties for design purposes must either be obtained experimentally at these time scales such as the work by Haney et al. (Haney et al., 2009), or shorter-term laboratory creep data must be reliably and accurately extrapolated to the longer times

needed for service. In the current work, the FT-H47-1 and H13-H47-2 cross-weld creep specimens were tested to durations of 2080.4 h and 3022.6 h, respectively, as shown in Fig. 4-18 and Fig. 4-56. Thus, the applicability of the cross-weld results is a valid concern, since there is at least a potential for non-representative behavior during short-term testing, for example if the more aggressive parameters of short-term tests (higher temperature and/or stress) lead to microstructure changes or creep mechanisms which will not be active during actual service conditions, which are typically at intermediate temperature (e.g. 600°C) and lower stress. Thus, this concern is addressed in two ways: the similarity of microstructure changes in CSEF steels during both short-term and long-term creep testing, and the various creep mechanisms which may be operable during short and/or long-term creep testing of CSEF steels and weldments. In the first aspect, the possibility of non-representative behavior from short-term creep testing arises from the influence of higher test stress and/or temperature on microstructural degradation processes (precipitate coarsening, subgrain coarsening, and dislocation density reduction) and creep damage processes (creep cavity nucleation, cavity growth, and creep crack growth). It was shown in the literature review that precipitate coarsening of $M_{23}C_6$ was influenced by changes in temperature and stress, as shown for example in Fig. 2-41, while MX precipitates appeared significantly more resistant to coarsening under both static exposure and creep exposure conditions as shown in Fig. 2-42. Subgrain coarsening was significantly more extensive during creep (subjected to stress) than during equivalent thermal exposure without stress as shown previously in Fig. 2-44. Aghajani et al. (Aghajani et al., 2009) reported that similar microstructural evolution processes were observed in long-term creep as well as in short term creep testing. They also reported that subgrain coarsening occurred to a significantly greater extent under applied stress during creep compared to the unstressed condition during aging (i.e. in material from the specimen gauge length, versus material obtained from the specimen grip). These observations from the literature suggest that the applied

stress level (and differences thereof) may be more important than changes in temperature when comparing laboratory testing versus service exposure conditions.

With regard to creep mechanisms for Grade 91 steel, there is some disagreement in the literature. Some researchers have stated that Grade 91 creep behavior may be sub-divided into multiple regions (Maruyama et al., 2017, 2016) which exhibit different values of creep stress exponent *n* and creep activation energy *Q* corresponding to changes in creep deformation or creep damage mechanisms as shown in Fig. 4-71. However, this view has been disputed by other researchers such as Wilshire and Scharning (Wilshire and Scharning, 2008), who proposed a new parametric model for creep behavior based on temperature-compensated stress ratio (σ/σ_{UTS}) and the activation energy *Qc* for matrix diffusion in steel. When applied to creep rupture datasets for CSEF steels (only base metals were considered), Wilshire and Scharning stated that the model was capable of satisfactorily predicting 10^5 h creep strength based on extrapolation from test durations of 5,000 h to 30,000 h. On this basis, Wilshire and Scharning concluded that the same creep mechanism was active in Grade 91 steels across a broad range of temperatures and stresses, namely, *diffusion-controlled dislocation creep*, and that the changes in stress exponent and activation energy which appeared to indicate changes in creep mechanism were actually caused by the interaction of minimum creep rate with variations in creep curve shape with changing test temperature and stress (Wilshire and Scharning, 2008). If the multi-region behavior view is accepted, then the relevance of short-term creep data would most likely depend on whether the short-term creep conditions were within the same region as the expected long-term creep conditions; if the two sets of conditions were in different regions, a potential change in mechanism could occur. In Fig. 4-71, it appears that for data in region L2 at 625°C /80 MPa (close to the short-term tests used in the current dissertation results), a shift to lower temperature and stress such as 600°C/40 MPa is projected to remain in the L2 region. If the view of Wilshire and Scharning is accepted,

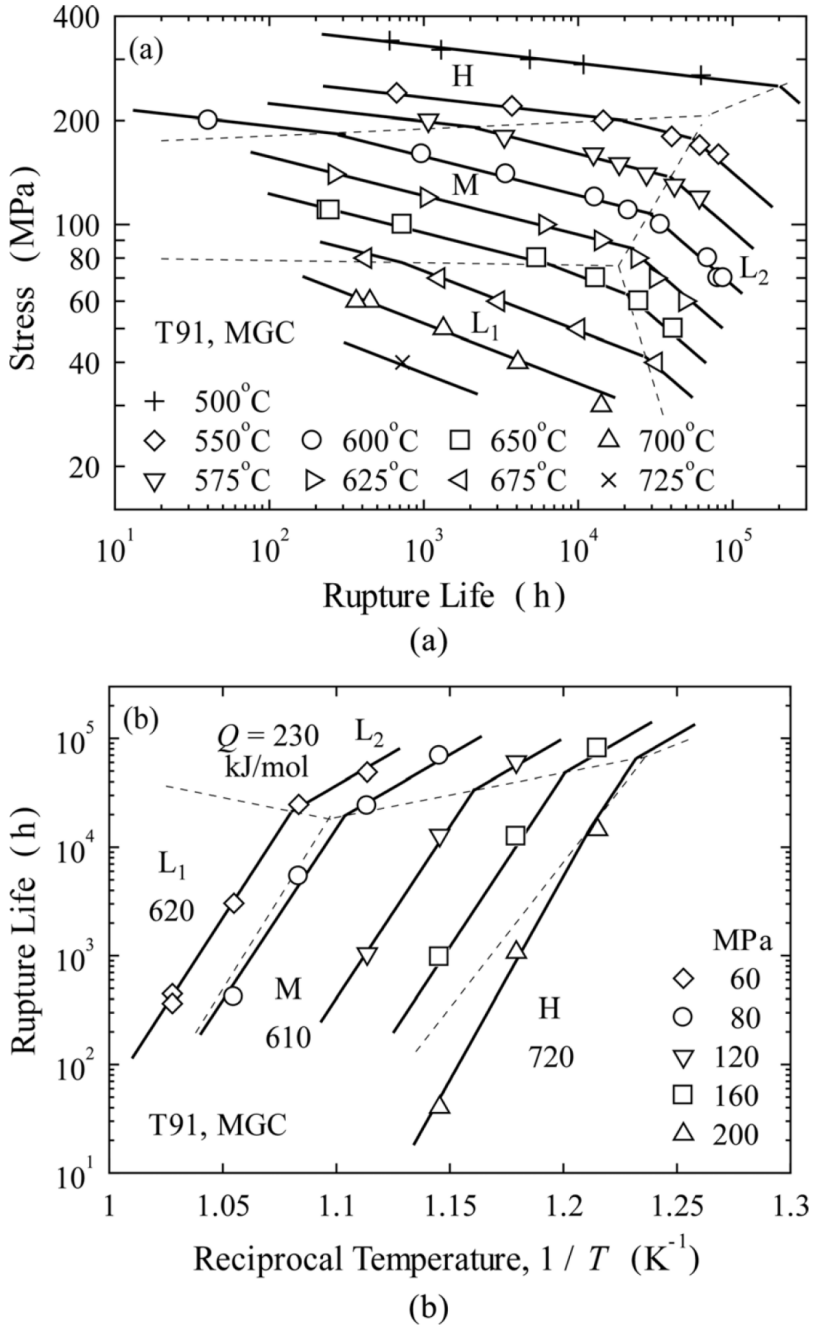


Figure 4-71. Graphs of creep data for a heat of Grade 91 steel with multi-region data fitting based on (a) stress and (b) temperature. Reproduced from Maruyama et al. (Maruyama et al., 2016).

then the creep mechanisms between the laboratory testing in the current dissertation and expected service conditions would be anticipated to be similar. Thus, in either case, it can be reasonably inferred that the short-term test results reported herein for dissimilar Grade 91 weldments are representative of the behavior that would be encountered under service stress and temperature levels.

4.4.5 Primary Considerations in Creep Behavior of the FT-H47 and H13-H47 Dissimilar Grade 91 Weldments

Based on the preceding discussions of the base metal composition characteristics and microstructure characteristics in dissimilar Grade 91 weldments, several factors are suggested as being more important in regard to the occurrence of Type IV creep damage. These factors are listed as follows in proposed order of significance and will be discussed briefly in turn: sulfur content, heat treatment conditions and resulting effects on microstructure and precipitates, and N:Al ratio.

Firstly, based on the presented results, sulfur content is suggested to be the most important factor influencing Type IV creep damage in the FT-H47 and H13-H47 dissimilar weldments. The importance of maintaining low sulfur content has been attributed in the literature to minimizing the formation of sulfide inclusions such as MnS, since a correlation between sulfur content and inclusion density has been reported (*Life Management of 9%Cr Steels: Evaluation of Metallurgical Risk Factors in Grade 91 Steel Parent Material*, 2018) in the literature as shown by Fig. 4-61. The current work showed an absence of the expected unambiguous correspondence between the highest sulfur content (0.008 wt.% in the FT material) and highest inclusion density. This could be potentially due to the magnification used for obtaining the SEM panoramas for image analysis (i.e. the magnification of 2500x may have been too low to resolve small sulfur inclusions) and/or to inhomogeneity in the FT material. The FT material is a forging and showed significant variability in the inclusion density between different measurement areas (refer to Fig. 4-2), as well as the occurrence of large inclusion

"stringers" as shown in Fig. 4-3, and thus it is possible that the measurement areas used for analysis may not have captured the full extent of the inclusion distribution. It should be noted that this type of behavior (high sulfur content without a correspondingly high inclusion density) has been shown in literature data such as the graph in Fig. 4-61.

Apart from this issue, it has been stated (*Life Management of 9%Cr Steels: Evaluation of Metallurgical Risk Factors in Grade 91 Steel Parent Material*, 2018) that sulfur content (correlated with increased inclusion density) is also accompanied by high content of other impurity elements such as, Sn, Sb, and Cu. However, in the current work, all three materials used in the dissimilar weldments had similar contents of As, Sn, and Sb which were below the current EPRI recommended limits, i.e. the FT material which exhibited much greater extent of creep damage did not have elevated As, Sn, or Sb content. Furthermore, in comparing the H47 and H13 materials in the H13-H47 weldment, the material with greater Type IV damage (H47) exhibited a higher sulfur content; other than S content, Cr content, As (higher in H47), and N:Al ratio (which was higher in H47), these materials had similar compositions. On this basis and together with the fact that the effect of sulfur cannot be altered after a heat is produced (i.e. as compared with an undesirable microstructure which can be altered by re-heat treatment), the current research suggests that difference in sulfur content is the primary factor which should be considered when ranking Grade 91 materials with otherwise similar characteristics, and furthermore that obtaining a low sulfur content should be of primary importance when procuring Grade 91 material.

Based on the observations of the current work, the heat treatment history and resulting precipitation characteristics are suggested as the second most important factor influencing the extent of Type IV creep damage. Although limited data and lack of information on prior processing history make it difficult to make firm connections between observed differences in precipitate characteristics and extent of Type IV creep damage, the results discussed in Section 4.2 for the FT-H47 dissimilar weldment still

suggest that the greatly increased creep damage in the FT-side HAZ is connected with a decreased extent of fine precipitates in the FT ICHAZ and also correlated with a decrease of fine precipitates in the FT base metal.

Finally, the correlation of N:Al ratio with creep damage in the two dissimilar weldments suggests that N:Al ratio is lower in importance in the ranking of Type IV creep damage factors, compared to the previous two factors, because while N:Al ratio did show a correlation with the difference in creep damage between the FT and H47 materials, it did not show the expected correlation with damage extent in the H13-H47 weldment.

Chapter 5 Creep Behavior and Creep Damage Characterization of Longitudinal Creep Specimens

Creep testing and characterization of Grade 91 weldments in the literature focuses almost exclusively on cross-weld creep testing of various sample sizes and geometries, such as the results and discussion presented in Chapter 4 of this dissertation. In the cross-weld configuration, the specimen is loaded in a transverse orientation relative to the welding direction (loading axis is perpendicular to the welding direction) which corresponds to the stress orientation of a longitudinal seam weld in piping, where the hoop stress due to internal pressure is perpendicular to the welding direction. The other loading orientation, in which the hoop stress is parallel to the welding direction, is less commonly explored and corresponds to the loading experienced by circumferential seam welds (girth welds). The girth weld geometry may be simulated in testing by using a sample which has its longitudinal axis oriented parallel to the welding direction. Both possibilities for loading orientation of a weldment were previously illustrated in Fig. 2-65. One of the principal differences between these loading modes is that in the iso-strain condition (circumferential seam welds) each region of the weld (BM, HAZ, WM) is subjected to nominally the same strain during the uniform portion of deformation (prior to necking). Therefore, preliminary creep experiments conducted in a previous project (Hobbs et al., 2015) and further microstructural characterization were reported herein using longitudinal creep loading to explore the creep deformation and cavitation behavior of the different regions in a Grade 91 weldment (BM, HAZ, and WM) when subjected to nominally identical strain until the onset of necking. Two different types of heat treatments were used—subcritical PWHT, and normalized and tempered (N&T)—in accordance with the permissible heat treatments for CSEF weldments in the ASME Boiler and Pressure Vessel Code Section I, Table PG-26 (*Section I: Rules of Construction for Power Boilers*, 2019).

5.1 Characteristics of the AEP Grade 91 Weldment

A Grade 91 submerged arc weldment designated as "AEP Grade 91 SAW," in the PWHT condition (774°C/8 h), was utilized for the current research from previous projects (Hobbs et al., 2015; Lundin and Liu, 1999). The weldment was previously fabricated from "AEP" base metal with the composition given in Table 3-1. The initial characterization of this weldment prior to creep testing is presented for the as-received PWHT condition and for two heat treatments which were subsequently performed. These heat treatments consisted of the following: extended subcritical PWHT at 774°C/56 h, for a total cumulative PWHT of 774°C/64 h, and a re-normalizing and tempering treatment consisting of 1066°C/2 h plus 774°C/3 h. The heat treatment conditions and resulting base metal hardness values measured on the Rockwell HRBW scale are summarized in Table 5-1.

The appearance of the as-received, subcritically PWHTed AEP Grade 91 SAW weldment is shown in Fig. 5-1. The weldment utilized a single V-groove geometry in 1-7/8" thick plate with 44 weld passes; note that due to the V-groove geometry and relatively small bead size, the formation of continuous, aligned regions of HAZ refined microstructure (wherein the weld deposit was re-heated into the intercritical temperature range) did not occur. The macroscopic appearance of the weldment in the 774°C/64 h PWHT condition is shown in Fig. 5-2; the appearance after the re-normalizing and tempering heat treatment is shown in Fig. 5-3. In the re-normalized and tempered condition, the base metal and weld deposit HAZ regions in the weldment have been eliminated due to the complete re-austenitization and on-cooling transformation to martensite which occurred in all regions of the weldment. As a result of the re-normalization, all of the HAZ regions within the weld deposit resulting from overlapping weld passes were also eliminated to produce a more uniform weld deposit microstructure; this is evident when comparing the weld deposit appearance in Fig. 5-1 versus Fig. 5-3.

Table 5-1. Summary of heat treatment parameters and measured base metal hardness values after heat treatment for the evaluated conditions of the AEP Grade 91 SAW weldment. Hardness values obtained from Hobbs et al. (Hobbs et al., 2015).

Heat Treatment Identifier	Heat Treatment Parameters	Base Metal Hardness after Heat Treatment (HRBW), Mean ± St.Dev.
"8 h PWHT" (subcritical PWHT)	- Original N&T (unknown) - Subcritical PWHT at 774°C/8 h	92.0 ± 0.2
"64 h PWHT" (subcritical PWHT)	- Original N&T (unknown) - Subcritical PWHT at 774°C/8 h - Additional subcritical PWHT at 774°C/56 h (for a cumulative total of 64 h)	90.3 ± 0.3
"N&T" (normalized and tempered)	- Original N&T (unknown) - Re-normalized at 1066°C/2 h and tempered at 774°C/3 h	94.6 ± 0.5

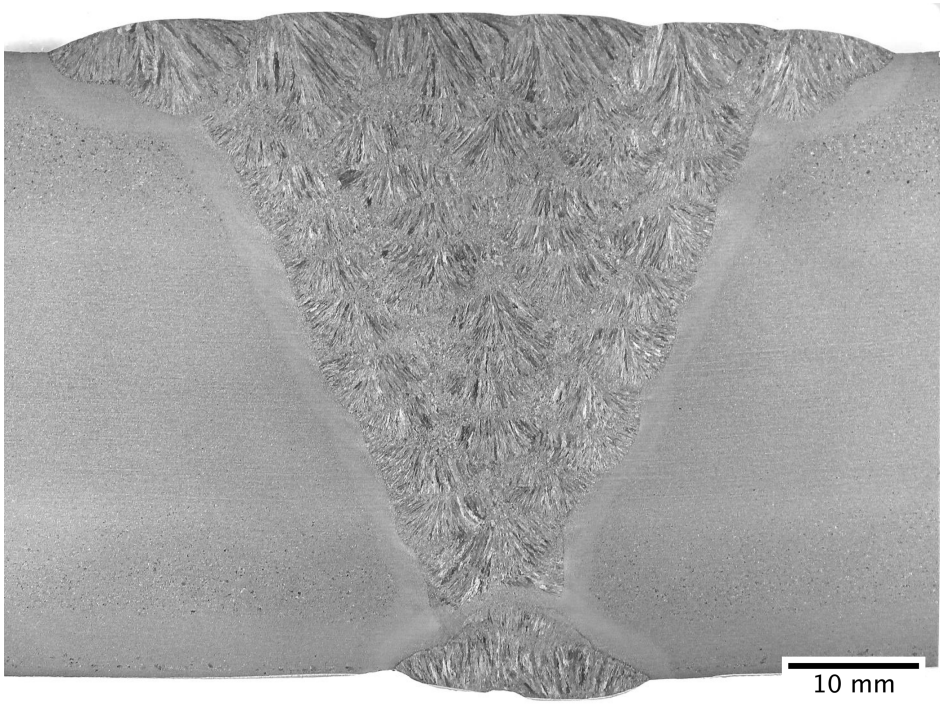


Figure 5-1. Cross-section macrograph of the AEP Grade 91 SAW weldment in the 8 h subcritical PWHT condition (774°C/8 h). Etchant: Fry's reagent. Reproduced from (Hobbs et al., 2015).



Figure 5-2. Cross-section macrograph showing the representative appearance of the AEP Grade 91 SAW weldment in the 64 h subcritical PWHT condition (774°C/64 h). Etchant: Fry's reagent. Reproduced from (Hobbs et al., 2015).

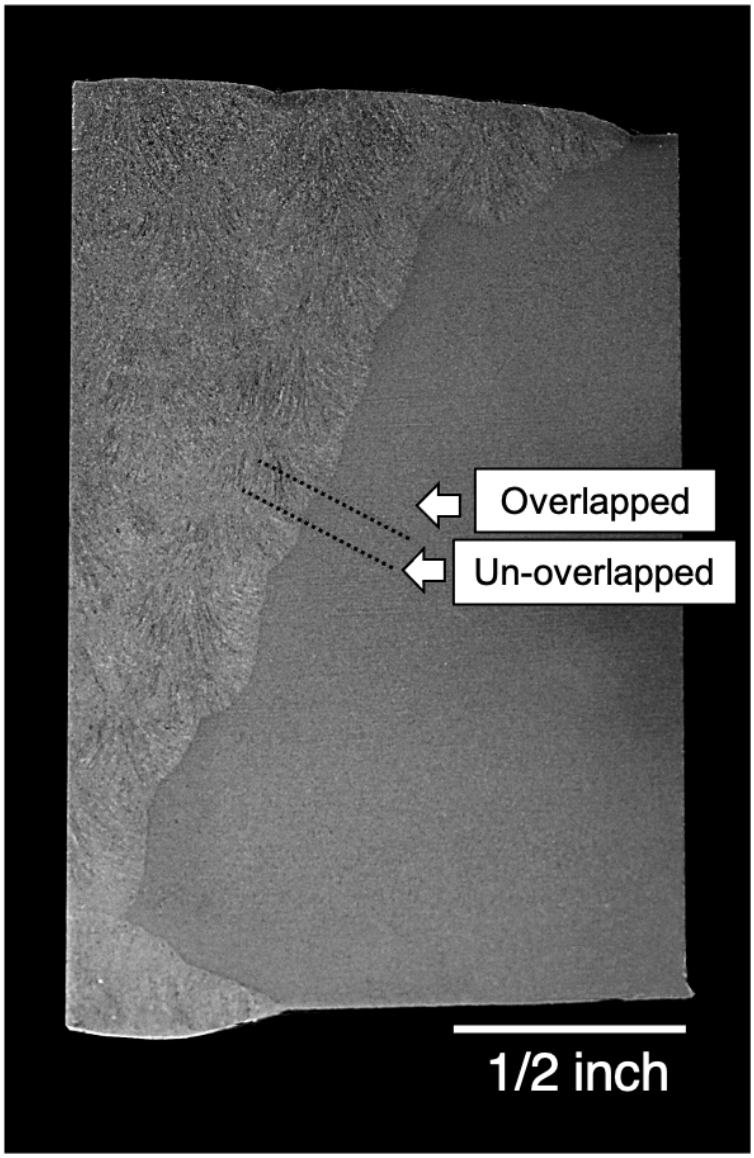


Figure 5-3. Cross-section macrograph showing the representative appearance of the AEP Grade 91 SAW weldment in the re-normalized and tempered condition (1066°C/2 h plus 774°C/3 h). The two dashed lines indicate the locations of two hardness traverses which were performed across the former overlapped and un-overlapped regions of the HAZ; the results are presented in Fig. 5-4. Etchant: Vilella's reagent. Reproduced from (Hobbs et al., 2015).

Hardness traverses were performed across the BM, HAZ, and weld deposit for two heat treatment conditions, in both overlapped and un-overlapped regions of the base metal HAZ. The overlapped region corresponds to an area where a subsequent weld pass re-heated the HAZ microstructure above the lower critical temperature (Ac1), while the un-overlapped region consists of the HAZ without any further exposure at temperatures above Ac1. The hardness data is shown in Fig. 5-4. From these plots, the N&T heat treatment produces a more uniform hardness distribution across the weld, as expected. There is no difference in hardness between former overlapped versus un-overlapped regions in the former HAZ region of the N&T sample, since the HAZ is eliminated during the re-normalization. The weld deposit exhibits a slight increase above the hardness of the adjacent former HAZ and BM, but the increase is minor (<10% relative to the BM hardness of 220HV) and overall the hardness traverse does not suggest a significant strength differential across the different regions of the weld. Although this hardness data was obtained at room temperature, the trend should be predictive for high temperature, based on the results of Li et al. (Li et al., 2003) for a P122 weldment which indicated that room temperature and high temperature hardness showed the same trends in values and the same location for the minimum hardness (refer back to Fig. 2-30). In the 64 h PWHT condition shown in Fig. 5-4, there is a slight hardness increase (indicating higher strength) in the weld deposit relative to the HAZ and base metal; as expected, the hardness differential is larger in the un-overlapped region of the HAZ, since the overlapped HAZ essentially receives further tempering from the additional thermal cycle(s) of subsequent weld passes.

5.2 Creep Behavior of Longitudinal Specimens from the AEP Grade 91 Weldment

Creep testing was previously performed (Hobbs et al., 2015) on several samples from the AEP Grade 91 submerged arc weldment to evaluate the behavior and creep damage accumulation of longitudinal specimens. For these longitudinal creep specimens, the tensile loading axis was parallel to the welding direction as described in Materials and

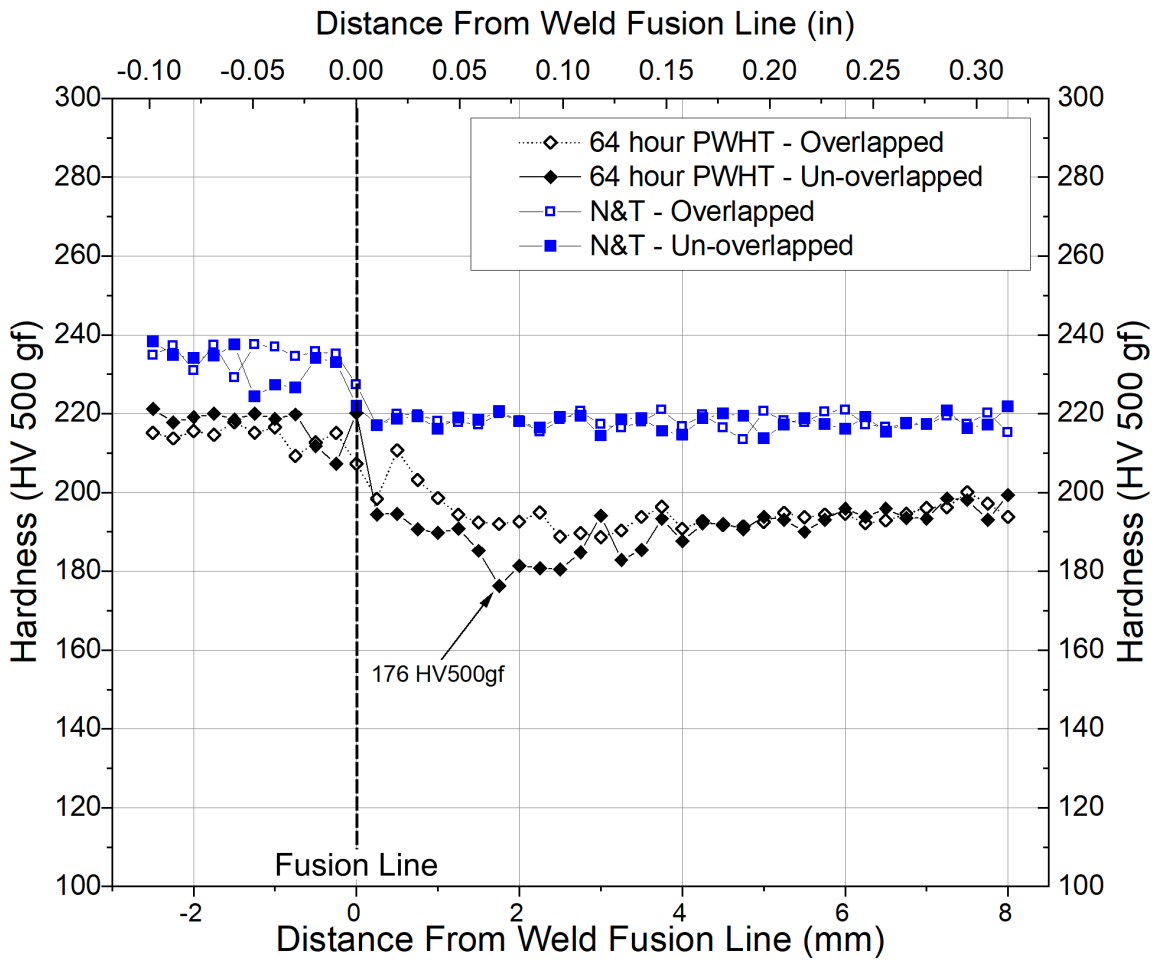


Figure 5-4. Measured microhardness traverses for the AEP Grade 91 SAW weldment in two conditions: subcritical PWHT, 774°C/64 h and re-normalized and tempered (N&T), 1066°C/2 h plus 774°C/3 h. The 64 h subcritical PWHT hardness traverse shows a hardness decrease in the un-overlapped HAZ with a minimum hardness value of 176 HV500gf. In comparison, the N&T hardness traverse shows a uniform hardness across the former HAZ and base metal regions. Data obtained from (Hobbs et al., 2015).

Experimental Procedures and shown in Fig. 3-1. As a result of this orientation, the entire sample length including the full gauge length contained all three microstructural regions in parallel (BM, HAZ, and WM) and thus these regions were subjected to nominally equal strain during the uniform deformation region of the test, prior to the onset of necking.

Creep testing was performed to rupture at 621°C/124 MPa; the resulting plots of creep strain versus elapsed time for the three longitudinal specimens (corresponding to the three heat treatments) are given in Fig. 5-5. Fig. 5-5 shows that the two subcritically PWHT samples exhibited significantly shorter rupture life than the N&T specimen; the 64 h PWHT specimen showed slightly higher elongation-to-rupture than the 8 h PWHT or N&T specimens, but both of the subcritical PWHT specimens showed significantly higher reduction of area than the N&T condition despite their shorter rupture times. Fig. 5-6 shows a comparison of the creep strain rate data determined from the measured creep data and the plot shows that the initial creep rate (the first few hours) is essentially identical between the three specimens. Comparing the subcritical PWHT specimens, both specimens exhibit similar creep rates, but the 8 h PWHT specimen shows a lower minimum creep rate (0.034 %/h) than the 64 h specimen (0.065 %/h); the tertiary creep rates are also similar for the two subcritical PWHT specimens. The N&T specimen shows a slight decrease in the slope of the creep rate with increasing test time and the minimum creep rate is approximately an order of magnitude lower (0.0076 %/h) than the 8 h PWHT specimen. Fig. 5-7 shows the creep rate data plotted versus normalized time to rupture and from this figure it is apparent that the 8 h PWHT and N&T specimens reach their minimum creep rate at approximately the same relative time (~0.3 $t_{R,max}$) while the 64 h PWHT condition reaches the minimum creep rate slightly sooner (~0.2 $t_{R,max}$). Fig. 5-7 also shows more clearly that the N&T specimen exhibits a greater increase in strain rate at the very end of life as compared to either of the subcritical PWHT samples (i.e. the slope of the strain rate curve is steeper for the

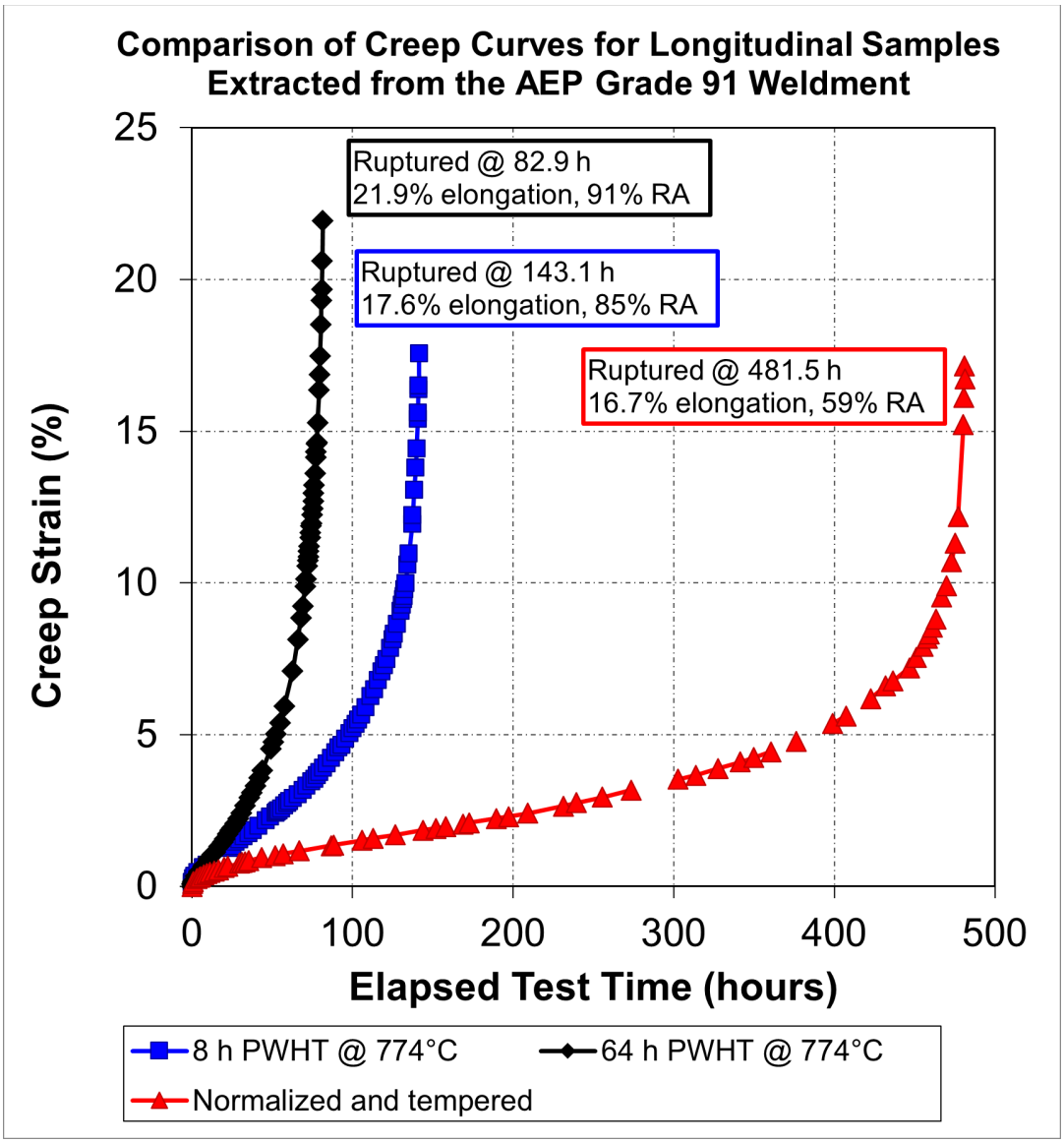


Figure 5-5. Plot of measured creep strain versus elapsed test time from three longitudinal creep specimens extracted from the AEP Grade 91 submerged arc weldment. "Longitudinal" refers to the orientation of the creep sample tensile axis with respect to the welding direction in the parent weldment; the creep sample tensile axis is parallel to the welding direction. Creep testing was performed at 621°C/124 MPa. Data from (Hobbs et al., 2015).

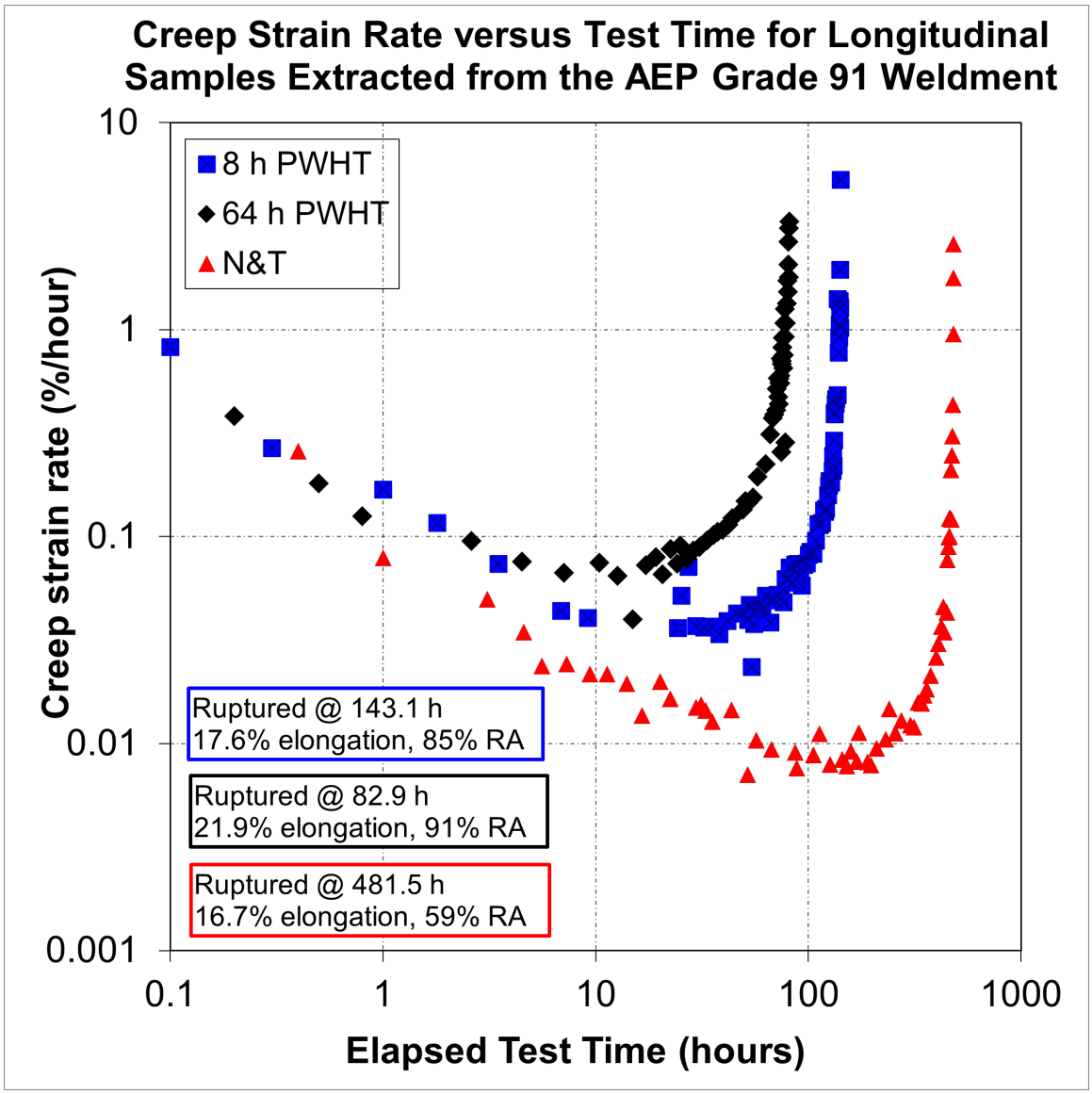


Figure 5-6. Plot of creep strain rate versus elapsed test time from measured creep data obtained from three longitudinal creep specimens extracted from the AEP Grade 91 submerged arc weldment. Creep testing was performed at 621°C/124 MPa.

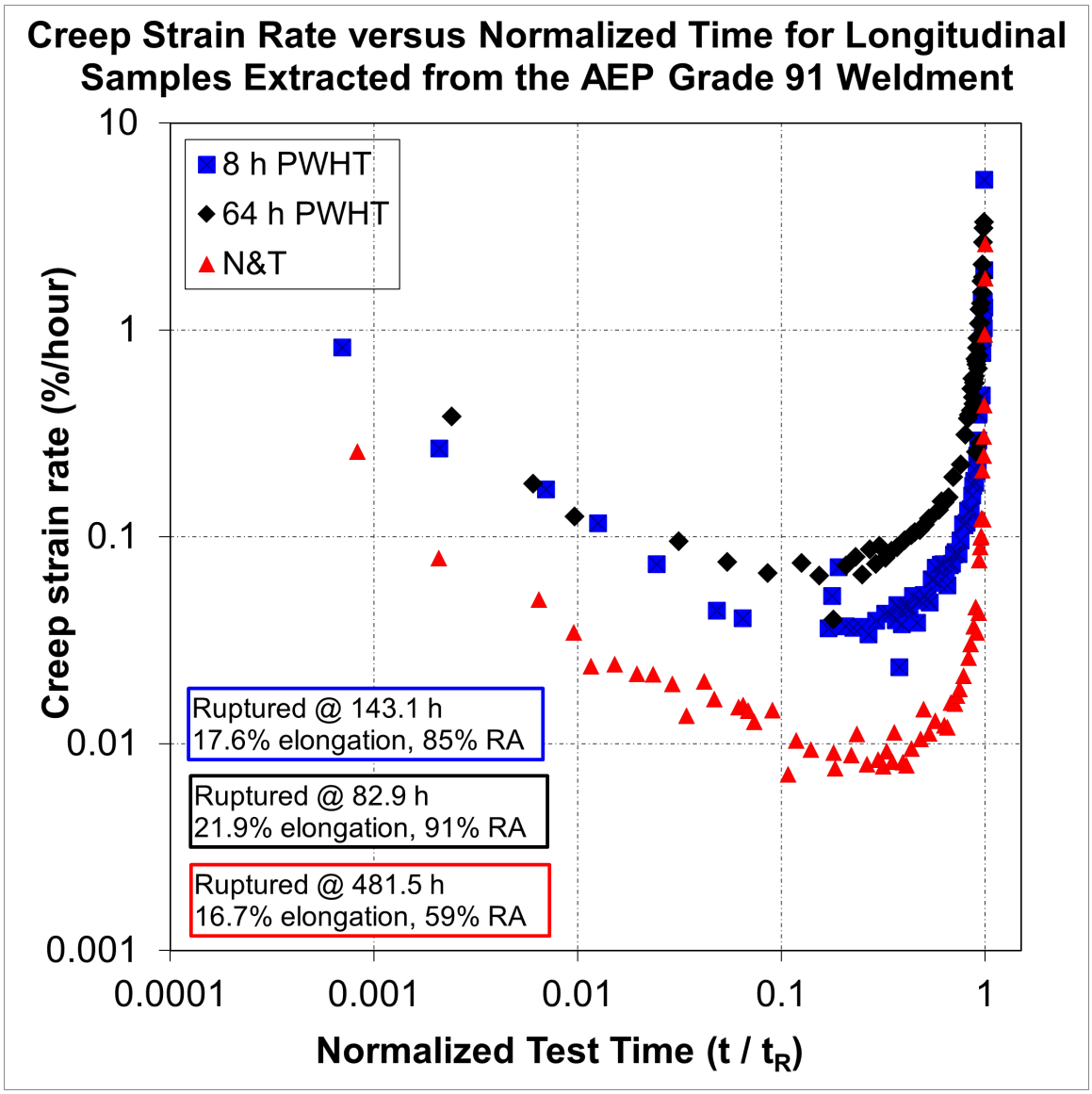


Figure 5-7. Plot of creep strain rate versus normalized test time from measured creep data obtained from three longitudinal creep specimens extracted from the AEP Grade 91 submerged arc weldment. Creep testing was performed at 621°C/124 MPa. Note that the 8 h PWHT and N&T specimens both reach their minimum creep rate at approximately the same time fraction (~0.3) while the 64 h PWHT specimen reaches the minimum creep rate at a slightly earlier fraction. Note also that the N&T specimen shows a significantly more rapid acceleration of creep rate at the very end of rupture life; this behavior is illustrated as a function of strain in Fig. 5-8.

N&T condition when the normalized test time approaches 1). Lastly, Fig. 5-8 shows a plot of creep strain rate versus average strain, from which it is clear that the N&T condition shows a steeper slope during strain accumulation, corresponding to a value of $d \log \varepsilon / d \varepsilon$ which is approximately twice as large.

The macroscopic appearance of the creep specimens after metallographic preparation revealed that the 8 h and 64 h subcritical PWHT specimens showed significant plastic deformation and necking at the rupture location, in accordance with the measured %RA values shown in the preceding creep plots. Fig. 5-9 and Fig. 5-10 show the macrographs of the 8 h PWHT specimen and 64 h PWHT specimen, respectively, and both specimens have a similar macrostructure. In both specimens, there is only a slight distinction between the HAZ and BM regions, so that the HAZ is visible although not clearly delineated; this is due to the etchant utilized for preparation. Additionally, both macrographs show evidence of plastic deformation occurring adjacent to the rupture location; the slight extent of microstructural banding in the base metal and HAZ is visibly deformed adjacent to rupture (refer to the arrows in Fig. 5-9 and Fig. 5-10. Fig. 5-11 shows the macrograph for N&T longitudinal specimen and it is immediately apparent that there is a difference in the extent of %RA in the WM compared to the former HAZ (recall that the HAZ was eliminated during the N&T treatment) and BM. The macrograph reveals that the deformation in the former HAZ and BM regions is significantly greater than in the WM; the deformation is visible by the distortion of the microstructural banding (refer to arrow in the macrograph). In the WM region of the N&T specimen, the extent of elongation and of %RA are both reduced in comparison to the former HAZ and BM, so that the WM appears to have relatively low ductility. The difference in ductility along the gauge length of each specimen is illustrated in Fig. 5-12, which shows that the 64 h PWHT condition exhibited the greatest overall %RA, both at the rupture location and along the gauge length. Fig. 5-12 indicates that the 64 h PWHT condition showed a similar trend of strain accumulation in the gauge length as the 8 h

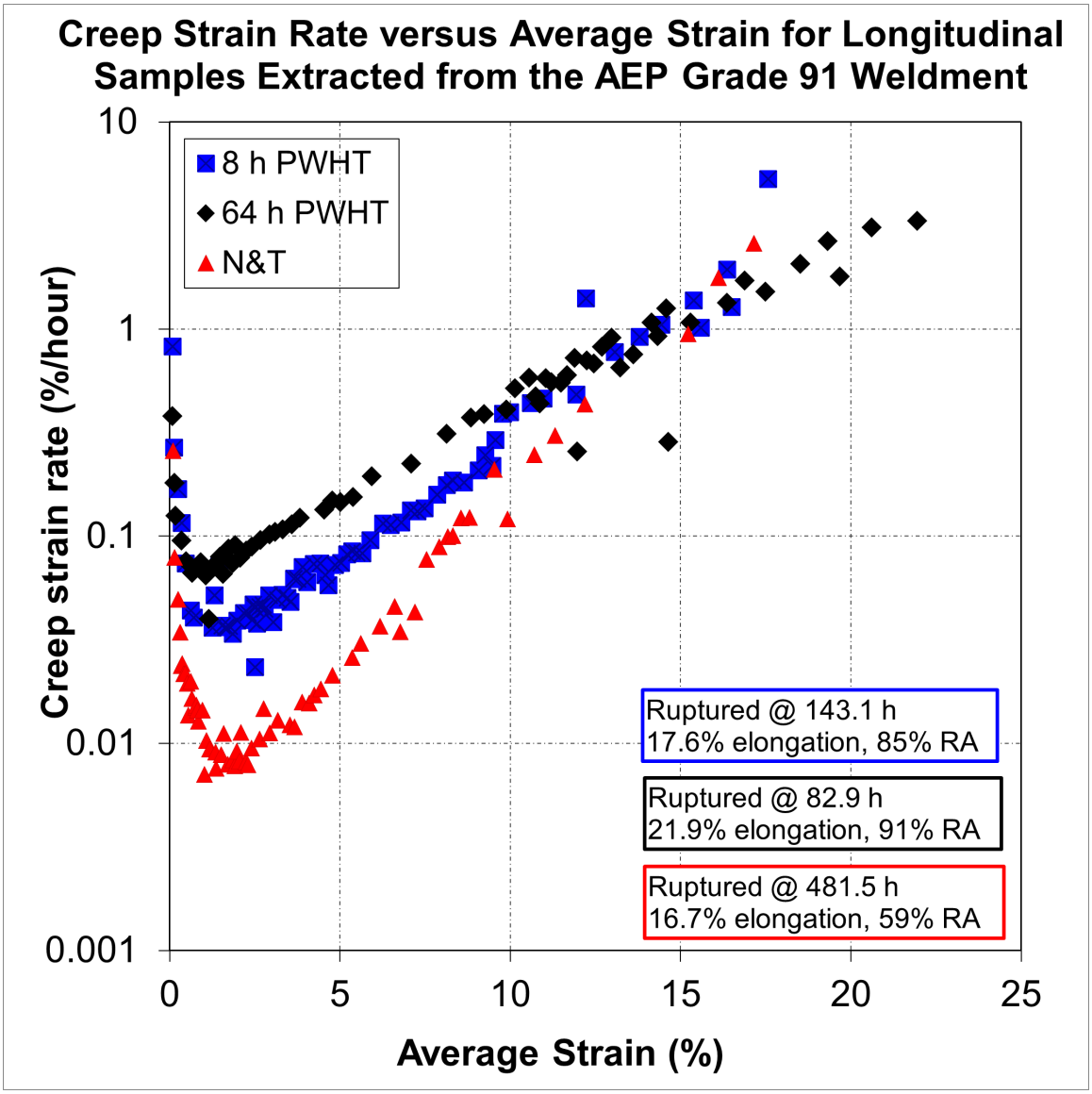


Figure 5-8. Plot of creep strain rate versus average strain from measured creep data obtained from three longitudinal creep specimens extracted from the AEP Grade 91 submerged arc weldment. Creep testing was performed at 621°C/124 MPa. Note that the N&T specimen shows a faster increase of creep strain rate as strain accumulation increases into the tertiary creep regime.

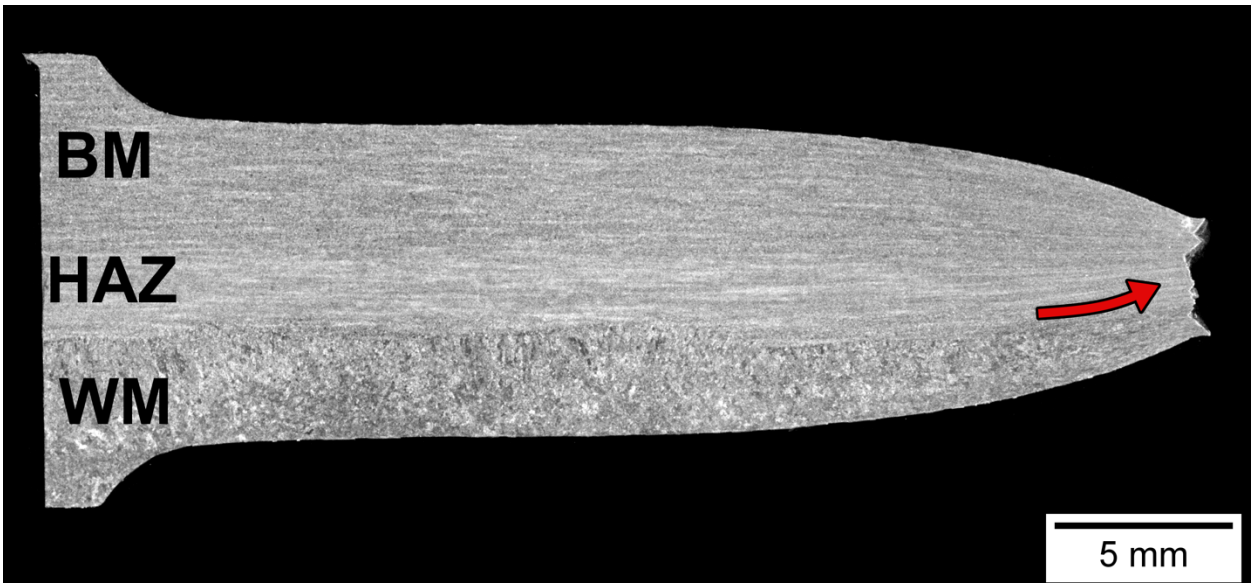


Figure 5-9. Optical macrograph of one half of the longitudinal creep specimen in the 8 h subcritical PWHT condition from the AEP Grade 91 weldment. Creep testing was performed at 621°C/124 MPa; total elongation was 17.6%, reduction of area was 85%. The arrow shows the distortion of microstructural banding that reveals the evidence of plastic deformation. Etchant: Vilella's reagent.

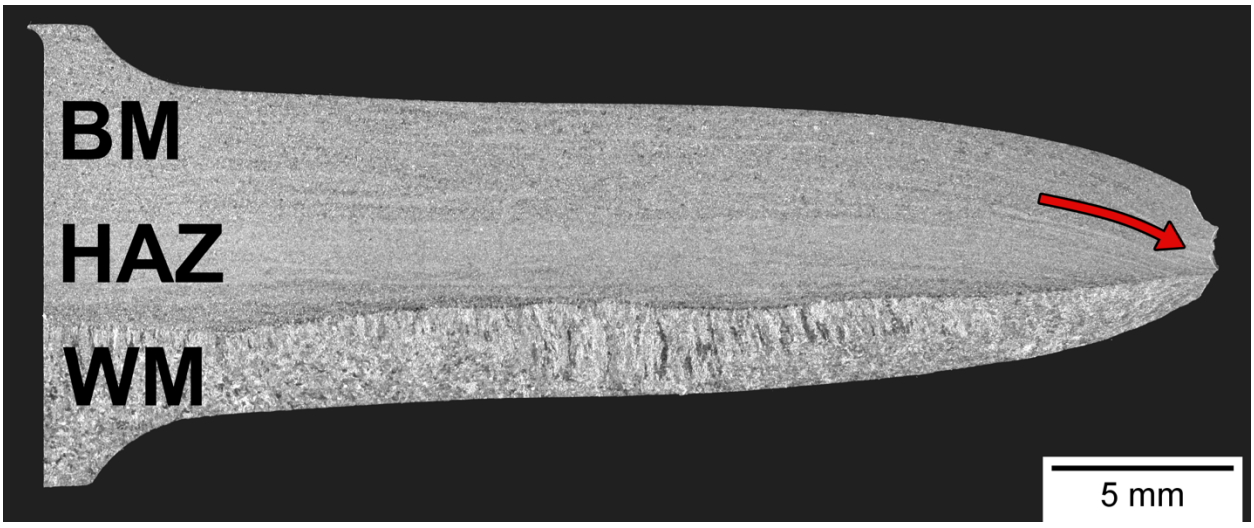


Figure 5-10. Optical macrograph of one half of the longitudinal creep specimen in the 64 h subcritical PWHT condition from the AEP Grade 91 weldment. Creep testing was performed at 621°C/124 MPa; total elongation was 21.9%, reduction of area was 91%. The arrow shows the distortion of microstructural banding that reveals the evidence of plastic deformation. Etchant: Vilella's reagent.



Figure 5-11. Optical macrograph of one half of the longitudinal creep specimen in the normalized and tempered (N&T) condition from the AEP Grade 91 weldment. Creep testing was performed at 621°C/124 MPa; total elongation was 16.7%, the overall reduction of area was 59%. Note that the WM region shows significantly less reduction in area than the former HAZ and BM regions (deformation noted by arrow). Etchant: Vilella's reagent.

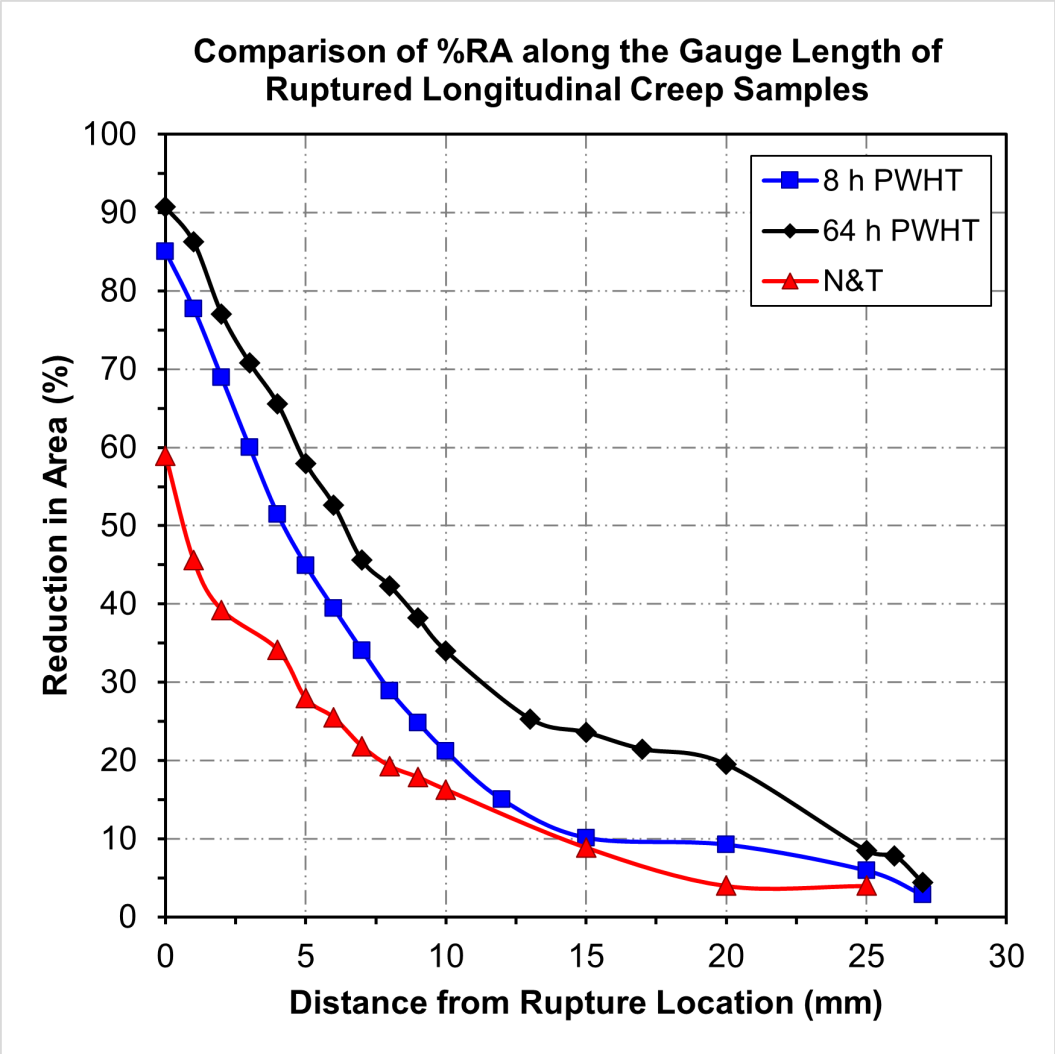


Figure 5-12. Measured profiles for reduction of area (%RA) along the gauge length of longitudinal creep samples from the AEP Grade 91 weldment. The profiles show the change in %RA along one half of the ruptured sample; the "0 mm" location in the graph corresponds to the rupture location, and the terminal location (25 or 27 mm) corresponds to the shoulder of each creep sample. Data from (Hobbs et al., 2015).

PWHT condition, but the magnitude of the strain accumulation was larger. In contrast, the N&T specimen showed both a lower %RA at the rupture location and decreased strain accumulation along the gauge length.

5.3 Creep Damage Characterization of the 64 h Subcritically Postweld Heat-Treated Longitudinal Creep Specimen

The results of the metallographic examination of the 64 h subcritical PWHT longitudinal creep sample are presented beginning with Fig. 5-13. Fig. 5-13 shows a low magnification optical macrograph of the region adjacent to the rupture location, with marked regions for higher magnification examination at distances of 1 mm, 2 mm, 4 mm, and 8 mm from rupture. From Fig. 5-13, it is apparent that severe plastic deformation occurred within several millimeters of the rupture location as can be seen from the distorted flow lines in the microstructure. Additionally, significant reduction of area is visible over the distance of ~8 mm shown in the macrograph. From the macrograph, it can be seen also that each of the regions (generally, the BM, HAZ, and WM) experienced a qualitatively similar amount of reduction of area; note that at the rupture location, necking clearly occurred to approximately equal extents in the weld metal as well as the base metal, in contrast to behavior for the N&T longitudinal specimen as described in a later section. At this low magnification, creep cavitation is not readily apparent.

Fig. 5-14 shows a comparison of the microstructure and extent of cavitation/voiding in the BM, FGHAZ, CGHAZ, and WM (weld metal) regions at a distance of 1 mm from rupture in the 64 h PWHT longitudinal specimen. The comparison shows that cavities or voids are present in each region at the 1 mm location; the cavities are distorted and elongated by the severe plastic deformation adjacent to rupture, corresponding to 86%RA from Fig. 5-12. The plastic deformation also obscures whether a significant difference in microstructure recovery (precipitate and subgrain coarsening) is evident between the individual regions at the 1 mm location. Fig. 5-15 shows the microstructure

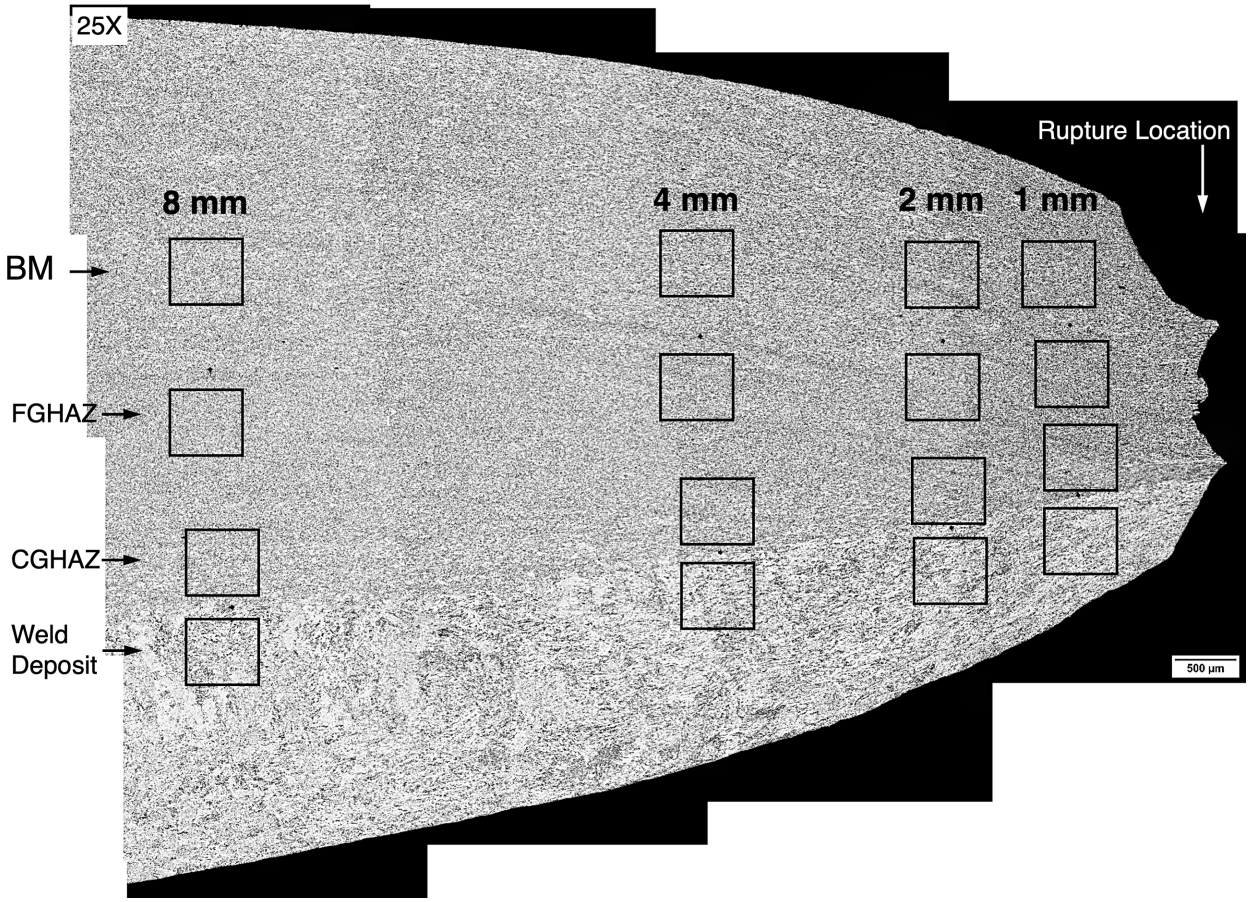


Figure 5-13. Optical light macrograph showing the appearance of the 64h subcritical PWHT longitudinal creep specimen, at the rupture location. The marked regions at the 1 mm, 2 mm, 4 mm, and 8 mm locations were selected for higher magnification examination. Etchant: Vilella's reagent.

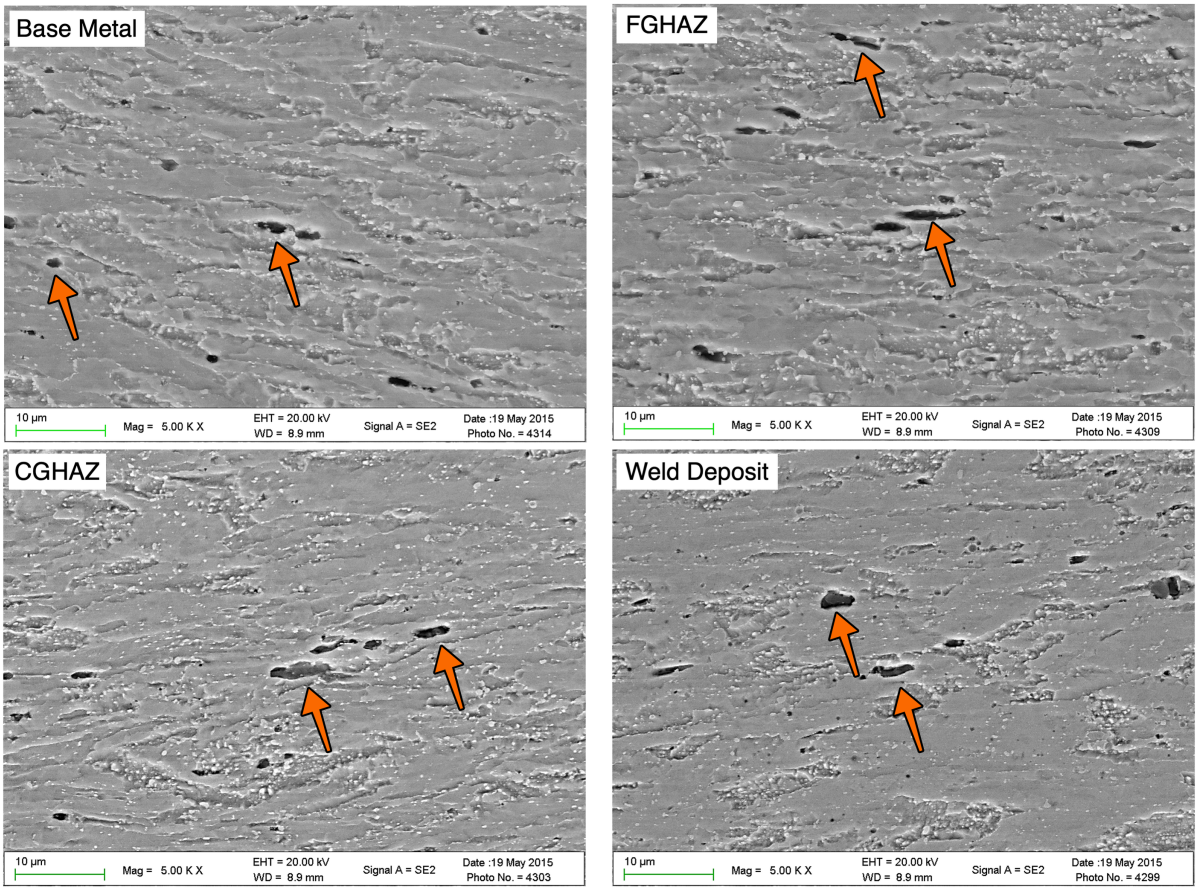


Figure 5-14. SE-SEM micrographs showing the microstructural appearance and extent of cavities/voids in the 64 h subcritical PWHT (774°C/64 h) longitudinal creep specimen at a distance of 1 mm from the rupture location. Note that all four individual regions in the weld show evidence of voiding/cavitation (orange arrows); additionally, the voids/cavities are distorted (elongated) due to severe plastic deformation at the 1 mm location (corresponding to 86%RA from Fig. 5-12). Etchant: Vilella's reagent.

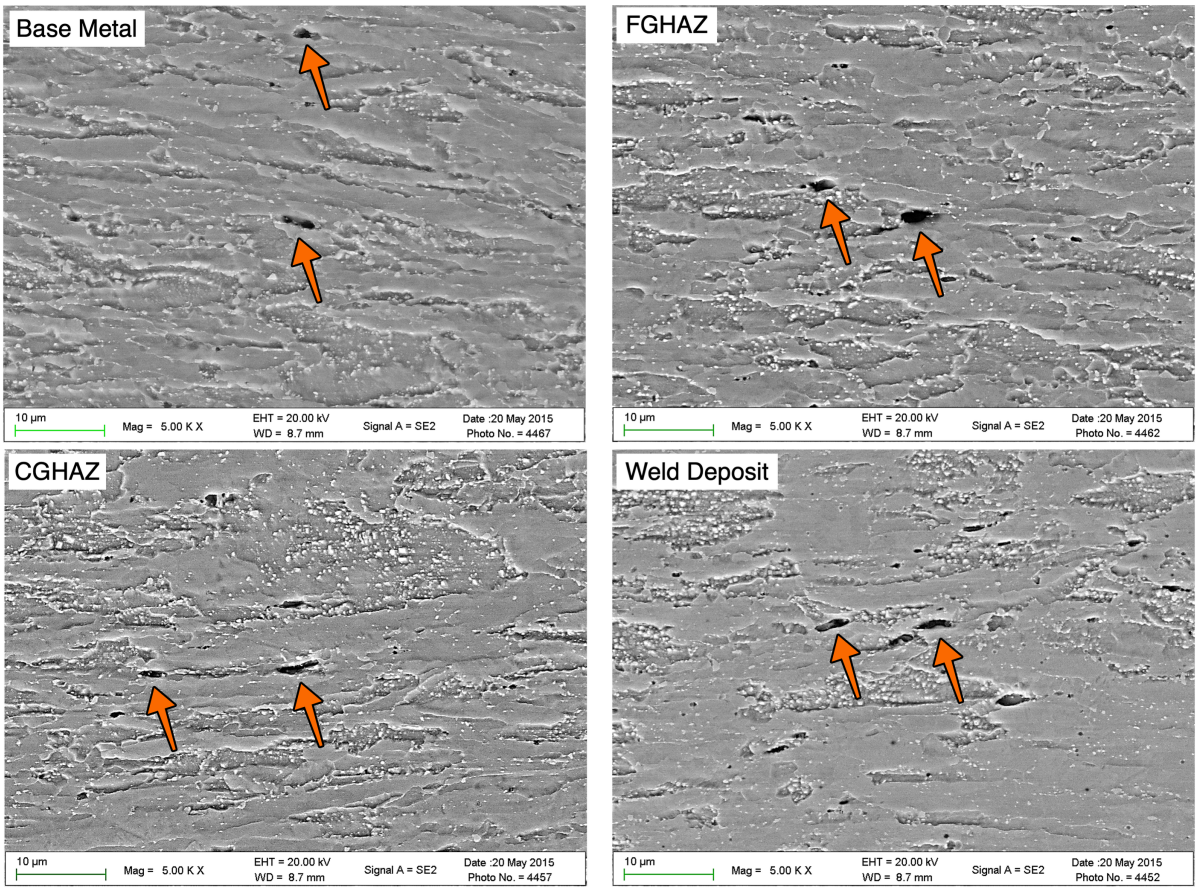


Figure 5-15. SE-SEM micrographs showing the microstructural appearance and extent of cavities/voids in the 64 h subcritical PWHT (774°C/64 h) longitudinal creep specimen at a distance of 2 mm from the rupture location. Note that all four individual regions in the weld show evidence of voiding/cavitation (orange arrows), but the extent is reduced from the 1 mm location in Fig. 5-14. The voids/cavities are still distorted (elongated) due to plastic deformation at the 2 mm location (corresponding to 77%RA from Fig. 5-12). Etchant: Vilella's reagent.

and extent of cavitation/voiding in the BM, FGHAZ, CGHAZ, and WM regions at a distance of 2 mm from rupture, corresponding to 77% RA from Fig. 5-12. At this location, cavities/voids are still present although to a lesser extent than the 1 mm location. The evidence of plastic deformation in the microstructure is still apparent in that the cavities/voids (orange arrows in the figures) are elongated and also in the fact that the FGHAZ, while exhibiting the formation of ferritic subgrains, appears "elongated" (i.e. the ferritic subgrain structure which normally appear equiaxed, is distorted by plastic deformation). Fig. 5-16 shows the microstructure and cavitation extent at a distance of 4 mm from the rupture location in the 64 h PWHT specimen, corresponding to 66% RA from Fig. 5-12. At this location, Fig. 5-16 indicates that the cavitation/voiding extent is further reduced from the 2 mm location, and the cavities appear significantly smaller than at the 2 mm location. Additionally at the 4 mm location, the cavities are noticeably less elongated and are nearly uniform in shape. In the base metal micrograph in Fig. 5-16, the cavities (orange arrows) are present along subgrain boundaries and are barely visible; in comparison, the cavities in the CGHAZ, FGHAZ, and WM are larger. Additionally, at the 4 mm location, the difference in substructure appearance is more apparent, such as the presence of subgrains. The microstructure and cavitation at the 8 mm location are shown in Fig. 5-17, which indicates that the extent of cavitation is minimal to none at this distance from rupture (which corresponds to 42%RA). In essence, only single cavities are visible in the field of view as shown by the orange arrows; additionally, the microstructure does not show any distortion from plastic deformation. The FGHAZ microstructure clearly reveals the presence of equiaxed ferritic subgrains and it is also clear that the FGHAZ has a refined structure compared to the other three regions. Small inclusions in the weld deposit (most likely, oxides) are visible and are not associated with cavitation. Lastly, Fig. 5-18 shows the microstructural appearance in the shoulder region (0%RA) of the 64 h PWHT specimen. No cavitation is observed and no distortion of the microstructure is apparent, although this region was subjected to some stress during creep testing (~64 MPa based

4 mm From Rupture – 5KX Comparison

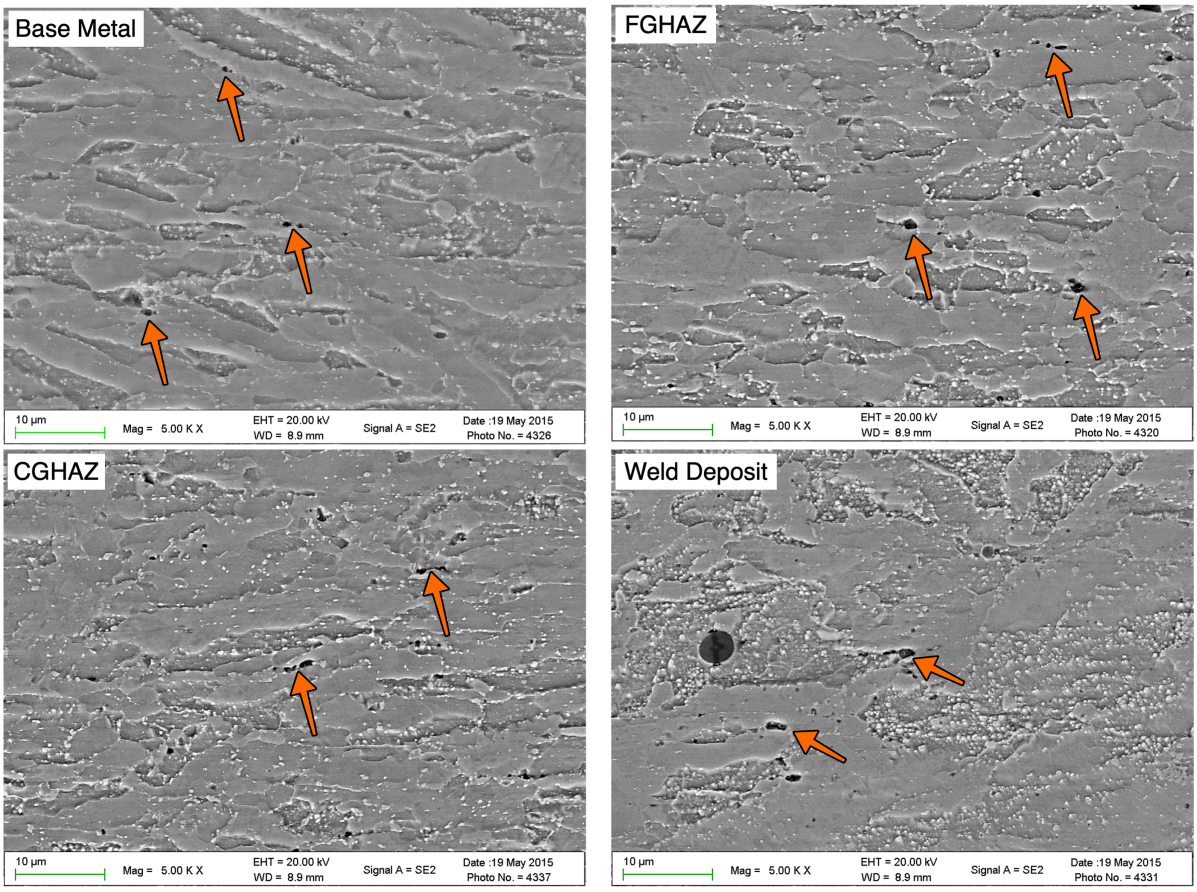


Figure 5-16. SE-SEM micrographs showing the microstructural appearance and extent of cavities/voids in the 64 h subcritical PWHT (774°C/64 h) longitudinal creep specimen at a distance of 4 mm from the rupture location. Note that all four individual regions in the weld show evidence of voiding/cavitation (orange arrows), but the cavity size is smaller and the extent is significantly reduced from the 1 mm location in Fig. 5-14. The voids/cavities are still slightly distorted (elongated) due to plastic deformation at the 4 mm location (corresponding to 66%RA from Fig. 5-12). Etchant: Vilella's reagent.

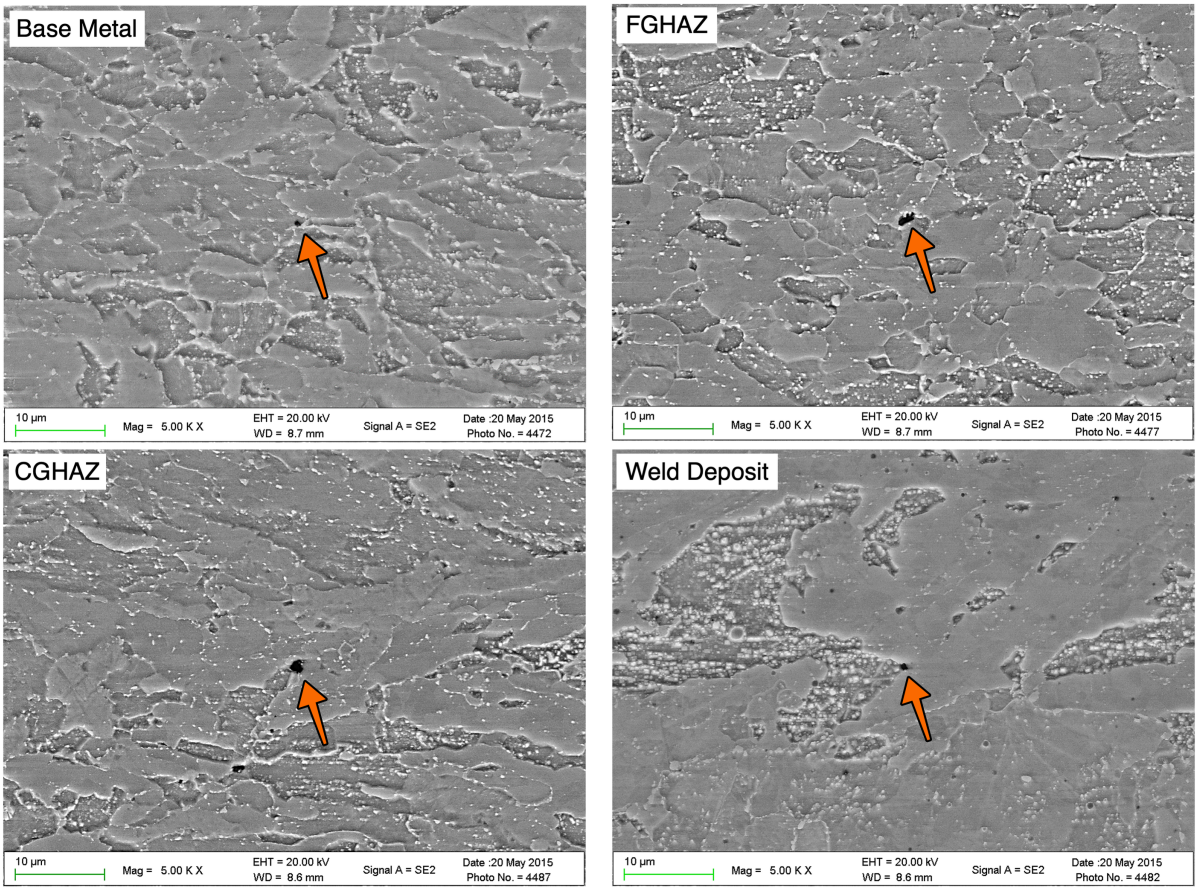


Figure 5-17. SE-SEM micrographs showing the microstructural appearance and extent of cavities/voids in the 64 h subcritical PWHT (774°C/64 h) longitudinal creep specimen at a distance of 8 mm from the rupture location. The extent of cavitation at the 8 mm location is minimal and very isolated, with only one or two cavities (orange arrows) in each micrograph; the voids/cavities are not distorted due to plastic deformation at this location (corresponding to 42%RA from Fig. 5-12). Additionally, the FGHAZ microstructure shows clear evidence of equiaxed ferritic subgrains. Etchant: Vilella's reagent.

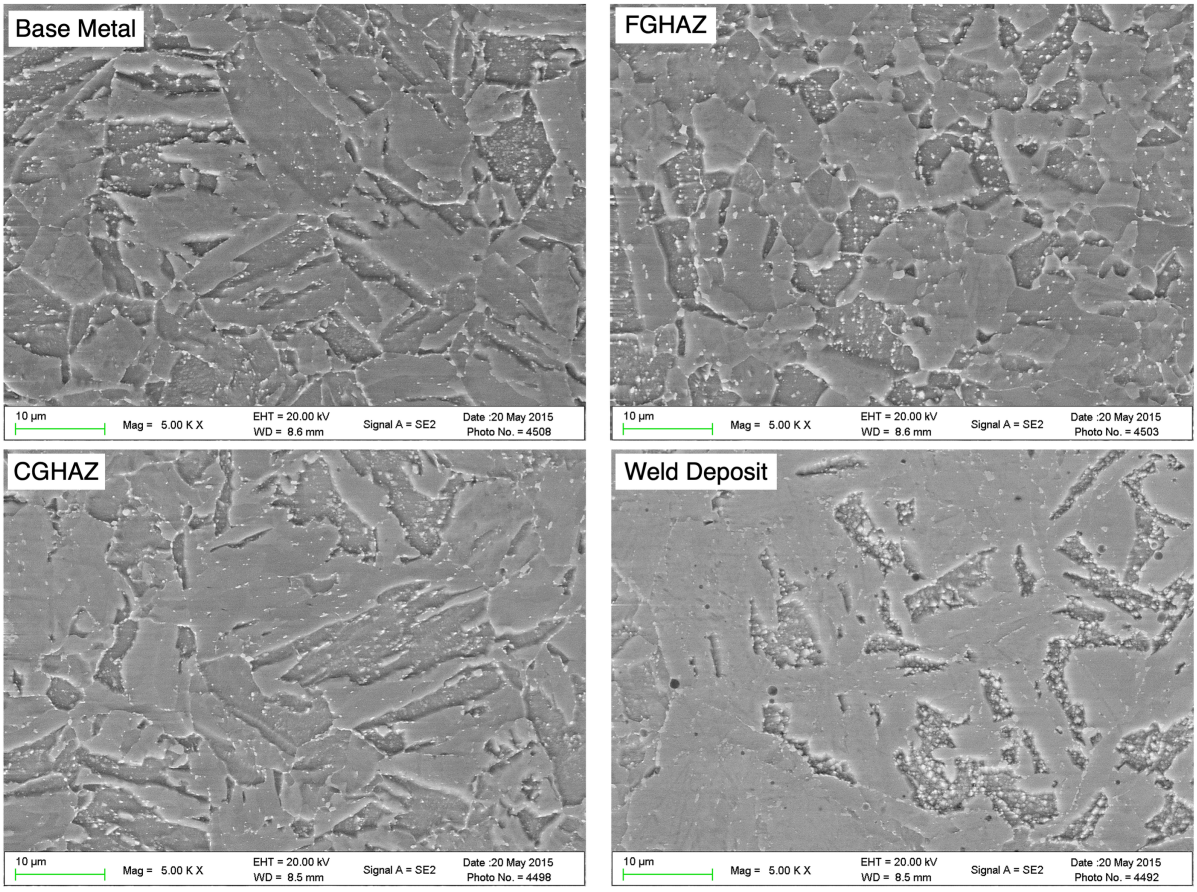


Figure 5-18. SE-SEM micrographs showing the microstructural appearance and extent of cavities/voids in the 64 h subcritical PWHT (774°C/64 h) longitudinal creep specimen, in the shoulder region located 4 mm from rupture (0 %RA at this location). In all four individual regions, no evidence of voiding/cavitation is observed. The FGHAZ microstructure shows clear evidence of equiaxed ferritic subgrains, while the CGHAZ, BM, and WM show a lath-like structure. Etchant: Vilella's reagent.

on shoulder diameter).

5.4 Creep Damage Characterization of the Normalized and Tempered Longitudinal Creep Specimen

The results of the metallographic examination of the N&T longitudinal creep sample are presented beginning with Fig. 5-19. Fig. 5-19 shows an optical macrograph of the N&T longitudinal creep specimen over the distance of approximately 0-10 mm from the rupture location. As discussed previously, in the N&T specimen the three regions (BM, "former" HAZ, and WM) are qualitatively similar in the sense that all three regions were fully transformed to austenite and subsequently transformed to martensite; thus, the microstructural gradient of the HAZ has been "erased" leaving only the "former" HAZ. At this low magnification, two primary differences resulting from creep exposure are apparent in the specimen: (i) the base metal side shows significantly more %RA than the weld deposit (WM) side (ii) macroscopic creep damage and cavitation is visible in the weld deposit (shown by the orange arrows in Fig. 5-19) but not in the former HAZ or BM. The marked regions in Fig. 5-20 shows the microstructural appearance and cavitation at a distance of 1 mm from the rupture location in the N&T longitudinal specimen. At this distance, cavitation is observed in all four regions (BM, former FGHAZ and CGHAZ, and WM) as denoted by the orange arrows in the micrographs; the cavities are elongated due to the plastic deformation which occurred adjacent to rupture (46% RA). More cavities were observed in the WM than in the other regions and appeared somewhat aligned, while in the other regions the cavities were mostly (although not entirely) isolated. It is also apparent from Fig. 5-20 that the microstructure is deformed in all four regions as evidenced by the elongated or flattened grain structure. Fig. 5-21 shows the appearance and cavitation (marked by orange arrows) at a distance of 2 mm from rupture. The extent of cavitation in the BM and former CGHAZ is reduced compared to the 1 mm location and the cavities appear less elongated, in agreement with the lower %RA (39%). In contrast, the creep damage

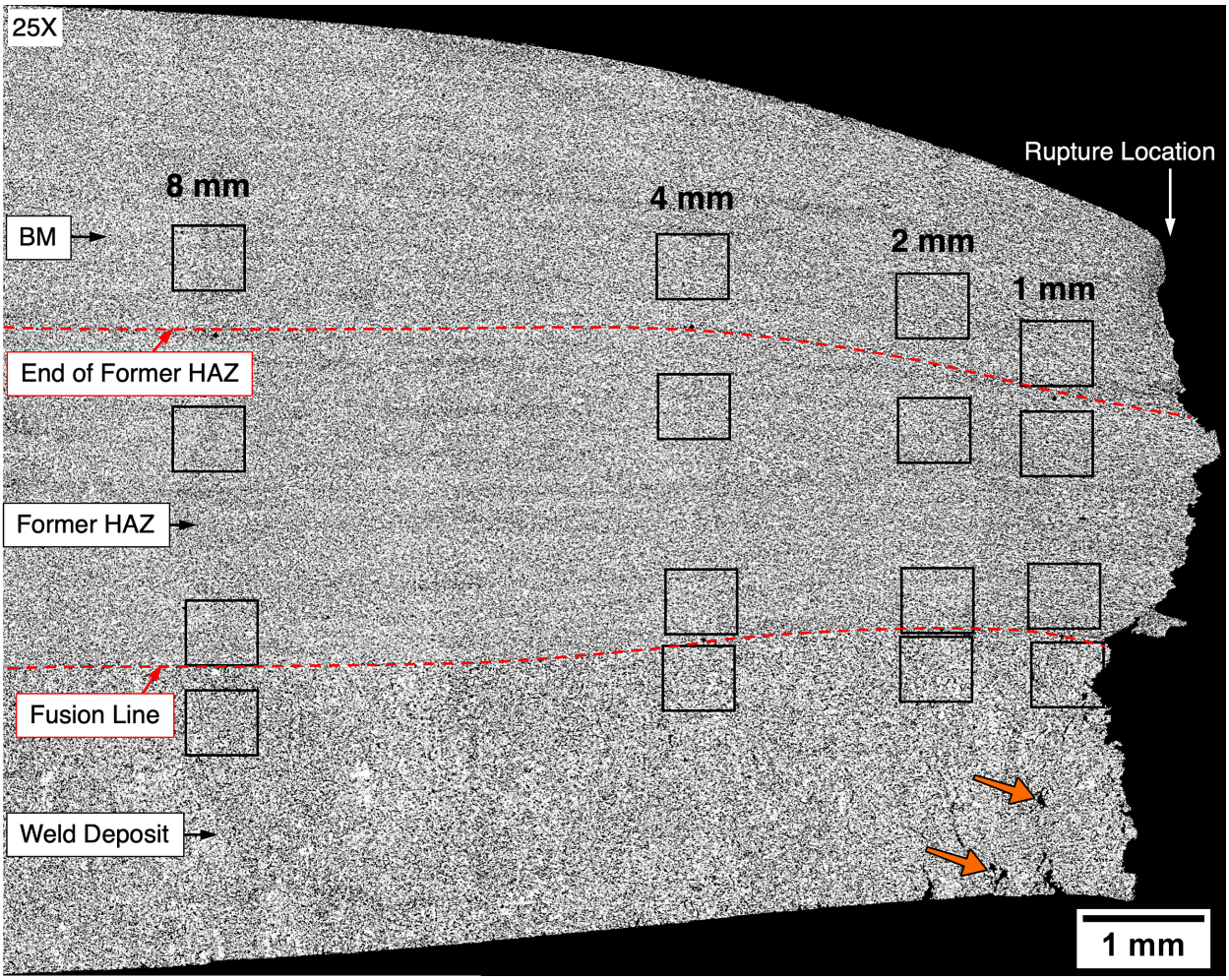


Figure 5-19. Optical light macrograph showing the appearance of the normalized and tempered (N&T) longitudinal creep specimen, at the rupture location. Creep testing was performed at 621°C/124 MPa; total elongation was 16.7%, the overall reduction of area was 59%, and rupture life was 481.5 h. The marked regions at the 1 mm, 2 mm, 4 mm, and 8 mm locations were selected for higher magnification examination. The two dashed red lines indicate the location of the fusion line and the approximate location of the "former HAZ" (the HAZ which was re-transformed to austenite during the N&T heat treatment, thus essentially eliminating the HAZ microstructure gradient which had previously been present). Note the significant difference in the reduction of area for the base metal (BM) region of the specimen as compared to the weld deposit (WM). Also, even at this low magnification, more extensive cavitation (orange arrows) is evident in the WM adjacent to the rupture location. Etchant: Vilella's reagent.

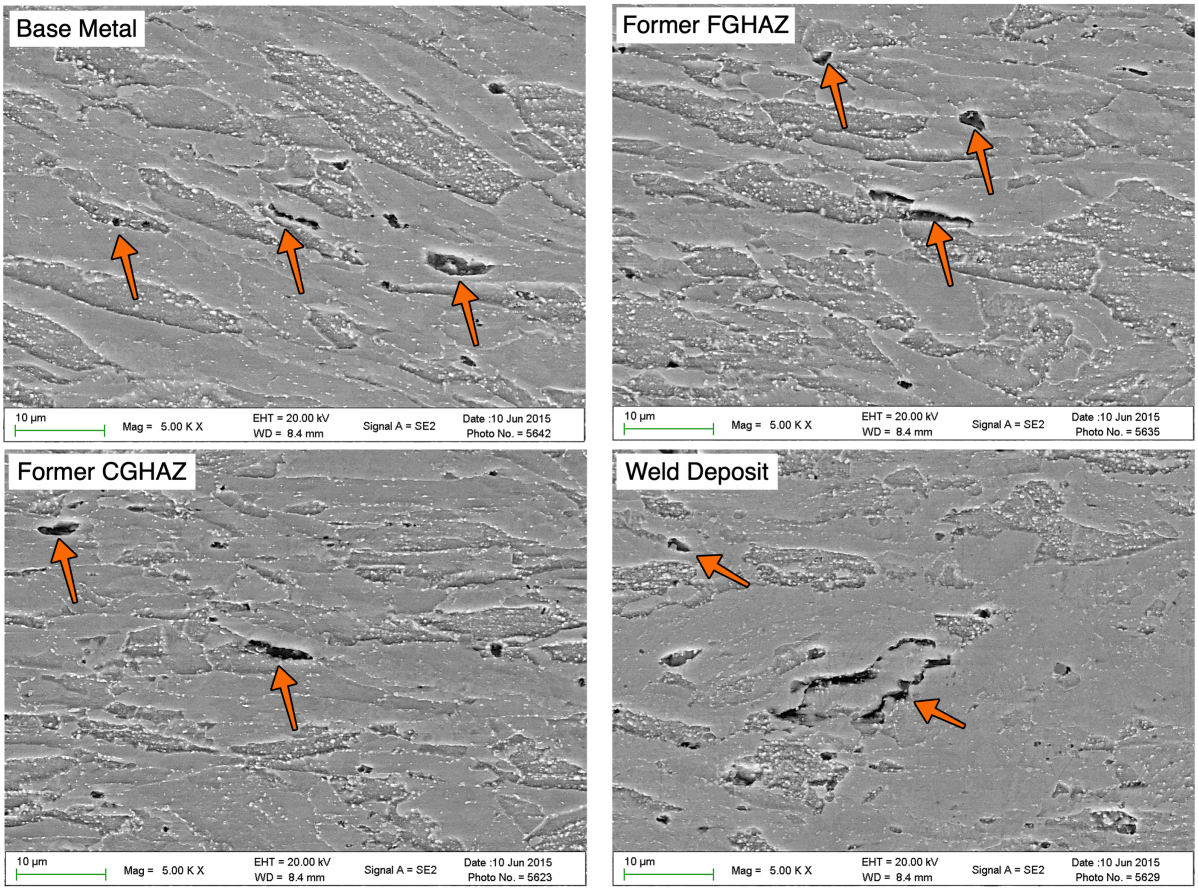


Figure 5-20. SE-SEM micrographs showing the microstructural appearance and extent of cavities/voids in the N&T longitudinal creep specimen at a distance of 1 mm from the rupture location. All four individual regions in the weld show evidence of voiding/cavitation (orange arrows); additionally, the voids/cavities are distorted (elongated) due to plastic deformation at the 1 mm location (corresponding to 46%RA from Fig. 5-12). Etchant: Vilella's reagent.

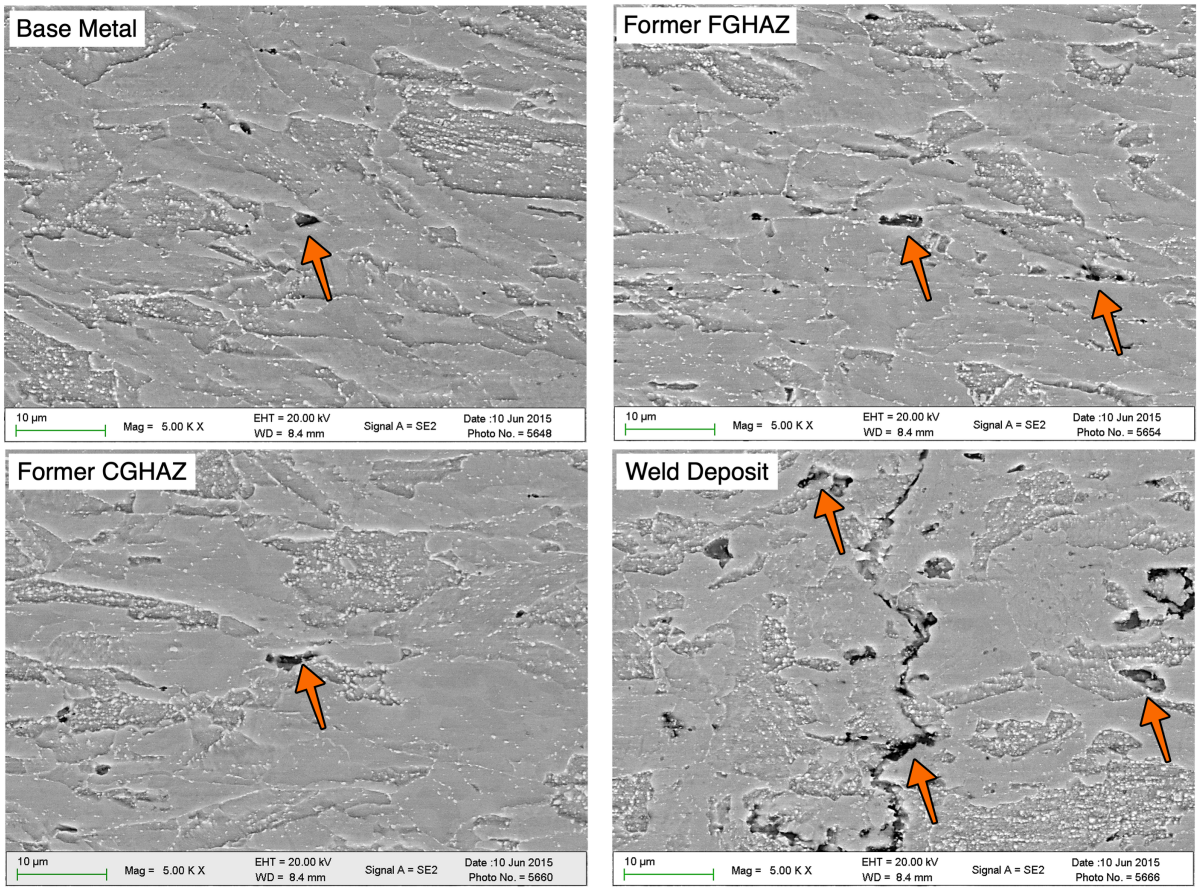


Figure 5-21. SE-SEM micrographs showing the microstructural appearance and extent of cavities/voids in the N&T longitudinal creep specimen at a distance of 2 mm from the rupture location. All four individual regions in the weld show evidence of voiding/cavitation (orange arrows); the cavitation in the WM region is particularly extensive and has the appearance of micro-cracking. The voids/cavities still show some distortion due to plastic deformation at the 2 mm location (corresponding to 39%RA from Fig. 5-12). Etchant: Vilella's reagent.

extent appears greater in the WM at the 2 mm location and the damage is linked to form a micro-crack, along with other cavities. At this location the reduction of area is 39% and the cavities still show slight elongation.

Fig. 5-22 shows the microstructure and extent of creep damage at a distance of 4 mm from the rupture location, corresponding to 34% RA from Fig. 5-12. Only minor evidence of creep cavitation is observed in the BM, former FGHAZ, and former CGHAZ regions, while the WM still shows significant cavitation. At the 4 mm location, the microstructure is not severely distorted and the tempered martensite lath structure is discernible in all four regions (due to the N&T heat treatment). Fig. 5-23 shows the microstructure and extent of creep damage at a distance of 8 mm from the rupture location, which corresponds to a lower deformation of 19% RA. In the BM, former CGHAZ, and former FGHAZ regions, there is minimal to no creep damage, but significant creep damage is observed in the WM region with some aligned cavities. The cavities do not show evidence of flattening or elongation at this location. Lastly, Fig. 5-24 shows the microstructure in the shoulder of the specimen, remote from rupture (36 mm). At this location, no creep damage is present and the microstructure is not distorted, but appears qualitatively similar in the four regions. The TMLS resulting from the N&T heat treatment is clearly visible in all four regions, including the former FGHAZ and former CGHAZ.

5.5 Discussion of Creep Behavior and Creep Damage in Longitudinal Specimens from the AEP Weldment

Several differences were observed when comparing the creep behavior and creep damage characterization of the 64 h subcritical PWHT and N&T longitudinal specimens as presented in the preceding preliminary results. Although the two conditions showed a similar order of magnitude of elongation during creep (~15 to 20%), the difference in reduction of area was much more significant (91% versus 59%, respectively) and this correlated much more closely with the observed extents of creep damage in the two

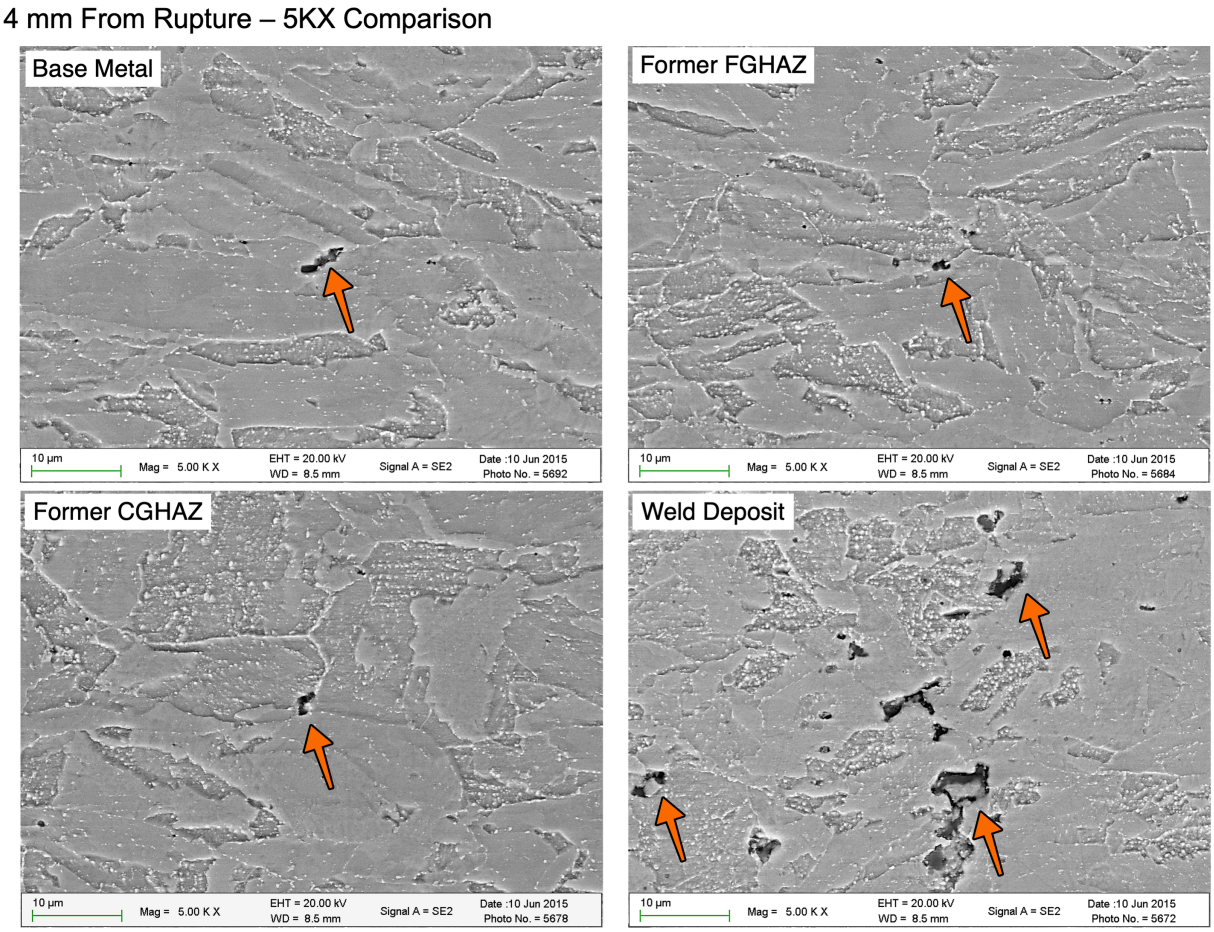


Figure 5-22. SE-SEM micrographs showing the microstructural appearance and extent of cavities/voids in the N&T longitudinal creep specimen at a distance of 4 mm from the rupture location. The BM, former FGHAZ, and former CGHAZ regions in the weld show minor evidence of voiding/cavitation (orange arrows), but the cavitation in the WM region remains the most extensive. The voids/cavities still show slight distortion due to plastic deformation at the 4 mm location (corresponding to 34%RA from Fig. 5-12). Etchant: Vilella's reagent.

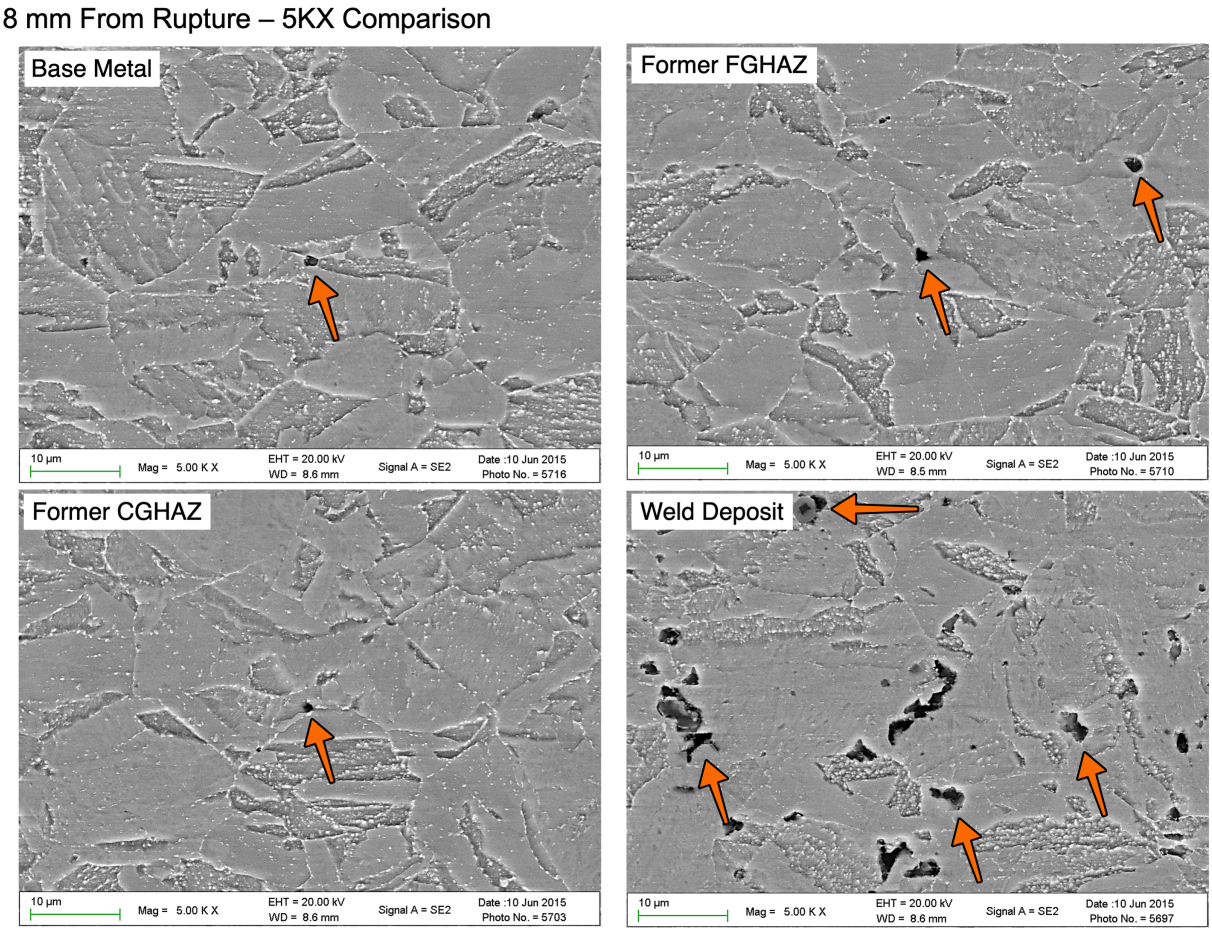


Figure 5-23. SE-SEM micrographs showing the microstructural appearance and extent of cavities/voids in the N&T longitudinal creep specimen at a distance of 8 mm from the rupture location. The cavitation in the BM, former FGHAZ, and former CGHAZ regions is minimal to essentially none (orange arrows), but the cavitation in the WM region remains extensive. The voids/cavities do not show evidence of elongation/distortion at the 8 mm location (corresponding to 19%RA from Fig. 5-12). Etchant: Vilella's reagent.

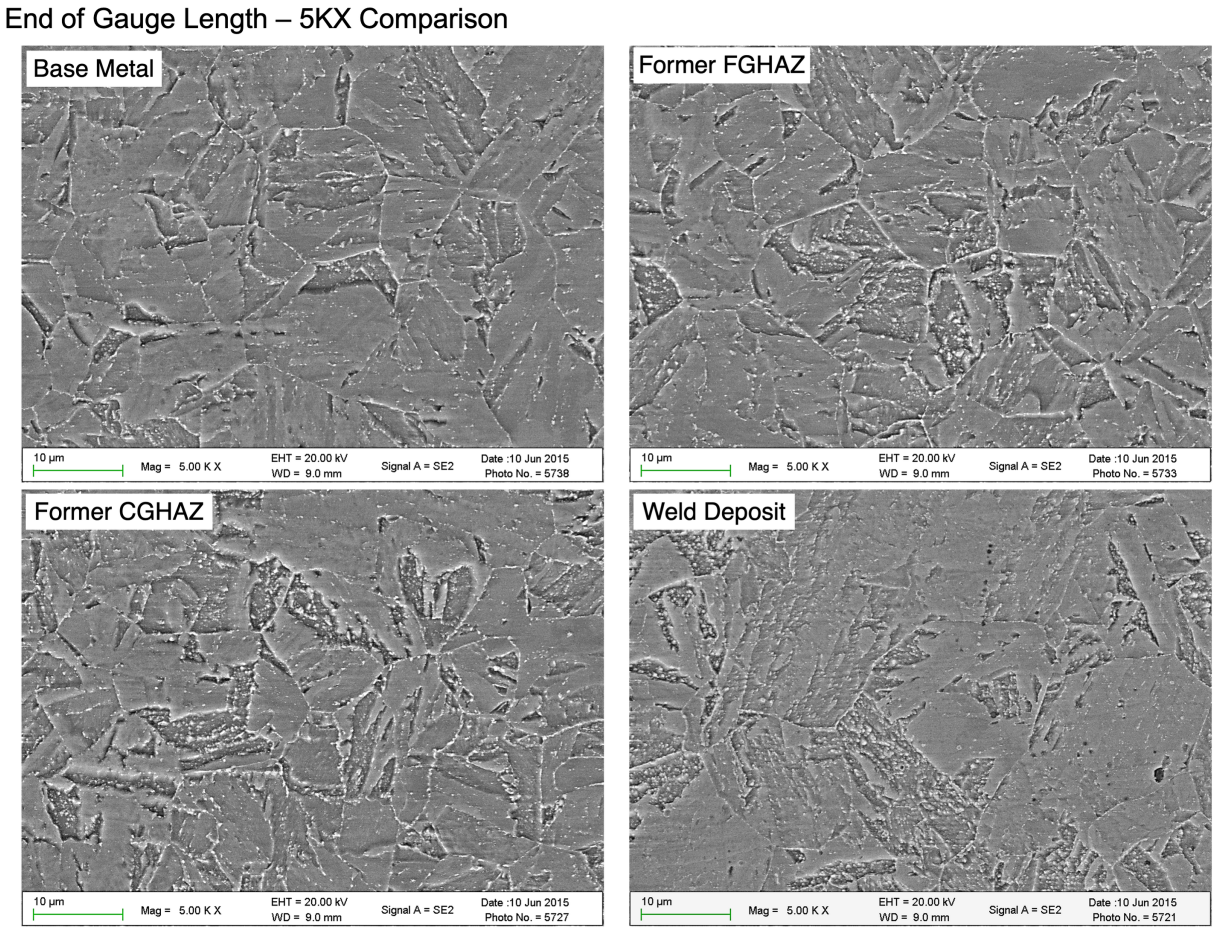


Figure 5-24. SE-SEM micrographs showing the microstructural appearance in the N&T longitudinal creep specimen in the shoulder region, at a distance of 36 mm from the rupture location. No cavitation is observed within this region due to the much lower stress (~64 MPa) during creep testing; the microstructural appearance is similar in all four individual regions due to the N&T heat treatment. Etchant: Vilella's reagent.

specimens. The 64 h PWHT specimen also showed a much more uniform reduction of area than the N&T specimen, which showed preferential %RA in the BM side of the specimen and reduced RA at the opposite, WM side of the specimen (cf. Fig. 5-13 to Fig. 5-19).

5.5.1 Comparison of the Longitudinal Creep Behavior of the Subcritical PWHT and N&T Heat Treatment Conditions

Overall, based on the preliminary presented results, the N&T condition showed more desirable creep behavior compared to the subcritical PWHT condition. From the creep data in Fig. 5-5 and Fig. 5-6, the N&T condition exhibited longer creep rupture life and lower minimum creep rate, and the N&T also showed a more uniform hardness profile across the weld and adjacent zones than the 64 h PWHT condition. The longer creep rupture life under laboratory testing conditions would most likely correspond to longer rupture life under service conditions as well, and this is reflected in the weld strength reduction factors (WSRF) in ASME Boiler and Pressure Vessel Code Section I (*Section I: Rules of Construction for Power Boilers*, 2019). Table PG-26 in this part of the ASME code describes the mandated multiplying factors which are used to reduce the allowable stress of welded Grade 91 components in elevated temperature service. In Table PG-26 in the code, subcritical PWHT and normalizing & tempering are both permissible as heat treatments for CSEF steel weldments; however, the WSRF values for the subcritical PWHT condition exact a much higher penalty on the allowable stress. In the subcritical PWHT condition, a reduction factor of 0.5 (50% penalty on allowable stress) is mandated for CSEF welds at all temperatures between 950 to 1200°F (use not permitted at higher temperatures). In contrast, CSEF welds in the N&T condition are given gradually decreasing WSRF values, beginning at 0.95 at 1000°F and decreasing to 0.77 at 1200°F. On this basis, the N&T condition would be more desirable for use in service components. However, the N&T heat treatment is not feasible to use "in the field," such as for heat treatment of circumferential welds between large pipe sections, due to the need for a furnace heat treatment rather than with heating blankets since an N&T

performed with heating blankets would create an intercritical HAZ region at the blanket edge, and also due to the increased potential for distortion at the higher temperature. For this reason, the N&T heat treatment for CSEF weldments is not as widely utilized as the longer creep rupture life evidenced by the data in Fig. 5-5 and Fig. 5-6 would initially suggest.

5.5.2 Comparison of 8 h and 64 h Subcritical PWHT Conditions

Another point of comparison in the longitudinal creep test results relates to the creep performance difference in the 8 h and 64 h subcritical PWHT specimens. As shown previously in Fig. 5-5 and Fig. 5-7, the 64 h condition showed an ~40% shorter rupture life and an ~90% higher value of minimum creep rate. The intent of the 64 h PWHT duration was to show the creep behavior that could be expected from a Grade 91 weldment in a "worst case" scenario if it was subjected to multiple PWHT cycles, for example eight cycles of 8 h with a cumulative effect. Multiple PWHT cycles could potentially occur over the course of component service life such as in cases where modification of a component is necessary or where weld repair is required due to reported NDE indications during an inspection. The 64 h PWHT represents a very severe cumulative PWHT, much greater than would be reasonably anticipated over the course of a component's actual service life. Hardness was measured for both conditions (see Table 2) which showed a slight hardness reduction after the 64 h PWHT. However, the microstructure of the 8 h subcritical PWHT specimen was not characterized for the preliminary results reported and thus a comparison of the 8 h and 64 h microstructure in the various regions (BM, IC/FG/CGHAZ, WM) is not presented here.

Although a comparison of the 8 h and 64 h microstructures cannot be made with the current results, it is possible to make some inferences about the expected microstructural differences based on the information from the literature review regarding the effects of tempering and creep exposure on the microstructure of CSEF steels and weldments. As discussed previously in the literature review, the primary

microstructural changes occurring during both tempering and creep, although to different extents, are precipitate coarsening, formation of equiaxed ferritic subgrains and subgrain coarsening, reduction of dislocation density, and potential precipitation of new phases (e.g. carbides during tempering, or Laves phase or Z-phase during creep). In the literature review, it was discussed that precipitate coarsening (primarily of $M_{23}C_6$) occurs more slowly during static thermal exposure such as PWHT and more rapidly during creep. Due to the significant difference in PWHT duration, it is certainly expected that the 64 h PWHT specimen would exhibit greater and further coarsening of $M_{23}C_6$ in the FG/ICHAZ, where coarsening and formation of equiaxed ferritic subgrains has already commenced due to the welding thermal cycle as shown in Fig. 5-18. Since these precipitates are frequently located along the subgrain boundaries, the 64 h PWHT condition would experience greater subgrain coarsening in the FG/ICHAZ, both during static thermal exposure and particularly during creep when plastic deformation is occurring. The expected difference in microstructure can be inferred from Fig. 2-53, which shows a comparison of 9Cr-1W steels tempered for 750°C/1 h and 750°C/20 h. The difference in subgrain coarsening (which is preceded by precipitate coarsening) is evident, with the 750°C/20 h Q&T showing a significant degradation of the elongated subgrain structure (TMLS) and formation of equiaxed ferritic subgrains. A similar form of microstructure change is expected for the 64 h PWHT condition compared to the 8 h condition, particularly in the FG/ICHAZ. Thus, the 64 h PWHT condition would be entering creep exposure with degraded TMLS and thus would be further susceptible to more immediate and more rapid microstructure change than the 8 h PWHT, which would explain the rapid progression into the tertiary creep regime after only ~10 h. As pointed out before, Abe (Abe, 2003) suggested based on Fig. 2-53 that the microstructure of 9Cr steels may develop toward a common "terminal" microstructure at the end of creep, consisting of coarsened carbides and equiaxed ferritic subgrains. In this respect, the 64 h PWHT condition would have degraded to a greater extent during heat treatment and would be closer to the "terminal" microstructure than the 8 h

PWHT, thus potentially explaining the decreased creep life of the 64 h PWHT longitudinal specimen.

Chapter 6 Conclusions

Based on the results reported in this dissertation, the following conclusions are stated pertaining to the cross-weld creep behavior of dissimilar Grade 91 shielded metal arc weldments and to the creep behavior of longitudinal creep specimens from a Grade 91 submerged arc weldment.

6.1 Conclusions Related to Cross-Weld Creep Testing of Grade 91 Weldments with Dissimilar Base Metals

As part of the dissertation research, the heat-affected zone (Type IV) creep behavior of dissimilar Grade 91 weldments comprised of Grade 91 forging and plate materials was evaluated through base metal characterization, cross-weld creep testing, and characterization of creep damage and microstructure in the tested weldment specimens. In this work, three different base metals were evaluated which had measured N:Al ratios of 2.41 (FT, forging), 11.33 (H13, plate), and 22.50 (H47, plate) and sulfur contents of 0.008 wt.%, 0.001 wt.%., and 0.003 wt.%, respectively. The following conclusions were determined based on the results obtained from this evaluation.

1. Cross-weld creep testing of Grade 91 base metals in a dissimilar weld configuration was effective for revealing differences in creep damage resistance and damage accumulation in the heat-affected zones (HAZs) of base metals which had identical heat treatments and similar chemical compositions except for certain differences including sulfur content, aluminum content, chromium content, and nitrogen to aluminum (N:Al) ratio.
2. The characterization of Type IV creep damage in the dissimilar weldments revealed unequal accumulation of creep damage in the respective base metal HAZs in each weldment and appeared to lend support to the position (Maruyama et al., 2017) that N:Al ratio is not an unequivocal indicator of creep damage susceptibility regardless of other factors. If lower N:Al ratio was categorically associated with greater propensity for Type IV creep damage, then it may be

expected that rupture would occur in the same base metal (that with the lowest N:Al ratio) in different weldments. However, the rupture location was different (i.e. occurred in a different base metal) in the two dissimilar weldments examined in this work. Specifically, in the FT-H47 creep specimen rupture occurred on the FT (forging) side with the lower N:Al ratio of 2.41, as would be expected. In the H13-H47 creep specimen, however, rupture occurred on the H47 (plate) side with a *higher* N:Al ratio of 22.50, in contrast to the general expectation based on literature.

3. In the FT-H47 weldment, creep rupture occurred in the FT ICHAZ region, and a much greater extent of creep cavitation was observed in the FT HAZ generally as compared to the isolated creep cavitation observed in the H47 HAZ. In the H13-H47 weldment, imminent creep rupture due to macro-crack formation and growth was observed in the H47 HAZ; a smaller micro-crack and significant creep cavitation were observed in the H13 HAZ. Overall, the difference in creep damage extent between two dissimilar base metals was significantly greater in the FT-H47 weldment than in the H13-H47 weldment.
4. An abrupt delineation between creep-damaged and undamaged areas was observed at the outer boundary of the FT HAZ, which suggests that Type IV creep cavitation was strongly influenced by microstructure evolution during welding, post weld heat treatment, and creep exposure because the thermal gradient in the HAZ with its consequent effect on microstructure evolution is the only parameter which could reasonably vary over the length scale involved (~200 μm distance between damaged and undamaged areas).
5. In the Grade 91 HAZ regions, creep cavitation typically exhibited a complex, irregular morphology rather than a spherical, rounded, or polyhedral morphology as revealed both by metallographic examination of polished and etched samples and by fractographic examination of cryo-cracked fracture surfaces. Many cavities appeared to be located at the intersection of multiple subgrain boundaries (i.e. at

subgrain boundary junctions). Locations with isolated cavitation such as the H47 HAZ revealed the random nature of creep damage accumulation since cavities were distributed in a widely separated manner.

6. The chemical compositions of the FT and H47 base metals showed similar correlations with extent of creep damage as has been reported in the literature for Grade 91 steels, but the behavior was not completely straightforward. The FT base metal with higher sulfur content and higher aluminum content showed a significantly higher extent of Type IV creep cavitation in cross-weld creep testing. However, differences between FT and H47 for other impurity elements associated with poor Grade 91 creep performance in the literature (As, Sb, Sn, Cu) did not show any significant correlation with the variation in creep damage. Additionally, the H47 side which exhibited less creep damage had three times higher Ni content, in contrast to the fact that elevated Ni content has been reported as a detrimental element for Grade 91 creep strength. The H13 and H47 base metals in the H13-H47 weldment, which both had similar chemical compositions, showed a more similar extent of Type IV creep damage than the FT and H47 base metals in the FT-H47 weldment.
7. The results of the inclusion analysis of the FT and H47 base metals did not show a clear difference in inclusion density between the two materials, which was unexpected due to the much higher sulfur content of the FT material. Although it is possible that a difference in inclusion content could be revealed by examining at higher magnifications than the 2500x SEM panoramas in the current work (such as at 5000x or 10000x) if the inclusion content contains a significant fraction of small inclusions, it is unknown whether such an examination would actually show a greater difference in inclusion content. The FT base metal (with higher sulfur content) showed that it contained a higher fraction of large inclusions than the H47 base metal.

8. The results of image analysis of FT and H47 HAZ microstructure suggested a correlation between the extent of Type IV creep damage in the FT and H47 HAZs and the precipitate characteristics in the FT and H47 ICHAZ regions. In the FT HAZ which showed a greater extent of creep damage, the precipitate distribution showed a 30-40% reduction in precipitates between 0.005 to 0.15 μm^2 in size. The greater extent of creep damage was attributed to the decrease in fine precipitates since it is known from the literature that the resistance to microstructure recovery depends on precipitate density and spacing. A reduced number of fine precipitates ($\leq$0.005 μm^2) in the FT ICHAZ corresponded to an ~50% increase in the calculated inter-particle spacing compared to the H47 ICHAZ for the specified particle size range.
9. A correlation was also observed between the measured ferritic subgrain size (post creep-test) and the extent of Type IV creep cavitation in the FT-H47 cross-weld specimen. The post-test subgrain size in the H47 FGHAZ and ICHAZ regions was smaller than the subgrain size in the FT FGHAZ and ICHAZ regions. No significant difference was found between the subgrain size of the FGHAZ and ICHAZ regions within the respective materials.
10. It was found that the ICHAZ precipitate distribution correlated with the initial base metal precipitate distribution after PWHT. Similarly to the FT ICHAZ precipitate distribution, the FT base metal after PWHT also showed a reduced extent of fine precipitates compared to the H47 base metal after PWHT, in agreement with the literature (Yu et al., 2013) regarding the effect of the precipitate size characteristics prior to welding upon the size characteristics after welding.
11. Although a number of possible explanations were explored to rationalize the difference in the FT and H47 ICHAZ precipitate distributions, the reasons for the reduced extent of fine precipitates in the FT ICHAZ were not clearly apparent. Preliminary thermodynamic calculations for the FT and H47 base metals did not

show a significant difference in either the $M_{23}C_6$ phase fraction at the PWHT temperature of 746°C or matrix diffusivity values, so the differences in precipitate distribution did not appear to originate from compositionally-based precipitation behavior.

12. Based on the combined results from the FT-H47 and H13-H47 dissimilar weldments, it is proposed that the extent of Type IV creep damage in these weldments was primarily influenced (in order) by sulfur content, microstructure and precipitation resulting from heat treatment, and N:Al ratio. Sulfur content is proposed to be a more important criterion than N:Al ratio during procurement of Grade 91 material, due to the fact that higher N:Al ratio was not unequivocally linked with higher damage resistance in the current results.

6.2 Conclusions Related to Creep Testing of Longitudinal Specimens from a Grade 91 Weldment

1. Creep testing of longitudinal specimens from a Grade 91 submerged arc weldment showed distinct differences in creep behavior and creep damage occurrence for two different types of heat treatment (subcritical postweld heat treatment versus normalizing and tempering).
2. For two different subcritical PWHT conditions (774°C/8 h and 774°C/64 h), the creep elongation (average strain to rupture) and creep ductility (reduction of area) were similar, but the shorter PWHT time showed approximately 70% longer rupture time. Comparatively, the N&T condition exhibited a similar level of elongation, but showed significantly lower creep ductility together with much longer rupture life (~5X longer than the 64 h PWHT condition).
3. All three conditions showed a similar primary creep rate, and the minimum creep rate achieved for each condition correlated with the trend in rupture times. All three conditions achieved the minimum creep rate at roughly the same point during testing when normalized by the total test time, but the N&T condition

exhibited the longest absolute time to reach the minimum creep rate and showed the lowest minimum creep rate of 0.0076 %/h.

4. For all three heat treatment conditions, the majority of the test duration occurred in the tertiary creep regime, in accordance with the typical behavior of Grade 91 material reported in the literature, such as by Abe (Abe, 2015). The N&T condition showed the highest increase in strain rate per increment of strain within the tertiary regime.
5. The N&T condition showed the lowest creep ductility in terms of %RA at the rupture location and also the lowest overall %RA along the gauge length. After an initial rapid decrease in %RA away from rupture, all three heat treatment conditions exhibited reduction of area even at locations which were not adjacent to the rupture location (20-25 mm from rupture) which suggests that a noticeable extent of uniform creep deformation occurred during testing, prior to necking and final rupture.
6. Comparing the 64 h PWHT condition to the N&T condition, the N&T condition showed a much greater overall occurrence of creep damage, particularly in the weld deposit, in contrast to its longer rupture time.
7. In the 64 h PWHT condition, creep cavitation was primarily observed at locations nearer to rupture (<4 mm from rupture), while in the N&T condition, significant creep damage was observed in the weld deposit along the gauge length at farther distances (8 mm) from rupture.
8. Comparing the subcritical PWHT results with the N&T result, both of which are permissible heat treatments for CSEF weldments according to Table PG-26 in the ASME Boiler and Pressure Vessel Code Section I, the N&T condition showed significantly longer (>3X) creep rupture life than the 8 h PWHT despite the much greater extent of creep cavitation in the N&T weld deposit. The longer creep life indicates that the N&T condition is preferable to the subcritical PWHT condition

in terms of weldment performance, but implementation of such an N&T heat treatment in the field is hampered by practical issues surrounding the heat treating of large power piping components.

6.3 Research Contribution

The following specific contributions were identified from the dissertation research and results as being helpful for industry users of Grade 91 material.

1. The results from the experiments with dissimilar Grade 91 weldments provided support for the position that N:Al ratio is not an unequivocal indicator of creep damage susceptibility regardless of other factors even for significant differences (factor of two). Thus, the results suggest that stringent controls on N:Al ratio may not be as necessary as anticipated.
2. Procedures were developed to quantitatively compare Grade 91 microstructures and precipitate characteristics using basic SEM capabilities which could be used in industry, without requiring the use of transmission electron microscopy.

Chapter 7 Future Work

Based on the findings of the current dissertation, several areas were identified as suggested directions for future research on Type IV creep damage development in Grade 91 steel weldments. These research areas would further increase the understanding of the primary factors which influence susceptibility to Type IV damage.

Direct measurement of strain using the DIC method has been reported for Grade 91 weldments by several researchers (Wang et al., 2021a, 2021b; Yu et al., 2014). These experiments were performed on weldments with identical base metals on each side, but work should be extended to dissimilar weldments having different Grade 91 base metals on each side. The application of DIC would allow the determination of whether the final creep strain differences (as evidenced by %RA at rupture) are due to a late accumulation of strain in the final portion of tertiary creep, or whether an initial difference is observed in creep strain accumulation from the beginning of the creep test. Instrumented DIC creep testing should also be coupled with interrupted creep testing of dissimilar Grade 91 weldments to determine how the development (nucleation and growth) of creep cavitation varies between different base metals in a dissimilar weldment and how this is connected to creep strain accumulation. Regardless of the nature of future creep testing, including DIC instrumented tests or interrupted tests, it will be critically important for the materials used in fabricating test weldments, and the test weldments themselves, to have a fully-defined processing history including original rolling conditions for plate material (rolling temperature, percent reduction), measured cooling rates from the processing temperature(s), and heat treatment records. Additionally, wherever possible, samples of material at each processing step (as-rolled, after normalizing, after tempering, etc.) should be preserved for evaluation. The availability of this processing information and associated samples in future experiments is necessary because the lack of information about the starting material conditions (e.g. forging parameters for the FT material and rolling parameters for the H13 and H47

plate materials, or cooling rates), together with the limited availability of microstructural data for image analysis in some cases (e.g. FT-H47 weldment after PWHT) made it more difficult to reach firm conclusions from observations gathered in the currently reported work.

Regarding longitudinally oriented creep specimens, DIC instrumented creep testing should also be integrated with the evaluation of longitudinally oriented creep specimens from Grade 91 weldments. Longitudinal creep tests should be conducted at different stress levels with DIC monitoring of strain accumulation in the various parallel regions within the specimen (BM, HAZ, and WM). A comparison of the stress dependence of creep behavior within the highest strain rate regions would potentially identify whether or not there is a linear stress dependence which, if observed, would point to discrete cavity nucleation such as at inclusions. Specifically regarding the work that was reported in this dissertation, the subcritical PWHT conditions (8 h and 64 h) showed significant difference in rupture time, although the strain behavior was similar. Since the intention of the 64 h PWHT was to show the expected performance of multiple PWHT cycles were needed, such as in the case of multiple weld repairs, the microstructural basis for the degraded performance of the 64 h PWHT should be further investigated beyond the introductory results presented in this dissertation. Additional creep testing with other Grade 91 weldments, particularly weldments which showed good creep performance with a more typical PWHT time of 1-4 h, would provide further understanding of the general response of Grade 91 weldments to extended PWHT, such as whether weldments with good creep performance with standard PWHT are additionally more resistant to degradation by extended PWHT than weldments which exhibit poor creep performance with standard PWHT conditions.

List of References

Abe, F., 2003. Effect of quenching, tempering, and cold rolling on creep deformation behavior of a tempered martensitic 9Cr-1W steel. Metall and Mat Trans A 34, 913–925. doi:10.1007/s11661-003-0222-x

Abe, F., 2004. Coarsening behavior of lath and its effect on creep rates in tempered martensitic 9Cr–W steels. Materials Science and Engineering: A, 13th International Conference on the Strength of Materials 387-389, 565–569. doi:10.1016/j.msea.2004.01.057

Abe, F., 2008. Precipitate design for creep strengthening of 9% Cr tempered martensitic steel for ultra-supercritical power plants. Science and Technology of Advanced Materials 9, 013002. doi:10.1088/1468-6996/9/1/013002

Abe, F., 2010. Heat-to-heat variation in long-term creep strength of some ferritic steels. International Journal of Pressure Vessels and Piping 87, 310–318. doi:10.1016/j.ijpvp.2010.03.014

Abe, F., 2015. Creep Behavior, Deformation Mechanisms, and Creep Life of Mod.9Cr-1Mo Steel. Metall and Mat Trans A 46, 5610–5625. doi:10.1007/s11661-015-3144-5

Abe, F., Nakazawa, S., Araki, H., Noda, T., 1992. The role of microstructural instability on creep behavior of a martensitic 9Cr-2W steel. MTA 23, 469–477. doi:10.1007/BF02801164

Abe, F., Tabuchi, M., Kondo, M., Tsukamoto, S., 2007. Suppression of Type IV fracture and improvement of creep strength of 9Cr steel welded joints by boron addition. International Journal of Pressure Vessels and Piping, Development of and Integrity Issues with New High Temperature High Strength Steels 84, 44–52. doi:10.1016/j.ijpvp.2006.09.013

Abe, F., Tanaka, H., Murata, M., 2007. Impurity effects on heat-to-heat variation in creep life for some heat resistant steels, in: Veivo, J., Auerkari, P. (Eds.),. Presented at the BALTICA VII Life Management and Maintenance for Power Plants, VTT, Helsinki, Finland, pp. 171–184.

Abràmoff, M.D., Magalhães, P.J., Ram, S.J., 2004. Image Processing with ImageJ. Biophotonics International 11, 36–42.

Abson, D.J., Rothwell, J.S., 2013. Review of type IV cracking of weldments in 9–12%Cr creep strength enhanced ferritic steels. International Materials Reviews 58, 437–473. doi:10.1179/1743280412Y.0000000016

Agamennone, R., Blum, W., Gupta, C., Chakravartty, J.K., 2006. Evolution of microstructure and deformation resistance in creep of tempered martensitic 9–12%Cr–2%W–5%Co steels. Acta Materialia 54, 3003–3014. doi:10.1016/j.actamat.2006.02.038

Aghajani, A., Somsen, Ch., Eggeler, G., 2009. On the effect of long-term creep on the microstructure of a 12% chromium tempered martensite ferritic steel. Acta Materialia 57, 5093–5106. doi:10.1016/j.actamat.2009.07.010

Ågren, J., Vassilev, G.P., 1984. Computer simulations of cementite dissolution in austenite. Materials Science and Engineering 64, 95–103. doi:10.1016/0025-5416(84)90076-4

Arreola-Herrera, R., Cruz-Ramírez, A., Rivera-Salinas, J.E., Romero-Serrano, J.A., Sánchez-Alvarado, R.G., 2018. The effect of non-metallic inclusions on the mechanical properties of 32 CDV 13 steel and their mechanical stress analysis by numerical simulation. Theoretical and Applied Fracture Mechanics 94, 134–146. doi:10.1016/j.tafmec.2018.01.013

Benci, J.E., Pope, D.P., George, E.P., 1988. Creep damage nucleation sites in ferrous alloys. Materials Science and Engineering: A, Workshop on the Mechanics and Physics of Crack Growth: Application to Life Prediction 103, 97–102. doi:10.1016/0025-5416(88)90555-1

Bonadé, R., Spätig, P., Schäublin, R., Victoria, M., 2004. Plastic flow of martensitic model alloys. Materials Science and Engineering: A, 13th International Conference on the Strength of Materials 387-389, 16–21. doi:10.1016/j.msea.2004.02.074

Brett, S.J., 2007. UK experience with modified 9%Cr (grade 91) steel. Energy Materials, Energy Mat. (UK) 2, 117–21. doi:10.1179/174892407X266707

Brett, S.J., Oates, D.L., Johnston, C., 2005. In-service Type IV cracking on a modified 9Cr (Grade 91) header. Presented at the ECCC Conference: Creep & Fracture in High Temperature Components - Design & Life Assessment Issues, London, pp. 563–572.

Das, C.R., Divya, M., Albert, S.K., Bhaduri, A.K., Murty, B.S., 2009. Microstructural evolution in the intercritical heat affected zone of a boron containing modified 9Cr-1Mo steel, in: Welding in the World. Institut International de la Soudure, pp. 511–515.

Dieter, G.E., 1986a. Stress and Strain Relationships for Elastic Behavior, in: Mechanical Metallurgy, McGraw-Hill Series in Materials Science and Engineering. McGraw-Hill, Inc., pp. 18–69.

Dieter, G.E., 1986b. Fracture, in: Mechanical Metallurgy, McGraw-Hill Series in Materials Science and Engineering. McGraw-Hill, Inc., pp. 241–272.

DiStefano, J.R., 1986. Summary of Modified 9Cr-1Mo Steel Development Program, 1975-1985 (No. ORNL-6303). Oak Ridge National Laboratory, Metals and Ceramics Division, Oak Ridge, TN.

Dronhofer, A., Pešicka, J., Dlouhý, A., Eggeler, G., 2003. On the nature of internal interfaces in tempered martensite ferritic steels. MEKU 94, 511–520. doi:10.3139/146.030511

Dyson, B.F., 1976. Constraints on diffusional cavity growth rates. Metal Science 10, 349–353. doi:10.1179/030634576790431417

Dyson, B.F., 1983. Continuous cavity nucleation and creep fracture. Scripta Metallurgica 17, 31–37. doi:10.1016/0036-9748(83)90065-0

Dyson, B.F., 1988. Creep and fracture of metals : mechanisms and mechanics. Revue de Physique Appliquee 23, 605–613. doi:10.1051/rphysap:01988002304060500

Eggeler, G., 1989. The effect of long-term creep on particle coarsening in tempered martensite ferritic steels. Acta Metallurgica 37, 3225–3234. doi:10.1016/0001-6160(89)90194-6

Eggeler, G., Nilsvang, N., Ilschner, B., 1987. Microstructural changes in a 12% chromium steel during creep. Steel Research 58, 97–103. doi:10.1002/srin.198701594

Francis, J.A., Cantin, G.M.D., Mazur, W., Bhadeshia, H.K.D.H., 2009. Effects of weld preheat temperature and heat input on type IV failure. Science and Technology of Welding and Joining 14, 436–442. doi:10.1179/136217109X415884

Francis, J.A., Mazur, W., Bhadeshia, H.K.D.H., 2006. Type IV cracking in ferritic power plant steels. Mater. Sci. Technol. 22, 1387–1395. doi:10.1179/174328406X148778

George, E.P., Li, P.L., Pope, D.P., 1987a. Creep cavitation in iron—I. Sulfides and carbides as nucleation sites. Acta Metallurgica 35, 2471–2486. doi:10.1016/0001-6160(87)90144-1

George, E.P., Li, P.L., Pope, D.P., 1987b. Creep cavitation in iron—II. Oxides as nucleation sites. Acta Metallurgica 35, 2487–2495. doi:10.1016/0001-6160(87)90145-3

Ghassemi Armaki, H., Chen, R., Maruyama, K., Igarashi, M., 2011. Creep Behavior and Degradation of Subgrain Structures Pinned by Nanoscale Precipitates in Strength-Enhanced 5 to 12 Pct Cr Ferritic Steels. Metall Mater Trans A 42, 3084–3094. doi:10.1007/s11661-011-0726-8

Ghassemi-Armaki, H., Chen, R.P., Maruyama, K., Igarashi, M., 2013. Contribution of recovery mechanisms of microstructure during long-term creep of Gr.91 steels. Journal of Nuclear Materials 433, 23–29. doi:10.1016/j.jnucmat.2012.09.026

Goodall, I.W., Skelton, R.P., 2004. The importance of multiaxial stress in creep deformation and rupture. Fatigue & Fracture of Engineering Materials & Structures 27, 267–272. doi:10.1111/j.1460-2695.2004.00743.x

Goyal, S., Laha, K., 2014. Creep life prediction of 9Cr–1Mo steel under multiaxial state of stress. Materials Science and Engineering: A 615, 348–360. doi:10.1016/j.msea.2014.07.096

Goyal, S., Laha, K., Das, C.R., Panneerselvi, S., Mathew, M.D., 2014. Effect of Constraint on Creep Behavior of 9Cr-1Mo Steel. Metall and Mat Trans A 45, 619–632. doi:10.1007/s11661-013-2025-z

Hales, R., 1994. The Role of Cavity Growth Mechanisms in Determining Creep-Rupture Under Multiaxial Stresses. Fatigue & Fracture of Engineering Materials & Structures 17, 579–591. doi:10.1111/j.1460-2695.1994.tb00257.x

Haney, E.M., Dalle, F., Sauzay, M., Vincent, L., Tournié, I., Allais, L., Fournier, B., 2009. Macroscopic results of long-term creep on a modified 9Cr–1Mo steel (T91). Materials Science and Engineering: A, 11th International Conference of Creep and Fracture of

Engineering Materials and Structures, CREEP 2008 510–511, 99–103. doi:10.1016/j.msea.2008.04.099

Hättestrand, M., Andrén, H.-O., 2001. Influence of strain on precipitation reactions during creep of an advanced 9% chromium steel. Acta Materialia 49, 2123–2128. doi:10.1016/S1359-6454(01)00135-5

Hobbs, C., Echivarre, M., Jania, C., Whitson, S., 2015. Creep performance and microstructural characterization of the Type IV Region in Grade 91 Steel Weldments (MSE 489 Senior Capstone Design: Final Report). University of Tennessee, Knoxville, TN.

Hoskins, W.C., Bohling, J.W., Lundin, C.D., Prager, M., 2017. Grade 91 Cross-Weld Creep Specimens from the Equity Engineering Group: A Summary of Activities and Experimental Results (Unpublished technical report), Materials Joining Group Reports. University of Tennessee, Knoxville, TN.

Jabar, S., Siefert, J.A., Strangwood, M., West, G.D., 2021. The Effect of Micro-Segregation on the Quantification of Microstructural Parameters in Grade 91 Steel. Metall Mater Trans A 52, 426–437. doi:10.1007/s11661-020-06062-y

Jaffee, R.I., 1979. Metallurgical problems and opportunities in coal-fired steam power plants. Metallurgical Transactions A 10, 139–164.

Kassner, M.E., Hayes, T.A., 2003. Creep cavitation in metals. International Journal of Plasticity 19, 1715–1748. doi:10.1016/S0749-6419(02)00111-0

Kimmins, S.T., Coleman, M.C., Smith, D.J., 1993. An overview of creep failure associated with heat affected zones of ferritic weldments, in: Creep and Fracture of Engineering Materials and Structures: Proceedings of the Fifth International Conference Held at University College, Swansea. Swansea, United Kingdom, pp. 681–694.

Kimmins, S.T., Smith, D.J., 1998. On the relaxation of interface stresses during creep of ferritic steel weldments. The Journal of Strain Analysis for Engineering Design 33, 195–206. doi:10.1243/0309324981512913

Kimura, K., Kushima, H., Sawada, K., 2009. Long-term creep deformation property of modified 9Cr–1Mo steel. Materials Science and Engineering: A, 11th International Conference of Creep and Fracture of Engineering Materials and Structures, CREEP 2008 510–511, 58–63. doi:10.1016/j.msea.2008.04.095

Kimura, K., Yaguchi, M., 2020. Evaluation of Stress Rupture Factors for Grade 91 Weldments. Journal of Pressure Vessel Technology 142. doi:10.1115/1.4046431

Komai, N., Tokiyoshi, T., Igari, T., Ohyama, H., Masuyama, F., Kimura, K., 2016. Experimental observation of creep damage evolution in seam-welded elbows of mod. 9Cr-1Mo steel. Materials at High Temperatures 33, 617–625. doi:10.1080/09603409.2016.1204063

Kostka, A., Tak, K.-G., Hellmig, R.J., Estrin, Y., Eggeler, G., 2007. On the contribution of carbides and micrograin boundaries to the creep strength of tempered martensite ferritic steels. Acta Materialia 55, 539–550. doi:10.1016/j.actamat.2006.08.046

Krauss, G., Marder, A.R., 1971. The morphology of martensite in iron alloys. Metallurgical Transaction 2, 2343. doi:10.1007/BF02814873

Kussmaul, K., Maile, K., Eckert, W., 1993. Influence of Stress State and Specimen Size on Creep Rupture of Similar and Dissimilar Welds, in: Hackett, E., Schwalbe, K.-H., Dodds, R. (Eds.), Constraint Effects in Fracture. ASTM International, 100 Barr Harbor Drive, PO Box C700, West Conshohocken, PA 19428-2959, pp. 341-341-20. doi:10.1520/STP18036S

Li, D., Shinozaki, K., Kuroki, H., Harada, H., Ohishi, K., 2003. Analysis of factors affecting type IV cracking in welded joints of high chromium ferritic heat resistant steels. Science and Technology of Welding and Joining 8, 296–302. doi:10.1179/136217103225005453

Life Management of 9%Cr Steels: Evaluation of Metallurgical Risk Factors in Grade 91 Steel Parent Material (No. 3002009678), 2018. Electric Power Research Institute (EPRI), Palo Alto, CA.

Liu, Z.-K., Höglund, L., Jönsson, B., ågren, J., 1991. An experimental and theoretical study of cementite dissolution in an Fe-Cr-C alloy. Metall Mater Trans A 22, 1745–1752. doi:10.1007/BF02646498

Lundin, C.D., Liu, P., 1999. Stress Rupture Behavior of Modifed 9Cr-1Mo (P91) Weldments in the Sub-Critically PWHT and N&T Condition (Unpublished technical report No. 98-24), PVRC Project Report. University of Tennessee.

Lundin, C.D., Zhou, G., Morrison, M., Prager, M., Sullivan, D., 1999. High Energy Piping: Compendium of Optical and Cryo-Crack Creep Damage Assessment. Materials Properties Council (MPC).

Lundin, C.D., Zhou, G., Prager, M., 1998. Cryo-Cracking: a technique for creep damage assessment in high temperature components. Materials at High Temperatures 15, 167–173. doi:10.1080/09603409.1998.11689596

Maki, T., 2012. Morphology and substructure of martensite in steels, in: Pereloma, E., Edmonds, D.V. (Eds.), Phase Transformations in Steels: Diffusionless Transformations, High Strength Steels, Modelling and Advanced Analytical Techniques. Elsevier Science & Technology, Cambridge, UNITED KINGDOM, pp. 34–58.

Manjoine, M.J., 1982. Creep-Rupture Behavior of Weldments. Welding Journal 61(2), 50s-57s.

Maruyama, K., Nakamura, J., Sekido, N., Yoshimi, K., 2017. Causes of heat-to-heat variation of creep strength in grade 91 steel. Materials Science and Engineering: A 696, 104–112. doi:10.1016/j.msea.2017.04.050

Maruyama, K., Nakamura, J., Yoshimi, K., 2016. Assessment of Long-Term Creep Rupture Strength of T91 Steel by Multiregion Rupture Data Analysis. Journal of Pressure Vessel Technology 138. doi:10.1115/1.4032647

Maruyama, K., Sawada, K., Koike, J., 2001. Strengthening Mechanisms of Creep Resistant Tempered Martensitic Steel. ISIJ International 41, 641–653. doi:10.2355/isijinternational.41.641

Maruyama, K., Sekido, N., Yoshimi, K., Yamamoto, Y., 2020. A Grain Size-Dependent Equation for Creep Rupture Life of Grade 91 Steel Verified Up To 233,000 Hours. Journal of Pressure Vessel Technology 142. doi:10.1115/1.4047442

Masuyama, F., 2010. Effect of specimen size and shape on creep rupture behavior of creep strength enhanced ferritic steel welds. International Journal of Pressure Vessels and Piping, International Conference WELDS 2009 87, 617–623. doi:10.1016/j.ijpvp.2010.08.006

Masuyama, F., Nishimura, N., Ozaki, M., 2004. Creep Properties of Gr. 91 Castings and Forgings With High Residual Elements, in: ASME/JSME 2004 Pressure Vessels and Piping Conference. American Society of Mechanical Engineers, pp. 19–26.

Materials Joining Group, 2014. Metallographic Examination of Creep Damage in High Energy Hot Reheat Piping (Unpublished technical report), MPC HEP Program Reports. University of Tennessee.

Mayr, P., Cerjak, H., 2008. The heat affected zone of boron alloyed creep resistant 9% chromium steels and their susceptibility to type IV cracking, in: Advances in Materials Technology for Fossil Power Plants - 5th International Conference, October 13, 2007 - October 15, 2007, Advances in Materials Technology for Fossil Power Plants - Proceedings from the 5th International Conference. ASM International, pp. 914–926.

Messner, M.C., Nassif, O., Ma, R., Truster, T.J., Cochran, K., Parks, D., Sham, T.-L., 2019. Combined crystal plasticity and grain boundary modeling of creep in ferritic-martensitic steels: II. The effect of stress and temperature on engineering and microstructural properties. Modelling Simul. Mater. Sci. Eng. 27, 075010. doi:10.1088/1361-651X/ab359f

Morito, S., Yoshida, H., Maki, T., Huang, X., 2006. Effect of block size on the strength of lath martensite in low carbon steels. Materials Science and Engineering: A, Proceedings of the International Conference on Martensitic Transformations 438-440, 237–240. doi:10.1016/j.msea.2005.12.048

Nassif, O., Truster, T.J., Ma, R., Cochran, K.B., Parks, D.M., Messner, M.C., Sham, T.-L., 2019. Combined crystal plasticity and grain boundary modeling of creep in ferritic-martensitic steels: I. Theory and implementation. Modelling Simul. Mater. Sci. Eng. 27, 075009. doi:10.1088/1361-651X/ab359c

Niu, T.-Y., Zhao, P., Zhu, G., Gong, J.-G., Xuan, F.-Z., 2021. Stress state dependent creep damage behavior of 9–12% Cr steel notched components. Materials Science and Engineering: A 804, 140762. doi:10.1016/j.msea.2021.140762

Panait, C., Zielinska-Lipiec, A., Koziel, T., Czyrska-Filemonowicz, A., Gourgues-Lorenzon, A.-F., Bendick, W., 2009. Evolution of dislocation density, size of subgrains and MX-type precipitates in a P91 steel during creep and during thermal ageing at 600 °C for more than 100,000 h. Materials Science and Engineering: A 527, 4062–4069. doi:10.1016/j.msea.2010.03.010

Panait, C.G., Bendick, W., Fuchsmann, A., Gourgues-Lorenzon, A.-F., Besson, J., 2010. Study of the microstructure of the Grade 91 steel after more than 100,000 h of creep exposure at 600 °C. International Journal of Pressure Vessels and Piping, ECCC Second International Creep Conference 87, 326–335. doi:10.1016/j.ijpvp.2010.03.017

Parker, J., 2014. Creep Cavitation in CSEF Steels, in: Advances in Materials Technology for Fossil Power Plants - Proceedings from the Seventh International Conference. Presented at the Advances in Materials Technology for Fossil Power Plants, ASM International, Waikoloa, Hawaii, USA, p. 20.

Parker, J., 2017. Creep ductility considerations for high energy components manufactured from creep strength enhanced steels. Materials at High Temperatures 34, 109–120. doi:10.1080/09603409.2016.1270720

Peŝiĉka, J., Dronhofer, A., Eggeler, G., 2004. Free dislocations and boundary dislocations in tempered martensite ferritic steels. Materials Science and Engineering: A, 13th International Conference on the Strength of Materials 387-389, 176–180. doi:10.1016/j.msea.2004.03.080

Pešička, J., Kužel, R., Dronhofer, A., Eggeler, G., 2003. The evolution of dislocation density during heat treatment and creep of tempered martensite ferritic steels. Acta Materialia 51, 4847–4862. doi:10.1016/S1359-6454(03)00324-0

Prager, M., 2000. The Omega Method–An Engineering Approach to Life Assessment. Journal of Pressure Vessel Technology 122, 273–280. doi:10.1115/1.556184

Raj, R., 1978. Nucleation of cavities at second phase particles in grain boundaries. Acta Metallurgica 26, 995–1006. doi:10.1016/0001-6160(78)90050-0

Riedel, H., 1987. Fracture at high temperatures. Springer, Berlin/Heidelberg.

Robson, J.D., Bhadeshia, H.K.D.H., 1996. Kinetics of precipitation in power plant steels. Calphad 20, 447–460. doi:10.1016/S0364-5916(97)00007-2

Sawada, K., Kimura, K., Tabuchi, M., 2013. Effect of Stress State on Microstructural Change During Creep in Grade 92 Steel Welded Joint, in: Advances in Materials Technology for Fossil Power Plants - Proceedings from the Seventh International Conference (October 22-25, 2013 Waikoloa, Hawaii, USA). ASM International, Waikoloa, Hawaii, USA, pp. 607–614.

Sawada, K., Kubo, K., Abe, F., 2003a. Contribution of coarsening of MX carbonitrides to creep strength degradation in high chromium ferritic steel. Materials Science and Technology 19, 732–738. doi:10.1179/026708303225010687

Sawada, K., Kushima, H., Hara, T., Tabuchi, M., Kimura, K., 2014. Heat-to-heat variation of creep strength and long-term stability of microstructure in Grade 91 steels. Materials Science and Engineering: A 597, 164–170. doi:10.1016/j.msea.2013.12.088

Sawada, K., Kushima, H., Tabuchi, M., Kimura, K., 2011. Microstructural degradation of Gr.91 steel during creep under low stress. Materials Science and Engineering: A 528, 5511–5518. doi:10.1016/j.msea.2011.03.073

Sawada, K., Suzuki, K., Kushima, H., Tabuchi, M., Kimura, K., 2008. Effect of tempering temperature on Z-phase formation and creep strength in 9Cr–1Mo–V–Nb–N steel. Materials Science and Engineering: A 480, 558–563. doi:10.1016/j.msea.2007.09.031

Sawada, K., Taneike, M., Kimura, K., Abe, F., 2003b. In situ observation of recovery of lath structure in 9% chromium creep resistant steel. Materials Science and Technology 19, 739–742. doi:10.1179/026708303225010696

Schüller, H.J., Hagn, L., Woitscheck, A., 1974. Risse im Schweißnahtbereich von Formstucken aus Heißdampfleitungen - Werkstoffuntersuchungen [Cracks in the weld region of fittings from superheated steam pipes - Material tests]. Der Maschinen Schaden 47, 1–13.

Section I: Rules of Construction for Power Boilers, 2019., 2019 ASME Boiler & Pressure Vessel Code. The American Society of Mechanical Engineers, New York, NY.

Service Experience with Grade 91 Components (No. EPRI Report 1018151), 2009. Electric Power Research Institute (EPRI).

Shassere, B.A., Yamamoto, Y., Babu, S.S., 2016. Toward Improving the Type IV Cracking Resistance in Cr-Mo Steel Weld Through Thermo-Mechanical Processing. Metallurgical and Materials Transactions A 47, 2188–2200. doi:10.1007/s11661-016-3387-9

Siefert, J.A., Parker, J.D., 2016. Evaluation of the creep cavitation behavior in Grade 91 steels. International Journal of Pressure Vessels and Piping 138, 31–44. doi:10.1016/j.ijpvp.2016.02.018

Siefert, J.A., Parker, J.D., Thomson, R., 2019. Cross-Weld Creep Performance in Grade 91 Steel: Macro-Based Assessment. Welding Journal 98, 63–77. doi:10.29391/2019.98.005

Siefert, J.A., Thomson, R.C., Parker, J.D., 2018. Microstructure Features Contributing to Heat Affected Zone Damage in Grade 91 Steel Feature Type Cross-Weld Tests, in: ASME 2018 Symposium on Elevated Temperature Application of Materials for Fossil, Nuclear, and Petrochemical Industries. Presented at the ASME 2018 Symposium on Elevated Temperature Application of Materials for Fossil, Nuclear, and Petrochemical Industries, American Society of Mechanical Engineers, Seattle, Washington, USA. doi:10.1115/ETAM2018-6709

Standard Test Methods for Determining Average Grain Size (ASTM Standard No. E112-13), 2013. ASTM International, West Conshohocken, PA.

Stevick, G.R., 1994. Failure of Welds at Elevated Temperatures (Welding Research Council Bulletin No. Bulletin 390). Welding Research Council.

Tabuchi, M., Takahashi, Y., 2012. Evaluation of Creep Strength Reduction Factors for Welded Joints of Modified 9Cr-1Mo Steel. J. Pressure Vessel Technol 134, 031401-031401-6. doi:10.1115/1.4006131

Taneike, M., Sawada, K., Abe, F., 2004. Effect of carbon concentration on precipitation behavior of M23C6 carbides and MX carbonitrides in martensitic 9Cr steel during heat treatment. Metall and Mat Trans A 35, 1255–1262. doi:10.1007/s11661-004-0299-x

The Benefits of Improved Control of Composition of Creep-Strength-Enhanced Ferritic Steel Grade 91 (No. EPRI Report 3002003472), 2014., Program 87 Materials and Repair. Electric Power Research Institute (EPRI), Palo Alto, CA.

Vander Voort, G., 1999. Metallography: principles and practice. ASM International, Materials Park, OH, USA.

Viswanathan, R., Stringer, J., 2000. Failure Mechanisms of High Temperature Components in Power Plants. J. Eng. Mater. Technol 122, 246–255. doi:10.1115/1.482794

Vitek, J.M., Klueh, R.L., 1983. Precipitation reactions during the heat treatment of ferritic steels. MTA 14, 1047–1055. doi:10.1007/BF02670443

Wang, C., Liu, X., Gui, J., Du, Z., Xu, Z., Guo, B., 2020. Effect of MnS inclusions on plastic deformation and fracture behavior of the steel matrix at high temperature. Vacuum 174, 109209. doi:10.1016/j.vacuum.2020.109209

Wang, L., 2010. Development of Predictive Formulae for the A_1 Temperature in Creep Strength Enhanced Ferritic Steels (Master of Science). The Ohio State University, Columbus, OH.

Wang, X., Wang, X., Wang, C., Zhang, Y.-L., Huang, Q.-S., 2020. Effect of multiaxial stress state on creep damage in ASME T92 welded joint. Fatigue & Fracture of Engineering Materials & Structures 43, 907–918. doi:https://doi.org/10.1111/ffe.13160

Wang, Y., Kannan, R., Li, L., 2016. Characterization of as-welded microstructure of heat-affected zone in modified 9Cr–1Mo–V–Nb steel weldment. Materials Characterization 118, 225–234. doi:10.1016/j.matchar.2016.05.024

Wang, Y., Kannan, R., Li, L., 2018. Correlation Between Intercritical Heat-Affected Zone and Type IV Creep Damage Zone in Grade 91 Steel. Metallurgical and Materials Transactions A 49, 1264–1275. doi:10.1007/s11661-018-4490-x

Wang, Y., Kannan, R., Li, L., 2020. Insight into Type IV cracking in Grade 91 steel weldments. Materials & Design 190, 108570. doi:10.1016/j.matdes.2020.108570

Wang, Y., Kannan, R., Zhang, L., Li, L., 2017. Microstructural Analysis of the As-Welded Heat-Affected Zone of a Grade 91 Steel Heavy Section Weldment. Welding Journal 203s–219s.

Wang, Y., Li, L., 2016. Microstructure evolution of fine-grained heat-affected zone in type IV failure of P91 welds. Welding Journal 95, 27s–36s.

Wang, Y., Li, L., Kannan, R., 2018b. Transition from Type IV to Type I cracking in heat-treated grade 91 steel weldments. Materials Science and Engineering: A 714, 1–13. doi:10.1016/j.msea.2017.12.088

Wang, Y., Zhang, W., Wang, Y., Feng, Z., 2021a. Characteristics of premature creep failure in over-tempered base metal of grade 91 steel weldment. International Journal of Pressure Vessels and Piping 192, 104396. doi:10.1016/j.ijpvp.2021.104396

Wang, Y., Zhang, W., Wang, Y., Lim, Y.C., Yu, X., Feng, Z., 2021b. Experimental evaluation of localized creep deformation in Grade 91 steel weldments. Materials Science and Engineering: A 799, 140356. doi:10.1016/j.msea.2020.140356

Watanabe, T., Tabuchi, M., Yamazaki, M., Hongo, H., Tanabe, T., 2006. Creep damage evaluation of 9Cr–1Mo–V–Nb steel welded joints showing Type IV fracture. International Journal of Pressure Vessels and Piping 83, 63–71. doi:10.1016/j.ijpvp.2005.09.004

Wey, M.Y., Sakuma, T., Nishizawa, T., 1981. Growth of Alloy Carbide Particles in Austenite. Transactions of the Japan Institute of Metals 22, 733–742. doi:10.2320/matertrans1960.22.733

Wilshire, B., Scharning, P.J., 2008. A new methodology for analysis of creep and creep fracture data for 9–12% chromium steels. International Materials Reviews 53, 91–104. doi:10.1179/174328008X254349

Xu, X., West, G.D., Siefert, J.A., Parker, J.D., Thomson, R.C., 2017. The Influence of Thermal Cycles on the Microstructure of Grade 92 Steel. Metall and Mat Trans A 48, 5396–5414. doi:10.1007/s11661-017-4306-4

Yaguchi, M., Ogata, T., Sakai, T., 2010. Creep strength of high chromium steels welded parts under multiaxial stress conditions. International Journal of Pressure Vessels and Piping, ECCC Second International Creep Conference 87, 357–364. doi:10.1016/j.ijpvp.2010.03.018

Yamamoto, Y., Santella, M.L., Yu, X., Babu, S.S., 2014. Effect of non-standard heat treatments on creep performance of creep-strength enhanced ferritic (CSEF) steel weldments, in: 7th International Conference on Advances in Materials Technology for Fossil Power Plants, October 22, 2013 - October 25, 2013, Advances in Materials Technology for Fossil Power Plants - Proceedings from the 7th International Conference. ASM International, pp. 1016–1024.

Yu, X., Babu, S.S., Terasaki, H., Komizo, Y., Yamamoto, Y., Santella, M.L., 2013. Correlation of precipitate stability to increased creep resistance of Cr–Mo steel welds. Acta Materialia 61, 2194–2206. doi:10.1016/j.actamat.2012.12.040

Yu, X., Feng, Z., Yamamoto, Y., 2014. In-Situ Full Field Creep Deformation Study of Creep Resistant Materials Welds. p. 9.

Zhang, W., Wang, X., Wang, Y., Yu, X., Gao, Y., Feng, Z., 2020. Type IV failure in weldment of creep resistant ferritic alloys: I. Micromechanical origin of creep strain localization in the heat affected zone. Journal of the Mechanics and Physics of Solids 134, 103774. doi:10.1016/j.jmps.2019.103774

Zhang, W., Wang, X., Wang, Y., Yu, X., Gao, Y., Feng, Z., 2020a. Type IV failure in weldment of creep resistant ferritic alloys: II. Creep fracture and lifetime prediction. Journal of the Mechanics and Physics of Solids 134, 103775. doi:10.1016/j.jmps.2019.103775

Zhao, L., Vermolen, F.J., Sietsma, J., Wauthier, A., 2006. Cementite dissolution at 860 °C in an Fe-Cr-C steel. Metall and Mat Trans A 37, 1841–1850. doi:10.1007/s11661-006-0127-6

Zhou, G., 1997. Metallurgical Causes for the Occurrence of Creep Damage in Longitudinally Seam-Welded Cr-Mo High Energy Piping (PhD dissertation). University of Tennessee, Knoxville, TN.

Vita

John Bohling was born in California to his parents, Mark and Sandra Bohling. He entered undergraduate studies at the University of Tennessee in 2006. He graduated with a B.S. in Materials Science and Engineering in 2010 and then began graduate studies at the University of Tennessee with the late Dr. Carl Lundin, professor of welding metallurgy until his retirement in 2020. John obtained his Master of Science degree in Materials Science and Engineering in 2016; his work focused on weldability investigations of heat-resistant austenitic stainless steel castings. He subsequently continued with doctoral studies focusing on creep damage in power plant steels. He defended his dissertation and obtained a PhD in Materials Science and Engineering in August 2021.